Exploring the Nature of Dark Energy with Modified Gravity and Machine Learning

Memoria de la Tesis Doctoral realizada por

Rubén Arjona Fernández

presentada ante el Departamento de Física Teórica
de la Universidad Autónoma de Madrid
para optar al Título de Doctor en Física Teórica

Tesis Doctoral dirigida por el **Prof. Savvas Nesseris**[1]

[1]Científico Titular del Instituto de Física Teórica UAM/CSIC

Departamento de Física Teórica
Universidad Autónoma de Madrid

Instituto de Física Teórica
UAM/CSIC

Madrid, Septiembre de 2021

A mi padre, físico teórico en ciernes.

Neither a lofty degree of intelligence nor imagination nor both together go to the making of genius. Love, love, love, that is the soul of genius.
Wolfgang Amadeus Mozart

Acknowledgments

Some time ago, I read in a newspaper a survey about the three main qualities a PhD student looks for in a supervisor, and they are: first, that they care and show love for them, second, that they have plenty of knowledge and third, that they are good at organizing. My supervisor Dr. Savvas Nesseris has all of those three virtues in abundance. How much I owe him for his selfless generosity and awareness, his intellect and good sense of humor. He has pushed me to get the best out of me by suggesting me to write my own articles and codes and collaborate with as many people as possible. I have found in him not only a mentor but also a friend.

Art is long and life is short. There is much to be thankful for in an adventure as exciting as that of a doctorate in Theoretical Physics. Thanks to Universidad Autónoma de Madrid expressing itself principally through Dr. Savvas Nesseris, I have been permitted to do what I like, and since I loved it, it was right to do it. Because I profoundly believe, as the poet Arthur H. King said, that "if you love, you may do what you like, because if you truly love, then what you like cannot fail to be right".

To Oscar Varela, for accepting to be my tutor even though he did not know me at all.

To Alessandro Melchiori, who accepted me to do a stay as part of my PhD for three months at La Sapienza even amidst these difficult times, and for his great intuition and sense of humor.

To wonderful researchers I have come in contact with during these years, Juan García-Bellido, Matteo Martinelli, Santiago Ávila, Guillermo Ballesteros, Daniel Figueroa and Pierre Fleury, for the things they have taught me.

To my CMB collaborators from Cantabria Enrique Martínez-González and Airam Marcos-Caballero, for all their support.

To my colleagues in Cosmology at the IFT, Llorent, Walter and Victor for their friendship and interesting conversations on Physics.

To my other friends at the IFT, Joan, Jorge, Jose and Francisco for the funny moments spent during lunch.

To the very good professors I had at Universidad Complutense de Madrid when I was a graduate student, Antonio L. Maroto, Gabriel A. Galindo, Artemio González, Federico Finkel, Antonio Dobado, Luis J. Garay, Felipe J. Llanes, José A. Ruiz Cembranos, Ignazio Scimemi, Francisco Domínguez-Adame, Enrique A. Maciá, which have influenced and inspired me.

To my close friends with whom I started my degree in physics, Daniel, Andrea, Rodrigo, Diego, Juan Carlos and Adrián, with whom I have shared so good moments.

To my dear wife Francesca, my soul mate who has given all so that I could become my very best. If I have arrived to this point in my life is because of her constant support and gentle care for me. I owe her everything. To my sons Gabriel and Emma, born while I was a PhD candidate and who have endured my absences, my long nights and weekends of intense work. Their affection more than compensates for all the efforts I have taken. Everything for them.

To my father, for being a pillar to me and the perfect example of love, dedication and wisdom. Who when I was about 11 years old started sharing with me books of Richard Feynman, Roger Penrose and Stephen Hawking. For the many hours we have spent discussing on Physics and the meaning of life. To my angelical mother who has always given me the best of advises and has invariably believed in me.

To my brothers Samuel, Daniel y David for all the funny moments we have each time we are together.

To my dear Italian family Arcangelo, Patrizia, Sara, Lidia and Lorenzo. For all their kindness and support.

To Arcangelo Distante, the father of Francesca, who has proven that he can show to a theoretical physicist how to do manual things and who had the belief that one day I would be "kidnapped" because I know physics.

To my grandparents, who have given me great support even though they hardly can understand what is my research about.

To my special friend José Abraham, for the many hours we have spent discussing about science.

To Guillermo Montero, the best high school teacher I could ever have and who initiated me in the wonders of Physics.

Finally, I acknowledge the use of the Hydra cluster at the Instituto de Física Teórica (IFT), on which some of the numerical computations for this thesis took place and acknowledge use of the codes: `RGTC`, `CLASS`, `MontePython 3` and the `HYREC-2` recombination module `Hyrec2020`. I also acknowledge support from Universidad Autónoma de Madrid for my Teaching Assistantship, the Research Project PGC2018-094773-B-C32 and the Centro de Excelencia Severo Ochoa Program SEV-2016-0597.

Madrid, September 2021

The scientist does not study nature for the usefulness that it may bring him;
He studies it for the joy it brings him, and this joy is due to the beauty in it.
Henri Poincaré

Statement

This dissertation is organized in three main parts: Foundations, Modified Gravity Theories and Machine Learning. The results presented on Chapters 4-8 and Chapters 11-18, and a few more papers that are under way, are based on original work done in collaboration with researchers from Madrid, Cantabria, Italy, Colombia, Korea and China during the course of my PhD, from October 2018 to June 2021. The references on the publications on which the above Chapters mentioned are based are listed below for convenience. The first part, Foundations, is composed of Chapters 1-2 where an overview of the standard model of Cosmology and the cosmological observations used in the analysis is presented. At the beginning of the second part, Modified Gravity Theories, there is Chapter 3 where it is displayed a motivation as to why one should explore theories beyond General Relativity. Chapters 4-8 are built on original work where the main theme is Modified Gravity. The third part, Machine Learning, starts with Chapter 9 where the use of Machine Learning (ML) in Cosmology is motivated, and on Chapter 10 there is a description on a particular ML technique used throughout this thesis known as the Genetic Algorithms. Then Chapters 11-18 are based on original work where the main topic is related to Machine Learning applied to cosmological observations. On Chapter 19 we summarize the conclusions. Finally, Appendices A and B describe some useful equations and tools necessary for the analysis of Chapters 4 and 5 while Appendix C shows a new publicly available growth rate likelihood for MontePython used on Chapters 6 and 7.

There are six more projects which are in a mature stage but they are not included in this thesis to not exceed the page limit and because they have not been published yet. These projects have the following topics: A novel null test with growth rate data and machine learning reconstructions, violations of the cosmic distance duality in non-linear electrodynamics and models with non-minimal couplings to gravity, the redshift drift of the BAO scale, a comparative analysis of Gaussian Processes and Genetic Algorithms with null tests of ΛCDM , the effect of lensing convergence and anisotropic dark energy in galaxy redshift surveys and a rigorous mathematical definition of the subhorizon and the quasi static approximation for modified gravity theories. Finally, the Genetic Algorithm and `EFCLASS` code were built on its own by the author of this thesis and used in several papers as it would be explained later. They are publicly available and can be found at the GitHub repository https://github.com/RubenArjona and at the website https://rubenarjoname.wixsite.com/mysite.

Rubén Arjona Fernández
Madrid, September 2021

1. **"Machine Learning improved fits of the sound horizon at the baryon drag epoch"**
   A. Aizpuru, **R. Arjona** and S. Nesseris,
   arXiv:2106.00428 [astro-ph.CO] HEP entry

2. **"A complementary consistency test of the Copernican principle via Noether's Theorem and machine learning forecasts"**
R. Arjona and S. Nesseris,
arXiv:2105.09049 [astro-ph.CO] HEP entry

3. **"Novel null tests for the spatial curvature and homogeneity of the Universe and their machine learning reconstructions"**
R. Arjona and S. Nesseris,
arXiv:2103.06789 [astro-ph.CO]
Phys. Rev. D 103, 103539 (2021) HEP entry

4. **"Machine Learning and cosmographic reconstructions of quintessence and the Swampland conjectures"**
R. Arjona and S. Nesseris,
arXiv:2012.12202 [astro-ph.CO]
Phys. Rev. D 103, 063537 (2021) HEP entry

5. **"Cosmological constraints with the Effective Fluid approach for Modified Gravity"**
W. Cardona, **R. Arjona**, A. Estrada and S. Nesseris,
JCAP 05 (2021) 064 arXiv:2012.05282 [astro-ph.CO] HEP entry

6. **"Machine Learning forecasts of the cosmic distance duality relation with strongly lensed gravitational wave events"**
R. Arjona, Hai-Nan Lin, S. Nesseris and Li Tang,
Phys. Rev. D 103, 103513 (2021) arXiv:2011.02718 [astro-ph.CO] HEP entry

7. **"Cosmological constraints on non-adiabatic dark energy perturbations"**
R. Arjona, J. García-Bellido and S. Nesseris,
arXiv:2006.01762 [astro-ph.CO]
Phys. Rev. D 102 (2020) 10, 103526 HEP entry

8. **"Machine Learning meets the redshift evolution of the CMB Temperature"**
R. Arjona,
arXiv:2002.12700 [astro-ph.CO]
JCAP 08 (2020) 009 HEP entry

9. **"Hints of dark energy anisotropic stress using Machine Learning"**
R. Arjona and S. Nesseris,
arXiv:2001.11420 [astro-ph.CO]
JCAP 11 (2020) 042 HEP entry

10. **"What can Machine Learning tell us about the background expansion of the Universe?"**
R. Arjona and S. Nesseris,
arXiv:1910.01529 [astro-ph.CO]
Phys. Rev. D 101 (2020) 12, 123525 HEP entry

11. **"Lensing convergence and anisotropic dark energy in galaxy redshift surveys"**
    W. Cardona, **R. Arjona** and S. Nesseris,
    arXiv:1907.10130 [astro-ph.CO] HEP entry

12. **"Analytic expressions for the background evolution of massive neutrinos and dark matter particles"**
    R. Arjona, W.Cardona and S.Nesseris,
    arXiv:1906.03160 [astro-ph.CO]
    JCAP 10 (2019) 060 HEP entry

13. **"Designing Horndeski and the effective fluid approach"**
    R. Arjona, W.Cardona and S.Nesseris,
    arXiv:1904.06294 [astro-ph.CO]
    Phys. Rev. D 100 (2019) 6, 063526 HEP entry

14. **"Unraveling the effective fluid approach for f(R) models in the subhorizon approximation"**
    R. Arjona, W.Cardona and S.Nesseris,
    arXiv:1811.02469 [astro-ph.CO]
    Phys. Rev. D 99 (2019) 4, 043516 HEP entry

Conference Proceedings

1. **"The effective fluid approach for modified gravity"**
    R. Arjona,
    arXiv:2010.04764 [astro-ph.CO] HEP entry
    Contribution to the 2nd Hermann Minkowski Meeting on the Foundations of Spacetime Physics, Albena, Bulgaria, 13-16 May 2019

It is not knowledge, but the act of learning,
not possession but the act of getting there,
which grants the greatest enjoyment.
Carl Friedrich Gauss

Abstract

As a branch of physical sciences, the field of Cosmology is rather peculiar; contrary to condensed-matter physics, quantum chemistry, or particle physics, Cosmology does not allow us to build controlled experiments on the object under study. We can only see what the Universe allows us to see, and attempt to correctly interpret its messages.

The detection of the accelerating expansion of the Universe lays out the most profound puzzle in contemporary physics. It insinuates that either the Universe is dominated by a component, dubbed Dark Energy (DE) that turns the pull of gravity into a repulsive force, or that General Relativity (GR), our currently best description of gravity breaks down at cosmological scales. Either way, it strongly challenges our knowledge of the basic laws of nature. Characterizing and understanding the origin and nature of the accelerated expansion is a truly broad and interdisciplinary venture.

Currently, the standard cosmological constant Λ cold dark matter model (ΛCDM) is our best phenomenological description of the data [1, 2]. However, since the first detection of DE, several alternatives to the ΛCDM model have also been developed, which roughly fall under the umbrella of two main categories. First, there are the so-called Modified Gravity (MG) models [3], which assume that GR is covariantly modified on large scales, the so-called Infrared (IR) modifications, in order to accommodate current observations [4]. These are well-motivated by high energy physics (Quantum Gravity and String Theory) and have diverse features from GR, e.g. a Newton's constant that can depend on time and scale, a different evolution of the matter density perturbations or distinct patterns in the emission of gravitational waves. The second category of theories that are serious contenders to ΛCDM are DE models with as yet unobserved scalar fields that dominate over the other matter species at late times which provide the pressure conditions to accelerate the Universe [5]. These DE models also exhibit perturbations, which will affect the large scale structure (LSS) of the Universe. As a result, in order to constrain the cosmological parameters to a percent level and discriminate between the various theories, DE perturbations should be well understood as they are expected to play an important role in the near future [6].

In this regard we could say that the purpose of this thesis resembles that of the Gordian Knot legend. There seems to be an intractable problem (untying an impossibly tangled knot or in this case unveiling the nature of DE) thus to solve the mystery different approaches and ways of thinking are needed. In this thesis the origin of DE in the form of MG theories is explored directly through the cosmological observations by applying Machine Learning (ML) algorithms which can remove biases due to a priori chosen models. Although the idea of cutting the Gordian Knot (following the analogy) has no yet been realised, we have made important progress in both directions.

In view of the plethora of DE and MG models, there has been an effort to provide a unified framework which encloses several of them like the Effective Field Theory (EFT) approach [7, 8] or the Effective Fluid approach (EFA) [9–11]. In this dissertation we have

focused on the latter which has the advantage that only a handful of variables are needed to compute, i.e. an equation of state $w(a)$, a pressure perturbation $\delta P(k,a)$, and an anisotropic stress $\sigma(k,a)$. In particular it will be shown that with simple modifications to the latest Cosmic Linear Anisotropy Solving System (`CLASS`) code, which we called `EFCLASS`, we provide competitive results in a much simpler and less error-prone approach in including the effects of modified gravity models.

A viable alternative that has been also explored in the quest to probe the nature of DE is more related to observations and statistics, which is the use of Machine Learning algorithms to perform model independent reconstruction of both the background expansion of the Universe but also the perturbations of matter on large scales with methods such as the Genetic Algorithms (GA), which can be best described as a stochastic search approach. The originality of our analysis is that we use a totally agnostic and non-parametric approach based on Machine Learning to explore the nature of dark energy and reconstruct its properties in a model independent fashion, which is much broader than traditional statistical inference and model selection. Our approach thus demonstrates that synergies between theory and machine learning can provide a deeper understanding of gravitation at large scales and identify possible hints of new physics in the form of modifications of gravity. Given the plethora and complexity of data coming from upcoming surveys in the near future, this will indubitably be a very rewarding approach.

Outline

The layout of this thesis is divided in three main parts: Foundations, Modified Gravity Theories and Machine Learning.

The first part deals with some fundamental aspects of Cosmology. In Chapter 1 we present an overview of the Standard Cosmological Model (ΛCDM) which is at present the concordance scenario and explains with high accuracy almost all observations, even though there are some tensions. We also describe some basic equations related to cosmological perturbation theory needed for subsequent chapters on Sec. 1.2 and then we point out some tensions or discrepancies that are currently under discussion concerning the successful ΛCDM paradigm, see Sec. 1.3. Since we will be using a plethora of cosmological observations throughout this thesis, we have devoted Chapter 2 to describe in great detail the observational probes used, both at the background and at the perturbation level.

The second part is related to Modified Gravity and Dark Energy models. In Chapter 3 we provide some motivation as to why this path is worthwhile. Chapters 4-8 are based on original work. In Chapters 4 and 5 we describe a mechanism to encompass and study a plethora of Dark Energy (DE) and Modified Gravity (MG) theories under the same footing through an effective fluid approach. This method allows for the correct background expansion in the models, all without sacrificing the accuracy of the results. In a nutshell, the Effective Fluid Approach works by rewriting the field equations of the MG model as GR and a DE fluid with an equation of state $w(a)$, a pressure perturbation $\delta P(k,a)$ and an anisotropic stress $\sigma(k,a)$. Especially the latter is crucial as sometimes it is ignored in analyses of MG models [12], something which might bias the results. In specific we show how this method works for $f(R)$ and Horndeski's theory of gravity and show how it can be implemented straightforwardly in a Boltzmann code, which solves the linear evolution of cosmological perturbations. We find that our simple modifications to the vanilla code are accurate to the level of $\sim 0.1\%$ with respect to the more complicated `hi_CLASS` code, see

Fig. 5.5. Then in Chapter 6 we perform a rigorous cosmological analysis on MG models using a Markov Chain Monte Carlo analyses and our effective fluid approach. In Chapter 7 we explore the possibility that dark energy might have a nonadiabatic component and we examine how it would affect several key cosmological observables. Finally, in Chapter 8 we provide exact analytic expressions for the density, pressure, average number density and pseudo-pressure for massive neutrinos and generic dark matter particles, both fermions and bosons and we compare our analytic expressions with the numerical implementation in a Boltzmann code.

The final part is focused on Machine Learning (ML) applied to Cosmology which is attracting attention due to its many applications. In Chapter 9 we motivate the importance and need to use these techniques and in Chapter 10 we present the Genetic Algorithms, a particular ML method which specialize in unsupervised symbolic regression of data and which would be used in the subsequent chapters. Chapters 11-18 are based on original work. In essence, in Chapter 11 we explore what can ML tell us about the background expansion of the Universe by estimating the deceleration parameter $q(z)$, a measure of the acceleration of the Universe, and we make a $\sim 4.5\sigma$ model independent detection of the accelerated expansion, but we also place constraints on the transition redshift of the acceleration phase ($z_{\rm tr} = 0.662 \pm 0.027$). We also find a deviation from ΛCDM at high redshifts, albeit within the errors, hinting toward the recently alleged tension between the SnIa/quasar data and the cosmological constant ΛCDM model at high redshifts ($z \gtrsim 1.5$). In Chapter 12 we extend our ML reconstruction analysis by including also cosmological data at the perturbation level, where we apply the Genetic Algorithms to explore the nature of DE in a model independent fashion by reconstructing quantities such as the growth index of matter density perturbations $\gamma(z)$, the linear DE anisotropic stress $\eta_{\rm DE}(z)$ and the adiabatic sound speed $c^2_{\rm s,DE}(z)$ of DE perturbations. We find a $\sim 2\sigma$ deviation of the equation of state $w(z)$ from -1 at high redshifts, the adiabatic sound speed is negative at the $\sim 2.5\sigma$ level at $z = 0.1$ and a $\sim 2\sigma$ deviation of the anisotropic stress from unity at low redshifts and $\sim 4\sigma$ at high redshifts. Thus, we provide mild hints at possible deviations from the ΛCDM model through either the presence of an non-adiabatic component in the DE sound speed or the presence of DE anisotropic stress. In Chapter 13 we present a model independent and non-parametric reconstruction of the redshift evolution of the Cosmic Microwave Background (CMB) temperature to place constraints on the cosmic distance duality relation and a temporal varying fine structure constant and in Chapter 14 we also explore the duality parameter with strongly lensed gravitational wave events and ML forecasts. In Chapter 15 we present reconstructions of quintessence and the Swampland conjectures using both ML and cosmography. Chapters 16 and 17 deal with novel null tests for the spatial curvature and homogeneity of the Universe and the Copernican principle via Noether's Theorem respectively and their ML reconstructions. Finally, in Chapter 18 we present ML improved fits of the sound horizon at the baryon drag epoch and show that they can strongly bias the derived constraints on the cosmological parameters using baryonic acoustic oscillations (BAO) data.

Introducción

Como rama de las ciencias físicas, el campo de la cosmología es bastante peculiar; contrariamente a la física de la materia condensada, la química cuántica o la física de partículas, la cosmología no nos permite construir experimentos controlados en el objeto en estudio. Solo podemos ver lo que el Universo nos permite ver e intentar interpretar correctamente sus mensajes.

La detección de la expansión acelerada del Universo plantea el rompecabezas más profundo de la física contemporánea. Insinúa que el Universo está dominado por un componente, denominado Energía Oscura (DE) que convierte la atracción de la gravedad en una fuerza repulsiva, o que la Relatividad General (GR), nuestra mejor descripción actual de la gravedad, se descompone a escalas cosmológicas. De cualquier manera, desafía fuertemente nuestro conocimiento de las leyes básicas de la naturaleza. Caracterizar y comprender el origen y la naturaleza de la expansión acelerada es una empresa verdaderamente amplia e interdisciplinaria.

Actualmente, la constante cosmológica estándar Λ modelo de materia oscura fría (ΛCDM) es nuestra mejor descripción fenomenológica de los datos [1, 2]. Sin embargo, desde la primera detección de DE, también se han desarrollado varias alternativas al modelo ΛCDM, que aproximadamente caen bajo el paraguas de dos categorías principales. En primer lugar, están los llamados modelos de gravedad modificada (MG) [3], que asumen que GR se modifica covariantemente a gran escala, las llamadas modificaciones de infrarrojos (IR), para adaptarse a las observaciones actuales [4]. Estos están bien motivados por la física de altas energías (gravedad cuántica y teoría de cuerdas) y tienen diversas características de GR, por ejemplo, una constante de Newton que puede depender del tiempo y la escala, una evolución diferente de las perturbaciones de la densidad de la materia o patrones distintos en la emisión de ondas gravitacionales. La segunda categoría de teorías que son serios contendientes de ΛCDM son los modelos DE con campos escalares aún no observados que dominan sobre las otras especies de materia en tiempos tardíos que proporcionan las condiciones de presión para acelerar el Universo [5]. Estos modelos DE también exhiben perturbaciones, que afectarán la estructura a gran escala (LSS) del Universo.

Como resultado, para restringir los parámetros cosmológicos a un nivel porcentual y discriminar entre las diversas teorías, las perturbaciones DE deben entenderse bien, ya que se espera que jueguen un papel importante en el futuro cercano [6].

En este sentido podríamos decir que el propósito de esta tesis se asemeja al de la leyenda del nudo gordiano. Parece haber un problema insoluble (desatar un nudo imposiblemente enredado o, en este caso, desvelar la naturaleza de la ED), por lo que para resolver el misterio se necesitan diferentes enfoques y formas de pensar. En esta tesis, el origen de la energía oscura en forma de teorías de gravedad modificada se explora directamente a través de las observaciones cosmológicas mediante la aplicación de algoritmos de aprendizaje automático (ML) que pueden eliminar los sesgos debidos a modelos elegidos a priori. Aunque la idea de cortar el nudo gordiano (siguiendo la analogía) aún no se ha realizado, hemos logrado importantes avances en ambas direcciones.

En vista de la plétora de modelos DE y MG, se ha hecho un esfuerzo por proporcionar un marco unificado que incluya varios de ellos, como el enfoque Effective Field Theory (EFT) [7, 8] o el enfoque Effective Fluid approach (EFA) [9–11]. En esta disertación nos hemos centrado en el último que tiene la ventaja de que solo se necesitan un puñado

de variables para calcular, es decir, una ecuación de estado $w(a)$, una perturbación de presión $\delta P(k,a)$, y una tensión anisotrópica $\sigma(k,a)$. En particular, se mostrará que con modificaciones simples al último código Cosmic Linear Anisotropy Solving System (`CLASS`), que llamamos `EFCLASS`, proporcionamos resultados competitivos en un enfoque mucho más simple y menos propenso a errores en la inclusión de los efectos de los modelos gravitatorios modificados.

Una alternativa viable que también se ha explorado en la búsqueda de sondear la naturaleza de la DE está más relacionada con las observaciones y la estadística, que es el uso de algoritmos de aprendizaje automático para realizar una reconstrucción independiente del modelo tanto de la expansión de fondo del Universo como de las perturbaciones de materia a gran escala con métodos como los algoritmos genéticos (GA), que se pueden describir mejor como un enfoque de búsqueda estocástica. La originalidad de nuestro análisis es que utilizamos un enfoque totalmente agnóstico y no paramétrico basado en el aprendizaje automático para explorar la naturaleza de la energía oscura y reconstruir sus propiedades de una manera independiente del modelo, que es mucho más amplia que la inferencia estadística tradicional y la selección de modelos. Por lo tanto, nuestro enfoque demuestra que las sinergias entre la teoría y el aprendizaje automático pueden proporcionar una comprensión más profunda de la gravitación a gran escala e identificar posibles indicios de nueva física en forma de modificaciones de la gravedad. Dada la plétora y la complejidad de los datos provenientes de las próximas encuestas en un futuro cercano, este será sin duda un enfoque muy gratificante.

Esquema

El diseño de esta tesis se divide en tres partes principales: Fundamentos, Teorías de la gravedad modificada y Aprendizaje automático.

La primera parte trata sobre algunos aspectos fundamentales de la cosmología. En el Capítulo 1 presentamos una descripción general del Modelo Cosmológico Estándar (ΛCDM) que es actualmente el escenario de concordancia y explica con alta precisión casi todas las observaciones, aunque existen algunas tensiones. También describimos algunas ecuaciones básicas relacionadas con la teoría de la perturbación cosmológica necesarias para los capítulos posteriores de la Sec. 1.2 y luego señalamos algunas tensiones o discrepancias que se están discutiendo actualmente con respecto al paradigma exitoso de ΛCDM, ver Sec. 1.3. Dado que utilizaremos una plétora de observaciones cosmológicas a lo largo de esta tesis, hemos dedicado el capítulo 2 a describir con gran detalle las sondas de observación utilizadas, tanto en el fondo como en el nivel de perturbación.

La segunda parte está relacionada con los modelos de Gravedad Modificada y Energía Oscura. En el Capítulo 3 proporcionamos alguna motivación sobre por qué vale la pena este camino. Los capítulos 4-8 se basan en trabajo original. En los Capítulos 4 y 5 describimos un mecanismo para abarcar y estudiar una plétora de teorías de Energía Oscura (DE) y Gravedad Modificada (MG) bajo la misma base a través de un enfoque de fluido efectivo. Este método permite la expansión de fondo correcta en los modelos, todo sin sacrificar la precisión de los resultados. En pocas palabras, el Enfoque Fluido Efectivo funciona reescribiendo las ecuaciones de campo del modelo MG como GR y un fluido DE con una ecuación de estado $w(a)$, una perturbación de presión $\delta P(k,a)$ y una tensión anisotrópica $\sigma(k,a)$. Especialmente este último es crucial, ya que a veces se ignora en análisis de modelos MG [12], algo que podría sesgar los resultados. En concreto,

mostramos cómo funciona este método para $f(R)$ y la teoría de la gravedad de Horndeski y mostramos cómo se puede implementar directamente en un código de Boltzmann, que resuelve la evolución lineal de las perturbaciones cosmológicas. Encontramos que nuestras modificaciones simples al código vanilla son precisas al nivel de $\sim 0.1\%$ con respecto al código `hi_CLASS` más complicado, ver la Fig. 5.5. Luego, en el Capítulo 6 realizamos un análisis cosmológico riguroso en modelos MG utilizando un análisis de Monte Carlo de la Cadena de Markov y nuestro enfoque de fluidos efectivo. En el capítulo 7 exploramos la posibilidad de que la energía oscura pueda tener un componente no adiabático y examinamos cómo afectaría a varios observables cosmológicos clave. Finalmente, en el capítulo 8 proporcionamos expresiones analíticas exactas para la densidad, presión, densidad numérica promedio y pseudopresión para neutrinos masivos y partículas genéricas de materia oscura, tanto fermiones como bosones, y comparamos nuestras expresiones analíticas con la implementación numérica en un código de Boltzmann.

La parte final se centra en el aprendizaje automático (ML) aplicado a la cosmología que está llamando la atención por sus múltiples aplicaciones. En el Capítulo 9 motivamos la importancia y la necesidad de usar estas técnicas y en el Capítulo 10 presentamos los Algoritmos Genéticos, un método ML particular que se especializa en la regresión simbólica no supervisada de datos y que se utilizará en los capítulos siguientes. Los capítulos 11-18 se basan en el trabajo original. En esencia, en el Capítulo 11 exploramos lo que ML puede decirnos sobre la expansión de fondo del Universo al estimar el parámetro de desaceleración $q(z)$, una medida de la aceleración del Universo, y hacemos una detección independiente del modelo $\sim 4.5\sigma$ de la expansión acelerada, pero también colocamos restricciones en la transición al corrimiento al rojo de la fase de aceleración ($z_{\rm tr} = 0.662 \pm 0.027$). También encontramos una desviación de ΛCDM en corrimientos al rojo altos, aunque dentro de los errores, lo que sugiere la tensión supuesta recientemente entre los datos de SnIa / cuásar y el modelo de constante cosmológica ΛCDM en corrimientos al rojo altos ($z \gtrsim 1.5$). En el capítulo 12 ampliamos nuestro análisis de reconstrucción de ML incluyendo también datos cosmológicos a nivel de perturbación, donde aplicamos los algoritmos genéticos para explorar la naturaleza de DE de una manera independiente del modelo reconstruyendo cantidades como el índice de crecimiento de perturbaciones de densidad de materia $\gamma(z)$, la tensión anisotrópica DE lineal $\eta_{\rm DE}(z)$ y la velocidad del sonido adiabático $c^2_{\rm s,DE}(z)$ de las perturbaciones DE. Encontramos una desviación $\sim 2\sigma$ de la ecuación del estado $w(z)$ de -1 a altos corrimientos al rojo, la velocidad del sonido adiabático es negativa en el nivel $\sim 2.5\sigma$ en $z = 0.1$ y una desviación $\sim 2\sigma$ de la tensión anisotrópica de la unidad en corrimientos al rojo bajos y $\sim 4\sigma$ en corrimientos al rojo altos. Por lo tanto, proporcionamos indicios leves sobre posibles desviaciones del modelo Λ CDM a través de la presencia de un componente no adiabático en la velocidad del sonido DE o la presencia de estrés anisotrópico DE. En el Capítulo 13 presentamos un modelo de reconstrucción independiente y no paramétrica de la evolución del corrimiento al rojo de la temperatura del Fondo Cósmico de Microondas (CMB) para imponer restricciones a la relación de dualidad distancia cósmica y una constante de estructura fina variable temporal y en En el capítulo 14 también exploramos el parámetro de dualidad con eventos de ondas gravitacionales con lentes fuertes y pronósticos de ML. En el capítulo 15 presentamos reconstrucciones de la quintaesencia y las conjeturas de Swampland utilizando tanto ML como cosmografía. Los capítulos 16 y 17 tratan de nuevas pruebas nulas para la curvatura espacial y homogeneidad del Universo y el principio copernicano a través del Teorema de Noether respectivamente y sus reconstrucciones ML. Finalmente, en el Capítulo 18 presentamos ML ajustes mejorados

del horizonte sonoro en la época de arrastre bariónico y mostramos que pueden sesgar fuertemente las restricciones derivadas sobre los parámetros cosmológicos usando datos de oscilaciones acústicas bariónicas (BAO).

Contents

Part I

Foundations

1

The Standard Cosmological Model

Einstein: What I most admire about your art, is your universality. You don't say a word, yet the world understands you!
Chaplin: True. But your glory is even greater! The whole world admires you, even though they don't understand a word of what you say.

1.1 Overview

Columbus was once at dinner with some dignitaries. It was after the first voyage to America, and somebody said, "It was not such a great thing after all. The ship did it easily enough; anybody could have done it." Columbus did not say anything, but later on he said, "Can any of you here make an egg stand on end?". Well, everybody tried it and could not do it at all. Columbus took the egg, gave it a light tap, and stood it on its end. They said, "Well, of course, anybody can do it that way". He said, "Yes, and anybody can do it when somebody shows them how it is done". There was nothing said about the egg could not be cooked or the shell had to be unbroken, or anything like that. Just, could you make the egg stand up. But the point with Columbus was that after somebody has done it, it is the easiest thing in the world and no great show at all. We as scientists should remember that we are doing science, as Stephen Hawking would say "in the shoulder of giants" and it is after countless hours of hard work that we get to master a certain subject and only then one could say it is "easy", and because of the efforts of thousands of researchers we now have an elegant mathematical description concerning the world around us.

In 1905 Albert Einstein published two papers that changed the course of physics of the twentieth century. The ideas conveyed led to two major revolutions in our understanding of the physical world, relativity and quantum mechanics [13]. They provide us with a picture about the relation between space and time and concerning the nature of matter and radiation. Later, in 1915 Albert Einstein published his theory of General Relativity (GR), which generalizes special relativity and describes a metric theory of gravity. It is one of the most well-tested theories that we have and surprisingly, it remains almost unchanged after more than one century. As applied to cosmology, the field equations of GR are used to describe the expansion of the Universe, the propagation of gravitational waves (which have recently been detected [14]), and the formation of Large Scale Structure (LSS) in the Universe, such as clusters of galaxies and super-clusters [15].

A striking aspect of GR is its prediction about the origin and evolution of the Uni-

verse, which can be understood with simple physical laws. One of its most interesting applications is Cosmology, which is the science that studies the Universe as a whole and tries to answer questions such as: How old is the Universe? What is the size and the geometry of the Universe? What is its composition? How did the Universe begin and how will it end? How did the matter and the structures that we observe in the Universe originate?

The field of Cosmology has transformed in what had previously been an assembly of largely untested speculation into an exact science, based on accurate astrophysical data and theoretical developments [16]. The best accepted physical model of our Universe is the Standard Cosmological Model (SCM) supplemented by an inflation mechanism through a scalar field named the inflaton [17]. Lately, the abundance with increasing precision of cosmological observations strongly indicates the existence of non-baryonic cold dark matter (CDM), and that the present Universe is in an epoch of accelerated expansion at redshifts $z \lesssim 1$ [18–20].

The SCM is also referenced as the Λ-Cold-Dark-Matter (ΛCDM) model and is so far the best explanation to describe the dynamical evolution of the late-time Universe [21]. However the ΛCDM model leaves many questions unanswered from the theoretical point of view, since it has to assume that ∼95% of the total component of the Universe is unknown. For this reason, the accelerating expansion of the Universe and the dark matter component still remain one of the biggest puzzles to solve in modern Cosmology.

Theoretical physicists have brought forward a plethora of possible origins of the cosmic acceleration, but all have challenges or objections. The most well known explanation is the cosmological constant, which can be traced back to Albert Einstein. In this theory, space is intrinsically filled with a very small level of vacuum energy, resulting from a slight missed cancellation in the quantum mechanics of elementary particles. But we do not know why the value of the cosmological constant has such a small value and yet nonzero [22, 23], nor can we derive it from our elementary particle theories.

The standard model of cosmology is a theoretical framework that accurately describes a large diversity of cosmological observables, ranging from the temperature anisotropies of the cosmic microwave background to the spatial distribution of galaxies. This model has a few free parameters representing fundamental quantities, like the geometry and expansion rate of the Universe, the amount and nature of dark energy and dark matter, and the sum of neutrino masses. Inferring the value of these parameters will expand our knowledge on the fundamental constituents and laws governing our Universe. Hence, one of most important goals of modern cosmology is to constrain the value of these parameters with the highest accuracy.

The SCM is built on five robust pillars [24]: i) The General Theory of Relativity, which provides the frame for the cosmological models and represents the most general theory describing a single metric that in four dimensions has field equations with at most second-order derivatives [25]. ii) The Cosmological Principle, which states that the spatial distribution of matter in the Universe is homogeneous and isotropic at large scales [26]. iii) The Hubble law, which proves to be the first observational basis for the expansion of the Universe [27]. iv) The Cosmic Microwave Background (CMB), whose uniformity in its temperature radiation is the best evidence for the isotropy of the observed Universe and whose small anisotropies (smaller than about one part in 10^5) provides strong constraints on the cosmological parameters [28]. v) The Big Bang Nucleosynthesis (BBN), that predicts the correct abundances for the light elements ^{1}H, ^{2}D, ^{3}He, ^{4}He, and ^{7}Li [29].

The theory of GR, described by a massless spin-2 field and formulated by A. Einstein in 1915-1916, is strongly based on four assumptions [30,31] that the Physics of Gravitation has to satisfy:

- *The Principle of Relativity*, which states that all the laws of Physics take the same form in any inertial reference.
- *The Principle of Equivalence*, which is equivalent to saying that the effects of the gravitational field can be cancelled by the acceleration of the reference frame.
- *The Principle of General Covariance*, which requires all the laws of Physics to be covariant (form-invariant) under general transformations of coordinates, i.e they have the same form in all reference frames for all observers. It is well known that the simplest way to construct laws of Physics (equations) satisfying invariance principles is to construct invariant actions.
- *The Principle of Causality*, i.e. that each point of space-time should admit a universally valid notion of past, present and future).

We will now mention the conventions and definitions that we will use throughout this thesis. Our convention for the metric signature is $(-+++)$ the Riemann and Ricci tensors are given respectively by $V_{b;cd} - V_{b;dc} = V_a R^a_{bcd}$ and $R_{ab} = R^s_{asb}$. We will use the Greek alphabet to write space-time indices and the Latin alphabet for the space indices. In the standard cosmological model one assumes the Einstein-Hilbert action

$$S = \int d^4x\sqrt{-g}\left[\frac{1}{2\kappa}R + \mathcal{L}_m\right], \tag{1.1}$$

where g is the determinant of the metric $g_{\mu\nu}$, R is the Ricci scalar, $\kappa \equiv \frac{8\pi G_N}{c^4}$ and $\mathcal{L}_m$ is the Lagrangian for matter fields. Applying the principle of least action to Eq. (1.1) one obtains the field equations

$$G_{\mu\nu} = \kappa\, T^{(m)}_{\mu\nu}, \tag{1.2}$$

where $G_{\mu\nu}$ is the Einstein tensor and $T^{(m)}_{\mu\nu}$ is the energy-momentum tensor for matter fields. For the Riemann and Einstein curvature tensors we will use the conventions of Misner, Thorne and Wheeler [32]:

$$R^{\mu}_{\nu\alpha\beta} = \partial_\alpha\Gamma^\mu_{\nu\beta} - \partial_\beta\Gamma^\mu_{\nu\alpha} + \Gamma^\mu_{\sigma\alpha}\Gamma^\sigma_{\nu\beta} - \Gamma^\mu_{\sigma\beta}\Gamma^\sigma_{\nu\alpha}, \tag{1.3}$$

$$G_{\mu\nu} = R_{\mu\nu} - \frac{1}{2}g_{\mu\nu}R, \tag{1.4}$$

where $R_{\mu\nu} = R^\alpha_{\mu\alpha\nu}$ is the Ricci curvature tensor and $R = R^\alpha_\alpha$ is the scalar curvature. The stress-energy tensor is defined with respect to the Lagrangian density for the matter fields as

$$T^{(m)}_{\mu\nu} = -\frac{2}{\sqrt{-g}}\frac{\delta\left(\sqrt{-g}\mathcal{L}_m\right)}{\delta g^{\mu\nu}}. \tag{1.5}$$

The ΛCDM model includes the Einstein Field Equations from GR

$$R_{\mu\nu} - \frac{1}{2}g_{\mu\nu}R = \kappa T_{\mu\nu} + \Lambda g_{\mu\nu}, \tag{1.6}$$

where Λ is the Cosmological Constant, $\kappa = \frac{8\pi G_N}{c^4}$ and G_N is the bare Newton's constant. In what follows we will set $c = 1$. The Bianchi identities imply the conservation of the energy momentum tensor

$$\nabla^\mu G_{\mu\nu} = 0 \longrightarrow \nabla^\mu T_{\mu\nu} = 0. \tag{1.7}$$

Finally, let us assume that the Universe can be described at the background level by a flat Friedmann-Lemaitre-Robertson-Walker (FLRW) metric, i.e

$$ds^2 = -dt^2 + a^2(t)\delta_{ij}dx^i dx^j, \tag{1.8}$$

then there are only two sets of non vanishing components of the Ricci tensor

$$R_{00} = -3\frac{\ddot{a}}{a} = -R/2 + 3H^2, \tag{1.9}$$

$$R_{ij} = \delta_{ij}\left[2\dot{a}^2 + a\ddot{a}\right], \tag{1.10}$$

which can be computed using the values for the Christoffel symbols

$$\Gamma^0_{00} = \Gamma^0_{0i} = \Gamma^0_{i0} = 0, \;\; \Gamma^0_{ij} = \delta_{ij}\dot{a}a, \;\; \Gamma^i_{0j} = \Gamma^i_{j0} = \delta_{ij}\frac{\dot{a}}{a}, \tag{1.11}$$

where the over-dots indicate derivatives with respect to time and all other $\Gamma^i_{\alpha\beta}$ is zero. For the Ricci scalar we have

$$R = 6\left[\frac{\ddot{a}}{a} + \left(\frac{\dot{a}}{a}\right)^2\right] = 12H^2 + 6\dot{H}. \tag{1.12}$$

The evolution of the scale factor is obtained considering the 00 component of the Einstein equations

$$R_{00} - \frac{1}{2}g_{00}R = 8\pi G T_{00}. \tag{1.13}$$

Since the 00 component of the energy-momentum tensor is the energy density ρ we can conclude that

$$\left(\frac{\dot{a}}{a}\right)^2 = \frac{8\pi G}{3}\rho, \tag{1.14}$$

which can also be written as

$$\frac{H^2}{H_0^2} = \frac{\rho}{\rho_{crit}}, \tag{1.15}$$

where $\rho_{crit} \equiv 3H_0^2/8\pi G$ and $H \equiv \dot{a}/a$ is known as the Hubble rate and characterizes the

expansion rate of the Universe, whose value today is denoted by H_0.

1.2 Cosmological Perturbation Theory

Perturbation theory is an essential instrument for making predictions for a variety of cosmological observations and is is also necessary to understand the formation and evolution of large-scale structures [15].

Let us assume that the Universe can be described at the background level, on large scales on the order of ∼100Mpc and more, by a flat Friedmann-Lemaitre-Robertson-Walker (FLRW) metric, then in order to study the perturbations of various cosmological models, we consider the perturbed FLRW metric, which in the Newtonian gauge[1] and including only the scalar perturbations can be written as:

$$ds^2 = -(1+2\Psi(\vec{x},t))dt^2 + a^2(t)(1-2\Phi(\vec{x},t))\delta_{ij}dx^i dx^j, \tag{1.16}$$

One of the motivations to choose this gauge is that the metric potentials Φ and Ψ are actually cosmological observables [35]. This metric can also be written as

$$\begin{aligned} g_{00}(\vec{x},t) &= -\left(1+2\Psi\right), \\ g_{0i}(\vec{x},t) &= 0, \\ g_{ij}(\vec{x},t) &= a(t)^2(1-2\Phi(\vec{x},t)). \end{aligned} \tag{1.17}$$

Since the metric (1.16) is diagonal, it is simple to invert it and at first order is given by

$$\begin{aligned} g^{00}(\vec{x},t) &= -\frac{1}{1+2\Psi} \simeq -1+2\Psi, \\ g^{0i}(\vec{x},t) &= 0, \\ g^{ij}(\vec{x},t) &= \frac{1}{a(t)^2(1-2\Phi(\vec{x},t))}\delta^{ij} \simeq \frac{1}{a(t)^2}\left(1+2\Phi\right)\delta^{ij}. \end{aligned} \tag{1.18}$$

In the absence of the potentials Ψ and Φ, Eq. (1.16) is the FLRW metric of the zero-order homogeneous, flat cosmology. Also, in the absence of expansion ($a = 1$) this metric describes a weak gravitational field. The Newtonian potential Ψ corresponds to the temporal perturbations to the metric, and Φ to the perturbation to the spatial curvature. In the derivation of the Christoffel symbols, the Ricci tensor and the Ricci scalar, we will treat Ψ and Φ as small quantities, since the perturbations in the Universe are small at the times and scales of interest, hence we will drop all terms quadratic in them.

It is worth noting that one can split the perturbations into those acting as scalars, vectors and tensors by performing a scalar-vector-tensor (SVT) decomposition, see for example [34]. What makes very useful the SVT decomposition is the fact that the Einstein equations for scalars, vectors and tensors do not mix at linear order and can then be

[1] Concerning the choice of a gauge, there is freedom in the variables one chooses to describe the fluctuations. In order to compare our results with [33, 34] we are working in the Newtonian gauge, since it is well known that the physical and measurable quantities must be gauge invariant.

treated separately. [36]. Eq. (1.16) contains only scalar perturbations since it is what dominates at large scales and contains the corresponding density perturbations. Notice that scalar perturbations formally means that the perturbations in $\Psi(\vec{x},t)$ and $\Phi(\vec{x},t)$ transforms as scalars as $\vec{x} \to \vec{x}'$; i.e they remain unchanged under a spatial coordinate transformation. Also they are the only ones that couple to matter perturbations and are the most important that couple to photon perturbation also [37]. We are not interested in vector perturbations at the moment since they are not produced by scalar field inflation [38]. Tensor perturbations are an important prediction of inflation and necessary for the study of the stochastic gravitational wave (GW) background.

In our derivation for the scalar perturbations we will follow Ref. [33]. Although we have computed by hand all the Einstein equations perturbatively around the zero-order homogeneous solution, we will not write down explicitly all the steps of the derivation since this calculation is completely straightforward, however a bit lengthy.

To derive the Einstein field equations, we first need to compute the perturbed connection coefficients. Recall that we are keeping those terms that are linear in Ψ and/or Φ,

$$\Gamma^{\beta}_{\mu\nu} = \frac{1}{2} g^{\beta\alpha} \left[g_{\alpha\mu,\nu} + g_{\alpha\nu,\mu} - g_{\mu\nu,\alpha} \right]. \tag{1.19}$$

Substituting Eqs. (1.17) and (1.18) into Eq. (1.19) gives

$$\Gamma^{0}_{00} = \Psi_{,0}, \tag{1.20}$$

$$\Gamma^{0}_{0i} = \Gamma^{0}_{i0} = \Psi_{,i} = ik_i\Psi, \tag{1.21}$$

$$\Gamma^{0}_{ij} = \delta_{ij} a^2 \left[H - 2H\left(\Phi + \Psi\right) - \Phi_{,0} \right], \tag{1.22}$$

$$\Gamma^{i}_{00} = \frac{ik^i}{a^2}\Psi, \tag{1.23}$$

$$\Gamma^{i}_{j0} = \Gamma^{i}_{0j} = \delta_{ij}\left(H - \Phi_{,0}\right), \tag{1.24}$$

$$\Gamma^{i}_{jk} = -i\Phi\left[\delta_{ik}k_j + \delta_{ij}k_k - \delta_{jk}k_i\right], \tag{1.25}$$

where $\Psi_{,0}$ and $\Phi_{,0}$ means derivative with respect to time. In Fourier space the spatial derivative i is replaced by $i\ k_i$. Notice also that both δ_{ij} and the 3-vector k_i are in Euclidean space, so we can freely interchange their upper and lower indices. In order to compute the 00 component of the Ricci tensor

$$R_{00} = \Gamma^{\alpha}_{00,\alpha} - \Gamma^{\alpha}_{0\alpha,0} + \Gamma^{\alpha}_{\beta\alpha}\Gamma^{\beta}_{00} - \Gamma^{\alpha}_{\beta 0}\Gamma^{\beta}_{0\alpha}, \tag{1.26}$$

we need to use the fact that

$$\Gamma^{i}_{00,i} = -\frac{k^2}{a^2}\Psi, \tag{1.27}$$

$$-\Gamma^{i}_{0i,0} = -3\left(\frac{\ddot{a}}{a} - H^2 - \Phi_{,00}\right), \tag{1.28}$$

$$\Gamma^{i}_{i\beta}\Gamma^{\beta}_{00} = -\Gamma^{i}_{i0}\Gamma^{0}_{00} = 3H\Psi_{,0}, \tag{1.29}$$

$$-\Gamma^{i}_{\beta 0}\Gamma^{\beta}_{0i} = -\Gamma^{i}_{j0}\Gamma^{j}_{0i} = -3\left(H^2 - 2H\Phi_{,0}\right). \tag{1.30}$$

Using the above expressions we find that

$$R_{00} = -3\frac{\ddot{a}}{a} - \frac{k^2}{a^2}\Psi + 3\Psi_{,00} + 3H\left(\Psi_{,0} + 2\Phi_{,0}\right), \tag{1.31}$$

where its zero-order agrees with Eq. (1.9). Similarly, the spatial part of the Ricci tensor is

$$\begin{aligned} R_{ij} = \delta_{ij}\left[\left(2a^2H^2 + a\ddot{a}\right)(1 - 2\Phi - 2\Psi) + a^2H\left(-6\Phi_{,0} - \Psi_{,0}\right) - a^2\Phi_{,00} - k^2\Phi\right] \\ + k_ik_j\left(\Psi - \Phi\right). \end{aligned} \tag{1.32}$$

Contracting the indices on the Ricci tensor we find the Ricci scalar

$$\begin{aligned} R &= g^{00}R_{00} + g^{ij}R_{ij}, \\ &= [-1 + 2\Psi]\left[-3\frac{\ddot{a}}{a} - \frac{k^2}{a^2}\Psi + 3\Phi_{,00} + 3H\left(\Psi_{,0} + 2\Phi_{,0}\right)\right] \\ &+ \frac{1 + 2\Phi}{a^2}\left[3\left\{\left(2a^2H^2 + a\ddot{a}\right)(1 - 2\Phi - 2\Psi) + a^2H\left(-6\Phi_{,0} - \Psi_{,0}\right) - a^2\Phi_{,00} - k^2\Phi\right\} + k^2\left(\Psi - \Phi\right)\right], \end{aligned} \tag{1.33}$$

it's zero-order agrees with Eq. (1.12). Considering small perturbations of the Ricci scalar

$$R = \bar{R} + \delta R, \tag{1.34}$$

where $\bar{R}$ represents the zero-order and δR the first order perturbation, if we subtract the zero-order from Eq. (1.33) and keep only the first order in Ψ and Φ we find

$$\delta R = 2\frac{k^2}{a^2}\Psi - 4\frac{k^2}{a^2}\Phi - 6H\left(\Psi_{,0} + 4\Phi_{,0}\right) - 6\Phi_{,00} - 12\dot{H}\Psi - 24H^2\Psi. \tag{1.35}$$

Finally we need to compute the Einstein tensor, which at first order the 00 component is

$$G_0^0 = g^{00}\left[R_{00} - \frac{1}{2}g_{00}R\right] = (-1 + 2\Phi)\,R_{00} - \frac{R}{2}, \tag{1.36}$$

$$\delta G_0^0 = 6H\Phi_{,0} + 6\Psi H^2 + 2\frac{k^2}{a^2}\Phi. \tag{1.37}$$

The spatial part of G_ν^μ gives

$$G_j^i = g^{ik}\left[R_{kj} - \frac{g_{kj}}{2}R\right] = \frac{\delta^{ik}\left(1 + 2\Phi\right)}{a^2}R_{kj} - \frac{\delta_{ij}}{2}R. \tag{1.38}$$

Using the expression for the Ricci scalar and the Ricci tensor we find

$$G_j^i = A\delta_{ij} + \frac{k_ik_j\left(\Psi - \Phi\right)}{a^2}, \tag{1.39}$$

where A has more than a dozen terms which we will not write down explicitly but on the GitHub repository https://github.com/RubenArjona we have a code written with Mathematica that shows all those derived terms. This code is based on the Riemann Geometry & Tensor Calculus (`RGTC`) package, see http://www-old.inp.demokritos.gr/sbonano/public_html/ for more details.

1.3 Tensions in the Concordance Model

Through the observations of distant Type Ia supernovae at the turn of the previous century, it was discovered that the Universe is undergoing a phase of accelerated expansion on very large scales,

apparently caused by a repulsive force, usually attributed to the cosmological constant [39, 40]. Since matter with positive pressure generates decelerated expansion, cosmologists suggested that the late-time acceleration of the Universe is sourced by an exotic energy component with negative pressure, known as *dark energy* (DE) [41, 42]. One of the simplest and earliest candidate of DE is the cosmological constant Λ. Further observations and theoretical developments led to a unified description for the formation and evolution of the Universe within the framework of General Relativity (GR), known as the standard Λ cold dark matter model (ΛCDM), that contains only six free parameters describing the matter and dark energy (DE) content of the Universe. This model is so far the best phenomenological fit to the data [1]. Even though this model fits very well the cosmological observations, it suffers from a few drawbacks, like the *fine tuning* and *coincidence problem* [43]. The first one, known as the *cosmological constant problem*, is associated with the large deviation between the theoretical value of Λ predicted by quantum field theories and its observed value [23]. The coincidence problem asks the question, *"Why are the densities of non relativistic matter and vacuum of the same order precisely today?"*, even though they evolve differently [44]. These problems have led to increased interest in models where GR is modified in a way to ease the aforementioned problems and produce the observed late time acceleration without creating new downsides [45].

While this framework is very successful, there also remain some tensions to resolve, such as the nature of the dominant cold dark matter component or the hotly debated Hubble constant tension, where the determination of H_0 deduced from physics of the early universe, i.e. the Cosmic Microwave Background (CMB) observations [1], is lower that the local determination of H_0 based on Cepheid variable-calibrated Type Ia supernovae (SnIa) [46] at the 4.4σ confidence level. Also, as mentioned in Ref. [47], results from other surveys such as DES [48], the SPT Collaboration [49] or the H0LiCOW collaboration [50], with few observational systematics between them, add to the idea that the tension is due more to the physics of the cosmological setting rather than experimental systematics, see Refs. [51–53] and references there in for a recent discussion. However, recent re-analyses have shown that the main bulk of the tension which remains between the CMB and local universe measurements is mainly due to the Cepheids [54].

Other tensions have also appeared [55]. Using quasars in high redshifts up to $z \simeq 7.5$, it was shown in Ref. [56] that a $\sim 4\sigma$ deviation of the dark energy equation of state $w(z)$ from the ΛCDM model exists, suggesting a time evolution of the DE equation of state at high redshifts. On the other hand, in Refs. [57, 58] it is mentioned that an enhanced lensing amplitude still present in the Planck 2018 CMB data can be explained by a positive curvature Universe, thus violating the underlying assumptions of the flat ΛCDM model. Also, the ΛCDM prediction of the amplitude of matter fluctuations defined as $S_8 \equiv \sigma_8 \left(\Omega_m/0.3\right))^{0.5}$, where σ_8 is the root mean square of matter fluctuations on a $8h^{-1}$Mpc scale, coming from the Planck CMB data (once calibrated) is about $2-3\sigma$ higher than the direct estimation coming from cosmic shear measurements [59].

As explained on Refs. [60, 61] there are some anomalies at $2-3\sigma$ on analysis of the CMB anisotropy which include a lack of power on large angular scales, differences on the best fit values of cosmological parameters, preference for odd parity correlations, the phenomena of cosmic birefringence, cold spot anomaly etc. It is worth also to mention the Lithium problem where it is observed five times less lithium than that the BBN predicts from measurements of old, metal-poor starts in the halo of the Milky Way. Finally, there are some issues in characterizing structures at small scales within the framework of the ΛCDM model such as the core-cusp problem, missing satellite problem, too big to fail problem etc. See Refs. [62, 63] for a review.

These issues have motivated several analyses trying to reassess the level of tensions and deviations from the ΛCDM model [64–70] or to resolve it with new physics [3]. The latter approach postulates that GR is only accurate on small scales and modifications at larger scales are needed. In Chapter 3 we will develop more on this related topic.

2

Observational Probes of Cosmology

Cosmology is standing on a golden age with the advent of current and upcoming observations of percent level precision. In this Chapter we present a thorough description of the cosmological data we will use in the subsequent chapters.

2.1 Background expansion

2.1.1 The $H(z)$ data

The Hubble expansion data are obtained in two complementary ways: by the clustering of galaxies or quasars and by the differential age method. The former approach is connected to the clustering of quasars or galaxies and is a direct probe of the Hubble expansion by determining the BAO peak in the radial direction [71]. The latter is connected to the redshift drift of distant objects over long time periods, usually a decade or longer, as in metric theories assuming the Friedmann-Lemaitre-Robertson-Walker metric, the Hubble parameter can also be expressed in terms of the time derivative of the redshift as $H(z) = -\frac{1}{1+z}\frac{dz}{dt}$ [72]. In specific, the $H(z)$ data measured via the differential age method are obtained by following the differential evolution of D_n4000, a spectral feature of very massive and passive galaxies. The main source of systematics is the astrophysical modelling of the stellar metallicity, namely via the M11 and BC03 models discussed in Ref. [73]. However, by implementing strict selection criteria it was shown in Ref. [73] that it is possible to keep the systematics under control. Furthermore, the $H(z)$ data are independent of any cosmology-based constraint, i.e. a fiducial cosmological model, they are assumed to be uncorrelated with each other and share no correlations with the SnIa data [73]. In this analysis we use the 36 points of the compilation from Ref. [9], which spans over a redshift range of $0.07 \leq z \leq 2.34$. The data are in the form (z_i, H_i, σ_{H_i}) and are explicitly shown in Table 2.1. For the likelihood for the $H(z)$ data we use a standard χ^2, given by

$$\chi^2_{\rm H} = \sum_{i=1}^{N} \left(\frac{H_i - H^{th}(z_i)}{\sigma_i} \right)^2 , \tag{2.1}$$

where th stands for the theoretical cosmological model under consideration. Since Eq. (2.1) has a quadratic form, we can then minimize the χ^2 analytically over H_0 and the result is

$$\chi^2_{\rm H} = A - \frac{B^2}{\Gamma}, \tag{2.2}$$

$$H_0 = \frac{B}{\Gamma}, \tag{2.3}$$

where the parameters A, B and Γ are defined as

$$A = \sum_{i}^{N_{\rm H}} \left(\frac{H_i}{\sigma_{H_i}} \right)^2 , \tag{2.4}$$

Table 2.1: The $H(z)$ data used in our analysis (in units of km s^{-1}Mpc^{-1}). This compilation, which was presented in Ref. [9], is partly based on those of Refs. [73] and [75].

z	$H(z)$	σ_H	Ref.	z	$H(z)$	σ_H	Ref.
0.07	69.0	19.6	[76]	0.48	97.0	62.0	[77]
0.09	69.0	12.0	[77]	0.57	96.8	3.4	[81]
0.12	68.6	26.2	[76]	0.593	104.0	13.0	[78]
0.17	83.0	8.0	[77]	0.60	87.9	6.1	[80]
0.179	75.0	4.0	[78]	0.68	92.0	8.0	[78]
0.199	75.0	5.0	[78]	0.73	97.3	7.0	[80]
0.2	72.9	29.6	[76]	0.781	105.0	12.0	[78]
0.27	77.0	14.0	[77]	0.875	125.0	17.0	[78]
0.28	88.8	36.6	[76]	0.88	90.0	40.0	[77]
0.35	82.7	8.4	[79]	0.9	117.0	23.0	[77]
0.352	83.0	14.0	[78]	1.037	154.0	20.0	[78]
0.3802	83.0	13.5	[73]	1.3	168.0	17.0	[77]
0.4	95.0	17.0	[77]	1.363	160.0	33.6	[82]
0.4004	77.0	10.2	[73]	1.43	177.0	18.0	[77]
0.4247	87.1	11.2	[73]	1.53	140.0	14.0	[77]
0.44	82.6	7.8	[80]	1.75	202.0	40.0	[77]
0.44497	92.8	12.9	[73]	1.965	186.5	50.4	[82]
0.4783	80.9	9.0	[73]	2.34	222.0	7.0	[83]

$$B = \sum_{i}^{N_{\rm H}} \frac{H_i \, E^{\rm th}(z_i)}{\sigma^2_{H_i}}, \tag{2.5}$$

$$\Gamma = \sum_{i}^{N_{\rm H}} \left(\frac{E^{\rm th}(z_i)}{\sigma_{H_i}} \right)^2, \tag{2.6}$$

where we denote the theoretical value of the Hubble parameter as $E^{\rm th}(z) = H^{\rm th}(z)/H_0$ and we set $N_{\rm H} = 36$. The aforementioned data can be used to measure the Hubble constant H_0, to determine the deceleration transition redshift, to constrain the spatial curvature of the Universe along with distance redshift data, but also constrain the non-relativistic matter and DE parameters, as shown in [74]. The Hubble constant H_0 has been the focus of an extended discussion in the literature, in light of a tension between local and high-redshift measurements of the parameter, see Ref. [51, 52] and references there in for a recent discussion.

2.1.2 The type Ia supernovae data

A type Ia supernovae is referred to a type of supernovae that occurs in a binary system of starts, where one of them is a white dwarf. The other star can be anything from a giant star to an even smaller white dwarf[1]. It is believed that Type Ia Supernovae (SNe Ia) are thermonuclear explosions in low mass stars, e.g. activated when the mass of a white dwarf is steer by the accretion of material from a companion above the maximum that can be supported by electron degeneracy pressure, which occurs at a critical mass, the Chandrasekhar limit of $\sim 1.4 M_\odot$ [84]. Since empirically SNe Ia follow photometric and spectroscopic sequences with regard to a consistent peak luminosity, these explosions can be used as standard candles to measure the distance to their host galaxies [85]. In

[1] https://en.wikipedia.org/wiki/Type_Ia_supernova

other words, Sne Ia exhibit an empirical relationship between their peak luminosity, and their light curve width (or "stretch") and color. This luminosity correction for the two parameters is the most common technique for standardising a compilation of SNe Ia. By fitting a light curve model to time-series photometry of SNe Ia it is possible to recover the supernovae parameters and infer their distances [86]. In fact, this process lead the way to the discovery of the accelerating expansion of the Universe [87]. Some empirical techniques used for this fitting the light curves are for example the Multi Colour Lightcurve Shape (`MLCS`) strategy [39] and `SALT2` (Spectral Adaptive Light Curve Template) where the later is used in most modern SN Ia analyses [86].

We use the Pantheon SnIa compilation of Ref. [88] of 1048 Supernovae Ia points in the redshift range $0.01 < z < 2.26$ along with their covariances. The apparent magnitude m_B is

$$m_{\rm B} = 5\log_{10}\left(\frac{d_{\rm L}(z)}{1{\rm Mpc}}\right) + 25 + M_B, \tag{2.7}$$

where $d_{\rm L}(z)$ is the luminosity distance and M_B the absolute magnitude. We then marginalize over the nuisance parameter M_B, as shown in the Appendix C of Ref. [89]. Then our final expression for the χ^2 is

$$\chi^2_{\rm SnIa} = A - \frac{B^2}{E} + \ln\left(\frac{E}{2\pi}\right), \tag{2.8}$$

where $A = \Delta\vec{m}\cdot\mathbf{C}^{-1}\cdot\Delta\vec{m}$, $B = \Delta\vec{m}\cdot\mathbf{C}^{-1}\cdot\Delta\vec{I}$ and $E = \vec{I}\cdot\mathbf{C}^{-1}\cdot\vec{I}$, while $\mathbf{C}$ is the SnIa covariance matrix, $\vec{I} = (1, 1, \cdots, 1)$ and $\Delta m \equiv m_{\rm B,i} - m_{\rm th}(z_i)$.

2.1.3 The baryon acoustic oscillations

The different BAO data used in our analysis comes from 6dFGS [90], SDDS [81], BOSS CMASS [91], WiggleZ [80], MGS [92] and BOSS DR12 [93], DES [94], Lya [95], DR - 14 LRG [96] and quasars [97]. The following functions that we will present now are used to describe the data. First, we define the ratio of the sound horizon at the drag redshift to the so called dilation scale:

$$d_z \equiv \frac{r_s(z_d)}{D_V(z)}, \tag{2.9}$$

where the comoving sound horizon is $r_s(z_d) = \int_{z_d}^{\infty}\frac{c_s(z)}{H(z)}dz$ and z_d is the redshift at the dragging epoch, see Eq. (4) of [98]. In the ΛCDM model the sound horizon can be approximated as

$$r_s(z_d) \simeq \frac{44.5\log\left(\frac{9.83}{\Omega_{\rm m,0}h^2}\right)}{\sqrt{1+10(\Omega_{\rm b,0}h^2)^{3/4}}}{\rm Mpc}, \tag{2.10}$$

while the dilation scale is given by

$$D_V(z) = \left[(1+z)^2 d_A(z)^2\frac{cz}{H(z)}\right]^{1/3}, \tag{2.11}$$

where we have defined the Hubble distance

$$D_H(z) = c/H(z). \tag{2.12}$$

Then, the 6dFGs and WiggleZ BAO data are specified as

z	d_z	σ_{d_z}
0.106	0.336	0.015
0.44	0.073	0.031
0.6	0.0726	0.0164
0.73	0.0592	0.0185

(2.13)

where their inverse covariance matrix is

$$C_{ij}^{-1} = \begin{pmatrix} \frac{1}{0.015^2} & 0 & 0 & 0 \\ 0 & 1040.3 & -807.5 & 336.8 \\ 0 & -807.5 & 3720.3 & -1551.9 \\ 0 & 336.8 & -1551.9 & 2914.9 \end{pmatrix} \tag{2.14}$$

with the χ^2 given by

$$\chi^2_{\rm 6dFS,Wig} = V^i C_{ij}^{-1} V^j, \tag{2.15}$$

and $V^i = d_{z,i} - d_z(z_i, \Omega_{\rm m,0})$. The BAO measurements for MGS and SDSS (LowZ and CMASS) are given by $D_V/r_s = 1/d_z$ via

z	$1/d_z$	σ_{1/d_z}
0.15	4.46567	0.168135
0.32	8.62	0.15
0.57	13.7	0.12

(2.16)

and the

$$\chi^2_{\rm MGS,SDSS} = \sum \left(\frac{1/d_{z,i} - 1/d_z(z_i, \Omega_{\rm m,0})}{\sigma_{1/d_{z,i}}} \right)^2. \tag{2.17}$$

At this point we should stress that these aforementioned data points were provided by their respective collaborations, 6dFGs and WiggleZ for the ones in Eq. (2.15) and MGS and SDSS for Eq. (2.17) in that exact form as this is how they are extracted from the raw data. Hence, we have not made any assumptions from our part at this stage.

The BAO data from DES are of the form $d_A(z)/r_s$ with $(z, d_A(z)/r_s, \sigma) = (0.81, 10.75, 0.43)$ and the χ^2 given by

$$\chi^2_{\rm DES} = \sum \left(\frac{d_A(z,i)/r_s - d_A(z_i, \Omega_{\rm m,0})/r_s}{\sigma_{d_A(z,i)/r_s}} \right)^2. \tag{2.18}$$

We also include the BAO data from Lya, which are of the form $f_{\rm BAO} = ((1+z)d_A/r_s, D_H/r_s)$ and are given by

z	$f_{\rm BAO}$	$\sigma_{f_{\rm BAO}}$
2.35	36.3	1.8
2.35	9.2	0.36

(2.19)

with the χ^2 given by

$$\chi^2_{\rm Lya} = \sum \left(\frac{f_{\rm BAO,i} - f_{\rm BAO}(z_i, \Omega_{\rm m,0})}{\sigma_{f_{\rm BAO}}} \right)^2. \tag{2.20}$$

Finally, the DR-14 LRG and quasars BAO data make the assumption of $r_{s,fid} = 147.78$ Mpc/h and are given by $D_V/r_s = 1/d_z$

z	$1/d_z$	σ_{1/d_z}
0.72	$\frac{2353}{r_{s,fid}}$	$\frac{62}{r_{s,fid}}$
1.52	$\frac{3843}{r_{s,fid}}$	$\frac{147}{r_{s,fid}}$

(2.21)

and the χ^2 given by

$$\chi^2_{\rm LRG,Q} = \sum \left(\frac{1/d_{z,i} - 1/d_z(z_i, \Omega_{\rm m,0})}{\sigma_{1/d_{z,i}}} \right)^2. \tag{2.22}$$

The total χ^2 is then given by

$$\chi^2_{\rm tot} = \chi^2_{\rm 6dFS,Wig} + \chi^2_{\rm MGS,SDSS} + \chi^2_{\rm DES} + \chi^2_{\rm Lya} + \chi^2_{\rm LRG,Q}. \tag{2.23}$$

Note that the previous equation carries the assumption that the data are independent, hence we can just add the χ^2 together. As some of the data points are from the same survey, there must

be galaxies in common between the overlapping datasets, and therefore some potentially strong covariances, something which poses an important limitation of our analysis.

In the particular cases, e.g. the WiggleZ data, where the correlations between the points, quantified in terms of a covariance matrix C_{ij}, are known, we have then included the C_{ij} in our analysis. However, in most cases the full correlations are in practice not publicly available or it is impossible to correctly estimate a covariance matrix, even if a few attempts have been made in the literature, e.g. for a similar discussion for the $f\sigma 8$ data see Ref. [99].

One way to resolve this important issue was proposed in Ref. [99], where the authors approximated the overall covariance matrix of the $f\sigma 8$ measurements as the percent fraction of overlapping volume between the surveys to the total volume of the two surveys combined. However, clearly this approach cannot take into account any negative correlations between the data as in general, the effect of the correlations can also be due to instrument systematics etc. Thus, approximating the covariance matrix with the percent overlap can potentially lead to a strongly biased covariance matrix.

On a related note, another limitation of this compilation of the BAO data is that some of the data points, e.g. those coming from 6dFGs and WiggleZ, are given in terms of the variable $d_z(z)$, while some other points, e.g. from MGS and SDSS, are given in terms of $1/d_z(z)$. This poses a problem as we have to make an implicit assumption about how the errors in those data points are distributed. For example, we always assume symmetric error bars, but if the errors are symmetric in $1/d_z(z)$, they will not be symmetric in $d_z(z)$ and vice versa. This further complicates the analysis as $d_z(z)$ and $1/d_z(z)$ are not raw data that can be reexpressed in a more consistent form, but they are derived data products which makes it impossible to rewrite them in the same form, without making further assumptions.

Finally, the BAO χ^2 terms in Eq. (2.23) depend on the sound horizon at the drag redshift $r_d = r_s(z_d)$ through Eq. (2.9), which is complicated to estimate model independently. In order to not assume a value for H_0, when we reconstruct this data set model independently on Chapters 11-17, when we fit the BAO data we have minimized the χ^2 over the quantity $r_{sh} = r_s \cdot h$, where r_s is the sound horizon at the drag redshift and h is the Hubble parameter. Hence, we avoid any bias of the results due to specifying a value of H_0.

2.1.4 Transversal and Radial BAO data

The 6 data points for the radial BAO Δz are taken from Table III of the SDSS-IV spectroscopic survey [100] coming from SDSS, SDSS-II, BOSS and eBOSS. As we did with the BAO data, to do not assume a value for H_0 in our reconstruction when we fit the radial BAO data we have minimized the χ^2 over the quantity $r_{sh} = r_s \cdot h$.

The angular BAO, also known as the transversal BAO scale data have been taken from Table I of Ref. [101] where 15 measurements of $\theta(z)$ are given and where the data have been derived without assuming a fiducial cosmology, following the approach of Ref. [102]. For convenience of the reader we also present the data points on Table 2.2. In particular, the compilation of the angular BAO data comes from luminous red galaxies, blue galaxies, quasar catalogs and from diverse releases of the Sloan Digital Sky Survey (SDSS), see Refs. [103–106]. For the fit of the transverse BAO we have also minimized the χ^2 over the quantity $r_{sh} = r_s \cdot h$.

2.1.5 Background CMB Temperature $T(z)$

In our analysis we use 37 points and the compilation can be found in Table 2.3. The main advantage of our compilation is that it spans over a wide redshift range of $0 \leq z \leq 3.025$. The compilation of the data is assumed to be uncorrelated since there is no public access to any correlation matrix. The background temperature of the CMB can be measured at both high and low redshifts. For the former, it can be recovered through fine-structure transitions of atomic or molecular species in cool absorption-line systems along the line of sight to high redshift quasars [107]. For low redshifts it can

Table 2.2: Angular BAO data taken from Table I of Ref. [101]

Catalog	z	$\theta(z)$	$\sigma_{\theta(a)}$	Ref.
SDSS-DR7	0.235	9.06	0.23	[106]
SDSS-DR7	0.365	6.33	0.22	[106]
SDSS-DR10	0.450	4.77	0.17	[105]
SDSS-DR10	0.470	5.02	0.25	[105]
SDSS-DR10	0.490	4.99	0.21	[105]
SDSS-DR10	0.510	4.81	0.17	[105]
SDSS-DR10	0.530	4.29	0.30	[105]
SDSS-DR10	0.550	4.25	0.25	[105]
SDSS-DR11	0.570	4.59	0.36	[104]
SDSS-DR11	0.590	4.39	0.33	[104]
SDSS-DR11	0.610	3.85	0.31	[104]
SDSS-DR11	0.630	3.90	0.43	[104]
SDSS-DR11	0.650	3.55	0.16	[104]
SDSS-DR12Q	2.225	1.77	0.31	[103]

be obtained from Sunyaev-Zel'dovich (SZ) effect in clusters of galaxies. The existing measurements at high redshifts still have large error bars and the majority of the points can be only treated as upper limits. However, in the near future, with high resolution spectroscopy with larger telescopes, the precision of these measurements can be competitive with local interstellar data. For the last data point of Table 2.3 we compute the error as

$$\sigma_T(z=3.025) = \sqrt{\frac{\sigma_u^2+\sigma_d^2}{2}} = 2.562, \tag{2.24}$$

where σ_i is the error on the temperature estimates and N is the number of the observational data used.

Since our χ^2 has a quadratic form

$$\chi^2_T = \sum_i^{N_T} \left(\frac{T_i - T^{th}(z_i)}{\sigma_{T_i}} \right)^2, \tag{2.25}$$

where $\mathrm{T}^{\mathrm{th}}(z) = \mathrm{T}_0\tilde{\mathrm{T}}(z)$ and $\tilde{\mathrm{T}}(z)$ is the dimensionless temperature, we can minimize the χ^2 analytically over T_0 finding

$$\chi^2_T = A - \frac{B^2}{\Gamma}, \tag{2.26}$$

$$T_0 = \frac{B}{\Gamma}, \tag{2.27}$$

where the parameters A, B and Γ are defined as

$$A = \sum_i^{N_T} \left(\frac{T_i}{\sigma_{T_i}} \right)^2, \tag{2.28}$$

$$B = \sum_i^{N_T} \frac{T_i\ \tilde{\mathrm{T}}(z_i)}{\sigma^2_{T_i}}, \tag{2.29}$$

$$\Gamma = \sum_i^{N_T} \left(\frac{\tilde{\mathrm{T}}(z_i)}{\sigma_{T_i}} \right)^2. \tag{2.30}$$

Table 2.3: Compilation of the CMB temperature-redshift relation T(z) measurements used in this analysis and related references. We used 37 data points.

z	T(K)	Ref.	z	T(K)	Ref.
0.000	2.72548 ± 0.00057	[108]	0.072	2.931 ± 0.017	[114]
0.023	2.72 ± 0.10	[109]	0.125	3.059 ± 0.032	[114]
0.152	2.90 ± 0.17	[109]	0.171	3.197 ± 0.030	[114]
0.183	2.95 ± 0.27	[109]	0.220	3.288 ± 0.032	[114]
0.200	2.74 ± 0.28	[109]	0.273	3.416 ± 0.038	[114]
0.202	3.36 ± 0.20	[109]	0.322	3.562 ± 0.050	[114]
0.216	3.85 ± 0.64	[109]	0.377	3.717 ± 0.063	[114]
0.232	3.51 ± 0.25	[109]	0.428	3.971 ± 0.071	[114]
0.252	3.39 ± 0.26	[109]	0.471	3.943 ± 0.112	[114]
0.282	3.22 ± 0.26	[109]	0.525	4.380 ± 0.119	[114]
0.291	4.05 ± 0.66	[109]	0.565	4.075 ± 0.156	[114]
0.451	3.97 ± 0.19	[109]	0.618	4.404 ± 0.194	[114]
0.546	3.69 ± 0.37	[109]	0.676	4.779 ± 0.278	[114]
0.550	4.59 ± 0.36	[109]	0.718	4.933 ± 0.371	[114]
2.418	9.15 ± 0.72	[110]	0.777	4.515 ± 0.621	[114]
1.777	7.20 ± 0.80	[111]	0.870	5.356 ± 0.617	[114]
1.973	7.9 ± 1	[112]	0.972	5.813 ± 1.025	[114]
2.338	10 ± 4	[113]	3.025	$12.1^{+1.7}_{-3.2}$	[115]
0.037	2.888 ± 0.039	[114]			

2.2 Large Scale Structure

2.2.1 The growth-rate data

The growth-rate $f\sigma_8$ compilation used in our analysis is given in Table I of Ref. [116], where the authors analyzed different subsets in the data and implemented Bayesian model comparison to test the internal robustness of the dataset. For convenience this compilation can also be found in Table 2.4. These data are obtained via the redshift-space distortions and in fact determine the combination $f\sigma_8(a) \equiv f(a) \cdot \sigma(a)$, which is a product of the growth rate $f(a) = \frac{dln\delta}{dlna}$ and the redshift-dependent rms fluctuations $\sigma(a) = \sigma_{8,0}\frac{\delta(a)}{\delta(1)}$ of the linear density field within spheres of radius $R = 8h^{-1}$Mpc. In this notation the parameter $\sigma_{8,0}$ is the value of the rms fluctuations today and is a direct measure of the amplitude of fluctuations in linear scales. The value of $f\sigma_8(a)$ can be directly determined from the ratio of the monopole to the quadrupole of the redshift-space power spectrum $P(k)$, which depends on the parameter $\beta = f/b_0$, where b_0 is the galaxy bias [117–119] and f is the growth rate assuming linear theory [117–119]. It can be shown that $f\sigma_8(a)$ is independent of the bias, as the latter completely cancels out from the previous expression.

Moreover, $f\sigma_8(a)$ has been shown to be a good discriminator of DE models [118]. For more details on the covariance matrix of the data and how to correct for the Alcock-Paczynski effect see Refs. [116], [120] and [121]. The advantage of using the combination $f\sigma_8$, instead of just the growth-rate $f(z)$, is that the former is directly associated to the power spectrum of peculiar velocities of galaxies [122].

To be more specific, the growth rate data set is constructed on the Gold-2017 compendium from [120] which has 18 independent measurements of $f\sigma_8(z)$, derived from redshift space distortion measurements from several surveys. Among these surveys, we note that the three WiggleZ [80]

Table 2.4: Compilation of the $f\sigma_8(z)$ data points used in the analysis along with the reference matter density parameter Ω_{m_0} which is needed for the growth correction.

z	$f\sigma_8(z)$	$\sigma_{f\sigma_8}(z)$	$\Omega_{m,0}^{\rm ref}$	Ref.
0.02	0.428	0.0465	0.3	[124]
0.02	0.398	0.065	0.3	[125], [126]
0.02	0.314	0.048	0.266	[127], [126]
0.10	0.370	0.130	0.3	[128]
0.15	0.490	0.145	0.31	[129]
0.17	0.510	0.060	0.3	[118]
0.18	0.360	0.090	0.27	[130]
0.38	0.440	0.060	0.27	[130]
0.25	0.3512	0.0583	0.25	[131]
0.37	0.4602	0.0378	0.25	[131]
0.32	0.384	0.095	0.274	[132]
0.59	0.488	0.060	0.307115	[133]
0.44	0.413	0.080	0.27	[80]
0.60	0.390	0.063	0.27	[80]
0.73	0.437	0.072	0.27	[80]
0.60	0.550	0.120	0.3	[134]
0.86	0.400	0.110	0.3	[134]
1.40	0.482	0.116	0.27	[135]
0.978	0.379	0.176	0.31	[136]
1.23	0.385	0.099	0.31	[136]
1.526	0.342	0.070	0.31	[136]
1.944	0.364	0.106	0.31	[136]

measurements are correlated, and their covariance matrix is given by

$$\mathbf{C}_{\rm WiggleZ} = 10^{-3} \begin{pmatrix} 6.400 & 2.570 & 0.000 \\ 2.570 & 3.969 & 2.540 \\ 0.000 & 2.540 & 5.184 \end{pmatrix}. \tag{2.31}$$

We also include four measurements from SDSS [123]. These points have a covariance matrix given by

$$\mathbf{C}_{\rm SDSS\text{-}IV} = 10^{-2} \begin{pmatrix} 3.098 & 0.892 & 0.329 & -0.021 \\ 0.892 & 0.980 & 0.436 & 0.076 \\ 0.329 & 0.436 & 0.490 & 0.350 \\ -0.021 & 0.076 & 0.350 & 1.124 \end{pmatrix}. \tag{2.32}$$

Hence our data set has $N = 22$ data points. This compilation was also used in Ref. [137], to place constraints on the dark-matter pressure, sound speed and viscosity. Some other compilations also exist in the literature (see Refs. [121, 138, 139]) but these contain duplicate points coming from the same surveys but in different years, as the goal of their analysis was to study the evolution of the $f\sigma_8$ tension over time. Here we will only focus on the compilation given in Table 2.4, as these points are unique and their statistical robustness has already been confirmed [116]. In Table 2.4 the RSD data points are given in different redshifts as $f\sigma_8^{\rm obs,i} = \left(f\sigma_8^{\rm obs}(z_1), \ldots, f\sigma_8^{\rm obs}(z_n)\right)$, while the theoretical prediction is given by $f\sigma_8^{\rm th}(\boldsymbol{\theta}_p) = \left(f\sigma_8^{\rm th}(z_1), \ldots, f\sigma_8^{th}(z_n)\right)$, which depends on the

Table 2.5: The $E_{\rm g}$ data used in this analysis as compiled by Refs. [145] and [139]. Note that some of the points in the previous references were duplicates as they come from the same surveys, albeit with combinations of different external probes, so we use only one of the measurements to avoid strong correlations. Here we only show the points we used in the analysis.

z	$E_{\rm g}$	$\sigma_{E_{\rm g}}$
0.267	0.43	0.13
0.270	0.40	0.05
0.305	0.27	0.08
0.320	0.40	0.09
0.554	0.26	0.07
0.570	0.30	0.07
0.600	0.16	0.09
0.860	0.09	0.07

cosmological model and the parameters θ_p. Note however, that some of the points are correlated with each other, and they also assume a fiducial cosmology that has to be corrected for due to the Alcock-Paczynski effect; see Refs. [116, 120, 121], and for earlier analyses see Refs. [140–142]. We give the values of the Ω_{m0} parameter for the fiducial flat ΛCDM model used in the fourth column of Table. 2.4.

2.2.2 The E_g data

The flat Friedmann-Lemaitre-Robertson-Walker (FLRW) metric, which can describe accurately the geometry of the Universe, reads $ds^2 = -(1+2\Psi)dt^2 + a(t)^2(1-2\Phi)dx^2$, where a is the scale factor and Ψ and Φ are the two scalar gravitational potentials. Then the gravitational slip, can be defined as the ratio of the gravitational potentials $\eta_{\rm DE} = \frac{\Phi}{\Psi}$, which in GR is equal to unity. These potentials satisfy the two Poisson equations in Fourier space:

$$-\frac{k^2}{a^2}(\Phi+\Psi) = 4\pi G_{\rm N}\Sigma(k,a)\rho_m\delta_m, \tag{2.33}$$

$$-\frac{k^2}{a^2}\Psi = 4\pi G_{\rm N}\mu(k,a)\rho_m\delta_m, \tag{2.34}$$

where $G_{\rm N}$ is the bare Newton's constant, while Σ and μ parameterize deviations in GR. In the case of GR these parameters have the value $\Sigma = 2$ and $\mu = 1$.

In order to test the aforementioned relations, the $E_{\rm g}$ statistic was created, aiming for it to be bias independent at linear order [143, 144]. The $E_{\rm g}$ test can be expressed as the expectation value of the ratio of lensing and galaxy clustering observables at a scale k as follows

$$E_{\rm g} = \left\langle \frac{a\nabla^2(\Psi+\Phi)}{3H_0^2 f\delta_m} \right\rangle. \tag{2.35}$$

To derive the gravitational slip in a model independent way, which it would be of interest to us on Chapter 12, we reconstruct two quantities through the $E_{\rm g}$ and $f\sigma_8$ data. The first quantity is $P_2(z)$ which is defined as $P_2 = \frac{\Omega_{\rm m,0}\Sigma}{f}$ and depends on the lensing potential and the growth rate. In GR this reduces to $P_2 = \frac{2\Omega_{\rm m,0}}{f}$, which implies that in GR we have $E_{\rm g} = \frac{\Omega_{\rm m,0}}{f}$. In general, $E_{\rm g}$ can be related to the P_2 statistic of Ref. [145] via $P_2 = 2E_{\rm g}$. The second quantity is P_3, expressed as $P_3 = \frac{(f\sigma_8(z))'}{f\sigma_8(z)}$, where the prime is the derivative with respect to $\ln a$. Then, the gravitational

slip can be derived in a model independent way as [145]

$$\eta_{\rm DE}(z) = \frac{3P_2(z)(1+z)^3}{2E(z)^2\left(P_3(z)+2+\frac{E'(z)}{E(z)}\right)} - 1, \tag{2.36}$$

where $E(z) \equiv H(z)/H_0$. The exact data points we used are given in Table 2.5 for completeness. Note that in our reconstruction we will use directly $E(z)$ so for this particular expression no value for H_0 is needed.

Part II

Modified Gravity Theories

3

Motivation: The Need to Go Beyond

Once we accept our limits, we go beyond them.
Albert Einstein

General Relativity (GR) is one of the most elegant and well-tested theories that we have and surprisingly, it remains almost unchanged after more than one century. The need of Modified Gravity (MG) theories, as a substitute to GR is motivated by both theoretical fundamental physics and cosmological observations [146]. From the theoretical point of view a quantum theory of gravity that describes space-time is still absent. For instance, it is well known that the Einstein-Hilbert (EH) action is not renormalizable at more than 2 loops and therefore cannot be conventionally quantized. In fact, this action needs to be supplemented by higher order terms in order for the resultant theory to be one-loop renormalizable [147, 148]. It has been shown [149–151] that when quantum loop corrections in field theory or higher order corrections in the low energy string dynamics are considered, the effective low energy gravitational action includes higher order curvature invariants. For example, when renormalizing GR to first loop order the Ricci scalar is modified as [149]

$$R \longrightarrow a_0(g_{\mu\nu})R + a_1(g_{\mu\nu}) + a_2(g_{\mu\nu}), \tag{3.1}$$

where

$$a_0(g_{\mu\nu}) = 1, \tag{3.2}$$

$$a_1(g_{\mu\nu}) = \left(\frac{1}{6} - \xi\right) R, \tag{3.3}$$

$$a_2(g_{\mu\nu}) = \frac{1}{180} R_{\alpha\beta;\delta} R^{\alpha\beta;\delta} - \frac{1}{180} R^{\alpha\beta} R_{\alpha\beta} - \frac{1}{6}\left(\frac{1}{5} - \xi\right) \Box R + \frac{1}{2}\left(\frac{1}{6} - \xi\right)^2 R^2. \tag{3.4}$$

The function $a_1(g_{\mu\nu})$ is related to the conformal coupling and $a_2(g_{\mu\nu})$ represents the Gauss Bonnet term and higher order correction to GR, which only contains terms with up to second derivatives of the metric. Hence, from the theoretical point of view, modifications of gravity are naturally expected when one tries to normalize GR as a perturbative field theory.

From the observational cosmological side, GR supplemented with the standard model of particle physics cannot account for the primordial accelerated expansion of the Universe necessary to solve the horizon and flatness problems. Also at large scales, there exists an undergoing phase of accelerated expansion caused by a repulsive force which GR itself cannot explain. The simplest explanation is the inclusion of a cosmological constant leading to a unified description for the formation and evolution of the Universe within the framework of GR, known as the standard Λ cold dark matter model (ΛCDM), that contains only six free parameters describing the matter and dark energy (DE) content of the Universe and could alleviate several problems in the Cold Dark Matter (CDM) scenario [152]. This model is so far the best phenomenological fit to the data [1, 153, 154], yet there exists also plenty of other models that could account for the accelerated

expanding Universe without the need of a cosmological constant Λ, whose nature still remains unknown.

The yet unsolved cosmological constant problem has driven an effort towards alternative explanations for the late-time accelerating phase of the Universe. In general, it is considered that there are two main approaches [155] to provide a physical description for the problem of dark matter and dark energy. One option is to keep GR and consider the existence of new fields in nature in order to describe the observations [156]. A more physical explanation could be that GR is not a good approximation to the effects of gravity at large scales; on scales larger than that of galaxy clusters ($\sim$ 10Mpc). This has led to the study of modified gravity models, see for example [157]. These are covariant geometric theories that account the observed accelerated expansion of the Universe to higher order curvature invariants that turn gravity into a repulsive interaction in the later times of the Universe age, but have undetectable effects at scales of the solar system (few AUs). They are usually formulated as covariant modifications to Einstein's theory of general relativity and provide a more credible and realistic alternative to ad-hoc models of dark energy and dark matter, as they can be motivated from high energy physics, see Refs. [158–163]. These modifications of GR are however not easily achieved as several tests carried out up to extragalactic scales are in very good agreement with GR [164, 165].

On the other hand, there exist Dark Energy (DE) models [5] where yet unobserved scalar fields would dominate the energy content at late times, avoiding fine-tuning issues as well as accelerating the Universe [166, 167]. Hence, in the case of modification with a scalar field, the common description to consider dark energy and modified gravity together is called scalar-tensor theory, been the Horndeski's theory an example. Both DE and MG models provide plausible, alternative scenarios for explaining the late-time acceleration of the Universe. It is known that both kinds of models can fit background astrophysical observations, as well as the standard model ΛCDM. These models are therefore degenerated at the background level despite several efforts to disentangle them with model independent approaches [168, 169]. Although the recent discovery of gravitational waves by the LIGO Collaboration [170] allows us to rule out some families of MG models [171–180] (e.g., from the so-called Horndeski theories[1] [182]), there remains a degeneracy between the two leading approaches.

Current and upcoming surveys will require sub-percent agreement in theoretical accuracy to test the different cosmological and gravity scenarios. Given the plethora of gravity models, it is crucial to have a standardized unified way to describe all of them and take them into account in Boltzmann solvers, i.e. codes that solve the linear evolution of cosmological perturbations, or in other words, the linearized Einstein and Boltzmann equations on an expanding background [183]. A critical aspect of this attempt is to be able to accurately compute a wide range of observables from the cosmological models, where current and coming surveys such as Euclid [2], LSST [3], WFIRST [4], SKA [5], and Stage 4 CMB [6] experiments will require sub-percent agreement in theoretical accuracy to test these different scenarios. The dynamics of cosmological perturbations, which have been extensively studied [184, 185], are governed by the coupled Boltzmann equations for radiative and matter species and Einstein equations for the metric. There exists already publicly-available Boltzmann codes that compute the CMB polarization, temperature, and matter power spectra, e.g., the Code for Anisotropies in the Microwave Background (CAMB) [186], and the Cosmic Linear Anisotropy Solving System (`CLASS`) [187] which are tested over a large range of cosmological parameters and are considered to be accurate to the sub-percent level. Among others, these codes are capable to probe different gravitational theories and their cosmological consequences, test models with current data and can help in the establishment of future experiments [188]. However,

[1] However, a recent work claims that the reduction of viable MG models is not as severe as previously announced [181].

[2] https://www.euclid-ec.org/

[3] https://www.lsst.org/

[4] https://wfirst.gsfc.nasa.gov/

[5] http://skatelescope.org/

[6] https://cmb-s4.org/

it is very difficult to take into account all the wide range of gravity models at a technical level and introduce them in an Boltzmann code since each model has its own structure, equations and parameters.

On Chapters 4 and 5 we fill this gap and present the effective fluid approach, see also Refs. [9, 10], which allows to map any modified gravity model as an effective dark energy fluid and then we show how to implement it in the Boltzmann solver code `CLASS` in a simple and straightforward way finding competitive results in a much simpler and less error-prone approach. This method has also the advantage that only a handful of variables are needed to compute to describe the fluid [189], i.e the equation of state $w(a)$ at the background level, the pressure perturbation $\delta P(a,k)$ or equivalently the sound speed $c_s^2(a,k)$, and the anisotropic stress $\sigma(a,k)$ at the linear perturbation. Let us recall that for the ΛCDM model ($w(a) = -1$, $\sigma(a,k) = 0$). This fluid approach makes easy the identification with well known single-field DE models like quintessence ($w(a) \geq -1$, $c_s^2 = 1$, $\sigma(a,k) = 0$) and K-essence ($w(a)$, $c_s^2(a)$, $\sigma(a,k) = 0$), where deviations from a non-zero anisotropic stress, which could be detected from weak-lensing [190], would exclude all standard DE models with a single field and would imply deviations from GR or if neglected, it could bias the cosmological parameters inferred from the data [191].

As we will see in the following chapters, although DE and MG models are certainly stimulated by different underlying physics, it is possible to study both kind of models on the same footing. In an effective fluid approach deviations from GR can be understood as an effective fluid contribution in such a way that comparison with DE models might become relatively simple [192–196]. Since both DE and MG models predict different behavior for these three functions, in an effective fluid approach different models can be, to a certain degree, distinguished.

The main idea of the effective fluid approach is to map any MG model to an effective DE fluid by rewriting the MG theory as GR plus an effective dark energy fluid. In order to do that one must write down the equations of motion of the MG model of interest, extract the Einstein tensor $G_{\mu\nu}$ and other matter components and what remains is defined as an effective dark energy fluid through the energy momentum tensor as

$$\kappa T^{(DE)}_{\mu\nu} = G_{\mu\nu} - \kappa T^{(m)}_{\mu\nu}, \tag{3.5}$$

where $\kappa = 8\pi G_N$ is a constant with G_N being the bare Newton's constant and $T^{(m)}_{\mu\nu}$ is the energy-momentum tensor for the matter fields. The main advantages of the effective fluid approach are that it makes it easier to include in Boltzmann codes, since they are written as GR plus a dark energy fluid, and it provides better physical intuition as one may compute compute dark energy perturbation quantities both at the background and at the linear perturbation level. In what follows we will apply the effective fluid approach to $f(R)$ theories (see Chapter 4) and a surviving class of Horndeski models (see Chapter 5) where we will also present the designer Horndeski (HDES) which has a background exactly equal to the standard cosmological model ΛCDM but at the perturbation level it has different signatures.

4

Unraveling the effective fluid approach for $f(R)$ models in the subhorizon approximation

The original content of this chapter is based on Ref. [9]. We provide explicit formulas for the effective fluid approach of $f(R)$ theories, such as the Hu & Sawicki and the designer models. Using the latter and simple modifications to the `CLASS` code, which we call `EFCLASS`, in conjunction with very accurate analytic approximations for the background evolution, we obtain competitive results in a much simpler and less error-prone approach. We also derive the initial conditions in matter domination and we find they differ from those already found in the literature for a constant w model. A clear example is the designer model that behaves as ΛCDM in the background, but has nonetheless dark energy perturbations. We then use the aforementioned models to derive constraints from the latest cosmological data, including supernovae, BAO, CMB, $H(z)$ and growth-rate data, and find they are statistically consistent to the ΛCDM model. Finally, we show that the viscosity parameter c^2_{vis} in realistic models is not constant as commonly assumed, but rather evolves significantly over several orders of magnitude, something which could affect forecasts of upcoming surveys.

4.1 Introduction

As discussed previously In Chapter 3, among the remaining MG models one finds an important class: $f(R)$ models [197–200]. Even though this kind of model might be fully degenerated at the background level (e.g., the so-called designer $f(R)$ models which can exactly mimic the background dynamics of a dark energy model with equation of state $w(z)$ [201–204]), the linear order perturbations could in principle be distinguishable from ΛCDM [205]. This is relevant as in general the DE perturbations can have a strong effect in the determination of the growth-index γ [206], even though with current growth data it is not possible to draw definite conclusions in favor of any $f(R)$ model [207, 208].

The study of perturbations in MG models is thus of great importance and one can find different approaches in the literature (e.g., [192, 193, 202, 203, 205, 209–224]). In Ref. [225] the authors restricted themselves to background histories consistent with a flat ΛCDM model and parameterized changes in both Poisson and anisotropy equations via two functions $\mu(a, k)$ and $\gamma(a, k)$; these two functions take into account possible deviations from GR in the relation between the Newtonian potentials as well as the relation between the potentials and matter perturbations. The parametric functions were implemented in a modified version of the code CAMB[1] [186] dubbed `MGCAMB`.[2] Since these parameterizations are only valid at late times, in Ref. [226] the authors modified `MGCAMB` to introduce new parameterizations which are valid at all times. A drawback in this approach to perturbations in MG models is that it fixes the background to ΛCDM while it is known that viable $f(R)$ models might differ from ΛCDM at the background level (e.g., Hu-Sawicki

[1] https://camb.info/

[2] http://aliojjati.github.io/MGCAMB/home.html

model [209]).

A different approach to study perturbations in MG models was carried out in Ref. [227] where the author studied perturbations in $f(R)$ models which exactly mimic the ΛCDM background by using the full set of covariant cosmological perturbation equations; the author modified the publicly available code CAMB, implemented this approach, and released a code called `FRCAMB`. [3] In Ref. [228] the author extended `FRCAMB` to take into account $f(R)$ models with a background different from ΛCDM; the code has not been released.

An Effective Field Theory (EFT) approach [7] to DE and MG models was pursued in Ref. [8] where authors had into account a fairly general theory with unbroken symmetries and implemented it in a code called `EFTCAMB`[4] (i.e., a modified version of CAMB). Although this approach does not use any quasi-static approximation and evolves the full dynamics of perturbations on linear scales, the mapping of specific models into an EFT formalism might be cumbersome.

The Planck Collaboration used `MGCAMB` and `EFTCAMB` in Ref. [229] to study cosmological constraints in both DE and MG models. Although the results depend on which data sets are regarded as well as on some assumptions (e.g., the equation of state $w(a)$, the sound speed $c_s^2(a,k)$, the anisotropic stress $\sigma(a,k)$), the authors did not find conclusive evidence for extensions to the standard model of cosmology.[5]

In Ref. [231] authors proposed the so-called Equation of State (EOS) approach for perturbations. In this approach $f(R)$ models can be expressed as a dark energy fluid at background and linearized perturbation order [192, 193], see also [194–196]. The authors used an elegant gauge-invariant formalism, without the sub-horizon approximation, where the modifications to GR are expressed as equation of state $w(a)$, entropy perturbation $\Gamma(a,k)$, and anisotropic stress $\Pi(a,k)$. The EOS approach was implemented in a modified version of the code `CLASS`[6] [232] in Ref. [233] where good agreement with previous studies and codes was found. In spite of addressing the problem of perturbations in $f(R)$ models in an elegant way, the EOS approach is not physically very intuitive: the interpretation of results and the perturbation variables in this formalism is not straightforward.

In this chapter we will also express $f(R)$ models as a dark energy fluid, but differently to the EOS approach in [231], as we will utilize the equation of state $w(a)$, the sound speed $c_s^2(a,k)$ and the anisotropic stress $\sigma(a,k)$ as variables describing the fluid [189]. This makes the comparison with popular DE models such as quintessence ($w(a) \geq -1$, $c_s^2 = 1$, $\sigma(a,k) = 0$) and K-essence ($w(a)$, $c_s^2(a)$, $\sigma(a,k) = 0$) relatively easy. This is of paramount importance in the case of the anisotropic stress because in $f(R)$ models generically one has $\sigma(a,k) \neq 0$ whereas in standard single-field DE models $\pi(a,k) = 0$, so that any convincing evidence of anisotropic stress would rule out all standard single-field DE models [189, 234]. Likewise, non-detection of anisotropic stress would get several classes of MG models into tensions with observations.

Since current galaxy surveys do not reach scales comparable to the cosmological horizon, one frequently uses a quasi-static approximation for the perturbation equations. The quasi-static approximation roughly amounts to neglecting time derivatives in the linearized Einstein equations while only keeping spatial derivatives; in addition one only takes into account modes whose wavelength is shorter than the cosmological horizon. Some previous studies and implementations (i.e. `FRCAMB`, `EFTCAMB`, `CLASS_EOS_FR`) did not apply the sub-horizon approximation to the perturbation equations. Nevertheless, the quasi-static approximation has been investigated in the context of MG theories in Refs. [12, 213] and has been implemented in `MGCAMB`. On the one hand, in Ref. [213] authors argue that general $f(R)$ models do not satisfy the quasi-static approximation; however, the sub-horizon approximation can be safely used in $f(R)$ models describing the current phase of accelerating expansion and fulfilling solar system tests.

[3] http://darklight.fisica.unimi.it/cosmonews/frcamb/

[4] http://eftcamb.org/

[5] However, in Ref. [230] authors found evidence for deviations of GR ($\gtrsim 3\sigma$) using various astronomical observations, including data from Planck.

[6] http://class-code.net/

On the other hand, in Ref. [12] authors argue that the quasi-static approximation breaks down outside the DE sound-horizon $k \ll k_J$, where $k_J(z) \equiv \frac{H(z)}{(1+z)c_s}$ is the physical Jeans scale, rather than outside the cosmological horizon; the authors disregarded the anisotropic stress in their analysis and also consider a constant DE sound speed c_s^2, both assumptions being not realistic for viable MG models. In this Chapter we will work out solutions to the perturbations equations in $f(R)$ models under the sub-horizon approximation. We will derive analytical solutions for DE perturbations and test them numerically showing that the quasi-static approximation actually performs quite well for this kind of MG model.

By placing MG and DE models on the same framework one is, in principle, able to disentangle the two kinds of models through different predictions for the equation of state $w(a)$, the sound speed $c_s^2(a,k)$, and the anisotropic stress $\sigma(a,k)$. Both DE sound speed and DE anisotropic stress are particularly important because they are closely related to the growth of structures and, therefore, might leave detectable traces in observables such as anisotropies in the Cosmic Microwave Background radiation (CMB) and Galaxy Counts (GC) [205, 235]. Although DE and Dark Matter (DM) perturbations are invisible, they affect both the CMB and the GC via, for instance, the integrated Sachs-Wolfe (ISW) effect and the lensing potential [192]. While the presence of DE anisotropic stress can enhance and stabilize the growth of matter perturbations [234–238], the DE sound speed might alter the level of clustering and the evolution of matter perturbations [239–241]. These properties are very important because one can use them to break background level degeneracies among different models [242, 243].

The most recent CMB data from the Planck satellite[7] as well as data from the Dark Energy Survey[8] are in good agreement with the standard cosmological model ΛCDM [1, 154], but this situation could potentially change by combining different probes and from upcoming galaxy surveys, stage IV CMB experiments, and gravitational wave observations (see, for instance, Refs. [48,178,244–250,250–263]). Despite the success of the ΛCDM model when fitting current data sets, its Bayesian evidence[9] is not extremely different from extended models [2, 266]. Furthermore, there remain unexplained issues with other data sets such as direct Hubble constant measurements, weak lensing data, and cluster counts where dynamically DE models or MG models could play a part (see, for instance, Refs. [2, 235, 267–275]).

This Chapter is organized as follows. In Sec. 4.2 we discuss the standard equations for perturbations in a Friedmann-Lemaitre-Robertson-Walker (FLRW) metric. First, in Subsection 4.2.1, we explain how $f(R)$ models can be mapped into a DE fluid and give analytical solutions for DE perturbations in general $f(R)$ models under the sub-horizon approximation. Secondly, we present results for some viable $f(R)$ models in Subsection 4.2.2. In Sec. 4.3 we show that our analytical solutions derived using the sub-horizon are in very good agreement with a full numerical evolution of the perturbation equations. Furthermore, we compare our implementation in the `CLASS` code with available codes such as `MGCAMB`, `CLASS_EOS_FR`, and `FRCAMB`. In Sec. 4.4 we clarify and discuss some points about viscosity in viable $f(R)$ models. Then, in Sec. 4.5 we present cosmological constraints for a few MG models within our methodology by using a Monte Carlo Markov Chain (MCMC) approach. We conclude in Sec. 4.6 and give details about our analytical computations and `CLASS` implementation in Appendices A.1 and A.2, respectively.

4.2 Theoretical framework

Let us assume that the Universe can be described at the background level by a FLRW metric, then in order to study the perturbations of various cosmological models, we consider the perturbed FLRW metric, which in the conformal Newtonian gauge can be written as:

$$ds^2 = a(\tau)^2 \left[-(1+2\Psi(\vec{x},\tau))d\tau^2 + (1-2\Phi(\vec{x},\tau))d\vec{x}^2\right], \tag{4.1}$$

[7] http://sci.esa.int/planck/

[8] https://www.darkenergysurvey.org/

[9] See, for instance, Refs. [264, 265] for a discussion about Bayesian evidence in cosmology.

where τ is the conformal time defined via $d\tau = dt/a(t)$ and we will follow the notation of Ref. [185].[10] At this point we can assume an ideal fluid with an energy momentum tensor

$$T^{\mu}_{\nu} = P\delta^{\mu}_{\nu} + (\rho + P)U^{\mu}U_{\nu}, \tag{4.2}$$

where ρ, P are the fluid density and pressure, while $U^{\mu} = \frac{dx^{\mu}}{\sqrt{-ds^2}}$ is its velocity four-vector given to first order by $U^{\mu} = \frac{1}{a(\tau)}(1-\Psi, \vec{u})$, which as can easily be seen satisfies $U^{\mu}U_{\mu} = -1$. Furthermore, $\vec{u} = \dot{\vec{x}}$, where $\dot{f} \equiv \frac{df}{d\tau}$, and the elements of the energy momentum tensor to first order of perturbations are given by:

$$\begin{aligned} T^0_0 &= -(\bar{\rho} + \delta\rho), & (4.3)\\ T^0_i &= (\bar{\rho} + \bar{P})u_i, & (4.4)\\ T^i_j &= (\bar{P} + \delta P)\delta^i_j + \Sigma^i_j, & (4.5) \end{aligned}$$

where $\bar{\rho}, \bar{P}$ are defined on the background and are functions of time only, while the perturbations $\delta\rho, \delta P$ are functions of $(\vec{x}, \tau)$ and $\Sigma^i_j \equiv T^i_j - \delta^i_j T^k_k/3$ is an anisotropic stress tensor.

Then, assuming GR we find that the perturbed Einstein equations in the conformal Newtonian gauge are given by [185]:

$$k^2\Phi + 3\frac{\dot{a}}{a}\left(\dot{\Phi} + \frac{\dot{a}}{a}\Psi\right) = 4\pi G_N a^2 \delta T^0_0, \tag{4.6}$$

$$k^2\left(\dot{\Phi} + \frac{\dot{a}}{a}\Psi\right) = 4\pi G_N a^2(\bar{\rho} + \bar{P})\theta, \tag{4.7}$$

$$\ddot{\Phi} + \frac{\dot{a}}{a}(\dot{\Psi} + 2\dot{\Phi}) + \left(2\frac{\ddot{a}}{a} - \frac{\dot{a}^2}{a^2}\right)\Psi + \frac{k^2}{3}(\Phi - \Psi) = \frac{4\pi}{3}G_N a^2 \delta T^i_i, \tag{4.8}$$

$$k^2(\Phi - \Psi) = 12\pi G_N a^2(\bar{\rho} + \bar{P})\sigma, \tag{4.9}$$

where we have defined the velocity $\theta \equiv ik^j u_j$, the anisotropic stress $(\bar{\rho} + \bar{P})\sigma \equiv -(\hat{k}_i\hat{k}_j - \frac{1}{3}\delta_{ij})\Sigma^{ij}$. We also need the evolution equations for the perturbations, given by the energy-momentum conservation $T^{\mu\nu}_{;\nu} = 0$ as:

$$\dot{\delta} = -(1+w)(\theta - 3\dot{\Phi}) - 3\frac{\dot{a}}{a}\left(c_s^2 - w\right)\delta, \tag{4.10}$$

$$\dot{\theta} = -\frac{\dot{a}}{a}(1-3w)\theta - \frac{\dot{w}}{1+w}\theta + \frac{c_s^2}{1+w}k^2\delta - k^2\sigma + k^2\Psi, \tag{4.11}$$

where we define the equation of state parameter $w \equiv \frac{\bar{P}}{\bar{\rho}}$ and the rest-frame sound speed of the fluid $c_s^2 \equiv \frac{\delta P}{\delta\rho}$. Following Ref. [235], we eliminate θ from Eqs. (4.10) and (4.11), resulting in a second order equation for δ:

$$\begin{aligned} \ddot{\delta} \;+\; & (\cdots)\dot{\delta} + (\cdots)\delta = -k^2\left((1+w)\Psi + c_s^2\delta - (1+w)\sigma\right) + \cdots \\ = \; & -k^2\left((1+w)\Psi + c_s^2\delta - \frac{2}{3}\pi\right) + \cdots, \end{aligned} \tag{4.12}$$

where the $(\cdots)$ indicates the presence of complicated expressions and we have defined the anisotropic stress parameter of the fluid as $\pi \equiv \frac{3}{2}(1+w)\sigma$. As also discussed in Ref. [235] the k^2 term will act as a source, driving the perturbations. However, since the potential scales as $\Psi \sim 1/k^2$ in relevant

[10] In more detail, our conventions are: (-+++) for the metric signature, the Riemann and Ricci tensors are given by $V_{b;cd} - V_{b;dc} = V_a R^a_{bcd}$ and $R_{ab} = R^s_{asb}$, while the Einstein equations are $G_{\mu\nu} = +\kappa T_{\mu\nu}$ for $\kappa = \frac{8\pi G_N}{c^4}$ and G_N is the bare Newton's constant. In what follows we will set the speed of light $c = 1$.

scales, the only terms that matter are the sound speed and the anisotropic stress. Therefore, we can define an effective sound speed as

$$c^2_{s,eff} = c^2_s - \frac{2}{3}\pi/\delta, \tag{4.13}$$

that characterizes the propagation of perturbations as well as the clustering properties on sub-horizon scales. We should also note that in principle the sound speed c^2_s can be both time and scale dependent, i.e., $c^2_s = c^2_s(\tau, k)$. For example, as noted in Ref. [276], the sound speed for a scalar field ϕ in the conformal Newtonian gauge for small scales is $c^2_{s,\phi} \simeq \frac{k^2}{4a^2m^2_\phi}$, where m_ϕ is the mass of the scalar field. On the other hand, c^2_s is equal to one only in the scalar field's rest-frame (see Chapter 11.2 of Ref. [276] for a quick derivation). Of course, one has the same situation in $f(R)$ theories because in practice they only contain a scalar degree of freedom[11] [12]. Therefore, we expect the sound speed to be scale dependent in modified gravity models, when we are not in the rest frame of the equivalent DE fluid.

Finally, in what follows we will use the scalar velocity perturbation $V \equiv ik_jT^j_0/\rho = (1+w)\theta$ instead of the velocity θ. The former has the advantage that it can remain finite when the equation of state w of the fluid crosses -1 (see also Ref. [278]). With this new variable the evolution equations, Eqs. (4.10)-(4.11), become

$$\delta' = 3(1+w)\Phi' - \frac{V}{a^2H} - \frac{3}{a}\left(\frac{\delta P}{\bar{\rho}} - w\delta\right), \tag{4.14}$$

$$V' = -(1-3w)\frac{V}{a} + \frac{k^2}{a^2H}\frac{\delta P}{\bar{\rho}} + (1+w)\frac{k^2}{a^2H}\Psi - \frac{2}{3}\frac{k^2}{a^2H}\pi, \tag{4.15}$$

where the prime $'$ is a derivative with respect to the scale factor a and $H(t) = \frac{da/dt}{a}$ is the Hubble parameter.

4.2.1 The f(R) models and the effective fluid approach

In this set up we can study a plethora of MG models either directly as in Ref. [205] or as an effective DE fluid [231]. For example, in the case of the $f(R)$ models, the modified Einstein-Hilbert action reads:

$$S = \int d^4x\sqrt{-g}\left[\frac{1}{2\kappa}f\left(R\right) + \mathcal{L}_m\right], \tag{4.16}$$

where $\mathcal{L}_m$ is the Lagrangian of matter and $\kappa = 8\pi G_N$ is a constant with G_N being the bare Newton's constant. Varying the action with respect to the metric, following the metric variational approach, we arrive at the following field equations [205]:

$$FG_{\mu\nu} - \frac{1}{2}(f(R) - R\,F)g_{\mu\nu} + (g_{\mu\nu}\Box - \nabla_\mu\nabla_\nu)\,F = \kappa\,T^{(m)}_{\mu\nu}, \tag{4.17}$$

where $F = f'(R)$, $G_{\mu\nu}$ is the Einstein tensor and $T^{(m)}_{\mu\nu}$ is the energy-momentum tensor for the matter fields. By adding and subtracting the Einstein tensor on the left hand side of Eq. (4.17) and moving everything to the right hand side we can rewrite the equations of motion as the usual Einstein equations plus an effective DE fluid, along with the usual matter fields [193]:

$$G_{\mu\nu} = \kappa\left(T^{(m)}_{\mu\nu} + T^{(DE)}_{\mu\nu}\right), \tag{4.18}$$

where

$$\kappa T^{(DE)}_{\mu\nu} = (1-F)G_{\mu\nu} + \frac{1}{2}(f(R) - R\,F)g_{\mu\nu} - (g_{\mu\nu}\Box - \nabla_\mu\nabla_\nu)\,F. \tag{4.19}$$

[11] $f(R)$ theories can be viewed as a non-minimally coupled scalar field in the Einstein frame. See, for instance, Ref. [277].

Due to the diffeomorphism invariance of the theory, it is very easy to show that the effective energy momentum tensor given by Eq. (4.19), indeed satisfies the usual conservation equation:

$$\nabla^{\mu} T_{\mu\nu}^{(DE)} = 0. \tag{4.20}$$

Clearly, the background equations are the same as in GR [185]:

$$\mathcal{H}^2 = \frac{\kappa}{3} a^2 \left(\bar{\rho}_m + \bar{\rho}_{DE}\right), \tag{4.21}$$

$$\dot{\mathcal{H}} = -\frac{\kappa}{6} a^2 \left(\left(\bar{\rho}_m + 3\bar{P}_m\right) + \left(\bar{\rho}_{DE} + 3\bar{P}_{DE}\right)\right). \tag{4.22}$$

While we assume that matter is pressureless ($\bar{P}_m = 0$), the effective DE density and pressure are given by:

$$\kappa \bar{P}_{DE} = \frac{f}{2} - \mathcal{H}^2/a^2 - 2F\mathcal{H}^2/a^2 + \mathcal{H}\dot{F}/a^2 - 2\dot{\mathcal{H}}/a^2 - F\dot{\mathcal{H}}/a^2 + \ddot{F}/a^2, \tag{4.23}$$

$$\kappa \bar{\rho}_{DE} = -\frac{f}{2} + 3\mathcal{H}^2/a^2 - 3\mathcal{H}\dot{F}/a^2 + 3F\dot{\mathcal{H}}/a^2, \tag{4.24}$$

where $\mathcal{H} = \frac{\dot{a}}{a}$ is the conformal Hubble parameter.[12] Using Eqs. (4.23) and (4.24) we see that the DE equation of state for the $f(R)$ models in the effective fluid description is given by:

$$w_{DE} = \frac{-a^2 f + 2\left((1+2F)\mathcal{H}^2 - \mathcal{H}\dot{F} + (2+F)\dot{\mathcal{H}} - \ddot{F}\right)}{a^2 f - 6(\mathcal{H}^2 - \mathcal{H}\dot{F} + F\dot{\mathcal{H}})}, \tag{4.25}$$

which is in agreement with the expression found in Ref. [205]. Thus it becomes clear that by working in the effective fluid approach, we can assign a density, pressure, velocity and anisotropic stress to the effective energy momentum tensor as in the general case of Eqs. (4.3)-(4.5). Then, we can find the effective quantities for the $f(R)$ model using the tensor of Eq. (4.19). As a result, the effective pressure, density and velocity perturbations are given by:

$$\frac{\delta P_{DE}}{\bar{\rho}_{DE}} = (...)\delta R + (...)\dot{\delta R} + (...)\ddot{\delta R} + (...)\Psi + (...)\dot{\Psi} + (...)\Phi + (...)\dot{\Phi}, \tag{4.26}$$

$$\delta_{DE} = (...)\delta R + (...)\dot{\delta R} + (...)\Psi + (...)\Phi + (...)\dot{\Phi}, \tag{4.27}$$

$$V_{DE} \equiv (1 + w_{DE})\theta_{DE} = (...)\delta R + (...)\dot{\delta R} + (...)\Psi + (...)\Phi + (...)\dot{\Phi}. \tag{4.28}$$

Moreover, in these models it is easy to see from the field equations that the difference of the potentials Φ and Ψ is given by

$$\Phi - \Psi = \frac{F_{,R}}{F}\delta R, \tag{4.29}$$

which implies that the anisotropic stress can be written as [185]

$$\bar{\rho}_{DE}\pi_{DE} = -\frac{3}{2}(\hat{k}_i\hat{k}_j - \frac{1}{3}\delta_{ij})\Sigma^{ij} = \frac{1}{\kappa}\frac{k^2}{a^2}\left(F_{,R}\delta R + (1-F)(\Phi - \Psi)\right). \tag{4.30}$$

In Appendix A.1 we give some other useful expressions related to the effective fluid variables.

[12] In what follows we denote the usual Hubble parameter as $H(t) = \frac{da/dt}{a}$ and the conformal one as $\mathcal{H}(\tau) = \frac{da/d\tau}{a}$. The two are related via $\mathcal{H}(\tau) = aH(t)$.

Sub-horizon approximation

Expressions in Eqs. (4.26)-(4.30) for DE perturbations might be cumbersome. Therefore, it is very convenient to work in the sub-horizon approximation, i.e., with modes deep in the Hubble radius ($k^2 \gg a^2H^2$), where we find that terms with time-derivatives are negligible compared to the ones scaling as k^2. For example, the perturbation in the Ricci scalar is

$$\delta R = -\frac{12(\mathcal{H}^2+\dot{\mathcal{H}})}{a^2}\Psi - \frac{4k^2}{a^2}\Phi + \frac{2k^2}{a^2}\Psi - \frac{18\mathcal{H}}{a^2}\dot{\Phi} - \frac{6\mathcal{H}}{a^2}\dot{\Psi} - \frac{6\ddot{\Phi}}{a^2}, \tag{4.31}$$

$$\simeq -\frac{4k^2}{a^2}\Phi + \frac{2k^2}{a^2}\Psi, \tag{4.32}$$

where the last line follows from the sub-horizon approximation. Then, using the equations of motion we find that the potentials can be written as:

$$\Psi = -4\pi G_N \frac{a^2}{k^2}\frac{G_{eff}}{G_N}\bar{\rho}_m\delta_m, \tag{4.33}$$

$$\Phi = -4\pi G_N \frac{a^2}{k^2}Q_{eff}\bar{\rho}_m\delta_m, \tag{4.34}$$

where the effective Newton's constant G_{eff} and Q_{eff} are given by [205]:

$$G_{eff}/G_N = \frac{1}{F}\frac{1+4\frac{k^2}{a^2}\frac{F_{,R}}{F}}{1+3\frac{k^2}{a^2}\frac{F_{,R}}{F}}, \tag{4.35}$$

$$Q_{eff} = \frac{1}{F}\frac{1+2\frac{k^2}{a^2}\frac{F_{,R}}{F}}{1+3\frac{k^2}{a^2}\frac{F_{,R}}{F}}, \tag{4.36}$$

where $F = \frac{df(R)}{dR}$, $F_{,R} = \frac{d^2f(R)}{dR^2}$. Note however, that in the effective fluid approach we have to introduce the DE density ρ_{DE}, which then means that from the Poisson equation for Φ we have:

$$-\frac{k^2}{a^2}\Phi = 4\pi G_N\left(\bar{\rho}_m\delta_m + \bar{\rho}_{DE}\delta_{DE}\right)$$

$$= 4\pi G_N Q_{eff}\bar{\rho}_m\delta_m, \tag{4.37}$$

or that

$$\bar{\rho}_m\delta_m = \frac{1}{Q_{eff}-1}\bar{\rho}_{DE}\delta_{DE}, \tag{4.38}$$

which can be used to find the evolution of the DE density perturbation in this regime. The previous expressions are also useful as in the sub-horizon approximation one can derive a second order differential equation for the matter density contrast in terms of G_{eff} [205]:

$$\delta_m''(a) + \left(\frac{3}{a} + \frac{H'(a)}{H(a)}\right)\delta_m'(a) - \frac{3}{2}\frac{\Omega_{m0}G_{eff}/G_N}{a^5H(a)^2/H_0^2}\delta_m(a) = 0, \tag{4.39}$$

where in this case primes $'$ denote derivatives with respect to the scale factor a. Finally, we can also define the anisotropic parameters $\eta \equiv \frac{\Psi-\Phi}{\Phi}$ and $\gamma \equiv \frac{\Phi}{\Psi}$ for which we then have,

$$\eta = \frac{2\frac{k^2}{a^2}\frac{F_{,R}}{F}}{1+2\frac{k^2}{a^2}\frac{F_{,R}}{F}}, \tag{4.40}$$

$$\gamma = \frac{1+2\frac{k^2}{a^2}\frac{F_{,R}}{F}}{1+4\frac{k^2}{a^2}\frac{F_{,R}}{F}}. \tag{4.41}$$

We can now apply the sub-horizon approximation and derive relatively simple expressions for all the effective DE perturbations in Eqs. (4.26)-(4.30). In practice, we have found that the

results depend on the way the approximation is applied and this is one of the main results of our Chapter.

Since δR in Eq. (4.31) has up to second order derivatives of Φ and Eq. (4.26) contains up to second order derivatives of δR, this means that the pressure perturbation has up to fourth order derivatives of the metric perturbation Φ. Eliminating all of the higher order perturbations via the sub-horizon approximation can cause significant deviations and instabilities in the system of effective fluid equations. We found that a better approach is to use Eq. (4.26) and repeatedly apply Eq. (4.29), thus reducing the number of higher order derivative terms and increasing the accuracy of the solutions.

Following this prescription and using the Poisson equations for the potentials, we find that the effective density, pressure and velocity perturbations are given by:

$$\frac{\delta P_{DE}}{\bar{\rho}_{DE}} \simeq \frac{1}{3F}\frac{2\frac{k^2}{a^2}\frac{F_{,R}}{F}+3(1+5\frac{k^2}{a^2}\frac{F_{,R}}{F})\ddot{F}k^{-2}}{1+3\frac{k^2}{a^2}\frac{F_{,R}}{F}}\frac{\bar{\rho}_m}{\bar{\rho}_{DE}}\delta_m, \tag{4.42}$$

$$\delta_{DE} \simeq \frac{1}{F}\frac{1-F+\frac{k^2}{a^2}(2-3F)\frac{F_{,R}}{F}}{1+3\frac{k^2}{a^2}\frac{F_{,R}}{F}}\frac{\bar{\rho}_m}{\bar{\rho}_{DE}}\delta_m, \tag{4.43}$$

$$\begin{aligned} V_{DE} &\equiv (1+w_{DE})\theta_{DE} \\ &\simeq \frac{\dot{F}}{2F}\frac{1+6\frac{k^2}{a^2}\frac{F_{,R}}{F}}{1+3\frac{k^2}{a^2}\frac{F_{,R}}{F}}\frac{\bar{\rho}_m}{\bar{\rho}_{DE}}\delta_m. \end{aligned} \tag{4.44}$$

Finally, the DE anisotropic stress parameter π_{DE} is given by

$$\begin{aligned} \pi_{DE} &= \frac{\frac{k^2}{a^2}(\Phi-\Psi)}{\kappa\,\bar{\rho}_{DE}} \\ &\simeq \frac{1}{F}\frac{\frac{k^2}{a^2}\frac{F_{,R}}{F}}{1+3\frac{k^2}{a^2}\frac{F_{,R}}{F}}\frac{\bar{\rho}_m}{\bar{\rho}_{DE}}\delta_m = \frac{\frac{k^2}{a^2}\frac{F_{,R}}{F}}{1-F+\frac{k^2}{a^2}(2-3F)\frac{F_{,R}}{F}}\delta_{DE}. \end{aligned} \tag{4.45}$$

Note that the DE anisotropic stress in Eq. (4.45) can also be written as

$$\pi_{DE}(a) = \frac{\frac{k^2}{a^2}f_1(a)}{1+\frac{k^2}{a^2}f_2(a)}\delta_{DE}(a), \tag{4.46}$$

where $f_1(a)=\frac{F_{,R}}{F(1-F)}$ and $f_2(a)=\frac{(2-3F)F_{,R}}{F(1-F)}$, which is reminiscent of Model 2 in Ref. [235], but with different functions in the numerator and the denominator. This is interesting as it seems that many popular ansatze for the DE anisotropic stress do not capture exactly all of the features of the $f(R)$ models.

On the other hand, using Eqs. (4.42) and (4.43), we see that the DE sound speed is given by

$$c^2_{s,DE} \simeq \frac{1}{3}\frac{2\frac{k^2}{a^2}\frac{F_{,R}}{F}+3(1+5\frac{k^2}{a^2}\frac{F_{,R}}{F})\ddot{F}k^{-2}}{1-F+\frac{k^2}{a^2}(2-3F)\frac{F_{,R}}{F}}, \tag{4.47}$$

which implies that the DE effective sound speed is

$$\begin{aligned} c^2_{s,eff} &\equiv c^2_{s,DE}-\frac{2}{3}\pi_{DE}/\delta_{DE} \\ &\simeq \frac{(1+5\frac{k^2}{a^2}\frac{F_{,R}}{F})\ddot{F}k^{-2}}{1-F+\frac{k^2}{a^2}(2-3F)\frac{F_{,R}}{F}}. \end{aligned} \tag{4.48}$$

As we will see later on, the effective sound-speed at late times tends to go to zero due to the fact that the $\ddot{F}$ term not only is suppressed by k^2, which in the sub-horizon approximation is

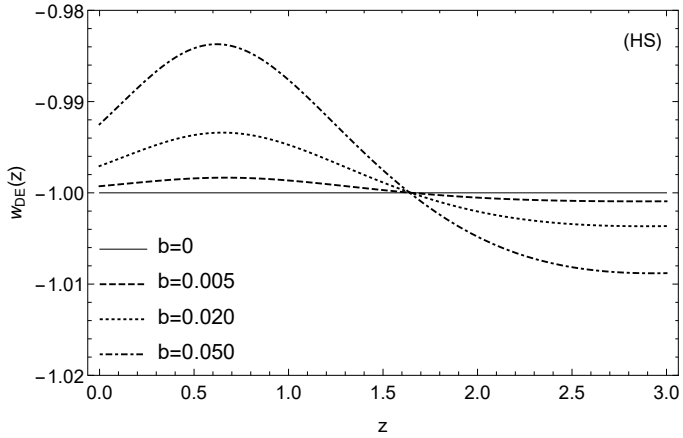

Figure 4.1: The DE equation of state $w_{DE}(z)$ for the HS model for $\Omega_{m0} = 0.3$, $n = 1$ and for a variety of values of the parameter b, with $b \in [0, 0.05]$. As can be seen, the equation of state crosses $w_{DE} = -1$ at approximately the same redshift $z \sim 1.65$. At early times, we have $1 + w_{DE} < 0$ thus violating the SEC.

much larger than the Hubble parameter or related quantities, but also because for viable models F in general is a slowly varying function. This implies that for these models there is no effective sound speed driving the DE perturbations, thus we expect that on large k and at late times the perturbations should become flat, in agreement with Ref. [235].

It is clear that for the ΛCDM model, i.e., $f(R) = R - 2\Lambda$, we have $F = 1$ and $F_{,R} = 0$ which implies that $w_{DE} = -1$ and $(\delta P_{DE}, \delta\rho_{DE}, \pi_{DE}) = (0, 0, 0)$ as expected. When the equation of state w_{DE} for an $f(R)$ model, e.g., the Hu & Sawicki (HS, hereafter) model, crosses the so-called phantom divide line ($w_{DE}(a) = -1$), problems could arise due to the presence of the $1 + w$ term in the denominator in Eq. (4.11) [119]. However, we see that in our case the perturbations remain finite despite the presence of the $1 + w$ term in the denominator in Eq. (4.11) as we can absorb the $1 + w$ term by introducing $V_{DE} = (1 + w_{DE})\theta_{DE}$ as mentioned earlier. Furthermore, the combination $(1 + w_{DE})\theta_{DE}$ always remains finite for viable $f(R)$ models as can be seen in Eq. (4.44). The simple analytical expressions given by Eqs. (4.42)-(4.44) are one of our main results.

Finally, for our effective DE fluid in Eq. (4.19) the most common energy conditions [279] can be written in terms of the effective DE density and pressure:

$$
\begin{aligned}
\textbf{NEC} &\implies \bar{\rho}_{DE} + \bar{P}_{DE} \geq 0, \\
\textbf{WEC} &\implies \bar{\rho}_{DE} \geq 0 \quad \text{and} \quad \bar{\rho}_{DE} + \bar{P}_{DE} \geq 0, \\
\textbf{DEC} &\implies \bar{\rho}_{DE} \geq 0 \quad \text{and} \quad \bar{\rho}_{DE} \geq \left|\bar{P}_{DE}\right|, \\
\textbf{SEC} &\implies \bar{\rho}_{DE} + 3\bar{P}_{DE} \geq 0 \quad \text{and} \quad \bar{\rho}_{DE} + \bar{P}_{DE} \geq 0,
\end{aligned}
$$

where NEC, WEC, DEC and SEC correspond respectively to the null, weak, dominant and strong energy conditions. As expected for an accelerating universe [280, 281], we have checked that the SEC is violated. Since the condition $\bar{\rho}_{DE} \geq 0$ holds, we find that the NEC, WEC and DEC can be translated into the following constraint for the DE equation of state $w_{DE} \geq -1$. As can be seen in Fig. 4.1 for the HS model, the NEC, WEC and DEC are violated for redshifts $z \gtrsim 1.65$ for reasonable values of the parameter b (see Eq. (4.56) in the next section), for $b \in [0, 0.05]$.

4.2.2 Results for specific f(R) models

So far, our analysis has been quite general and here we work out a couple of examples. In this section we will present our results for two specific models, namely, the HS model and the so-called designer (DES) model which has an expansion history equal to the ΛCDM model. These models are interesting because they satisfy solar system tests and give a proper matter era. Note, however, that in the literature one finds other $f(R)$ models sharing these properties (see, for instance, Refs. [215, 282, 283]), but to simplify our presentation we only focus on the two aforementioned models.

Since modifications to GR are expected to become important at late times, we consider a universe only containing matter and an effective DE fluid.[13] The system of differential equations that we are interested in is, hence, given by Eqs. (4.6), (4.9), (4.14), (4.15):

$$\delta_m' = 3\Phi' - \frac{V_m}{a^2 H}, \tag{4.49}$$

$$V_m' = -\frac{V_m}{a} + \frac{k^2}{a^2 H}\Psi, \tag{4.50}$$

$$\delta_{DE}' = 3(1+w_{DE})\Phi' - \frac{V_{DE}}{a^2 H} - \frac{3}{a}\left(\frac{\delta P_{DE}}{\bar{\rho}_{DE}} - w_{DE}\delta_{DE}\right), \tag{4.51}$$

$$V_{DE}' = -(1-3w_{DE})\frac{V_{DE}}{a} + \frac{k^2}{a^2 H}\frac{\delta P_{DE}}{\bar{\rho}_{DE}} + (1+w_{DE})\frac{k^2}{a^2 H}\Psi - \frac{2}{3}\frac{k^2}{a^2 H}\pi_{DE}, \tag{4.52}$$

$$\frac{k^2}{a^2}\Phi = -\frac{3}{2}(\Omega_m\delta_m + \Omega_{DE}\delta_{DE}) - 3H^2(a\Phi' + \Psi), \tag{4.53}$$

$$\frac{k^2}{a^2}(\Phi - \Psi) = 3\Omega_{DE}\pi_{DE}, \tag{4.54}$$

where the prime $'$ denotes a derivative with respect to scale factor a, we have assumed that the matter component is cold ($w_m \simeq 0$) and pressureless ($c_{s,m}^2 \simeq 0$), $\Omega_m = \Omega_{m0}a^{-3}$, $\Omega_{DE} = H^2 - \Omega_m$, and finally that the effective DE density, pressure and velocity perturbations are given by Eqs. (4.42),(4.43) and (4.44), respectively.

The HS model

The HS model [209] has a lagrangian[14] given by

$$f(R) = R - m^2\frac{c_1(R/m^2)^n}{1 + c_2(R/m^2)^n}, \tag{4.55}$$

where c_1, c_2 are two free parameters, $m^2 \simeq \Omega_{m0}H_0^2$ is of the order of the Ricci scalar R_0, H_0 is the Hubble constant, Ω_{m0} is the dimensionless matter density today; and m and n are positive constants with n usually taking positive integer values i.e., $n = 1, 2, \cdots$. In the rest of our Chapter we assume $n = 1$.

After simple algebraic manipulations Eq. (4.55) can also be written as [286]

$$f(R) = R - \frac{m^2 c_1}{c_2} + \frac{m^2 c_1/c_2}{1 + c_2(R/m^2)^n}$$

[13] In this Chapter we focus on the late-time evolution of the Universe, but it is possible that MG theories play a part in earlier stages as well, namely, the inflationary period. There exist $f(R)$ models that give a unified description of early- and late-time accelerating phases of the Universe [284, 285] and our effective fluid approach could in principle also be applied in these scenarios.

[14] The Starobinsky model [215] has a lagrangian $f(R) = R - c_1\, m^2\left[1 - \left(1 + R^2/m^4\right)^{-n}\right]$ and the results we obtain are very similar to those for the HS model. To keep our presentation simple we will only present results for the HS model.

$$
\begin{aligned}
&= R - 2\Lambda\left(1 - \frac{1}{1+(R/(b\,\Lambda)^n}\right)\\
&= R - \frac{2\Lambda}{1+\left(\frac{b\Lambda}{R}\right)^n},
\end{aligned}
\tag{4.56}
$$

where $\Lambda = \frac{m^2 c_1}{2c_2}$ and $b = \frac{2c_2^{1-1/n}}{c_1}$. In this form it is clear that this model can be arbitrarily close to ΛCDM, depending on the parameters b and n. Moreover, for $n > 0$ it has the limits [286]:

$$
\begin{aligned}
\lim_{b\to 0} f(R) &= R - 2\Lambda,\\
\lim_{b\to \infty} f(R) &= R.
\end{aligned}
\tag{4.57}
$$

Since the HS model tends to ΛCDM for $b \to 0$, it can be considered as a small perturbation around the ΛCDM model. Therefore, it should come as no surprise that the HS model can successfully pass the solar system tests.

Furthermore, in Ref. [286] it was shown that for small values of the parameter b one is always able to find an analytic approximation to the Hubble parameter that works to a level of accuracy better than $\sim 10^{-5}\%$ when the parameter b is of the order of $b \sim [0.001 - 0.1]$, thus making the approximations very useful. Then, the Hubble parameter $H(t) = \frac{da/dt}{a}$ can be well approximated by

$$
H_{HS}(a)^2 = H_\Lambda(a)^2 + b\;\delta H_1(a)^2 + b^2\;\delta H_2(a)^2 + \cdots\,,
\tag{4.58}
$$

where the functions $\delta H_1(a)$ and $\delta H_2(a)$ are given in the Appendix of [286].

From Eqs. (4.25),(4.56),(4.58) and considering a universe only containing matter and DE, we can calculate the DE equation of state as a series expansion in terms of b

$$
w_{DE}(a) \simeq -1 - \frac{12\left(a^3(\Omega_{m0}-1)\Omega_{m0}\left(a^3(\Omega_{m0}-1)-\Omega_{m0}\right)\left(8a^3(\Omega_{m0}-1)+\Omega_{m0}\right)\right)}{\left(\Omega_{m0}-4a^3(\Omega_{m0}-1)\right)^4} b + \cdots\,,
\tag{4.59}
$$

while the DE anisotropic stress will be given by

$$
\begin{aligned}
\pi_{DE}(a) &= \frac{1}{F}\frac{\frac{k^2}{a^2}\frac{F_{,R}}{F}}{1+3\frac{k^2}{a^2}\frac{F_{,R}}{F}}\frac{\bar\rho_m}{\bar\rho_{DE}}\delta_m\\
&\simeq \left(\frac{k^2}{a^2}\frac{1}{H_0^2}\frac{4a^9(1-\Omega_{m0})^2}{3\left(\Omega_{m0}+4a^3(1-\Omega_{m0})\right)^3}b + \cdots\right)\frac{\bar\rho_m}{\bar\rho_{DE}}\delta_m.
\end{aligned}
\tag{4.60}
$$

From the system of differential equations (4.49)-(4.54) and the DE perturbations (4.42)-(4.45) we can derive approximate solutions in a matter dominated regime ($H(a)^2/H_0^2 \simeq \Omega_{m0}a^{-3}$):

$$
w_{DE}(a) \simeq -1 - \frac{12a^3 b(1-\Omega_{m0})}{\Omega_{m0}} + \cdots\,,
\tag{4.61}
$$

$$
\frac{\delta P_{DE}(a)}{\bar\rho_{DE}(a)} \simeq b(1-\Omega_{m0})^2\left(\frac{8a^7k^2}{9\Omega_{m0}^3H_0^2} - \frac{66a^5H_0^2}{k^2\Omega_{m0}} + \cdots\right)\frac{\Omega_m(a)}{\Omega_{DE}(a)}\delta_m,
\tag{4.62}
$$

$$
\pi_{DE} \simeq b\left(\frac{4a^7k^2(1-\Omega_{m0})^2}{3\Omega_{m0}^3H_0^2} + \cdots\right)\frac{\Omega_m(a)}{\Omega_{DE}(a)}\delta_m,
\tag{4.63}
$$

$$
\delta_m(a) \simeq \delta_0\left(a + \frac{3\Omega_{m0}H_0^2}{k^2}\right),
\tag{4.64}
$$

$$
V_m(a) \simeq -\delta_0\sqrt{a\Omega_{m0}} + \cdots\,,
\tag{4.65}
$$

$$
\delta_{DE}(a) \simeq -\delta_0\, b\,(1-\Omega_{m0})\left(\frac{a^5k^2}{3\Omega_{m0}^2H_0^2} + \frac{8a^4}{35\Omega_{m0}} - \frac{495a^3H_0^2}{13k^2} - \cdots\right),
\tag{4.66}
$$

$$V_{DE}(a) \simeq \delta_0\, b\, (1-\Omega_{m0}) \left(-\frac{396\, a^{5/2} H_0^2 \sqrt{\Omega_{m0}}}{13k^2} - \frac{32a^{7/2}}{5\sqrt{\Omega_{m0}}} + \cdots \right), \tag{4.67}$$

$$\Phi(a) \simeq -\frac{3}{2}\delta_0 \frac{\Omega_{m0} H_0^2}{k^2} + \cdots, \tag{4.68}$$

where $\Omega_m(a) = \Omega_{m0} a^{-3}$ and in this limit $\Omega_{DE}(a) \simeq 1 - \Omega_{m0}$. Also, as can be seen from the above expressions, the dominant contributions in the sub-horizon limit and in the matter-dominated regime are $\delta_{DE} \propto k^2 a^5$ and $V_{DE} \propto a^{7/2}$. When numerically solving the system of differential equations (4.49)-(4.54), we will use the above solutions as initial conditions.

The DES model

The DES model [201, 202, 204], which has a background exactly that of the ΛCDM model, has a lagrangian given by

$$f(R) = R - 2\Lambda + \alpha\, H_0^2 \left(\frac{\Lambda}{R-3\Lambda} \right)^{c_0} {}_2F_1 \left(c_0, \frac{3}{2} + c_0, \frac{13}{6} + 2c_0, \frac{\Lambda}{R-3\Lambda} \right), \tag{4.69}$$

where $c_0 = \frac{1}{12}\left(-7 + \sqrt{73}\right)$ and α is a free dimensionless parameter.

While for the DES model the background is much simpler than for the HS model (in the DES model the expansion history matches that of the ΛCDM model, i.e., $H^2_{DES}(a) = H^2_{\Lambda CDM}(a)$, Eq. (4.69) makes more complicated the expressions for all the effective DE quantities. We have found an approximation around $a \simeq 0$ that works very well in the range $a \in [0, 1]$; it reads

$$F(a) \simeq 1 + f_{R,0} \frac{\Omega_{m0}^{-c_0-1}}{{}_2F_1\left(c_0+1, c_0+\frac{3}{2}; 2c_0+\frac{13}{6}; 1-\Omega_{m0}\right)} a^{3(1+c_0)} + \mathcal{O}(a^{3(2+c_0)}), \tag{4.70}$$

where $f_{R,0} \equiv F(a=1) - 1$. For viable models, the parameter $f_{R,0}$ has typical values on the order $f_{R,0} \sim -10^{-4}$ (see, for instance, Ref. [203]).[15]

Following the same approach as for the HS model we have found approximate solutions in a matter dominated regime

$$w_{DE}(a) = -1, \tag{4.71}$$

$$\frac{\delta P_{DE}}{\bar{\rho}_{DE}} \simeq \left(-\frac{2(c_0+1) f_{R,0} k^2 a^{3c_0+4} \Omega_{m0}^{-c_0-2}}{9\, g_0} + \cdots \right) \frac{\Omega_m(a)}{\Omega_{DE}(a)} \delta_m, \tag{4.72}$$

$$\pi_{DE} \simeq \left(-\frac{(c_0+1) f_{R,0} k^2 a^{3c_0+4} \Omega_{m0}^{-c_0-2}}{3\, g_0} + \cdots \right) \frac{\Omega_m(a)}{\Omega_{DE}(a)} \delta_m, \tag{4.73}$$

$$\delta_m(a) \simeq \delta_0 \left(a + \frac{3\Omega_{m0} H_0^2}{k^2} \right), \tag{4.74}$$

$$V_m(a) \simeq -\delta_0 \sqrt{a\Omega_{m0}} + \cdots, \tag{4.75}$$

$$\delta_{DE}(a) \simeq \frac{\delta_0 f_{R,0} a^{1+3c_0} \Omega_{m0}^{-1-c_0} \left(a(1+2c_0)k^2 + 36 c_0 \Omega_{m0} \right)}{9\, g_0\, (1-\Omega_{m0})} + \cdots, \tag{4.76}$$

$$V_{DE}(a) \simeq 0 + \cdots, \tag{4.77}$$

$$\Phi(a) \simeq -\frac{3}{2}\delta_0 \frac{\Omega_{m0} H_0^2}{k^2} + \cdots, \tag{4.78}$$

where $g_0 = {}_2F_1\left(1+c_0, \frac{3}{2}+c_0, \frac{13}{6}+2c_0, 1-\Omega_{m0}\right)$. In the next section, we will use these approximations as initial conditions for the numerical evolution in the effective fluid approach.

[15] For illustration purposes we note that the right-hand side of Eq. (4.70) evolves roughly as $F(a) \approx 1 + 0.85\, f_{R,0}\, \Omega_{m0}^{-0.57} a^{3.386}$. We however do not use this expression in our computations.

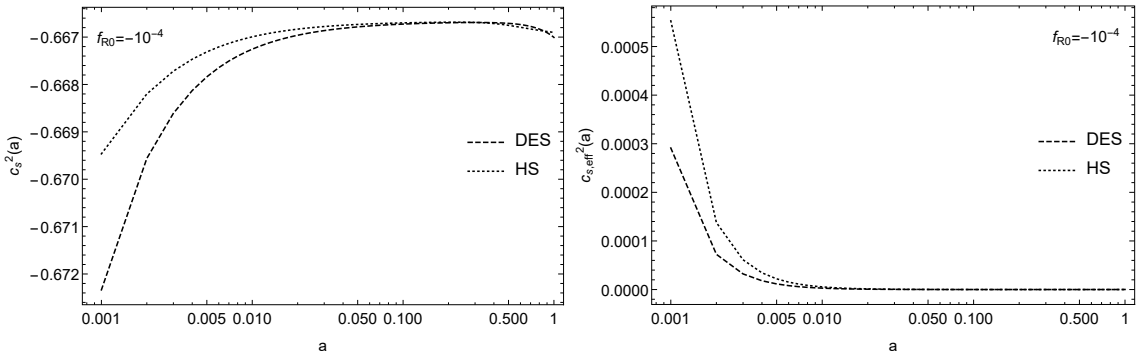

Figure 4.2: The DE fluid sound speed $c^2_{s,DE}$ (left) and the DE effective sound speed $c^2_{s,eff}$ (right) given by Eqs. (4.47) and (4.48) for both the HS (dotted line) and DES (dashed lines) models for $\Omega_{m0} = 0.3$, $k = 300H_0$ and $f_{R,0} = -10^{-4}$. As can be seen, for both models the DE sound speed remains close to $c^2_{s,DE} \sim -\frac{2}{3}$ while the DE effective sound speed is close to $c^2_{s,eff} \sim 0^+$.

Note that in Ref. [278] the authors derived approximations to the evolution of the DE density contrast $\delta_{DE} \simeq \delta_0(1+w)\left(\frac{a}{1-3w} + \frac{3H0^2\Omega_{m0}}{k^2}\right)$ and velocity perturbation $V_{DE} \simeq -\delta_0(1+w)H_0\sqrt{\Omega_{m0}}a^{1/2}$. Clearly, in both cases when $w = -1$, as is the case for the DES model, we would have that $(\delta_{DE}, V_{DE}) = (0, 0)$ as expected. However, we have seen that the DE perturbations in the DES model (despite having $w_{DE} = -1$) have in general a dependence on the scale factor a which is quite different. Therefore, care should be used when applying the expressions of Ref. [278] as initial conditions and instead one should derive again the correct expressions as we have done.

4.3 Numerical solution of the evolution equations

4.3.1 Evolution of perturbations

Here we present the results of the numerical solution of the evolution equations (4.49)-(4.54). In all cases we will assume $\Omega_{m0} = 0.3$, $k = 300H_0$, $f_{R0} = -10^{-4}$ and $\sigma_{8,0} = 0.8$, where $f_{R,0} = F(a = 1) - 1$, unless otherwise specified. We set the initial conditions well inside the matter dominated regime at $a = 10^{-3}$. The reason we choose the specific value of $k = 300H_0 \sim 0.1\ h/\text{Mpc}$ for the wave-number is that it corresponds to the largest value of k we can choose without entering the non-linear regime.

Before we proceed with the discussion of our results, it is instructive to show the evolution of the DE sound speed $c^2_{s,DE}$ and the DE effective sound speed $c^2_{s,eff}$ given by Eqs. (4.47) and (4.48), respectively, for both the HS and DES models. The plots are shown in Fig. 4.2, where we show $c^2_{s,DE}$ (left) and $c^2_{s,eff}$ (right) for both the HS (dotted line) and DES (dashed lines) models. As can be seen, for both models the DE sound speed remains close to $c^2_{s,DE} \sim -\frac{2}{3}$ while the effective sound speed is close to $c^2_{s,eff} \sim 0^+$. On the one hand, this behavior implies that at early times while the DE effective sound speed is positive, the DE perturbations are expected to grow. On the other hand, at late times as the DE effective sound speed goes to zero asymptotically the DE perturbations are expected to reach a plateau and stop growing.

In Figs. 4.3 and 4.4 we present our results for the perturbation variables $(\delta_m, V_m, \delta_{DE}, V_{DE})$ and the potentials (Φ, Ψ), respectively. As noted before, the DE perturbations reach a plateau and then flatten out for both models, as expected from the fact that the DE effective sound speed goes to zero at late times (see Fig. 4.2). Also, in all cases, the DE velocity perturbation remains significantly suppressed with respect to the rest of the variables. Furthermore, the potentials remain approximately equal until $a \sim 0.1$, which as seen in Fig. 4.2 corresponds to the epoch when roughly $c^2_{s,eff} \sim 0$, and then diverge from each other significantly due to the presence of the

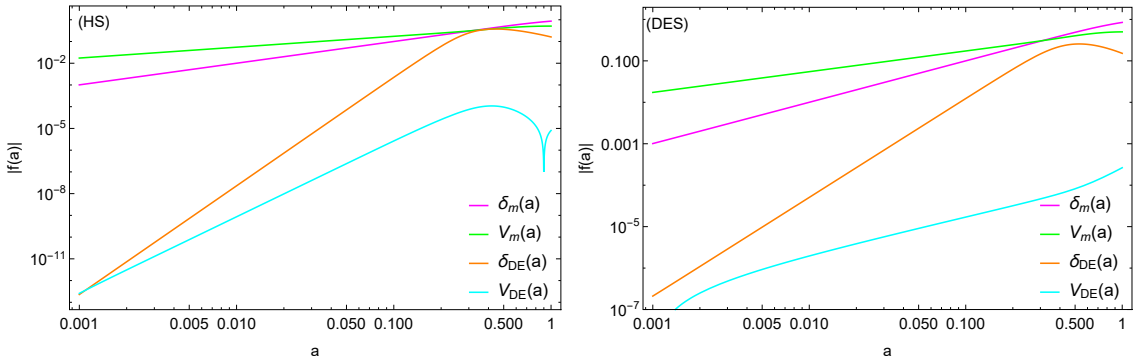

Figure 4.3: The evolution of the matter and effective DE perturbation variables $(\delta_m, V_m, \delta_{DE}, V_{DE})$ for the HS (left) and the DES (right) models for $\Omega_{m0} = 0.3$, $k = 300H_0$, $\delta_0 = 1$, and $f_{R,0} = -10^{-4}$. As described in the text, the DE perturbations reach a plateau and then flatten out for both models, as expected from the fact that the DE effective sound speed given by Eq. (4.48) goes to zero at late times (see Fig. 4.2). Also, in all cases, the DE velocity perturbation remains significantly suppressed with respect to the rest of the variables.

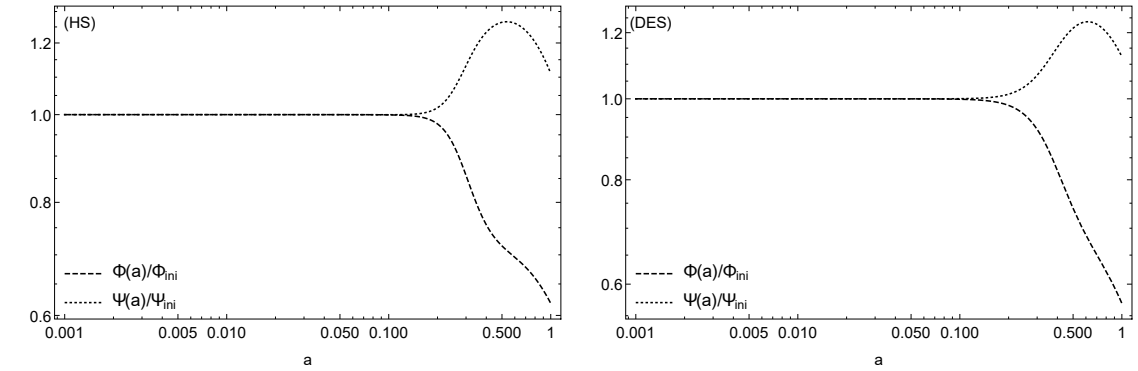

Figure 4.4: The evolution of the potentials Φ and Ψ for the HS (left) and the DES (right) models for $\Omega_{m0} = 0.3$, $k = 300H_0$, $\delta_0 = 1$, and $f_{R,0} = -10^{-4}$. Due to a non-vanishing DE anisotropic stress the potentials diverge from each other at late times.

anisotropic stress.

4.3.2 Growth rate of matter perturbations

Next we will also present our results for the growth rate of matter perturbations parameter $f\sigma_8(a) \equiv f(a) \cdot \sigma(a)$, where $f(a) = \frac{dln\delta}{dlna}$ is the growth rate and $\sigma(a) = \sigma_{8,0}\frac{\delta(a)}{\delta(1)}$ is the redshift-dependent root mean square (rms) fluctuations of the linear density field within spheres of radius $R = 8h^{-1}$Mpc, while the parameter $\sigma_{8,0}$ is its value today. This parameter is important as it can be shown to be not only independent of the bias b_0, but also a good discriminator of DE models [118].

In this section we will also compare our results with those of Ref. [203] that follow a direct brute-force solution of the differential equations of the $f(R)$ model, dubbed "Full $f(R)$" from now on. There is of course also the equation of state approach of Ref. [231] and we have explicitly checked that our results are in excellent agreement with it; thus, to avoid an overload in both the presentation and the plots, in what follows we will only present the comparison with the "Full $f(R)$" approach.

Both aforementioned approaches are exact, in the sense of having no approximations, however the one of Ref. [203] suffers from the problem that the relevant equations are extremely stiff

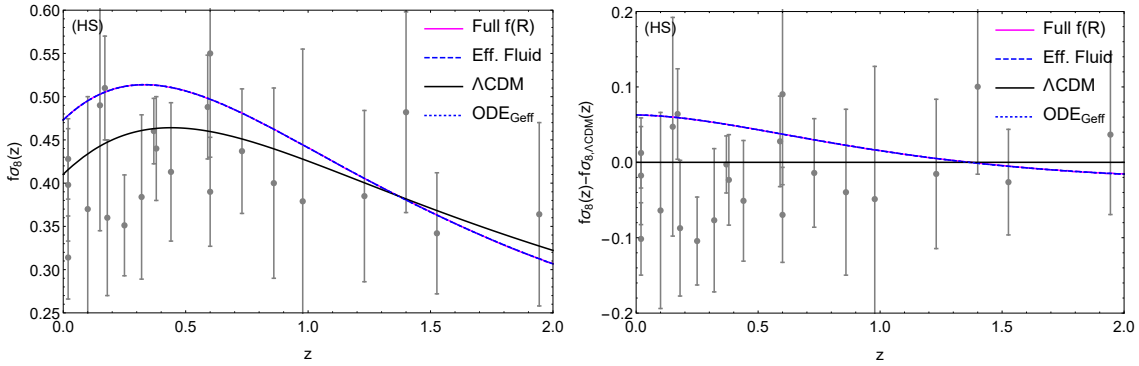

Figure 4.5: The evolution of the $f\sigma_8(z)$ parameter for the HS model for $\Omega_{m0} = 0.3$, $k = 300H_0$, $f_{R,0} = -10^{-4}$ and $\sigma_{8,0} = 0.8$ versus the $f\sigma_8$ data compilation from Ref. [116]. On the left panel we show the theoretical curves for the "Full $f(R)$" brute-force solution based on Ref. [203] (magenta line), our effective fluid approach which we call "Eff. Fluid" (blue dashed line), the ΛCDM model (black line) and the numerical solution of Eq. (4.39) dubbed "ODE_{Geff}" (dotted blue line). On the right panel we show the difference of the aforementioned theoretical curves with respect to that of the ΛCDM model. As can be seen, the agreement with all approaches is excellent.

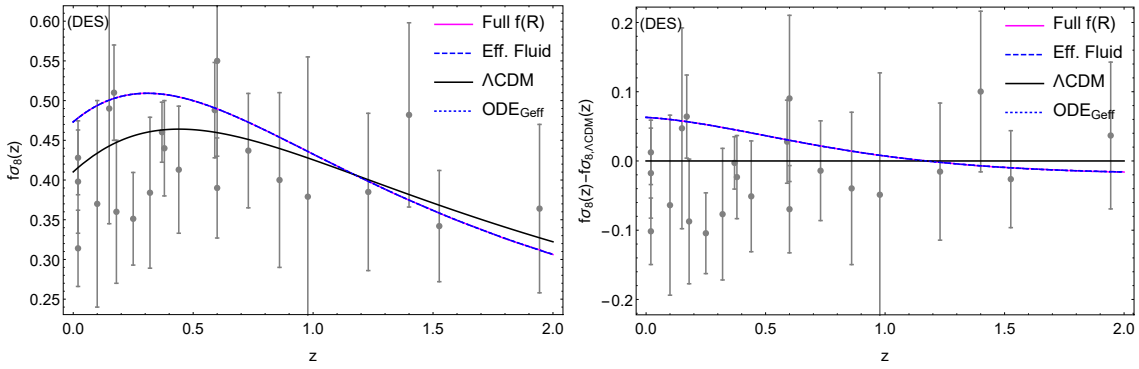

Figure 4.6: The evolution of the $f\sigma_8(z)$ parameter for the DES model for $\Omega_{m0} = 0.3$, $k = 300H_0$, $f_{R,0} = -10^{-4}$ and $\sigma_{8,0} = 0.8$ versus the $f\sigma_8$ data compilation from Ref. [116]. On the left panel we show the theoretical curves for the "Full $f(R)$" brute-force solution based on Ref. [203] (magenta line), our effective fluid approach which we call "Eff. Fluid" (blue dashed line), the ΛCDM model (black line) and the numerical solution of Eq. (4.39) dubbed "ODE_{Geff}" (dotted blue line). On the right panel we show the difference of the aforementioned theoretical curves with respect to that of the ΛCDM model. As can be seen, the agreement with all approaches is excellent.

numerically, while in the one of Ref. [231] the fluid equations are written in terms of a gauge-invariant entropy perturbation which cannot be easily translated to simple analytic expressions for the effective pressure, density contrast and velocity perturbations such as Eqs. (4.42), (4.43) and (4.44) presented here.

In Figs. 4.5 and 4.6 we show the evolution of the $f\sigma_8(z)$ parameter for the HS and DES models respectively, for $\Omega_{m0} = 0.3$, $k = 300H_0$, $f_{R,0} = -10^{-4}$ and $\sigma_{8,0} = 0.8$ versus the $f\sigma_8$ data compilation from Ref. [116]. On the left panel we show the theoretical curves for the "Full $f(R)$" brute-force solution based on Ref. [203] (magenta line), our effective fluid approach which we call "Eff. Fluid" (blue dashed line), the ΛCDM model (black line) and the numerical solution of Eq. (4.39) dubbed "ODE_{Geff}" (dotted blue line). On the right panel we show the difference of the aforementioned theoretical curves with respect to that of the ΛCDM model. As can be seen, the agreement with all approaches is excellent.

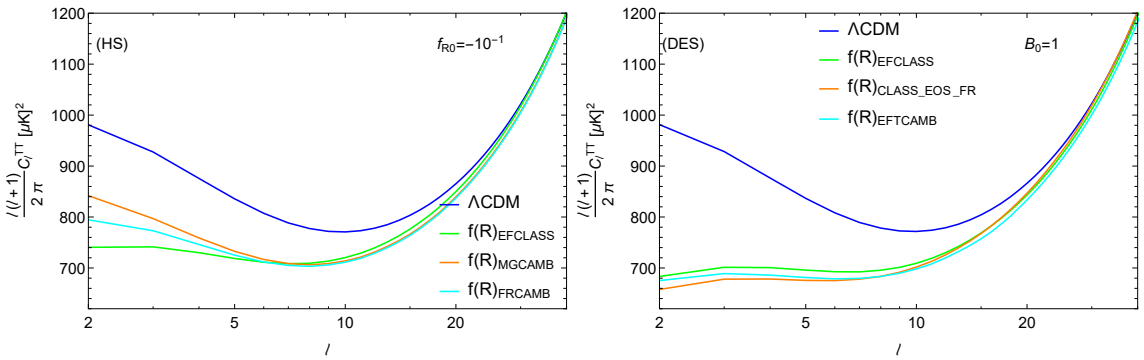

Figure 4.7: The low multipoles of the unlensed CMB TT power spectrum for the HS model (left panel) and the DES model (right panel). We compare several codes: our own modifications to `CLASS` which we call `EFCLASS`, the codes `MGCAMB` and `FRCAMB` for the HS model and the codes `CLASS_EOS_FR` and `EFTCAMB` for the DES model. We find that in the case of the DES model all approaches are in very good agreement, but in the case of the HS model, which also requires modifying the background evolution, there is significant disagreement at $l \in [2, 5]$ as the codes `MGCAMB` and `FRCAMB` do not take into account the change of the background properly. For these plots we assume $(n_s, A_s) = (1, 2.3 \times 10^{-9})$, $f_{R,0} = -10^{-1}$ for the HS model and $B_0 = 1$, which corresponds to $f_{R,0} \simeq -0.159285$ for the DES model for $\Omega_{m0} = 0.3$, while the rest of the parameters are as in the previous plots.

4.3.3 CMB power spectrum

We now also present the results for the CMB power spectra for both models and we compare our predictions with those of several other codes. As we show in Appendix A.2, our implementation of the effective fluid approach in the `CLASS` code [232], while much simpler, also gives results in excellent agreement with other codes, such as `EFTCAMB` [8], `MGCAMB` [225], `FRCAMB` [227], `CLASS_EOS_FR` [233]. In all cases, we took extreme care in order to match the various cosmological parameters between the codes and we explicitly tested that in the limit of the ΛCDM model, all codes agree with each other within the numerical errors. The fact that our implementation is consistent with that of Ref. [233], which is exact, shows the sub-horizon approximation can be safely applied in the models we discussed (see Fig. 4.7). This agrees with results in Ref. [213]: for $f(R)$ models that predict an accelerated expansion of the Universe and satisfy the local gravity constraints, the sub-horizon approximation is accurate.

In order to check with other results for the DES model in the literature, we find it advantageous to introduce the B_0 parameter defined as

$$B_0 = \frac{F_{,R}}{F} \frac{R'(a)}{aH'(a)/H(a)}\Big|_{a=1}. \tag{4.79}$$

The main reason for this choice is that the effects of the modified gravity models on the ISW would be small for $f_{R,0} = -10^{-4}$ that we used in the previous plots. Thus in order to make the effect more visible and still be able to compare with other analyses, we will choose the value $B_0 = 1$, which corresponds to $f_{R,0} \simeq -0.159285$ for the DES model for $\Omega_{m0} = 0.3$. For the HS model we will use $f_{R,0} = -10^{-1}$ and in both cases the rest of the parameters are as in the previous plots.

We also fix the spectral index n_s and amplitude A_s to $(n_s, A_s) = (1, 2.3 \times 10^{-9})$, so that we can isolate the effects of the $f(R)$ models from the effects of a non-flat primordial spectrum. As we have mentioned in previous sections, for large values of the parameter b the HS model behaves as a matter dominated model and we actually expect the CMB spectrum at low multipoles to be nearly completely flat (also due to our choice of $n_s = 1$).

In Fig. 4.7 we present the low multipoles of the CMB TT power spectrum for the HS model (left panel) and the DES model (right panel). We compare several codes: our own modifications

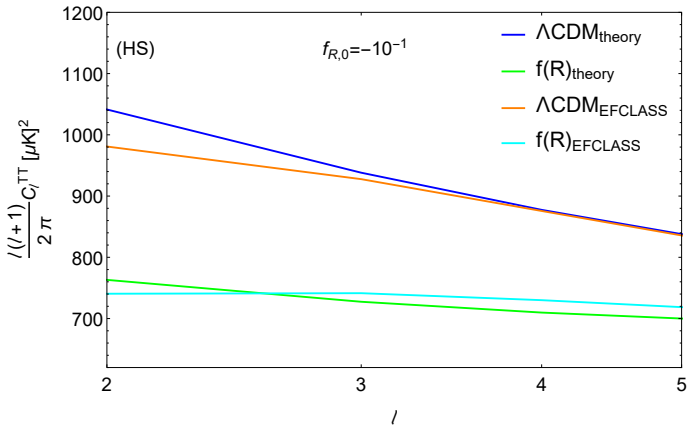

Figure 4.8: A comparison of the low multipoles of the unlensed CMB TT power spectrum ($l \in [2,5]$) for the HS and ΛCDM models between our own modifications to `CLASS` (`EFCLASS`) and a direct theoretical calculation using the expressions for the ISW effect given in Appendix A.1. We find that in both cases there is excellent agreement. For this plot again we assume $(n_s, A_s) = (1, 2.3 \times 10^{-9})$ and $f_{R,0} = -10^{-1}$, while the rest of the parameters are as in the previous plots.

to `CLASS` which we call `EFCLASS`, the codes `MGCAMB` and `FRCAMB` for the HS model and the codes `CLASS_EOS_FR` and `EFTCAMB` for the DES model. We find that in the case of the DES model all approaches are in very good agreement, but in the case of the HS model, which also requires modifying the background evolution, there is significant disagreement at $l \in [2,5]$ as the codes `MGCAMB` and `FRCAMB` do not take into account the change of the background properly.

Although disagreement between the codes for the HS model can be explained by the fact that the other codes do not treat the background properly, we also compare our results with a direct theoretical calculation of the ISW effect, see Fig. 4.8. The relevant formulas for the theoretical calculation of the ISW effect are given for completeness in Appendix A.1. In Fig. 4.8 we show the comparison of the low multipoles of the CMB TT power spectrum ($l \in [2,5]$) for the HS and ΛCDM models between our own modifications to `CLASS` (`EFCLASS`) and a direct theoretical calculation. We find that in both cases there is excellent agreement. For this plot again we assume $(n_s, A_s) = (1, 2.3 \times 10^{-9})$, $f_{R,0} = -10^{-1}$, while the rest of the parameters are as in the previous plots. We find that in the case of the HS model, the agreement between the direct theoretical calculation and our `CLASS` modifications (green and cyan lines respectively) is well below $\sim 2\%$.

4.4 Evolution of the viscosity parameter

In principle the anisotropic stress parameter is the lowest multipole in the Boltzmann hierarchy after the density and velocity perturbations. As a result, it should also follow an evolution equation. Since the properties of DE are currently unknown, one can assign a viscosity parameter c_{vis}^2 and a phenomenological evolution equation as in Ref. [239]:

$$\begin{aligned} \dot{\sigma} + 3\mathcal{H}\frac{c_a^2}{w}\sigma &= \frac{8}{3}\frac{c_{vis}^2}{1+w}\theta \\ &= \frac{8}{3}\frac{c_{vis}^2}{(1+w)^2}V_{DE}, \end{aligned} \tag{4.80}$$

whereas in previous sections we have introduced the parameter $V_{DE} = (1+w)\theta$ and the adiabatic sound speed is $c_a^2 = w - \frac{\dot{w}}{3\mathcal{H}(1+w)} = w - \frac{aw'}{3(1+w)}$ where dots are conformal time derivatives and primes scale factor derivatives. Also, note that there is a difference in the definition of the anisotropic stress compared to Ref. [239]. Since we follow the notation of Ref. [185] we have $\pi_{DE} = w\Pi_{\rm WH}$,

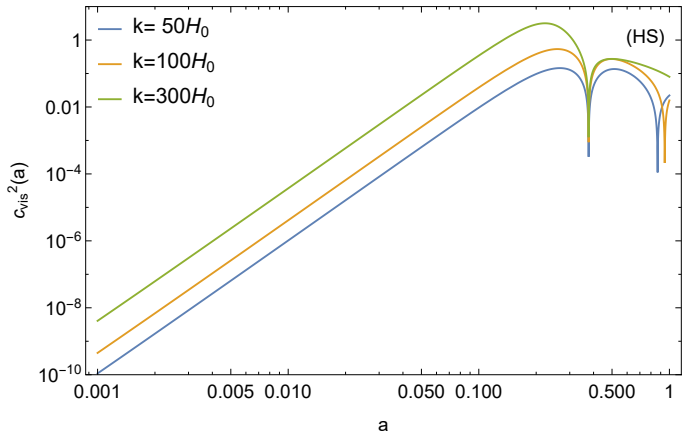

Figure 4.9: The evolution of the viscosity $c^2_{vis}(a)$ parameter for the HS model for $\Omega_{m0} = 0.3$, $f_{R,0} = -10^{-4}$ and values of the wavenumber $k/H_0 = [50, 100, 300]$. As can be seen, the parameter changes by more than 7 orders of magnitude over the range $a \in [10^{-3}, 1]$.

where $\pi_{DE} = \frac{3}{2}(1+w)\sigma$ is the anisotropic stress in this Chapter and $\Pi_{\rm WH}$ is the anisotropic stress parameter of Ref. [239].

The parameterization of Eq. (4.80) is also useful if one wants to explore the properties of a generalized dark matter fluid, as was done in Ref. [287] or place constraints in imperfect fluids [237]. In our case we actually know the underlying DE model, which is our $f(R)$ effective fluid, so using Eq. (4.80) we can reconstruct the viscosity parameter, something which would be of great interest for forecasts for upcoming surveys.

After changing variables from conformal time to scale factor in Eq. (4.80) we can solve for the viscosity parameter as:

$$c^2_{vis} = \frac{aH(1+w)}{4V_{DE}w}\left(3c_a^2(1+w)\pi_{DE} + w(a\pi'_{DE} - 3w\pi_{DE})\right). \tag{4.81}$$

In the case of the HS model it can easily be seen from the previous equation that at early times, in matter domination in particular, the viscosity parameter scales as

$$c^2_{vis} \simeq \frac{14}{3}\frac{1-\Omega_{m0}}{\Omega^2_{m0}}\, b\, k^2\, a^4. \tag{4.82}$$

In the case of the DES model, we have that while $c^2_{vis} \to 0$ there is clearly anisotropic stress in this model as in the RHS of Eq. (4.80) the term $(1+w)$ in the denominator cancels out with c^2_{vis} to give a non-zero result.

In Fig. 4.9 we show the evolution of the viscosity parameter c^2_{vis} given by Eq. (4.81) as a function of scale factor a for the HS model for $\Omega_{m0} = 0.3$, $f_{R,0} = -10^{-4}$ and values of the wave number $k/H_0 = [50, 100, 300]$. As can be seen, the parameter changes by more than 7 orders of magnitude over the range $a \in [10^{-3}, 1]$ which means that in realistic models, like the HS $f(R)$ model, c^2_{vis} clearly cannot be considered as a constant parameter, as is the usual assumption when performing forecasts for future surveys like Euclid [248].

4.5 Cosmological constraints

4.5.1 Data

Here we present the results of our analysis from fitting the latest cosmological observations including the supernovae type Ia (SnIa), Baryon Acoustic Oscillations (BAO), CMB, the Hubble expansion

H(z) and growth $f\sigma_8$ data. In particular, we use the Pantheon SnIa data of Ref. [88], the BAO points from 6dFGS [90], SDDS [81], BOSS CMASS [91], WiggleZ [80], MGS [92] and BOSS DR12 [93]. We also use the CMB shift parameters based on the *Planck 2015* release [267], as derived by Ref. [288].[16] For more details regarding the data used see Chapter 2.

4.5.2 Methodology

Our total likelihood function $L_{\rm tot}$ can be given as the product of the various likelihoods as

$$L_{\rm tot} = L_{\rm SnIa} \times L_{\rm BAO} \times L_{\rm H(z)} \times L_{\rm cmb} \times L_{\rm growth},$$

which can also be translated to the total χ^2 via $\chi^2_{\rm tot} = -2\log L_{\rm tot}$ or

$$\chi^2_{\rm tot} = \chi^2_{\rm SnIa} + \chi^2_{\rm BAO} + \chi^2_{\rm H(z)} + \chi^2_{\rm cmb} + \chi^2_{\rm growth}. \tag{4.83}$$

In order to study the statistical significance of our constraints we will use the well known Akaike Information Criterion (AIC) [289]. Assuming Gaussian errors the AIC estimator is given by

$$\mathrm{AIC} = -2\ln\mathcal{L}_{\rm max} + 2k_p + \frac{2k_p(k_p+1)}{N_{\rm dat}-k_p-1}\,, \tag{4.84}$$

where $N_{\rm dat}$ and k_p indicate the total number of data points and the number of free parameters (see also [290]) of our models, respectively. In our case we have 1048 data points from the Pantheon set, 3 CMB shift parameters, 9 BAO points, 22 growth-rate data and 36 $H(z)$ points for a total of $N_{\rm dat} = 1118$.

The usual interpretation of the AIC estimator is that a smaller value implies a better fit to the data. However, in order to compare different models, we need to use the pair difference which can be written as $\Delta\mathrm{AIC} = \mathrm{AIC}_{\rm model} - \mathrm{AIC}_{\rm min}$. This relative difference can be interpreted with the Jeffreys' scale as follows: $4 < \Delta\mathrm{AIC} < 7$ indicate a positive evidence against the model with higher value of $\mathrm{AIC}_{\rm model}$ and $\Delta\mathrm{AIC} \geq 10$ suggests strong evidence. Finally, when we have that $\Delta\mathrm{AIC} \leq 2$ then this is interpreted as an indication of the consistency of the two models. However, note that the Jeffreys' scale in general has been shown to lead to misleading conclusions, thus it has to be interpreted with care [291]. To summarize, our χ^2 is given by Eq. (4.83) and the parameter vectors (assuming a flat Universe) are given by: $p_{\Lambda\rm CDM} = \left(\Omega_{m0}, 100\Omega_b h^2, h, \sigma_{8,0}\right)$ for the ΛCDM ; and $p_{f(R)} = \left(\Omega_{m0}, 100\Omega_b h^2, \alpha, h, \sigma_{8,0}\right)$ for the $f(R)$ models (when studying the DES model $\alpha = f_{R,0}$ whereas for the HS model $\alpha = b$). Then, the best-fit parameters and their uncertainties were obtained via the MCMC method based on a Metropolis-Hastings algorithm. The MCMC code for Mathematica used in the analysis is freely available at `http://members.ift.uam-csic.es/savvas.nesseris/`. Moreover, we assumed priors for the parameters given by $\Omega_{m0} \in [0.1, 0.5]$, $\Omega_b h^2 \in [0.001, 0.08]$, $\alpha = (-f_{R,0}, b) \in [0, 1]$, $h \in [0.4, 1]$, $\sigma_{8,0} \in [0.1, 1.8]$ and obtained approximately $\sim 10^5$ points for each of the three models.

4.5.3 Results

In Figs. 4.10, 4.11 and 4.12 we show the 68.3%, 95.4% and 99.7% confidence contours for the ΛCDM, the DES and the HS models, respectively, along with the one-dimensional marginalized likelihoods for various parameter combinations. In these plots we also highlight, with either a red point or a black dashed line, the Planck 2015 concordance cosmology. The latter is based on the TT,TE,EE+lowP spectra, a flat ΛCDM model and the values are shown in Table 4.1. In all cases we find the best-fit $\sigma_{8,0}$ parameter is roughly $\sim 2.5\sigma$ away from the Planck 2015 best-fit, thus reaffirming the mild tension between low redshift probes and Planck [120]. However, it should be

[16] When this work was written the likelihoods of the Planck 2018 data release were not publicly available.

Table 4.1: ΛCDM parameters with 68% limits based on TT,TE,EE+lowP and a flat ΛCDM model (middle column) or a wCDM model (right column); see Table 4 of Ref. [267] and the Planck chains archive.

Parameter	Value (ΛCDM)	Value (wCDM)
$\Omega_b h^2$	0.02225 ± 0.00016	0.02229 ± 0.00016
$\Omega_c h^2$	0.1198 ± 0.0015	0.1196 ± 0.0015
n_s	0.9645 ± 0.0049	0.9649 ± 0.0048
H_0	67.27 ± 0.66	> 81.3
Ω_m	0.3156 ± 0.0091	$0.203^{+0.022}_{-0.065}$
w	-1	$-1.55^{+0.19}_{-0.38}$
σ_8	0.831 ± 0.013	$0.983^{+0.100}_{-0.055}$

Table 4.2: The best-fit (top row) and mean (bottom row) parameters for the ΛCDM, the DES and the HS models respectively. Note that $\alpha = (-f_{R,0}, b)$.

Model	Ω_{m0}	$100\Omega_b h^2$	$log_{10}(\alpha)$	h	$\sigma_{8,0}$
Best-fit values					
ΛCDM	0.313 ± 0.006	2.226 ± 0.013	–	0.674 ± 0.004	0.760 ± 0.029
DES	0.314 ± 0.006	2.226 ± 0.014	-8.821 ± 1.946	0.674 ± 0.005	0.753 ± 0.043
HS	0.315 ± 0.006	2.224 ± 0.014	-8.186 ± 1.510	0.674 ± 0.005	0.757 ± 0.036
Mean values					
ΛCDM	0.314 ± 0.006	2.224 ± 0.014	–	0.674 ± 0.004	0.760 ± 0.029
DES	0.314 ± 0.006	2.225 ± 0.014	-6.391 ± 1.916	0.674 ± 0.005	0.738 ± 0.043
HS	0.314 ± 0.006	2.225 ± 0.014	-6.176 ± 1.567	0.674 ± 0.005	0.750 ± 0.035

Table 4.3: The χ^2 and AIC parameters for the ΛCDM, the DES and the HS models respectively.

Model	χ^2	AIC	ΔAIC
ΛCDM	1086.62	1094.660	0
DES	1086.63	1096.684	2.028
HS	1086.61	1096.664	2.008

mentioned that there exist several minima in the likelihood with respect to the modified gravity parameters $f_{R,0}$ and b due to the presence of degeneracies in the growth factor, something which has already been studied in standard GR DE models in Ref. [292].

Furthermore, we find that a mild tension between Planck and low redshift probes remains even in the case of the $f(R)$ models since in general these cannot predict a decreasing G_{eff} which is required by the growth data, in agreement with Refs. [120], [293]. It should be stressed though, that the first year results from the Dark Energy Survey, whose precision is now comparable to that of Planck [154], hints that the tension might be decreasing. Although the central values measured by the Dark Energy Survey for $\sigma_{8,0}$ and Ω_{m0} are a bit lower compared to those of Planck, it was shown in Ref. [154] that the corresponding Bayes factor are similar; thus, the two datasets are becoming more consistent.

In Tables 4.2 and 4.3 we show the best-fit, mean values of the model parameter, and also the values for the χ^2 and AIC parameters for the ΛCDM, the DES and the HS models respectively. As can be seen from Tables 4.2 and 4.3, we find that as the difference in the AIC parameters is roughly ~ 2, then all three models seem to be statistically consistent with each other.

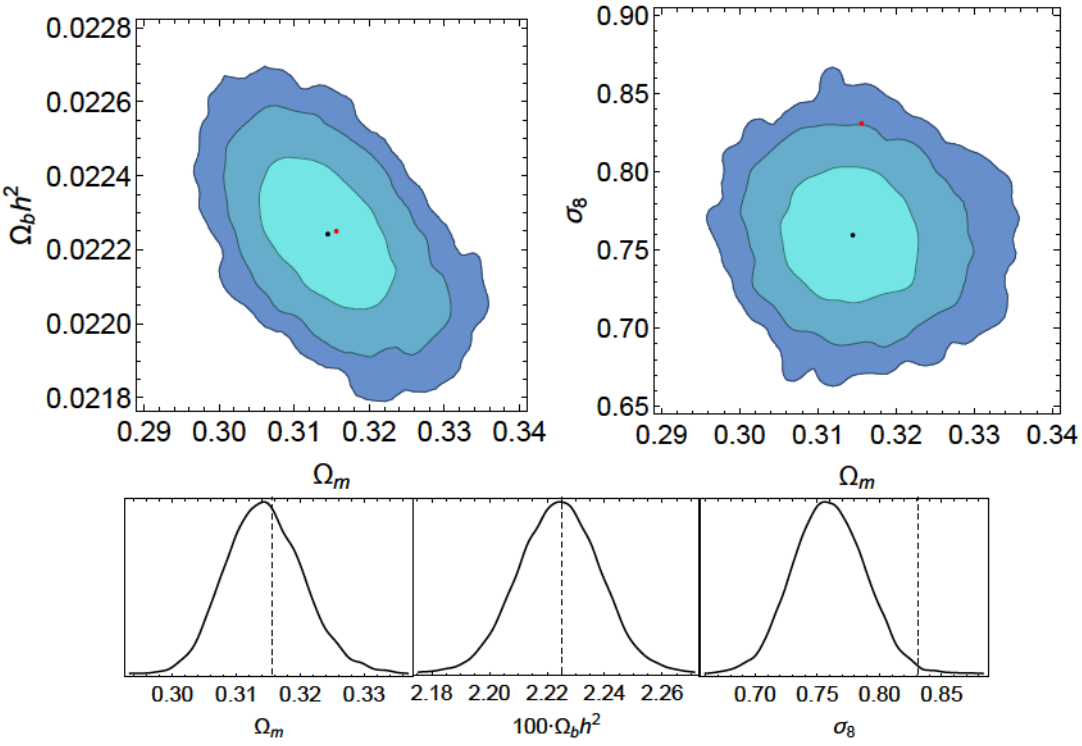

Figure 4.10: The 68.3%, 95.4% and 99.7% confidence contours (top) and the one-dimensional marginalized likelihoods (bottom) for various parameter combinations for the ΛCDM model. The red point and black dashed lines correspond to the concordance Planck 2015 ΛCDM parameters given in Table 4.1. The black point indicates the mean value from the MCMC analysis.

4.6 Conclusions

In this chapter, we discussed in-depth the effective fluid approach and perturbation theory in the context of $f(R)$ theories. We presented several new results, in particular regarding the effective DE fluid components of the energy momentum tensor, the effective velocity of the fluid V_{DE} given by Eq. (4.44), the effective pressure and sound speed given by Eqs. (4.42) and (4.48). We used these expressions in our modifications of the popular `CLASS` code, which we call `EFCLASS`. They provide a much simpler and less error-prone approach in including the effects of modified gravity models.

We then considered specific $f(R)$ models: the well known designer $f(R)$ model (DES), which mimics exactly ΛCDM at the background level, and the Hu-Sawicki (HS) model which can evade solar system tests. For these models, we calculated the solutions of the DE fluid in the matter dominated era, which we later used as initial conditions for the numerical solution of the system. In this regard, we anticipated the evolution of the numerical solutions by studying the behavior of the DE effective sound speed at both early and late times. As shown, the DE effective sound speed is positive at early times, but then quickly it goes to zero at late times and as a result, the DE perturbations first grow quickly, but then at late times flatten out and reach a plateau. We also found that the numerical solutions of the matter perturbations are in good agreement with the $f\sigma_8$ data and we later on used them in our MCMC analysis. Finally, we also confirmed that for these models the Strong Energy Condition (SEC) is violated, in agreement with the expectation for an accelerating Universe.

With these at hand, we then presented `EFCLASS`, namely our modifications of the `CLASS` code, and compared it with other codes in the literature, such as `EFTCAMB`, `CLASS_EOS_FR` and `FRCAMB`. The differences between our modifications, discussed in Appendix A.2, are twofold. First,

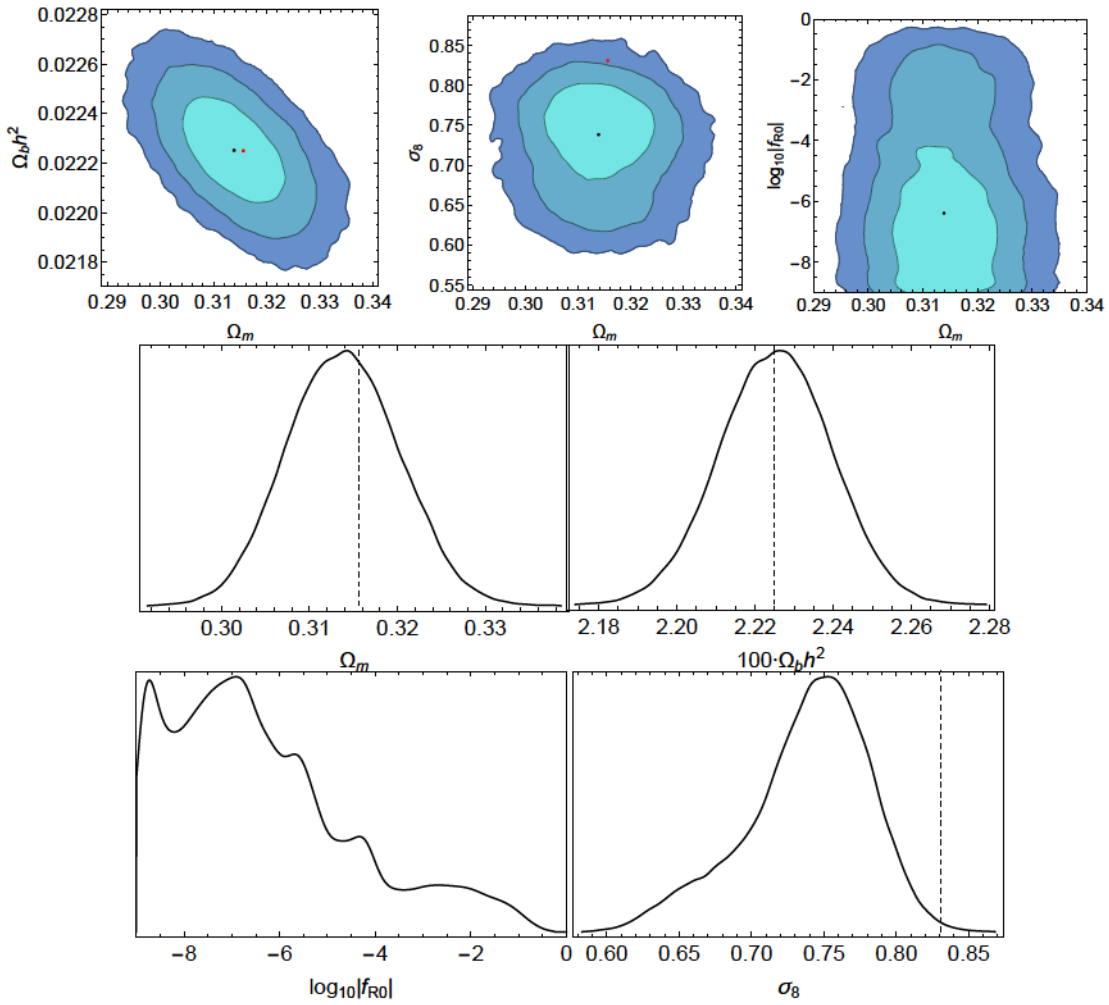

Figure 4.11: The 68.3%, 95.4% and 99.7% confidence contours (top) and the one-dimensional marginalized likelihoods (bottom) for various parameter combinations for the DES model. The red point and black dashed lines correspond to the concordance Planck 2015 ΛCDM parameters given in Table 4.1. The black point indicates the mean value from the MCMC analysis.

in contrast to other codes we treat the background of the $f(R)$ models properly by including the correct evolution of the Hubble parameter. In particular, in the case of the HS model we implement very accurate (better than $< 10^{-5}\%$) second order analytic approximations for the Hubble parameter $H(z)$. Second, our modifications are overall much simpler and less error-prone than the ones found in other codes, as we use the effective fluid approach variables, namely the effective velocity of the fluid V_{DE} given by Eq. (4.44) and the anisotropic stress given by Eqs. (4.45). As a result, since we also properly modify the background in the case of $f(R)$ model, we clearly go beyond the simple comparison of Boltzmann codes as was done in Ref. [294]. While for the DES model we find that our results are in good agreement with expectations and other codes, we find a big difference in the case of the HS model, as the other codes currently ignore the necessary modifications to the background.

An important and related issue is also that the viscosity parameter c^2_{vis} actually is not constant as commonly assumed, but rather evolves significantly, as shown in Fig. 4.9 where we can see the parameter change by more than 7 orders of magnitude over the range $a \in [10^{-3}, 1]$. This means that in realistic models, like the Hu-Sawicki $f(R)$ model, c^2_{vis} clearly cannot be considered as a constant parameter, as is the usual assumption when performing forecasts for future surveys,

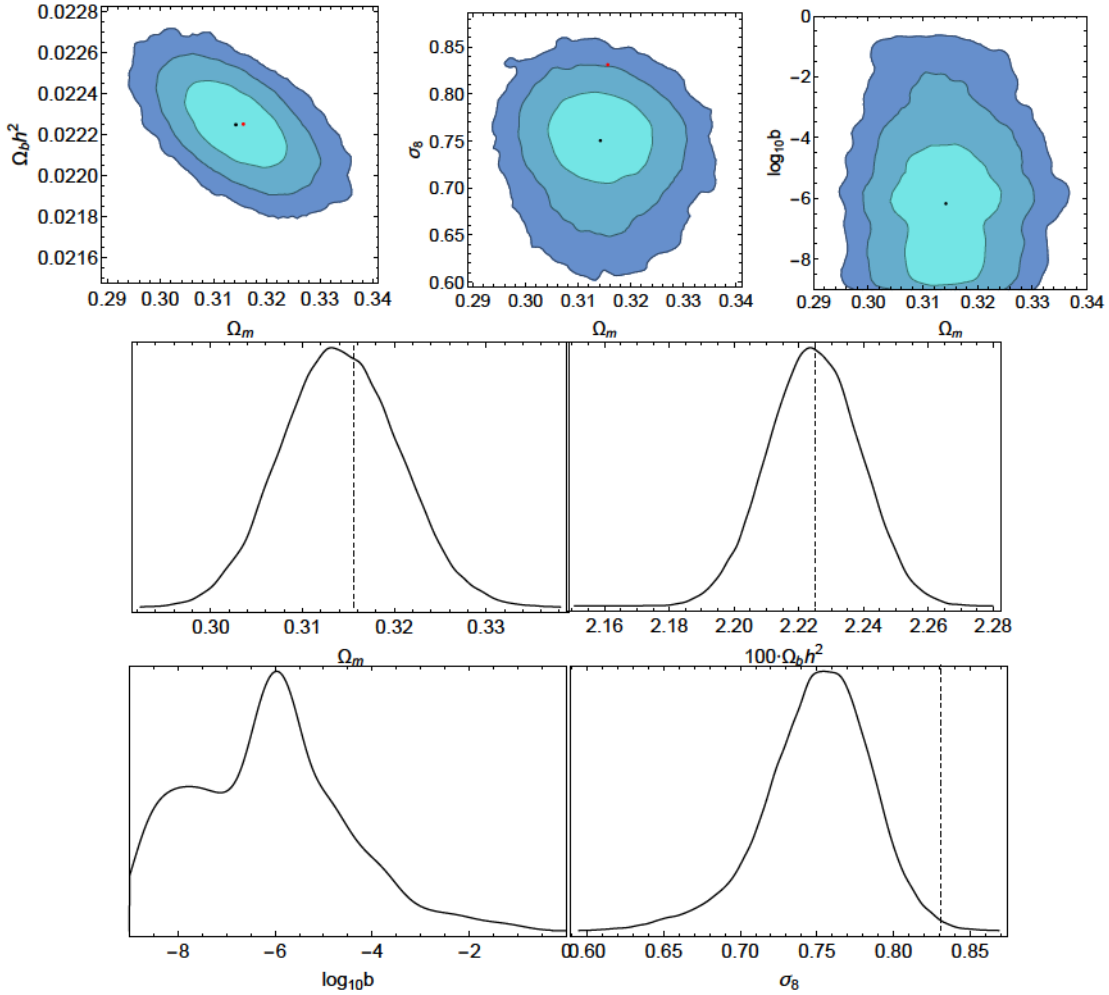

Figure 4.12: The 68.3%, 95.4% and 99.7% confidence contours (top) and the one-dimensional marginalized likelihoods (bottom) for various parameter combinations for the HS model. The red point and black dashed lines correspond to the concordance Planck 2015 ΛCDM parameters given in Table 4.1. The black point indicates the mean value from the MCMC analysis.

something which in the future should be taken into account.

Finally, we also presented results from our MCMC analysis using the latest cosmological probes including SnIa, BAO, CMB, $H(z)$ and growth $f\sigma_8$ data. We presented a complete analysis and a Bayesian comparison of the ΛCDM, DES and HS models. The confidence contours and one-dimensional marginalized likelihoods from the MCMC analysis were shown in Figs. 4.10, 4.11 and 4.12, while in Tables 4.2 and 4.3 we showed the best-fit, mean values of the model parameters, but also the values for the χ^2 and AIC parameters for the ΛCDM, the DES and the HS models respectively. We found that as the difference in the AIC parameters is roughly ~ 2, then all three models can be assumed to be statistically consistent with each other.

To summarize, we showed that by using our new expressions for the DE effective fluid description of the $f(R)$ models as described earlier and the simple modifications to the `CLASS` code in conjunction to the very accurate analytic approximations for the background evolution, we can obtain competitive results in a much simpler and less error-prone approach. In particular, the correct treatment of the background evolution is very important, as in the near future we will have access to cosmological data that constrain the background to less than 1 percent, thus our theoretical predictions must also be at least as accurate.

5

Designing Horndeski and the effective fluid approach

The original content of this chapter is based on Ref. [10]. We present a family of designer Horndeski models, i.e. models that have a background exactly equal to that of the ΛCDM model but perturbations given by the Horndeski theory. Then, we extend the effective fluid approach to Horndeski theories, providing simple analytic formulae for the equivalent dark energy effective fluid pressure, density and velocity. We implement the dark energy effective fluid formulae in our code `EFCLASS`, a modified version of the widely used Boltzmann solver `CLASS`, and compare the solution of the perturbation equations with those of the code `hi_CLASS` which already includes Horndeski models. We find that our simple modifications to the vanilla code are accurate to the level of $\sim 0.1\%$ with respect to the more complicated `hi_CLASS` code. Furthermore, we study the kinetic braiding model both on and off the attractor and we find that even though the full case has a proper ΛCDM limit for large n, it is not appropriately smooth, thus causing the quasistatic approximation to break down. Finally, we focus on our designer model (HDES), which has both a smooth ΛCDM limit and well-behaved perturbations, and we use it to perform Markov Chain Monte Carlo analyses to constrain its parameters with the latest cosmological data. We find that our HDES model can also alleviate the soft 2σ tension between the growth data and Planck 18 due to a degeneracy between σ_8 and one of its model parameters that indicates the deviation from the ΛCDM model.

5.1 Introduction

As we have previously mentioned, given the wide range of both DE and MG models it is useful to have a unified framework which encompasses several of them. It turns out that such a theory exists since 1974 when Horndeski found the most general Lorentz-invariant extension of GR in four dimensions [182]. This theory can be obtained by using a single scalar field and restricting the equations of motion to being second order in time derivatives. The Horndeski Lagrangian comprehends theories such as Kinetic Gravity Braiding, Brans-Dicke and scalar tensor gravity, single field quintessence and K-essence theories, as well as $f(R)$ theories in their scalar-tensor formulation [295]. Although the range of models encompassed by the Horndeski Lagrangian was severely reduced (see, for instance, [171–181, 296, 297]) with the recent discovery of gravitational waves by the LIGO Collaboration [170], an interesting remaining subclass of models (including $f(R)$ theories [197–200] and Kinetic Gravity Braiding [298]) is well worth an investigation.

In Chapter 4 we employed an effective fluid approach to study $f(R)$ theories [9]. Even though it is not easy to obtain expressions for quantities describing perturbations (e.g., pressure perturbation δP) in MG models [6], by using the quasistatic and subhorizon approximations we found analytical expressions for the effective DE perturbations as well as the quantities describing the effective DE fluid, namely, $w(a)$, $c_s^2(a,k)$, and $\sigma(a,k)$. We implemented our approach in the code `CLASS`[1] [232] and found excellent agreement with the so-called Equation of State (EOS)

[1] http://class-code.net/

approach [231, 233], which does not use any approximation. In this Chapter we extend our work to the remaining part of the Horndeski Lagrangian which contains $f(R)$ theories as a special case. Horndeski theories have been implemented in the code `hi_CLASS` [299] which solves the full set of dynamical equations without using the quasistatic approximation. In our approach we find analytical expressions for the effective DE perturbations that give us a better understanding of the underlying physics and also allow us to compare with our numerical implementation. Moreover, we show that it is possible to find 'designer Horndeski theories' matching a given background evolution. We implement one such a model in the `hi_CLASS` code and show there is good agreement with our approach, namely, our effective fluid approach assuming both quasistatic and subhorizon approximations performs quite well.

The Chapter is organized as follows. In Sec. 5.2 we discuss the equations for perturbations in a Friedmann-Lemaitre-Robertson-Walker (FLRW) metric and set our notation. Then, we introduce the Horndeski Lagrangian and discuss both background and perturbation equations in Sec. 5.3. In Sec. 5.4 we study the remaining subclass of Horndeski theories by utilizing the effective fluid approach, we discuss the subhorizon and quasistatic approximations and present analytical results for two classes of models, those in which we have dark energy anisotropic stress and those in which we do not. In Sec. 5.5 we show analytical results for a family of models named 'designer Horndeski' which mimic the ΛCDM background and in Sec. 5.6 we compare our analytical solutions for DE perturbations with a fully numerical solution of the system of differential equations and show they are in very good agreement. We then constrain the parameter space for a viable designer Horndeski model in Sec. 5.7 and in Sec. 5.8 we present our conclusions. In Appendices B.1 and B.2 we give details about our analytical computations.

5.2 Theoretical framework

As a reminder and to set out our notation for this Chapter, in the standard cosmological model one assumes the Einstein-Hilbert action

$$S = \int d^4x\sqrt{-g}\left[\frac{1}{2\kappa}R + \mathcal{L}_m\right], \tag{5.1}$$

where g is the determinant of the metric $g_{\mu\nu}$, R is the Ricci scalar, $\kappa \equiv \frac{8\pi G_N}{c^4}$ and $\mathcal{L}_m$ is the Lagrangian for matter fields.[2] Applying the principle of least action to Eq. (5.1) one obtains the field equations

$$G_{\mu\nu} = \kappa\, T^{(m)}_{\mu\nu}, \tag{5.2}$$

where $G_{\mu\nu} \equiv R_{\mu\nu} - \frac{1}{2}g_{\mu\nu}R$ is the Einstein tensor and $T^{(m)}_{\mu\nu}$ is the energy-momentum tensor for matter fields. At this point one needs to make assumptions about the geometrical properties and the matter content in the Universe. First, since observations indicate the Universe on large scales is statistically homogeneous and isotropic [300, 301] (also having tiny inhomogeneities which can be treated within linear perturbation theory), one further assumes a perturbed FLRW metric.

In this Chapter we are working with a slightly different definition of the metric to that of Chapter 4 (see Eq. (4.1)) since in the literature, specially when working with Horndeski's theory it is common to work with the cosmic time t and with a positive sign in front of the Newtonian potential Φ, where in Eq. (4.1) we previously had placed a minus sign. Hence, we will repeat part of the analysis derived in Chapter 4 but with the considerations mentioned before. To start we will assume the following perturbed FLRW metric

$$ds^2 = -\left(1 + 2\Psi(\vec{x}, t)\right) dt^2 + a(t)^2(1 + 2\Phi(\vec{x}, t))d\vec{x}^2, \tag{5.3}$$

[2] Throughout this Chapter we set the speed of light $c = 1$ and $\kappa = 8\pi G_N$ with G_N being the bare Newton's constant. Our conventions are: $(-+++)$ for the metric signature, the Riemann and Ricci tensors are given respectively by $V_{b;cd} - V_{b;dc} = V_a R^a_{bcd}$ and $R_{ab} = R^s_{asb}$.

where a is the scale factor, $\vec{x}$ represents spatial coordinates, t is the cosmic time and Ψ and Φ are the gravitational potentials in the Newtonian gauge. Second, one can suppose the matter fields are ideal fluids (with small perturbations) having an energy-momentum tensor given by

$$T^{\mu}_{\nu} = P\delta^{\mu}_{\nu} + (\rho + P)U^{\mu}U_{\nu}, \tag{5.4}$$

where P is the pressure, ρ is the energy density, and $U^{\mu} = \left(1 - \Psi, \frac{\vec{u}}{a(t)}\right)$ is the velocity four-vector. As a result, the elements of the energy-momentum tensor up to first order are given by :

$$T^{0}_{0} = -(\bar{\rho} + \delta\rho), \tag{5.5}$$

$$T^{0}_{i} = (\bar{\rho} + \bar{P})a(t)u_i, \tag{5.6}$$

$$T^{i}_{j} = (\bar{P} + \delta P)\delta^{i}_{j} + \Sigma^{i}_{j}, \tag{5.7}$$

where $\bar{\rho}$ is the background energy density, $\bar{P}$ is the background pressure, $u_i = a(t)\dot{x}_i$, $\Sigma^{i}_{j}(\vec{x},\tau) \equiv T^{i}_{j} - \delta^{i}_{j}T^{k}_{k}/3$ is an anisotropic stress tensor, and $\delta\rho(\vec{x},\tau)$ and $\delta P(\vec{x},\tau)$ are the density and pressure perturbations, respectively.[3]

5.2.1 Background

If one only considers zero order quantities in the Einstein field equations (5.2), then there are two independent Friedmann equations describing the background evolution of the Universe:

$$H^2 = \frac{\kappa}{3}\bar{\rho}, \tag{5.8}$$

$$H^2 + \dot{H} = -\frac{\kappa}{6}\left(\bar{\rho} + 3\bar{P}\right), \tag{5.9}$$

where $H \equiv \frac{\dot{a}}{a}$ is the cosmic Hubble parameter.[4]

5.2.2 Linear perturbations

Considering just the first order perturbations in the Einstein field equations (5.2) we obtain

$$-\frac{k^2}{a^2}\Phi + 3\frac{\dot{a}}{a}\left(\frac{\dot{a}}{a}\Psi - \dot{\Phi}\right) = \frac{\kappa}{2}\delta T^{0}_{0}, \tag{5.10}$$

$$k^2\left(\frac{\dot{a}}{a}\Psi - \dot{\Phi}\right) = \frac{\kappa}{2}a(\bar{\rho} + \bar{P})\theta, \tag{5.11}$$

$$-\frac{k^2}{3a^2}(\Phi + \Psi) + \left(2\frac{\ddot{a}}{a} + \frac{\dot{a}^2}{a^2}\right)\Psi + \frac{\dot{a}}{a}\left(\dot{\Psi} - 3\dot{\Phi}\right) - \ddot{\Phi} = \frac{\kappa}{6}\delta T^{i}_{i}, \tag{5.12}$$

$$-k^2(\Phi + \Psi) = \frac{3\kappa}{2}a^2(\bar{\rho} + \bar{P})\sigma, \tag{5.13}$$

where we defined the velocity $\theta \equiv ik^j u_j$ and wrote the anisotropic stress as $(\bar{\rho} + \bar{P})\sigma \equiv -(\hat{k}_i\hat{k}_j - \frac{1}{3}\delta_{ij})\Sigma^{ij}$.

From the conservation of the energy-momentum tensor $T^{\mu\nu}_{;\nu} = 0$ one obtains the equations for the evolution of perturbations. Defining the equation of state parameter as $w \equiv \frac{\bar{P}}{\bar{\rho}}$ and the sound speed $c_s^2 \equiv \frac{\delta P}{\delta\rho}$ we find the equations governing the evolution of density and pressure perturbations are given by

$$\dot{\delta} = -(1 + w)(\frac{\theta}{a} + 3\dot{\Phi}) - 3\frac{\dot{a}}{a}\left(c_s^2 - w\right)\delta, \tag{5.14}$$

[3] In our notation, a dot over a function f denotes the derivative with respect to the cosmic time : $\dot{f} \equiv \frac{df}{dt}$. In addition, Greek indices run from 0 to 3 whereas Latin indices take on values from 1 to 3.

[4] The conformal Hubble parameter $\mathcal{H}$ and the Hubble parameter H are related via $\mathcal{H} = aH$.

$$\dot{\theta} = -\frac{\dot{a}}{a}(1-3w)\theta - \frac{\dot{w}}{1+w}\theta + \frac{c_s^2}{1+w}\frac{k^2}{a}\delta - \frac{k^2}{a}\sigma + \frac{k^2}{a}\Psi, \tag{5.15}$$

The system of differential equations (5.14)-(5.15) presents problems when the equation of state crosses -1 because there is a singularity. However, a simple change of variable turns out to be helpful in solving this inconvenience. We will use the scalar velocity perturbation $V \equiv ik_jT_0^j/\rho = (1+w)\theta$ instead of the velocity θ. In terms of this new variable the evolution equations (5.14)-(5.15) become

$$\delta' = -3(1+w)\Phi' - \frac{V}{a^2H} - \frac{3}{a}\left(\frac{\delta P}{\bar{\rho}} - w\delta\right), \tag{5.16}$$

$$V' = -(1-3w)\frac{V}{a} + \frac{k^2}{a^2H}\frac{\delta P}{\bar{\rho}} + (1+w)\frac{k^2}{a^2H}\Psi - \frac{2}{3}\frac{k^2}{a^2H}\pi, \tag{5.17}$$

where a prime $'$ denotes a derivative with respect to the scale factor and we defined the anisotropic stress parameter $\pi \equiv \frac{3}{2}(1+w)\sigma$.

5.3 Horndeski

Horndeski theory constitutes the most general Lorentz-invariant extension of GR in four dimensions and encompasses several DE and MG models. Although in its most general form the Horndeski Lagrangian has several free functions, the recent discovery of gravitational waves by the LIGO Collaboration significantly constrained the allowed models. In particular, it has been shown that the constraint on the speed of Gravitational Waves (GWs) must satisfy [173]

$$-3\cdot 10^{-15} \leq c_g/c - 1 \leq 7\cdot 10^{-16}, \tag{5.18}$$

which for Horndeski theories implies that

$$G_{4X} \approx 0, \quad G_5 \approx \text{const.}, \tag{5.19}$$

as can be seen from the sound speed formula for tensor perturbations [302]

$$c_T^2 = \frac{G_4 - XG_{5\phi} - XG_{5X}\ddot{\phi}}{G_4 - 2XG_{4X} - X\left(G_{5X}\dot{\phi}H - G_{5\phi}\right)}. \tag{5.20}$$

In this section we will derive evolution equations for the remaining parts of the Horndeski Lagrangian, namely,

$$S[g_{\mu\nu},\phi] = \int d^4x\sqrt{-g}\left[\sum_{i=2}^{4}\mathcal{L}_i\left[g_{\mu\nu},\phi\right] + \mathcal{L}_m\right], \tag{5.21}$$

where

$$\mathcal{L}_2 = G_2(\phi,X) \equiv K(\phi,X), \tag{5.22}$$

$$\mathcal{L}_3 = -G_3(\phi,X)\,\Box\phi, \tag{5.23}$$

$$\mathcal{L}_4 = G_4(\phi)\,R. \tag{5.24}$$

Here ϕ is a scalar field, $X \equiv -\frac{1}{2}\partial_\mu\phi\partial^\mu\phi$ is a kinetic term, and $\Box\phi \equiv g^{\mu\nu}\nabla_\mu\nabla_\nu\phi$; K, G_3 and G_4 are free functions of ϕ and X.[5] Since we are mainly interested in the late-time dynamics of the Universe, hereafter we will further assume $\mathcal{L}_m$ is the Lagrangian of a CDM component. As has been mentioned in [177], although the functions K, G_3 and G_4 are able to modify the background with a general dependence on X and ϕ, this does not hold at the perturbations level.

[5] From now on we define $G_i \equiv G_i(\phi,X)$, $G_{i,X} \equiv G_{iX} \equiv \frac{\partial G_i}{\partial X}$ and $G_{i,\phi} \equiv G_{i\phi} \equiv \frac{\partial G_i}{\partial \phi}$ where $i = 2,3,4$.

For instance, $K(\phi, X)$ encloses the k-essence and quintessence theory and is partly responsible for the background and the perturbations, however $K(\phi)$ does not contribute to the perturbations.

The term $G_3(\phi, X)$ includes the kinetic gravity braiding with $G_{3X} \neq 0$ being in charge of combining the kinetic term of the scalar and the metric, but the term $G_3(\phi)$ only modifies the background as a dynamical dark energy. Finally, G_4 is the only function that is able to modify the non-minimal coupling of the scalar to the Ricci curvature.

Among the theories embedded in the action (5.21) one finds, for example:

- **f(R) theories.** When interpreted as a non-minimal coupled scalar field, these theories can be written using [303]

$$K = -\frac{Rf_{,R} - f}{2\kappa}, \quad G_4 = \frac{\phi}{2\sqrt{\kappa}}, \tag{5.25}$$

  where $\phi \equiv \frac{f_{,R}}{\sqrt{\kappa}}$ has units of mass and $f_{,R} \equiv \dfrac{df}{dR}$.

- **Brans-Dicke theories.** In our notation we have

$$K = \frac{\omega_{BD} X}{\phi\sqrt{\kappa}} - V(\phi), \quad G_4 = \frac{\phi}{2\sqrt{\kappa}}, \tag{5.26}$$

  where $V(\phi)$ is the field potential and ω_{BD} is the Brans-Dicke parameter [304].

- **Kinetic gravity braiding.** This kind of scalar-tensor models exhibit mixing of scalar and tensor kinetic terms [298] and can be written as

$$K = K(X), \quad G_3 = G_3(X), \quad G_4 = \frac{1}{2\kappa}. \tag{5.27}$$

- **Non-minimal coupling (NMC) model [305].** In our notation and for a coupling constant ζ

$$K = \omega(\phi)X - V(\phi), \quad G_4 = \left(\frac{1}{2\kappa} - \frac{\zeta\phi^2}{2}\right), \quad G_3 = 0. \tag{5.28}$$

  In the context of inflation, a Higgs-like inflation model corresponds to $\omega(\phi) = 1$, $V(\phi) = \lambda\left(\phi^2 - \nu^2\right)^2/4$.

- **Cubic Galileon [305].** The simplest case is when

$$K = -X, \quad G_3 \propto X, \quad G_4 = \frac{1}{2\kappa}, \tag{5.29}$$

- **4-dimensional static and spherical symmetric solution of Black Hole with scalar hair [306].**

$$K = X, \quad G_3 = -\frac{\alpha \log(-X)}{\sqrt{\kappa}}, \quad G_4 = \frac{1}{2\kappa}. \tag{5.30}$$

As previously done for the Einstein-Hilbert action (5.1), here we apply the principle of least action to (5.21) in order to find evolution equations for both the gravitational field and the scalar field. Varying Eq. (5.21) with respect to the metric and the scalar field one finds[6] [302]

$$\delta\left(\sqrt{-g}\sum_{i=2}^{4}\mathcal{L}_i\right) = \sqrt{-g}\left[\sum_{i=2}^{4}\mathcal{G}^i_{\mu\nu}\delta g^{\mu\nu} + \sum_{i=2}^{4}\left(P^i_\phi - \nabla^\mu J^i_\mu\right)\delta\phi\right] + \text{total derivative}, \tag{5.31}$$

[6] See Appendix B.1 for a derivation of the field equations.

which allows us to find the field equations. First, the gravitational field equation is given by

$$\sum_{i=2}^{4}\mathcal{G}^{i}_{\mu\nu}=\frac{1}{2}T^{(m)}_{\mu\nu}, \tag{5.32}$$

where we have defined

$$\mathcal{G}^{2}_{\mu\nu} = -\frac{1}{2}K_X\nabla_\mu\phi\nabla_\nu\phi-\frac{1}{2}Kg_{\mu\nu} \tag{5.33}$$

$$\mathcal{G}^{3}_{\mu\nu} = \frac{1}{2}G_{3X}\Box\phi\nabla_\mu\phi\nabla_\nu\phi+\nabla_{(\mu}G_3\nabla_{\nu)}\phi-\frac{1}{2}g_{\mu\nu}\nabla_\lambda G_3\nabla^\lambda\phi \tag{5.34}$$

$$\mathcal{G}^{4}_{\mu\nu} = G_4G_{\mu\nu}+g_{\mu\nu}\left(G_{4\phi}\Box\phi-2XG_{4\phi\phi}\right)-G_{4\phi}\nabla_\mu\nabla_\nu\phi-G_{4\phi\phi}\nabla_\mu\phi\nabla_\nu\phi, \tag{5.35}$$

and $T^{(m)}_{\mu\nu}$ is the energy-momentum tensor of a CDM component. Note that from Eq. (5.32) we retrieve the GR field equations (5.2) if we set $K=G_3=0$ and $G_4=\frac{1}{2\kappa}$. Second, the scalar field equation reads

$$\nabla^\mu\left(\sum_{i=2}^{4}J^{i}_{\mu}\right)=\sum_{i=2}^{4}P^{i}_{\phi}, \tag{5.36}$$

where

$$P^{2}_{\phi}=K_\phi,\quad P^{3}_{\phi}=\nabla_\mu G_{3\phi}\nabla^\mu\phi,\quad P^{4}_{\phi}=G_{4\phi}R, \tag{5.37}$$

$$J^{2}_{\mu}=-\mathcal{L}_{2X}\nabla_\mu\phi,\quad J^{3}_{\mu}=-\mathcal{L}_{3X}\nabla_\mu\phi+G_{3X}\nabla_\mu X+2G_{3\phi}\nabla_\mu\phi,\quad J^{4}_{\mu}=0. \tag{5.38}$$

As it is mentioned in Ref. [302], one could think $\nabla^\mu J^i_\mu$ leads to higher than second-order derivatives. However, this is not the case since commutations of higher derivatives can be substituted by the curvature tensor and are hence canceled. In particular, one can prove that

$$\nabla_\mu\left(\Box\phi\nabla^\mu\phi+\nabla^\mu X\right)=\left(\Box\phi\right)^2-\left(\nabla_\alpha\nabla_\beta\phi\right)^2-R_{\mu\nu}\nabla^\mu\phi\nabla^\nu\phi, \tag{5.39}$$

which will be of paramount importance when we will discuss perturbation equations.

It is possible to find a relatively simple expression for the scalar field equation (5.36) if we consider the case $i=3$, namely,

$$0=2G_{3\phi}\Box\phi+\nabla^\mu G_{3\phi}\nabla_\mu\phi+\nabla_\mu\phi\nabla^\mu G_{3X}\Box\phi+\underbrace{\nabla^\mu\left(G_{3X}\nabla_\mu X\right)+G_{3X}\left(\Box\phi\right)^2+G_{3X}\nabla_\mu\phi\nabla^\mu\Box\phi}. \tag{5.40}$$

The terms on top of the brace in Eq. (5.40) can be expanded as

$$\nabla^\mu G_{3X}\nabla_\mu X+\underbrace{G_{3X}\Box X+G_{3X}\left(\Box\phi\right)^2+G_{3X}\nabla^\mu\phi\nabla_\mu\Box\phi}=0, \tag{5.41}$$

and the terms on top of the brace in Eq. (5.41) can in turn be written as

$$G_{3X}\left[\nabla^\mu\phi\nabla_\mu\Box\phi+\left(\Box\phi\right)^2+\Box X\right]=G_{3X}\left[\nabla_\mu\left(\Box\phi\nabla^\mu\phi+\nabla^\mu X\right)\right]. \tag{5.42}$$

Using Eq. (5.39) in Eq. (5.42) we find

$$G_{3X}\left[\nabla^\mu\phi\nabla_\mu\Box\phi+\left(\Box\phi\right)^2+\Box X\right]=G_{3X}\left[\left(\Box\phi\right)^2-\left(\nabla_\alpha\nabla_\beta\phi\right)^2-R_{\mu\nu}\nabla^\mu\phi\nabla^\nu\phi\right], \tag{5.43}$$

and the scalar field equation (5.36) can be written as

$$\begin{aligned} &-\nabla_\mu K_X\nabla^\mu\phi-K_X\Box\phi-K_\phi+2G_{3\phi}\Box\phi+\nabla_\mu G_{3\phi}\nabla^\mu\phi+\nabla_\mu G_{3X}\Box\phi\nabla^\mu\phi+\nabla_\mu G_{3X}\nabla^\mu X\\ &+G_{3X}\left[\left(\Box\phi\right)^2-\left(\nabla_\alpha\nabla_\beta\phi\right)^2-R_{\mu\nu}\nabla^\mu\phi\nabla^\nu\phi\right]-G_{4\phi}R=0. \end{aligned} \tag{5.44}$$

In what follows, in order to simplify the notation we will denote the kinetic term of the scalar field evaluated at the background simply by X and its linear order perturbation as δX.

5.3.1 Background

Thus far the discussion of the field equations has been quite general. Now, as previously done in Sec. 5.2, we assume a perturbed FLRW as given in Eq. (5.3). If we consider only zero order quantities in the gravitational field equation (5.32), we obtain

$$\mathcal{E} \equiv \sum_{i=2}^{4} \mathcal{E}_i = -\rho_m, \tag{5.45}$$

$$\mathcal{P} \equiv \sum_{i=2}^{4} \mathcal{P}_i = 0, \tag{5.46}$$

where

$$\mathcal{E}_2 \equiv 2XK_X - K, \quad \mathcal{E}_3 \equiv 6X\dot{\phi}HG_{3X} - 2XG_{3\phi}, \quad \mathcal{E}_4 \equiv -6H^2G_4 - 6H\dot{\phi}G_{4\phi}, \tag{5.47}$$

$$\mathcal{P}_2 \equiv K, \quad \mathcal{P}_3 \equiv -2X\left(G_{3\phi} + \ddot{\phi}G_{3X}\right), \quad \mathcal{P}_4 \equiv 2\left(3H^2 + 2\dot{H}\right)G_4 + 2\left(\ddot{\phi} + 2H\dot{\phi}\right)G_{4\phi} + 2\dot{\phi}^2 G_{4\phi\phi}. \tag{5.48}$$

Eqs. (5.45)-(5.46) are the modified Friedmann equations describing the background evolution of the Universe. Collecting terms they respectively read

$$2XK_X - K + 6X\dot{\phi}HG_{3X} - 2XG_{3\phi} - 6H^2G_4 - 6H\dot{\phi}G_{4\phi} + \rho_m = 0, \tag{5.49}$$

$$K - 2X\left(G_{3\phi} + \ddot{\phi}G_{3X}\right) + 2\left(3H^2 + 2\dot{H}\right)G_4 + 2\left(\ddot{\phi} + 2H\dot{\phi}\right)G_{4\phi} + 2\dot{\phi}^2 G_{4\phi\phi} = 0. \tag{5.50}$$

Note that from Eqs. (5.49)-(5.50) we respectively retrieve the Friedmann equations (5.8)-(5.9) if we set $K = G_3 = 0$ and $G_4 = \frac{1}{2\kappa}$. Rearranging terms in Eqs. (5.49)-(5.50) we can define an effective DE density

$$\bar{\rho}_{DE} = \dot{\phi}^2 K_X - K + 3\dot{\phi}^3 HG_{3X} - \dot{\phi}^2 G_{3\phi} + 3H^2\left(\frac{1}{\kappa} - 2G_4\right) - 6H\dot{\phi}G_{4\phi}, \tag{5.51}$$

and an effective DE pressure

$$\bar{P}_{DE} = K - \dot{\phi}^2\left(G_{3\phi} + \ddot{\phi}G_{3X}\right) + 2\dot{\phi}^2 G_{4\phi\phi} + 2\left(\ddot{\phi} + 2H\dot{\phi}\right)G_{4\phi} - \left(3H^2 + 2\dot{H}\right)\left(\frac{1}{\kappa} - 2G_4\right), \tag{5.52}$$

in such a way that we can write the modified Friedmann equations Eqs. (5.49)-(5.50) as

$$3H^2 = \kappa\left(\bar{\rho}_{DE} + \rho_m\right) \tag{5.53}$$

$$-\left(2\dot{H} + 3H^2\right) = \kappa\bar{P}_{DE}, \tag{5.54}$$

where we are assuming that matter is pressureless $\bar{P}_m = 0$ as indicated by current constraints [307]. The effective DE density and pressure in Eqs. (5.51)-(5.52) allow us to define an effective DE equation of state as

$$w_{DE} = \frac{K - \dot{\phi}^2\left(G_{3\phi} + \ddot{\phi}G_{3X}\right) - \left(3H^2 + 2\dot{H}\right)\left(\frac{1}{\kappa} - 2G_4\right) + 2\left(\ddot{\phi} + 2H\dot{\phi}\right)G_{4\phi} + 2\dot{\phi}^2 G_{4\phi\phi}}{\dot{\phi}^2 K_X - K + 3\dot{\phi}^3 HG_{3X} - \dot{\phi}^2 G_{3\phi} + 3H^2\left(\frac{1}{\kappa} - 2G_4\right) - 6H\dot{\phi}G_{4\phi}}. \tag{5.55}$$

Let us now consider the scalar field equation (5.44) and only keep zero order quantities, that is to say,

$$K_\phi - (K_X - 2G_{3\phi})\left(\ddot{\phi} + 3H\dot{\phi}\right) - K_{\phi X}\dot{\phi}^2 - K_{XX}\ddot{\phi}\dot{\phi}^2 + G_{3\phi\phi}\dot{\phi}^2 + G_{3\phi X}\dot{\phi}^2\left(\ddot{\phi} - 3H\dot{\phi}\right) -$$

$$3G_{3X}\left(2H\dot{\phi}\ddot{\phi}+3H^2\dot{\phi}^2+\dot{H}\dot{\phi}^2\right)-3G_{3XX}H\dot{\phi}^3\ddot{\phi}+6G_{4\phi}\left(2H^2+\dot{H}\right)=0, \tag{5.56}$$

which fully agrees with [308]. Note that defining

$$J_\mu \equiv \sum_{i=2}^{4} J_\mu^i, \tag{5.57}$$

$$P_\phi \equiv \sum_{i=2}^{4} P_\phi^i, \tag{5.58}$$

we can write the scalar field equation (5.36) as

$$\nabla_\mu J^\mu = P_\phi, \tag{5.59}$$

and it becomes clear that there exists a Noether current for Lagrangians invariant under constant shifts of the field $\phi \to \phi + c$ [298], namely,

$$J_\mu = \left(\mathcal{L}_{2X}+\mathcal{L}_{3X}-2G_{3\phi}\right)\nabla_\mu\phi - G_{3X}\nabla_\mu X. \tag{5.60}$$

Taking into consideration that $X=\frac{1}{2}\dot{\phi}^2$, the charge density of the Noether current can be written as

$$J \equiv J_0 = \dot{\phi}\left(K_X - 2G_{3\phi} + 3H\dot{\phi}G_{3X}\right), \tag{5.61}$$

so that the scalar field equation is given by the simple expression

$$\dot{J}+3HJ=P_\phi. \tag{5.62}$$

When $P_\phi = 0$ then it is easy to see that the solution to the previous equation is

$$J=\frac{J_c}{a^3}, \tag{5.63}$$

where J_c is a constant. When $J_c = 0$, then the system is on the attractor solution, but when $J_c \neq 0$ then the system is not on the attractor and as we will see in Sec. 5.4.2 interesting dynamics may arise.

5.3.2 Linear perturbations

Considering only first order quantities in the gravitational field equations (5.32) one obtains [309, 310]

$$A_1\dot{\Phi}+A_2\dot{\delta\phi}+A_3\frac{k^2}{a^2}\Phi+A_4\Psi+\left(A_6\frac{k^2}{a^2}-\mu\right)\delta\phi-\rho_m\delta_m=0, \tag{5.64}$$

$$C_1\dot{\Phi}+C_2\dot{\delta\phi}+C_3\Psi+C_4\delta\phi-\frac{a\rho_m V_m}{k^2}=0, \tag{5.65}$$

$$B_1\ddot{\Phi}+B_2\ddot{\delta\phi}+B_3\dot{\Phi}+B_4\dot{\delta\phi}+B_5\dot{\Psi}+B_6\frac{k^2}{a^2}\Phi+\left(B_7\frac{k^2}{a^2}+3\nu\right)\delta\phi \tag{5.66}$$

$$+\left(B_8\frac{k^2}{a^2}+B_9\right)\Psi=0,$$

$$G_4\left(\Psi+\Phi\right)+G_{4\phi}\delta\phi=0. \tag{5.67}$$

Note that when $K = G_3 = 0$ and $G_4 = \frac{1}{2\kappa}$, Eqs. (5.64)-(5.67) respectively correspond to the GR limit given by Eqs. (5.10)-(5.13) with $\sigma_m = 0$.

If we now consider the scalar field equation (5.44) and take into account only first order quantities we find

$$D_1\ddot{\Phi} + D_2\ddot{\delta\phi} + D_3\dot{\Phi} + D_4\dot{\delta\phi} + D_5\dot{\Psi} + \left(D_7\frac{k^2}{a^2} + D_8\right)\Phi + \left(D_9\frac{k^2}{a^2} - M^2\right)\delta\phi + \left(D_{10}\frac{k^2}{a^2} + D_{11}\right)\Psi = 0. \tag{5.68}$$

Expressions for the coefficients A_i, μ, ν, B_i, C_i and D_i can be found in Appendix B.2 and are in agreement with those found in [309, 310], except for D_8 which is actually equal to zero as can be seen by using the expression found in [310] and using the background equations of motion for the scalar field.

5.4 The effective fluid approach

We have seen in the previous section that the gravitational field equations for the Horndeski Lagrangian can be written in such a way that they resemble those found in Sec. 5.2 where we assumed GR and a perfect fluid. Indeed, defining an effective DE density and pressure given by Eqs. (5.51)-(5.52) makes it possible to obtain an effective DE equation of state (see Eq. (5.55)). As mentioned in Sec. 5.1, a fluid can be described by its equation of state, sound speed, and anisotropic stress, so in what follows we will explicitly derive those quantities.

In this section we will present relatively simple expressions for the effective DE sound speed and anisotropic stress under the subhorizon and quasistatic approximations. Actually, by defining an effective DE fluid we are considering a DE effective energy-momentum tensor $T^{DE}_{\mu\nu}$ obtained via the gravitational field equations (5.32) and defined explicitly as follows:

$$\begin{aligned} G_{\mu\nu} &= \kappa\left(T^{(m)}_{\mu\nu} + T^{(DE)}_{\mu\nu}\right), \\ \kappa T^{(DE)}_{\mu\nu} &= G_{\mu\nu} - 2\kappa\sum_{i=2}^{4}\mathcal{G}^i_{\mu\nu}. \end{aligned} \tag{5.69}$$

Since we are taking into consideration expressions up to linear order, $T^{DE}_{\mu\nu}$ also contains small perturbations which allow us to define quantities such as DE effective perturbations in the pressure, density, and velocity. These can be extracted from the DE effective energy-momentum tensor $T^{DE}_{\mu\nu}$ by considering the decomposition of the tensor into its components, given by Eqs. (5.5)-(5.7). Qualitatively, these expressions have the following structure which resembles to that of the $f(R)$ case (see Chapter 4):

$$\frac{\delta P_{DE}}{\bar{\rho}_{DE}} = (...)\delta\phi + (...)\dot{\delta\phi} + (...)\ddot{\delta\phi} + (...)\Psi + (...)\dot{\Psi} + (...)\Phi + (...)\dot{\Phi} + (...)\ddot{\Phi}, \tag{5.70}$$

$$\delta_{DE} = (...)\delta\phi + (...)\dot{\delta\phi} + (...)\Psi + (...)\Phi + (...)\dot{\Phi}, \tag{5.71}$$

$$V_{DE} = (...)\delta\phi + (...)\dot{\delta\phi} + (...)\Psi + (...)\Phi + (...)\dot{\Phi}. \tag{5.72}$$

where (...) indicates expressions which might be cumbersome. It is therefore very helpful to work out these expressions under the subhorizon and quasistatic approximations in order to gain a better understanding.

We have explained in great detail the way we carry out the subhorizon and quasistatic approximations in Chapter 4, but in a nutshell, the former refers to only considering modes deep in the Hubble radius, i.e. those for which $k^2 \gg a^2H^2$, while the latter refers to neglecting derivatives of the potentials during matter domination as they are roughly constant but also terms of similar order as $\partial_\eta \sim 1/\eta \sim aH(a)$. For example, the perturbation in the Ricci scalar is

$$\delta R = -\frac{12(\mathcal{H}^2 + \dot{\mathcal{H}})}{a^2}\Psi - \frac{4k^2}{a^2}\Phi + \frac{2k^2}{a^2}\Psi - \frac{18\mathcal{H}}{a^2}\dot{\Phi} - \frac{6\mathcal{H}}{a^2}\dot{\Psi} - \frac{6\ddot{\Phi}}{a^2},$$

$$\simeq \quad -\frac{4k^2}{a^2}\Phi + \frac{2k^2}{a^2}\Psi.$$

Following the same procedure and applying the subhorizon approximation to the linearized gravitational field equations (5.64),(5.67), and to the linearized scalar field equation (5.68), one finds, respectively,

$$A_3\frac{k^2}{a^2}\Phi + A_6\frac{k^2}{a^2}\delta\phi - \kappa\rho_m\delta_m \simeq 0, \tag{5.73}$$

$$B_6\frac{k^2}{a^2}\Phi + B_8\frac{k^2}{a^2}\Psi + B_7\frac{k^2}{a^2}\delta\phi \simeq 0, \tag{5.74}$$

$$D_7\frac{k^2}{a^2}\Phi + \left(D_9\frac{k^2}{a^2} - M^2\right)\delta\phi + D_{10}\frac{k^2}{a^2}\Psi \simeq 0. \tag{5.75}$$

Note that since $B_7 = 4G_{4\phi}$ and $B_6 = B_8$ (see Appendix B.2), Eq. (5.74) leads to no anisotropic stress $\Phi = -\Psi$ when G_4 is a constant.

Solving Eqs. (5.73)-(5.75) for Φ, Ψ and $\delta\phi$ one finds

$$\frac{k^2}{a^2}\Psi = -\frac{\kappa}{2}\frac{G_{\rm eff}}{G_N}\bar{\rho}_m\delta, \tag{5.76}$$

$$\frac{k^2}{a^2}\Phi = \frac{\kappa}{2}Q_{\rm eff}\bar{\rho}_m\delta, \tag{5.77}$$

$$\delta\phi = \frac{(A_6B_6 - B_6B_7)\,\rho_m\delta_m}{(A_6^2B_6 - 2A_6B_6B_7 + B_6^2D_9)\,\frac{k^2}{a^2} - B_6^2M^2}, \tag{5.78}$$

where $G_{\rm eff}$ and $Q_{\rm eff}$ are Newton's effective constant

$$\frac{G_{\rm eff}}{G_N} = \frac{2\left[(B_6D_9 - B_7^2)\,\frac{k^2}{a^2} - B_6M^2\right]}{(A_6^2B_6 + B_6^2D_9 - 2A_6B_7B_6)\,\frac{k^2}{a^2} - B_6^2M^2}, \tag{5.79}$$

$$Q_{\rm eff} = \frac{2\left[(A_6B_7 - B_6D_9)\,\frac{k^2}{a^2} + B_6M^2\right]}{(A_6^2B_6 + B_6^2D_9 - 2A_6B_7B_6)\,\frac{k^2}{a^2} - B_6^2M^2}, \tag{5.80}$$

and we make use of the following correspondence $A_3 = B_6 = B_8$, $D_7 = B_7$ and $D_{10} = A_6$ (see Appendix B.2). One can also define the following anisotropic stress parameters

$$\eta \equiv \frac{\Psi + \Phi}{\Phi} = \frac{(A_6 - B_7)\,B_7\frac{k^2}{a^2}}{(A_6B_7 - B_6D_9)\,\frac{k^2}{a^2} + B_6M^2}, \tag{5.81}$$

$$\gamma \equiv -\frac{\Phi}{\Psi} = \frac{(A_6B_7 - B_6D_9)\,\frac{k^2}{a^2} + B_6M^2}{(B_7^2 - B_6D_9)\,\frac{k^2}{a^2} + B_6M^2}. \tag{5.82}$$

The aforementioned expressions for Newton's effective constant and the anisotropic stress parameters are in agreement with the ones in Ref. [309].

The subhorizon approximation is also useful as the evolution equations for the growth of matter perturbations δ_m given by Eqs. (5.16)-(5.17) can be reduced to a single differential equation (which we have already seen), where the variable $G_{\rm eff}$ plays a primary role:

$$\delta_m''(a) + \left(\frac{3}{a} + \frac{H'(a)}{H(a)}\right)\delta_m'(a) - \frac{3}{2}\frac{\Omega_{m,0}G_{\rm eff}/G_N}{a^5H(a)^2/H_0^2}\delta_m(a) = 0, \tag{5.83}$$

with $G_{\rm eff}$ given by Eq. (5.79) and initial conditions $\delta_m(a_i) = a_i$ and $\delta_m'(a_i) = 1$ for an initial value for the scale factor a_i deep in the matter era.

In what follows, we will present the effective DE perturbations under the subhorizon and quasistatic approximations for two classes of models: those in which there is DE anisotropic stress and those where DE anisotropic stress vanishes.

5.4.1 Horndeski models with DE anisotropic stress

We now apply the subhorizon and quasistatic approximations in Eqs. (5.70)-(5.72) using the same prescription as in Ref. [9]. We also found, in agreement with Ref. [308], that the quasistatic approximation breaks down for this model due to the rapid oscillations of the scalar field, so if we eliminate the scalar field, then this can slightly increase the accuracy of the numerical solutions of the effective fluid equations. To eliminate $\delta\phi$ and its derivatives, we use Eq. (5.67) and insert the resulting equations in Eqs. (5.70)-(5.72).

Then, by keeping the dominant k^2 terms (the subhorizon approximation) and dropping time derivatives of the potentials (the quasistatic approximation) in Eqs. (5.70)-(5.72) we find

$$\frac{\delta P_{DE}}{\bar{\rho}_{DE}} \simeq \frac{1}{3\mathcal{F}_4}\frac{\frac{k^4}{a^4}\mathcal{F}_1+\frac{k^2}{a^2}\mathcal{F}_2+\mathcal{F}_3}{\frac{k^4}{a^4}\mathcal{F}_5+\frac{k^2}{a^2}\mathcal{F}_6}\frac{\bar{\rho}_m}{\bar{\rho}_{DE}}\delta_m, \tag{5.84}$$

$$\delta_{DE} \simeq \frac{\frac{k^4}{a^4}\mathcal{F}_7+\frac{k^2}{a^2}\mathcal{F}_8+\mathcal{F}_9}{\frac{k^4}{a^4}\mathcal{F}_5+\frac{k^2}{a^2}\mathcal{F}_6}\frac{\bar{\rho}_m}{\bar{\rho}_{DE}}\delta_m, \tag{5.85}$$

$$V_{DE} \simeq a\frac{\frac{k^2}{a^2}\mathcal{F}_{10}+\mathcal{F}_{11}}{\frac{k^2}{a^2}\mathcal{F}_5+\mathcal{F}_6}\frac{\bar{\rho}_m}{\bar{\rho}_{DE}}\delta_m, \tag{5.86}$$

for the effective DE pressure perturbation, effective DE density perturbation, and effective DE velocity perturbation, respectively (the interested reader can find the expressions for $\mathcal{F}_i$ in Appendix B.2). It is now also possible to obtain an expression for the effective DE anisotropic stress under the subhorizon approximation

$$\begin{aligned}\pi_{DE} &= \frac{\frac{k^2}{a^2}(\Phi+\Psi)}{\kappa\,\bar{\rho}_{DE}} \simeq \frac{\frac{k^2}{a^2}\mathcal{F}_4^2 B_7\left(B_7-A_6\right)}{\frac{k^2}{a^2}\mathcal{F}_5+\mathcal{F}_6}\frac{\bar{\rho}_m}{\bar{\rho}_{DE}}\delta_m \\ &\simeq \frac{\frac{k^4}{a^4}\mathcal{F}_4^2 B_7\left(B_7-A_6\right)}{\frac{k^4}{a^4}\mathcal{F}_7+\frac{k^2}{a^2}\mathcal{F}_8+\mathcal{F}_9}\delta_{DE}.\end{aligned} \tag{5.87}$$

Having found expressions for the effective DE equation of state (see Eq. (5.55)) and the effective DE anisotropic stress (Eq. (5.87)), the only missing ingredient for an effective fluid description of the Horndeski Lagrangian is the sound speed. This quantity can easily be found using our equations for the effective DE pressure perturbation (5.84) and the effective DE density perturbation (5.85). The DE sound speed reads

$$\begin{aligned}c_{s,DE}^2 &\equiv \frac{\delta P_{DE}}{\delta\rho_{DE}} \\ &= \frac{1}{3}\frac{\frac{k^4}{a^4}\mathcal{F}_1+\frac{k^2}{a^2}\mathcal{F}_2+\mathcal{F}_3}{\frac{k^4}{a^4}\mathcal{F}_7+\frac{k^2}{a^2}\mathcal{F}_8+\mathcal{F}_9}.\end{aligned} \tag{5.88}$$

Due to the presence of anisotropic stress, perturbations on subhorizon scales in the effective DE fluid are not driven by the sound speed (5.88), but by an effective DE sound speed defined as [9, 235]

$$\begin{aligned}c_{s,eff}^2 &\equiv c_{s,DE}^2-\frac{2}{3}\pi_{DE}/\delta_{DE} \\ &= \frac{1}{3}\frac{\frac{k^4}{a^4}\left(\mathcal{F}_1-2\mathcal{F}_4^2 B_7\left(B_7-A_6\right)\right)+\frac{k^2}{a^2}\mathcal{F}_2+\mathcal{F}_3}{\frac{k^4}{a^4}\mathcal{F}_7+\frac{k^2}{a^2}\mathcal{F}_8+\mathcal{F}_9}.\end{aligned} \tag{5.89}$$

Finally, it is clear that for the cosmological constant model, i.e. $\mathcal{L}_2=-\frac{\Lambda}{\kappa}$, $\mathcal{L}_3=0$, $\mathcal{L}_4=\frac{1}{2\kappa}R$, $\mathcal{L}_5=0$, we have $K=-\frac{\Lambda}{\kappa}$, $G_3=0$, $G_4=\frac{1}{2\kappa}$ and $G_5=0$, which implies that $w_{DE}=-1$ and $(\delta P_{DE},\delta\rho_{DE},\pi_{DE})=(0,0,0)$ as expected.

f(R) models

Thus far we have kept the discussion quite general, that is to say, we did not specify any function in the Horndeski Lagrangian (5.21). To mention an example, we will present the results for $f(R)$ models. With the definitions in Eqs. (5.25) and using units where $\kappa = 1$, one obtains

$$\begin{aligned}
B_7 &= 2A_6 = 2, \quad B_6 = B_8 = 2\phi, \quad D_9 = 0, \quad \mathcal{F}_1 = \mathcal{F}_4 = -1/2, \quad \mathcal{F}_2 = -\frac{15\ddot{F}}{4}, \\
\mathcal{F}_3 &= -\frac{2F\ddot{F}}{4F_{,R}}, \quad \mathcal{F}_5 = -\frac{3F}{2}, \quad \mathcal{F}_6 = -\frac{F^2}{2F_{,R}}, \quad \mathcal{F}_7 = -1 + \frac{3F}{2}, \quad \mathcal{F}_8 = \frac{(F-1)\,F}{2F_{,R}}, \\
\mathcal{F}_9 &= 0, \quad \mathcal{F}_{10} = -\frac{3\dot{F}}{2}, \quad \mathcal{F}_{11} = -\frac{F\dot{F}}{4F_{,R}}, \quad M^2 = -K_{\phi\phi} = \frac{1}{2f_{RR}},
\end{aligned} \tag{5.90}$$

where

$$K_\phi = \frac{dK}{d\phi} = \frac{dK}{dR}\frac{dR}{d\phi} = \frac{1}{2f_{,RR}}\left(Rf_{,RR}\right) = -\frac{R}{2}, \tag{5.91}$$

$$K_{\phi\phi} = \frac{d}{d\phi}\left(\frac{dK}{d\phi} = -\frac{R}{2}\right) = \frac{1}{f_{,RR}}\frac{d}{dR}\left(-\frac{R}{2}\right) = -\frac{1}{2f_{RR}}, \tag{5.92}$$

and $F = f_{,R}$, $F_{,R} = f_{,RR}$. Then, the effective DE fluid quantities read

$$\frac{\delta P_{DE}}{\bar{\rho}_{DE}} \simeq \frac{1}{3F}\frac{2\frac{k^2}{a^2}\frac{F_{,R}}{F} + 3(1+5\frac{k^2}{a^2}\frac{F_{,R}}{F})\ddot{F}k^{-2}}{1+3\frac{k^2}{a^2}\frac{F_{,R}}{F}}\frac{\bar{\rho}_m}{\bar{\rho}_{DE}}\delta_m, \tag{5.93}$$

$$\delta_{DE} \simeq \frac{1}{F}\frac{1-F+\frac{k^2}{a^2}(2-3F)\frac{F_{,R}}{F}}{1+3\frac{k^2}{a^2}\frac{F_{,R}}{F}}\frac{\bar{\rho}_m}{\bar{\rho}_{DE}}\delta_m, \tag{5.94}$$

$$V_{DE} \simeq \frac{a\dot{F}}{2F}\frac{1+6\frac{k^2}{a^2}\frac{F_{,R}}{F}}{1+3\frac{k^2}{a^2}\frac{F_{,R}}{F}}\frac{\bar{\rho}_m}{\bar{\rho}_{DE}}\delta_m, \tag{5.95}$$

$$\begin{aligned}
\pi_{DE} &\simeq \frac{1}{F}\frac{\frac{k^2}{a^2}\frac{F_{,R}}{F}}{1+3\frac{k^2}{a^2}\frac{F_{,R}}{F}}\frac{\bar{\rho}_m}{\bar{\rho}_{DE}}\delta_m \\
&\simeq \frac{\frac{k^2}{a^2}\frac{F_{,R}}{F}}{1-F+\frac{k^2}{a^2}(2-3F)\frac{F_{,R}}{F}}\delta_{DE},
\end{aligned} \tag{5.96}$$

$$c^2_{s,DE} \simeq \frac{1}{3}\frac{2\frac{k^2}{a^2}\frac{F_{,R}}{F} + 3(1+5\frac{k^2}{a^2}\frac{F_{,R}}{F})\ddot{F}k^{-2}}{1-F+\frac{k^2}{a^2}(2-3F)\frac{F_{,R}}{F}}, \tag{5.97}$$

$$c^2_{s,eff} \simeq \frac{(1+5\frac{k^2}{a^2}\frac{F_{,R}}{F})\ddot{F}k^{-2}}{1-F+\frac{k^2}{a^2}(2-3F)\frac{F_{,R}}{F}}. \tag{5.98}$$

These results are in perfect agreement with the expressions derived in Chapter 4, see Eqs. (4.42)-(4.48).

5.4.2 Horndeski models with no dark energy anisotropic stress

With the same approach that we followed in (5.4.1) we compute the DE perturbations for models where the is no DE anisotropic stress, i.e $\Phi = -\Psi$. With this restriction it is easy to see from Eq. (5.67) that $G_{4\phi} = 0$. Then applying this condition under the subhorizon approximation in Eqs. (5.70)-(5.72) leads to

$$\frac{\delta P_{DE}}{\bar{\rho}_{DE}} \simeq \frac{1}{3}\frac{\frac{k^2}{a^2}\hat{\mathcal{F}}_2 + \hat{\mathcal{F}}_3}{\frac{k^4}{a^4}\hat{\mathcal{F}}_5 + \frac{k^2}{a^2}\hat{\mathcal{F}}_6}\frac{\bar{\rho}_m}{\bar{\rho}_{DE}}\delta_m, \tag{5.99}$$

$$\delta_{DE} \simeq \frac{\frac{k^4}{a^4}\hat{\mathcal{F}}_7 + \frac{k^2}{a^2}\hat{\mathcal{F}}_8 + \hat{\mathcal{F}}_9}{\frac{k^4}{a^4}\hat{\mathcal{F}}_5 + \frac{k^2}{a^2}\hat{\mathcal{F}}_6}\frac{\bar{\rho}_m}{\bar{\rho}_{DE}}\delta_m, \tag{5.100}$$

$$V_{DE} \simeq a\frac{\frac{k^2}{a^2}\hat{\mathcal{F}}_{10} + \hat{\mathcal{F}}_{11}}{\frac{k^2}{a^2}\hat{\mathcal{F}}_5 + \hat{\mathcal{F}}_6}\frac{\bar{\rho}_m}{\bar{\rho}_{DE}}\delta_m, \tag{5.101}$$

and since $\Phi = -\Psi$ the anisotropic parameters read

$$\eta \equiv \frac{\Psi + \Phi}{\Phi} = 0, \tag{5.102}$$

$$\gamma \equiv -\frac{\Phi}{\Psi} = 1, \tag{5.103}$$

as expected, while the DE anisotropic stress parameter is zero $\pi_{DE} = 0$. Our general expression for the DE sound speed (5.88) reduces in this case to

$$c^2_{s,DE} = \frac{\frac{k^2}{a^2}\hat{\mathcal{F}}_2 + \hat{\mathcal{F}}_3}{\frac{k^4}{a^4}\hat{\mathcal{F}}_7 + \frac{k^2}{a^2}\hat{\mathcal{F}}_8 + \hat{\mathcal{F}}_9}, \tag{5.104}$$

which is equal to the DE effective sound speed since $\pi_{DE} = 0$. Here we will show results for a few specific models embedded in the Horndeski Lagrangian.

Quintessence

We can recover the Lagrangian of Quintessence by choosing the following functions

$$K = X - V(\phi), \qquad G_4 = \frac{1}{2\kappa} \tag{5.105}$$

where ϕ is the scalar field, X is the kinetic term defined as $X = -\frac{1}{2}g^{\mu\nu}\partial_\mu\phi\partial_\nu\phi$ and $V(\phi)$ is the potential. Using a variational approach one finds that the effective pressure, density and velocity perturbations for Quintessence theories are given by

$$\begin{aligned} \delta P_{DE} &= \left(\dot{\phi}\dot{\delta\phi} - \Psi\dot{\phi}^2\right) - V_\phi\delta\phi, \\ \rho_{DE}\delta_{DE} &= \left(\dot{\phi}\dot{\delta\phi} - \Psi\dot{\phi}^2\right) + V_\phi\delta\phi, \qquad (5.106) \\ V_{DE} &= \frac{k^2}{a}\dot{\phi}\delta\phi, \qquad (5.107) \end{aligned}$$

and these expressions are in agreement with [276]. Also, the DE anisotropic stress parameter π_{DE} is zero since for Quintessence $\Psi = -\Phi$. We find that under the subhorizon approximation

$$A_6 = 0, \quad B_6 = -2, \quad D_9 = -K_X, \quad M^2 = -K_{\phi\phi}, \tag{5.108}$$

so that the effective pressure, density and velocity perturbations for Quintessence theories are given by

$$\frac{\delta P_{DE}}{\bar{\rho}_{DE}} \simeq \frac{\dot{\phi}^2}{2k^2/a^2}\frac{\bar{\rho}_m}{\bar{\rho}_{DE}}\delta_m, \tag{5.109}$$

$$\delta_{DE} \simeq \frac{\dot{\phi}^2}{2k^2/a^2}\frac{\bar{\rho}_m}{\bar{\rho}_{DE}}\delta_m, \tag{5.110}$$

$$V_{DE} \simeq 0. \tag{5.111}$$

It is thus straightforward, using Eqs. (5.109) and (5.110), to see that the DE sound speed is given by

$$c^2_{s,DE} = 1. \tag{5.112}$$

Moreover, we also find that in the subhorizon approximation

$$\begin{aligned} \delta\phi &\simeq 0, \\ \Psi &\simeq -\frac{\bar{\rho}_m \delta_m a^2}{2k^2}, \end{aligned} \tag{5.113}$$

K-essence

In our notation the Lagrangian of K-essence theories is specified by the functions [311, 312]

$$K(\phi, X) = P(\phi, X), \qquad G_4 = \frac{1}{2\kappa}, \tag{5.114}$$

and as usual through the variation of the action it is possible to find expressions for the pressure, density, and velocity perturbations

$$\delta P_{DE} = P_\phi \delta\phi + P_X \left(\dot{\phi}\dot{\delta\phi} - \dot{\phi}^2\Psi\right), \tag{5.115}$$

$$\rho_{DE}\delta_{DE} = \delta\phi\left(P_{X\phi}\dot{\phi}^2 - P_\phi\right) - \dot{\phi}\left(P_X + P_{XX}\dot{\phi}^2\right)\left(\dot{\phi}\Psi - \dot{\delta\phi}\right), \tag{5.116}$$

$$V_{DE} = \frac{k^2}{a} P_X \dot{\phi}\delta\phi. \tag{5.117}$$

Since for K-essence $\Psi = -\Phi$ the DE anisotropic stress parameter π_{DE} vanishes. We find that under the subhorizon approximation

$$A_6 = 0, \quad B_6 = -2, \quad D_9 = -P_X, \quad M^2 = -P_{\phi\phi}, \tag{5.118}$$

and therefore the DE perturbations for K-essence theories are given by

$$\frac{\delta P_{DE}}{\bar{\rho}_{DE}} \simeq \frac{P_X\dot{\phi}^2}{2k^2/a^2}\frac{\bar{\rho}_m}{\bar{\rho}_{DE}}\delta_m, \tag{5.119}$$

$$\delta_{DE} \simeq \frac{\dot{\phi}^2\left(P_X + P_{XX}\dot{\phi}^2\right)}{2k^2/a^2}\frac{\bar{\rho}_m}{\bar{\rho}_{DE}}\delta_m, \tag{5.120}$$

$$V_{DE} \simeq 0, \tag{5.121}$$

and the DE sound speed reads

$$c^2_{s,DE} = \frac{P_X}{P_X + 2XP_{XX}}, \tag{5.122}$$

in agreement with Refs. [311, 312]. The perturbations of the scalar field and the gravitational potential are respectively given by

$$\begin{aligned} \delta\phi &\simeq 0, \\ \Psi &\simeq -\frac{\bar{\rho}_m \delta_m a^2}{2k^2}. \end{aligned} \tag{5.123}$$

Kinetic gravity braiding

An interesting DE model is the kinetic gravity braiding (KGB) which is characterized by the following Lagrangian

$$K = K(X), \qquad G_3 = G_3(X), \qquad G_4 = \frac{1}{2\kappa}. \tag{5.124}$$

Since G_4 is constant it is easily shown from Eq. (5.74) that the KGB model has no DE anisotropic stress and therefore the anisotropic parameters

$$\eta \equiv \frac{\Psi + \Phi}{\Phi} = 0, \tag{5.125}$$

$$\gamma \equiv -\frac{\Phi}{\Psi} = 1. \tag{5.126}$$

Furthermore, it follows that the effective Newton's constant $G_{\rm eff}/G_N$ is given by

$$G_{\rm eff}/G_N = \frac{M^2 - D_9 \frac{k^2}{a^2}}{M^2 - (D_9 + A_6^2/2)\frac{k^2}{a^2}}. \tag{5.127}$$

The effective DE density and pressure $\bar{\rho}_{DE}$ and $\bar{P}_{DE}$ read, respectively,

$$\kappa\bar{\rho}_{DE} = -K + \dot{\phi}^2\left(-G_{3\phi} + K_X + 3G_{3X}H\dot{\phi}\right), \tag{5.128}$$

$$\kappa\bar{P}_{DE} = K - \dot{\phi}^2\left(G_{3\phi} + G_{3X}\ddot{\phi}\right), \tag{5.129}$$

and therefore the DE equation of state is given by

$$w_{DE} = \frac{K - \dot{\phi}^2\left(G_{3\phi} + G_{3X}\ddot{\phi}\right)}{-K + \dot{\phi}^2\left(-G_{3\phi} + K_X + 3G_{3X}H\dot{\phi}\right)}. \tag{5.130}$$

We also find that the scalar field equation at the background level is

$$K_\phi - (K_X - 2G_{3\phi})\left(\ddot{\phi} + 3H\dot{\phi}\right) - K_{X\phi}\dot{\phi}^2 - K_{XX}\ddot{\phi}\dot{\phi}^2 + G_{3\phi\phi}\dot{\phi}^2 + G_{3X\phi}\dot{\phi}^2\left(\ddot{\phi} - 3H\dot{\phi}\right)$$
$$-3G_{3X}\left(2H\ddot{\phi}\dot{\phi} + 3H^2\dot{\phi}^2 + \dot{H}\dot{\phi}^2\right) - 3G_{3XX}H\ddot{\phi}\dot{\phi}^3 = 0. \tag{5.131}$$

As a specific example we now discuss the KGB model of Ref. [308] defined by

$$K(X) = -X \tag{5.132}$$

$$G_3(X) = \frac{1}{\sqrt{\kappa}}\left(\kappa r_c^2 X\right)^n = \alpha X^n, \tag{5.133}$$

where n and α are parameters in the model. A number of reasons make the KGB an attractive model. First, it passes the recent observational constraints from gravitational waves. Second, it is known that this model connects the original Galileon model [298] and the ΛCDM model by the parameter n, at least for the background and first order perturbations: linear perturbations of the KGB model reduce to those of ΛCDM (original Galileon) for $n = \infty$ ($n = 1$) [308].

The charge density of the Noether current Eq. (5.61) is in this case

$$J_0 = \dot{\phi}\left(3\dot{\phi}G_{3X}H - 1\right), \tag{5.134}$$

and satisfies the differential equation

$$\dot{J}_0 + 3HJ_0 = 0, \tag{5.135}$$

whose solution reads

$$J_0 = \frac{J_c}{a^3}, \tag{5.136}$$

with J_c a constant. It is therefore clear that J_0 approaches zero as the Universe expands. The simplest attractor solution is located at $J_0 = 0$ and has two branches, namely,

$$\dot{\phi} = 0, \tag{5.137}$$

and

$$\dot{\phi} = \frac{1}{3G_{3X}H}. \tag{5.138}$$

Because the first case has ghostly perturbations, as it is shown in [308], we will focus on the attractor solution Eq. (5.138). Using Eqs. (5.53) and (5.134) we find that the modified Friedmann equation is given by

$$\left(\frac{H}{H_0}\right)^2 = (1-\Omega_{m,0})\left(\frac{H}{H_0}\right)^{-\frac{2}{2n-1}} + \Omega_{m,0}a^{-3}, \tag{5.139}$$

where we have neglected radiation. The background equation of the KGB model reduces to that of ΛCDM for $n=\infty$ as can be seen from Eq. (5.139). Also, one can easily find an expression for the parameter α by using Eq. (5.139) at the present epoch

$$\alpha = \left(\frac{2^{n-1}}{3n}\right)\left(\frac{1}{6\,(1-\Omega_{m,0})}\right)^{\frac{2n-1}{2}}. \tag{5.140}$$

The DE equation of state becomes

$$w_{DE} = \frac{\bar{P}_{DE}}{\bar{\rho}_{DE}} = \frac{2\dot{H}}{3\,(2n-1)} - 1, \tag{5.141}$$

and through Eq. (5.138) it is also possible to find an analytical expression for the kinetic term

$$\begin{aligned} X &= \frac{1}{2}a^2H^2\phi'(a)^2 \\ &= 3H_0^2(1-\Omega_{m,0})\left(\frac{H}{H_0}\right)^{\frac{2n}{1-2n}}, \end{aligned} \tag{5.142}$$

where the prime stands for the derivative with respect to the scale factor.

To derive the ΛCDM limit for the perturbations in this model we rewrite Eqs. (5.67) and (5.68) in terms of the kinetic term perturbation $\delta X = \dot{\phi}\dot{\delta\phi} - \dot{\phi}^2\Psi$. Then, for $n\to\infty$ the former equation reduces to $\delta X\left(-\frac{2}{a} - \frac{H'(a)}{H(a)} + O(1/n)\right)$, while the latter equation gives

$$\delta\dot{X} + 3H\delta X = 0, \tag{5.143}$$

which implies that the kinetic term perturbation decays as $\delta X \sim 1/a^3$ and thus can be ignored at late time. Since DE perturbations in the KGB model are proportional to δX for large n, then they reduce to zero as expected for the ΛCDM model.

Finally, it should be noted that a standard hydrodynamical description of the KGB in terms of an effective fluid, has been studied in Ref. [313]. There, it was shown that the KGB model can also be described in terms of an imperfect fluid with a chemical potential, in which the equations of motion reduce to the standard diffusion equation. However, in our current analysis we will only focus on the ideal fluid approach, which is totally equivalent, as we are interested in finding simple analytic solutions and with comparing with our previous work.

5.5 Designer Horndeski

In this section we will address the shortcomings found in the KGB model defined by Eqs. (5.132)-(5.133). We will show that it is possible, starting from the Lagrangian (5.124), to find a model corresponding to a given background but yet having different perturbations. Using the modified Friedmann equation and the scalar field conservation equation, we can find specific designer models such that the background is always that of the ΛCDM model, namely, having $w_{DE}=-1$. This is particularly useful in detecting deviations from ΛCDM at the perturbations level and is a natural expansion of our earlier work [9, 204]. We start with the modified Friedmann equation, which can be written as

$$-H(a)^2 - \frac{K(X)}{3} + H_0^2\Omega_m(a) + 2\sqrt{2}X^{3/2}H(a)G_{3X} + \frac{2}{3}XK_X = 0. \tag{5.144}$$

while the scalar field conservation equation can be written as

$$\frac{J_c}{a^3} - 6XH(a)G_{3X} - \sqrt{2}\sqrt{X}K_X = 0, \tag{5.145}$$

where J_c is a constant which quantifies our deviation from the attractor, as in the case of the KGB model [308]. We now have two equations given by (5.144) and (5.145), but three unknown functions $(G_{3X}(X), K(X), H(a))$ thus the system is undetermined. Therefore, we need to specify one of the three unknown functions $(G_{3X}(X), K(X), H(a))$ and determine the other two using Eqs. (5.144) and (5.145). To facilitate this, we express the Hubble parameter as a function of the kinetic term X, ie $H = H(X)$ and then solve the previous equations to find $(G_{3X}(X), K(X))$. Doing so yields:

$$\begin{aligned} K(X) &= -3H_0^2\Omega_{\Lambda,0} + \frac{J_c\sqrt{2X}H(X)^2}{H_0^2\Omega_{m,0}} - \frac{J_c\sqrt{2X}\Omega_{\Lambda,0}}{\Omega_{m,0}}, \\ G_{3X}(X) &= -\frac{2J_cH'(X)}{3H_0^2\Omega_{m,0}}. \end{aligned} \tag{5.146}$$

With Eqs. (5.146) we can make a whole family of designer models that behave as ΛCDM at the background level but have different perturbations. We now proceed to specify some examples using our formalism.

5.5.1 Example 1

Choosing $K(X) = 0$ and solving Eqs. (5.146) we find

$$\begin{aligned} K(X) &= 0, \\ G_3(X) &= -\frac{\sqrt{2J_c}\sqrt{\Omega_{\Lambda,0}\left(2J_c\sqrt{X} + 3\sqrt{2}H_0^2\Omega_{m,0}\right)}}{3H_0X^{1/4}\Omega_{m,0}}, \end{aligned} \tag{5.147}$$

and the derivative of the scalar field $\phi'(a)$ is

$$\phi'(a) = \frac{3a^2H_0^2\Omega_{\Lambda,0}}{J_cH(a)}, \tag{5.148}$$

where the prime is the derivative with respect to the scale factor. However, this model has the problem that it does not have a smooth limit to ΛCDM when $J_c = 0$.

5.5.2 Example 2

On the other hand, specifying $G_3(X)$ leads to another interesting designer model, defined as

$$\begin{aligned} G_3(X) &= G_{30}X, \\ K(X) &= -3H_0^2\Omega_{\Lambda,0} + \frac{9H_0^2(X - X_0)^2G_{30}^2\sqrt{X}\Omega_{m,0}}{2\sqrt{2}J_c} - \frac{\sqrt{2}J_c\sqrt{X}\Omega_{\Lambda,0}}{\Omega_{m,0}} \end{aligned} \tag{5.149}$$

where the kinetic term is defined as

$$X = \frac{3G_{30}H_0X_0\Omega_{m,0} - 2J_cH(a)}{3G_{30}H_0^2\Omega_{m,0}}, \tag{5.150}$$

and X_0 is an integration constant. However, this model has the problem that at early times the perturbations do not go to zero and we do not recover GR, since the kinetic term goes to infinity as it grows as $X \sim H(a)$.

5.5.3 Example 3 (HDES)

To solve the previous shortcomings we follow a different approach. First, we demand that the kinetic term behaves as $X = \frac{c_0}{H(a)^n}$, where $c_0 > 0$ and $n > 0$. Then, from Eqs. (5.145) and (5.144) we find:

$$\begin{aligned} G_3(X) &= -\frac{2J_c c_0^{1/n} X^{-1/n}}{3H_0^2\Omega_{m,0}}, \\ K(X) &= \frac{\sqrt{2}J_c c_0^{2/n} X^{\frac{1}{2}-\frac{2}{n}}}{H_0^2\Omega_{m,0}} - 3H_0^2\Omega_{\Lambda,0} - \frac{\sqrt{2}J_c\sqrt{X}\Omega_{\Lambda,0}}{\Omega_{m,0}}. \end{aligned} \tag{5.151}$$

This specific model solves both previous problems, i.e., it has a smooth limit to ΛCDM and it also recovers GR when $J_c \sim 0$, thus we will designate this model as *HDES* and focus on it in what follows.

5.5.4 Comparison with the α parameters

To facilitate comparisons with the literature we also provide the expressions for our designer HDES model in terms of the α_i functions, where $i = M, K, B, T$. The functions $G_i(\phi, X)$ and α_i are connected in the following manner [299]:

$$\begin{aligned} M_*^2 &\equiv 2\left(G_4 - 2XG_{4X} - \dot{\phi}HXG_{5X} + XG_{5\phi}\right), \\ \alpha_M &\equiv \frac{d\ln M_*^2}{d\ln a}, \\ H^2M_*^2\alpha_K &\equiv 2X\left(G_{2X} + 2XG_{2XX} - 2G_{3\phi} - 2XG_{3\phi X}\right) \\ &+ 12H\dot{\phi}X\left[G_{3X} + XG_{3XX} - 3G_{4\phi X} - 2XG_{4\phi XX}\right] \\ &+ 12H^2X\left[G_{4X} - G_{5\phi} + X\left(8G_{4XX} - 5G_{5\phi X}\right)\right. \\ &+ \left. 2X^2\left(2G_{4XXX} - G_{5\phi XX}\right)\right] \\ &+ 4H^3\dot{\phi}X\left(3G_{5X} + 7XG_{5XX} + 2X^2G_{5XXX}\right), \\ H^2M_*^2\alpha_B &\equiv 2\dot{\phi}\left(XG_{3X} - G_{4\phi} - 2XG_{4\phi X}\right) \\ &+ 8HX\left(G_{4X} + 2XG_{4XX} - G_{5\phi} - XG_{5\phi X}\right) \\ &+ \frac{2H^2\phi' X}{a}\left(3G_{5X} + 2XG_{5XX}\right), \\ M_*^2\alpha_T &\equiv 4X\left(G_{4X} - G_{5\phi}\right) - 2X\left(\ddot{\phi} - 2H\dot{\phi}\right)G_{5X}, \end{aligned} \tag{5.152}$$

where the dot is the derivative with respect to the cosmic time, $M_*^2(\tau)$ is the cosmological strength of gravity, α_T is the tensor speed excess, α_B is called the braiding and α_K is referred to as the kineticity. For more information on these α_i functions see [314]. At all times we require $D = \alpha_K + \frac{3}{2}\alpha_B^2 > 0$ so that there are no ghostly instabilities and that $\alpha_{M,K,B,T} \simeq 0$ at early times, so as to recover GR.

For our HDES designer model given by Eqs. (5.151), we have that the α_i functions of Eq. (5.152) are given by

$$M_*^2 \equiv 1, \tag{5.153}$$

$$\alpha_M \equiv \frac{d\ln M_*^2}{d\ln a} = 0, \tag{5.154}$$

$$\alpha_K \equiv -\frac{4\sqrt{2}\sqrt{c_0}J_c(n-2)H(a)^{-\frac{n}{2}}}{H_0^2n^2\Omega_{m,0}}, \tag{5.155}$$

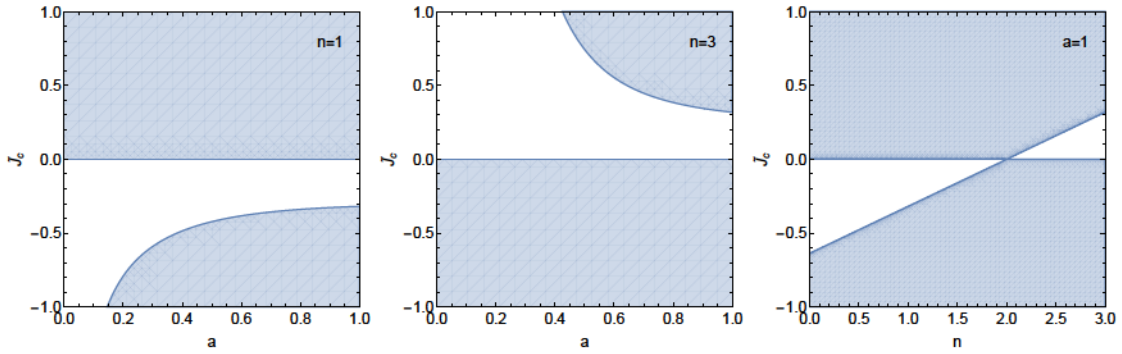

Figure 5.1: The allowed parameter space (shaded region) so that $D > 0$ for $n = 1$ (left) and $n = 3$ (center) and $a = 1$ for $\Omega_{m,0} = 0.3$. In the case of $n = 2$, all values of $\tilde{J}_c$ are allowed.

$$\alpha_B \equiv \frac{4\sqrt{2}\sqrt{c_0}J_c H(a)^{-\frac{n}{2}}}{3H_0^2 n\Omega_{m,0}}, \tag{5.156}$$

$$\alpha_T \equiv 0. \tag{5.157}$$

Since in Eqs. (5.155)-(5.156) we have a degeneracy with the coefficients c_0 and J_c, they appear together as $\sqrt{c_0}J_c$, we can choose to absorb c_0 in the definition of J_c. Finally, it is straightforward to see that our α_i functions are dimensionless since through dimensional analysis we found that $[c_0] = H_0^{n+2}$, $[J_c] = H_0$, the kinetic term $[X] = H_0^2$, $[K] = H_0^2$ and $[G_{3X}] = H_0^{-2}$.

Notice that not all designer models satisfy the above conditions, so in what follows we consider only HDES, given by Eq. (5.151). Then, the stability condition $D = \alpha_K + \frac{3}{2}\alpha_B^2 > 0$ for our model Eq. (5.151) gives

$$\tilde{J}_c\left(4\tilde{J}_c - 3\sqrt{2}(n-2)\Omega_{m,0}\left(\frac{H(a)}{H_0}\right)^{n/2}\right) > 0, \tag{5.158}$$

where we have set $\tilde{J}_c = J_c/H_0$ and $\tilde{c}_0 = c_0/H_0^{n+2} = 1$.

Then, inequality (5.158) implies that in order for the system to be stable we must have either $\tilde{J}_c > 0$ for $0 < n \leq 2$ or a complicated set of expressions that can however be easily derived from Eq. (5.158) with algebraic manipulations. For $n = 2$ the inequality is automatically satisfied for any value of $\tilde{J}_c$ as $\alpha_K = 0$ as can be seen from Eq. (5.155). We show the complicated parameter space that is allowed for $n = 1$ and $n = 3$ as a function of scale factor a but also as a function of n for $a = 1$, in Fig. 5.1.

5.5.5 Analytic solutions for the growth

Furthermore, in this case we can also find approximate solutions to the growth equation Eq. (5.83) in matter domination for $n = 2$. To do this, we first do a series expansion around $a = 0$ to the $G_{\rm eff}$ of Eq. (5.79), which gives:

$$G_{\rm eff}/G_N = 1 + \frac{\sqrt{2}\tilde{J}_c}{3\Omega_{m,0}H(a)/H_0}, \tag{5.159}$$

which we can use to solve Eq. (5.83) in matter domination, where $H(a)/H_0 \simeq \sqrt{\Omega_{m,0}a^{-3}}$. Then, we get

$$\delta_m(a) = \frac{3^{5/3}\Omega_{m,0}^{5/4}\Gamma\left(\frac{8}{3}\right)}{2^{5/4}\tilde{J}_c^{5/6}}a^{-1/4}I_{\frac{5}{3}}\left(\frac{2^{7/4}\sqrt{\tilde{J}_c}}{3\Omega_{m,0}^{3/4}}a^{3/4}\right), \tag{5.160}$$

where $I_n(z)$ is the modified Bessel function of the first kind and $\Gamma(n)$ is the usual Gamma function. Using Eq. (5.160) and the definition of the growth rate $f\sigma_8(a) \equiv f(a)\cdot\sigma(a) = \sigma_8 a\delta_m'(a)/\delta_m(a=1)$,

we can calculate the latter exactly. However, it is instructive to perform a series expansion around $a = 1$, which gives:

$$f\sigma_8(a) \simeq \sigma_8\left(\frac{1}{2}\left(\frac{5\alpha_1}{\alpha_2}-3\right)+\frac{1}{4}\left(-\frac{5\alpha_1}{\alpha_2}+\frac{2\sqrt{2}\tilde{J}_c}{\Omega_{m,0}^{3/2}}+9\right)(a-1)+\cdots\right), \tag{5.161}$$

where we have defined the parameters

$$\alpha_1 = {}_0F_1\left(\frac{5}{3};\frac{2\sqrt{2}\tilde{J}_c}{9\Omega_{m,0}^{3/2}}\right), \tag{5.162}$$

$$\alpha_2 = {}_0F_1\left(\frac{8}{3};\frac{2\sqrt{2}\tilde{J}_c}{9\Omega_{m,0}^{3/2}}\right), \tag{5.163}$$

where ${}_0F_1(c_1, z)$ is a hypergeometric function.

As can be seen from Eq. (5.161) there is a strong degeneracy between $\tilde{J}_c$ and σ_8, which can also be demonstrated by doing a series expansion of $f\sigma_8(a = 1)$ for small $\tilde{J}_c$, which gives

$$f\sigma_8(a=1) \simeq \sigma_8\left(1+\frac{\tilde{J}_c}{4\sqrt{2}\Omega_{m,0}^{3/2}}+\cdots\right). \tag{5.164}$$

which implies that if we keep the growth today given constant, i.e., $f\sigma_8(a = 1) = C_0 = \text{const.}$ then σ_8 will scale roughly as

$$\sigma_8 \simeq C_0\left(1-\frac{\tilde{J}_c}{4\sqrt{2}\Omega_{m,0}^{3/2}}+\cdots\right). \tag{5.165}$$

Since $\Omega_{m,0}$ is strongly constrained from Planck, we expect that the low redshift $f\sigma_8$ data will exhibit a degeneracy between $\tilde{J}_c$ and σ_8. More specifically, by inspecting Eq. (5.165) we expect a strong negative correlation between the two parameters and this is exactly what we see from the actual Markov Chain Monte Carlo (MCMC) that we present in later sections. This degeneracy is interesting as it can potentially alleviate the soft 2σ tension between the growth rate data ($\sigma_8 = 0.88$) and Planck ($\sigma_8 = 0.831$), which has been extensively discussed in the literature, see Ref. [116, 120] and references therein.

5.6 Numerical solutions

Here we present the numerical solutions of the two models, the KGB and HDES, that we described in the previous section.

5.6.1 The KGB model

The attractor

To explore the possibility of working outside the attractor we only need to use Eqs. (5.53) and (5.134), as these constrain J_c and α with $H(a = 1) = H_0$. To parameterize the deviation from the attractor we will use the parameter J_c. An illustrative example is found in Fig. 5.2 where we plot the dark energy density Ω_{DE} with respect to the scale factor for several values of n (left) and J_c (right). The values of values for J_c were chosen so as to highlight the differences of these models with respect to GR.

In the KGB model the DE density can be written via Eq. (5.51) as

$$\Omega_{DE} = \frac{\rho_{DE}}{\rho_c}, \tag{5.166}$$

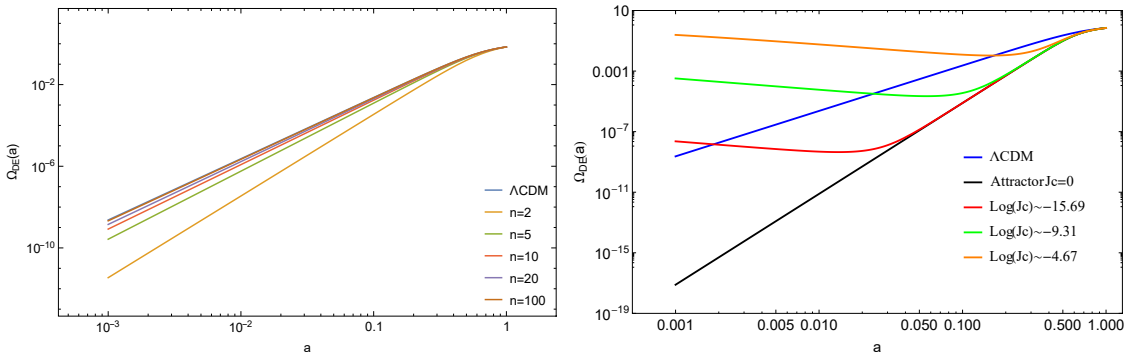

Figure 5.2: The DE density for the KGB model for various values of n (left) and for the KGB model (n=1) for the attractor and three general cases outside the attractor given by different values of J_c, chosen so as to highlight the differences of these models with respect to GR. The left panel clearly shows that as n grows the DE density approaches that of the ΛCDM model.

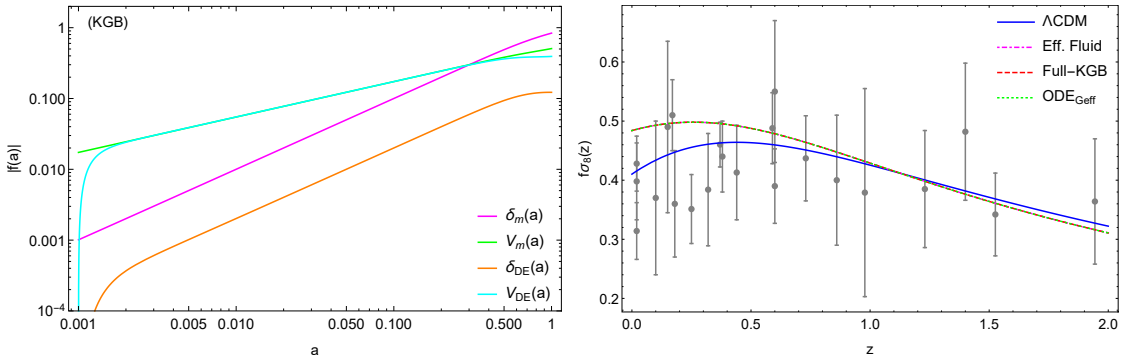

Figure 5.3: Left: The evolution of the matter and effective DE perturbation variables $(\delta_m, V_m, \delta_{DE}, V_{DE})$ for the KGB with $n = 2$. Right: The evolution of the $f\sigma_8(z)$ parameter for the KGB model with $n = 2$ and $\sigma_{8,0} = 0.8$ versus the $f\sigma_8$ data compilation from Ref. [116]. Here we show the theoretical curves for the "Full KGB" brute-force solution, the effective fluid approach, the ΛCDM model and the numerical solution of the $G_{\rm eff}$ equation. As can be seen, the agreement with all approaches is excellent.

$$\rho_{DE} \quad = \quad -K + K_X\dot{\phi}^2 - G_{3\phi}\dot{\phi}^2 + 3G_{3X}H\dot{\phi}^3. \tag{5.167}$$

From Fig. 5.2 we can see that working outside the attractor for the KGB model ($n = 1$) we might find new parts of the parameter space and new phenomenology. In the right panel of Fig. 5.2, we see that the orange line can be ruled out because it predicts a very high value for the DE density at early times. The red and green lines, although outside the attractor solution, are plausible solutions that are interesting to analyze in more depth.

Numerical solution

In this section we present the results of the numerical solution of the evolution equations. In all cases we will assume $\Omega_{m,0} = 0.3$, $k = 300H_0$ and $\sigma_{8,0} = 0.8$, unless otherwise specified. The reason we choose the specific value of $k = 300H_0 \sim 0.1\ h/\text{Mpc}$ for the wave-number is that it corresponds to the largest value of k we can choose without entering the non-linear regime. Finally, we set the initial conditions for the DE variables to zero at $a_i = 10^{-3}$, when we are well inside the matter dominated regime.

Next we will also present our results for the growth rate of matter perturbations parameter

$f\sigma_8(a) \equiv f(a) \cdot \sigma(a)$, where $f(a) = \frac{dln\delta}{dlna}$ is the growth rate and $\sigma(a) = \sigma_{8,0}\frac{\delta(a)}{\delta(1)}$ is the redshift-dependent rms fluctuations of the linear density field within spheres of radius $R = 8h^{-1}$Mpc, while the parameter $\sigma_{8,0}$ is its value today. The $f\sigma_8(a)$ parameter is important as it can be shown to be not only independent of the bias b_1, but also a good discriminator of DE models. The reason for this is that in linear theory the quadrupole contribution to the galaxy power spectrum in redshift space is sensitive only to the combination $f\sigma_8(a)$.

Specifically, here we will compare the numerical solutions for the following cases:

- The numerical solution of the full system of equations given by Eqs. (5.64)-(5.67), which however we rewrite in terms of $\delta X = \dot{\phi}\dot{\delta\phi} - \dot{\phi}^2\Psi$ as the system is more stable this way. We call this case "Full KGB".
- The numerical solution of the effective fluid approach given by Eqs. (5.16)-(5.17). We call this case "Eff. Fluid".
- The numerical solution of the growth factor equation (5.83). We call this case "ODE-Geff".
- The ΛCDM model.

In the left panel of Fig. 5.3 we show the evolution of the matter and effective DE perturbation variables $(\delta_m, V_m, \delta_{DE}, V_{DE})$ for the KGB for $n = 2$. In the right panel we show the evolution of the $f\sigma_8(z)$ parameter for the KGB model for $n = 2$ and $\sigma_{8,0} = 0.8$ versus the $f\sigma_8$ data compilation from Ref. [116]. We show the theoretical curves for the "Full KGB" brute-force solution, the effective fluid approach, the ΛCDM model and the numerical solution of the $G_{\rm eff}$ equation. As can be seen, the agreement with all approaches is excellent.

An interesting thing to note in Fig. 5.3 is that $V_{DE} > \delta_{DE}$ and $V_{DE} \sim V_m$ at intermediate redshift. The reason for this is that in the effective fluid approach the DE velocity perturbations are not always subdominant, as it would be expected in a general DE fluid. This can be seen by remembering that the velocity perturbations are actually a component of the effective energy momentum tensor, namely the T^0_i part, thus they contain some of the main contributions of the Modified Gravity (MoG) theory and can be in some cases rather large. See, for example, Eqs. (5.6) and (5.17) for the definition of V_{DE} and Eqs. (5.65) and (5.72) for all of the extra terms that are rewritten as V_{DE}.

As an example, also consider the case of quintessence and k-essense, where V_{DE} is proportional to the scalar field perturbations, see Eqs. (5.107) and (5.117) respectively. In the case of $f(R)$, V_{DE} is given by (5.95) and is proportional to $\dot{F}/F$, which parameterizes the deviations from GR, so it is a proxy for the $f(R)$ modified gravity perturbations.

However, in the case of the KGB model the subhorizon approximation fails when the parameter n is large. This can easily be seen by calculating the large n limit of the $G_{\rm eff}$ parameter via Eq. (5.79):

$$G_{\rm eff}/G_N \simeq 1 + \frac{2a^3(1-\Omega_{m,0})}{5\Omega_{m,0}}, \tag{5.168}$$

which at $a = 1$ tends to $G_{\rm eff}/G_N \simeq \frac{3}{5} + \frac{2}{5\Omega_{m,0}}$, which is different from unity as expected at this limit. However, in general deviations of $G_{\rm eff}/G_N$ from unity on such scales are not problematic as screening mechanisms play an important role. In any case, our finding is in agreement with what was previously found in Ref. [308], namely: the quasistatic approximation breaks down for the model due to the rapid oscillations of the scalar field. As a result, in what follows we will only focus on our new designer model, which does not suffer from this issue.

5.6.2 Designer Model

We now focus on our designer model HDES, given by Eq. (5.151). Again, we will consider the numerical solutions for the following cases:

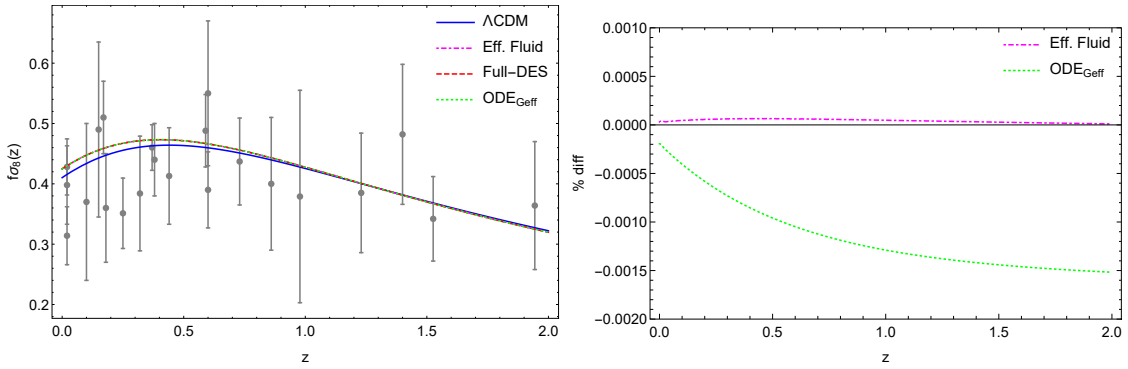

Figure 5.4: Left: We show the evolution of the $f\sigma_8(z)$ parameter for the HDES model with $n = 2$, $\tilde{J}_c = 5 \cdot 10^{-2}$ and $\sigma_{8,0} = 0.8$ versus the $f\sigma_8$ data compilation from Ref. [116]. The values of values for $\tilde{J}_c$ were chosen so as to highlight the differences of these models with respect to GR. Here we show the theoretical curves for the HDES model for the "Full-DES" brute-force numerical solution, the effective fluid approach, the ΛCDM model and the numerical solution of the $G_{\rm eff}$ equation. As can be seen, the agreement with all approaches is excellent. Right: The percent difference between the "Full-DES" brute-force numerical solution and the effective fluid approach (magenta dot dashed line) and the numerical solution of the growth factor equation (5.83) (green dotted line).

- The numerical solution of the full system of equations given by Eqs. (5.64)-(5.67), which however we rewrite in terms of $\delta X = \dot{\phi}\dot{\delta\phi} - \dot{\phi}^2\Psi$ as the system is more stable this way. We call this case "Full-DES".
- The numerical solution of the effective fluid approach given by Eqs. (5.16)-(5.17). We call this case "Eff. Fluid".
- The numerical solution of the growth factor equation (5.83). We call this case "ODE-Geff".
- The ΛCDM model.

As mentioned in the previous sections, we can absorb the constant c_0 in that of J_c, so we will only vary the latter, i.e., we set $\tilde{c}_0 = 1$. Furthermore, since the model is stable for all values of J_c when $n = 2$, we will consider this case when studying cosmological constraints. Again, we use $\Omega_{m,0} = 0.3$, $k = 300H_0$ and $\sigma_{8,0} = 0.8$, unless otherwise specified.

In the left panel of Fig. 5.4 we show the evolution of the $f\sigma_8(z)$ parameter for the HDES model with $n = 2$, $\tilde{J}_c = 5 \cdot 10^{-2}$ and $\sigma_{8,0} = 0.8$. The values of values for $\tilde{J}_c$ were chosen so as to highlight the differences of these models with respect to GR. We show the theoretical curves for the HDES model for the "Full-DES" brute-force numerical solution, the effective fluid approach, the ΛCDM model and the numerical solution of the $G_{\rm eff}$ equation. As can be seen, the agreement with all approaches is excellent. In the right panel of the same figure we show the percent difference between the "Full-DES" brute-force numerical solution and the effective fluid approach (magenta dot dashed line) and the numerical solution of the growth factor equation (5.83) (green dotted line).

5.6.3 Modifications to CLASS and the ISW effect.

Here we will present our modifications to the CLASS Boltzmann code, which we call `EFCLASS`. We will compare the outcome with the `hi_CLASS` code, which solves the full set of dynamical equations but at the cost of significantly more complicated modifications. At the same time, we will also compare with a brute force calculation of the integrated sachs wolfe (ISW) effect as in our previous work with $f(R)$.

In order to modify the CLASS code in our effective fluid approach we only need two functions, the DE velocity and the anisotropic stress [9]. In the case of the HDES model, the anisotropic stress π_{DE} is zero, as can be seen from Eq. (5.67), since $G_{4\phi} = 0$. Therefore, we only need the DE velocity which we can easily be obtained from Eq. (5.101), however we found that this approach is not very stable numerically. Hence, in order to have a consistent solution, we solve Eq. (5.17) for V_{DE} and since $w_{DE} = -1$, the only variable we need is the effective pressure δP_{DE} given by Eq. (5.99). The expressions are rather cumbersome, but for $n = 1$ we have

$$V_{DE} \simeq \left(-\frac{14\sqrt{2}}{3} \Omega_{m,0}^{-3/4} \tilde{J}_c \; H_0 \; a^{1/4} \right) \frac{\bar{\rho}_m}{\bar{\rho}_{DE}} \delta_m. \tag{5.169}$$

In the left panel of Fig. 5.5 we show the low-ℓ multipoles of the TT CMB spectrum for a flat universe with $\Omega_{m,0} = 0.3$, $n_s = 1$, $A_s = 2.3 \cdot 10^{-9}$, $h = 0.7$ and $(\tilde{c_0}, \tilde{J}_c, n) = (1, 2 \cdot 10^{-3}, 1)$. Our EFCLASS code is denoted by the green line, hi_CLASS by the orange line and for reference the ΛCDM with a blue line. On the right panel of Fig. 5.5 we show the percent difference of our code with hi_CLASS as a reference[7]. As can be seen, our simple modification achieves roughly $\sim 0.1\%$ accuracy across all multipoles.

We also compare our results with a brute force calculation of the Integrated Sachs-Wolfe (ISW) effect. In this case the power spectrum is given by [315]:

$$C_\ell^{\rm ISW} = 4\pi \int \frac{dk}{k} I_\ell^{\rm ISW}(k)^2 \frac{9}{25} \frac{k^3 P_\zeta}{2\pi^2}, \tag{5.170}$$

where $I_\ell^{\rm ISW}(k)$ is a kernel that depends on the line of sight integral of the growth and a bessel function and P_ζ is the power spectrum (see Ref. [315] and Appendix A of Ref. [9]), and is given by the primordial power spectrum times a transfer function

$$\frac{k^3 P_\zeta}{2\pi^2} = A_s \left(\frac{k}{k_0} \right)^{n_s - 1} T(k)^2, \tag{5.171}$$

where A_s is the primordial amplitude, k_0 is the pivot scale and $T(k)$ is the usual matter-radiation Bardeen, Bond, Kaiser and Szalay (BBKS) transfer function (see Eq. (7.71) in Ref. [316]).

In Fig. 5.6 we present the results for the calculation of the ISW effect and a comparison with CLASS/hi_CLASS for the ΛCDM model (left) and the HDES model (right), for the same parameters as in Fig. 5.5. We see that there is excellent agreement for all multipoles, except $\ell = 2$. The reason for this is that we have used the BBKS formula for the transfer function $T(k)$ which is very accurate at small scales, but only at the level of 10% on large scales, i.e., small multipoles.

5.7 Cosmological constraints

Here we present the cosmological constraints for the $n = 2$ HDES and ΛCDM models discussed in previous sections. We use the latest cosmological observations including the supernovae type Ia (SnIa), Baryon Acoustic Oscillations (BAO), CMB and the Hubble expansion H(z) data. Specifically, we use the Pantheon SnIa compilation of Ref. [88], the BAO measurements from 6dFGS [90], SDDS [81], BOSS CMASS [91], WiggleZ [80], MGS [92], BOSS DR12 [93] and DES Y1 [94]. For the CMB we use the shift parameters (R, l_a) based on the *Planck 2018* release [1] and as derived by Ref. [317]. We assume the existence of three families of neutrinos with $N_{\rm eff} = 3.046$. For more details regarding the data used see Chapter 2.

With these in mind, our total likelihood function $L_{\rm tot}$ can be given as the product of the separate likelihoods of the data (we assume they are statistically independent) as follows:

$$L_{\rm tot} = L_{\rm SnIa} \times L_{\rm BAO} \times L_{\rm H(z)} \times L_{\rm CMB} \times L_{\rm growth},$$

[7] In this case we did not use $n = 2$ as we found that in this case hi_CLASS crashes and we cannot compare with that code.

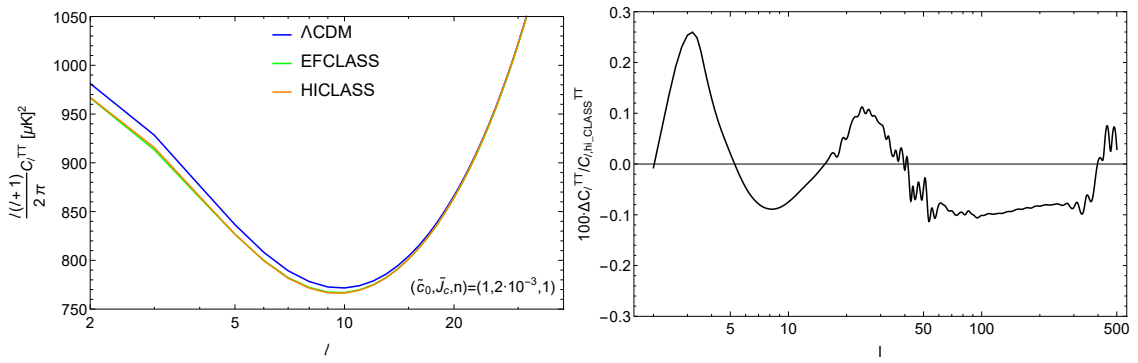

Figure 5.5: Left: The low-ℓ multipoles of the TT CMB spectrum for a flat universe with $\Omega_{m,0} = 0.3$, $n_s = 1$, $A_s = 2.3 \cdot 10^{-9}$, $h = 0.7$ and $(\tilde{c_0}, \tilde{J_c}, n) = (1, 2 \cdot 10^{-3}, 1)$. The values of values for $\tilde{J_c}$ were chosen so as to highlight the differences of these models with respect to GR. Our `EFCLASS` code is denoted by the green line, `hi_CLASS` by the orange line and for reference the ΛCDM with a blue line. Right: The percent difference of our code with `hi_CLASS` as a reference. As can be seen, our simple modification achieves roughly $\sim 0.1\%$ accuracy across all multipoles.

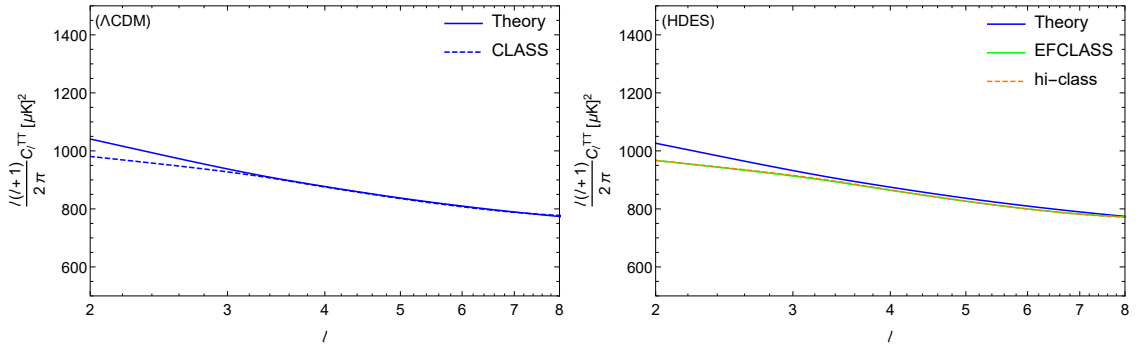

Figure 5.6: The ISW effect and a comparison with `CLASS`/`hi_CLASS` for the ΛCDM model (left) and the HDES model (right), for the same parameters as in Fig. 5.5. We see that there is excellent agreement for all multipoles, except $\ell = 2$ due to the use of the BBKS transfer function which is accurate only up to 10% at large scales.

which is related to the total χ^2 via $\chi^2_{\rm tot} = -2 \log L_{\rm tot}$ or

$$\chi^2_{\rm tot} = \chi^2_{\rm SnIa} + \chi^2_{\rm BAO} + \chi^2_{\rm H(z)} + \chi^2_{\rm cmb} + \chi^2_{\rm growth}. \tag{5.172}$$

Calculating the best-fit is not enough, but we also need to study the statistical significance of our constraints. To achieve this we make use of the well known Akaike Information Criterion (AIC) [289] previously used in Chapter 4, see Eq. (4.84). For other similar statistical tools see also Ref. [290]. In this analysis we have 1048 data points from the Pantheon set, 3 from the CMB shift parameters, 10 from the BAO measurements, 22 from the growth measurements and finally 36 $H(z)$ points, for a total of $N_{\rm dat} = 1118$.

Finally, our total χ^2 is given by Eq. (5.172) while the parameter vectors (assuming a spatially flat Universe) are given by: $p_{\Lambda\rm CDM} = \left(\Omega_{m,0}, 100\Omega_b h^2, h, \sigma_8\right)$ for the ΛCDM and $p_{\rm HDES} = \left(\Omega_{m,0}, 100\Omega_b h^2, h, \tilde{J}_c, \sigma_8\right)$ for the HDES model. Using the aforementioned cosmological data and methodology, we can obtain the best-fit parameters and their uncertainties via the MCMC method based on a Metropolis-Hastings algorithm. The MCMC code for Mathematica used in the analysis is freely available at `http://members.ift.uam-csic.es/savvas.nesseris/`. The priors we assumed for the parameters are given by $\Omega_{m,0} \in [0.1, 0.5]$, $\Omega_b h^2 \in [0.001, 0.08]$, $\tilde{J}_c \in [-1, 12]$, $h \in [0.4, 1]$, $\sigma_8 \in [0, 2]$ and we sample $\sim 10^5$ MCMC points for each of the two models.

Table 5.1: ΛCDM parameters with 68% limits based on TT,TE,EE+lowP and a flat ΛCDM model (middle column) or a wCDM model (right column); see Ref. [1] and the Planck chains archive.

Parameter	Value (ΛCDM)	Value (wCDM)
$\Omega_b h^2$	0.02225 ± 0.00016	0.02229 ± 0.00016
$\Omega_c h^2$	0.1198 ± 0.0015	0.1196 ± 0.0015
n_s	0.9645 ± 0.0049	0.9649 ± 0.0048
H_0	67.27 ± 0.66	> 81.3
Ω_m	0.3156 ± 0.0091	$0.203^{+0.022}_{-0.065}$
w	-1	$-1.55^{+0.19}_{-0.38}$
σ_8	0.831 ± 0.013	$0.983^{+0.100}_{-0.055}$

Table 5.2: The best-fit parameters for the ΛCDM and the HDES ($n = 2$) models respectively.

Model	$\Omega_{m,0}$	$100\Omega_b h^2$	$\tilde{J}_c$	h	σ_8
Best-fit values					
ΛCDM	0.311 ± 0.006	2.243 ± 0.014	0	0.680 ± 0.004	0.758 ± 0.025
HDES	0.313 ± 0.006	2.240 ± 0.014	-0.309 ± 0.244	0.678 ± 0.004	0.911 ± 0.068

Table 5.3: The χ^2 and AIC parameters for the ΛCDM and the HDES models respectively.

Model	χ^2	AIC	ΔAIC
ΛCDM	1087.64	1095.68	0
HDES	1086.30	1096.35	0.678

5.7.1 Results

In Figs. 5.7 and 5.8 we show the 68.3%, 95.4% and 99.7% confidence contours for the ΛCDM and the HDES models, respectively, along with the one-dimensional (1D) marginalized likelihoods for all parameter combinations in the familiar triangle plot. We also highlight with a black point the mean MCMC values and with a red point the Planck 2018 concordance cosmology. The latter is based on the TT,TE,EE+lowP spectra, a flat ΛCDM model and the values are shown in Table 5.1.

In Tables 5.2 and 5.3 we show the best-fit values of the model parameters and the values for the χ^2 and AIC parameters for the ΛCDM and the HDES model respectively. As can be seen from Tables 5.2 and 5.3, we find that as the difference in the AIC parameters is roughly ~ 0.68, then both models seem to be statistically equivalent with each other. Furthermore, as seen in Fig. 5.8, there is a clear negative correlation between $\tilde{J}_c$ and σ_8 as we saw in Sec. 5.5.5 and Eq. (5.165) due to the strong degeneracy between the parameters. This degeneracy is useful as it can potentially alleviate and relax the tension that has been recently observed, see Refs. [116, 120]. In particular, in Fig 5.9 we show the 68.3%, 95.4% and 99.7% confidence contours for the ΛCDM (left) and the HDES ($n = 2$) (right) models respectively in the $(\Omega_{m,0}, \sigma_8)$ plane. As can be seen, for the HDES model, the best-fit in the $(\Omega_{m,0}, \sigma_8)$ plane moves toward higher values of σ_8, closer to those of Planck.

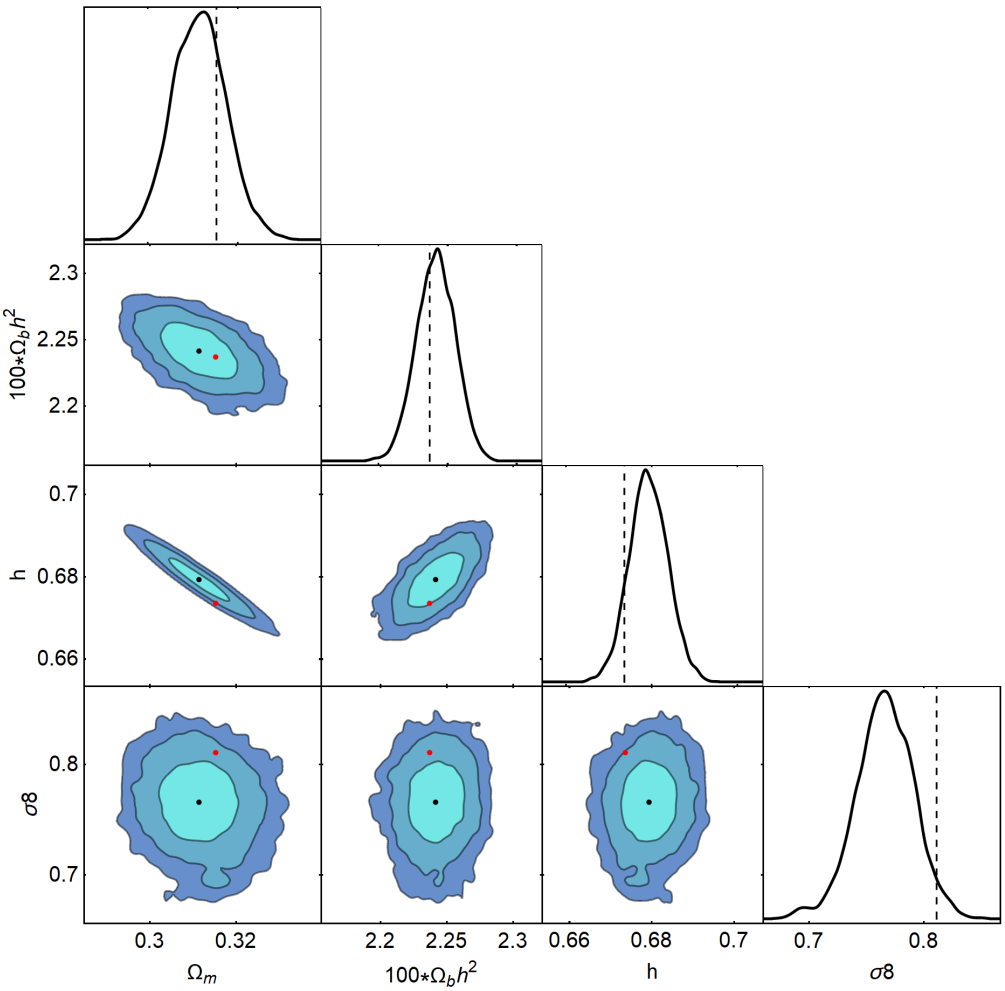

Figure 5.7: The 68.3%, 95.4% and 99.7% confidence contours for the ΛCDM model, along with the 1D marginalized likelihoods for all parameter combinations. We also highlight with a black point the mean MCMC values and with a red point or dashed vertical line the Planck 2018 concordance cosmology. The latter is based on the TT,TE,EE+lowP spectra, a flat ΛCDM model and the values are shown in Table 5.1.

5.8 Conclusions

The recent discovery of gravitational waves emission from a binary neutron star merger with an optical counterpart, signified a major breakthrough in astrophysics and cosmology as it provided a direct measurement of the speed of propagation of gravitational waves. This observation not only represented an important advance for astronomy, but it also served to greatly reduce the number of alternative models aiming at explaining the current accelerating phase of the Universe. In particular, since the constraint on the speed of propagation of gravitational waves is extremely close to the speed of light, the Horndeski Lagrangian simplified to only three functions. Although this means a notable progress in constraining cosmological models, degeneracies with the ΛCDM model remain and must be further investigated.

In this Chapter we used an effective fluid approach to study the remaining Horndeski La-

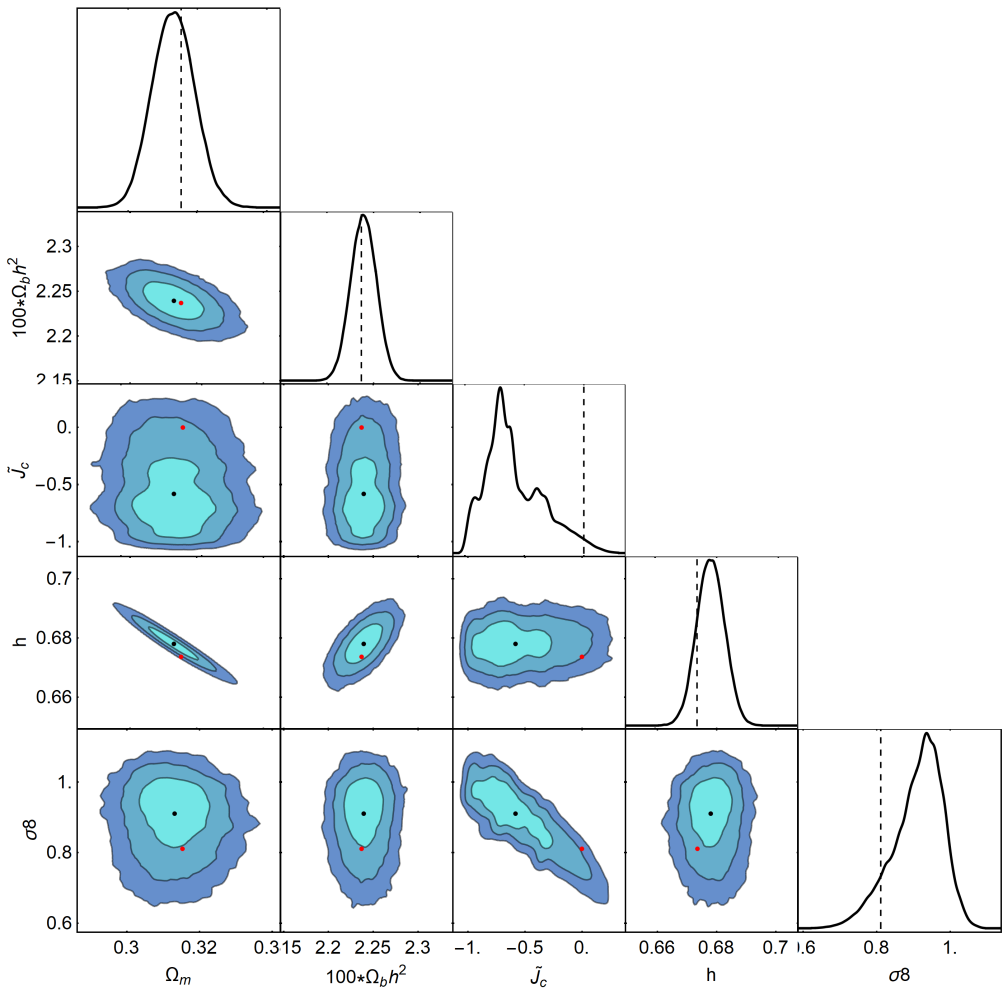

Figure 5.8: The 68.3%, 95.4% and 99.7% confidence contours for the HDES ($n = 2$) model, along with the 1D marginalized likelihoods for all parameter combinations. We also highlight with a black point the mean MCMC values and with a red point or dashed vertical line the Planck 2018 concordance cosmology. The latter is based on the TT,TE,EE+lowP spectra, a flat ΛCDM model and the values are shown in Table 5.1.

grangian. This formalism makes it possible to compare models with different underlying physics (e.g., DE and MG models) in a relatively easy way: each model is mapped to three functions describing the effective fluid, namely, the equation of state w, the sound speed c_s^2, and the anisotropic stress π. Even though the remaining Horndeski Lagrangian is now simpler than its original version, finding exact analytical solutions can be quite laborious. Nevertheless, the subhorizon and quasistatic approximations are pretty helpful at overcoming this difficulty.

One of our main results is the set of Eqs. (5.84)-(5.89). These equations along with the equation of state Eq. (5.55) describe the remaining Horndeski Lagrangian in an effective fluid approach under the subhorizon and quasistatic approximations. In this Chapter, we provide explicit expressions for the effective fluid description of several DE and MG models.

In order to exemplify our results and since we focused on explanations to the late-time accelerating universe, we carried out an analysis where only DM and an effective DE fluid are

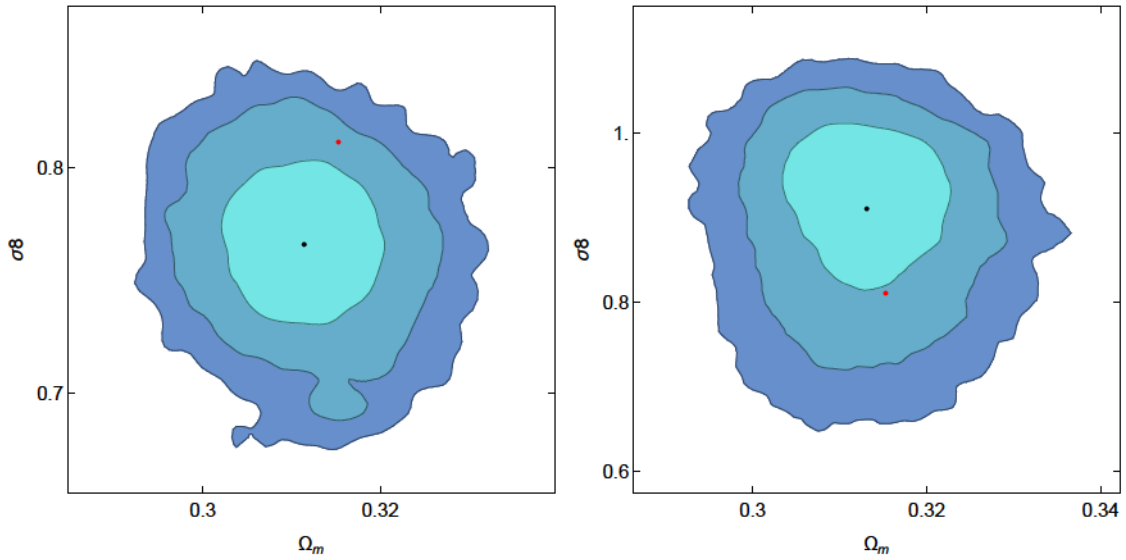

Figure 5.9: The 68.3%, 95.4% and 99.7% confidence contours for the ΛCDM (left) and the HDES ($n = 2$) (right) models respectively in the $(\Omega_{m,0}, \sigma_8)$ plane. We also highlight with a black point the mean MCMC values and with a red point or dashed vertical line the Planck 2018 concordance cosmology. The latter is based on the TT,TE,EE+lowP spectra, a flat ΛCDM model and the values are shown in Table 5.1.

taken into consideration. A particularly interesting model also included in our formalism is the KGB model. In Sec. 5.6 we show our analytical solutions agree pretty well with a full numerical solution of the system of differential equations describing the DM and effective DE perturbations. We also confirm that the subhorizon approximation breaks down for the KGB model due to the rapid oscillations of the scalar field in the large n limit, in agreement with Ref. [308]. Also, for the KGB model the background equation for the expansion history $H(a)$ can only be found numerically for $n > 1$, thus slowing down the codes significantly.

Due to these problems, we propose a completely new class of Horndeski models based on the designing principle, i.e., fixing the background to a specific model, usually that of the ΛCDM and then determining the Lagrangian. Given the freedom in specifying the remaining functions of the Horndeski Lagrangian, we propose a way to find families of models which match a particular background expansion, i.e., the equation of state w_{DE}. Since current observations are in good agreement with the standard ΛCDM at the background level, we provide equations specifying a $w_{DE} = -1$ designer Horndeski model (see Eqs. (5.151)), which we call HDES. Furthermore, for this model we are able to find exact solutions for the growth $\delta_m(a)$ in the matter domination epoch by solving Eq. (5.83). The solutions we found are given by Eq. (5.161) and they imply a degeneracy between σ_8 and the parameter of the HDES model $\tilde{J}_c$, which can approximately be described via Eq. (5.165).

Although fixing the background to ΛCDM is a common practice, the treatment of the perturbations might not be rigorous enough in current studies. Public codes solving the perturbation equations for the Horndeski Lagrangian (e.g., `hi_CLASS`) use ad hoc parametrizations for the α_i functions which differ significantly from our findings that approximate a realistic model (see Eqs. (5.153)-(5.157)), see for example Refs. [318–320].

We implemented the parametrized version for the DE effective fluid of our $w_{DE} = -1$ designer Horndeski HDES model in the public code `CLASS`, which we call `EFCLASS`, by following the straightforward implementation explained in Chapter 4. For the sake of comparison and in order to check the validity of our effective fluid approach, we compared results from our code `EFCLASS` with the public code `hi_CLASS`, which solves numerically the full perturbation equations.

In Fig. 5.5 we show the CMB angular power spectrum computed with both codes and as can be seen in the right panel of Fig. 5.5, the agreement is remarkable and on average on the order of $\sim 0.1\%$. Since the `hi_CLASS` code does not utilize either the subhorizon or the quasistatic approximation, but our `EFCLASS` does it, we conclude our effective fluid approach is quite accurate and powerful. Furthermore, the main advantage of our method is that while `hi_CLASS` requires significant and non-trivial modifications, our `EFCLASS` code practically only requires the implementation of Eq. (5.169), which is trivial.

We further investigated our $w_{DE} = -1$ designer Horndeski HDES model by computing cosmological constraints with recent data sets using an MCMC analysis. The results of our MCMC analysis are shown in Tables 5.2 and 5.3, where we present the best-fit values of the model parameters and the values for the χ^2 and AIC parameters for the ΛCDM and the HDES model respectively. We find that as the difference in the AIC parameters is roughly ~ 0.68, then both models seem to be statistically equivalent with each other. Furthermore, as seen in Fig. 5.8, there is a clear negative correlation between $\tilde{J}_c$ and σ_8. This can be understood, as we saw in Sec. 5.5.5, due to the strong degeneracy between the parameters described by Eq. (5.165). This degeneracy is useful as it can potentially alleviate the σ_8 tension that has been recently observed, see Ref. [116, 120].

6

Cosmological constraints with the Effective Fluid approach for Modified Gravity

The original content of this chapter is based on Ref. [321]. Cosmological constraints of Modified Gravity (MG) models are seldom carried out rigorously. First, even though general MG models evolve differently (i.e., background and perturbations) to the standard cosmological model, it is usual to assume a ΛCDM background. This treatment is not correct and in the era of precision cosmology could induce undesired biases in cosmological parameters. Second, neutrino mass is usually held fixed in the analyses which could obscure its relation to MG parameters. In Chapters 4 and 5 we showed that by using the Effective Fluid Approach we can accurately compute observables in fairly general MG models. An appealing advantage of our approach is that it allows for a pretty easy implementation of this kinds of models in Boltzmann solvers (i.e., less error–prone) while having a useful analytical description of the effective fluid to understand the underlying physics. This Chapter illustrates how the effective fluid approach can be used to carry out proper analyses of cosmological constraints in MG models. We investigated three MG models including the sum of neutrino masses as a varying parameter in our Markov Chain Monte Carlo analyses. Two models (i.e., Designer $f(R)$ [DES-fR] and Designer Horndeski [HDES]) have a background matching ΛCDM, while in a third model (i.e., Hu & Sawicki $f(R)$ model [HS]) the background differs from the standard model. In this way we estimate how relevant the background is when constraining MG parameters along with neutrinos' masses. We implement the models in the popular Boltzmann solver `CLASS` and use recent, available data (i.e., Planck 2018, CMB lensing, BAO, SNIa Pantheon compilation, H_0 from SHOES, and RSD Gold-18 compilation) to compute tight cosmological constraints in the MG parameters that account for deviation from the ΛCDM model. For both the DES-fR and the HS model we obtain $\log_{10} b < -8$ at 68% confidence when all data are included. In the case of the HDES model we find a somewhat weaker value of $\log_{10} J_c > -5$ at 68% confidence. We also find that constraints on MG parameters are a bit weakened when compared to the case where neutrinos' masses are held fixed in the analysis.

6.1 Introduction

As the available parameter space has shrank remarkably via the measurement of the speed of propagation of the gravitational waves by the event GW170817 and its optical counterpart GRB170817A [171,173,322], there are a few remaining models which deserve attention as well as proper analyses. Nevertheless, many analyses of the remaining models, especially the ones where the background expansion differs significantly from the ΛCDM model, do not consider the background expansion properly and just fix it to either the ΛCDM or a constant w model, as was observed in Refs. [9,10]. This obviously biases the results as it introduces biases in the cosmological parameters and spurious tensions with the data. However, some recent analyses have also acknowledged this discrepancy and newer versions of the Boltzmann solvers now have support for the correct backgrounds in some cases [323].

On the other hand, the so-called Effective Fluid Approach presented in Chapters 4 and 5 has the advantage that it provides a unified approach to analyse all models under the same umbrella, allows for the correct background expansion in the models, all without sacrificing the accuracy of the results [9–11]. In a nutshell and as a reminder, the Effective Fluid Approach works by rewriting the field equations of the MG model as GR and a DE fluid with an equation of state w, a pressure perturbation δP and an anisotropic stress σ. Especially the latter is crucial as sometimes it is ignored in analyses of MG models [12], something which might bias the results [191]. Moreover, through a joint Machine Learning analysis applied to the latest cosmological data hints of dark energy anisotropic stress were found [324] as we will also discuss on Chapter 12.

In the Effective Fluid Approach we also assume that in the relevant scales, where linear theory applies, the sub-horizon and quasi-static approximations hold. With these, general analytical expressions for the equation of state, the pressure perturbation, and the anisotropic stress were found in in Chapters 4 and 5. With the latter, one may then just solve numerically the evolution equations for the perturbations, found for example in Ref. [185].

Thus, the main advantage of the Effective fluid approach is that once one has the expressions for the variables w, δP and σ, it is very straightforward to also implement them in standard Boltzmann codes, such as `CLASS`, with very minimal modifications. We have already shown how his is done with the `EFCLASS` code, which implements the aforementioned approach, where it finding that `EFCLASS` and `hi_CLASS` [299], a modification of `CLASS` that solves numerically the whole set of perturbation equations for Horndeski, agree to better than 0.1%, see Fig. 5.5.

Recently, a comparison of different approaches to the quasi-static approximation in Horndeski models was made by Ref. [325], by applying this approximation to either the field equations, as done in the Effective fluid approach, or the equations for the two metric potentials Φ and Ψ and finally, the use of the attractor solution derived within the Equation of State approach [231]. It was found that all three approaches agree exactly on small scales and that in general, this approach is valuable in future model selections analyses for models beyond the ΛCDM model.

In this analysis we use the Effective Fluid approach and our `EFCLASS` code, for the background and first order perturbations, to obtain cosmological constraints with the latest cosmological data sets: we include the Pantheon SNe compilation [88], the Planck 2018 CMB data [1], the H_0 Riess measurement [46], various BAO points [90, 92, 326], and a new redshift space distortions (RSD) likelihood (see Ref. [327] for the "Gold 2018" compilation of Ref. [116]). An important aspect of our investigation is that we take into consideration neutrino mass as a varying parameter. Neutrino mass is usually held fixed in analyses which could obscure its relation to MG parameters. The role of massive neutrinos in modified gravity was first investigated in [328] by considering $f(R)$ gravity. The implementation in Boltzmann solvers of $f(R)$ gravity including neutrino mass as a varying parameter was carried out in [329,330], where cosmological constraints were also computed.

The chapter is organised as follows. In Sec. 6.2 we present the models we consider and the results of our MCMC analysis with `EFCLASS`, in Sec. 6.3 we conclude and lastly, in Appendix C we present some details on our RSD likelihood.

6.2 Cosmological Constraints

In our MCMC analysis with `EFCLASS` we will consider the $f(R)$ Designer model and the Hu & Sawicki model defined in Eqs. (4.69) and (4.56) of Chapter 4 respectively and the Horndeski Designer model (HDES) defined in Eq. (5.151) of Chapter 5.

6.2.1 Methodology

In order to compute cosmological constraints we use the following data sets. Firstly, we utilise the 2018 release by the Planck Collaboration including temperature and polarisation anisotropies of the CMB (`TTTEEE`) as well as CMB lensing (`lensing`) [1]. Secondly, we include measurements of

Parameter	Range
$\log_{10} b_\pi$	$[-10, 0]$
$\log_{10} b_{hs}$	$[-10, -1]$
$\log_{10} J_c$	$[-10, 0]$

Table 6.1: Flat prior bounds used in the MCMC analyses. Prior range for other parameters is set as in Table 1 of Ref. [331]

Baryon Acoustic Oscillations (`BAO`) from Refs. [90, 92, 326]. Thirdly, Pantheon supernovae (`SNe`) from [88] were also incorporated in the analysis. Fourthly, we employed local Hubble measurement (`H0`) from Ref. [46] as a Gaussian prior. Finally, we coded a new likelihood for a compilation of Redshift-Space-Distortions (`RSD`) measurements (see Appendix C and Ref. [327]).

The cosmological models previously discussed in Section 6.2 were implemented in our Boltzmann solver `EFCLASS`. For a given cosmological model and a set of cosmological parameters we can compute the solution for both background and linear perturbations, that is, we can predict observables such as the matter power spectrum and the CMB angular power spectrum. Since the parameter space not only includes cosmological parameters, but also several nuissance parameters, it becomes hard to find the best fit model as well as the relevant statistical information. The usual approach is to use Markov Chain Monte Carlo (MCMC) techniques [242, 332] and we will do so.

We explore the parameter space of the cosmological models with the code `Montepython` [333, 334] which works along with `EFCLASS`: theoretical predictions are computed and compared to observations through likelihood functions $\sim 10^5$ times. The MCMC procedure allows us not only to find the best fit model parameters, but also to obtain the relevant countours confidence. In our analysis we use the set of flat priors in Table 6.1.

6.2.2 Results

DES-fR model

In Fig. 6.1 we show the 68% and 95% confidence contours for the DES-fR model. Vertical dashed and horizontal dotted lines indicate the values obtained by the Planck Collaboration in their analyses for the standard cosmological model ΛCDM (last column in Table 2 of Ref. [1]). The relevant statistical information (i.e., mean values and 68% confidence limits) is shown in Table 6.2. We see there is good agreement for common parameters in both DES-fR and ΛCDM models. Although error on neutrino masses get significantly reduced as we add more data, we can only set an upper limit when combining all data sets. In the case of the MG parameter b_π we do not observe any degeneracy with other parameters in the model. It is interesting that the constraints on MG, although still prior dominated, present different tendencies according to the combination of data sets: i) RSD push the MG constraints towards GR, while the H_0 tension remains unresolved; ii) if we exclude RSD from the data sets, we notice a preference for a MG scenario, but still hitting the prior bound on the right and not solving the problem with H_0; iii) a similar situation occurs when we exclude supernovae, H_0, and RSD from the data sets, because there is a preference for MG (prior dominated though) while obtaining a H_0 value that agrees very well with Planck Collaboration results for ΛCDM . Finally, we note that our derived value for the parameter

$$\sigma_8 = 0.815^{+0.009}_{-0.007} \qquad (68\%), \tag{6.1}$$

when including the whole data set, agrees very well with the value found by DES Collaboration $\sigma_8 = 0.807^{+0.062}_{-0.041}$ for the ΛCDM model [154].

Parameter	Planck	{...}+lensing	{...}+BAO	{...}+SNe	{...}+H_0	{...}+RSD
ω_b	$0.02234^{-0.00017}_{+0.00015}$	$0.02235^{-0.00016}_{+0.00015}$	$0.02252^{-0.00012}_{+0.00013}$	$0.02246^{-0.00013}_{+0.00014}$	0.02250 ± 0.00013	$0.02255^{-0.00017}_{+0.00011}$
ω_{cdm}	0.1204 ± 0.0014	$0.1204^{-0.0014}_{+0.0012}$	$0.1191^{-0.0009}_{+0.0010}$	$0.1192^{-0.0009}_{+0.0010}$	$0.1188^{-0.0009}_{+0.0008}$	$0.1185^{-0.0009}_{+0.0010}$
H_0	$66.64^{-0.78}_{+1.63}$	$66.70^{-0.80}_{+1.48}$	67.96 ± 0.57	$67.91^{-0.47}_{+0.55}$	$68.18^{-0.39}_{+0.49}$	$68.42^{-0.47}_{+0.41}$
$\ln 10^{10} A_s$	$3.047^{-0.016}_{+0.014}$	$3.047^{-0.016}_{0.015}$	3.051 ± 0.011	3.047 ± 0.015	3.032 ± 0.009	$3.051^{-0.018}_{+0.014}$
n_s	$0.9643^{-0.0047}_{+0.0049}$	$0.9646^{-0.0040}_{+0.0047}$	0.9679 ± 0.0037	$0.9676^{-0.0041}_{+0.0033}$	$0.9694^{-0.0038}_{+0.0046}$	$0.9693^{-0.0039}_{+0.0036}$
τ_{reio}	$0.0548^{-0.0080}_{+0.0072}$	$0.0545^{-0.0082}_{+0.0071}$	$0.0580^{-0.0058}_{+0.0060}$	$0.0560^{-0.0071}_{+0.0075}$	$0.0492^{-0.0051}_{+0.0048}$	$0.0584^{-0.0092}_{0.0068}$
Σm_ν	< 0.171	< 0.158	< 0.064	< 0.058	< 0.054	< 0.043
$\log_{10} b_\pi$	$[-10, 0]$	$[-10, 0]$	-4^{-1}_{+3}	$[-10, 0]$	$-1.1^{-0.6}_{+0.8}$	< -8

Table 6.2: Mean values and 68% confidence limits on cosmological parameters for the DES-fR model. Here {...} stands for the inclusion of data from column on the left.

Parameter	Planck	{...}+lensing	{...}+BAO	{...}+SNe	{...}+H_0	{...}+RSD
ω_b	$0.02233^{-0.00015}_{+0.00018}$	0.02238 ± 0.00016	0.02247 ± 0.00013	$0.02247^{-0.00016}_{+0.00013}$	$0.02257^{-0.00015}_{+0.00016}$	$0.02256^{-0.00012}_{+0.00013}$
ω_{cdm}	$0.1205^{-0.0014}_{+0.0013}$	$0.1201^{-0.0013}_{+0.0012}$	0.1191 ± 0.0010	$0.1191^{-0.0009}_{+0.0011}$	$0.1184^{-0.0008}_{+0.0007}$	0.1182 ± 0.0008
H_0	$66.38^{-0.72}_{+1.89}$	$66.68^{-0.81}_{+1.70}$	$67.90^{-0.49}_{+0.59}$	$67.91^{-0.59}_{+0.52}$	$68.57^{-0.38}_{+0.40}$	$68.59^{-0.33}_{+0.43}$
$\ln 10^{10} A_s$	3.046 ± 0.016	3.044 ± 0.014	3.046 ± 0.014	3.044 ± 0.015	$3.039^{-0.010}_{+0.011}$	$3.050^{-0.016}_{+0.013}$
n_s	$0.9638^{-0.0043}_{+0.0051}$	$0.9650^{-0.0045}_{+0.0047}$	$0.9684^{-0.0040}_{+0.0037}$	$0.9680^{-0.0043}_{+0.0035}$	$0.9694^{-0.0031}_{+0.0029}$	$0.9702^{-0.0035}_{+0.0037}$
τ_{reio}	$0.0535^{-0.0079}_{+0.0077}$	$0.0536^{-0.0072}_{+0.0074}$	$0.0557^{-0.0069}_{+0.0073}$	$0.0544^{-0.0082}_{+0.0073}$	$0.0519^{-0.0055}_{+0.0053}$	$0.0584^{-0.0083}_{0.0066}$
Σm_ν	< 0.151	< 0.143	< 0.064	< 0.061	< 0.026	< 0.032
$\log_{10} b_{hs}$	$[-10, -1]$	> -3	> -6	> -4	> -4	< -7

Table 6.3: Mean values and 68% confidence limits on cosmological parameters for the HS model. Here {...} stands for the inclusion of data from column on the left.

HS model

In Fig. 6.2 we depict 68% and 95% confidence contours for the HS model using a number of data sets. Dashed-vertical and dotted-horizontal lines are the parameter values that the Planck Collaboration reported for its analysis using ΛCDM model (last column in Table 2 of Ref. [1]). Table 6.3 contains relevant statistical information for our analysis: we show mean values and 68% limits for the HS model. Again, cosmological parameters which are common to both ΛCDM and HS models are in good agreement with Planck Collaboration's results. As in the case for the DES-fR model we can only find an upper limit for the neutrino masses which is slightly smaller for the HS model. Also in this case MG constraints are prior dominated and we observe a preference for departure from GR in most probe combination, the exception being the case including RSD. The latter again goes towards GR while not solving the H_0 discrepancy with the local value. Interestingly, in Ref. [335] the authors analyzed galaxy morphology and placed the following constraint for the HS model $f_{R0} < 1.4 \times 10^{-8}$. By using the whole data set we find

$$\sigma_8 = 0.816^{+0.008}_{-0.007} \qquad (68\%), \tag{6.2}$$

which perfectly agrees with the value found for the DES-fR model.

HDES model

Fig. 6.3 shows confidence contours for the cosmological parameters in the HDES model. We see good agreement in parameters that also play a part in ΛCDM model; the values found by the Planck Collaboration (last column in Table 2 of Ref. [1]) are depicted as vertical-dashed and horizontal-dotted lines in Fig. 6.3. As for the DES-fR and HS models, in this case the neutrino masses remain unconstrained in our analysis and we can only set an upper limit. Concerning the MG parameter we observe that results are not decisive since posteriors are mostly affected by the prior distribution. Although there exist preference for departure from GR when including H_0 and RSD in the data set, the constraints hit the prior bound on the right. Interesting in this case RSD push the constraints far from GR, whereas in the case of DES-fR and HS models the whole data

Parameter	Planck	{...}+lensing	{...}+BAO	{...}+SNe	{...}+H_0	{...}+RSD
ω_b	$0.02233^{-0.00015}_{+0.00017}$	$0.02236^{-0.00016}_{+0.00017}$	0.02242 ± 0.00013	$0.02238^{-0.00020}_{+0.00014}$	$0.02257^{-0.00015}_{+0.00014}$	$0.02257^{-0.00017}_{+0.00013}$
ω_{cdm}	0.1205 ± 0.0014	0.1204 ± 0.0013	0.1195 ± 0.0009	$0.1197^{-0.0010}_{+0.0014}$	0.1180 ± 0.0009	0.1182 ± 0.0009
H_0	$66.67^{-0.76}_{+1.52}$	$66.95^{-0.73}_{+1.36}$	67.78 ± 0.50	$67.81^{-0.72}_{+0.54}$	$68.68^{-0.46}_{+0.44}$	$68.60^{-0.49}_{+0.47}$
$\ln 10^{10} A_s$	$3.046^{-0.018}_{+0.016}$	$3.049^{-0.017}_{+0.015}$	3.045 ± 0.013	$3.048^{-0.011}_{+0.014}$	$3.049^{-0.018}_{+0.010}$	$3.046^{-0.018}_{+0.014}$
n_s	$0.9640^{-0.0045}_{+0.0049}$	$0.9646^{-0.0044}_{+0.0043}$	$0.9671^{-0.0037}_{+0.0035}$	$0.9658^{-0.0065}_{+0.0069}$	$0.9716^{-0.0032}_{+0.0030}$	$0.9700^{-0.0037}_{+0.0038}$
τ_{reio}	$0.0539^{-0.0086}_{+0.0075}$	$0.0552^{-0.0084}_{+0.0074}$	$0.0544^{-0.0063}_{+0.0062}$	$0.0554^{-0.0052}_{+0.0064}$	$0.0583^{-0.0094}_{+0.0059}$	$0.0560^{-0.0087}_{0.0056}$
Σm_ν	< 0.134	< 0.115	< 0.056	< 0.043	< 0.038	< 0.037
$\log_{10} J_c$	$[-10, 0]$	$[-10, 0]$	< -0.3	< -9	$-1.^{-0.2}_{+0.5}$	> -5

Table 6.4: Mean values and 68% confidence limits on cosmological parameters for the HDES model. Here {...} stands for the inclusion of data from column on the left.

set prefer the GR limit. Finally we note that our derived

$$\sigma_8 = 0.814^{+0.009}_{-0.007} \qquad (68\%), \tag{6.3}$$

taking into consideration the full data set agrees well with values found for DES-fR and HS models.

In Table 6.4 we show mean values and 68% confidence bounds for the cosmological parameters in the HDES model.

6.3 Conclusions

Over the past decades several cosmological models have emerged as a plausible explanation for the late-time accelerating expansion of the Universe. In this Chapter we investigated three MG models which satisfy solar system tests and also fulfil constraints on the speed of propagation of GWs, namely: DES-fR, HS, and the HDES models.

It is possible to interpret MG models as an effective fluid and we followed this approach in this work. We implemented DES-fR, HS, and HDES models in the Boltzmann solver `EFCLASS` which uses sub-horizon and quasi-static approximations when solving the perturbation equations. We showed in Chapters 4 and 5 that the observables are accurately computed (i.e., better than 0.1% as compared to outputs from codes which do not use any approximation, see Fig. 5.5) while having the advantage of analytical expressions describing MG as an effective fluid.

When constraining the parameter space for the HS model is usual to assume a ΛCDM background. This is however incorrect as the background for the HS model is in general different from the ΛCDM model. In this Chapter we dropped this assumption and solved the perturbations equations taking into consideration the background evolution too. We found constraints which are in good agreement with results by the Planck Collaboration when the parameter spaces overlap. We also note that the constraints on the MG parameter are dominated by the prior hence unconstrained by current data sets. As the HS model has an additional parameter than the ΛCDM model, the former will be severely penalized in any Bayesian model comparison.

Since data indicate a preference for the standard model it is interesting to study models which exactly match the ΛCDM background. These models might rely on new physics while also behaving differently at the perturbations level with respect to the ΛCDM model. By investigating these kinds of models we can also reveal whether or not current data sets can discriminate alternative models from the concordance model. In this Chapter we investigated two models, namely, a designer $f(R)$ (DES-fR) and a designer Horndeski model (HDES).

When considering common cosmological parameters, constraints for the DES-fR model do not exhibit significant discrepancies with results by the Planck Collaboration for the standard model. Concerning the MG parameter we note the results depend on the probe combination. Most cases are dominated by the prior and hence unconstrained. The full data set however, prefers the GR limit. One reason for this might be the strong constraints from the RSD likelihood. As the surveys that make the RSD measurements assume a ΛCDM model in their analysis, the data

themselves maybe a bit biased. While this in general can be corrected, up to a point, with the AP correction as mentioned in the Appendix, some residual bias may remain. While this is an important point, it is however outside the scope of our present analysis, thus we leave it for future work.

Regarding the constraints for the HDES model we also find good agreement with parameters also appearing in the ΛCDM model. Here constraints on MG are also inconclusive as the posteriors are prior dominated. Interestingly, in this case the full data set shows a slight preference for a departure from GR.

In summary, our results do not conclusively indicate the presence of modifications to GR. Since our MG constraints are prior dominated we conclude ΛCDM is still the preferred model. Where data sets overlap, our results fully agree with the investigation carried out by the Planck Collaboration [229].

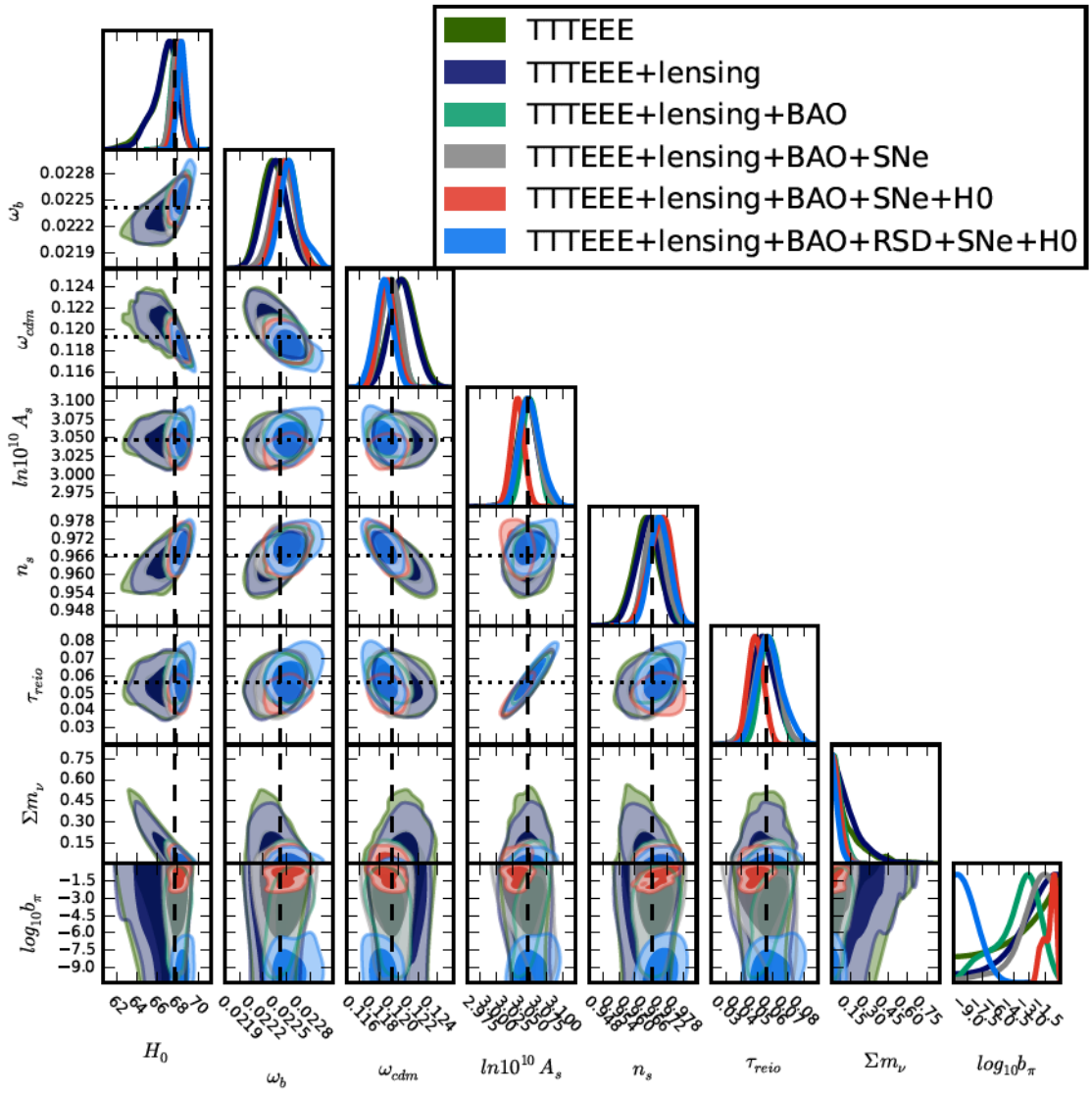

Figure 6.1: 1D marginalised likelihoods as well as confidence contours (i.e., 68% and 95%) for the DES-fR model. The dashed vertical and horizontal dotted lines correspond to the results obtained by the Planck Collaboration for the ΛCDM parameters (last column in Table 2 of Ref. [1]). TTTEEE stands for CMB temperature and E-mode polarisation anisotropies correlations and cross-correlations, lensing stands for CMB lensing, BAO stands for Baryonic Acoustic Oscillations, SNe stands for supernovae, H0 stands for the Hubble constant, and RSD stands for redshift space distortions.

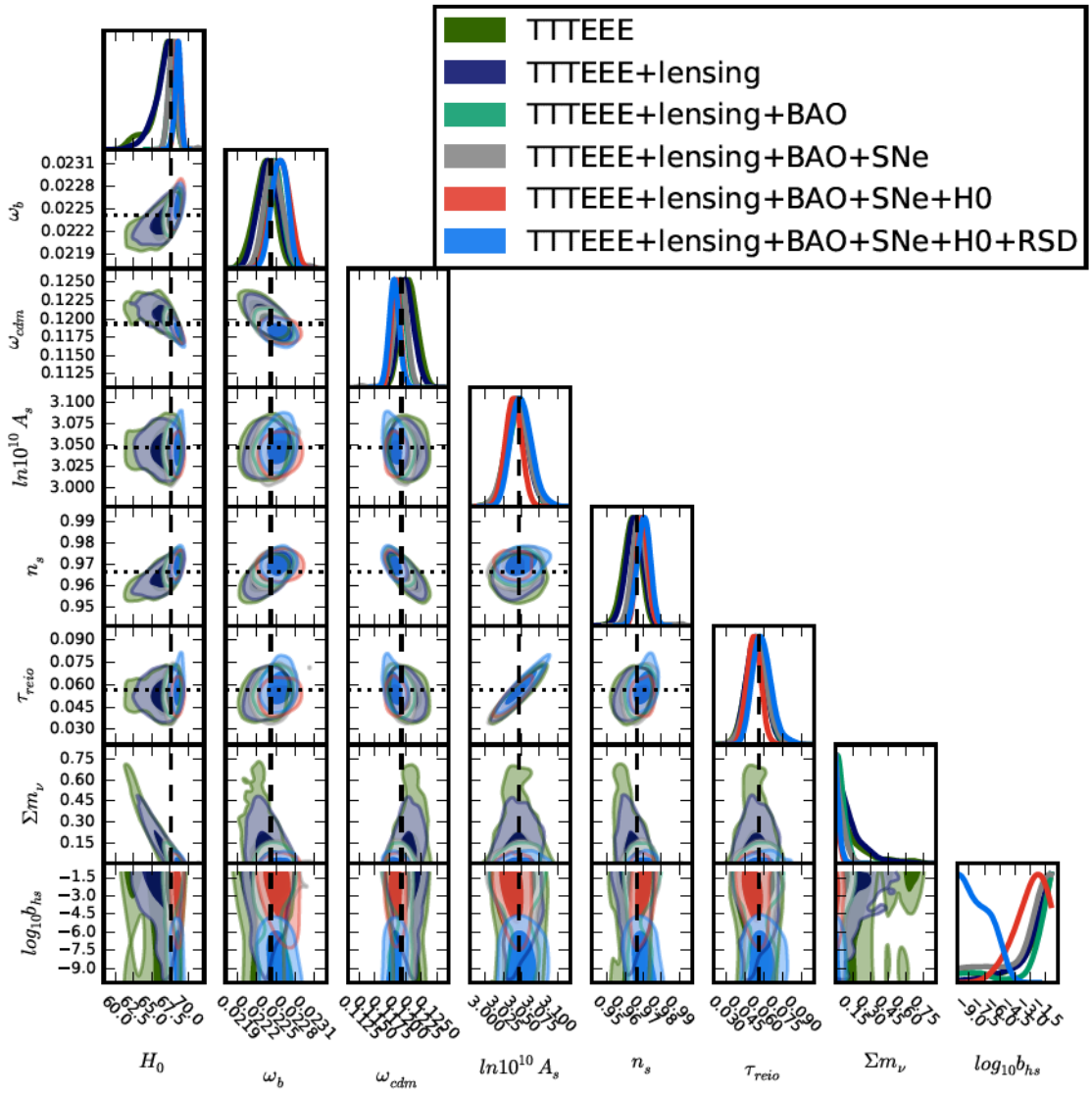

Figure 6.2: 1D marginalised likelihoods as well as confidence contours (i.e., 68% and 95%) for the HS model. The dashed vertical and horizontal dotted lines correspond to the results obtained by the Planck Collaboration for the ΛCDM parameters (last column in Table 2 of Ref. [1]). TTTEEE stands for CMB temperature and E-mode polarisation anisotropies correlations and cross-correlations, lensing stands for CMB lensing, BAO stands for Baryonic Acoustic Oscillations, SNe stands for supernovae, H0 stands for the Hubble constant, and RSD stands for redshift space distortions.

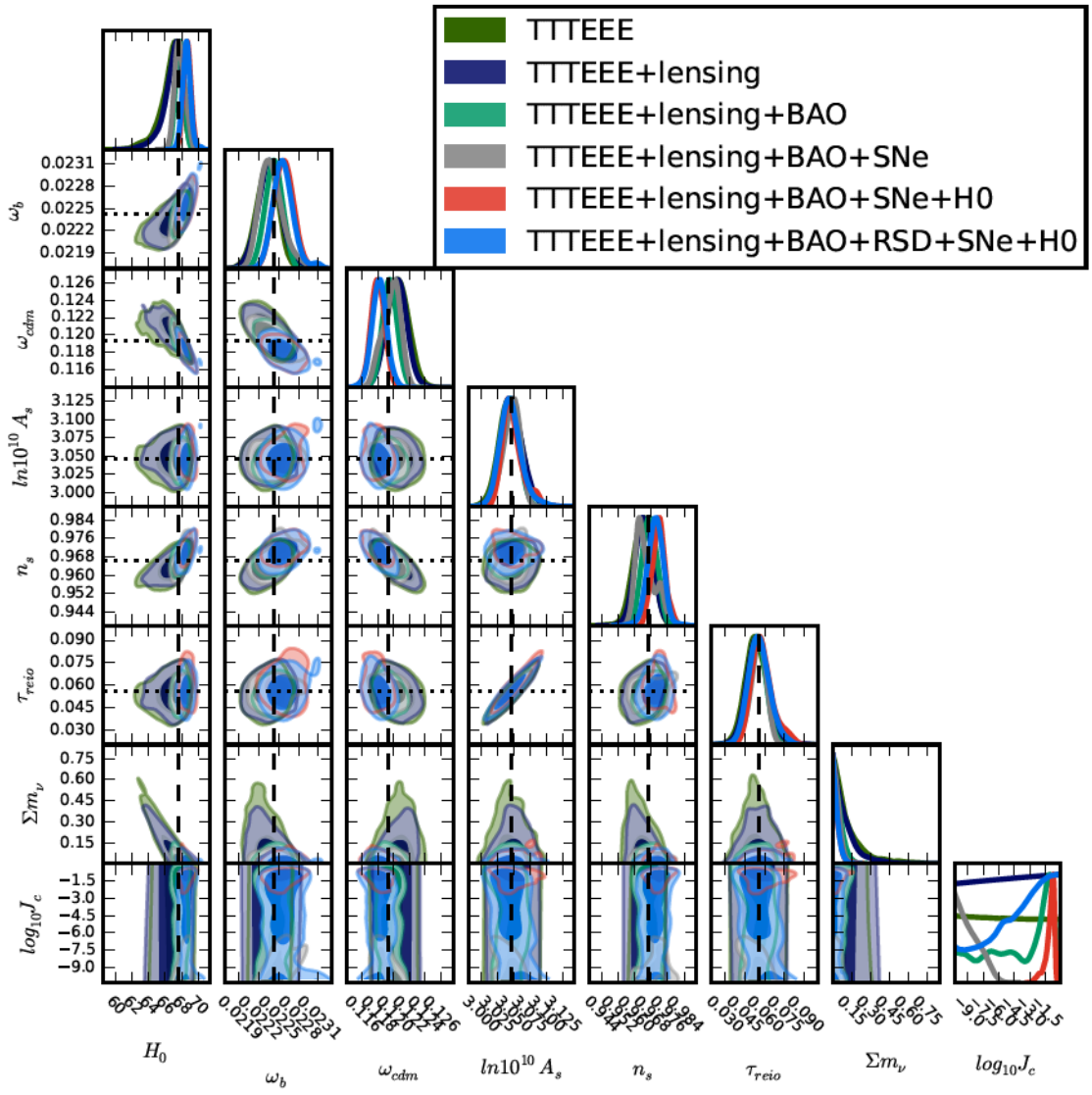

Figure 6.3: 1D marginalised likelihoods as well as confidence contours (i.e., 68% and 95%) for the HDES model. The dashed vertical and horizontal dotted lines correspond to the results obtained by the Planck Collaboration for the ΛCDM parameters (last column in Table 2 of Ref. [1]). TTTEEE stands for CMB temperature and E-mode polarisation anisotropies correlations and cross-correlations, lensing stands for CMB lensing, BAO stands for Baryonic Acoustic Oscillations, SNe stands for supernovae, H0 stands for the Hubble constant, and RSD stands for redshift space distortions.

7

Cosmological constraints on non-adiabatic dark energy perturbations

The original content of this chapter is based on Ref. [327]. The exact nature of dark energy is currently unknown and its cosmological perturbations, when dark energy is assumed not to be the cosmological constant, are usually modeled as adiabatic. Here we explore the possibility that dark energy might have a nonadiabatic component and we examine how it would affect several key cosmological observables. We present analytical solutions for the growth rate and growth index of matter density perturbations and compare them to both numerical solutions of the fluid equations and an implementation in the Boltzmann code `CLASS`, finding that they all agree to well below one percent. We also perform a Monte Carlo analysis to derive constraints on the parameters of the nonadiabatic component using the latest cosmological data, including the temperature and polarization spectra of the Cosmic Microwave Background as observed by Planck, the Baryon Acoustic Oscillations, the Pantheon type Ia supernovae compilation and lastly, measurements of Redshift Space Distortions (RSD) of the growth rate of matter perturbations. We find that the amplitude of the nonadiabatic pressure perturbation is consistent with zero within 1σ. Finally, we also present a new, publicly available, RSD likelihood for MontePython based on the "Gold 2018" growth rate data compilation, see Appendix C for more details.

7.1 Introduction

As we have been discussing extensively in Chapters 4, 5 and 6, although Dark Energy (DE) and Modified Gravity (MG) models seem at a first glance quite dissimilar, however it is possible to unify them within the same framework. One way to do this is to map the MG models, to linear order, to some DE fluid via the effective fluid approach. Then, MG models can be interpreted as DE fluids described by an equation of state $w(a)$, a pressure perturbation $\delta P(k,a)$, and an anisotropic stress $\sigma(k,a)$ [9,10,192–196]. Hence, the evolution of the background is determined by $w(a)$, while the evolution of the perturbations is governed by $\delta P(k,a)$ and $\sigma(k,a)$, both of which are time and scale-dependent. In this case however, the effective fluid DE pressure perturbation $\delta P(k,a)$ could also be interpreted as containing both an adiabatic and a nonadiabatic contribution, as we will see later on in Sec. 7.2.

On the other hand, the presence of DE anisotropic stress has the interesting side-effect that the DE sound speed $c^2_{\rm s,DE}$ can in general be negative, without sacrificing the overall stability of the perturbations. This is true as long as the effective sound speed, which is the sum of the DE sound speed and the anisotropic stress, is always positive [235]. Moreover, it can be shown that a varying adiabatic sound speed of DE perturbations can mimic anisotropic stresses [236, 237].

In this Chapter we will consider a holistic approach and also consider nonadiabatic DE perturbations, motivated by the following reasons. First, in Ref. [324], and we will cover it also on Chapter 12, it was shown with a machine learning approach, based on the Genetic Algorithms, that current data seem to give hints for the existence of DE anisotropic stress, thus going beyond

simple DE models within GR. This could also leave open the possibility for a nonadiabatic DE component, as then the DE component could originate from a higher energy model, usually of the MG type. Second, the previous observation is crucial since, as mentioned earlier and will be seen in detail in the following sections, when MG models are described by the effective fluid approach, equivalently they can also be modeled as a DE fluid with a nonadiabatic component. Hence, we conclude that a nonadiabatic DE component could arise naturally in a wide class of models.

Finally, Primordial Black Holes (PBH) can be a significant component of Dark Matter [336] and give rise to entropy perturbations at early times on very small scales. They grow like isocurvature energy density perturbations and may eventually generate a significant component on large scales [337]. Note that PBH as dark matter behaves as an adiabatic component on very large scales, since it follows the large scale curvature perturbations just like baryons and photons. It is only on small scales that it has an isocurvature component, which is also highly non-Gaussian and can grow to become relevant at late times, around vacuum energy domination. While the PBH entropy perturbations happen on very different scales from those of DE, this clearly provides another mechanism for giving rise to a nonadiabatic component in the dark sector.

Here we consider the effects of the nonadiabatic DE perturbations on the LSS of the Universe, as the latter is directly affected by the underlying gravitational theory, something which allows us to easily search for deviations from GR. A main probe of LSS is the matter density perturbations, which in linear theory can be parameterized through the growth parameter $\delta_m = \frac{\delta\rho_m}{\bar{\rho}_m}$ and the growth rate $f \equiv \frac{d\ln\delta_m}{d\ln a}$, which is the former's logarithmic derivative while $\bar{\rho}_m$ is the background matter density and $\delta\rho_m$ its perturbation to linear order. The growth rate can also be parameterized via the growth index γ parameter [338], which in the ΛCDM model is equal to $\gamma \simeq 6/11$, hence making it easier to look for deviations from GR. The growth index is defined as the exponent of the growth rate $f(z) = \Omega_m^{\gamma}(z)$ and, as in the ΛCDM model the growth rate is scale-invariant on large scales, this makes γ a useful discriminator of DE models [339].

One of the main advantages of the growth rate is that it encodes information about how gravity affects the LSS, as the latter requires only linear physics, which is well understood. This means the growth can be a particularly useful probe [340]. Similarly, the growth index can help discriminate models both between DE and MG (see Ref. [141, 208]) and between ΛCDM [207] and MG models that are fully degenerate at the background level [9, 201–204] as we have seen in earlier Chapters.

Some of the first constraints on the sound speed of DE were reported in Ref. [341] by using WMAP data. However, given the data at the time, no significant sensitivity on the adiabatic sound-speed was reported. On the other hand, nonadiabatic perturbations were studied within the context of a decaying vacuum cosmology in Ref. [342], where they were found to only have an effect on larger scales. Constraints on nonadiabatic DE models using only growth RSD data were reported in Ref. [343] which used a particular parameterization for the nonadiabatic DE perturbations based on a linear combination of the intrinsic and entropy perturbations $\Gamma(a)$ and $S(a)$ [343]. Using a conjoined analysis of the $f\sigma_8$ and $H(z)$ data no deviations from ΛCDM were found. Another similar analysis with only growth RSD data was done in Ref. [344], which did not find any deviations from the standard cosmological model. Finally, a related approach in the search of primordial entropy perturbations was presented in Ref. [345] and was constrained by the Cosmic Microwave Background (CMB) data in Ref. [346].

In the next sections we will present a broader approach by considering a general ansatz for the nonadiabatic DE perturbations and we will use the latest cosmological data, including Planck 18, BAO and RSD measurements to constrain its model parameters. The structure of our Chapter is as follows. In Sec. 7.2 we present the theoretical background of our analysis and a realistic parameterization for the nonadiabatic DE pressure perturbations, along with analytic solutions for the growth of matter density perturbations and the growth index γ, while in Sec. 7.3 we compare our numerical and analytical solutions against an implementation of the nonadiabatic perturbations in the Boltzmann code `CLASS`. In Sec. 7.4 we present our results from a Monte Carlo Markov Chain (MCMC) analysis using the latest cosmological data, while in Sec. 7.5 we discuss our

conclusions. Finally, in Appendix C we present an implementation of the redshift space distortions (RSDs) likelihood for MontePython.

7.2 Theory

For the benefit of the reader, following we will repeat a few basic equations covered already on Chapter 4 to avoid the need to scroll upward and recall some useful expression we will use in our analysis. We will consider a spatially flat universe and assume that the scalar perturbations of the metric can be described by the perturbed Friedmann-Lemaitre-Robertson-Walker metric in the conformal Newtonian gauge

$$ds^2 = a^2\left[-(1+2\psi)d\tau^2 + (1-2\phi)dx_i dx^i\right], \tag{7.1}$$

where $a = a(\tau) = \frac{1}{1+z}$ is the scale factor, z is the redshift and $d\tau = dt/a$ is the conformal time in terms of the cosmic time t.

We assume that a DE fluid is responsible for the accelerated expansion of the universe and that its background evolution can be described by an equation of state $w = \bar{P}/\bar{\rho}$, while its fluctuations can be described by a pressure perturbation δP and anisotropic stress σ. The energy momentum tensor of the fluid can be written as

$$T^\mu_\nu = P\delta^\mu_\nu + (\rho + P)U^\mu U_\nu, \tag{7.2}$$

where the overhead bar $\bar{\rho}$ denotes a background quantity, $U^\mu \equiv dx^\mu/\sqrt{-ds^2}$ is the four velocity, given to linear order by $U^\mu \simeq \frac{1}{a}\left(1-\psi, u^i\right)$ for $u^i = dx^i/d\tau$ and the density and pressure include both background and perturbations, i.e. $\rho = \bar{\rho} + \delta\rho$ and $P = \bar{P} + \delta P$. The components of the energy momentum tensor are then given by

$$T^0_0 = -(\bar{\rho} + \delta\rho), \tag{7.3}$$

$$T^0_i = (\bar{\rho} + \bar{P})u_i, \tag{7.4}$$

$$T^i_j = (\bar{P} + \delta P)\delta^i_j + \Sigma^i_j, \tag{7.5}$$

where Σ^i_j is the anisotropic stress tensor, which is traceless $\Sigma^i_i = 0$ and can also be written via the σ parameter as $(\bar{\rho} + \bar{P})\sigma \equiv -(\hat{k}^i\hat{k}_j - \frac{1}{3}\delta^i_j)\Sigma^j_i$.

The evolution equations of the fluid variables $\delta = \frac{\delta\rho}{\bar{\rho}}$ and velocity of the DE fluid $\theta = ik^j u_j$ can be found by the conservation of the energy momentum tensor $T^{\mu\nu}{}_{;\nu} = 0$ and are given by [185, 278]:

$$\dot{\delta} = -(1+w)\left(\theta - 3\dot{\phi}\right) - 3\mathcal{H}\left(\frac{\delta P}{\bar{\rho}} - w\delta\right), \tag{7.6}$$

$$\dot{\theta} = -\mathcal{H}(1-3w)\theta - \frac{\dot{w}}{1+w}\theta + \frac{\delta P/\bar{\rho}}{1+w}k^2 - k^2\sigma + k^2\psi, \tag{7.7}$$

where $\mathcal{H} \equiv \frac{\dot{a}}{a}$ is the conformal Hubble parameter and k is the wavenumber of the Fourier mode of the perturbations, which in GR are decoupled.

In general, is is most convenient to describe the DE pressure perturbation in the rest frame $\delta\hat{P}$, denoted here by a hat, which is defined as the frame where the fluid is at rest, i.e. $\hat{\theta} = 0$. Then, the pressure perturbation in the rest frame can be expressed in terms of the energy density ρ and entropy S as $\hat{P} = \hat{P}(\rho, S)$ as [347]

$$\delta\hat{P} = \left.\frac{\partial\hat{P}}{\partial\rho}\right|_S \delta\hat{\rho} + \left.\frac{\partial\hat{P}}{\partial S}\right|_\rho \delta\hat{S}, \tag{7.8}$$

where the DE density and entropy perturbations at the rest frame are given by $\hat{\delta\rho}$ and $\hat{\delta S}$ respectively. In principle, the nonadiabatic contribution may come from some internal degrees of freedom, as for example happens in the quintom model [6]. We can straight-forwardly identify the DE rest frame sound speed as

$$\hat{c}_s^2 \equiv \left.\frac{\partial\hat{P}}{\partial\rho}\right|_S, \tag{7.9}$$

which is equal to one for quintessence, but is in the range $\hat{c}_s^2 \in [0,1]$ for k-essence or other models [276]. For modified gravity models it can even be negative, in which case one would presume that a negative value would cause instabilities in the perturbations, unless there is anisotropic stress to stabilize them [235].

We can now decompose the pressure perturbation in terms of the sound speed $\hat{c}_s^2$ and a nonadiabatic part $\hat{\delta P}_{\rm nad}$ as

$$\hat{\delta P} = \hat{c}_s^2\bar{\rho}\hat{\delta} + \hat{\delta P}_{\rm nad}, \tag{7.10}$$

where both quantities are defined in the DE rest frame and the nonadiabatic contribution at the rest frame can be identified as

$$\hat{\delta P}_{\rm nad} = \left.\frac{\partial\hat{P}}{\partial S}\right|_\rho \hat{\delta S}. \tag{7.11}$$

In order to use the aforementioned expressions for the pressure perturbation in any other frame besides the DE rest frame, we have to change gauge by considering a general coordinate transformation between the hatted (DE rest frame) and the unhatted (general) frame [6, 185]:

$$x^\mu = \hat{x}^\mu + d^\mu, \tag{7.12}$$

where $d^\mu = (\alpha(\vec{x},\tau), \vec{\nabla}\beta(\vec{x},\tau) + \vec{\epsilon}(\vec{x},\tau))$, for some functions α, β and ϵ. Then, the perturbation variables transform as [185]

$$\delta = \hat{\delta} - \alpha\frac{\dot{\bar{\rho}}}{\bar{\rho}}, \tag{7.13}$$

$$\theta = \hat{\theta} - \alpha k^2, \tag{7.14}$$

$$\delta P = \hat{\delta P} - \alpha\dot{\bar{P}}, \tag{7.15}$$

where in the rest frame we have that $\hat{\theta} = 0$. We can use Eq. (7.14) to eliminate α, as $\hat{\theta} = 0$, thus finding from Eq. (7.15)

$$\delta P = \hat{\delta P} - 3\mathcal{H}c_a^2\bar{\rho}\frac{(1+w)\theta}{k^2}, \tag{7.16}$$

where $c_a^2 = \frac{\dot{\bar{P}}}{\dot{\bar{\rho}}} = w - \frac{\dot{w}}{3\mathcal{H}(1+w)}$ is the so-called adiabatic sound speed and we have used the background conservation equation

$$\dot{\bar{\rho}} + 3\mathcal{H}(1+w)\bar{\rho} = 0. \tag{7.17}$$

Using Eqs. (7.10), (7.13) and (7.17) in Eq. (7.16) we can write the pressure perturbation in any gauge as

$$\delta P = \hat{c}_s^2\bar{\rho}\delta + \hat{\delta P}_{\rm nad} + 3\mathcal{H}\left(\hat{c}_s^2 - c_a^2\right)\bar{\rho}\frac{(1+w)\theta}{k^2}, \tag{7.18}$$

which is in agreement with Ref. [6]. Thus, our final expressions for the evolution equations for the DE perturbations in the conformal Newtonian gauge are given by

$$\begin{aligned}\dot{\delta}_{\rm DE} &= -(1+w)\left(\theta_{\rm DE} - 3\dot{\phi}\right) - 3\mathcal{H}\left(\hat{c}_s^2 - w\right)\delta_{\rm DE} \\ &- 9\mathcal{H}^2\left(\hat{c}_s^2 - c_a^2\right)\frac{(1+w)\theta_{\rm DE}}{k^2} - 3\mathcal{H}\frac{\hat{\delta P}_{\rm nad}}{\bar{\rho}},\end{aligned} \tag{7.19}$$

$$\dot{\theta}_{\rm DE} = -\mathcal{H}(1-3\hat{c}_s^2)\theta_{\rm DE} + \frac{k^2\hat{c}_s^2}{1+w}\delta_{\rm DE} - k^2\sigma + k^2\psi + \frac{\delta\hat{P}_{\rm nad}/\bar{\rho}}{1+w}k^2. \quad (7.20)$$

Compared to Refs. [185] and [278], the last terms in Eqs. (7.19) and (7.20) are new. The latter, ignoring any nonadiabatic contributions, are commonly used in the Boltzmann codes to model the behavior of the DE perturbations. In order to include them in the aforementioned codes, we will henceforth assume that the DE fluid in the rest frame also has a nonadiabatic component $\delta\hat{P}_{\rm nad}$.

This extra component however, can in principle destabilize the perturbations. To demonstrate this, we follow Ref. [235] and we eliminate θ from Eqs. (7.19)-(7.20), resulting in a second order equation for the growth of DE perturbations $\delta_{\rm DE}$:

$$\begin{aligned}\ddot{\delta}_{\rm DE} &+ (\cdots)\dot{\delta}_{\rm DE} + (\cdots)\delta_{\rm DE} = \\ &= -k^2\left((1+w)\psi + \hat{c}_s^2\delta_{\rm DE} + \delta\hat{P}_{\rm nad}/\bar{\rho} - \frac{2}{3}\pi\right) + \cdots,\end{aligned} \quad (7.21)$$

where the dots $(\cdots)$ indicate the presence of complicated expressions and we have redefined the anisotropic stress parameter of the DE fluid as $\pi \equiv \frac{3}{2}(1+w)\sigma$. Here we focus solely on the last k^2 term, which as discussed in Ref. [6], it will act as a source driving the perturbations. However, since the potential scales as $\psi \sim 1/k^2$ in matter domination, the only terms that matter are the sound speed, the nonadiabatic perturbation and the anisotropic stress. Therefore, we can define an effective sound speed as

$$c_{s,\rm eff}^2 = \hat{c}_s^2 + \frac{\delta\hat{P}_{\rm nad}}{\bar{\rho}\,\delta_{\rm DE}} - \frac{2}{3}\pi/\delta_{\rm DE}, \quad (7.22)$$

which has to be positive for the perturbations to be stable at all scales.

In order to solve Eqs. (7.19) and (7.20), we need to choose a parameterization for the DE nonadiabatic pressure perturbations, something which is non-trivial in general without using an underlying model. Hence, in order to keep our results general enough, in what follows we will attempt to motivate an ansatz for the evolution of the pressure perturbations, by using a realistic $f(R)$ to determine the behavior of δP at early and late times. As dark energy is only expected to dominate at late times, the initial conditions will not affect our results, but we will still discuss them for completeness. In particular, here we will consider a case which is motivated by the effective fluid approach of Refs. [9,10] and as an example we will consider the designer $f(R)$ model, see Ref. [9], which is constructed so that the background expansion corresponds exactly to ΛCDM but to linear order, it can have perturbations [204]. This implies that $w=-1$ and from Eq. (7.18) we have that for the designer $f(R)$ model

$$\frac{\delta\hat{P}_{\rm nad,des}}{\bar{\rho}} = \frac{\delta P}{\bar{\rho}} - \hat{c}_s^2\delta_{\rm DE} - 3\mathcal{H}\left(\hat{c}_s^2 - c_a^2\right)\frac{V_{\rm DE}}{k^2}, \quad (7.23)$$

where $\frac{\delta P}{\bar{\rho}}$ and $\delta_{\rm DE}$ are given by Eqs. (42) and (43) of Ref. [9], $V_{\rm DE} = (1+w)\theta_{\rm DE}$, while $\hat{c}_s^2 = 1$ for $f(R)$. Note that for this model, in general we have $V_{\rm DE} \neq 0$ even if $w=-1$ [9].

We plot this function for the designer $f(R)$ model for $\Omega_{m0}=0.3$, $f_{R0}=-10^{-4}$ and $w=-1$ in Fig. 7.1, where we see that at both early and late times, the nonadiabatic component evolves as a power law of the form $\delta\hat{P}_{\rm nad}/\bar{\rho} \simeq c_0 a^n k^2/H_0^2$. Specifically, we find that [9]

$$n = \frac{9}{4} + \frac{\sqrt{73}}{4} \simeq 4.386, \quad (7.24)$$

$$c_0 = -\frac{5+\sqrt{73}}{36}g(\Omega_{m0})f_{R0}, \quad (7.25)$$

where

$$g(\Omega_{m0}) \simeq \frac{\Omega_{m0}^{-\frac{17}{12}-\frac{\sqrt{73}}{12}}}{{}_2F_1\left[\frac{\sqrt{73}+5}{12}, \frac{\sqrt{73}+11}{12}; \frac{\sqrt{73}+6}{6}; 1-\Omega_{m0}\right]}. \quad (7.26)$$

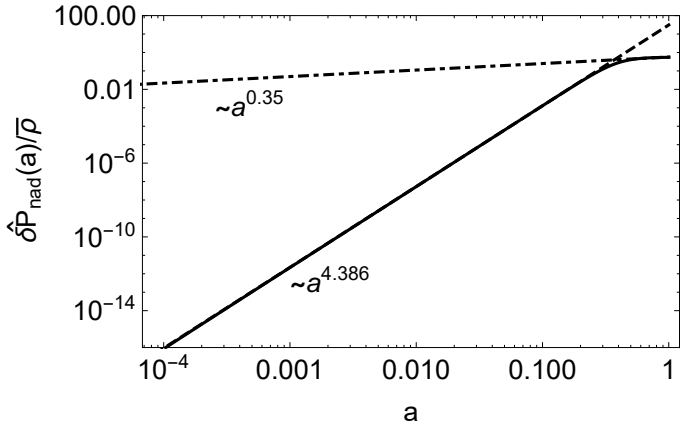

Figure 7.1: The evolution of $\frac{\delta\hat{P}_{\rm nad}}{\bar{\rho}}$ for the designer $f(R)$ model obtained using the effective fluid approach of Ref. [9], for $\Omega_{m0}=0.3$, $f_{R0}=-10^{-4}$, $k=300\,H_0$ and $w=-1$. As seen, at different times the nonadiabatic component evolves as a power law of the form $\frac{\delta\hat{P}_{\rm nad}}{\bar{\rho}}\sim c_0 a^n k^2$. The solid black line corresponds to the prediction from the designer $f(R)$ model, while the dashed and dot-dashed lines correspond to the asymptotic limits at early and late times respectively.

Inspired by this functional form, in what follows we will assume the rather general ansatz

$$\frac{\delta\hat{P}_{\rm nad}}{\bar{\rho}} = c_0\, a^n k^2/H_0^2, \tag{7.27}$$

where (c_0, n) are parameters to be determined; however the exponent n has to be positive so as to ensure the nonadiabatic DE perturbation vanishes at early times, and thus we will assume the prior $n\in(0,\infty)$. In the next sections we will present constraints on the parameters (c_0, n) in the case of $w=$const and of no DE anisotropic stress ($\sigma=0$).

7.2.1 The initial conditions

Here will now discuss the initial conditions for the DE perturbations in both gauges and in two different regimes, in matter and radiation domination. First, we consider the initial conditions in the conformal Newtonian gauge in matter domination, for which we follow Ref. [278]. In a similar vein we consider two regimes: 1) the DE perturbations are larger than the sound horizon, $k\ll aH/\hat{c}_s$ or equivalently that $\hat{c}_s^2=0$; 2) the small scales solutions $k\gg aH/\hat{c}_s$, which implies that the terms scaling as k^2 dominate of over the rest.

In any case, the initial conditions for matter and the potential (assuming no anisotropic stress) in matter domination are unchanged and given by [278]

$$\delta_m(a) = \delta_0\left(a+\frac{3H_0^2\Omega_{m0}}{k^2}\right), \tag{7.28}$$

$$V_m(a) = -\delta_0 H_0\sqrt{\Omega_{m0}}\,a^{1/2}, \tag{7.29}$$

$$\phi = -\frac{3}{2}\delta_0\frac{H_0^2\Omega_{m0}}{k^2}, \tag{7.30}$$

where δ_0 is a normalization set at early times from inflation, while $V_i\equiv(1+w_i)\theta_i$.

In the first case ($k\ll aH/\hat{c}_s$) we find that the initial conditions for the DE density and velocity perturbations are given by

$$\delta_{\rm DE}(a) = \delta_0(1+w)\left(\frac{a}{1-3w}+\frac{3H_0^2\Omega_{m0}}{k^2}\right)-\frac{c_0k^2a^n\left(6+\frac{9}{n+3w}-\frac{2ak^2/H_0^2}{n\Omega_{m0}-3\Omega_{m0}w+\Omega_{m0}}\right)}{H_0^2(2n+3)}, \tag{7.31}$$

$$V_{\rm DE}(a) = -\delta_0(1+w)H_0\sqrt{\Omega_{m0}}\,a^{1/2} + \frac{c_0 k^4 a^{n+\frac{1}{2}}}{H_0^3\left(n+\frac{3}{2}\right)\sqrt{\Omega_{m0}}}. \tag{7.32}$$

In the second case ($k \gg aH/\hat{c}_s$) we find that the initial conditions for the DE density and velocity perturbations are given by

$$\delta_{\rm DE}(a) = \frac{3}{2}(1+w)\delta_0\frac{H_0^2\Omega_{m0}}{\hat{c}_s^2 k^2} - \frac{c_0 k^2 a^n}{\hat{c}_s^2 H_0^2}, \tag{7.33}$$

$$V_{\rm DE}(a) = -\frac{9}{2}(1+w)(\hat{c}_s^2-w)\frac{H_0^3\Omega_{m0}^{3/2}}{\hat{c}_s^2\,k^2}a^{-1/2} + \frac{c_0 k^2\sqrt{\Omega_{m0}}a^{n-\frac{1}{2}}(n-3w)}{\hat{c}_s^2 H_0}\left[1 - \frac{9H_0^2\Omega_{m0}(\hat{c}_s^2-w)}{ak^2} + \frac{81H_0^4\Omega_{m0}^2(\hat{c}_s^2-w)^2}{a^2k^4}\right]. \tag{7.34}$$

Note that in the previous sets of equations, the dark energy perturbations have non-vanishing values, even for $w=-1$. This is clearly a smoking gun signal for modified gravity, as the usual dark energy perturbations within GR exactly vanish for the cosmological constant ($w=-1$). Finally, we find that in both cases the last terms containing c_0, are new compared to Ref. [278] and correspond to the contribution of the nonadiabatic term.

For the simpler case of a constant adiabatic DE sound-speed $\hat{c}_s^2$, the initial conditions in the synchronous gauge in radiation domination where first derived in Ref. [348] as a series expansion in terms of $k\tau$. Here we generalize this approach by also considering the nonadiabatic pressure perturbation and we follow Refs. [185, 348]. Since we have to expand in terms of $k\tau$ we find that in this case it is more convenient to consider the different regimes for the index n of the power law of our ansatz given by Eq. (7.27). Specifically, as we have already mentioned, n has to be positive in order for the nonadiabatic pressure perturbation to vanish at early times, so we will consider the regimes $n\in(0,1)$, $n\in[1,2)$, $n\in[2,3)$ and $n\geq 3$, since then the scalar factor dominates differently at early times.

Then, by expanding the Einstein and fluid equations in terms of $k\tau$, following Refs. [185,348], we find the initial conditions for the DE density $\delta_{\rm DE}$ and velocity $\theta_{\rm DE}$ perturbations for $n\in(0,1)$

$$\delta_{\rm DE}(a) = \frac{\delta_0(3\hat{c}_s^2-4)(k\tau)^2(w+1)}{6\hat{c}_s^2-12w+8} + \frac{c_0k^2}{4H_0^2(3\hat{c}_s^2-6w+4)(\hat{c}_s^2-w)} \cdot \left[4\left(w\left((k\tau)^2-9w+12\right)-4\right) - 3\hat{c}_s^2\left(\left((k\tau)^2-6\right)w+4\right)\right], \tag{7.35}$$

$$\theta_{\rm DE}(a) = -\frac{\delta_0\hat{c}_s^2k(k\tau)^3}{6\hat{c}_s^2-12w+8} + \frac{c_0k^3(k\tau)w\left(\hat{c}_s^2\left((k\tau)^2-6\right)+12w-8\right)}{4H_0^2(w+1)(3\hat{c}_s^2-6w+4)(\hat{c}_s^2-w)}. \tag{7.36}$$

For $n\in[1,2)$ we have that

$$\delta_{\rm DE}(a) = \frac{\delta_0(3\hat{c}_s^2-4)(k\tau)^2(w+1)}{6\hat{c}_s^2-12w+8} + \frac{3ac_0k^2(w-1)}{H_0^2(2\hat{c}_s^2-3w+1)}, \tag{7.37}$$

$$\theta_{\rm DE}(a) = -\frac{\delta_0\hat{c}_s^2k(k\tau)^3}{6\hat{c}_s^2-12w+8} + \frac{ac_0k^3(k\tau)(3w-1)}{3H_0^2(w+1)(-2\hat{c}_s^2+3w-1)}. \tag{7.38}$$

For $n\in[2,3)$ we have that

$$\delta_{\rm DE}(a) = \frac{\delta_0(3\hat{c}_s^2-4)(k\tau)^2(w+1)}{6\hat{c}_s^2-12w+8} + \frac{3a^2c_0k^2(3w-4)}{H_0^2(6\hat{c}_s^2-12w+8)}, \tag{7.39}$$

$$\theta_{\rm DE}(a) = -\frac{\delta_0\hat{c}_s^2k(k\tau)^3}{6\hat{c}_s^2-12w+8} + \frac{a^2c_0k^3(k\tau)(3w-2)}{2H_0^2(w+1)(-3\hat{c}_s^2+6w-4)}, \tag{7.40}$$

while for $n\geq 3$ the contribution from the nonadiabatic pressure perturbation of Eq. (7.27) is subdominant and we recover the results of Ref. [348].

7.2.2 Approximate solutions and the growth index

Here we present analytic solutions to the evolution equations (7.19) and (7.20), as well as analytic expressions for the growth index γ at late times. We note that the forthcoming approximations are only used to gain insight and intuition on the effects of the nonadiabatic term on the growth and the LSS and are not used in `CLASS` or the MCMC analysis later on, for which we solve the corresponding equations numerically.

One way to determine how the nonadiabatic DE pressure perturbation, and DE in general, affects the growth of matter density perturbation $\delta_m \equiv \frac{\delta\rho_m}{\bar{\rho}_m}$, is to rewrite the fluid equations for matter and DE as a second order differential equation for δ_m. To do so, we assume homogeneity, isotropy and neglect neutrinos, which is a viable approximation since in such small scales our data is not affected by them. Then, the growth of matter can be followed with the second order differential equation [244, 349–351]

$$\delta_m''(a) + \left[\frac{3}{a} + \frac{H'(a)}{H(a)}\right]\delta_m'(a) - \frac{3\Omega_{m_0}H_0^2\,G_{\rm eff}(a)}{2a^5H(a)^2\,G_N}\delta_m(a) = 0, \tag{7.41}$$

where the effects of DE or a modified gravity theory, such as $f(R)$, at the perturbations level can be taken into account by the effective Newtonian constant $G_{\rm eff}(a)$.

To find the effects of the nonadiabatic pressure perturbation we follow Ref. [278], where it was shown that for a DE fluid with constant equation of state w during matter domination $Q \equiv G_{\rm eff}(a)/G_N$ is given by

$$Q - 1 = \left(\frac{1-\Omega_m}{\Omega_m}\right)\left(\frac{1+w}{1-3w}\right)a^{-3w} \equiv Q_0 a^{-3w}. \tag{7.42}$$

To find a similar expression of Q during dark energy domination, which is a solution on small scales $k \gg aH/\hat{c}_s$, that takes into account the nonadiabatic component $\delta\hat{P}_{\rm nad}/\bar{\rho}$ we do the following. Defining the scalar velocity perturbation as $V \equiv ik_jT_0^j/\rho = (1+w)\theta$, Eqs. (7.19) and (7.20) can be rewritten, in the conformal Newtonian gauge, as

$$\delta'_{\rm DE} = -\frac{V_{\rm DE}}{Ha^2}\left(1 + \frac{9a^2H^2\left(\hat{c}_s^2 - c_a^2\right)}{k^2}\right) - \frac{3}{a}\left(\hat{c}_s^2 - w\right)\delta_{\rm DE} + 3(1+w)\phi' - \frac{3}{a}\frac{\delta\hat{P}_{\rm nad}}{\bar{\rho}}, \tag{7.43}$$

$$V'_{\rm DE} = -(1-3\hat{c}_s^2)\frac{V_{\rm DE}}{a} + \frac{k^2}{Ha^2}\hat{c}_s^2\delta_{\rm DE} + (1+w)\frac{k^2}{Ha^2}\psi + \frac{\delta\hat{P}_{\rm nad}}{\bar{\rho}}\frac{k^2}{Ha^2} - \frac{(1+w)k^2}{Ha^2}\sigma, \tag{7.44}$$

where the prime $'$ is the derivative with respect to the scale factor a and we are assuming there is no DE anisotropic stress, i.e $\sigma = 0$, and hence $\phi = \psi$. In Eq. (7.44), in order to not have large velocity perturbations it is expected that the terms that scale as k^2 cancel out, hence

$$\delta_{\rm DE} = \frac{3}{2}(1+w)\frac{H_0^2\Omega_m}{\hat{c}_s^2k^2}\delta_0 - \frac{\delta\hat{P}_{\rm nad}/\bar{\rho}}{\hat{c}_s^2}, \tag{7.45}$$

where we have used that $k^2\phi = -\frac{3}{2}\delta_0H_0^2\Omega_m$ which is the solution for the perturbation equations in matter domination [278]. Then using Eqs. (7.43) and (7.45) we find

$$V_{\rm DE} = -3Ha(\hat{c}_s^2 - w)\delta - 3Ha\frac{\delta\hat{P}_{\rm nad}}{\bar{\rho}}. \tag{7.46}$$

Now we can compute Q in the dark energy domination regime as

$$Q - 1 = \frac{\rho_{\rm DE}\Delta_{\rm DE}}{\rho_m\Delta_m}, \tag{7.47}$$

where $\Delta \equiv \delta + \frac{3aHV}{k^2}$ is the gauge invariant density perturbation. In matter domination we have that $\Delta_m = \delta_0 a$, while for DE we have that

$$\Delta_{\rm DE} \simeq \frac{3}{2}(1+w)\frac{H_0^2\Omega_m}{\hat{c}_s^2k^2}\delta_0 - \frac{\delta\hat{P}_{\rm nad}/\bar{\rho}}{\hat{c}_s^2}, \tag{7.48}$$

which is similar to the initial condition given by Eq. (7.33). From Eq. (7.48) we see that the dominant term comes from the contribution of the nonadiabatic part, as the latter scales as k^2, see Eq. (7.27), hence Q can be expressed as

$$Q - 1 \simeq -\frac{1-\Omega_m}{\Omega_m}\frac{\delta\hat{P}_{\rm nad}/\bar{\rho}}{\delta_0 \hat{c}_s^2} a^{-1-3w}. \tag{7.49}$$

Analytic solutions for the growth

Modeling the nonadiabatic pressure perturbation as in Eq. (7.27), Q can be written as

$$Q(k,a) = 1 - \frac{1-\Omega_m}{\Omega_m}\frac{c_0 k^2}{\delta_0 \hat{c}_s^2 H_0^2} a^{n-1-3w}. \tag{7.50}$$

In order to solve Eq. (7.41) with $Q \equiv G_{\rm eff}(k,a)/G_N$ given by Eq. (7.50) we need to make an approximation due to the appearance of the term a^{n-1}, which makes it difficult to find analytic solutions. As we expect that $n \sim O(1)$ at late times (see Fig. 7.1), then we make a series expansion of the term a^{n-1} around $n = 1$ of the form

$$\begin{aligned} a^{n-1} &\simeq 1 + (n-1)\ln a + \cdots \\ &\simeq 1 - (n-1)\ln(1+z) + \cdots, \end{aligned} \tag{7.51}$$

where in the second step we used that $a = \frac{1}{1+z}$. Since we are interested in the evolution of the growth at low redshifts, we replace the term $\ln(1+z)$ with an average $b_0 = \langle \ln(1+z) \rangle$, which in the range $z \in [0,2]$ is approximately $b_0 \simeq 0.6479$. Hence, under this approximation Newton's constant becomes

$$Q(k,a) \simeq 1 - \frac{1-\Omega_m}{\Omega_m}\frac{c_0 k^2}{\delta_0 \hat{c}_s^2 H_0^2}\left(1 - b_0\,(n-1)\right) a^{-3w}. \tag{7.52}$$

Then, by making the change of variables $a^{-3w} \equiv x$ and inserting Eq. (7.49) into Eq. (7.41) we find

$$\delta_m(a) = a\,{}_2F_1\left[\frac{1}{4} - \frac{5}{12w} + B, \frac{1}{4} - \frac{5}{12w} - B, 1 - \frac{5}{6w}; -\frac{1-\Omega_{\rm m0}}{\Omega_{\rm m_0}} a^{-3w}\right], \tag{7.53}$$

where

$$B = -\frac{1}{12w}\sqrt{(1-3w)^2 + 24\delta B}, \tag{7.54}$$

$$\delta B = -\frac{c_0 k^2}{\delta_0 \hat{c}_s^2 H_0^2}\left(1 - b_0\,(n-1)\right). \tag{7.55}$$

To compare our analytical results with the full numerical solution from the evolution equations (7.19)-(7.20) in the next sections we will use the combination $f\sigma_8(a)$ which is a measurable quantity and is defined as

$$\begin{aligned} f\sigma_8(a) &\equiv f(a)\cdot\sigma(a) \\ &= \frac{\sigma_{8,0}}{\delta_m(1)} a\delta_m'(a), \end{aligned} \tag{7.56}$$

where $\sigma(a) = \sigma_{8,0}\frac{\delta_m(a)}{\delta_m(1)}$ is the redshift-dependent rms fluctuations of the linear density field at $R = 8h^{-1}$Mpc while the parameter $\sigma_{8,0}$ is its value today. Since in order to derive the solution of Eq. (7.53) we have neglected radiation, neutrinos and baryons, we note that the solution is only valid at late times.

The growth rate index γ

Finally, we briefly discuss the growth index γ in the presence of DE perturbations. The latter affect the evolution of the matter density contrast $\delta_m \equiv \frac{\delta\rho_m}{\rho_m}$ and its growth rate $f(a) \equiv \frac{d\ln\delta_m}{d\ln a}$. When we ignore DE perturbations, the latter can be approximated as [206, 338, 352]

$$f(a) = \Omega_{\rm m}(a)^{\gamma(a)}, \tag{7.57}$$

where the growth index γ is given by

$$\begin{aligned}\gamma(a) &= \gamma_m(a) \\ &= \frac{\ln f(a)}{\ln\Omega_{\rm m}(a)} \\ &\simeq \frac{3(1-w)}{5-6w} + \cdots,\end{aligned} \tag{7.58}$$

which for ΛCDM reduces to $\gamma \sim \frac{6}{11}$ and by γ_m we denote the contribution to the growth index coming from the CDM and the background evolution only. When we include the DE perturbations assuming they are sourced from an anisotropic stress, the growth index picks up a correction [206]

$$\gamma = \gamma_m + \gamma_{\rm DE}, \tag{7.59}$$

where the contribution coming from the DE perturbations is given by

$$\gamma_{\rm DE} \simeq -\frac{3(1+w)}{18w^2-21w+5} + \cdots. \tag{7.60}$$

From now on we will refer to $\Omega_m(a)$ as Ω as a shorthand. If we include DE perturbations the growth index for the matter can be written to first order as

$$\begin{aligned}\gamma &= \frac{\ln(f(\Omega))}{\ln(\Omega)} \\ &= \frac{3(\delta B+w-1)}{6w-5} - \frac{3(\Omega-1)((\delta B+w-1)(9\delta B(4w-3)-3w+2))}{2\left((5-6w)^2(12w-5)\right)} + \cdots,\end{aligned} \tag{7.61}$$

We can split the growth index into two parts: the contribution from the CDM component and the background expansion denoted as γ_m, and the contribution from the nonadiabatic component, denoted as $\gamma_{\rm DE}$. Then we have

$$\gamma = \gamma_m + \gamma_{\rm DE}, \tag{7.62}$$

and we find from Eq. (7.61) that

$$\gamma_m = \frac{3(w-1)}{6w-5} + \frac{3(3w-2)(w-1)(\Omega-1)}{2(5-6w)^2(12w-5)} + \cdots, \tag{7.63}$$

$$\gamma_{DE} = \frac{3\delta B}{6w-5} + (\Omega-1)\left(-\frac{3\delta B(6w(6w-11)+29)}{2\left((5-6w)^2(12w-5)\right)} - \frac{27\delta B^2(4w-3)}{2\left((5-6w)^2(12w-5)\right)}\right) + \cdots \tag{7.64}$$

where δB is given by Eq. (7.55). These expressions are similar to those when DE perturbations are included, originally derived in Ref. [206], but now the extra contribution comes instead from the nonadiabatic pressure perturbation.

7.2.3 Discussion on the scale-dependent growth

Large scale structure surveys measure the growth rate $f\sigma_8(z)$ by using the values from the multipoles of the redshift-space galaxy two-point correlation function at late times, see for example

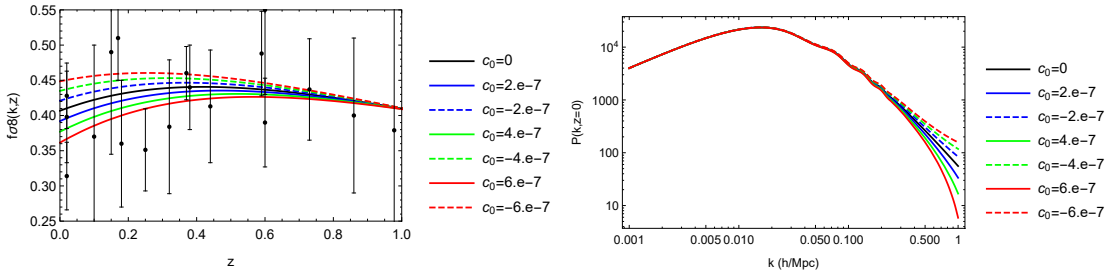

Figure 7.2: Left panel: the evolution of the scale-dependent growth rate $f\sigma_8(k,z)$ for various values of c_0 and $n = 0.5$. In this case the growth was calculated with `CLASS` via $\delta(k,z) \equiv \sqrt{\frac{P(k,z)}{P(k,0)}}$ for $k = 0.1h/\text{Mpc}$. The points correspond to the "Gold 2018" growth rate $f\sigma_8$ compilation shown in Table 2.4. Right panel: the matter power spectrum $P(k,z)$ at $z = 0$, for various values of c_0 and $n = 0.5$. In both cases we assumed $\Omega_{m0} = 0.3$, $w = -0.8$, $h = 0.67$.

Ref. [353]. This requires modeling the multipoles at the redshift z either by assuming a fiducial cosmological model, so as to compute the shape of the real-space power spectrum, or by assuming the growth is scale-independent from the onset of some early redshift and then assuming another fiducial model at early times. Both approaches can in principle be problematic if dark energy causes the growth to be strongly scale-dependent, so it would be ideal to directly model the multipoles in the particular scale-dependent cosmology at hand and do the parameter inference at the multipole level. However, this approach is computationally extremely prohibitive for doing Monte Carlo analyses, so we do not consider it here opting instead to examine how the scale-dependence of the growth affects our results.

One way to examine this dependence would be to create mock $f\sigma_8(z)$ data using an N-body simulation of the nonadiabatic dark energy model and then check whether the input fiducial cosmology can be recovered, as was done for example in Ref. [354]. In particular, the authors of Ref. [354] found that this scale-dependence of the growth can significantly bias the parameter constraints. However, such an analysis is beyond the scope of our thesis, so instead in the next section we will extensively study how strong this scale-dependence is by comparing the analytical and `Mathematica` numerical solutions to those of `CLASS`, as well as by studying the scale-dependence of the growth as a function of the wave-number k.

7.3 Comparison with CLASS and numerical solutions

Here we present in detail how the nonadiabatic DE pressure perturbation, given by the ansatz of Eq. (7.27), affects several key cosmological quantities, such as the scale-dependent growth $f\sigma_8(k,z)$, the matter power spectrum $P(k,z)$ and the CMB TT power spectrum C_ℓ^{TT}.

To do this, we implemented the nonadiabatic pressure perturbation as given by Eq. (7.27), along with the initial conditions in radiation domination in the synchronous gauge, given by Eqs. (7.35)-(7.40), in the Boltzmann code `CLASS` [187, 232]. To test our modifications, we also compare the numerical results from `CLASS` with the numerical solution in `Mathematica` of the fluid equations (7.19) and (7.20), but also with the analytical solutions of Sec. 7.2.2.

We should note that there is a difference between the normalization used in `CLASS`, which uses units of Mpc and thus affects the initial values of the perturbations δ_0, and in the numerical solution of the evolution equations (7.19) and (7.20) in `Mathematica`, where we set $\delta_0 = 1$, so that $\delta_m(a) \sim a$ in matter domination, and k is expressed in units of H_0. For example, a wavenumber of $k = 0.1\text{Mpc}^{-1}$ in `CLASS` corresponds to $k = 0.1\frac{3000}{h}H_0 = \frac{300}{h}H_0$ in our notation[1]. Then, the coefficient c_0 is rescaled by a factor of $c_{0,\text{CLASS}} \to c_{0,\text{Math}}\left(\frac{3000}{h}\right)^2 \frac{\delta_{0,\text{CLASS}}}{\delta_{0,\text{Math}}}$ between the two

[1]Similarly, a wavenumber of $k = 0.1h\text{Mpc}^{-1}$ is equivalent to $k = 0.1 \cdot 3000H_0 = 300H_0$.

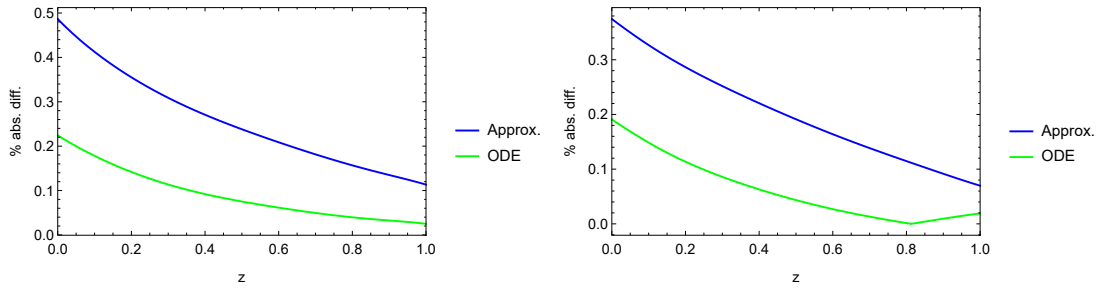

Figure 7.3: Left panel: The absolute percentage difference of $f\sigma_8(z)$ between the numerical solution from the evolution equations Eq. (7.20) (green line, denoted "ODE") and the analytical approximation of Eq. (7.53) (denoted "Approx.") with respect to the numerical solution from our `CLASS` implementation for $c_0 = 2\cdot 10^{-7}$. Right panel: same as the left panel, but for $c_0 = -2\cdot 10^{-7}$. For both plots we assume $\Omega_m = 0.3$, $w = -0.8$, $\hat{c}_s^2 = 1$, $h = 0.67$, $k = 0.1h/\text{Mpc}$ and $\sigma_8 = 0.8$.

frameworks. In what follows, we will express all values of c_0 in the dimensionless picture, i.e. $c_0 = c_{0,\text{Math}}$, as that is easier to test numerically with any ordinary differential equation solver, not only `CLASS`. In what follows we will assume a fiducial cosmology with $\Omega_m = 0.3$, $w = -0.8$, $\hat{c}_s^2 = 1$, $h = 0.67$, $k = 0.1h/\text{Mpc}$ and $\sigma_8 = 0.8$, unless otherwise specified.

First, in Fig. 7.2 we show the dependence of the growth rate $f\sigma_8(k,z)$ and the matter power spectrum $P(k,z)$ on the parameter c_0 keeping n fixed. In the left panel we show the evolution of the scale-dependent growth rate $f\sigma_8(k,z)$ for various values of c_0 and $n = 0.5$. In this case the growth was calculated with `CLASS` via $\delta(k,z) \equiv \sqrt{\frac{P(k,z)}{P(k,0)}}$ for $k = 0.1h/\text{Mpc}$. As can be seen, the amplitude of the pressure perturbation ansatz c_0 has a strong effect on the growth rate $f\sigma_8(k,z)$ at late times $z < 1$, and thus we expect it to be tightly constrained in the MCMC analysis in the next section.

We also tested our codes by calculating the growth for $w = -1$ and as expected, we find that the main effect indeed comes from the nonadiabatic perturbations. This test is important as the usual dark energy perturbations within GR exactly vanish for the cosmological constant model ($w = -1$), so any difference of the growth from its expected ΛCDM value would be a smoking gun signal for modified gravity.

On the other hand, in the right panel of Fig. 7.2 we show the matter power spectrum $P(k,z)$ at $z = 0$, for various values of c_0 and $n = 0.5$. As can be seen, the effect of the nonadiabatic perturbations in this case is to suppress or enhance power, depending on the sign of c_0, an effect similar to that observed in Ref. [355] for a mixed DE-DM model and in Ref. [356] for a similar ansatz. Note that in general the matter power spectrum $P(k,z)$ at scales $k \sim 0.1 - 10\ h/\text{Mpc}$ can be constrained by Lyman alpha data [357], however as those observations are beyond the scope of this work we do not consider them in this analysis.

Next, we compare the results for the growth rate between `CLASS`, `Mathematica` and the analytical approximation to the growth equation. In Fig. 7.3 we show the absolute percentage difference of $f\sigma_8(z)$ between the numerical solution from the evolution equations (7.20) (green line, denoted "ODE") and the analytical approximation of Eq. (7.53) (denoted "Approx.") with respect to the numerical solution from `CLASS` for $c_0 = 2\cdot 10^{-7}$. In the right panel we show the same functions as in the left one, but for $c_0 = -2\cdot 10^{-7}$. As seen in Fig. 7.3, with the approximation we have sub-percent agreement between the analytic approximation and the numerical one at late times. Note however, that neither the analytical solutions in `Mathematica` (denoted "ODE") nor the analytical solutions of Eq. (7.53) (denoted "Approx.") include radiation, neutrinos or baryons, and hence their range of validity in terms of the wavenumber k is limited to $k \geq k_{eq}$. Here we only consider them in order to gain physical insight on the behavior of this model.

In Fig. 7.4 we show the scale-dependence of the growth rate and a comparison with the solution from `CLASS`. In particular, in the left panel we show the present value of the scale-dependent

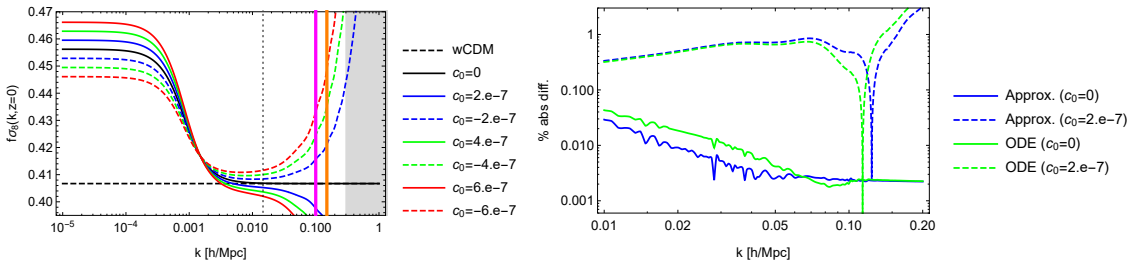

Figure 7.4: Left: The present value of the scale-dependent growth $f\sigma_8(k, z = 0)$ as a function of the wavenumber k. The dashed black line is the scale independent growth in GR (neglecting radiation, neutrinos and baryons) given by the solution to Eq. (7.7), the vertical dotted line corresponds to the scale of equality $k_{\rm eq} \simeq 0.073\ \Omega_{m,0}h^2/{\rm Mpc}$, while the grey region denotes the non-linear regime [358]. The vertical magenta and orange lines correspond to the effective wavenumber for SDSS and WiggleZ, while the colored lines correspond to various values of c_0. Right: The scale-dependence of the absolute percent difference of the approximate solution for $c_0 = 0$ (blue line) and $c_0 = 2\cdot 10^{-7}$ (blue dashed line) and the `Mathematica` numerical solution for $c_0 = 0$ (green line) and $c_0 = 2 \cdot 10^{-7}$ (green dashed line) against the solution from `CLASS`. In both cases we assumed $\Omega_{m0} = 0.3$, $w = -0.8$, $h = 0.67$.

growth $f\sigma_8(k, z = 0)$ as a function of the wavenumber k. The dashed black line is the scale independent growth in GR (neglecting radiation, neutrinos and baryons) given by the solution to Eq. (7.7), the vertical dotted line corresponds to the scale of equality $k_{\rm eq} \simeq 0.073\ \Omega_{m,0}h^2/{\rm Mpc}$, while the grey region denotes the non-linear regime [358]. The vertical magenta and orange lines correspond to the effective wavenumber for SDSS and WiggleZ of $k = 0.1h/{\rm Mpc}$ and $k = 0.15h/{\rm Mpc}$ respectively, while the colored lines correspond to various values of c_0. At $k \sim k_{eq}$ (vertical dotted line) the dashed black and solid black lines agree perfectly, while the deviations at small k are due to radiation, neutrinos etc included in `CLASS`.

In the right panel of Fig. 7.4 we show the scale-dependence of the absolute percent difference of the approximate solution for $c_0 = 0$ (blue line) and $c_0 = 2 \cdot 10^{-7}$ (blue dashed line) and the `Mathematica` numerical solution for $c_0 = 0$ (green line) and $c_0 = 2 \cdot 10^{-7}$ (green dashed line) against the solution from `CLASS`. As can be seen, especially close to the scales where the data are, i.e. $0.1 < k\ ({\rm Mpc}/h) < 0.15$, the agreement is below 1%. At higher k the difference rises somewhat above 1%, but we then quickly enter the non-linear regime where, as mentioned earlier, our calculations are not valid.

In Fig. 7.5 we also compare the predictions for the growth index γ as a function of redshift for $c_0 = 2\cdot 10^{-7}$ and $n = 0.5$ for five different cases: $\gamma = \frac{3(w-1)}{6w-5}$ (dashed green line), the analytical expression when inverting Eq. (7.57) for the wCDM model (solid green line), the analytical approximation to first order of Eq. (7.61) (dashed blue line), the analytical expression when inverting Eq. (7.57) with the growth given by Eq. (7.53) for the nonadiabatic model model (dot-dashed blue line) and the numerical solution of the fluid equation for the nonadiabatic model model (solid blue line). As can be seen, in all cases the agreement between the exact numerical result (solid blue line) and the two approximations is on average of the order of a percent.

Finally, in Fig. 7.6 we show the effect of the nonadiabatic pressure perturbation, given by Eq. (7.27), on the TT CMB spectrum (left) and its low multipoles (right). Overall, the effect is either to enhance or suppress power on large scales, i.e. small multipoles, with the rest of the TT spectrum remaining unchanged. Thus, in our MCMC analysis in the next section, we expect the main constraint from the Planck 18 data to come from the integrate Sachs-Wolfe (ISW) part of the TT CMB spectrum.

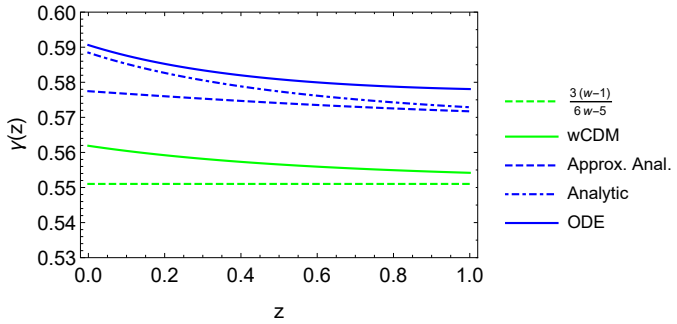

Figure 7.5: The growth index γ as a function of redshift for $\Omega_{m0} = 0.3$, $k = 0.1\ h/\mathrm{Mpc}$, $c_0 = 2{\cdot}10^{-7}$, $n = 0.5$ and $w = -0.8$ for five different cases: $\gamma = \frac{3(w-1)}{6w-5}$ (dashed green line), the analytical expression when inverting Eq. (7.57) for the wCDM model (solid green line), the analytical approximation to first order of Eq. (7.61) (dashed blue line), the analytical expression when inverting Eq. (7.57) with the growth given by Eq. (7.53) for the nonadiabatic model model (dot-dashed blue line) and the numerical solution of the fluid equation for the nonadiabatic model model (solid blue line).

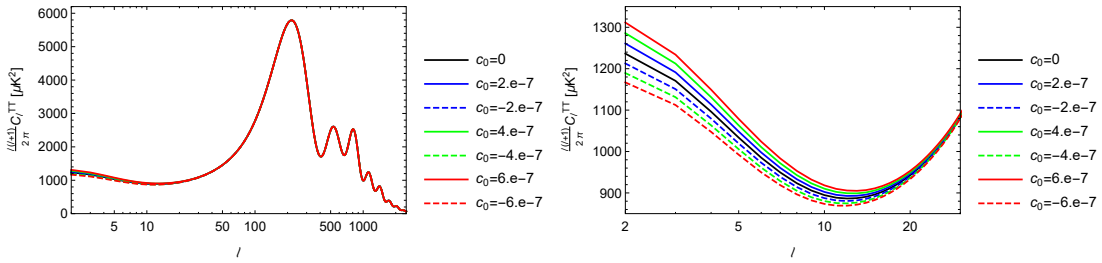

Figure 7.6: The effect of the nonadiabatic pressure perturbation, given by Eq. (7.27), on the TT CMB spectrum (left) and its low multipoles (right). As can be seen, the effect is either to enhance or suppress power on small multipoles, with the rest of the TT spectrum remaining unchanged. In both cases we assumed $\Omega_{m0} = 0.3$, $w = -0.8$, $h = 0.67$.

7.4 MCMC results

Here we discuss how MontePython [333,334] was used to place constraints via an MCMC approach on the parameters of the ansatz for the nonadiabatic pressure perturbation given by Eq. (7.27). We used the Planck 2018 CMB data and in particular we add the "Planck_highl_TTTEEE", "Planck_lowl_EE", "Planck_lowl_TT" temperature and polarization likelihoods (collectively called CMB later on), as well as the CMB lensing "Planck_lensing" likelihood [1].

We also add the BOSS DR-12 data [326], the 6dF BAO points from Ref. [90], the MGS BAO points from [92] and the Pantheon SnIa compilation of Ref. [88]. Finally, we also include an RSD likelihood for MontePython, presented here for the first time, based on the "Gold 2018" growth rate $f\sigma_8$ compilation given in Table I of Ref. [116]. We discuss the new likelihood in detail in the Appendix.

As seen in the previous section, the nonadiabatic DE pressure perturbation, as given by Eq. (7.27), may affect the clustering of objects, by either suppressing or enhancing it. The non-linear regime in Boltzmann codes like `CLASS` is taken into account with routines like Halofit [358], which is calibrated with ΛCDM N-body simulations in order to emulate the effects of non-linearities on small scales $[0.1 < k\,(\mathrm{Mpc}/h) \lesssim 10]$ for a range of ΛCDM parameters. Halofit should not be expected to work well, if at all, in models that deviate significantly from this scenario. Indeed, simulations of Warm Dark Matter (WDM) models demonstrate that Halofit overestimates the power spectrum at small scales [359]. Hence, one should be careful when using Halofit, especially

when the model under consideration induces scale-dependent corrections to the matter power spectrum, as in our case here. As a result, we have decided to turn off Halofit in our analysis.

We then ran MCMC chains for the wCDM model and the nonadiabatic model for two data combinations each: CMB+BAO+SnIa and CMB+BAO+SnIa+RSD in order to assess the constraining power of the new RSD likelihood. For the wCDM model we ran four chains with roughly 200,000 points, while for the nonadiabatic model we ran 19 chains with roughly 2,000,000 points in total in order to make sure all the parameters, described below, were well converged.

Specifically, for the MCMC runs of the wCDM model we consider the following parameters: the DE equation of state parameter w, assuming it is constant, the baryon and cold dark matter density parameters $\Omega_{b,0}h^2$ and $\Omega_{c,0}h^2$ respectively, the angular scale of the acoustic oscillations θ, the optical depth to Thomson scattering from reionization τ and the two parameters of the primordial power spectrum A_s and n_s. In a nutshell, our parameter vector for the wCDM model is then $p_{w\rm CDM} = \left(w, \Omega_{b,0}h^2, \Omega_{c,0}h^2, \theta, A_s, n_s\right)$. On the other hand, for the MCMC runs of the nonadiabatic model, we include the parameters of the wCDM model, along with the two nonadiabatic parameters c_0 and n of Eq. (7.27). Then, our parameter vector for the nonadiabatic model is $p_{\text{non-ad}} = \left(w, \Omega_{b,0}h^2, \Omega_{c,0}h^2, \theta, A_s, n_s, c_0, n\right)$.

In Fig. 7.7 we show the confidence contours for wCDM using CMB+Lensing+BAO+SnIa (green contours) and the CMB+Lensing+BAO+SnIa+RSD (blue contours), while in Tables 7.1-7.2 we present the 68% mean values and 95% confidence regions, for some of the parameters of the model. As can be seen, the contours are a bit shifted to higher values of $\sigma_{8,0}$ and w when the RSD data included. This is consistent with the well-known tension for σ_8 between low and high redshift probes [120].

Next, in Fig. 7.8 we present the constraints for the nonadiabatic model. In particular we show the confidence contours using CMB, Lensing, BAO and SnIa (green contours) and the CMB, Lensing, BAO, SnIa and RSD (blue contours), while in Tables 7.3-7.4 we present the 68% mean values and 95% confidence regions, for some of the parameters of the model. As can be seen, the amplitude of the nonadiabatic perturbation c_0 is consistent with zero, while n is very close to $n \sim 1/2$ as expected from the toy model based on the $f(R)$ designer model.

7.5 Conclusions

In this Chapter we have explored the effects of a nonadiabatic DE pressure perturbation on the CMB and LSS. First, we derived the extra contribution of this nonadiabatic component on the DE perturbation equations, given by the last terms in Eqs. (7.19) and (7.20). Since currently it is unknown if DE has a nonadiabatic component and, even if it does, the behavior of $\frac{\hat{\delta P}_{\rm nad}}{\hat{\rho}}$ is unknown, we took advantage of the effective fluid approach of Refs. [9]- [10] in order to construct a realistic ansatz.

Param	best-fit	mean$\pm\sigma$	95% lower	95% upper
n_s	0.9622	$0.965^{+0.0039}_{-0.0041}$	0.9571	0.973
w	-1.024	$-1.03^{+0.033}_{-0.032}$	-1.095	-0.9673
$\Omega_{\rm m,0}$	0.3109	$0.3058^{+0.0076}_{-0.0082}$	0.2903	0.3215
$10^{+9}A_s$	2.086	$2.104^{+0.03}_{-0.033}$	2.041	2.169
$\sigma_{8,0}$	0.8152	$0.8191^{+0.011}_{-0.011}$	0.7973	0.8412

Table 7.1: The best-fit, mean, 1σ errors and 95% confidence limits for the wCDM model for the data combination CMB+Lensing+BAO+SnIa. In this case the minimum was found for $\chi^2 = 3810$.

Param	best-fit	mean$\pm\sigma$	95% lower	95% upper
n_s	0.9692	$0.9663^{+0.0039}_{-0.004}$	0.9584	0.9742
w	-1.005	$-1.013^{+0.029}_{-0.028}$	-1.07	-0.9554
$\Omega_{\rm m,0}$	0.3061	$0.3064^{+0.0071}_{-0.0082}$	0.2917	0.3217
$10^{+9}A_s$	2.112	$2.101^{+0.03}_{-0.032}$	2.037	2.164
$\sigma_{8,0}$	0.8114	$0.8115^{+0.01}_{-0.0099}$	0.7911	0.8314

Table 7.2: The best-fit, mean, 1σ errors and 95% confidence limits for the wCDM model for the data combination CMB+Lensing+BAO+SnIa+RSD. In this case the minimum was found for $\chi^2 = 3826$.

Param	best-fit	mean$\pm\sigma$	95% lower	95% upper
n_s	0.966	$0.9651^{+0.0038}_{-0.004}$	0.9571	0.973
w	-0.9978	$-1.027^{+0.033}_{-0.027}$	-1.086	-0.9743
$10^{+7}c_0$	-0.3492	$-0.2056^{+0.400}_{-0.400}$	-1.000	1.000
n	0.4127	$0.5019^{+0.083}_{-0.12}$	0.200	0.800
$\Omega_{\rm m,0}$	0.3083	$0.3063^{+0.0074}_{-0.0074}$	0.2914	0.3211
$10^{+9}A_s$	2.098	$2.104^{+0.029}_{-0.032}$	2.041	2.168
$\sigma_{8,0}$	0.8078	$0.819^{+0.01}_{-0.011}$	0.7983	0.8402

Table 7.3: The best-fit, mean, 1σ errors and 95% confidence limits for the nonadiabatic model for the data combination CMB+Lensing+BAO+SnIa. In this case the minimum was found for $\chi^2 = 3809$.

Param	best-fit	mean$\pm\sigma$	95% lower	95% upper
n_s	0.9638	$0.9662^{+0.004}_{-0.0041}$	0.9582	0.9742
w	-1.023	$-1.016^{+0.031}_{-0.027}$	-1.071	-0.9608
$10^{+7}c_0$	-0.08274	$0.001678^{+0.36}_{-0.28}$	-0.7133	0.7427
n	0.5417	$0.4843^{+0.12}_{-0.11}$	0.200	0.800
$\Omega_{\rm m,0}$	0.3041	$0.3059^{+0.0076}_{-0.0074}$	0.291	0.3206
$10^{+9}A_s$	2.097	$2.099^{+0.029}_{-0.031}$	2.037	2.162
$\sigma_{8,0}$	0.8136	$0.8122^{+0.0097}_{-0.01}$	0.7925	0.832

Table 7.4: The best-fit, mean, 1σ errors and 95% confidence limits for the nonadiabatic model for the data combination CMB+Lensing+BAO+SnIa+RSD. In this case the minimum was found for $\chi^2 = 3827$.

In particular, using the designer $f(R)$ model, we derived the expected behavior of this nonadiabatic component both at early and late times, finding that in either era it can be modeled as a power law. Inspired by this, we then assumed the ansatz given by Eq. (7.27), where from the $f(R)$ model we expect $n \sim 0.5$. We then solved the fluid equations and implemented it into the Boltzmann code `CLASS`. Moreover, using an approach similar to that of Ref. [206], we were able to find analytical approximations to the growth rate of matter perturbations $f\sigma_8(z)$ of better than 0.5% when compared with our numerical implementation in `CLASS`.

Since we expect the DE perturbations to have an effect, if at all, at late times when they are growing, we anticipate the nonadiabatic component will affect the CMB only at late times

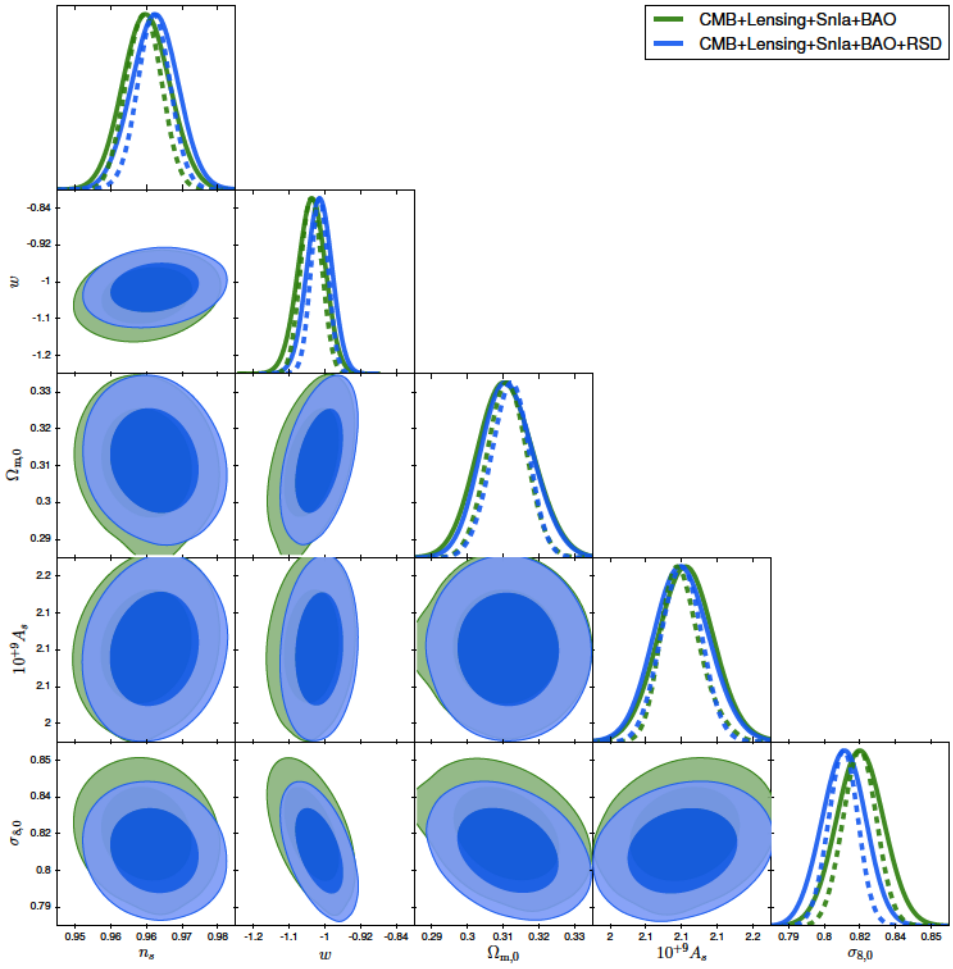

Figure 7.7: The confidence contours for the wCDM model using the data combinations of Planck+Lensing+BAO+SnIa (green contours) and Planck+Lensing+BAO+SnIa+RSD (blue contours).

and on large scales. Equivalently, this implies that it affects the low multipoles via the ISW effect and using our implementation in `CLASS`, we confirmed this. Furthermore, availing ourselves of the modifications in `CLASS`, we also performed MCMC analyses using the latest cosmological data. Here, we used CMB, BAO and SnIa data, as well as a new RSD likelihood for MontePython, which we presented in this work for the first time. By doing this analysis we found that the parameter c_0 is consistent with zero at 1σ, while $n \sim 0.5$ is in agreement with the expectation from the designer $f(R)$ model.

In conclusion, we have shown that a nonadiabatic DE pressure perturbation could have measurable effects on the CMB and other key cosmological observables such as the growth rate of matter density perturbations and the matter power spectrum. Using the latest cosmological data, including RSDs, and assuming a power-law for the nonadiabatic DE component given by Eq. (7.27), we constrained its amplitude and found it is consistent with zero and GR at 1σ.

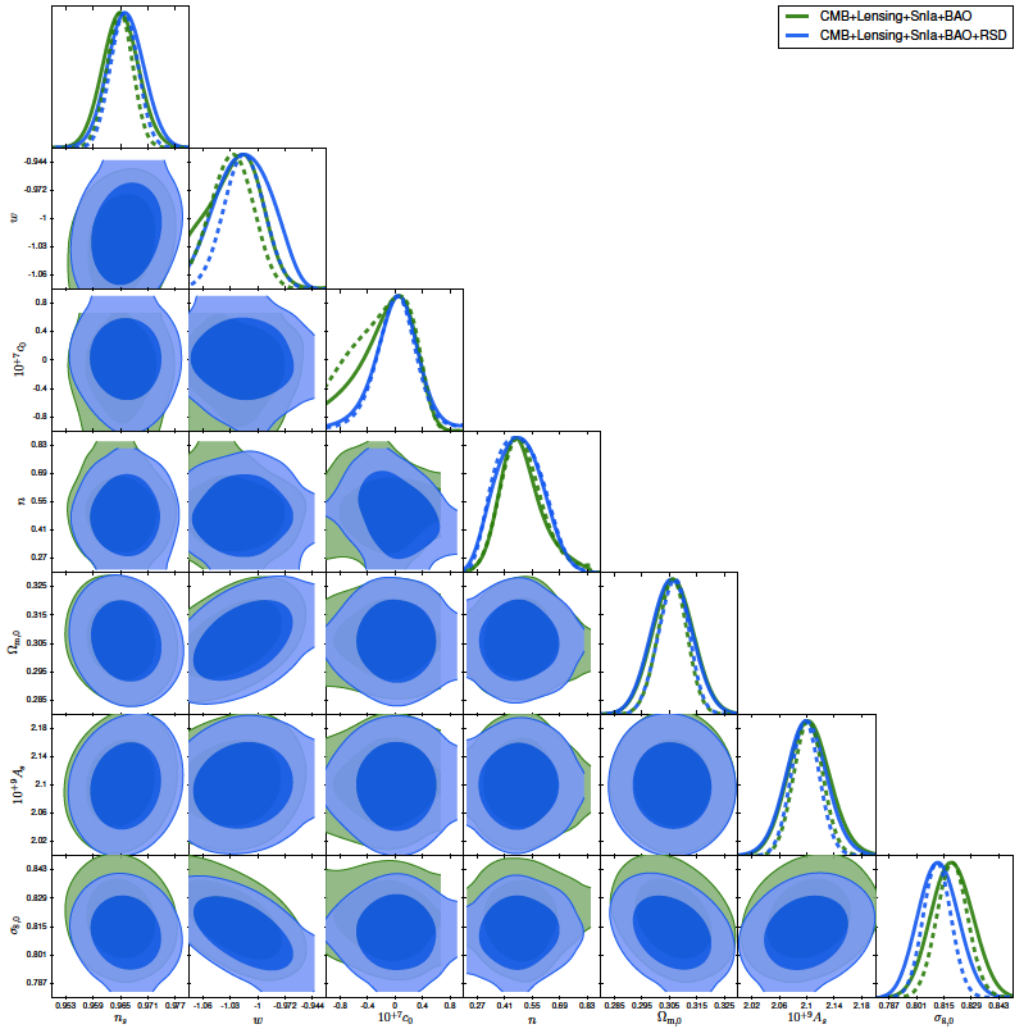

Figure 7.8: The confidence contours for wCDM with nonadiabatic DE perturbations using the data combinations of Planck+Lensing+BAO+SnIa (green contours) and Planck+Lensing+BAO+SnIa+RSD (blue contours). Some of the contours appear to be truncated due to a peculiarity of the MontePython plotting routines and not due to our choice of the prior.

8

Analytic expressions for the background evolution of massive neutrinos and dark matter particles

The original content of this chapter is based on Ref. [360]. We provide exact analytic expressions for the density, pressure, average number density and pseudo-pressure for massive neutrinos and generic dark matter particles, both fermions and bosons. We then focus on massive neutrinos and we compare our analytic expressions with the numerical implementation in the `CLASS` Boltzmann code. We find that our modifications including the exact analytic expressions are in agreement to better than $10^{-4}\%$ with the default `CLASS` implementation in the estimation of the CMB power spectrum; our modifications do not have an impact on the performance of the code. We also provide several specific limits of our expressions at the relativistic regime, but also at late times for the neutrino equation of state.

8.1 Introduction

Over the past decades Dark Matter (DM) has become a fundamental ingredient in the standard model of cosmology [361]. Although we know relatively little about its nature, it is clear that taking into consideration DM when modelling the Universe makes it possible to explain a wide variety of astrophysical observations [1, 154, 267, 362]. Nowadays, it is commonly believed that DM comprises beyond Standard Model particles which move slowly with respect to the speed of light and whose interaction with other particles does not go beyond gravity: the so-called Cold Dark Matter (CDM). However, in the Standard Model of particle physics there exist candidates with similar properties which can account for a fraction of the DM in the Universe. Neutrinos weakly interact with other particles and their speed of propagation is different at late- and early-times in the cosmic evolution: in the beginning their speed of propagation is very close to the speed of light and recently they became non-relativistic. This sort of DM is usually dubbed non-Cold Dark Matter (nCDM).

Even though there is compelling evidence for flavour neutrino oscillations which implies that neutrinos are massive particles [363–368], current constraints do not fully determine their absolute mass scale [369–371]. Nevertheless, this situation is expected to change with upcoming galaxy surveys which will be able to measure the galaxy distribution on scales comparable to the horizon [372]. Since massive neutrinos suppress power on small scales [373], accurate measurements of the matter power spectrum will lead to a detection of their absolute mass scale thus reducing our ignorance of the abundance of DM in the Universe [372, 374, 375]. Furthermore, measurement of neutrino masses could give hints about new fundamental theories having the Standard model of particle physics as a low-energy limit.

Due to their weakly interacting nature, neutrinos obey a collisionless Boltzmann equation. However, since neutrinos are massive particles the evolution of their phase-space distribution function is not trivial [185]. In order to find the unperturbed density and pressure for neutrinos current

implementations in Boltzmann solvers, such as CAMB[1] [186] and `CLASS`[2] [376, 377], employ numerical methods. Shortcomings of the numerical approach include non-trivial weighting scheme to carry out the numerical integration, possible limited precision, increase of computing time, but more importantly hindering the understanding of the underlying physics. In this Chapter we show that a careful analytical treatment of the integrals makes it possible to overcome these difficulties. We provide explicit analytical solutions for the neutrino's unperturbed density, pressure, number density, and pseudo-pressure. Our expressions agree with previous phenomenological attempts of analytical approximations[3] and also with the fully numerical implementation of the code `CLASS`. We have implemented our solutions in `CLASS` and verified that the fully numerical approach (current implementation in `CLASS`) and the fully analytical approach are in very good agreement. These changes in the code leave precision and computing time unchanged.

This Chapter is organized as follows. Firstly, in Section 8.2 we derive our main results, namely, analytical expressions for the background evolution of massive fermions and bosons that are either relativistic or non-relativistic at decoupling. Secondly, in order to compare with previous phenomenological attempts of analytical approximations we provide asymptotic expansions at late times for the quantities governing the neutrino background evolution in Section 8.3. Thirdly, in Section 8.4 we implement our analytical expressions for massive neutrinos in the code `CLASS` and compare with the current numerical implementation in the code. Finally, we conclude in Section 8.5.

8.2 Theoretical framework

In this section we will derive simple analytic expressions for several key quantities that are relevant for the background evolution of massive particles, such as the average number density $n(a)$, the density $\rho(a)$ and pressure $P(a)$ of a particle given its phase-space distribution. For the implementation in Boltzmann codes, it is also useful to calculate the derivative of the so-called pseudo-pressure, which we denote by $psP(a)$. All of these quantities are given by the following expressions:[4]

$$n(a) = \int d^3p f_0(p), \tag{8.1}$$

$$\rho(a) = \int d^3p E(p) f_0(p), \tag{8.2}$$

$$P(a) = \int d^3p \frac{p^2}{3E(p)} f_0(p), \tag{8.3}$$

$$psP(a) = \int d^3p \frac{p^4}{3E(p)^3} f_0(p), \tag{8.4}$$

where p is the physical momentum of the particles, a is the scale factor, E is the energy, while the distribution $f_0(p)$ is given by

$$f_0(p) = \frac{g_s}{e^{\frac{E(p)}{T}} \pm 1}, \tag{8.5}$$

where g_s is the degeneracy of the species, T is the temperature of the particles and the $\pm$ corresponds to fermions/bosons respectively.[5]

As the Universe expands and cools down, the temperature will reach the decoupling temperature T_D and all interactions will freeze out, so that the phase space distribution of Eq. (8.5)

[1] https://camb.info/

[2] http://class-code.net/

[3] See, for instance, Ref. [287].

[4] Note that here and in what follows, we will use natural units in which $c = \hbar = k_B = 1$.

[5] We ignore the chemical potential μ in our analysis as in all realistic particles, it is much smaller than the temperature. Moreover, current bounds on the common value of the neutrino degeneracy parameter indicate that a neutrino chemical potential can be safely neglected [378–385].

of a particle with mass M will remain frozen [368, 386]

$$f_0(p) \quad = \quad f_{eq}\left(p\frac{a(\eta)}{a(\eta_D)}, T_D\right) = \frac{g_s}{e^{\frac{\sqrt{p^2a^2/a_D^2+M^2}}{T_D}}+1}. \tag{8.6}$$

Here η is the conformal time, f_{eq} is the distribution at thermal equilibrium, the subscript D denotes decoupling, $a_D \equiv a(\eta_D)$, and $a \equiv a(\eta)$. Thus, we will consider two separate cases for the distribution $f_0(p)$ at the decoupling temperature T_D:

1. The particles are relativistic, with energy $E(p) \sim p$;
2. The particles are non-relativistic, with energy $E(p) = \sqrt{p^2 + M^2}$.

Note that this will only affect the distribution $f_0(p)$ and not the energy in the integrand, which can be allowed to be time-dependent. Following, we will present the analytical expressions for the thermodynamic quantities for both fermions and bosons that are relativistic and non-relativistic in Section 8.2.1 and Section 8.2.2 respectively.

8.2.1 Relativistic fermions and bosons at decoupling

In this section we are mainly interested in massive neutrinos and we will specifically focus on them, but our results are readily applicable to other massive relics that are relativistic at decoupling. Neutrino decoupling happened at $T_D \sim 1\,\mathrm{MeV}$ or $z \sim 10^{10}$, so at that point neutrinos are still relativistic and their distribution can be written as

$$f_0(p) = \frac{g_s}{e^{\frac{p}{T_\nu(a)}}+1}. \tag{8.7}$$

Taking into account the expansion of the Universe, we see that the physical momentum p will be redshifted and can be written in terms of the comoving momentum Q as $p = Q/a$, where $a = \frac{1}{1+z}$ is the scale factor and z is the redshift. After neutrino decoupling the temperature scales as $T_\nu(a) = T_{\nu,0}/a$ and $T_{\nu,0} \simeq \left(\frac{4}{11}\right)^{1/3} T_{\rm cmb}$ is the neutrino temperature today with a value $T_{\nu,0} \sim 1.68 \cdot 10^{-4}\,\mathrm{eV}$. Therefore, the combination $Q/T_{\nu,0}$ will be constant and does not depend on the redshift, thus the distribution is frozen.

Defining $T_{\nu,0}$ as $T_{\nu,0} = \widetilde{T}$, the previous equations for the evolution variables can be written as

$$n(a) \quad = \quad \frac{4\pi g_s}{a^3}\int_0^\infty dQ\; Q^2 \frac{1}{e^{\frac{Q}{\widetilde{T}}}+1}, \tag{8.8}$$

$$\rho(a) \quad = \quad \frac{4\pi g_s}{a^4}\int_0^\infty dQ\; Q^2 \frac{\left(Q^2+a^2M^2\right)^{1/2}}{e^{\frac{Q}{\widetilde{T}}}+1}, \tag{8.9}$$

$$P(a) \quad = \quad \frac{4\pi g_s}{3a^4}\int_0^\infty dQ\; Q^4 \frac{\left(Q^2+a^2M^2\right)^{-1/2}}{e^{\frac{Q}{\widetilde{T}}}+1}, \tag{8.10}$$

$$psP(a) \quad = \quad \frac{4\pi g_s}{3a^4}\int_0^\infty dQ\; Q^6 \frac{\left(Q^2+a^2M^2\right)^{-3/2}}{e^{\frac{Q}{\widetilde{T}}}+1}, \tag{8.11}$$

In the previous equations all the integrals are of the form

$$I_{n,k} \equiv \int_0^\infty dQ\; Q^n \frac{\left(Q^2+a^2M^2\right)^{k/2}}{e^{\frac{Q}{\widetilde{T}}}+1}, \tag{8.12}$$

where (n, k) are integers. In order to calculate $I_{n,k}$ analytically, we multiply the numerator and denominator with the term $e^{\frac{-Q}{\widetilde{T}}}$ and then we use the expansion $\frac{x}{1+x} = \sum_{\beta=1}^{\infty}(-1)^{\beta+1}x^\beta$ for $x \leq 1$,

which in our case is possible as $e^{\frac{-Q}{\widetilde{T}}} \leq 1$ for all $Q \in [0, \infty)$, thus our series will always converge. Then, we have

$$\begin{aligned} I_{n,k} &= \int_0^\infty dQ\; Q^n \frac{e^{\frac{-Q}{\widetilde{T}}} \left(Q^2 + a^2 M^2\right)^{k/2}}{e^{\frac{-Q}{\widetilde{T}}} + 1} \\ &= \sum_{\beta=1}^{\infty} (-1)^{\beta+1} \int_0^\infty dQ\; Q^n \left(Q^2 + a^2 M^2\right)^{k/2} e^{\frac{-\beta Q}{\widetilde{T}}}. \end{aligned} \tag{8.13}$$

To solve the previous integral we use Eq. (3.389.2) from Ref. [387]

$$\int_0^\infty z^{2\nu-1} \left(u^2 + z^2\right)^{\alpha-1} e^{-\mu z} dz = \frac{u^{2\nu+2\alpha-2}}{2\sqrt{\pi}\Gamma(1-\alpha)} G^{3,1}_{1,3}\left(\begin{matrix} 1-\nu \\ 1-\alpha-\nu, 0, \frac{1}{2} \end{matrix}\middle| \frac{\mu^2 u^2}{4}\right), \tag{8.14}$$

where Re $\mu > 0$, Re $\nu > 0$, $|\arg u < \frac{\pi}{2}|$ and $G^{m,n}_{p,q}\left(\begin{matrix} a_1, \ldots, a_n & a_{n+1}, \ldots, a_p \\ b_1, \ldots, b_m & b_{m+1}, \ldots, b_q \end{matrix}\middle| z\right)$ is the Meijer-G function. With this expression we find that

$$I_{n,k} = \sum_{i=1}^{\infty} (-1)^{i+1} \frac{(aM)^{1+k+n}}{2\sqrt{\pi}\Gamma(-k/2)} G^{3,1}_{1,3}\left(\begin{matrix} \frac{1-n}{2} \\ -\frac{1}{2}(1+k+n), 0, \frac{1}{2} \end{matrix}\middle| \frac{x_i^2}{4}\right), \tag{8.15}$$

where for convenience we have set $x_i = \frac{iaM}{\widetilde{T}}$. Next we will provide the explicit expressions for each of the key background quantities mentioned earlier.

Average number density

The average number density $n(a)$ corresponds to the parameters $(n, k) = (2, 0)$, so combining Eqs. (8.8) and (8.15) gives the well known result:

$$n(a) = \frac{6\pi g_s \zeta(3)}{a^3} \widetilde{T}^3. \tag{8.16}$$

The density

The density corresponds to the parameters $(n, k) = (2, 1)$ and the final result can be found to be

$$\begin{aligned} \rho(a) &= g_s M^4 \sum_{i=1}^{\infty} (-1)^i\, G^{3,1}_{1,3}\left(\begin{matrix} -\frac{1}{2} \\ -2, 0, \frac{1}{2} \end{matrix}\middle| \frac{x_i^2}{4}\right) \\ &= 2\pi^2 g_s M^4 \sum_{i=1}^{\infty} (-1)^i \frac{1}{x_i^3} \left(-\frac{2}{\pi} x_i^2 + 3 x_i K_0(x_i) + \left(x_i^2 - 6\right) K_1(x_i)\right), \end{aligned} \tag{8.17}$$

where $K_\nu(x) = H_\nu(x) - Y_\nu(x)$ is the Struve K function, $H_\nu(x)$ is the Struve H function and $Y_\nu(x)$ the usual Bessel Y function of the second kind [388]. In the relativistic limit, where $M = 0$, we find

$$\rho(a) = \frac{7\pi^5 g_s}{30 a^4} \widetilde{T}^4. \tag{8.18}$$

The derivative $\frac{d\rho}{dM}(a)$, which is also useful in calculations in Boltzmann solvers, corresponds to $(n, k) = (2, -1)$ and is given by

$$\begin{aligned} \frac{d\rho(a)}{dM} &= 2 g_s M^3 \sum_{i=1}^{\infty} (-1)^{i+1}\; G^{3,1}_{1,3}\left(\begin{matrix} -\frac{1}{2} \\ -1, 0, \frac{1}{2} \end{matrix}\middle| \frac{x_i^2}{4}\right), \\ &= 2\pi^2 g_s M^3 \sum_{i=1}^{\infty} (-1)^i \frac{1}{x_i} \left[x_i K_0(x_i) - K_1(x_i)\right]. \end{aligned} \tag{8.19}$$

Pressure

The pressure corresponds to the set of parameters $(n,k)=(4,-1)$ and as a result we have

$$\begin{aligned} P(a) &= \frac{2g_sM^4}{3}\sum_{i=1}^{\infty}(-1)^{i+1}\,G^{3,1}_{1,3}\left(\begin{matrix}-\frac{3}{2}\\ -2,0,\frac{1}{2}\end{matrix}\middle|\frac{x_i^2}{4}\right), \\ &= \frac{2g_s\pi^2M^4}{3}\sum_{i=1}^{\infty}(-1)^{i}\,\frac{(3-x_i^2)}{x_i^3}\left(-\frac{2x_i^2}{(3-x_i^2)\pi}+x_i\;K_0(x_i)-2K_1(x_i)\right). \end{aligned} \tag{8.20}$$

In the relativistic limit, where $M=0$, we find

$$P(a)=\frac{7\pi^5g_s}{90a^4}\widetilde{T}^4=\frac{\rho(a)}{3}, \tag{8.21}$$

as expected for relativistic particles.

Pseudo pressure

The pseudo-pressure corresponds to the set of parameters $(n,k)=(6,-3)$

$$\begin{aligned} psP(a) &= \frac{4g_sM^4}{3}\sum_{i=1}^{\infty}(-1)^{i+1}\,G^{3,1}_{1,3}\left(\begin{matrix}-\frac{5}{2}\\ -2,0,\frac{1}{2}\end{matrix}\middle|\frac{x_i^2}{4}\right), \\ &= \frac{2\pi^2g_sM^4}{3}\sum_{i=1}^{\infty}(-1)^{i}\,\frac{1}{x_i^3}\left(-\frac{2}{\pi}(x_i^2+x_i^4)-3x_i(x_i^2-1)K_0(x_i)+(x_i^4+3x_i^2-6)K_1(x_i)\right). \end{aligned} \tag{8.22}$$

In the relativistic limit, where $M=0$, we find

$$psP(a)=\frac{7\pi^5g_s}{90a^4}\widetilde{T}^4\equiv P(a)=\frac{\rho(a)}{3}. \tag{8.23}$$

Results for massive bosons

In the case of bosons, the analytical expressions for the background are very similar to the ones found for fermions. The only difference is the factor $(-1)^i$ that appears in the sum which has to be replaced by (-1). Hence, the density and pressure are

$$\rho(a) = 2\pi^2g_sM^4\sum_{i=1}^{\infty}\frac{1}{x_i^3}\left(\frac{2}{\pi}x_i^2-3x_iK_0(x_i)-\left(x_i^2-6\right)K_1(x_i)\right), \tag{8.24}$$

$$P(a) = \frac{2\pi^2g_sM^4}{3}\sum_{i=1}^{\infty}\frac{(3-x_i^2)}{x_i^3}\left(\frac{2x_i^2}{(3-x_i^2)\pi}-x_i\;K_0(x_i)+2K_1(x_i)\right), \tag{8.25}$$

and for the average number density we obtain the well known result

$$n(a)=\frac{8\pi g_s}{a^3}\tilde{T}^3. \tag{8.26}$$

In the relativistic limit where $M=0$, we find

$$P(a)=\frac{4\pi^5}{45a^4}g_s\tilde{T}^4=\frac{\rho(a)}{3}. \tag{8.27}$$

Free-streaming length

Similarly, we can also calculate the free-streaming length, i.e., the typical distance particles travel between interactions, which is defined via [389, 390]:

$$k_{FT}(t) = \left(\frac{4\pi G\bar{\rho}(t)a(t)^2}{v_{th}^2(t)}\right)^{1/2}, \tag{8.28}$$

$$\lambda_{FT}(t) = 2\pi\frac{a(t)}{k_{FT}(t)} = 2\pi\sqrt{\frac{2}{3}}\frac{v_{th}}{H(t)}, \tag{8.29}$$

where $v_{th} \equiv \frac{\langle p\rangle}{m}$ is the thermal velocity and $\langle p\rangle$ the average particle momentum. After the particles become non-relativistic we can calculate the average momentum, by using the results in the previous sections for non-relativistic massive particles, as follows

$$\langle p\rangle = \frac{\int d^3p\; p\; f_0(p)}{\int d^3p\; f_0(p)} \tag{8.30}$$

$$= \frac{7\pi^4}{180\zeta(3)}T_\nu(a) \tag{8.31}$$

$$\simeq 3.15137\;\frac{T_{\nu,0}}{a}. \tag{8.32}$$

Finally, we have that the free-streaming length is

$$\lambda_{FT}(t) = 2\pi\sqrt{\frac{2}{3}}\frac{7\pi^4}{180\zeta(3)}\frac{T_{\nu,0}}{maH}$$

$$\simeq 8.14996\;\frac{1}{aH(t)/H_0}\left(\frac{\mathrm{eV}}{m}\right)h^{-1}\mathrm{Mpc}, \tag{8.33}$$

which is in good agreement with the result of Ref. [389, 390].

8.2.2 Non-relativistic fermions and bosons at decoupling

When we have massive fermions that are non-relativistic at decoupling ($M_X \gg T_D$) their distribution function after the freeze out or decoupling can be written as [386]

$$f_X(p) = f_{eq}\left(p\frac{a(\eta)}{a(\eta_D)}, T_D\right) = \frac{g_s}{e^{\frac{\sqrt{p^2a^2/a_D^2+M^2}}{T_D}}+1}, \tag{8.34}$$

where the subscript D denotes decoupling and $a_D \equiv a(\eta_D)$, $a \equiv a(\eta)$. Defining $\tilde{T} = T_0$, the comoving momentum Q as $p = Q/a$ and the temperature parameter $T_0 \equiv Ta \equiv T_D a_D$, following a similar approach as in Section 8.2.1 we can compute the average number density, the energy density and pressure as

$$n(a) = \frac{4\pi g_s}{a^3}\int_0^\infty dQ\; Q^2\frac{1}{e^{\frac{\sqrt{Q^2+a_D^2M^2}}{\tilde{T}}}+1}, \tag{8.35}$$

$$\rho(a) = \frac{4\pi g_s}{a^4}\int_0^\infty dQ\; Q^2\frac{\left(Q^2+a^2M^2\right)^{1/2}}{e^{\frac{\sqrt{Q^2+a_D^2M^2}}{\tilde{T}}}+1}, \tag{8.36}$$

$$P(a) = \frac{4\pi g_s}{3a^4}\int_0^\infty dQ\; Q^4\frac{\left(Q^2+a^2M^2\right)^{-1/2}}{e^{\frac{\sqrt{Q^2+a_D^2M^2}}{\tilde{T}}}+1}. \tag{8.37}$$

Average number density

To solve Eq. (8.35) we first perform a change of variables to hyperbolic functions. Then, using Eq. (3.547.2) from Ref. [387] we find

$$n(a) = \frac{4\pi}{a^3} g_s a_D^3 M^3 \sum_{i=1}^{\infty} (-1)^{i+1} \frac{K_2(y_i)}{y_i}, \tag{8.38}$$

where $K_n(z)$ is the modified Bessel function of the second kind and $y_i = \frac{i a_D M}{\tilde{T}}$.

The density

Using Eq. (7.6.1) from Ref. [391] we find after some algebraic manipulations that the density can be written as

$$\rho(a) = \frac{4\pi g_s}{a^4} \sum_{n=0}^{\infty} \sum_{i=1}^{\infty} (-1)^{i+n} \frac{\Gamma(n-1/2)\,\Gamma(n+3/2)}{\pi\Gamma(n+1)} \frac{2^n a_D^{n+2} M^{3-n} \tilde{T}^{n+1}}{a^{2n-1} i^{n+1}} K_{n+2}(y_i), \tag{8.39}$$

where $K_n(z)$ is the modified Bessel function of the second kind and $y_i = \frac{i a_D M}{\tilde{T}}$.

The pressure

Following the same procedure as with the density, we find that the pressure can be written as

$$P(a) = \frac{4\pi g_s}{3a^4} \sum_{n=0}^{\infty} \sum_{i=1}^{\infty} (-1)^{i+1} \frac{\Gamma(n+5/2)}{\Gamma(1/2-n)\,\Gamma(n+1)} \frac{a_D M}{(aM)^{2n+1}} \left(\frac{2 a_D M \tilde{T}}{i}\right)^{n+2} K_{n+3}(y_i), \tag{8.40}$$

where again $K_n(z)$ is the modified Bessel function of the second kind and $y_i = \frac{i a_D M}{\tilde{T}}$.

Numerical results

We compared the analytical expressions for the average number density, density and pressure Eqs. (8.38)-(8.40), with the numerical integration of Eqs. (8.35)-(8.37) for some realistic values of WIMP particles like neutralinos [392, 393] $z_D \sim 10^{13}, m_X \sim 25\,\mathrm{GeV}, T_D \sim 1\,\mathrm{GeV}$ and found that the agreement is better than $10^{-18}\%$ for only 4 iterations.

Results for massive bosons

In the case of bosons, the analytical expressions for the background are very similar to the ones found for fermions, the only difference being the factor $(-1)^{i+1}$ that appears in the sum which has to be replaced by 1. Hence

$$n(a) = \frac{4\pi}{a^3} g_s a_D^3 M^3 \sum_{i=1}^{\infty} \frac{K_2(y_i)}{y_i}, \tag{8.41}$$

$$\rho(a) = \frac{4\pi g_s}{a^4} \sum_{n=0}^{\infty} \sum_{i=1}^{\infty} \frac{(-1)^{n+1}\,\Gamma(n-1/2)\,\Gamma(n+3/2)}{\pi\Gamma(n+1)} \frac{2^n a_D^{n+2} M^{3-n} \tilde{T}^{n+1}}{a^{2n-1} i^{n+1}} K_{n+2}(y_i), \tag{8.42}$$

$$P(a) = \frac{4\pi g_s}{3a^4} \sum_{n=0}^{\infty} \sum_{i=1}^{\infty} \frac{\Gamma(n+5/2)}{\Gamma(1/2-n)\,\Gamma(n+1)} \frac{a_D M}{(aM)^{2n+1}} \left(\frac{2 a_D M \tilde{T}}{i}\right)^{n+2} K_{n+3}(y_i). \tag{8.43}$$

In the non relativistic limit $M_X \gg T_D$, we can find semi-analytical expressions valid for fermions and bosons for the average number density (8.35), density (8.36) and pressure (8.37) in the following way

$$n(a) = \frac{4\pi g_s}{a^3} e^{-M/T_D} \int_0^\infty dQ\, Q^2 e^{-\frac{Q^2}{2Ma_D^2 T_D}} = \left(\frac{a_D}{a}\right)^3 (2\pi g_s M T_D)^{3/2}\, e^{-M/T_D}, \tag{8.44}$$

$$\begin{aligned}\rho(a) &= \frac{4\pi g_s}{a^4} e^{-M/T_D} \int_0^\infty dQ\, Q^2 \left(Q^2 + a^2M^2\right)^{1/2} e^{-\frac{Q^2}{2Ma_D^2 T_D}} \\ &= 2\pi g_s \left(\frac{a_D}{a}\right)^2 M^3 T_D e^{\beta - M/T_D} K_1(z),\end{aligned} \tag{8.45}$$

$$\begin{aligned}P(a) &= \frac{4\pi g_s}{3a^4} e^{-M/T_D} \int_0^\infty dQ\, \frac{Q^4 e^{-\frac{Q^2}{2Ma_D^2 T_D}}}{\left(Q^2 + a^2M^2\right)^{1/2}} \\ &= \frac{\pi g_s M^3 e^{\beta - M/T_D}}{3} \left[MK_0(z) + (2\left(\frac{a_D}{a}\right)^2 T_D - M)K_1(z)\right],\end{aligned} \tag{8.46}$$

where we have to consider the series expansion $\sqrt{Q^2 + a_D^2 M^2} \sim a_D M + \frac{Q^2}{2a_D M} + O(Q)^4$ in the exponential and also assume that $e^{\frac{\sqrt{Q^2+a_D^2M^2}}{\tilde{T}}} \gg 1$. Again $K_n(\beta)$ is the modified Bessel function of the second kind and $\beta = \frac{a^2 M}{4a_D^2 T_D}$.

8.3 Asymptotic expansions at late times

The Struve K function $K_\nu(z)$ is a particular solution of the inhomogeneous Bessel differential equation

$$\frac{d^2w}{dz^2} + \frac{1}{z}\frac{dw}{dz} + \left(1 - \frac{\nu^2}{z^2}\right) w = \frac{(z/2)^{\nu-1}}{\sqrt{\pi}\,\Gamma\left(\nu + \frac{1}{2}\right)} \tag{8.47}$$

and it admits the following asymptotic expansion for large values of the argument z with fixed ν [388]:

$$K_\nu(z) \sim \frac{1}{\pi} \sum_{k=0}^{\infty} \frac{\Gamma(k + \frac{1}{2})}{\Gamma(\nu + \frac{1}{2} - k)} \left(\frac{z}{2}\right)^{\nu - 2k - 1}, \tag{8.48}$$

which can be used to obtain asymptotic expansions for the quantities in the previous section. Specifically, we find

$$\rho(a) = \frac{6\pi g_s \widetilde{T}^3 M}{a^3} \left(\zeta(3) + \frac{15\widetilde{T}^2\zeta(5)}{2a^2M^2} \cdots\right), \tag{8.49}$$

$$\frac{d\rho(a)}{dM} = \frac{6\pi g_s \widetilde{T}^3}{a^3} \left(\zeta(3) - \frac{15\widetilde{T}^2\zeta(5)}{2a^2M^2} \cdots\right), \tag{8.50}$$

$$P(a) = \frac{30\pi g_s \widetilde{T}^5}{Ma^5} \left(\zeta(5) - \frac{63\widetilde{T}^2\zeta(7)}{32a^2M^2} \cdots\right), \tag{8.51}$$

$$psP(a) = \frac{945\pi g_s \widetilde{T}^7}{M^3a^7} \left(\zeta(7) - \frac{85\widetilde{T}^2\zeta(9)}{a^2M^2} \cdots\right). \tag{8.52}$$

Keeping the zero-order terms for the density and the pressure gives an approximation at late times for the equation of state $w \equiv \frac{P}{\rho}$ as

$$w(a) = \frac{5\zeta(5)}{\zeta(3)} \frac{\widetilde{T}^2}{M^2} a^{-2}, \tag{8.53}$$

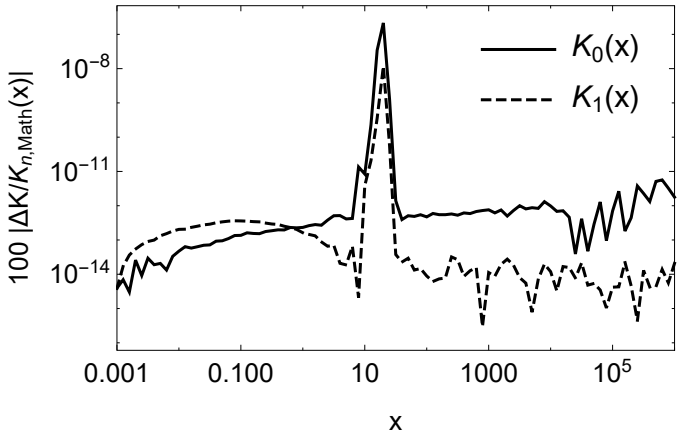

Figure 8.1: The percent difference of the implementation in the CEPHES library vs. the arbitrary precision code of Mathematica for $K_0(x)$ (solid black line) and $K_1(x)$ (dashed black line) for $x \in [10^{-3}, 10^6]$.

which is accurate to a few percent at late times $z < 10$. This expression is also in excellent agreement with the ansatz of Ref. [287] that at late times the equation of state scales as $w(a) \sim 1/a^2$. Moreover, Eq. (8.53) also provides us with the exact numerical coefficient $\frac{5\zeta(5)}{\zeta(3)} \frac{\tilde{T}^2}{M^2}$.

8.4 Numerical results and implementation in CLASS

Here we present numerical comparisons between our analytic results for massive neutrinos, see Sec. 8.2.1, and numerical calculations of the quantities based on double precision calculations from `CLASS`, arbitrary precision calculations in Mathematica and the CEPHES library[6] that we used to implement the Struve K functions in C.

A lower limit on the neutrino mass of approximately $m_\nu \sim 0.06$eV is settled by the existence of three-flavour oscillations (Refs. [365–367]), independently of their nature (Dirac or Majorana) and this is the value that we will use in what follows.

First, we compare the implementation of the Struve K functions in CEPHES with Mathematica's arbitrary precision calculations. The results of this comparison are shown in Fig. 8.1, where we present the percent difference of the implementation in the CEPHES library vs. the arbitrary precision code of Mathematica for $K_0(x)$ (solid black line) and $K_1(x)$ (dashed black line) for $x \in [10^{-3}, 10^6]$. We find that in both cases, on average the agreement between the two codes is on the order of $\sim 10^{-12}\%$ for both functions, thus we are confident in our numerical implementation in what follows.

Next, we compare our numerical implementation of the analytical expressions for the neutrino density and pressure given by Eqs. (8.17) and (8.20), with the numerical integration done in `CLASS`. For this comparison we assumed no relativistic species and only 1 massive neutrino of mass $m_\nu = 0.06\,\mathrm{eV}$, while keeping all other parameters in `CLASS` in their default values. The results of the comparison are shown in Fig. 8.2, where we present the percent difference between the default version of `CLASS` and our analytical expressions for the density (left) and the pressure (right) for 10, 50 and 100 terms (black, green and blue lines) of the analytical expressions given by Eqs. (8.17) and (8.20). We find that keeping 50 terms in the expansion yields an accuracy of $10^{-4}\%$ on average for the density and pressure, without affecting the computational performance.

Then we also compare the results of the CMB power spectrum for our implementation and that of the default version of `CLASS`. The results of the comparison are shown in Fig. 8.3, where

[6] https://www.netlib.org/cephes/index.html

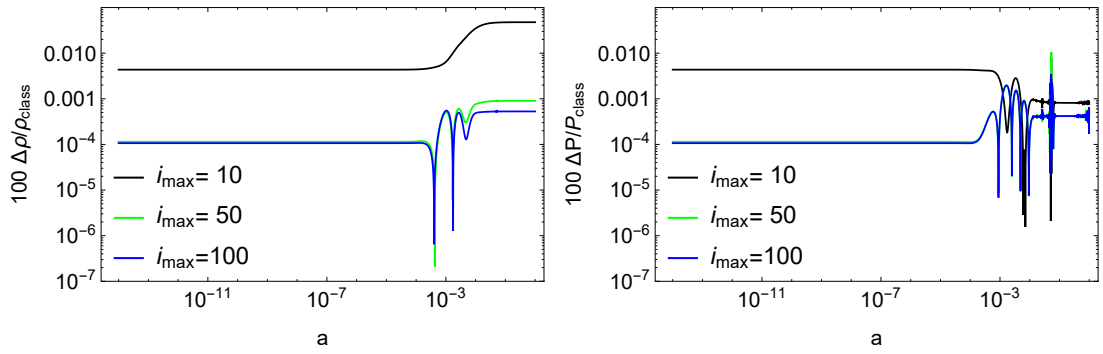

Figure 8.2: The percent difference between the default version of `CLASS` and our analytical expressions for the density (left) and the pressure (right) for 10, 50 and 100 terms (black, green and blue lines). We find that keeping 50 terms in the expansion yields an accuracy of $10^{-4}\%$ on average for the density and pressure, without affecting the performance of the code.

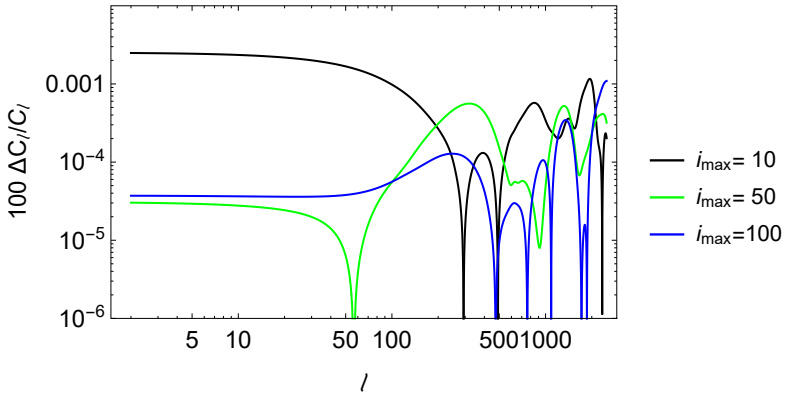

Figure 8.3: The percent difference in the CMB power spectrum for 10 terms in the expansion (black line), 50 terms (green line) and 100 iterations (blue line). We find that keeping 50 terms in the expansion yields an accuracy of $10^{-4}\%$ on average for the CMB spectrum, without having an impact on the performance of the code. We have smoothed the data a bit to remove the oscillatory behavior at high multipoles, but this does not affect our conclusions.

we present the percent difference in the CMB power spectrum for 10 terms in the expansion (black line), 50 terms (green line) and 100 iterations (blue line). We find that keeping 50 terms in the expansion yields an accuracy of $10^{-4}\%$ on average for the C_ℓ^{TT} of the CMB spectrum, without having an impact on the performance of the code.

We also test the approximation for the equation of state $w(z)$ of the neutrinos at late times, given by Eq. (8.53). The comparison for one massive neutrino of mass $m_\nu = 0.06\,\text{eV}$ is shown in Fig. 8.4, where we present the percent difference in the equation of state $w(a)$ between the numerical results (solid black line) and the approximation of Eq. (8.53) (dashed line), for which $w(a) \sim a^{-2}$. As can be seen in the inset plot, at late times ($z < 10$) the agreement is better that 1%, thus validating the ansatz of Ref. [287]. Finally, we have also checked and confirmed that using a slightly larger neutrino mass, such as $m_\nu = 0.15 - 0.30\,\text{eV}$, does not affect the precision of our comparison with `CLASS`.

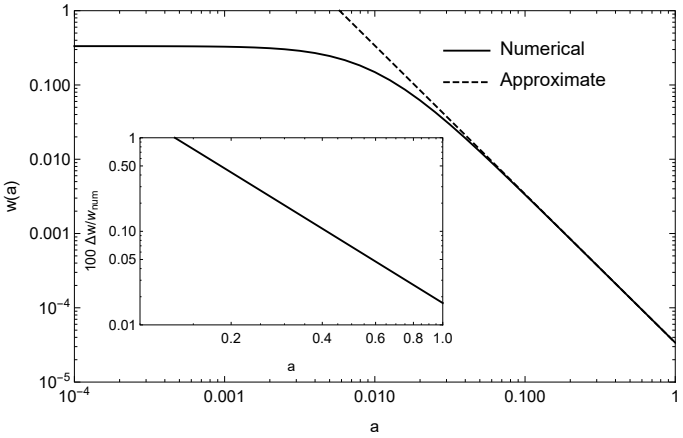

Figure 8.4: The percent difference in the equation of state $w(a)$ between the numerical results and the approximation of $w(a) \sim a^{-2}$ given by Eq. (8.53), for which at late times ($z < 10$), the agreement is better that 1%.

8.5 Conclusions

In this Chapter we presented simple but exact analytical expressions for the background evolution of the density $\rho(a)$, the pressure $P(a)$ and the average number density $n(a)$ for massive particles, both fermions and bosons. In both cases we considered the case when the particles are either relativistic or non-relativistic at the time of decoupling. We find that for non-relativistic massive particles the expressions are somewhat more cumbersome due to the presence of a double sum but in principle these results could be useful in future studies of dark matter candidates, such as WIMPs or any of the hypothetical superpartners of the leptons (sneutrino, etc.).

We also specifically tested our expressions, given by Eqs. (8.17) and (8.20) for the density and pressure respectively, in the case of massive neutrinos that are still relativistic at decoupling ($z \sim 10^{10}$), assuming one neutrino with mass of $m_\nu = 0.06\,\mathrm{eV}$. We implemented our analytical expressions in the Boltzmann code `CLASS` and found that by keeping 50 terms in the sum, e.g., in Eqs. (8.17) and (8.20), it is possible to achieve better than $10^{-4}\%$ accuracy with respect to the default implementation in `CLASS`. Our modifications in the code do not have an impact in the computational performance and avoid the involved quadrature integration scheme at the background level. Our analytical expressions provide validation for the current numerical implementations in public Boltzmann codes. By comparing CMB angular power spectra, we find the agreement between our analytical approach and the current numerical implementation is better than $10^{-4}\%$.

The main advantage of our approach is that our expressions are both exact and analytic, thus they can also provide useful intuition about the behavior of the background quantities for massive particles and how they affect the CMB. Moreover, our analytical expressions allow us to compute quantities such as the entropy density $s = (\rho + P)/T$ or the conserved number $Y = n/s$. For instance, it is possible to derive the exact behavior of the neutrino equation of state $w(a)$ at late times ($z < 10$) and show it behaves as $w \sim a^{-2}$ to better than 1%, in agreement with the ansatz of Ref. [287], thus demonstrating how fast massive neutrinos can become non-relativistic.

Part III

Machine Learning

9

Motivation: What can Machine Learning tell us about the background expansion and large scale structure of the Universe?

That there exists rules to be checked at all is some sort of miracle.
Richard Feynman

Cosmology has now reached a level of precision allowing it to become a complementary probe of particle and fundamental physics. Observations of current and future surveys such as LSST [394], DES [154], eBOSS [395], J-PAS [396], DESI [397], SKA [398] and 21-cm data [399] will allow us to probe the whole epoch from recombination to now and provide a vast amount of data for a broad span of redshifts with hundreds of thousands of supernovas type Ia, along with millions of galaxies and quasars. Clearly, the acquisition of such vast amounts of data means that traditional statistical inference is impractical, as the dimensionality of the data will also increase exponentially, a phenomenon known as 'curse of dimensionality" [400]. This makes it an excellent testing ground for Machine Learning (ML) methods as the latter are ideal in cases where traditional fitting methods give poor results or completely fail, such as in the case of big data, but also when the parameter space is very large, too complex or not well enough understood, as is the case of Dark Energy (DE). Let us recall that ML is a subset of artificial intelligence that aims to build mathematica models that describe a given set of data. It can also be defined as the study of computer algorithms that improve automatically through experience and by the use of data [1]. ML approaches have been proven to be successful at processing and extracting essential information from large amounts of data and can get rid of the problem of model bias [401], while also being very effective in testing the consistency of the dataset model independently and also for searching tensions or systematics. As a result, machine learning will play a big role in testing accurately the standard model of cosmology, but will also help in the search for new physics and tensions in the data by placing tighter constraints on cosmological parameters [402–404].

As we discussed in Chapter 1, the standard cosmological model is at the moment the best candidate to explain the accelerated expansion of the Universe as it is in excellent agreement with all of the current data [1]. However, there is a plethora of other models as well, many of which are included in the pipelines of upcoming surveys, such as Euclid [405]. These models range from canonical scalar fields [166, 406, 407], scalar fields with a generalized kinetic terms [167, 408] or a nonminimal couplings [409–411] in addition to general relativity (GR), coupled DE models [412], modifications of the Einstein-Hilbert action [413], the Chaplygin gas [414] or extra dimensions [415]. For further reviews see [197–200, 276, 349, 405, 416].

This huge landscape of DE models makes the interpretation of the cosmological observations difficult as the results, e.g. the value of the matter content of the Universe Ω_{m0}, depend on the particular model chosen. For example, the Planck mission provides an accurate value for the

[1] see https://en.wikipedia.org/wiki/Machine_learning

matter density parameter today $\Omega_{m0} = 0.315 \pm 0.007$, see Ref. [1], however this value is specific to the ΛCDM model as it was obtained assuming the ΛCDM model, hence is model dependent. To remove biases due to choosing an *a priori* defined model, it is important to use machine learning reconstruction techniques and model independent approaches, see for example [168]. These offer several advantages of traditional fitting and reconstruction methods.

First, the results derived from model independent methods are general, reflecting the underlying physics in an unbiased way as described by the data themselves. The results do not depend on our prior choices and assumptions for what the underlying theory might be. A key example is the reconstruction of the luminosity distance of the Type Ia supernovae, see [417], where no assumptions were made regarding the curvature of the Universe or by imposing an underlying model for DE. Still, the reconstruction can describe the data equally well or even better than the cosmological model and without any free parameters. This method can be applied to other data, not only related to the expansion of the Universe, but also its matter perturbations that cause the large scale structure, thus a main goal of this thesis is to combine all the possible available cosmological observations to provide unbiased results for the key parameters that describe the Universe.

Secondly, while a central goal of modern ML research is to learn and extract important features directly from data [418], ML methods have also been applied to reconstruct null tests of ΛCDM, i.e. quantities that are supposed to be exactly constant for all redshifts [168, 419–424]. Some of these algorithms have been applied to tests that are model independent, i.e. a function that only depends on observed quantities and does not rely on the model. These null tests are useful to check for possible tensions or systematics in the data, or could hint towards new physics. Some of the advantages are that any deviations at any redshift from the expected value imply the failure of any assumptions made [425]. Null tests have been already applied for the concordance ΛCDM model [168, 426, 427], interacting DE models [428], the growth-rate data [404, 425, 429], the cosmic curvature [424, 430–432], to probe the scale-independence of the growth of structure in the linear regime [339] and the homogeneity of the Universe [433].

A third advantage of ML algorithms is that they can capture features of whole classes of theories, without the need to limit the analysis on a specific model, allowing to discriminate among the plethora of Modified Gravity (MG) theories and search for hints of new physics. In MG models it is well known that Newton's constant is time and scale dependent. This means that in order to constrain its evolution we have to use a specific model, for example the f(R) theories presented in Chapter 4. However, using machine learning methods, it is possible to constrain it successfully and even identify deviations from GR, see Ref. [417]. In this regard one could also find constraints on the Etherington relation, that is a relation between the angular diameter distance and the luminosity distance that holds for any metric theory of gravity when the number of photons is conserved. Any deviations from the expected value can be due to either new physics or couplings of the photons to the axions. As we will see in the subsequent Chapters these algorithms may provide hints to yet undiscovered physics and are ideal for poorly understood phenomena like dark energy or modifications of gravity.

Finally, ML has already lead to many contributions in cosmology [401]. ML methods have been used to reduce the scatter in cluster mass estimates [434], to distinguish between standard and modified gravity theories from statistically similar weak lensing maps [260], and have been found to be useful for the next generation CMB experiments [435], N-body simulations [436], cosmological parameters inference [437], dark energy model comparison [438], supernova classification [439] and strong lensing probes [440]. In the context of GW physics, ML can be a useful tool since it can tackle challenges that upcoming GW astronomy is fronting [441, 442] such as a fast and systematic method to characterize properly the signal and the detector, accurate reconstructions of GW signals and a correct estimate of their statistical and systematic errors, and can help to improve and be more sensitive to different searching techniques such as matched-filtering [443], cross-correlation methods [444] and time-coincident detection of coherent excess power between several detectors [445]. ML algorithms have been used to improve the sensitivity of ground-based GW detectors, to reduce and characterize non-astrophysical detector noise and also it has been

applied for fast determinations of parameter estimation [446, 447]. See Ref. [448] for a review on several ML methods. ML is able to process GW signals on real-time, for example the algorithm named Deep Filtering [449] based on neural networks has been created for parameter estimation, reaching a similar performance compared to matched-filtering but faster. In the last few years ML techniques have also been applied with success for glitch classification [450], earthquake prediction [451] and to supplement existing Bayesian methods [452]. It is worth also mentioning the recent progress of neural networks in producing in a fast manner one and two dimensional marginalised Bayesian posteriors [453] for GW parameter estimation, showing how ML can give results very similar to Bayesian statistics [454]. Neural Networks (NN) have been also tested on open data, for example in Ref. [455] the authors searched for a gravitational wave signal from an isolated neutron star from a remnant of GW170817. NN were applied as well in continuous gravitational waves from unknown spinning neutron stars [456] and for gravitational-wave transients associated with gamma-ray bursts [457]. Other applications, general reports and reviews for the use of GW data analysis with ML can be found in Refs. [402, 458–463].

In what follows, see Chapter 10, we will describe a particular class of ML methods, the Genetic Algorithms (GA), which specialize in unsupervised symbolic regression of data and we use them to perform our analysis. This means that the GA can reconstruct an analytic function that describes the data, using one or more variables. One of the advantages of the GA against other symbolic regression methods, such as Neural Networks, is that the GA provides analytical functions that describe the data provided. Then, in the coming Chapters (11-18) we present a unified ML analysis of all the currently available cosmological data in order to reconstruct several key background and perturbations variables in a model-independent manner in order to explore the nature of DE.

10
The Genetic Algorithms

10.0.1 Mathematical formalism

In this Section we will now discuss the theoretical background and the particular implementation of the Genetic Algorithms (GA) used in our analysis. The GA are a particular class of stochastic optimization ML methods that specialize in unsupervised symbolic regression of data by reconstructing analytically, using one or more variables, a function that describes the data. This is achieved by mimicking the theory of evolution via the notion of natural selection, as expressed by the genetic operations of mutation and crossover. In a nutshell, a set of test functions evolves over long periods of time under the influence of the stochastic operators of crossover, i.e. the joining of two individuals to make an offspring, and mutation, i.e. a random alteration of an individual.

Mathematically, these operations can be described via an example as follows. Assuming we have two functions $f_1(x) = 1+x+x^2$ and $f_2(x) = \sin(x)+\cos(x)$, then the mutation operation will stochastically, i.e. randomly, modify the coefficients, the exponents but also the various functions present in the expressions. For example, after the mutation operation is applied the functions might be changed to $f_1(x) = 1 + 2x + x^2$ and $f_2(x) = \sin(x^2) + \cos(x)$, where in the first case the coefficient of the second term changed from one to two and in the second case, $x = x^1$ was changed to x^2. On the other hand the crossover operation randomly combines the two functions to produce two more, e.g. in the aforementioned example the GA might combine the terms $1 + 2x$ from f_1 and $\cos(x)$ to make $\widetilde{f_1}(x) = 1 + 2x + \cos(x)$, while the remaining parts will combine to $\widetilde{f_2}(x) = x^2 + \sin(x^2)$.

As the GA is a stochastic approach by nature, the probability that a population of functions will produce offspring is frequently assumed to be proportional to its fitness to the data, this being a χ^2 statistic in our whole analysis. Specifically, we choose the $\mathcal{N}$ best-fitting functions, where $\mathcal{N} = sel \times pop$, sel is the selection percentage (usually $sel \sim 10\%$) and pop is the population size (usually $pop = 100$), so that the mutation and crossover stochastic operators are applied to these chosen functions. The stochastic nature of the mutation operator in this case means that a function is changed randomly, with the various coefficients and exponents drawn from a uniform random distribution $\mathbf{X} \sim U(-9, 9)$, while the crossover is applied upon two uniform randomly chosen functions, from the whole set of best-fitting GA functions. For example, if there are 10 best-fitting GA functions, the GA will randomly choose for the crossover two out of the ten and proceed to apply the crossover operation as described in the previous paragraph. This is done by choosing a uniformly distributed random number in the range between one and the length of the expression, such that the two functions can be intermixed. Finally, the mutation will also be applied randomly, as described before, only if a uniformly random drawn number $\mathbf{X} \sim U[0, 1]$ does not exceed the mutation rate, typically set to 0.3. For further details on the GA and some applications to cosmology see Refs. [169, 464].

The reconstruction procedure then proceeds as follows, see also Fig. 10.1 for a flowchart of the list of steps of a usual GA. First, we select a set of analytic functions, commonly called the "grammar", with which we set up the first generation. In this first step we also impose any necessary priors dictated either by physical or mathematical reasons. For example, we may impose

Table 10.1: The grammars used in the GA analysis, which include polynomials, exponentials, fractions, constants, trigonometric functions, logarithms etc. More complicated forms are automatically created by the mutation and crossover operations as described in the text.

Grammar type	functions
Polynomials	c, x, $1+x$
Fractions	$\frac{x}{1+x}$
Trigonometric	$\sin(x)$, $\cos(x)$, $\tan(x)$
Exponentials	e^x, x^x, $(1+x)^{1+x}$
Logarithms	$\log(x)$, $\log(1+x)$

that the value of the luminosity distance at $z = 0$ is zero, i.e. $d_{\rm L}(z = 0) = 0$ or that the Hubble parameter today is $H(z = 0) = H_0$. Hence, we make no assumptions on the curvature of the Universe or on any modified gravity model.

Note that we do not only use grammars including simple polynomials, but we also include several other functions, see Table 10.1 for a complete list. More complicated forms like $e^{f(z)}$ and $f(z)^{g(z)}$ are then automatically created by the mutation and crossover operations as described earlier. Also, it should be stressed that the choice of the grammar and the population size has already been tested in Ref. [464][1]. Similarly, the seed numbers are also crucial as they are used to create the initial population of functions used later on by the GA. This is clearly analogous to the initialization of weights in a neural network.

After we have constructed this initial population of functions, the fitness of each member is determined by a χ^2 statistic using the data and the best-fitting functions in every generation are selected via a tournament selection, see Ref. [464] for more details. Afterwards, the two stochastic operations of the mutation and the crossover are consecutively applied and the whole process is repeated several thousands of times so as to ensure convergence. In an analogy to traditional Monte Carlo approaches, we also reran the GA with a plethora of different random seeds, so as to explore the functional space.

10.0.2 Error analysis

After the GA has converged, the final output is a set of differentiable and continuous functions of the redshift z. In order to obtain an estimate of the errors in the reconstructed functions we follow the path integral approach of Refs. [169, 417]. We approximate the errors using the path integral approach expanded, for a limited set of functions, around the best fit GA. Whilst this may not be representative of the true errors, we find they agree well with Fisher matrix and bootstrap Monte-Carlo analyses [169].

Then, given a function $f(x)$ which is reconstructed by the GA, the "path integral" approach of Ref. [169] can provide us with the 1σ error $\delta f(x)$. Moreover, in principle the GA may in fact consider any possible function as it is exploring the functional space and even though possibly poor fits may be discarded, they can indeed contribute in the total probability when integrating over the likelihood and as a result, they have to be taken into account in the error calculations.

This approach has been well-tested by comparing the GA errors against Fisher and Bootstrap MCMC analyses, and in Ref. [169] (see Fig. 2) it was demonstrated that the "path integral" approach gives robust and reliable errors, not affected by the error reconstruction method. For the "path integral" approach employed here, we assume the errors correspond to 1σ, which is equal to one standard deviation of a normal deviation around the GA best-fit. This is similar to error

[1] See for example Fig. 2 of Ref. [464] for the effect of the population size on the convergence and a discussion in page 5 for the effects of the grammar.

propagation assuming that the error in a quantity is given by $\sigma_f = f'(p)\delta p$, where p in this case is a parameter. Having extensively tested the GA against Fisher matrix and Bootstrap MCMCs in Ref. [169], where the GA was confirmed to give robust error estimates, we find this assumption of the error propagation to be appropriate for the data used here. Then, we can treat the values of the function f as random variables described by a normal distribution

$$\mathcal{L}(f) = \frac{e^{-\frac{(f-f_{\rm GA})^2}{2\delta f^2}}}{\sqrt{2\pi}\delta f}. \tag{10.1}$$

This assumption is justified in the context of the "path integral" approach, thus to good approximation the GA error can in fact be taken to be Gaussian, see also Eqs. (2.5) and (2.6) in Ref. [169].

Then, the error propagated to any quantity formed by the function f, eg $g = g(f)$ can be estimated by using the definition of the standard deviation $\delta g^2 = \langle g^2\rangle - \langle g\rangle^2$ and the expectation value $\langle g\rangle = \int_{-\infty}^{+\infty} g(f)\ \mathcal{L}(f)df$. For example, we demonstrate this approach for the simple example of $g(f) = f^2$, where we would expect the error of g to be $\delta g = 2f_{\rm GA}\delta f + \cdots$. Indeed, we find

$$\begin{aligned} \langle g^2\rangle &= 3\delta f^4 + f_{\rm GA}^4 + 6\delta f^2 f_{\rm GA}^2 \\ \langle g\rangle^2 &= \left(\delta f^2 + f_{\rm GA}^2\right)^2, \end{aligned} \tag{10.2}$$

which gives

$$\begin{aligned} \delta g &= \sqrt{2\delta f^4 + 4\delta f^2 f_{\rm GA}^2} \\ &\simeq 2f_{\rm GA}\delta f + \cdots, \end{aligned} \tag{10.3}$$

in agreement with the expected value.

10.0.3 General considerations

Even though with the GA we do not make assumptions on a particular DE model, such as the ΛCDM, it may happen that the data contain some model assumptions. A notorious such example is the JLA SnIa compilation [465], where the cosmological parameters have to fitted simultaneously with variables of astrophysical origin, such as the light-curve parameters. In a similar vein, in the Pantheon compilation [88], some model dependence still remains, even though the light-curve parameters have already been marginalized over. This is due to the fact that the SnIa surveys have to include in the analysis particular peculiar velocity corrections, assuming the ΛCDM model and linear theory [466]. Furthermore, in order to derive the covariance matrix, frequently a fiducial model is assumed [88]. As we will see on Chapter 11, the best-fit is close to the ΛCDM model in our analysis, hence we can safely assume that these effects do not affect the reconstruction process.

Also, there exist other non-parametric approaches such as Gaussian processes (GP). These assume the data can be described by a stochastic Gaussian process, where one can later on map to any cosmological function of interest [145, 467–469]. Even though the GP necessitate choosing both a kernel and a fiducial model for the mean value, in Ref. [467] it has been shown that these assumptions do not affect the results of the reconstruction. However, the GA have the advantage over the GP that they do not need a physical model with prior assumptions, for example of a flat Universe or a DE model, other than the choice of the grammar and this only affects the convergence rate [464]. By comparing plots of the same reconstructed parameter we can see that both reconstruction methods give similar errors, see for example the plot of $H(z)$ in Fig. 2 of Ref. [145] with that of the left panel of Fig. 2 of Ref. [419].

Finally, we should stress that it has been demonstrated with the use of mock data sets that the GA can successfully recover the underlying physical model. For example, in the case of generic, i.e. non-physically motivated, mock data this was done in Ref. [169] (see Fig. 2), where as it can be seen the GA matches both the underlying fiducial model and also gives error estimates

that are similar with other approaches (Fisher and MCMC). Similarly, in the case of cosmological data the ability of the GA to recover the fiducial model was tested in Ref. [470] (see Fig. 6) and Ref. [471] (see Figs. 7-9) with a variety of mock cosmological data, while using several quite different fiducial models such as the ΛCDM and modified gravity theories, but also models that violate the distance duality relation. For other successful symbolic regression methods applied in physics and cosmology see [472–479].

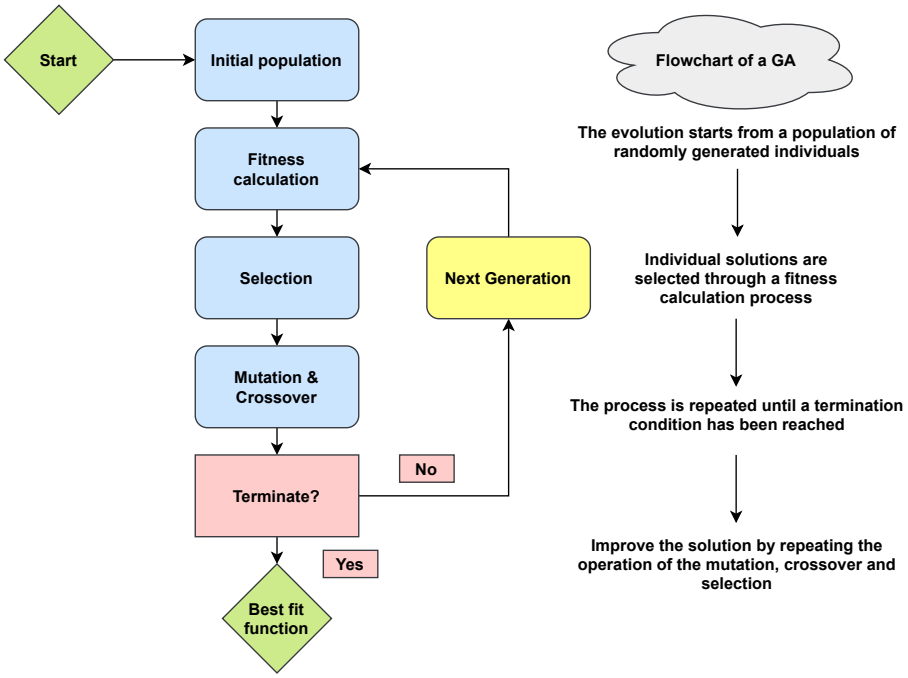

Figure 10.1: Flowchart of the list of steps of a usual Genetic Algorithm.

11

The Background Expansion of the Universe

The original content of this chapter is based on Ref. [419]. Machine learning (ML) algorithms have revolutionized the way we interpret data in astronomy, particle physics, biology and even economics, since they can remove biases due to a priori chosen models. Here we apply a particular ML method, the genetic algorithms (GA), to cosmological data that describes the background expansion of the Universe, namely the Pantheon Type Ia supernovae and the Hubble expansion history $H(z)$ datasets. We obtain model independent and nonparametric reconstructions of the luminosity distance $d_L(z)$ and Hubble parameter $H(z)$ without assuming any dark energy model or a flat Universe. We then estimate the deceleration parameter $q(z)$, a measure of the acceleration of the Universe, and we make a $\sim 4.5\sigma$ model independent detection of the accelerated expansion, but we also place constraints on the transition redshift of the acceleration phase ($z_{\rm tr} = 0.662 \pm 0.027$). We also find a deviation from ΛCDM at high redshifts, albeit within the errors, hinting toward the recently alleged tension between the SnIa/quasar data and the cosmological constant ΛCDM model at high redshifts ($z \gtrsim 1.5$). Finally, we show the GA can be used in complementary null tests of the ΛCDM via reconstructions of the Hubble parameter and the luminosity distance.

11.1 Introduction

As we have been discussing, Cosmology has reached a stage of near percent level precision ans has a wide range of theoretical models that describe rigorous and accurate measurements. However, the explanation as to why the Universe is undergoing a period of accelerated expansion still remains an open question and the cause of this phenomenon is usually attributed to a dark energy (DE) component [5].

In this Chapter we will apply a particular ML method, the genetic algorithms (GA) to cosmological data that describes the background expansion of the Universe, namely the Pantheon Type Ia supernovae and the Hubble rate $H(z)$ datasets. The GA have been used in many disciplines ranging from astrophysics, e.g. to determine the photometric redshift [480], to find the optimum parameters for cosmic ray injection and propagation [481], to fit dusty galaxies [482], to perform galaxy classification [483], in particle physics to constrain the MSSM [484, 485] or resonances in Lambda reactions [486], but also in finance [487, 488] and biology [489]. More recently, they have also been applied to cosmology for data reconstruction [168, 169, 324, 403, 417, 420, 464, 490, 491]. One of the most effective use of these methods is the reconstruction of null tests, i.e. pass/fail test made of variables of a theory that should always be constant for all values of the parameters, and can be used to test theories in a model independent way. In light of the near future experiments that will gather a vast amount of data, such as Euclid and LSST, it is necessary to perform model independent tests to check for possible tensions that could be due to systematics or new physics.

The structure of our Chapter is as follows. In Sec. 11.2 we present the theoretical background of the GA approach we use in our analysis, in Sec. 11.3 we present our reconstructions and the results on the deceleration parameter, the transition redshift and the two null tests based on the Hubble parameter and luminosity distance. Finally, in Sec. 11.4 summarize our results and present

our conclusions.

11.2 The Genetic Algorithms

Here we present the theoretical background of the implementation of the GA in our analysis. In this chapter we consider the Pantheon Type Ia Supernovae (SnIa) and $H(z)$ data sets (see Chapter 2 for more details), so in practice, the procedure to reconstruct them, proceeds as follows. First, we choose an orthogonal basis of functions, traditionally called the "grammar", with which an initial population of functions is constructed. These function are randomly picked so that every member of the population codifies an initial guess for both the luminosity distance $d_{\rm L}(z)$ and the Hubble parameter $H(z)$. While this choice for the grammar might seem crucial for the symbolic regression, it has been shown in Ref. [464] that it only affects the rate of convergence of the GA.

In this first step one may also impose any necessary physical priors, for example that the value of the Hubble parameter today is $H(z=0)=H_0$ or that the luminosity distance at $z=0$ is zero, i.e. $d_{\rm L}(z=0)=0$. This step is important as we want to avoid any unphysical functions that could unnecessarily delay the convergence of our GA code. We also demand that all functions reconstructed by the GA are continuous and differentiable, without any singularities in the redshift range covered by the data, so as to avoid overfitting or any spurious reconstructions. These are the only physical assumptions we do and we make no assumption on any particular DE or modified gravity model or even on the curvature of the Universe.

After the initial population has been constructed, the fitness of each member is estimated by a χ^2 statistic, using as input the SnIa and $H(z)$ data. Afterwards, using a tournament selection, see Ref. [464] for more details, the best-fitting functions in every generation are chosen and the two stochastic operations of the crossover and the mutation are applied. In order to ensure convergence this procedure is then repeated hundreds of times and with various random seeds, so as to properly explore the functional space.

The final output of the GA code is a couple of two continuous and differentiable functions of the redshift z that describe the Hubble parameter $H(z)$ and the luminosity distance $d_{\rm L}(z)$ respectively. However, the GA on its own does not provide any estimate of the errors of the reconstructed functions, something which is necessary for the statistical interpretation of the data. To do so, we implement the path integral approach of Refs. [169, 417], explained also in Sec. 10.0.2, where the errors are estimated by calculating analytically a path integral over all functions that may be surveyed by the GA. This error reconstruction method has been exhaustively examined and compared against a bootstrap Monte-Carlo by Ref. [169].

At this point it should be noted that while no assumptions on a particular cosmological model, such as the ΛCDM were made, sometimes the data themselves may not be completely model-independent. As explained in Sec. 10.0.3, some model dependence may still remain since the SnIa surveys have to take into account specific corrections regarding the peculiar velocities, assuming linear theory and the ΛCDM model [466]. Moreover, a fiducial background model is typically assumed in order to derive the covariance matrix of the data [88]. In our case we can safely assume that these effects have a very small effect on the reconstruction process as the best-fit is close to the ΛCDM model.

11.3 Analysis and results

11.3.1 The data

The null tests we will consider here are the $\mathrm{Om}(z)$ statistic [426, 427] and a new null test derived from the luminosity distance, that we present here for the first time. We thus propose applying ML methods, in particular the GA, to fit to the Pantheon Type Ia supernovae (SnIa) data compilation [88] and the $H(z)$ data compilation of Ref. [9] to obtain a model independent reconstruction of the

luminosity distance $d_L(z)$ and of the Hubble parameter $H(t) \equiv \frac{\dot{a}}{a}$, where $a(t)$ is the scale factor in the Robertson-Walker metric, and the dot stands for a derivative with respect to the cosmic time t.

In our analysis we use 1048 data points in the range $z \in [0, 2.26]$, along with their covariances, from the Pantheon set [88], and 36 points in the range $z \in [0, 2.34]$ from the $H(z)$ compilation, presented in Table 2.1. On the other hand, we make no assumptions for H_0 and derive it directly from the $H(z)$ data, as we will see later on. Finally, for the likelihood for the $H(z)$ data we use a standard χ^2, given by

$$\chi^2_{\rm H} = \sum_{i=1}^{N} \left(\frac{H_i - H_{\rm GA}(z_i)}{\sigma_i} \right)^2 , \tag{11.1}$$

while for the SnIa data we use the expressions found in Appendix C of Ref. [89]. Note that in our analysis we use the two data sets in the following manner: we use the $H(z)$ data for the deceleration parameter $q(z)$ and the $\mathrm{Om_H}$ null test, while for the $\mathrm{Om_{dL}}$ null test we will use the SnIa data.

11.3.2 The reconstructions

We reconstruct the Hubble parameter by applying the GA to the $H(z)$ data, while the value of the Hubble parameter H_0 was derived through minimizing the χ^2 analytically as the χ^2 is quadratic in H_0, see Sec. 2.1.1 and also Ref. [140]. For the SnIa, due to the degeneracy between the absolute magnitude M and the Hubble parameter H_0, we used the value extracted from the $H(z)$ data, given below. In both cases, no assumptions such as a flat Universe or a specific DE model were made, hence our results are almost completely model independent.

Note that sometimes the data are themselves model dependent, with an infamous example being the SnIa, as one must optimize parameters in the lightcurve function simultaneously with those of the assumed model. Furthermore, a covariance matrix is typically inferred based on an assumed background model, usually ΛCDM. However, since in our case the best-fit is close to ΛCDM and the errors are much larger than the effects of the model-bias in the covariance, we can safely assume for now that these effects have a minimal effect to the minimization.

In order to make sure we are not biasing our analysis due to the specific value of the random seed we have performed several simulations with different random seed numbers. We have also demanded that all functions, along with their derivatives, are continuous and have no singularities in the range covered by the data. As an example, the genetic evolution of several different initializations of the GA code with different seed random numbers for the SnIa data as a function of the generation number can be seen in Fig. 11.1. In most cases, the GA has converged very quickly in the evolutionary history and in the majority of cases, the obtained χ^2 is smaller than that of the ΛCDM model.

Following this approach and taking into account the constraints mentioned earlier, we find the best-fit GA functions to be

$$H_0 = (69.27 \pm 12.00)\ \mathrm{km/s/Mpc}, \tag{11.2}$$

$$H(z) = H_0 \left(1 + z \left(0.652 + 0.228z - 0.017z^3\right)^2\right), \tag{11.3}$$

$$d_L(z) = \frac{c}{H_0} z \left(1 + z \left(-0.054z - 0.146e^{0.347z} + 0.999\right)^2\right), \tag{11.4}$$

where c is the speed of light and the constraint on H_0 was derived directly from the $H(z)$ data. The best-fit χ^2 for the GA and ΛCDM models are given in Table 11.1, while plots of the Hubble parameter and the distance modulus $\mu(z) = 5\log_{10}\left(d_L(z)/\mathrm{Mpc}\right) + 25$ versus ΛCDM and the data are given in Fig. 11.2. The agreement with the best-fit ΛCDM model ($\Omega_{m0} = 0.299 \pm 0.022$) for the distance modulus $\mu(z)$ is at a subpercent level with ΛCDM until $z \sim 1.5$, but then it deviates similarly, albeit within the errors, to the reconstruction of Refs. [56, 492] that used SnIa and quasar data.

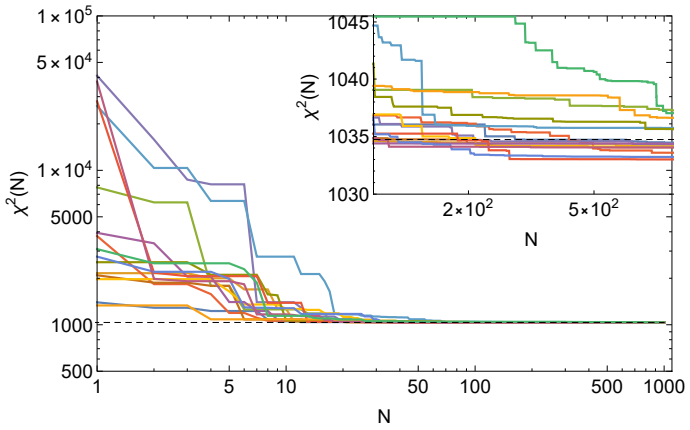

Figure 11.1: The genetic evolution of several different initializations of the GA code with different seed random numbers for the SnIa data as a function of the generation number. In most cases the GA has converged very quickly in the evolutionary history and reaches a lower χ^2 than ΛCDM does.

Table 11.1: The χ^2 for ΛCDM and GA using the Pantheon SnIa and $H(z)$ data.

	SnIa	$H(z)$
$\chi^2_{\Lambda\text{CDM}}$	1034.73	19.476
χ^2_{GA}	1034.30	17.683

In order to make sure that the observed deviation from ΛCDM is not affected by the choice of the particular dataset, we removed the last two points at high redshifts (at $z = 1.914$ and $z = 2.26$) of the Pantheon SnIa compilation in order to test the robustness of our results. We found that the GA fit is actually unaffected, with the χ^2 values being respectively $\chi^2 = 1033.2$ for the ΛCDM and $\chi^2 = 1032.94$ for the GA best-fit, where the latter in this case was found to be

$$d_L(z) = \frac{c}{H_0} z \left(1 + z(0.871 - 0.131z - 0.001z^4)^2\right). \tag{11.5}$$

Specifically, we find that for the original dataset the difference of the distance moduli at $z = 2.305$ is $\mu_{\text{GA}} - \mu_{\Lambda\text{CDM}} = -0.200284$, while after removing the last two points we have $\mu_{\text{GA}} - \mu_{\Lambda\text{CDM}} = -0.246619$. In order to verify that our analysis is indeed robust, we extended it by repeated removing two random points, at any redshift this time, and then ran the reduced data set over the GA pipeline. In all cases we found that the behavior of the GA best-fit remains unchanged.

Therefore, since the residuals in the reduced dataset are clearly consistent with the ones of the complete set, as shown in the right panel of Fig. 11.2, we are confident our analysis is robust and is not affected by the choice of the specific dataset. Thus, having determined the functional forms of $H(z)$ and the luminosity distance, we can now use them to place model independent tests on the background expansion of the Universe and reconstruct null tests of the ΛCDM model.

The most critical parameter in determining whether the Universe is accelerating or not, is the deceleration parameter which is given by

$$q(z) = -\frac{\ddot{a}a}{\dot{a}^2} = -1 + (1+z)\frac{H'(z)}{H(z)}, \tag{11.6}$$

where dots stand for derivatives with respect to the cosmic time t, while primes for derivatives with respect to the redshift z, where $a(t) = \frac{1}{1+z}$. The advantage of this parameter over the DE equation of state $w(z)$ is that the former only requires the knowledge of $H(z)$ and not that of cosmological parameters such as Ω_{m0} [168].

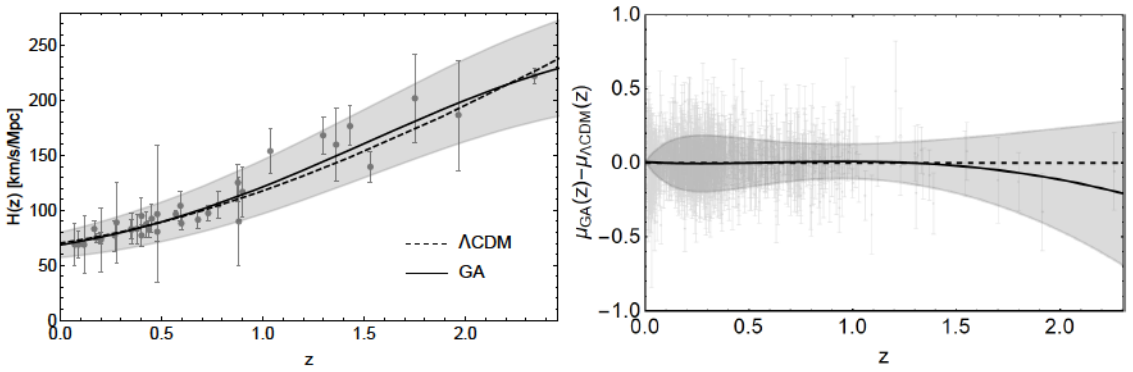

Figure 11.2: Left: The $H(z)$ data compilation along with the ΛCDM best-fit (dashed line) and the GA best-fit (solid black line). Right: The difference between the GA best-ft distance modulus of the Pantheon SnIa data (black line) and that of the ΛCDM model (dashed line). The Pantheon SnIa data are shown as grey points in the background.

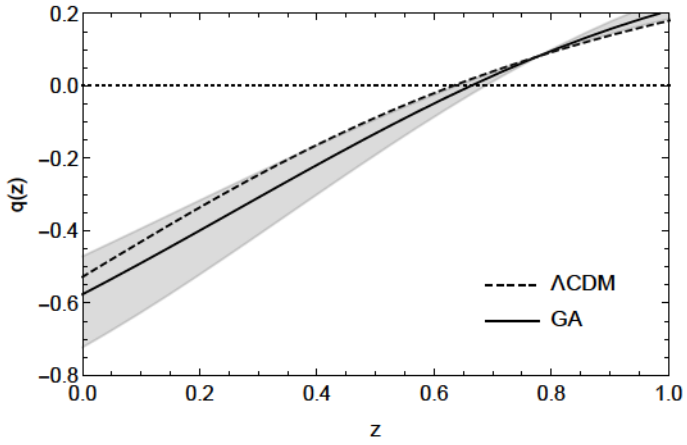

Figure 11.3: The deceleration parameter given by Eq. (11.6) as reconstructed by using Eq. (11.3). The shaded region corresponds to the 1σ errors, while the transition redshift $z_{\rm tr}$ corresponds to the point where $q(z)$ crosses zero.

For the Universe to accelerate today, we require (due to historical reasons) that $q_0 < 0$, e.g. for the ΛCDM model we have $q_{0,\Lambda\rm CDM} = -1 + 3\Omega_{m0}/2 \simeq -0.528 \pm 0.011$ for the Planck best-fit $\Omega_{m0} = 0.315$ [1] and $q_{0,\Lambda\rm CDM} = -0.613 \pm 0.043$ for the ΛCDM best-fit to the $H(z)$ data of $\Omega_{m0} = 0.258 \pm 0.029$. Using the GA reconstruction of the Hubble parameter given by Eq. (11.3) we can calculate the deceleration parameter given by Eq. (11.6) and the result is given in Fig. 11.3. The present value of the deceleration parameter is found to be $q_0 \equiv q(z=0) = -0.575 \pm 0.132$, a $\sim 4.5\sigma$ detection of the accelerated expansion of the Universe in a model-independent way.

We can also estimate the value of the transition redshift, i.e. the redshift where the deceleration parameter changes sign, see Refs [74, 493–497] for a list of recent estimates. From the GA reconstruction we find that $z_{\rm tr} = 0.662 \pm 0.027$, while for the ΛCDM the latter is equal to $z_{\rm tr,\Lambda CDM} = -1 + 2^{1/3}\left(\Omega_{m0}^{-1} - 1\right)^{1/3} = 0.632 \pm 0.018$ for Planck and $z_{\rm tr,\Lambda CDM} = 0.791 \pm 0.091$ for the $H(z)$ ΛCDM best-fit. While the precision of these measurements seems worse than that of ΛCDM, in our case we have made very minimal assumptions and have not assumed any DE model.

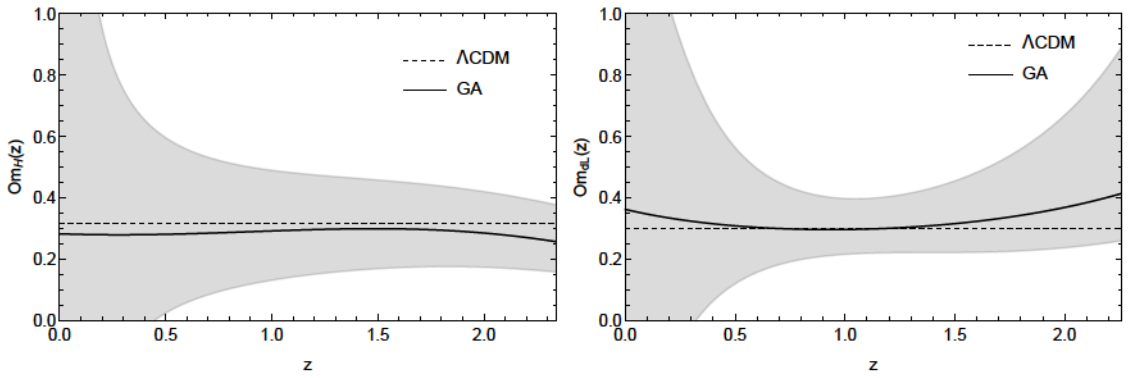

Figure 11.4: The reconstruction of the $\mathrm{Om_H}(z)$ (left) and $\mathrm{Om_{dL}}(z)$ (right) statistics respectively, along with the 1σ errors (gray regions). Both cases are consistent with the ΛCDM model (dashed line).

11.3.3 The null tests

Next we focus on the reconstruction of the null tests for the ΛCDM model. The first null test we will consider is the $\mathrm{Om}(z)$ statistic of Ref. [426], which only requires knowledge of the Hubble parameter $H(z)$ and allows us to discriminate ΛCDM from other DE models, see Refs [168]. It is defined as[1]

$$\mathrm{Om_H}(z) \equiv \frac{H(z)^2/H_0^2 - 1}{(1+z)^3 - 1}. \tag{11.7}$$

Here we also present a different, but at the same time complementary, null test of the ΛCDM by extracting the matter density Ω_{m0} from the luminosity distance instead of the Hubble parameter. To do this, we use the Lagrange inversion theorem which states that given an analytic function, we can estimate the Taylor series expansion of the inverse function, i.e. given the function $y = f(x)$, where f is analytic at a point p and $f'(p) \neq 0$ the theorem allows us to solve the equation for x and write it as a power series $x = g(y)$, see [388].

We now apply the Lagrange inversion theorem to the luminosity distance $d_L(z, \Omega_{m0})$ and from now on we will restrict ourselves at late times, when DE dominates over the other components, such as radiation and neutrinos. Then, the analytical expression of the luminosity distance for the ΛCDM model, assuming a flat Universe but neglecting radiation and neutrinos, is given by

$$\begin{aligned} d_L(z,\Omega_{m0}) &= \frac{c}{H_0}(1+z)\int_0^z \frac{1}{H(x)}dx \\ &= \frac{c}{H_0}\frac{2(1+z)}{\sqrt{\Omega_{m0}}}\left({}_2F_1\left(\frac{1}{6},\frac{1}{2},\frac{7}{6},\frac{\Omega_{m0}-1}{\Omega_{m0}}\right) - \frac{{}_2F_1\left(\frac{1}{6},\frac{1}{2},\frac{7}{6},\frac{\Omega_{m0}-1}{\Omega_{m0}(1+z)^3}\right)}{\sqrt{1+z}}\right). \end{aligned} \tag{11.8}$$

To derive the $\mathrm{Om_{dL}}(z)$ test we first do a series expansion on Eq. (11.8) around $\Omega_{m0} = 1$ and keep the first 10 terms in order to obtain a reliable unbiased estimation and avoid theoretical systematic errors. Then, we apply the Lagrange inversion theorem to invert the series and to write the matter density Ω_{m0} as a function of the luminosity distance d_L, i.e $\mathrm{Om_{dL}} = \mathrm{Om_{dL}}(z, d_L)$. For example, the first two terms of the expansion are

$$\mathrm{Om_{dL}}(a, d_L) = 1 - \frac{7a\left(\frac{H_0}{c}d_L - \frac{2-2\sqrt{a}}{a}\right)}{6 + \sqrt{a}\,(a^3 - 7)} + \cdots, \tag{11.9}$$

[1]We use the notation $\mathrm{Om_H}$ with the subscript H to discriminate this null test from the one we will introduce later on and which is based on the luminosity distance $d_L(z)$.

where the scale factor a is related to the redshift z as $a = \frac{1}{1+z}$. This null test has the main advantage that it does not require taking derivatives of the data as we use the luminosity distance directly.

The reconstruction of both null tests of the ΛCDM model is shown in Fig. 11.4, in the left panel for the $\mathrm{Om_H}$ and the right panel for the $\mathrm{Om_{dL}}$ respectively. We find that both null tests are in agreement with ΛCDM at the 1σ level. While the errors of the distance modulus $\mu(z)$ and the $\mathrm{Om_{dL}}$ test, shown in Figs. 11.2 and 11.4 respectively, seem somewhat larger compared to those in Refs. [168, 169], the latter used the Union 2.1 set but did not include the systematic errors, thus underestimating the errors regions. On the other hand, the Pantheon compilation both statistical and systematic errors are included in the publicly available data [2]. As a result, even though the Pantheon set has roughly twice as many points than the Union 2.1, the inclusion of the systematic errors of the Pantheon in the analysis, brings the error estimates for $\mu(z)$ and $\mathrm{Om_{dL}}$ to the same level as those in Refs. [168, 169].

11.4 Conclusions

In summary, ML methods are revolutionizing the way we interpret data since they can help to remove biases due to choosing *a priori* a specific defined model. This is more important than ever as the endeavor to explain the accelerated expansion of the Universe has led to a plethora of DE models, which make the interpretation of the data difficult as the results are model dependent. This can lead to model bias, thus affecting the conclusions drawn about fundamental physics.

We have shown that applying the GA to the SnIa and $H(z)$ data can be used to reconstruct the expansion history of the Universe and help determine the current deceleration parameter and transition redshift in a model independent fashion. The datasets we use are the Pantheon Type Ia Supernovae compilation of Ref. [88] and the $H(z)$ based on the differential age method and the clustering of galaxies or quasars by Moresco *et al.* (shown in Table 2.1 of Sec. 2.1.1), both being state-of-the-art at the moment. Given that we only have one realization of "real" data at the moment, one could possibly use mock datasets to test the GA approach as a reconstruction method. This however, has already been done, see for example [169, 420]. By considering subsamples of the Pantheon dataset at high redshifts we also confirmed that our results are robust.

We also find a $\sim 4.5\sigma$ detection of the accelerated expansion, contrary to recent claims by Ref. [498, 499], where the authors claimed that there is little to no evidence for acceleration. The main differences between our work and that of Ref. [498], is that in the latter the authors used the (now outdated) Joint Lightcurve Analysis (JLA) catalogue by Ref. [465], while here we use the much more recent Pantheon sample by Ref. [88]. The Pantheon sample was created by analyzing together recent observations of SnIa from the Pan-STARRS1 survey and from other previously available low redshift subsamples from other surveys, in order to create a uniform dataset that would have the same quality cuts and systematics.

Besides the choice of the SnIa data, our Chapter and that of Ref. [498], also differ in the fact that while our approach is completely nonparametric and model-independent, Ref. [498] assumes Gaussian priors for the absolute magnitude M, the stretch x and the color c, as seen in Eq. (4) in their paper, each with a mean value and a standard deviation. Then, these six new parameters are fitted along with the cosmological parameters. However, as was pointed out in [500], the observed distributions of these parameters are far from redshift-independent, thus biasing their results.

Furthermore, our method has several advantages compared to other methods found in the literature like the GP. In particular, while the GP requires the choice of a kernel function and a fiducial model, usually taken to be a Gaussian and ΛCDM respectively, our approach assumes

[2] The systematic errors are included in the "sys_full_long.txt" file, which is publicly available from the Pantheon GitHub page https://github.com/dscolnic/Pantheon. For the SnIa likelihood in our analysis, we use the following free and publicly available code, see https://members.ift.uam-csic.es/savvas.nesseris/codes.html.

neither and is completely theory agnostic. Also, compared to the approach of Ref. [498], our approach is completely nonparametric.

In summary, we showed how the GA can be used to reconstruct complementary null tests of the ΛCDM model via reconstructions of both the Hubble parameter and the luminosity distance and we found that both are consistent with ΛCDM within the errors.

12

Hints of dark energy anisotropic stress using Machine Learning

The original content of this chapter is based on Ref. [324]. Recent analyses of the Planck data and quasars at high redshifts have suggested possible deviations from the flat Λ cold dark matter model (ΛCDM), where Λ is the cosmological constant. Here we use machine learning methods to investigate any possible deviations from ΛCDM at both low and high redshifts by using the latest cosmological data. Specifically, we apply the Genetic Algorithms to explore the nature of dark energy (DE) in a model independent fashion by reconstructing its equation of state $w(z)$, the growth index of matter density perturbations $\gamma(z)$, the linear DE anisotropic stress $\eta_{\rm DE}(z)$ and the adiabatic sound speed $c^2_{\rm s,DE}(z)$ of DE perturbations. We find a $\sim 2\sigma$ deviation of $w(z)$ from -1 at high redshifts, the adiabatic sound speed is negative at the $\sim 2.5\sigma$ level at $z = 0.1$ and a $\sim 2\sigma$ deviation of the anisotropic stress from unity at low redshifts and $\sim 4\sigma$ at high redshifts. These results hint towards either the presence of an non-adiabatic component in the DE sound speed or the presence of DE anisotropic stress, thus hinting at possible deviations from the ΛCDM model.

12.1 Introduction

In Sec. 1.3 we discussed about the tensions in the ΛCDM model. These issues have motivated several analyses trying to reassess the level of deviations from the ΛCDM model [64–70] or to resolve it with new physics [3]. The latter approach postulates that GR is only accurate on small scales and modifications at larger scales are needed. One side-effect of this deviation from GR is that the Newtonian potentials Φ and Ψ are now in general not equal, thus resulting to an anisotropic stress which could be detected from weak-lensing [190]. The anisotropic stress is usually modeled via the parameter $\eta_{\rm DE} \equiv \frac{\Phi}{\Psi}$, where Φ and Ψ are the Newtonian potentials, taken to be equal in GR in the absence of anisotropic stresses from other sources such as neutrinos. Thus, any deviation of $\eta_{\rm DE}$ from unity would point to modified gravity or if neglected, it could bias the cosmological parameters inferred from the data [191].

If this modification of gravity is interpreted via the effective fluid approach [9, 10], then the presence of anisotropic stress also implies that the sound speed of propagation of the DE perturbations $c^2_{\rm s,DE}$ can be negative. However, the perturbations can still remain stable if the effective sound speed, defined as the sum of the DE sound speed and the anisotropic stress, is positive [235]. Therefore, if direct measurements of $c^2_{\rm s,DE}$ find that it is negative, this would be a smoking gun signature for the existence of an anisotropic stress and possible modifications of gravity. Furthermore, it has been shown that the effects of the anisotropic stress can be mimicked by a varying adiabatic sound speed of DE perturbations [236, 237]. A related quantity is also the $F(z)$ test of Ref. [501], which is proportional to the DE sound speed and is supposed to be equal to zero for the ΛCDM model. As both $F(z)$ and $c^2_{\rm s,DE}$ are related, here we will only consider the latter.

The large scale structure (LSS) of the Universe provides a natural testbed to search for

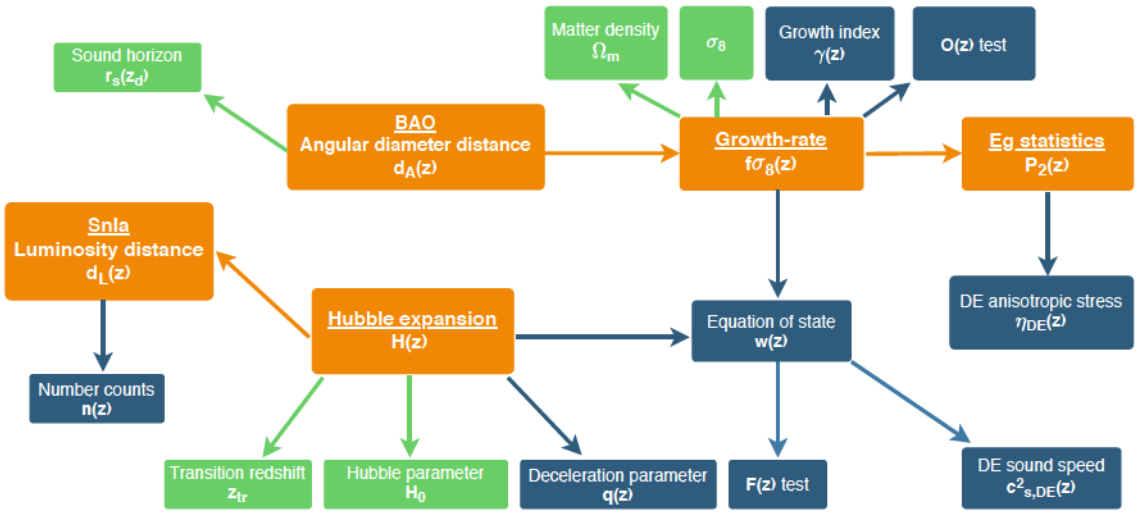

Figure 12.1: A flowchart of the fitting process using the machine learning approach. The orange blocks represent primary quantities reconstructed directly from the data, i.e. the ML best-fits, the blue blocks represent quantities reconstructed from the latter, such as $w(z)$, and the green blocks stand for the derived (secondary) parameters. The flowchart shows the interplay between the different data and derived parameters, something which is reflected in our analysis.

deviations from GR, since it is very sensitive to the underlying gravitational theory which directly affects the evolution of matter density perturbations. In linear theory these are parameterized via the growth parameter $\delta_m = \frac{\delta\rho_m}{\bar{\rho}_m}$ and its logarithmic derivative $f \equiv \frac{d\ln\delta_m}{d\ln a}$ called the growth-rate, where $\bar{\rho}_m$ is the background matter density and $\delta\rho_m$ its perturbation to linear order. The growth-rate can also be expressed in terms of the γ parameter, which is useful when looking for deviations from GR, as in the ΛCDM model $\gamma \simeq 6/11$ and is defined via $f(z) = \Omega_m^{\gamma}(z)$. In the ΛCDM model the fact that the growth rate is scale-invariant on large scales makes it a key discriminator [339].

The main advantage of the growth is that over time it can provide information about gravity and DE and how both can be evolving as the Universe expands. The reason for this is that LSS observations in cosmology have the advantage of requiring only linear physics, which makes them an especially clean and highly successful probe [340]. They can help in understanding what is the expansion rate of the Universe and how do structures form within the cosmological background. At the perturbations level, the growth of matter perturbations provides a useful tool to investigate the matter distribution in the Universe, and, more importantly, it can be measured from observations. The measurement of the growth index provides an efficient way to discriminate between modified gravity models and DE models which are developed in the context of GR [141]. The effect of DE on the growth of perturbations is therefore an important tool in discriminating models from ΛCDM [207] and models that are fully degenerate at the background level [9, 201–204].

As we have discussed in Chapter 9, Machine Learning (ML) will play a big role in testing accurately the standard model of cosmology, but will also help in the search for new physics and tensions in the data by placing tighter constraints on cosmological parameters [402–404]. While a central goal of modern ML research is to learn and extract important features directly from data [418], ML methods have also been applied to reconstruct null tests of ΛCDM, i.e. quantities that are supposed to be exactly constant for all redshifts [168, 419–424]. In this paper we present a unified ML analysis of all the currently available cosmological data in order to reconstruct several key background and perturbations variables in a model-independent manner in order to explore the nature of DE. For example, such variables include the DE equation of state and the DE anisotropic stress, which we then use to test for deviations from ΛCDM.

The structure of our paper is as follows: In Section 12.2 we present the theoretical background of our work and our notation, in Section 12.3 we describe in detail the cosmological data

we used in our analysis, in Section 12.4 we present the details of our implementation of the ML approach, while in Section 12.5 we present our methodology and the minimal assumptions we made for the reconstruction of the data. Then, in Section 12.6 we present the exact fits of the reconstruction and our main results, while in Section 12.7 we present our Conclusions.

12.2 Theory

Here we present some theoretical material regarding the quantities we reconstruct in what follows. The DE equation of state $w(z) \equiv \frac{P}{\rho}$ and the deceleration parameter $q(z) \equiv -\frac{\ddot{a}}{aH(a)^2}$ can be written as [490]

$$w(z) = -1 + \frac{1}{3}(1+z)\frac{d\ln(\Omega_{\rm DE}(z))}{dz}, \tag{12.1}$$

$$q(z) = -1 + (1+z)\frac{d\ln(H(z))}{dz}, \tag{12.2}$$

where $\Omega_{\rm DE}(z) \equiv H(z)^2/H_0^2 - \Omega_{m,0}(1+z)^3$ is the DE energy density. When $w(z) = -1$ we recover the ΛCDM model, for which $q_0 = q(z=0) = -1 + \frac{3\Omega_{m0}}{2}$. Here and in what follows we will neglect radiation as it is negligible at late times when we perform our reconstructions. We also constrain the DE adiabatic sound speed $c^2_{\rm s,DE}(z)$, which can be written in terms of the DE equation of state $w(z)$ as

$$\begin{aligned} c^2_{\rm s,DE}(z) &= \frac{\delta P_{\rm DE}}{\delta \rho_{\rm DE}} \\ &\simeq w(z) + \frac{1+z}{3}\frac{w'(z)}{1+w(z)}. \end{aligned} \tag{12.3}$$

We also consider the number counts of luminous sources, which are given by [502]

$$n(z) = \frac{4\pi \mathcal{N}_0 d_{\rm L}(z)^2}{H(z)(1+z)^2}, \tag{12.4}$$

where $\mathcal{N}_0 \equiv \int_0^\infty \mathcal{N}_0(L)dL$ is the total number of sources per proper volume integrated over all luminosities. Next we also present the variables related to the matter density perturbations, in particular the growth index $\gamma(a)$, which is defined via [338]

$$f(a) = \Omega_{\rm m}(a)^{\gamma(a)}, \tag{12.5}$$

where $f(a) = \frac{d\ln\delta_m}{d\ln a}$ is the logarithmic derivative of the growth of matter perturbations $\delta_m(a) \equiv \frac{\delta\rho_m}{\rho_m}$, the matter density is given by $\Omega_{\rm m}(a) = \frac{\Omega_{\rm m,0}a^{-3}}{H(a)^2/H_0^2}$ and $H(a) \equiv \frac{\dot{a}}{a}$, is the Hubble parameter as a function of the dimensionless scale factor $a = \frac{1}{1+z}$ that describes the expansion of the universe. Solving for the growth index we find that it can be expressed as

$$\gamma(a) = \frac{\ln(f(a))}{\ln(\Omega_{\rm m}(a))} = \frac{\ln(f(a))}{\ln\left(\frac{\Omega_{\rm m,0}a^{-3}}{H(a)^2/H_0^2}\right)}. \tag{12.6}$$

We can now proceed to re express the various quantities contained in Eq. (12.6) with ones that can be reconstructed directly from the data. Assuming a homogeneous and isotropic universe in GR, with no DE perturbations and neglecting neutrinos, then the growth factor $\delta_m(a)$ satisfies the differential equation:

$$\delta_m''(a) + \left(\frac{3}{a} + \frac{H'(a)}{H(a)}\right)\delta_m'(a) - \frac{3}{2}\frac{\Omega_{\rm m,0}}{a^5 H(a)^2/H_0^2}\delta_m(a) = 0. \tag{12.7}$$

At this point it should be noted that while here we neglect neutrinos in order to streamline the analysis, in general they can have a large effect on the amplitude and slope at LSS scales. Regarding the growth, what is measurable is not exactly the growth $\delta_m(a)$, but the combination

$$\begin{aligned} f\sigma_8(a) &\equiv f(a)\cdot\sigma(a) \\ &= \frac{\sigma_8}{\delta_m(1)}\, a\, \delta_m'(a), \end{aligned} \tag{12.8}$$

where $f(a)$ is the growth rate and $\sigma(a) = \sigma_8 \frac{\delta_m(a)}{\delta_m(1)}$ is the redshift-dependent rms fluctuations of the linear density field at $R = 8h^{-1}$Mpc while the parameter σ_8 is its value today. The combination of $f\sigma_8(a)$ is bias-free as both $f(a)$ and $\sigma_8(a)$ have a dependence on bias which is the inverse of the other, thus cancels out, and it has been shown to be a good discriminator of DE models [118]. Performing direct manipulations of the definition of $f\sigma_8$ of Eq. (12.7) and Eq. (12.8) one can show, see also Ref. [292], that

$$\frac{\delta_m(a)}{\delta_m(1)} = \frac{1}{\sigma_8}\int_0^a \frac{f\sigma_8(x)}{x}dx \tag{12.9}$$

$$H(a)^2/H_0^2 = \frac{3\Omega_{m,0}}{a^4 f\sigma_8(a)^2}\int_0^a dx f\sigma_8(x)\int_0^x dy \frac{f\sigma_8(y)}{y}, \tag{12.10}$$

but also the useful relations:

$$\sigma_8 = \int_0^1 \frac{f\sigma_8(x)}{x}dx \tag{12.11}$$

$$\Omega_{\rm m,0} = \frac{1}{3\int_0^1 dx \frac{f\sigma_8(x)}{f\sigma_8(1)}\int_0^x dy \frac{1}{y}\frac{f\sigma_8(y)}{f\sigma_8(1)}}. \tag{12.12}$$

Combining Eqs. (12.6) and (12.9)-(12.10), we obtain our main result for the growth index:

$$\gamma(a) = \frac{\ln\left(\frac{f\sigma_8(a)}{\int_0^a \frac{f\sigma_8(x)}{x}dx}\right)}{\ln\left(\frac{af\sigma_8(a)^2}{3\int_0^a dx f\sigma_8(x)\int_0^x dy \frac{f\sigma_8(y)}{y}}\right)}. \tag{12.13}$$

The main advantages of Eq. (12.13) are that it only requires knowledge of $f\sigma_8(a)$ and does not depend on Ω_{m0} or $H(a)$, σ_8 or any other parameter. Finally, exploiting the Noether symmetries of Eq. (12.7) we can define a conserved charge that has to be constant at all times and redshifts, thus is an ideal null test. Following this procedure, in Ref. [429] it was shown that a null test for the growth can be written as

$$\mathcal{O}(z) = a^2 E(a)\frac{f\sigma_8(a)}{f\sigma_8(1)}e^{I(z)}, \tag{12.14}$$

$$I(z) = -\frac{3}{2}\Omega_{m_0}\int_1^a \frac{\sigma_{8_0} + \int_1^x \frac{f\sigma_8(y)}{y}dy}{x^4 E(x)^2 f\sigma_8(x)}dx, \tag{12.15}$$

where we define $\sigma_{8_0} \equiv \sigma_8(a=1)$ for simplicity and we have set $E(a) \equiv \frac{H(a)}{H_0}$. It is clear that Eq. (12.15) has to be constant for all redshifts z and moreover, $\mathcal{O}(z)$ has to be equal to 1 as any deviation from unity might hint towards a deviation from the FLRW metric, non zero DE perturbations, a deviation from GR or a tension between the $H(z)$ and $f\sigma_8$ data.

12.3 The data

The data used in this analysis is explained in detailed in Chapter 2. In specific we have used the Hubble expansion data $H(z)$, the supernovae type Ia data, the baryon acoustic oscillations data, the growth-rate data and the E_g data.

12.4 The Genetic Algorithms

A full description on how the Genetic Algorithms operate can be found in Chapter 10. There we have also discussed the error analysis treatment and now we will expand that part to accommodate it to the expressions we are seeing in this Chapter. One can derive for example the error of the Om statistic, which can be reconstructed using the GA best-fit $H_{\rm GA}(z)$, see Chapter 11 and Ref. [419]. The Om statistic is a null test, i.e. a true/false statement or equivalently a consistency test, that has to be true at all redshifts if the ΛCDM is the real underlying physical model. It is derived by solving the Friedmann equation [168, 426]

$$H(z)^2/H_0^2 = \Omega_{\rm m,0}(1+z)^3 + 1 - \Omega_{\rm m,0}, \tag{12.16}$$

for $\Omega_{\rm m,0}$ using simple algebraic manipulations, so its value should be equal to that of $\Omega_{\rm m,0}$ if and only if the ΛCDM is the true model. Thus, using a model-independent approach to reconstruct the Hubble parameter $H(z)$ we can probe for deviations from ΛCDM in a straight-forward manner. Noting that the Om statistic is defined as

$$\mathrm{Om}(z) \quad = \quad \frac{H(z)^2/H_0^2 - 1}{(1+z)^3 - 1}, \tag{12.17}$$

then, using the aforementioned approach we find the error on the Om statistic is

$$\delta\mathrm{Om}(z) \quad = \quad \frac{2H_{\rm GA}(z)\delta H(z)/H_0^2}{(1+z)^3 - 1}, \tag{12.18}$$

as expected for traditional error propagation as well.

Similarly, one can derive the error propagation of a quantity that depends on two reconstructed quantities by the GA. The procedure is exactly the same as before and we now consider the example of the DE energy density parameter $\Omega_{\rm DE} = \frac{H(z)^2}{H_0^2} - \Omega_{\rm m,0}(1+z)^3$, where we assume the two reconstructed quantities are $H(z)$ and $\Omega_{\rm m,0}$, each being described by a normal distribution. In this case the error on $\Omega_{\rm DE}$ can be found to be:

$$\delta\Omega_{\rm DE}(z)^2 \simeq 4\frac{H(z)^2}{H_0^2}\frac{\delta H(z)^2}{H_0^2} + (1+z)^6\delta\Omega_{\rm m,0}^2 + \cdots, \tag{12.19}$$

again in agreement with the expected value from standard error propagation.

We also have to calculate quantities that contain derivatives, such as the DE equation of state or the deceleration parameter. In this case we will assume that we can model the error propagation as a variation of the functions during the evolution of the functional space of the GA, i.e. $\delta f = \delta(f)$. This is in agreement with the previous approach as if we assume $g = f^2$ then we have $\delta g = 2f\delta f$ as expected. We can further assume that the variational δ commutes with derivatives, i.e. $\delta(\frac{df}{dx}) = \frac{d}{dx}(\delta f(x))$. The reason for this is that we can always assume that at any point x functions f that are close to the best-fit, can be written as $f \simeq f_{\rm GA} + \delta f$, so that $\frac{df}{dx} \simeq \frac{df_{\rm GA}}{dx} + \frac{d\delta f}{dx}$, which implies $\delta(\frac{df}{dx}) \simeq \frac{df}{dx} - \frac{df_{\rm GA}}{dx} \simeq \frac{d\delta f}{dx}$ as mentioned before. For example, in the case of the deceleration parameter we have:

$$q_{\rm GA}(z) \quad = \quad -1 + (1+z)\frac{d\ln H_{\rm GA}}{dz}, \tag{12.20}$$

which implies that the error is

$$\delta q(z) \quad = \quad (1+z)\delta\left[\frac{d\ln H}{dz}\right] = (1+z)\frac{d}{dz}\left[\delta\ln H\right] = (1+z)\frac{d}{dz}\left[\frac{\delta H}{H_{\rm GA}}\right]. \tag{12.21}$$

Similarly, we will assume that the variational δ commutes with integrals, an assumption commonly made in variational calculus, so that for example for the σ_8 parameter we have:

$$\sigma_{8,\rm GA} \quad = \quad \int_0^1 \frac{f\sigma_{8,\rm GA}(x)}{x}dx \tag{12.22}$$

and the corresponding error on the derived GA best-fit is

$$\delta\sigma_8 \quad = \quad \int_0^1 \frac{\delta f\sigma_8(x)}{x} dx. \tag{12.23}$$

Then, for the matter density parameter Ω_{m0} we also have

$$\Omega_{m,0\mathrm{GA}} \quad = \quad \frac{1}{3\int_0^1 dx \frac{f\sigma_{8\mathrm{GA}}(x)}{f\sigma_{8\mathrm{GA}}(1)} \int_0^x dy \frac{1}{y} \frac{f\sigma_{8\mathrm{GA}}(y)}{f\sigma_{8\mathrm{GA}}(1)}} = \frac{1}{3\int_0^1 dx F(x) \int_0^x dy \frac{1}{y} F(y)}, \tag{12.24}$$

where $F(x) = \frac{f\sigma_{8\mathrm{GA}}(x)}{f\sigma_{8\mathrm{GA}}(1)}$. Then, the error is

$$\frac{\delta\Omega_{m,0}}{3\Omega_{m,0}^2} \quad = \quad \left| \int_0^1 dx \left[\delta F(x) \int_0^x dy \frac{F(y)}{y} + F(x) \int_0^x dy \frac{\delta F(y)}{y} \right] \right|, \tag{12.25}$$

where we have set

$$\delta F(a) \quad = \quad \delta\left(\frac{f\sigma_8(a)}{f\sigma_8(1)}\right) = \frac{\delta f\sigma_8(a)}{f\sigma_{8\mathrm{GA}}(1)} - \frac{f\sigma_{8\mathrm{GA}}(a)}{f\sigma_{8\mathrm{GA}}(1)^2}\, \delta f\sigma_8(1). \tag{12.26}$$

12.5 Methodology

We will now describe how to reconstruct using the GA the Hubble parameter $H(z)$ from the Hubble expansion history $H(z)$ data, the luminosity distance $d_{\mathrm{L}}(z)$ from the Pantheon Type Ia supernovae (SnIa) data, the angular diameter distance $d_{\mathrm{A}}(z)$ from Baryon Acoustic Oscillations (BAO), $f\sigma_8(z)$ from the growth-rate data obtained via the redshift-space distortions (RSD) and $P_2(z)$ from the E_{g} data.

These functions will in turn be used to reconstruct the DE anisotropic stress $\eta_{\mathrm{DE}}(z)$ (see Sec. 2.2.2 for a more detailed explanation), the growth index $\gamma(z)$, the DE equation of state $w(z)$ and the DE adiabatic sound speed $c^2_{\mathrm{s,DE}}(z)$. Furthermore, we will also reconstruct the growth rate null test $\mathcal{O}(z)$ presented in Ref. [429] as a consistency test of the ΛCDM model and the number counts of luminous sources $n(z)$. We also derive the matter density $\Omega_{\mathrm{m,0}}$ and the root mean square (rms) density fluctuation σ_8 from the $f\sigma_8$ data, the value of the Hubble constant H_0 and the sound horizon at the drag epoch r_{d} from the BAO data.

As mentioned in the previous section, in order to reconstruct the data we will only make very few minimal physical or mathematical assumptions, but we will make no assumption of a DE model or that the spatial curvature of the Universe is zero, i.e. flatness. However, we will assume homogeneity, isotropy and the Friedmann-Robertson-Walker (FRW) metric. Specifically we have assumed:

1. The Hubble parameter today is given by the Hubble constant $H(z=0) = H_0$. Then, H_0 is estimated directly from the $H(z)$ data.
2. We assume the Hubble law at low redshifts $d_{\mathrm{L}}(z \simeq 0) \simeq \frac{c}{H_0} z$. We use the Hubble constant H_0 from the $H(z)$ fit to break the degeneracies with the absolute SnIa magnitude.
3. Similarly, at low redshifts we assume $d_{\mathrm{A}}(z \simeq 0) \simeq \frac{c}{H_0} z$ due to the Hubble law. We make no assumptions for the sound horizon at drag redshift r_{d}, which is minimized over.
4. The Universe at early times went through a phase of matter domination ($z \simeq 100$), so the linear growth behaves as $\delta_m(a) \simeq a$ at high redshifts.

We also note that the growth rate data has a dependence on the fiducial model which can be corrected by rescaling the measurements by the ratios of $H(z)D_{\mathrm{A}}(z)$ as it is explained in

Ref. [120]. Finally, the SnIa contain some model dependence, as one must optimize parameters in the lightcurve function simultaneously with those of the assumed model. This mainly affects the covariance matrix, which is typically inferred based on an fiducial background model, usually ΛCDM. However, since in our case the best-fit is close to ΛCDM and the errors are much larger than the effects of the model-bias in the covariance, we can safely assume for now that these effects have a minimal effect on the minimization.

For illustration purposes we also present in Fig. 12.1 a flowchart of the whole fitting process. To estimate the errors on these reconstructed quantities we use the *Path Integral* approach developed by Refs. [169, 417], where one calculates analytically a path integral over the whole functional space that can be scanned by the GA. Then this error is propagated onto the various derived quantities with the error propagation approach described in detail in Sec. 10.0.2.

12.6 Results

Here we present the results of our analysis by considering all data separately. Specifically we show the reconstructions of all relevant quantities including the DE equation of state $w_{\rm DE}(z)$, the DE adiabatic sound speed $c^2_{\rm s,DE}(z)$, the growth index $\gamma(z)$, the $\mathcal{O}(z)$ test, the DE anisotropic stress $\eta_{\rm DE}(z)$, the number counts of luminous sources $n(z)$ and σ_8.

First, we fit the BAO data without assuming the value of H_0 given by the $H(z)$ reconstruction. To perform the reconstruction of the BAO data we minimize the χ^2 over the quantity $r_{\rm sh} = r_{\rm s} \cdot h$, where $r_{\rm s}$ is the sound horizon at the drag redshift and h is the Hubble parameter, thus avoiding any bias of the results due to a specific value of H_0. This reconstruction will affect the growth-rate $f\sigma_8$, and thereby the growth index γ and the $O(z)$ test, but also the secondary parameters: $\Omega_{\rm m,0}$ and σ_8. This in turn affects the equation of state $w(z)$ and the dark energy sound speed $c^2_{\rm s,DE}$ since they depend on the value of $\Omega_{\rm m,0}$, see Eq. (12.1). Finally, the DE anisotropic stress also depends on the $f\sigma_8$ reconstruction.

In particular, the plots of the reconstructed quantities are shown in Fig. 12.2 for the SnIa and $H(z)$ data, while in Fig. 12.3 for the $f\sigma_8$ and $E_{\rm g}$ data. In both cases, we show both the ΛCDM best-fit (blue line) and the GA best-fit (red line), while the red and grey shaded region correspond to the 1σ confidence region for the GA and ΛCDM respectively and the actual data are shown as grey points in the background. The best-fit functions are then as follows:

$$H(z)/H_0 = \left(1 + z\left(-0.676 - 0.221z + 0.018z^3\right)^2\right), \tag{12.27}$$

$$d_{\rm L}(z) = \frac{c}{H_0} z\left(1 + z\left(0.872 - 0.133z - 0.002z^2\right)^2\right), \tag{12.28}$$

$$\frac{H_0}{c} d_{\rm A}(z) = D_{\rm A}(z) = \frac{z}{(1+z)^2}\left(1 + z\left(0.885 - 0.175z + 0.025z^2 - 0.00003z^5\right)^2\right), \tag{12.29}$$

$$f\sigma_8(a) = f_0\left(a - a^4\left(-1.675 + 0.870a + 0.001a^2\right)^2\right), \tag{12.30}$$

$$P_2(a) = \left(-0.434a - 0.414ae^{0.666a} - 0.011a^{2.060}\right)^2, \tag{12.31}$$

where $f_0 = 1.06477$, while we also find the following derived parameters

$$\sigma_8 = 0.805 \pm 0.246, \tag{12.32}$$

$$\Omega_{\rm m,0} = 0.254 \pm 0.025, \tag{12.33}$$

$$\gamma_0 = 0.5549 \pm 0.0003, \tag{12.34}$$

$$r_{\rm sh} = 101.873 \pm 2.078 \text{ Mpc/h}, \tag{12.35}$$

$$w_{\rm GA,0} = -0.932 \pm 0.177. \tag{12.36}$$

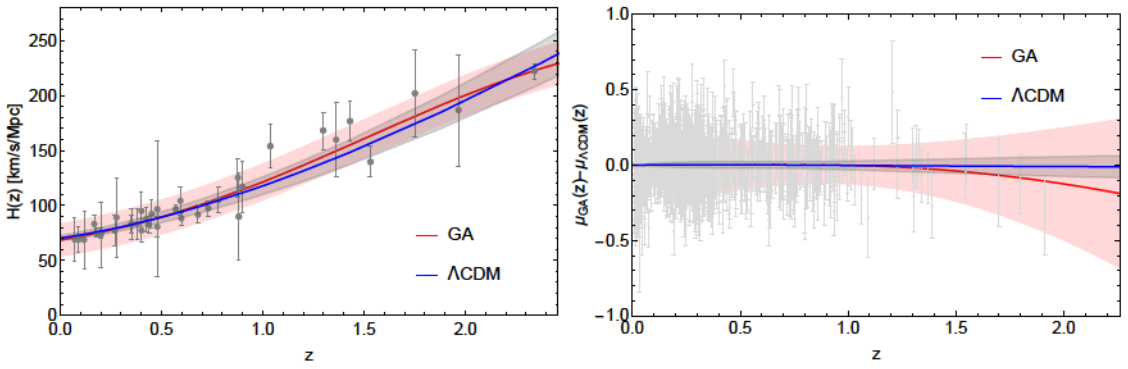

Figure 12.2: Left: The $H(z)$ data compilation along with the ΛCDM best-fit (blue line) and the GA best-fit (red line). Right: The difference between the GA best-fit distance modulus of the Pantheon SnIa data (red line) and that of the ΛCDM model (blue line). In both cases the red and grey shaded regions correspond to the 1σ confidence region for the GA and ΛCDM respectively, and the actual data are shown as grey points in the background.

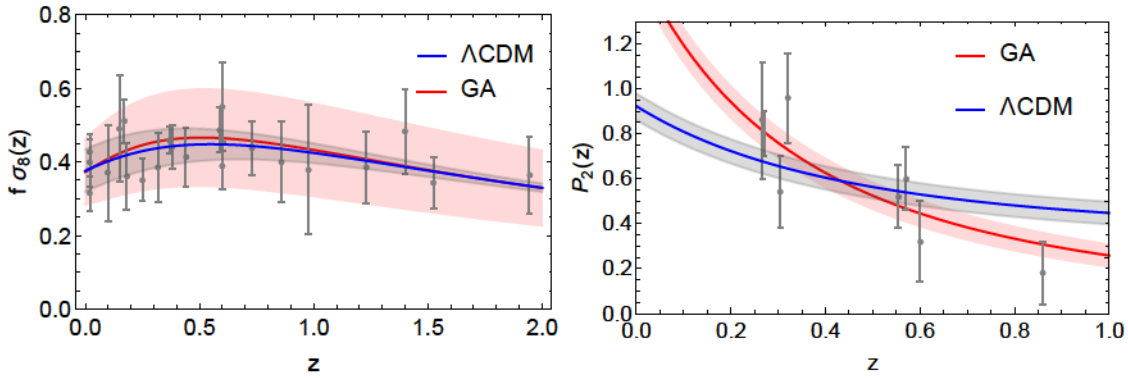

Figure 12.3: Left: The $f\sigma_8$ data compilation along with the ΛCDM best-fit (blue line) and the GA best-fit (red line). The GA reconstruction follows both the data and the ΛCDM model closely. Right: The P_2 parameter of Ref. [145] along with the E_g data given in Table 2.5. In both cases the red and grey shaded regions correspond to the 1σ confidence region for the GA and ΛCDM respectively, and the actual data are shown as grey points in the background.

Note that $E(z) = H(z)/H_0$ is reconstructed directly from the $H(z)$ data, without assuming a value of H_0. However, using Eq. (2.3) of Chapter 2 we can derive a value for H_0 as well, while from the $H(z)$ data we also get

$$q_{\rm GA,0} = -0.543 \pm 0.118, \tag{12.37}$$

$$z_{\rm GA,tr} = 0.641 \pm 0.023, \tag{12.38}$$

where z_{tr} is the value of the transition redshift, i.e. the redshift at which the deceleration parameter changes sign.

In Fig. 12.4 we show the DE equation of state $w(z)$ given by Eq. (12.1) (left panel) and the adiabatic sound speed $c^2_{\rm s,DE}$ (right panel), where the latter is given by Eq. (12.3). As can be seen, the equation of state $w(z)$ is consistent with ΛCDM at low redshifts, but shows a mild 2σ tension at $z \sim 1$, thus hinting that deviations from the ΛCDM could happen at higher redshifts as claimed in Ref. [56]. In the case of the adiabatic sound speed we focus on small redshifts as the earliest we can reconstruct it from the Hubble data is at $z > 0.07$. As we can see, the adiabatic sound speed is evolving and is negative at the $\sim 2.5\sigma$ level at $z = 0.1$, which implies that DE either has a dominant non-adiabatic component at small redshifts or it should have anisotropic stress, as

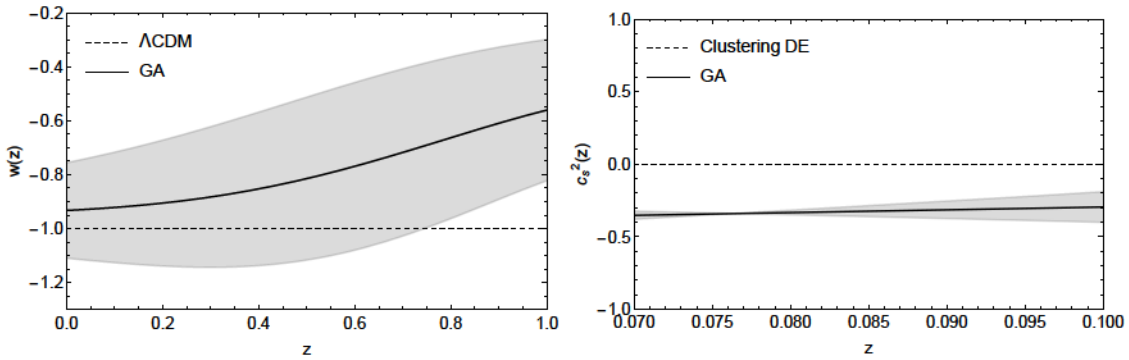

Figure 12.4: Left: The DE equation of state $w(z)$ given by Eq. (12.1), using the GA reconstruction of the Hubble data and the value of $\Omega_{\rm m,0}$ found from the growth data. We find that at high redshifts ($z \gtrsim 0.8$) there is a mild $\sim 1.5\sigma$ deviation from the ΛCDM model. The dashed line corresponds to the theoretical prediction of the ΛCDM model, while the solid black line and the grey region to the GA best-fit and the 1σ errors. Right: The adiabatic DE sound speed $c^2_{\rm s,DE}$ given by Eq. (12.3). The dashed line corresponds to clustering DE with $c_s^2 = 0$, while the solid black line and the grey region to the GA best-fit and the 1σ errors.

otherwise the matter density perturbations would be unstable [235].

In the left panel of Fig. 12.5 we show the $\mathcal{O}(z)$ test of Refs. [420, 429] given by Eq. (12.15). The dashed line corresponds to the theoretical prediction of the ΛCDM model, while the solid black line and the grey region to the GA best-fit and the 1σ errors. We find that the test is consistent with ΛCDM within the errors. In the right panel of Fig. 12.5 we show the anisotropic stress parameter $\eta_{\rm DE}(z)$ given by Eq. (2.36). The dashed line corresponds to the theoretical prediction of the ΛCDM model (no DE anisotropic stress), while the solid black line and the grey region to the GA best-fit and the 1σ errors. We find that there are deviations present at both low and high redshifts at the $\sim 2\sigma$ and $\sim 4\sigma$ level respectively.

In the left panel of Fig. 12.6 we show the number counts of luminous sources given by Eq. (12.4). The dashed line corresponds to the theoretical prediction of the ΛCDM model, while the solid black line and the grey region to the GA best-fit and the 1σ errors. We find that the reconstructions agree with the theoretical prediction of the ΛCDM model within the errors. In the right panel of Fig. 12.6 we show the growth index of the matter density perturbations $\gamma(z)$, which is given by Eq. (12.13) and which we find to be consistent within the errors with the theoretical predictions of the ΛCDM model.

The deviations found in the DE anisotropic stress reconstructed from the $E_{\rm g}$ data and the DE equation of state $w(z)$ using the $H(z)$ data may hint either to unaccounted for systematics, possibly non-negligible radiative processes or new physics. For example, a potential source of the deviations observed with the $E_{\rm g}$ data may be due to the lensing magnification. In Refs. [503, 504] it was shown that lensing magnification modifies both the galaxy-galaxy lensing correlations and the galaxy-galaxy correlations. As a result, lensing magnification both introduces systematic errors in the determination of $E_{\rm g}$ and makes it bias dependent. For a more in-depth discuss of the systematics see also Ref. [139].

We should note that traditionally one would compare the χ^2 per degree of freedom (dof), where the latter is traditionally defined as the number of points (36 $H(z)$ + 1048 SnIa + (4 + 3 + 2 + 2 + 1) BAO + 22 growth + 8 $E_{\rm g}$ = 1126 points in our analysis) minus the number of free parameters of the model in question. As the GA have no free parameters, we cannot compare the dof between the GA and the ΛCDM model.

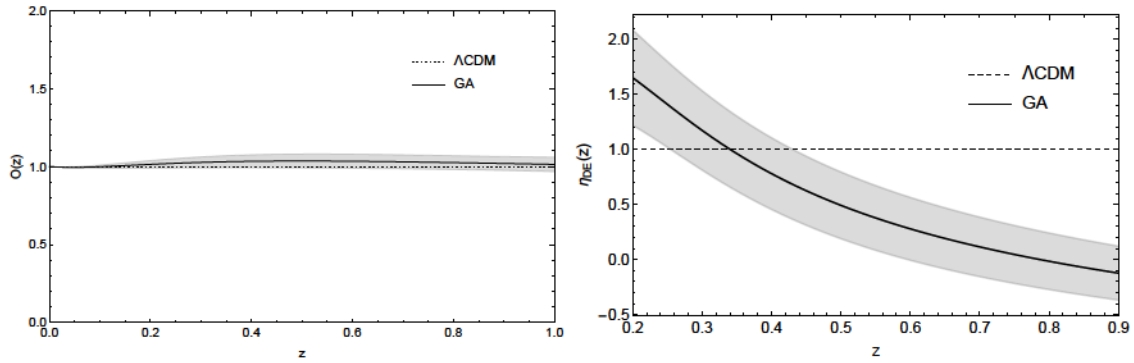

Figure 12.5: Left: The $\mathcal{O}(z)$ test of Refs. [420, 429] given by Eq. (12.15). The dashed line corresponds to the theoretical prediction of the ΛCDM model (no DE anisotropic stress), while the solid black line and the grey region to the GA best-fit and the 1σ errors. We find that the test is consistent with ΛCDM within the errors. Right: The anisotropic stress parameter $\eta_{\rm DE}(z)$ given by Eq. (2.36). The dashed line corresponds to the theoretical prediction of the ΛCDM model (no DE anisotropic stress), while the solid black line and the grey region to the GA best-fit and the 1σ errors. We find that there are deviations present at both low and high redshifts at the $\sim 2\sigma$ and $\sim 4\sigma$ level respectively.

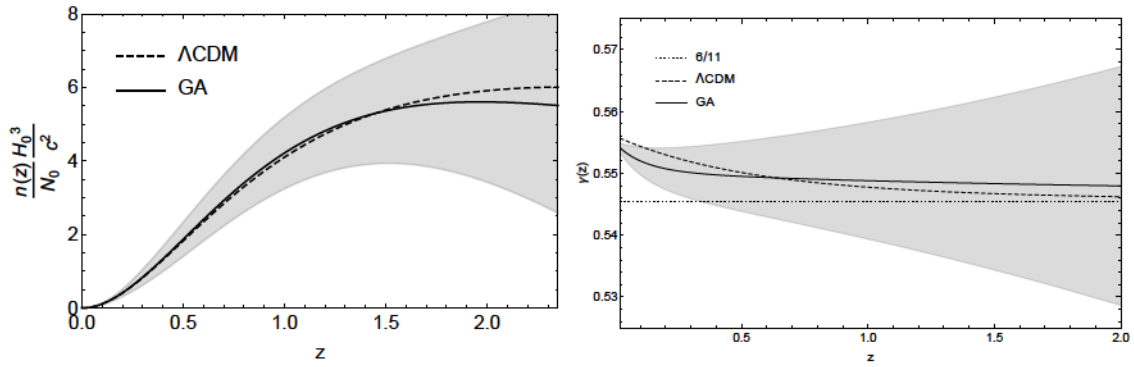

Figure 12.6: Left: The number counts of luminous sources given by Eq. (12.4). The dashed line corresponds to the theoretical prediction of the ΛCDM model, while the solid black line and the grey region to the GA best-fit and the 1σ errors. Right: The growth index $\gamma(z)$ of the matter density perturbations given by Eq. (12.13). The dashed line corresponds to the ΛCDM model, the dotted line to the rough estimate $\gamma \sim \frac{6}{11}$, while the solid black line and the grey region to the GA best-fit and the 1σ errors. We find that both reconstructions are consistent with the ΛCDM model.

12.7 Conclusions

In summary, we use the Genetic Algorithms (GA), a specific machine learning method, to reconstruct the evolution of the background history of the Universe and the matter density perturbations, based on a plethora of cosmological data including SnIa, BAO, $H(z)$, $E_{\rm g}$ and growth rate data. The GA can provide another method to probe underlying physical models, whilst also giving error estimates in agreement with approaches such as Fisher and MCMC [169]. In particular this has been shown to be the case with cosmological data based on several different fiducial models such as the ΛCDM model and modified gravity theories [471], but also models that violate the distance duality relation [470].

Using then the GA and the cosmological data described in Sec. 12.3, we find that there is a $\sim 2\sigma$ deviation of $w(z)$ from -1 at high redshifts, the adiabatic sound speed $c^2_{\rm s,DE}$ is evolving and

is negative at the $\sim 2.5\sigma$ level at $z = 0.1$, while using the $E_{\rm g}$ data we find a $\sim 2\sigma$ deviation of the anisotropic stress $\eta_{\rm DE}(z)$ from unity at low redshifts and $\sim 4\sigma$ at high redshifts, thus suggesting the presence of significant deviations from the ΛCDM model. The reconstructions of these quantities in terms of the redshift z, along with the 1σ error regions, is shown in Figs. 12.4 and 12.5.

As mentioned earlier, our approach has been validated via the use of mocks, see Refs. [470, 471], so clearly then the aforementioned deviations from the ΛCDM model present a problem as they hint towards two possibilities, either the presence of unaccounted for systematics and possibly non-negligible radiative processes, as might be the case for the $E_{\rm g}$ data, or new physics in the form of modifications of gravity. The latter case is quite plausible, as the deviations come from very different data sets with very different systematics, i.e. the equation of state $w(z)$ and $c^2_{\rm s,DE}$ from the $H(z)$ data, the growth index from the growth data coming from the RSD measurements and the $\eta_{\rm DE}(z)$ from the $E_{\rm g}$ data.

Specifically, the fact that the adiabatic sound speed $c^2_{\rm s,DE}$ is both evolving and negative, implies that the DE perturbations would be unstable unless there exists either a strong anisotropic stress, coming for example from some modification of gravity, so that the total effective sound speed is positive, as shown in Ref. [235] or a non-adiabatic DE component [327]. In particular, using the effective fluid approach it can be shown that in $f(R)$ models, like the Hu-Sawicki or the designer model, the sound speed of the effective DE fluid is negative and the matter perturbations are stable due to the anisotropic stress [9], hence lending more support to modified gravity scenarios.

A possible caveat in our analysis is that there is some overlap between the BAO and $H(z)$ data, which could induce spurious correlations between the two data sets. Since unfortunately, we do not have access to the covariance matrices, we are not able to take this covariance into account, thus possibly underestimating the errors in our analysis, hence we analyze them separately. This is also the case for the $E_{\rm g}$ and the growth rate data, which come from overlapping surveys, however again we do not have the covariance matrices.

However, our approach is completely agnostic as we made no assumptions about the nature of DE or the spatial curvature of the Universe during the fitting of our data. This is one of the main advantages of our ML approach compared to other traditional or non-parametric methods such as cosmography which suffers from convergence issues at high redshifts or Gaussian processes that assume a fiducial model. As the GA can provide model-independent reconstructions of key parameters that describe DE, then if indeed there are no systematics in the data, the observed model-independent deviations from ΛCDM could point to the existence of new physics. The possibility of such an exciting prospect could be further strengthened by the upcoming cosmological surveys like LSST [394].

13

Machine Learning meets the redshift evolution of the CMB Temperature

The original content of this chapter is based on Ref. [403]. We present a model independent and non-parametric reconstruction with a Machine Learning algorithm of the redshift evolution of the Cosmic Microwave Background (CMB) temperature from a wide redshift range $z \in [0, 3]$ without assuming any dark energy model, an adiabatic universe or photon number conservation. In particular we use the Genetic Algorithms (GA) which avoid the dependency on an initial prior or a cosmological fiducial model. Through our reconstruction we constrain new physics at late times. We provide novel and updated estimates on the β parameter from the parametrisation $\mathrm{T}(z) = \mathrm{T}_0(1+z)^{1-\beta}$, the duality relation $\eta(z)$ and the cosmic opacity parameter $\tau(z)$. Furthermore we place constraints on a temporal varying fine structure constant α, which would have signatures in a broad spectrum of physical phenomena such as the CMB anisotropies. Overall we find no evidence of deviations within the 1σ region from the well established ΛCDM model, thus confirming its predictive potential.

13.1 Introduction

Our current knowledge for the evolution of the Universe as a whole from the first fraction of a second to our present day, about 13.6 billion years later, rests upon the successful hot Big Bang cosmological model [505]. It is built on the robust theoretical framework of General Relativity (GR) and based on well tested observations such as the expansion of the Universe [506], the relative abundance of light elements [507] and the cosmic microwave background (CMB) [508]. The presence of the latter is considered to be the best indication for a primordial expanding state of the Universe originating from an initial high density state to become an almost perfect isotropic blackbody radiation at a temperature of about 3K and whose emission we receive around $380,000$ years after the Big Bang.

The hot Big Bang model predicts that the CMB photon energy is redshifted with the cosmic expansion. In other words, the Universe has a hot and dense past and cools as it expands adiabatically according to the linear average temperature-redshift relation (TRR) of the CMB, $\mathrm{T}_{\mathrm{CMB}}(z) = \mathrm{T}_0(1+z)$ where $\mathrm{T}_0 = (2.72548 \pm 0.00057)\mathrm{K}$ is the local measurement of the CMB temperature today i.e. at $z = 0$ [108] and $\mathrm{T}_{\mathrm{CMB}}(z)$ represents the temperature measured by an observer at redshift z. This relation is not confined to a specific metric theory, holding in the framework of GR and the electromagnetic theory of Maxwell under the assumption that photons are massless, the CMB is thermal radiation, the first law of thermodynamics is true and that the expansion of space is isotropic [509]. Although this linear temperature relation is well established [113] and departures from it would require important distortions in the Planck spectrum of the CMB [510], it can be modified for example [511] by adding extra components such as a decaying vacuum energy density or some process of quantum gravitational origin that could affect the adiabatic photon production (or destruction), due to late inflationary models induced by a

scalar field, in string theory models where axions and photons could be mixed [512] or theories with deviations from homogeneity and isotropy.

To constrain deviations from adiabatic evolution, the following power-law $\mathrm{T_{CMB}}(z) = \mathrm{T_0}(1+z)^{1-\beta}$ is commonly used, where β is the parameter of the theory and $\beta > 0$ or $\beta < 0$ would be compatible with net photon production or destruction respectively [510]. It is also of great interest models where some fundamental constants are not space-time invariant, such as the fine structure constant α. This effect can be found for example in theories with extra compact dimensions (aiming to unify gravity and other fundamental forces), where the cosmic evolution of the scale factor will have a time dependence on the coupling constants [513]. A different possibility is the inclusion of a new scalar field with couplings to the Maxwell scale factor $F_{ab}F^{ab}$ whose evolution involves a variation of α [514].

One of the first convincing evidence for a cosmic expansion came in 1998 as a result of an unanticipated dimming through the observed light of type Ia supernovae (SNIa) [87]. Although the cosmic acceleration has been asserted through other independent probes like the CMB [515], baryon acoustic oscillations (BAO) [80] or the Hubble parameter [1], the presence of some cosmic opacity that can contribute to astronomical photometric measurements of distant SNe Ia is still an open possibility [516]. As mentioned in Ref. [517], opacity sources could come from the non-conservation of the photon number density, which in turns changes the temperature-redshift and the distance duality relation, or from MG theories with non-minimal couplings between the electromagnetic Lagrangian and a new scalar field [518]. If there is some extra dimming contribution, this would have an imprint in the cosmological parameters and the expansion rate inferred from SNe Ia measurements. Hence, testing the cosmic opacity parameter denoted as $\tau(z)$ and in turn the duality relation $\eta(z)$ where both are related through the parametrization $e^{\tau(z)/2} = \eta(z)$ [517] is of great interest.

Machine Learning algorithms are successful at processing and extracting crucial information from large amounts of data and can remove the problem of model bias [401]. They are also very useful to test the consistency of the dataset in a model independent approach and also to search for tensions or systematics. In this Chapter we will use a particular Machine Learning (ML) algorithm, the genetic algorithms (GA). The robustness of the GA resides in the fact that is a non-parametric method and does not require an initial prior or a cosmological fiducial model [169, 464]. Even though the temperature-redshift relation (TRR) appears to be well established, measurements of the connection between the redshift and the CMB temperature serves as an important cosmological probe. Among others, it can help to confirm the assumption of photon number conservation, the CMB is thermal radiation, entropy conservation and that the expansion of space is isotropic. It provides also a way to discriminate alternative cosmologies [519, 520]. Measurements of the TRR can be also used to measure the local expansion rate H_0 through the time evolution of the background $\mathrm{T_{CMB}}(z)$ [509].

In this Chapter we implement the GA which is a model independent and non-parametric algorithm to reconstruct the evolution of the CMB temperature from a wide redshift range $z \in [0, 3]$ without assuming any dark energy model, an adiabatic universe or photon number conservation. We then provide novel and updated estimates on the β parameter from the parametrisation $\mathrm{T_{CMB}}(z) = \mathrm{T_0}(1+z)^{1-\beta}$, the duality relation $\eta(z)$ and the cosmic opacity $\tau(z)$. Furthermore we place constraints on temporal variations fine structure constant α, which could affect among others the CMB anisotropies [521, 522]. We want to stress that our constraints are not independent of each other since all of them parameterize in diverse ways potential deviations from the temperature-redshift relation.

This Chapter is organized as follows. In Section 13.2 we present the notation and methodology of our analysis with the minimal assumptions made for the reconstruction of the data. In Section 13.3 we compare our error analysis of the GA with the Fisher matrix approach and in Section 13.4 we describe the data used and our implementation for the error analysis. Finally, in Section 13.5 we present our constraints and results and in Section 13.6 we present our Conclusions.

13.2 Analysis

In this section we apply the GA to reconstruct the background temperature of the CMB $\mathrm{T_{CMB}}(z)$ given in Table 2.3. Hereafter we will express $\mathrm{T(z)} \equiv \mathrm{T_{CMB}}(z)$. In our analysis we use 37 points of the compilation from Table 2.3 which spans over a wide redshift range of $0 \leq z \leq 3.025$. The data is in the form (z_i, T_i, σ_{T_i}). Since our χ^2 has a quadratic form

$$\chi^2_T = \sum_i^{N_T} \left(\frac{T_i - T^{th}(z_i)}{\sigma_{T_i}} \right)^2 , \tag{13.1}$$

where $\mathrm{T^{th}}(z) = \mathrm{T_0}\tilde{\mathrm{T}}(z)$ and $\tilde{\mathrm{T}}(z)$ is the dimensionless temperature, we can minimize the χ^2 analytically over T_0 finding

$$\chi^2_T = A - \frac{B^2}{\Gamma}, \tag{13.2}$$

$$T_0 = \frac{B}{\Gamma}, \tag{13.3}$$

where the parameters A, B and Γ are defined as

$$A = \sum_i^{N_T} \left(\frac{T_i}{\sigma_{T_i}} \right)^2 , \tag{13.4}$$

$$B = \sum_i^{N_T} \frac{T_i\ \tilde{\mathrm{T}}(z_i)}{\sigma^2_{T_i}}, \tag{13.5}$$

$$\Gamma = \sum_i^{N_T} \left(\frac{\tilde{\mathrm{T}}(z_i)}{\sigma_{T_i}} \right)^2 , \tag{13.6}$$

and we denote the theoretical value $\mathrm{T^{th}}(z)$ of the background temperature of the CMB obtained from the GA as $\mathrm{T^{th}}(z) = \mathrm{T}^{GA}(z)$. Then $\tilde{\mathrm{T}}(z) = \mathrm{T}^{GA}(z)/\mathrm{T_0}$ and we set $N_T = 37$. Our best-fit function found is

$$T^{GA}(z) = T_0 \left(1 + z \left(e^{0.00123 z^2} - 0.03581 z + 0.00678 z^2 \right) \right), \tag{13.7}$$

and our own assumption is that the value of the background temperature of the CMB T(z) today is given by $\mathrm{T}(z=0) = \mathrm{T_0}$ where $\mathrm{T_0}$ is obtained directly from Eq. (13.3). The best-fit χ^2 for the GA is $\chi^2 = 28.816$, which is smaller than that of the ΛCDM model with a χ^2 of $\chi^2 = 29.176$ or that with the Fisher matrix approach with $\chi^2 = 28.892$, see Sec. 13.3. In the left panel of Fig. 13.1 we present the $\mathrm{T}(z)$ data compilation shown as grey points along with the ΛCDM best-fit (dashed line) and the GA best-fit (solid black line). The shaded gray regions corresponds to the 1σ errors of the GA. For the evaluation of the GA errors on the reconstructed quantities we make use of the path integral approach, first derived in [169, 417], where one calculates analytically a path integral over the functional space that can be scanned by the GA. We have also tested our GA approach leaving free the function $f_{GA}(z)$ as $\mathrm{T}^{GA}(z) = \mathrm{T_0}(1+z)^{1-f_{GA}(z)}$ finding a similar χ^2 with Eq. (13.7). We want to clarify that although the GA provide a smooth and differentiable function at all redshifts they are a non-parametric algorithm, hence the traditional statistical comparison based on Bayesian inference is ambiguous. Then the use of quantitative criterion such as the Bayesian Information Criterion (BIC), Akaike Information Criterion (AIC) or Evidence Ratio cannot be used in this case to make a fair and consistent comparison. For this reason we compare the best-fit χ^2 for the GA and ΛCDM as can be seen in Table (13.1).

In what follows, we present some theoretical context for the remaining derived quantities we will reconstruct and in Fig. 13.2 we present a flowchart of our fitting process for illustration

Table 13.1: The χ^2 for ΛCDM and GA using the $T(z)$ data.

	$T(z)$
$\chi^2_{\Lambda CDM}$	29.176
χ^2_{GA}	28.816

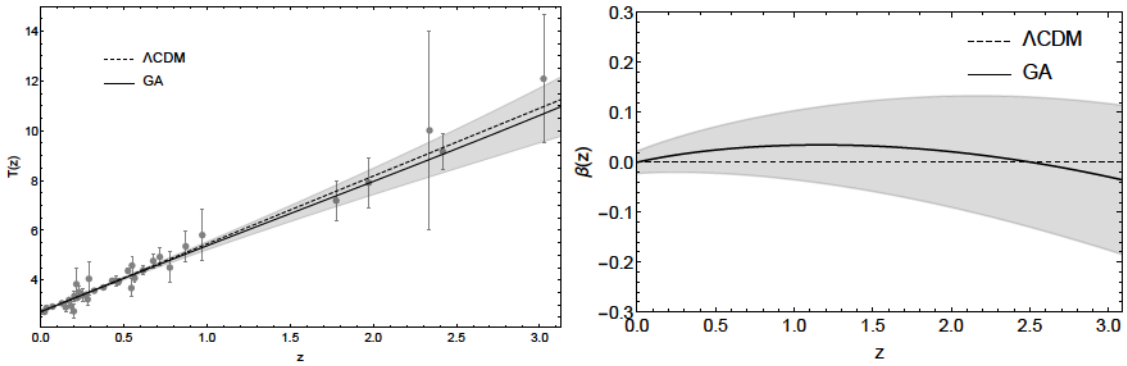

Figure 13.1: Left: The T(z) data compilation shown as grey points along with the ΛCDM best-fit (dashed line) and the GA best-fit (solid black line). The shaded gray regions corresponds to the 1σ errors of the GA. Right: The reconstruction of the β parameter. Both cases are consistent with the ΛCDM model.

purposes. We stress that the robustness of the GA approach resides in the fact that is a non-parametric method and does not require an initial prior or a cosmological fiducial model, obtaining constraints in a model independent approach. We also make a reminder that these constraints are not independent of each other since all of them parameterize potential deviations from the background temperature relation of the CMB.

13.2.1 β parameter

If we assume that the expansion of the Universe is adiabatic, then the hot Big Bang model predicts that the CMB temperature evolves proportional to $(1+z)$. One can parameterize possible deviations to this linear law as

$$T(z) = T_0(1+z)^{1-\beta}, \tag{13.8}$$

where β is a parameter that would account for adiabatic photon production $\beta > 0$ or destruction $\beta < 0$. This phenomena can occur for example in decaying dark energy models [523] where DE interacts with matter by the creation of photons, affecting in turn the CMB spectrum [524]. From Eq. (13.8) we find that we can write β as the logarithmic derivative of T(z)

$$\beta(z) = 1 - (1+z)\frac{d\ln\left(T(z)/T_0\right)}{dz}, \tag{13.9}$$

where T(z) represents our best-fit reconstructed function, Eq. (13.7), and T_0 our derived parameter, Eq. (13.3). In the right panel of Fig. 13.1 we present our reconstruction of the β parameter where the dashed line is the prediction from ΛCDM and the GA best-fit is the solid black line. The shaded gray regions corresponds to the 1σ errors of the GA. We find that our model independent approach is consistent with an adiabatic universe and the conservation of photon number.

13.2.2 Duality relation and the cosmic opacity

The distance duality relation (DDR) defines a connection between the luminosity distance d_L and the angular diameter distance d_A in the following way

$$\eta(z) \equiv \frac{d_L}{(1+z)^2 d_A} = 1, \tag{13.10}$$

where any deviations from $\eta(z) \neq 1$ would be a hint for new physics, e.g. that the Universe is opaque. This relation is valid under the condition of the conservation of photon number in cosmic evolution, gravity must be described by a metric theory and the travel of photons along null geodesics [525] holding true for all curved space-times. The DDR has been tested from different datasets ranging from radio galaxies and ultra compact radio sources [526], The CMB [527–529], Baryon Acoustic Oscillations (BAO) [530, 531], H 21cm signal from disk galaxies [532], Gamma Ray Bursts [533] and high redshift quasars [534] among others. If we assume the temperature-redshift relation of the CMB from the ΛCDM model, i.e. $\mathrm{T}(z) = \mathrm{T}_0(1+z)$, then the factor $1+z$ can be written as $1+z = \mathrm{T}(z)/\mathrm{T}_0$. Inserting this relation into the rhs of Eq. (13.10) we find that

$$\frac{d_L}{d_A} = (1+z)^2 = \left(\frac{T(z)}{T_0}\right)^2. \tag{13.11}$$

Substituting the ratio $\frac{\mathrm{d_L}}{\mathrm{d_A}} = \left(\frac{\mathrm{T}(z)}{\mathrm{T}_0}\right)^2$ from Eq. (13.11) in Eq. (13.10) we see that the DDR can also be written in terms of the redshift temperature relation of the CMB as

$$\left(\frac{T(z)}{T_0(1+z)}\right)^2 \equiv \eta(z), \tag{13.12}$$

as it is also shown in Ref. [535] and which should be equal to unity in the ΛCDM model. The above relation is directly connected to the cosmic opacity $\tau(z)$ as we will show below and therefore we can use our GA reconstruction on $\eta(z)$ and $\tau(z)$ to constrain the transparency of the universe.

If we have an opaque universe, the photon flux collected by the observers is lowered by a factor $e^{-\tau(z)}$, and the observed luminosity distance $d_{L,obs}$ can be expressed as [517]

$$d_{L,obs}(z) = d_{L,true}(z) e^{\tau(z)/2}, \tag{13.13}$$

where $\tau(z)$ denotes the opacity parameter between an observer at $z = 0$ and a source at z, and physically it gives us information about how transparent is the universe or in other words it connotes the optical depth associated to the cosmic absorption. This parameter can mimic a dark energy behaviour [533] and reconstructions for the parameter $\tau(z)$ have been done in the past [536–538] and recently it has been tested from Gravitational Waves mock data from the third generation of the Einstein Telescope and using Gaussian Processes [517]. From Eq. (13.10) and Eq. (13.13) we can see that

$$e^{\tau(z)/2} = \eta(z), \tag{13.14}$$

then using Eq. (13.12) we see that $\tau(z)$ and our reconstruction for $\mathrm{T}(z)$ are connected in the following way

$$\tau(z) = 4 \ln\left(\frac{T(z)/T_0}{(1+z)}\right). \tag{13.15}$$

13.2.3 Fine structure constant

Fundamental constants, which we assume to be constant over space-time, are described operationally, meaning that nature does not force it to be constant. They are not given by the theory and must be obtained experimentally. For a review on the variation of fundamental constants see [539]. Here we will probe the interesting case where the fine structure constant $\alpha = \frac{e^2}{\hbar c}$ is not invariant

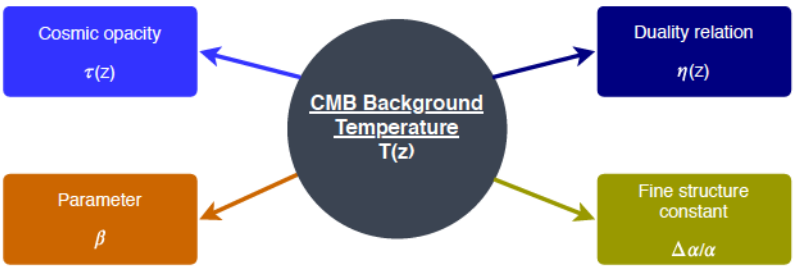

Figure 13.2: A flowchart of the reconstructed functions using our Machine Learning algorithm for the T(z) data.

and we will express its relative variation as $\Delta\alpha/\alpha$. If there are eventually signatures of a variation it would have imprints in different physical mechanisms such as the CMB anisotropies [522]. Constraints on this variation, both temporal and spatial, have been performed already [514, 540–545], and this variation can be produced for example through an evolving scalar field which is coupled to the electromagnetic Lagrangian [514] producing violations in the photon number conservation. This will give rise to both, variations of the fine structure constant and violations of the standard $T_{CMB}(z)$ law. A class of models where this occurs is the Bekenstein-Sanvik-Barrow-Magueijo (BSBM) model [546], where the electric charge is allowed to vary. Although such theories preserve the local gauge and Lorentz invariance, the fine structure constant will vary during the matter dominated era. The corresponding action is

$$S = \int d^4x\sqrt{-g}\left(\mathcal{L}_g + \mathcal{L}_m - \frac{\omega}{2}\partial_\mu\psi\partial^\mu\psi - e^{-2\psi}\mathcal{L}_{em}\right), \tag{13.16}$$

where $\mathcal{L}_g = \frac{1}{16\pi G}R$ is the Hilbert-Einstein Lagrangian plus the matter fields $\mathcal{L}_m$, the third term is the kinetic term for the scalar field ψ and, finally, the last term couples the scalar field with the standard electromagnetic Lagrangian $\mathcal{L}_{em} = \frac{F^{\mu\nu}F_{\mu\nu}}{4}$. Then the governing evolution equation of the radiation energy reads

$$\dot{\rho}_\gamma + 4H\rho_\gamma = 2\dot{\psi}\rho_\gamma, \tag{13.17}$$

with

$$\frac{\alpha}{\alpha_0} = \exp^{2(\psi-\psi_0)}. \tag{13.18}$$

For this type of models, assuming adiabaticity, the relation between the evolution of the CMB temperature T(z) and the variation of the fine structure constant is expressed as [547]

$$T(z)/T_0 \sim (1+z)\left(1+\frac{1}{4}\frac{\Delta\alpha}{\alpha}\right). \tag{13.19}$$

Since $\Delta\alpha/\alpha$ is expected to be small experimentally, a more general phenomenological relation that can be tested observationally and can be seen as a good approximation for a wider range of couplings is expressed as [540]

$$T(z)/T_0 \sim (1+z)\left(1+\varepsilon\frac{\Delta\alpha}{\alpha}\right), \tag{13.20}$$

or instead

$$\frac{\Delta T_{CMB}}{T} = \frac{T_{CMB}(z) - T_{CMB,std}(z)}{T_{CMB,std}(z)} \sim \varepsilon\frac{\Delta\alpha}{\alpha}, \tag{13.21}$$

where $T_{CMB,std}(z)$ represents the evolution of the CMB temperature in the ΛCDM model, i.e $T_{CMB,std}(z) = T_0(1+z)$. The coefficient ε depends on the specific model under consideration and

it is commonly assumed to be of order unity [541], hence we will consider as a test case $\varepsilon = 1$. Writing $\frac{\Delta\alpha}{\alpha}$ as a function of T(z) we find

$$\frac{\Delta\alpha}{\alpha} \sim -\frac{(1+z) - T(z)/T_0}{\varepsilon\,(1+z)}. \tag{13.22}$$

This relation Eq. (13.22), can be tested for both, time and/or spatial variations of α [547]. To test for spatial variations of the fine structure, we would have to resolve the CMB temperature at the cluster location using multi-frequency measurements of the thermal Sunyaev Zel'dovich effect (TSZ). This has already been performed in [514, 541] and we plan to do a similar study using the GA but such analysis is left for a future work. In this Chapter we will limit to constrain how the fine structure constant α changes with distance, or in other words, test its temporal evolution using the CMB temperature at redshift between 0 and 3, with the data compilation found in Table 2.3 which comes from SZ observations at low redshifts and from observations of spectral lines at high redshift. To the best of our knowledge, this is the first time that temporal variations on the fine-structure constant $\frac{\Delta\alpha}{\alpha}$ are constrained in a model independent and non parametric approach using the GA.

13.3 Fisher matrix approach

To evaluate the rigor of the path integral approach for the error analysis of the GA we compare it numerically with the Fisher matrix approach. We chose the following function which could be used to test deviations from the ΛCDM model

$$f(z;a,b) = T_0(1+z)^{1+ax+bx^2}, \tag{13.23}$$

where z is the redshift and a and b are constant numbers. Then we fitted the model $f(z;a,b)$ of Eq (13.23) by minimizing the χ^2

$$\chi^2(a,b) = \sum_i \left(\frac{y_i - f(z_i;a,b)}{\sigma_{y_i}}\right)^2. \tag{13.24}$$

The best-fit value is given by $(a,b)_{min} = (a = -0.0264 \pm 0.0502, b = 0.0106 \pm 0.0231)$ with a $\chi^2_{min} = 28.892$. The shaded gray region from Fig. 13.3 is the 1σ error following a Fisher Matrix approach [169]. The error of our best-fitted function $f(z;a,b)$ is obtained from

$$\sigma_f(z)^2 = \sum_{i,j} C_{ij}\partial_i f(z;a,b)\partial_j f(z;a,b)\mid_{min}, \tag{13.25}$$

which is evaluated at the best fit [548] and the dummy variables (i,j) correspond to our parameters (a,b). The covariance matrix C_{ij} is obtained from the inverse of the Fisher matrix $C_{ij} = F_{ij}^{-1}$ where

$$F_{ij} = \frac{1}{2}\partial_{ij}\chi^2(a,b)\mid_{min}, \tag{13.26}$$

evaluated at the best-fit. Comparing the shaded gray regions from the Fisher matrix method see Fig. 13.3 and the GA approach, see Fig. 13.1 we see that the path integral approach [169, 417] is robust.

13.4 Data compilation and error analysis

In our analysis we use 37 points and the compilation can be found in Table 2.3 of Chapter 2. The main advantage of our compilation is that it spans over a wide redshift range of $0 \leq z \leq 3.025$, thus testing the β parameter, the duality relation $\eta(z)$, the cosmic opacity parameter $\tau(z)$ and temporal variations on the fine structure constant $\frac{\Delta\alpha}{\alpha}$ up to high redshifts.

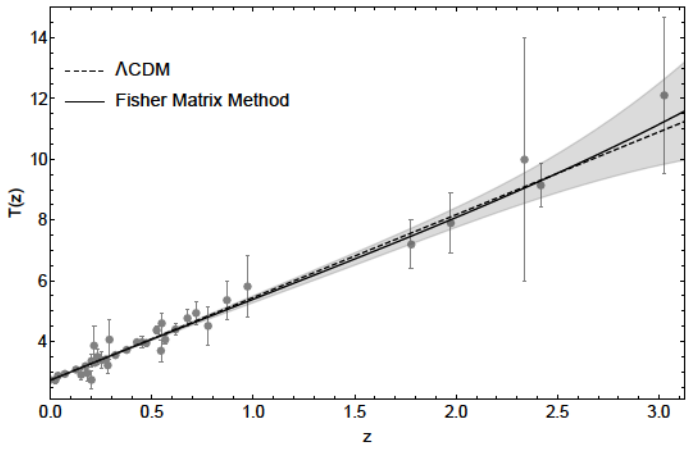

Figure 13.3: The T(z) data compilation shown as grey points along with the ΛCDM best-fit (dashed line) and the Fisher matrix method best-fit (solid black line). The shaded gray regions corresponds to the 1σ errors of the Fisher matrix method and is consistent with the GA approach, see Fig. 13.1.

The 1σ errors of β, $\eta(z)$, $\tau(z)$ and $\frac{\Delta\alpha}{\alpha}$ were computed following the traditional error propagation, since it has been shown [324] that is in agreement with the errors obtained using the definition of the standard deviation $\delta g^2 = \langle g^2\rangle - \langle g\rangle^2$, where g is a quantity formed by a function f. For the β parameter, since it is defined as

$$\beta(z) = 1 - (1+z)\frac{d\ln\left(T(z)/T_0\right)}{dz}, \tag{13.27}$$

following the aforementioned approach we find that the error of β, e.g. $\delta\beta$ is

$$\delta\beta(z) = -(1+z)\frac{d\left(\delta T(z)/T(z)\right)}{dz}, \tag{13.28}$$

where T(z) is our best-fit function given by the GA and its 1σ error obtained through the path integral approach is δT(z). Similarly we can derive the rest of the errors. For the duality relation $\eta(z)$ we have that

$$\eta(z) = \left(\frac{T(z)/T_0}{(1+z)}\right)^2, \tag{13.29}$$

then

$$\delta\eta(z) = \frac{2T(z)\delta T(z)}{T_0^2(1+z)^2}. \tag{13.30}$$

For the cosmic opacity parameter defined as

$$\tau(z) = 4\ln\left(\frac{T(z)/T_0}{(1+z)}\right), \tag{13.31}$$

we have

$$\delta\tau(z) = \frac{4}{T(z)/T_0}\ln\left(\delta T(z)/T_0\right), \tag{13.32}$$

and finally for the variation of the fine structure constant

$$\frac{\Delta\alpha}{\alpha} = -\frac{(1+z) - T(z)/T_0}{\varepsilon\,(1+z)}, \tag{13.33}$$

we found the following

$$\delta\left(\frac{\Delta\alpha}{\alpha}\right) = \frac{1}{(1+z)\varepsilon}\frac{\delta T(z)}{T_0}. \tag{13.34}$$

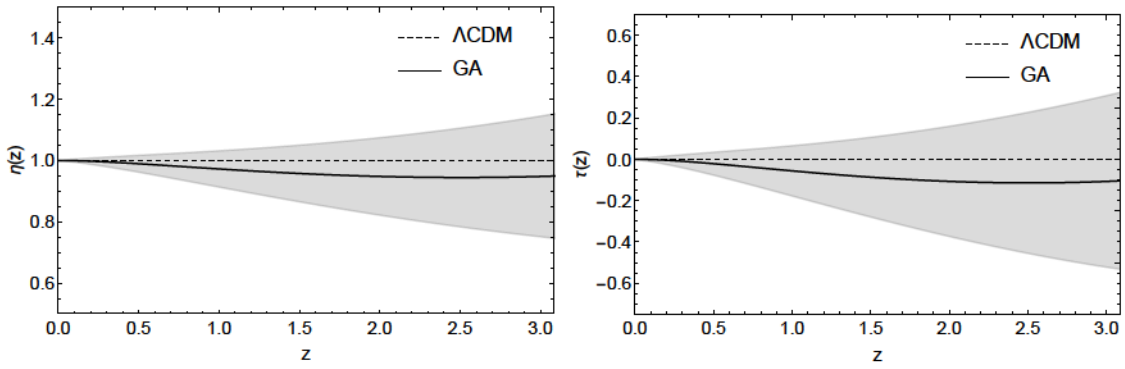

Figure 13.4: Left: The reconstruction of the duality relation $\eta(z)$. Right: The reconstruction of the cosmic opacity $\tau(z)$. In both cases the ΛCDM best-fit corresponds to the dashed line and the GA best-fit to the solid black line along with the 1σ errors (gray regions). Both cases are consistent with the ΛCDM model.

13.5 Results

In this Section we present our best-fit reconstructions for the parameter β, the duality relation $\eta(z)$, the opacity parameter $\tau(z)$ and temporal variations on the fine structure constant $\frac{\Delta\alpha}{\alpha}$. Inserting our reconstructed T(z) function Eq. (13.7) in Eqs. (13.9),(13.12),(13.15) and (13.22) we derived the following constraints at redshift $z = 0$

$$\beta(z=0) = 0.0000 \pm 0.0224, \tag{13.35}$$
$$\eta(z=0) = 1.0000 \pm 0.0002\,, \tag{13.36}$$
$$\tau(z=0) = 0.0000 \pm 0.0004, \tag{13.37}$$
$$\frac{\Delta\alpha}{\alpha}(z=0,\varepsilon=1) = 0.0000 \pm 0.0001, \tag{13.38}$$

and at redshift $z = 3.025$ where we have our last data point

$$\beta(z=3.025) = -0.0309 \pm 0.1475, \tag{13.39}$$
$$\eta(z=3.025) = 0.9483 \pm 0.1986\,, \tag{13.40}$$
$$\tau(z=3.025) = -0.1062 \pm 0.4188, \tag{13.41}$$
$$\frac{\Delta\alpha}{\alpha}(z=3.025,\varepsilon=1) = -0.0262 \pm 0.1020. \tag{13.42}$$

From the numbers given above, we can see that both at low and high redshifts our constraints are consistent with the ΛCDM model. In the left and right panel of Fig. 13.4 we show the reconstruction of the duality relation $\eta(z)$ and the cosmic opacity parameter $\tau(z)$ respectively. In both cases the expected value from ΛCDM corresponds to the dashed line and the GA best-fit to the solid black line along with the 1σ errors (gray regions). Both cases are consistent with photon number conservation and a transparent universe and hence with the ΛCDM model. Finally, in Fig. 13.5 we show our reconstruction of the variation of the fine structure constant for $\varepsilon = 1$ which is consistent with a non varying constant within the 1σ region. Overall, for all our reconstructions we find no evidence of deviations within the 1σ region from the well established ΛCDM model.

13.6 Conclusions

We have presented a model independent and non-parametric reconstruction of data coming from the redshift evolution of the CMB temperature which spans over a redshift range of $0 \leq z \leq 3.025$

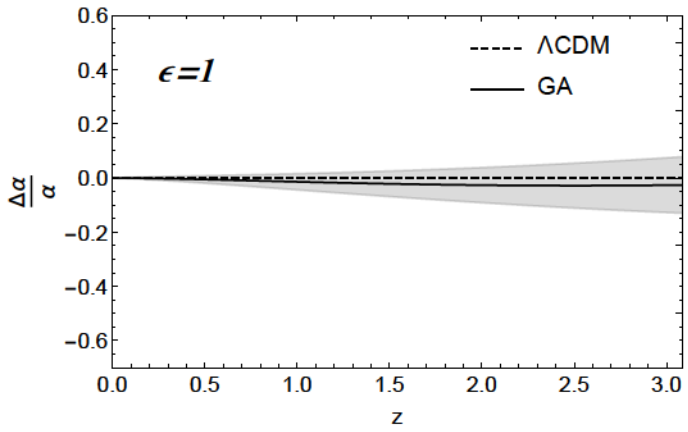

Figure 13.5: The reconstruction of the temporal variation of the fine structure constant $\frac{\Delta\alpha}{\alpha}$ for $\varepsilon = 1$. The dashed line corresponds to a non varying constant and the GA best-fit to the solid black line along with the 1σ errors (gray regions). We found that our reconstruction is consistent with a fine structure constant that is not temporally varying.

with a Machine Learning algorithm without assuming any dark energy model, an adiabatic universe or photon number conservation. In particular we used the GA which avoids the dependency on an initial prior or a cosmological fiducial model. From our reconstruction we have provided constraints and updated estimates in a novel approach on the β parameter from the parametrisation $\mathrm{T}(z) = \mathrm{T}_0(1+z)^{1-\beta}$, the duality relation $\eta(z)$ and the cosmic opacity parameter $\tau(z)$. Furthermore we place constraints on a temporal varying fine structure constant α, which would have signatures in a broad spectrum of physical phenomena such as the CMB anisotropies. It is important to notice that our constraints are not independent of each other since all of them parameterize in diverse ways potential deviations from the temperature-redshift relation. Within uncertainties, our model independent approach is consistent with the standard view of $\mathrm{T} \propto (1+z)$ having found no strong discrepancies within the 1σ region with the ΛCDM model. Finally, our results demonstrate that a transparent universe is preferred at 1σ.

14

Machine learning forecasts of the cosmic distance duality relation with strongly lensed gravitational wave events

The original content of this chapter is based on Ref. [549]. We use simulated strongly lensed gravitational wave events from the Einstein Telescope to demonstrate how the luminosity and angular diameter distances, $d_L(z)$ and $d_A(z)$ respectively, can be combined to test in a model independent manner for deviations from the cosmic distance duality relation and the standard cosmological model. In particular, we use two machine learning approaches, the Genetic Algorithms and Gaussian Processes, to reconstruct the mock data and we show that both approaches are capable of correctly recovering the underlying fiducial model and can provide percent-level constraints at intermediate redshifts when applied to future Einstein Telescope data.

14.1 Introduction

The first detection of gravitational waves (GWs) by the LIGO/Virgo collaboration was not just limited to the discovery of new astrophysical objects, but it was also instrumental in furthering our understanding of the fundamental properties of gravity and cosmology, by providing tests of gravity in the strong field regime. These observations from black hole and neutron star mergers have, figuratively speaking, shone a light on the population of compact objects in the Universe and the mechanism by which they are formed [550], given some of the most rigorous direct tests to date of General Relativity (GR) [551, 552] and provided the first measurement of a cosmological parameter, the Hubble constant H_0, using GW sources [553].

Moreover, the observation of the binary neutron star merger GW170817 availed us of the opportunity to test gravity both in the strong regime and at large scales, as it was followed by the nearly simultaneous detection of its optical counterpart and allowed us to strongly constrain the GW propagation speed to $|c_g - c| \lesssim \mathcal{O}\left(10^{-15}\right)$ [554], thus challenging a wide range of modified gravity scenarios which are candidates to explain the current acceleration of the Universe [171–174, 180, 555]. The impact of GW observations will be further extended by third generation ground based detectors like the Einstein Telescope (ET) [556] and the space-based interferometer LISA [557].

Similarly to photons, GWs can be gravitationally lensed by the presence of galaxies and clusters of galaxies, producing a deflection in their trajectories, thus generating multiple detection events. This phenomenon is quite intriguing because the clustered matter that lies in between the GW source and the observer can enhance the observed signal [558]. This in turn can cause the luminosity distance to the source and therefore its redshift, if combined with the Hubble parameter H_0 constraints [559], to be underestimated. Sequentially, this would lead to an overestimation of the chirp mass [560].

With the upgraded sensitivity of the third generation of GW detectors, such as the Einstein

Telescope (ET), the detection sensitivity of the GW events would be accordingly improved. Thus, with the sufficiently large number of detectable events foreseen [561, 562], it is expected that some of these events could be gravitationally lensed, thus allowing the creation of a considerably large catalogue of strongly lensed GWs event within a few years of operation. For an extensive analysis on how GW lensing is enriched with concrete signatures and features and can be used to search for deviations of GR see Ref. [563].

As the GW passes through near massive astrophysical objects, its path would be modified producing gravitational lensing [564–566]. Since its first proposal [567], efforts have been placed to search for signatures of gravitational lensing in binary black hole events from current detectors such as LIGO and Virgo [568] but with no strong evidence of this effect [569]. However, as the sensitivity of the detectors improve further, it is plausible to observe lensing effects with future detectors such as aLIGO, the ET [570] and the space-based detector LISA [571]. In Ref. [572] the authors improved previous analysis of GW lensing events by including effects created by the ellipticity of lensing galaxies, lens environments and magnification bias. Indeed, these observations could lead to new applications in astrophysics, cosmology and fundamental physics [573–579].

One of the advantages of strongly lensed GW events comes from their ability to provide simultaneous measurements of both the luminosity and angular diameter distance, i.e $d_L(z)$ and $d_A(z)$ respectively, which in turn could be used to probe fundamental properties of the standard cosmological model. One such example of a possible probe is the cosmic distance duality relation (DDR), also known as the Etherington relation, which relates the luminosity distance to the angular diameter distance at any redshift z via [580]

$$d_L(z) = (1+z)^2 d_A(z), \tag{14.1}$$

which is valid for any metric theory of gravity like GR and under the condition that the number of gravitons or photons, depending in which context it is applied, is conserved and that they travel along null geodesics in a pseudo-Riemannian spacetime [526]. At this point we can introduce the duality parameter

$$\begin{aligned} \eta(z) &\equiv \frac{d_L(z)}{(1+z)^2 d_A(z)} \\ &\equiv (1+z)^{\epsilon(z)} \end{aligned} \tag{14.2}$$

where $\eta(z)$ is a function that accounts for possible deviations from unity and is equal to unity when the DDR holds, while in the last line we have introduced a phenomenological parameter $\epsilon(z)$, usually assumed to be constant, i.e. $\epsilon(z) \simeq \epsilon_0 =$constant. Notice that on Chapter 13 we have already constrained the duality relation but with the redshift evolution of the CMB Temperature.

As we have seen, any violation of the DDR relation at any redshift, i.e $\eta(z) \neq 1$ or $\epsilon_0 \neq 0$, would be a hint of new physics, which in the case of photons could be caused by different mechanisms, such as the annihilation of photons by the intergalactic dust [581], the coupling of photons with other particles like axions [582] and the variation of fundamental constants [529]. In fact several works have been devoted to test the DDR relation [403, 470, 471, 526–528, 530–534, 583–587].

As mentioned earlier, in our analysis ϵ_0 is a phenomenological parameter that parameterizes deviations from the standard DDR, i.e. any values that are different from zero imply a deviation from the standard model. Clearly, any such deviations will be small, as otherwise they would be immediately obvious in a plethora of observations, including strong and weak lensing. Indeed, in Ref. [470] it was shown that current Type Ia supernovae (SnIa) and Baryon Acoustic Oscillations (BAO) data constrain the parameter to be $\epsilon_0 = 0.013 \pm 0.029$ and that there is no evidence for a redshift evolution of $\epsilon(z)$. The latter was shown by splitting the data in two bins, in $0 < z < 0.9$ and $z \geq 0.9$, and testing if both bins give consistent results for the reconstruction of the parameter ϵ_0 in each bin. In particular, it was found that the values of ϵ_0 in both bins were the same, note however that this analysis was made using data in small redshifts ($z < 1.5$), so deviations might be present at higher redshifts.

Furthermore, in Ref. [470] it was found that future large scale structure surveys like Euclid will be able to improve upon the the constraints on ϵ_0 from currently available BAO and type Ia supernovae (SnIa) by a factor of six. In particular, current BAO and SnIa data provide a constraint of $\epsilon_0 = 0.013 \pm 0.029$, while Euclid will improve this to $\epsilon_0 = -0.0008 \pm 0.0049$, which is a tighter constraint on ϵ_0 by a factor of six [470].

Since $\epsilon(z)$ relates two geometric variables, i.e. the luminosity and angular diameter distances, then strong lensing (either with light or GWs) is ideally suited to constrain it, while in the case of weak lensing the effect is less clear, but as was shown in Ref. [470], the bulk of the constraining power will come from improving the bounds on Ω_m, thus breaking the degeneracies between Ω_m and ϵ.

In this Chapter we show how to reconstruct the DDR relation using mock datasets of strongly lensed GWs, as they allow us to measure both the angular diameter and luminosity distance is complementary to the approach of Ref. [588], where $\eta(z)$ was constrained using mocks of strongly lensed SnIa, based on the Large Synoptic Survey Telescope (LSST) survey. Both methods have the advantage of allowing for measurements of the duality parameter without relying on multiple datasets, hence it is competitive with other more traditional tests of the DDR relation where the latter is constrained through the combination of SnIa and BAO observations, as for example it has been forecast for future surveys [470].

In Ref. [589] the authors proposed a novel method to test the cosmic distance duality relation using the strongly lensed GWs from the Einstein Telescope and in Ref. [590] mock data points were generated for this ground-based detector, while a parameterized approach was used to constrain the DDR relation. Here we present a broader analysis by presenting a slightly different methodology which allows us to directly make robust $\eta(z)$ mocks, based on the mocks of d_L and d_A and then we use Genetic Algorithms (GA) and Gaussian Processes (GP), two non-parametric and symbolic regression subclasses of machine learning methods, to reconstruct $\eta(z)$ directly without any underlying model.

The parametric and non-parametric methods, like the GA, were extensively compared using mock data in Ref. [470], where it was shown that the two approaches are consistent with each other, albeit the errors in the reconstructed quantities are slightly larger for the GA due to its non-parametric nature. On the other hand, a model for the duality parameter η, based on axion physics was studied in Ref. [471]. Since axions couple to the standard model and photons, it is expected that some of the axions will be converted to photons and vice versa, thus leading to a surplus or deficit of photons. Since the DDR assumes the photon number conservation, this implies axions lead to a violation of the DDR and an duality parameter which is different from unity. Using mock data it was shown in Ref. [471], that both the GA and the GP can consistently reconstruct the cosmological distances and the duality parameter η in agreement with each other and the fiducial model, within the errors, thus we are confident for our reconstruction methods.

Here we follow the approach of Ref. [471], especially as we also use mock GW events, albeit we assume that they can be lensed so that we also extract the angular diameter distance. Using the mock data, where we know the fiducial cosmology, allows us to assess the quality of the fit and determine whether the GA and the GP can successfully determine the underlying model.

Our Chapter is organized as follows: In Sec. 14.2 we describe the methodology to generate the ET mock data points and the machine learning (ML) implementation. In Sec. 14.3 we present our reconstructions for the GP and GA, while in Sec. 14.4 we perform a comparative analysis. Finally in Sec. 14.5 we summarize our conclusions.

14.2 Methodology

14.2.1 Strongly lensed GW events

The angular diameter distance d_A from strong lensing

Here we will now consider the case when a GW emission is strongly lensed by a foreground galaxy, whose mass profile can be modeled by the singular isothermal sphere (SIS) model [591]. We will assume however that GWs propagate following geometric optics[1], i.e. we neglect wave effects, see Ref. [566] for more details. With this setup then we assume the two images will appear at angular positions θ_1 and θ_2 with respect to the lensing galaxy. See Fig. 14.1 the geometrical illustration of the lensing system. Thus, the Einstein radius $\theta_E = |\theta_1 - \theta_2|/2$ will be given by [591]

$$\theta_E = \frac{4\pi\sigma_{\rm SIS}^2 d_A(z_l, z_s)}{c^2 d_A(z_s)}, \tag{14.3}$$

where the velocity dispersion of the lens galaxy is given by $\sigma_{\rm SIS}$, the angular diameter distances from the observer to the source and from the lens to the source are given by $d_A(z_s)$ and $d_A(z_l, z_s)$ respectively, z_l and z_s are the redshifts of the lens and source respectively. We can rearrange Eq. (14.3) to obtain the distance ratio, which will be given by

$$R_A \equiv \frac{d_A(z_l, z_s)}{d_A(z_s)} = \frac{c^2\theta_E}{4\pi\sigma_{\rm SIS}^2}. \tag{14.4}$$

If the angular positions and the velocity dispersion are well measured, which would require a precise localization of the GW sources that should be achievable with a network of interferometers[2], then we can obtain the distance ratio R_A from Eq. (14.4).

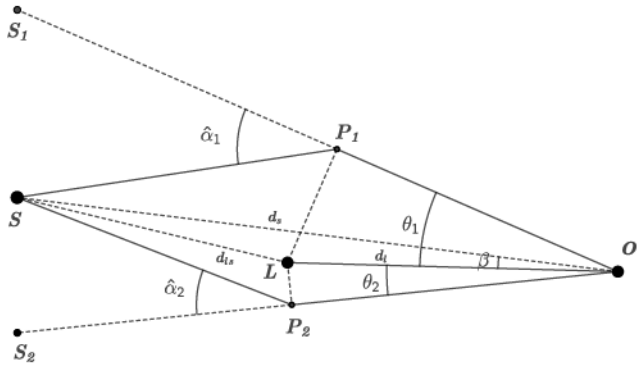

Figure 14.1: The geometry of gravitational lensing. The source (S) at redshift z_s is strongly lensed by a foreground galaxy (L) at redshift z_l. The observer (O) sees two images (S1 and S2) at angular positions θ_1 and θ_2, respectively. The actual angular position of the source with respect to the line-of-sight from observer to lens is β.

[1]The frequency of a gravitational wave produced by the merger of Neutron Star-Black Hole (NS-BH) or Neutron Star-Neutron Star (NS-NS) binary, is about several hundred Hertz and the corresponding wavelength ($\sim 10^6$ m) is much smaller than the scale of lens galaxy ($\sim$ kpc). Hence, it is unnecessary to consider the wave effect.

[2]The angular separation between the images in a typical strongly lensing system is about several arcseconds [592]. In order to identify the images, the angular resolution of GW detectors should be better than arcseconds. A larger network of interferometers is necessary in order to reach such a high accuracy.

As the two images propagating along different paths will take different amounts of time to reach Earth, then the time delay between the images will be given by [591]

$$\Delta t = \frac{(1+z_l)}{c}\frac{d_A(z_l)d_A(z_s)}{d_A(z_l,z_s)}\Delta\phi, \tag{14.5}$$

where

$$\Delta\phi = \frac{(\theta_1-\beta)^2}{2} - \Psi(\theta_1) - \frac{(\theta_2-\beta)^2}{2} + \Psi(\theta_2), \tag{14.6}$$

is the Fermat potential difference between two paths, β is the actual angular position of the source, and $\Psi(\theta)$ is the rescaled projected gravitational potential of the lens galaxy. From equation (14.5) we can thus obtain the time-delay distance

$$D_{\Delta t} \equiv \frac{d_A(z_l)d_A(z_s)}{d_A(z_l,z_s)} = \frac{c}{1+z_l}\frac{\Delta t}{\Delta\phi}. \tag{14.7}$$

If the gravitational potential of the lens galaxy can be measured from photometric and spectroscopic observations, and if the time delay between two images can be well measured, we can obtain the time-delay distance $D_{\Delta t}$ according to Eq. (14.7).

In a spatially flat universe, the angular diameter distance from lens to source, $d_A(z_l,z_s)$, can be expressed in terms of $d_A(z_s)$ and $d_A(z_l)$ as [589]

$$d_A(z_l,z_s) = d_A(z_s) - \frac{1+z_l}{1+z_s}d_A(z_l). \tag{14.8}$$

Equation (14.8), together with equations (14.4) and (14.7) allow us to uniquely solve for $d_A(z_s)$, which reads

$$d_A(z_s) = \frac{1+z_l}{1+z_s}\frac{R_A D_{\Delta t}}{1-R_A}, \tag{14.9}$$

where R_A and $D_{\Delta t}$ are given by equations (14.4) and (14.7), respectively. The error on $d_A(z_s)$ propagates from the errors on R_A and $D_{\Delta t}$. Using the standard error propagating formula, and assuming that R_A and $D_{\Delta t}$ are uncorrelated, we obtain,

$$\frac{\delta d_A(z_s)}{d_A(z_s)} = \sqrt{\left(\frac{\delta R_A}{R_A(1-R_A)}\right)^2 + \left(\frac{\delta D_{\Delta t}}{D_{\Delta t}}\right)^2}, \tag{14.10}$$

where

$$\frac{\delta R_A}{R_A} = \sqrt{\left(\frac{\delta\theta_E}{\theta_E}\right)^2 + 4\left(\frac{\delta\sigma_{\rm SIS}}{\sigma_{\rm SIS}}\right)^2}, \tag{14.11}$$

and

$$\frac{\delta D_{\Delta t}}{D_{\Delta t}} = \sqrt{\left(\frac{\delta\Delta t}{\Delta t}\right)^2 + \left(\frac{\delta\Delta\phi}{\Delta\phi}\right)^2}. \tag{14.12}$$

In order for our method to work, we must independently measure the following observables: (z_l, z_s, Δt, $\Delta\phi$, θ_E, $\sigma_{\rm SIS}$). If a GW event is accompanied by electromagnetic counterparts, the redshifts of the lens and source can be measured spectrometrically with negligible uncertainty, just as in the strongly lensed quasar or galaxy case [593, 594]. The time delay between two images can be measured by comparing the light curves of two images at percentage level [595]. Especially, in the strongly lensed GW case, due to the transient property of GW signal, the time delay can be measured with negligible uncertainty. The difference of Fermat potentials $\Delta\phi$, and the velocity dispersion of lens galaxy $\sigma_{\rm SIS}$, can be measured through photometric and spectroscopic observations of the lens galaxy [594, 596]. The Einstein radius, $\theta_E = |\theta_1 - \theta_2|/2$, can be obtained by measuring the image positions θ_1 and θ_2. The measurements of the latter three observables, however, may be uncertain. Following Ref. [597], we assume 0.6%, 1.0% and 5.0% uncertainties on $\Delta\phi$, θ_E, $\sigma_{\rm SIS}$, respectively. Having obtained all the observables, $d_A(z_s)$ and its uncertainty can be derived from Eqs. (14.9)–(14.12). We see that the uncertainty on $d_A(z_s)$ mainly comes from the uncertainty on $\sigma_{\rm SIS}$. The uncertainties on the rest observables will not strongly affect our results. To improve the accuracy, more accurate determinations of the velocity dispersion are required.

The luminosity distance d_L from GW signals

We now consider an unlensed GW source. In this case the luminosity distance to the source can be directly obtained by matching the GW signals to the GW templates. GW detectors based on the interferometers, such as ET, measure the change of difference of two optical paths caused by the pass of GW signals. In general, the response of a GW detector on GW signals will depend on the spacetime strain, which is the linear combination of the two polarization states $h_+(t)$ and $h_\times(t)$

$$h(t) = F_+(\theta, \varphi, \psi)h_+(t) + F_\times(\theta, \varphi, \psi)h_\times(t), \tag{14.13}$$

where the beam-pattern functions $F_+(\theta, \varphi, \psi)$ and $F_\times(\theta, \varphi, \psi)$ do not only depend on the configuration of the detector, but they also depend on the position of the GW source (θ, φ) and the polarization angle ψ. For example, in the case of the ET, the beam-pattern functions can be found in Ref. [598].

In the post-Newtonian and stationary phase approximation, the strain $h(t)$ can be written in the the Fourier space by [598, 599]

$$\mathcal{H}(f) = \mathcal{A}f^{-7/6}\exp[i(2\pi f t_0 - \pi/4 + 2\psi(f/2) - \varphi_{(2,0)})], \tag{14.14}$$

where f is the GW frequency, t_0 is the time of merger. The explicit expressions of the phase terms $\psi(f/2)$ and $\varphi_{(2,0)}$ can be found in Ref. [600], but they are unimportant in our study here. The Fourier amplitude in Eq. (14.14) is given by

$$\mathcal{A} \quad = \quad \frac{1}{d_L}\sqrt{F_+^2(1+\cos^2\iota)^2 + 4F_\times^2\cos^2\iota}\sqrt{\frac{5\pi}{96}}\pi^{-7/6}\mathcal{M}_c^{5/6},$$

where ι is the inclination angle, d_L is the luminosity distance, $\mathcal{M}_c = M\eta^{3/5}$ is the chirp mass, $M = m_1 + m_2$ is the total mass, $\eta = m_1m_2/M^2$ is the symmetric mass ratio, m_1 and m_2 are the component masses of the binary in the comoving frame. Here and after, we work in the natural units, so $c = G = 1$. In the case of a GW source at redshift z, $\mathcal{M}_c$ in equation (14.15) should be interpreted as the chirp mass in the observer frame, which can be related to that of the comoving frame via $\mathcal{M}_{c,\rm obs} = (1+z)\mathcal{M}_{c,\rm com}$. Finally, it should be noted that the exponential term on the right-hand side of Eq. (14.14) is just a phase term, which is unimportant in our analysis.

The signal-to-noise ratio (SNR) of the detector's response to a GW signal is given by [599]

$$\rho_i = \sqrt{\langle\mathcal{H}, \mathcal{H}\rangle}, \tag{14.15}$$

where the inner product may be defined as

$$\langle a, b\rangle = 4\int_{f_{\rm lower}}^{f_{\rm upper}} \frac{\tilde{a}(f)\tilde{b}^*(f) + \tilde{a}^*(f)\tilde{b}(f)}{2}\frac{df}{S_h(f)}, \tag{14.16}$$

and in the latter equation, $\tilde{a}$ and a^* stand for the Fourier transformation and complex conjugation of a, respectively, while $S_h(f)$ is the one-side noise power spectral density (PSD) of ET, $f_{\rm lower} = 1$ Hz and $f_{\rm upper} = 2f_{\rm LSO}$ are the lower and upper cutoffs of the frequency, $f_{\rm LSO} = 1/(6^{3/2}2\pi M_{\rm obs})$ is the orbit frequency at the last stable orbit, $M_{\rm obs} = (1+z)(m_1+m_2)$ is the total mass in the observer frame. Finally, the PSD for ET is given by [601]

$$S_h(f) \quad = \quad 10^{-50}(2.39\times10^{-27}x^{-15.64} + 0.349x^{-2.145} + 1.76x^{-0.12} + 0.409x^{1.1})^2\ \text{Hz}^{-1},$$

where x is the GW frequency in unit of 100Hz, i.e., $x = f/100$Hz. For the ET, three arms interfere with each other in pairs, hence the combined SNR is given by

$$\rho = \left[\sum_{i=1}^{3}\rho_i^2\right]^{1/2}. \tag{14.17}$$

In general, there is degeneracy between the luminosity distance d_L and inclination angle ι, so the uncertainty on d_L may be large. However, if the GW event is accompanied by a short gamma-ray burst (GRB), we can assume that the inclination angle is small, since GRB is expected to be produced in a narrow beam. In this case the degeneracy between d_L and ι breaks, and the uncertainty on d_L can be estimated as

$$\delta d_L = \sqrt{\left(\frac{2d_L}{\rho}\right)^2 + (0.05 z d_L)^2}\,, \tag{14.18}$$

where the $0.05z$ term represents the uncertainty arising from weak lensing effect caused by the intergalactic medium along the line-of-sight.

The above discussion is applicable for unlensed GW events. However, the situation is subtle for strongly lensed GW events. Due to the magnification effect of lensing, the luminosity distance determined from the strongly lensed GW signals is not the true distance. Since the amplitude of GW signal $\mathcal{A}$ is magnified by the lensing effect by a factor of $\sqrt{\mu_\pm}$ [602], and the luminosity distance d_L is inversely proportional to $\mathcal{A}$, the true luminosity distance should be $d_L^{\rm true} = \sqrt{\mu_\pm} d_L^{\rm obs}$. If the magnification factor $\sqrt{\mu_\pm}$ can be independently determined through photometric observations, we can obtain the true distance $d_L^{\rm true}$. The uncertainty of $\mu_\pm$ will also propagate to d_L. Therefore, the total uncertainty on $d_L(z_s)$ is given by

$$\frac{\delta d_L^{\rm total}}{d_L} = \sqrt{\left(\frac{2}{\rho}\right)^2 + (0.05 z_s)^2 + \frac{1}{4}\left(\frac{\delta \mu_\pm}{\mu_\pm}\right)^2}\,. \tag{14.19}$$

Due to the contamination of the image flux by the foreground lensing galaxy, the magnification factor is highly uncertain. Here we follow Ref. [597] and assume a 20% uncertainty on $\mu_\pm$.

Theoretically, only the merger of NS-NS or NS-BH binaries may be accompanied by a short GRB, while the merger of BH-BH binary is expected to have no electromagnetic counterpart. Our method requires the direct measurement of source redshift, which is achievable only for NS-NS or NS-BH mergers. Unfortunately, according to numerical simulations [570], most of the lensed GW events are produced by the BH-BH merger. Without the redshift for the BH-BH events, they cannot be directly used to test DDR. If, however, the GW event can be precisely localized, it is possible to infer the redshift of GW source statistically [603], but will introduce additional uncertainty.

14.2.2 The mock DDR data points

The fiducial cosmological distances

In order to forecast direct measurements of the duality parameter $\eta(z)$ from the ET, we use mock distance data points based on individual measurements of the luminosity and angular diameter distances $d_L(z)$ and $d_A(z)$ respectively, as described previously. To join the two measurements and derive the $\eta(z)$ data points, we follow the pioneering work of Ref. [588] using a Markov Chain-Monte Carlo (MCMC) approach to create mock samples.

In an nutshell we can summarize this approach as follows. First, we assume a fiducial cosmology based on the cosmological constant Λ and Cold Dark Matter (ΛCDM) model with a Hubble constant $H_0 = 70$ km s^{-1} Mpc^{-1}, a matter density parameter $\Omega_{m,0} = 0.3$ and assuming flatness ($\Omega_k = 0$). Then, based on the redshift distribution of sources, see Fig. 1 in Ref. [590] and Fig. 2 in Ref. [570] for either NS-NS or NS-BH, we calculate at every point in redshift the corresponding angular diameter distance $d_A(z)$ and the luminosity distance $d_L(z)$ via the methodology of Ref. [590] as described earlier. At this point, we also introduce a modification of the luminosity distance so that the observed luminosity distance would be proportional to the "bare" one as:

$$d_{L,\rm obs}(z) = (1+z)^{\epsilon(z)} d_{L,\rm bare}(z), \tag{14.20}$$

such that it corresponds to a duality parameter $\eta(z) = (1+z)^{\epsilon(z)}$, which should be equal to unity if no deviations are present, i.e. $\epsilon(z) \to 0$ in the ΛCDM model and $\eta(z) = 1$. In particular, we assume that to lowest order, any deviations are small enough that we can assume a constant $\epsilon(z) = \epsilon_0$. In general, any such deviations on the GW sector could be due to modifications of gravity, see for example Ref. [471]. Specifically, in what follows we will assume four specific scenarios: the vanilla ΛCDM case for $\epsilon_0 = 0$ and three more cases with one mild and two stronger deviations of the duality relation with $\epsilon_0 = (0.01,\ 0.05,\ 0.1)$.

As mentioned earlier, current supernovae and BAO data constrain the parameter to be $\epsilon_0 = 0.013 \pm 0.029$ and there is no evidence for a redshift evolution of $\epsilon(z)$, while that Euclid will be able to improve the constraints by a factor of six [470]. Thus, our choices of the ϵ_0 are realistic at the lower end ($\epsilon_0 \sim 0.01$) and high enough to sufficiently test our methodology at the higher end ($\epsilon_0 \sim 0.1$). In any case the constant $\epsilon(z) = \epsilon_0$ is the simplest ansatz used to test for deviations from the duality relation and it does not really affect our analysis or our conclusions.

The mock samples of $\eta(z)$

After we have calculated the fiducial values of the cosmological distances, we can then make mock samples of the duality parameter $\eta(z)$ directly via the following procedure: First, at each redshift we create mock distances $d_A(z_s)$ and $d_L(z_s)$ based on a Gaussian distribution using the fiducial values and 1σ errors based on the methodology of Ref. [588], such that for the mock we have

$$(D_{i,\mathrm{mock}}, \sigma_{i,\mathrm{mock}}) \to \mathcal{N}(D_{i,\mathrm{fid}}, \sigma_{i,\mathrm{fid}}), \tag{14.21}$$

where $i = 1 \ldots N_{\mathrm{lens}}$, D_i represents either d_A or d_L, while $\sigma_{i,\mathrm{fid}}$ are the errors and $\mathcal{N}(\mu, \sigma)$ stands for a normal distribution with mean μ and standard deviation σ. Then, to make a mock sample of $\eta(z_i)$ values we can use Eq. (14.2) and finally, we employ an MCMC-like approach to obtain the mean values and the errors of the data points as follows:

1. Using the mock distances at each redshift $D_{i,\mathrm{mock}}$ we draw 10,000 random samples from the assumed distribution for $D_{i,\mathrm{mock}}$.
2. We then estimate $\eta(z_i)$ at each redshift z_i for each of the 10,000 random points using Eq. (14.2) to obtain 10,000 realisations of the distribution of $\eta(z_i)$.
3. We estimate the mean and standard deviation of $\log_{10}\eta(z_i)$ at each redshift point to create our final mock sample.

The main advantage of this MCMC-like approach is that it does not depend on error propagation for the various quantities, which could be highly non-trivial for complicated modified gravity models, but it also preserves the statistical properties of the samples. This allows us to obtain our results without any further dependence on the cosmological model and in Ref. [471] it was shown that this approach allows for the creation of mocks that have minimal external biases, theoretical, statistical or otherwise. For example, this means that we no longer have to assume that the distributions of the $\log_{10}\eta(z_i)$ data points are sufficiently Gaussian, as implied by standard error propagation and which may bias the results by introducing artificial deviations from the fiducial model.

Finally, we should note that we chose to make mocks of $\log_{10}\eta(z_i)$ instead of simply $\eta(z_i)$, as we found that the distribution of the latter is somewhat non-gaussian, while on the other hand, $\log_{10}\eta(z_i)$ is very close to being normally distributed around zero, i.e. $\log_{10}\eta(z_i) \sim \mathcal{N}(0, \sigma_{\log_{10}\eta(z_i)})$. Then, having created the $\log_{10}\eta(z_i)$ samples, we consider a likelihood $\mathcal{L}$ of the form [588]:

$$-2\ln\mathcal{L} = \sum_{i=1}^{N_{\mathrm{lens}}} \left(\frac{\log_{10}\eta(z_i) - \log_{10}\eta^{\mathrm{th}}(z_i)}{\sigma_{\log_{10}\eta(z_i)}} \right)^2 \tag{14.22}$$

where $\eta^{\mathrm{th}}(z_i)$ is the theoretical value of $\eta(z_i)$. In our actual analysis we will consider the somewhat optimistic case of $N_{\mathrm{lens}} = 100$ as an optimistic case for the possible number of events that could be detected in the coming decades.

14.2.3 Machine learning

Machine learning (ML) is a subset of artificial intelligence designed to model a given dataset. ML approaches have been proven to be successful at processing and extracting essential information from large amounts of data and can get rid of the problem of model bias [401], while also being very effective in testing the consistency of the dataset model independently and also for searching tensions or systematics. See Chapter 9 for a more lengthy motivation and the use of ML algorithms applied to GW physics.

In what follows we will describe two particular classes of ML methods, the Genetic Algorithms (GA) and the Gaussian Processes (GP) which we use to perform our analysis. One of the advantages of the GA against other symbolic regression methods, such as Neural Networks, is that the GA provides analytical functions that describe the data provided. In our Chapter we have also used the GP to compare our results with the GA, but it is beyond the scope of this work to compare all of the different symbolic regression ML approaches.

The Genetic Algorithms

The theoretical background of the implementation of the GA in our analysis can be found on Chapter 10.

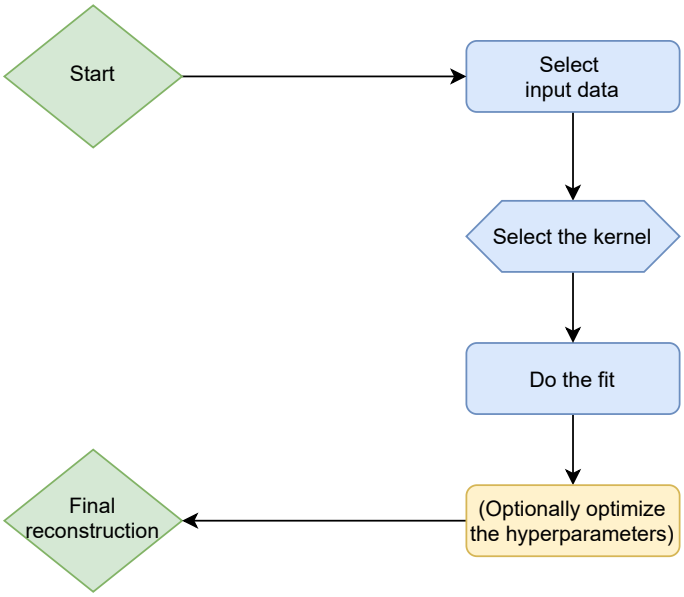

Figure 14.2: Flowchart of the list of steps of a usual Gaussian Process.

In this analysis we reconstruct the DDR parameter $\log_{10}\eta(z_i)$ directly from the data, and the procedure to its reconstruction proceeded as follows. First, our predefined grammar consisted on the following orthogonal basis of functions: exp, log, polynomials etc. and a set of operations $+, -, \times, \div$, see Table 10.1 for a complete list.

We also imposed a prior motivated by physical reasons. The only assumption made is that $\eta(z)$ is equal to 1; at out present time $z = 0$. This is natural to expect since mechanisms where the DDR is violated are cumulative, as photons interact with interceding constituents along the line of sight. Hence, such an event does not have time to occur at vanishing redshifts. This can also be seen by taking the limit for $z = 0$ at Eq. (14.2) and assuming the Hubble law, i.e. $\lim_{z\to 0}\eta(z) = 1$. Finally, we make no assumptions on the curvature of the Universe or any modified gravity or dark energy model.

We also required that all functions reconstructed by the GA are continuous and differ-

entiable, without any singularities in the redshift probed by the data, avoiding in this manner overfitting or any spurious reconstructions.

Once the initial population has been constructed, the fitness of each member is evaluated by a χ^2 statistic, using the $\eta(z)$ data points directly as input. Afterwards, using a tournament selection, see Ref. [464] for more details, the best-fitting functions in each generation are chosen and the two stochastic operations (crossover and mutation) are used. In order to assure convergence, the GA process is then repeated thousands of times and with various random seeds, so as to properly explore the functional space. Then the final output of the code is a function of $\eta(z)$ that describes the evolution of the DDR.

Finally, the error estimates of the reconstructed function are determined via the path integral approach, which was originally implemented in Refs. [169, 417] and is explained in detail on Sec. 10.0.2.

The Gaussian Processes

We also use the Gaussian Processes approach in order to provide an alternative to the GA reconstruction and minimize any potential biases due to the reconstruction approach. Traditionally, a Gaussian process (GP) is defined as an ensemble of random variables that have a joint Gaussian distribution [604]. The GP in general is determined by the mean, usually assumed to be zero or some fiducial model, and the covariance. In our case the GP random variables stand for the duality parameter $\log_{10}\eta(z_i)$.

On the other hand, the covariance function, also known as a kernel, is denoted by $k(x,\tilde{x})$ and encodes the correlations of two different GP random variables denoted by x and $\tilde{x}$, which in our case correspond to the values of the duality parameter $\eta(z)$ at different values of z, i.e. two different data points of the data set. In summary then, the kernel is used to join up the data points in order to build a function. In practice, the kernel is related to the input data as it is used as a measure of the similarity between points, i.e. a covariance function, and is used to predict the value for an unseen point from training data.

Lately the GPs have been used in the reconstruction of a plethora of cosmological datasets, see e.g. [404, 467, 605–612], while the proper choice of the kernel remains a hotly debated issue in the literature, as it can strongly affect the GP reconstruction. In Ref. [613] it was found that a kernel that works quite well for cosmological datasets is the so-called Matérn class of kernels, given by [604]:

$$k(x,\tilde{x}) = \sigma_M^2 \frac{2^{1-\nu}}{\Gamma(\nu)} \left(\frac{\sqrt{2\nu}(x-\tilde{x})}{\ell} \right)^{\nu} K_\nu \left(\frac{\sqrt{2\nu}(x-\tilde{x})}{\ell} \right),$$

where K_ν is a modified Bessel function, ν determines the shape of the covariance function, which asymptotes to the Gaussian limit as $\nu \to \infty$, while $\Gamma(\nu)$ is the gamma function.

Furthermore, the parameter ℓ describes the length scales over which the function varies, while the parameter σ_M corresponds to the magnitude of these variations. The parameter ν is further chosen to be a half-integer to minimize the dependence on the Bessel function [613]. High values of ν make the GP smoother but for $\nu \geq 7/2$ the results are practically indistinguishable from each other, so we make the choice $\nu = 5/2$. Overall, we find that altering either the GP kernels or ν does not impact the performance of the GP. In our analysis we use the GP Python package `george` [614] to reconstruct of $\log_{10}\eta(z)$ with the kernel as described above. Also note that in the GP the log-likelihood given by Eq. (14.22) is used, by maximising it, to optimise the value of any hyperparameters in the kernel.

Finally, similarly to the GA case described in the previous section, we have also imposed a prior on the GP reconstructions which is motivated by physical reasons. Specifically, we again demand that $\eta(z)$ is equal to unity at out present time $z = 0$, i.e. $\eta(z = 0) = 1$. Again, this is necessary to ensure our reconstructions are physical, while at the same time keeping our analysis general enough.

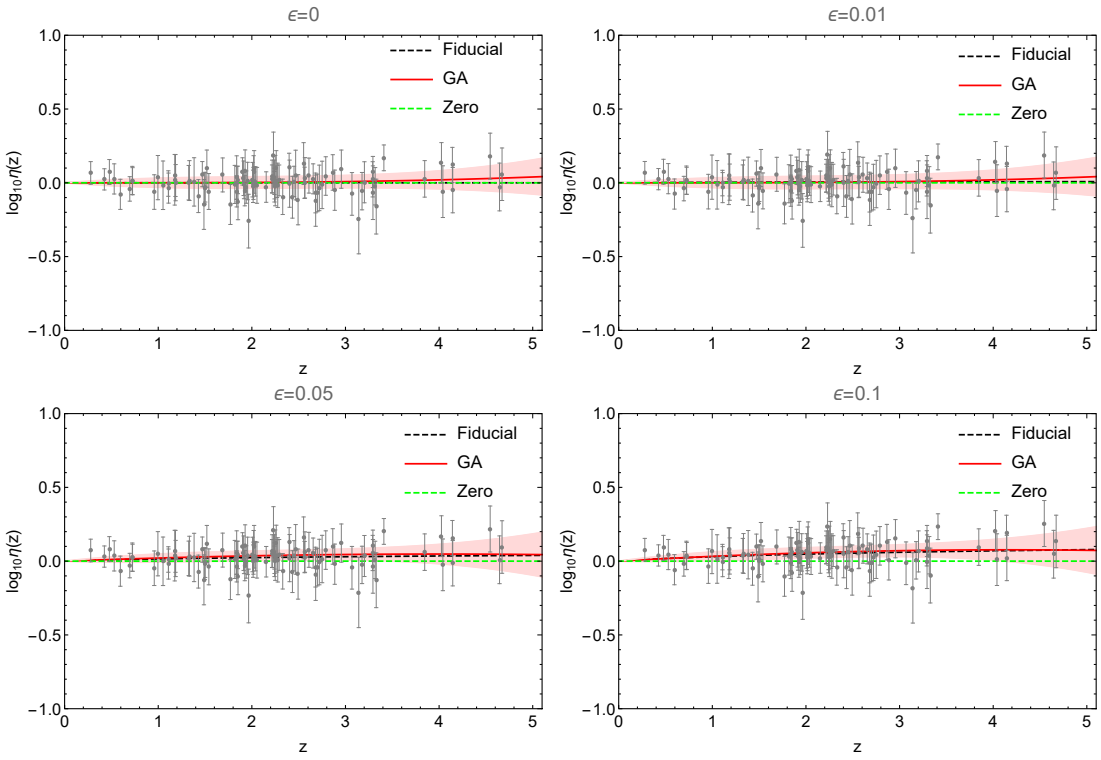

Figure 14.3: The $\eta(z)$ mocks along with the fiducial model given by Eq. (14.2) (black dashed line), the case of $\log_{10}\eta = 0$ (dashed green line), the corresponding best-fit (solid colored line) for the GA for $\epsilon = (0, 0.01, 0.05, 0.10)$ in the top left, top right, bottom left and bottom right panels respectively. In all cases the $\eta(z)$ data points are shown in the background as gray points with their 1σ errorbars and the shaded band corresponds to the 1σ confidence region for the GA (red band).

14.3 Results

We will now present the results of the reconstruction for both the GA and GP approaches.[3] Note that in both cases the input data are the values of $\log_{10}\eta_i$ in the form of sets of points given by $(z, \log_{10}\eta_i, \sigma_{\log_{10}\eta_i})$, which are the inputs to the GP and GA and can be used to create a likelihood, as discussed in the previous point. In the case of the GA the data enter only via the likelihood of Eq. (14.22), while on the other hand the GP builds a function that essentially joins up the data points according to the GP kernel, but also uses the data (via the likelihood) to optimise the value of any hyperparameters.

In Figs. 14.3 and 14.4 we show a particular realization of the $\log_{10}\eta(z_i)$ mocks for $N_{\rm lens} = 100$, along with the fiducial model (dashed black line), the case of $\log_{10}\eta = 0$ (dashed green line), and the corresponding best-fit (solid colored line) for the GA and the GP for $\epsilon = (0, 0.01, 0.05, 0.10)$ in the top left, top right, bottom left and bottom right panels respectively. The data points are shown in the background as gray points with their 1σ errorbars and the shaded band corresponds to the 1σ confidence region for the GA (red band) and the GP (magenta band) in the two plots.

Note that for the different values of ϵ for the mocks, we keep the same random seed number so that our analysis is not complicated by statistical fluctuations and the interpretation of our results is more straightforward. The apparent lack of events at high redshifts is due to the expected redshift distribution of the BH-NS and NS-NS events, see Fig. 1 in Ref. [590] and Fig. 2 in Ref. [570], which

[3]Both codes are very efficient and it takes a few seconds for the GA and less than a second for the GP to converge, which is comparable to other traditional parametric approaches.

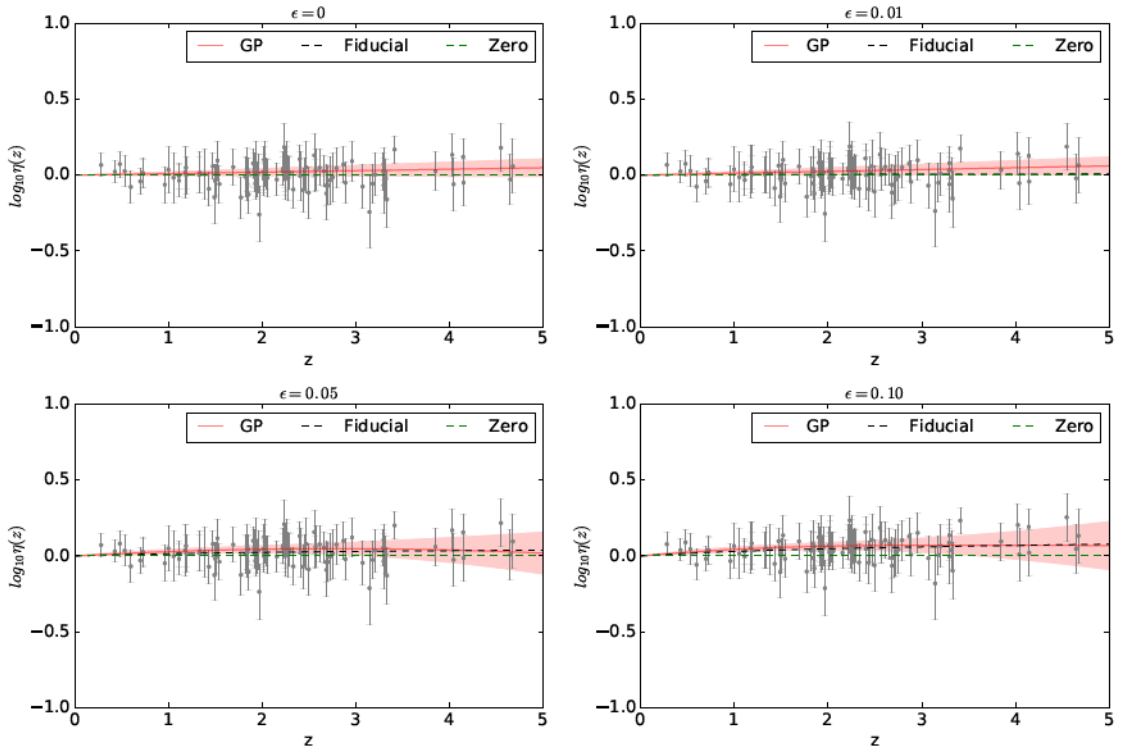

Figure 14.4: The $\eta(z)$ mocks along with the fiducial model given by Eq. (14.2) (black dashed line), the case of $\log_{10}\eta = 0$ (dashed green line), the corresponding best-fit (solid colored line) for the GP for $\epsilon = (0, 0.01, 0.05, 0.10)$ in the top left, top right, bottom left and bottom right panels respectively. In all cases the $\eta(z)$ data points are shown in the background as gray points with their 1σ errorbars and the shaded band corresponds to the 1σ confidence region for the GP (magenta band).

also has the side-effect of increasing the errors of the reconstructions and making the fits increase with redshift at high z. The expected probability density of events as a function of redshift, i.e. the redshift distribution of the BH-NS and NS-NS events for the ET, was determined in Ref. [570] by using the intrinsic merger rates of these objects with the help of a population synthesis evolutionary code.

The only physical prior used in the reconstruction was the assumption that $\lim_{z\to 0}\eta(z) \to 1$, which follows naturally from the definition of $\eta(z)$ via Eq. (14.2) and the fact that, at zero redshift the causes of any deviation (for example either axions for light or modified gravity for the GW) have had no time to yet act, which is necessary to ensure that our results are physical.

As can be seen in Figs. 14.3 and 14.4, in all cases both the GA and the GP capture the behavior of the data points accurately and remain close to the fiducial model, well within the 1σ region. In particular, on average the difference between the GA or GP best-fit and the fiducial model remains close to a percent level in all reconstructions. Furthermore, for both ML approaches we find that the reconstructed errors are consistent with each other, thus we are confident in our reconstruction as the GA and the GP are in principle rather different reconstruction methods. In particular, we see in both the GA and GP cases that when $\epsilon = (0.05, 0.10)$ both ML approaches find a clear deviation from the null hypothesis, i.e. $\log_{10}\eta = 0$ (dashed green line) for $0 \leq z \leq 3.5$. For higher redshifts, due to the lack of points the errors of the reconstruction become larger and the statistical significance of the detection diminishes[4].

[4]As a consistency test of our approach, we also fit the parameterization $\eta(z) = (1+z)^{\epsilon_0}$, with ϵ_0 =cosntant, to the mock data and we discuss our results in Appendix 14.4.

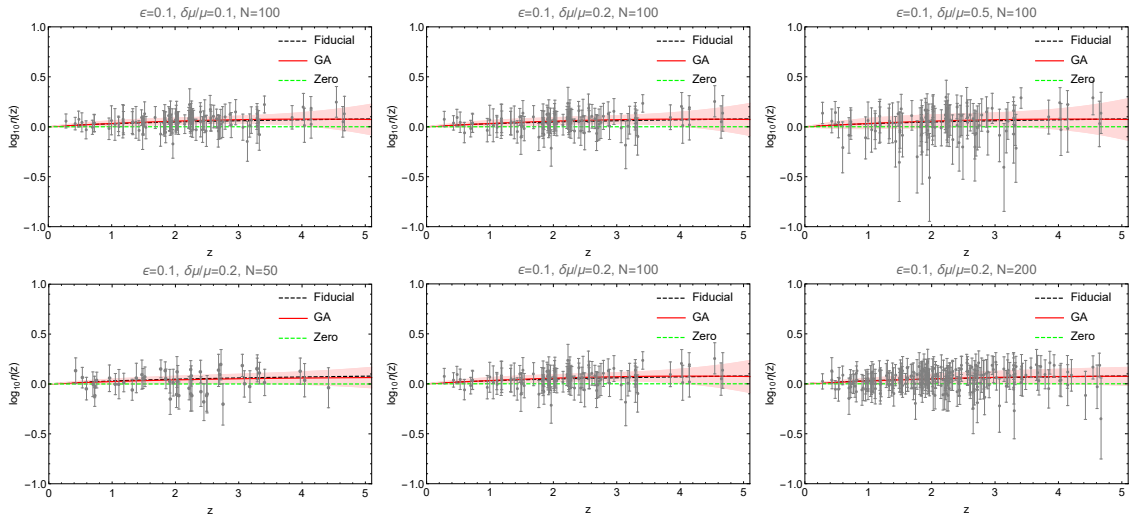

Figure 14.5: The $\eta(z)$ mocks along with the fiducial model given by Eq. (14.2) (black dashed line), the case of $\log_{10}\eta = 0$ (dashed green line), the corresponding best-fit (solid colored line) for the GA for $(\epsilon = 0.10, \delta\mu/\mu = 0.1, N = 100)$, $(\epsilon = 0.10, \delta\mu/\mu = 0.2, N = 100)$ $(\epsilon = 0.10, \delta\mu/\mu = 0.5, N = 100)$, $(\epsilon = 0.10, \delta\mu/\mu = 0.2, N = 50)$, $(\epsilon = 0.10, \delta\mu/\mu = 0.2, N = 100)$, $(\epsilon = 0.10, \delta\mu/\mu = 0.2, N = 200)$ in the top left, top center, top right, bottom left, bottom center and bottom right panels respectively. In all cases the $\eta(z)$ data points are shown in the background as gray points with their 1σ errorbars and the shaded band corresponds to the 1σ confidence region for the GA (red band).

Finally, we also vary two key parameters of our analysis, the amplification error $\delta\mu/\mu$ and the number of events N. Using the GA, we reconstruct $\eta(z)$ with the amplification error $\delta\mu/\mu$ taking the values $[0.1, 0.2, 0.5]$ and then we do the same with the number of lenses with $N = [50, 100, 200]$ events for the case of $\epsilon = 0.1$. We show the results in Fig. 14.5 and we find that as expected, increasing the amplification error (top row of plots in Fig. 14.5) has no obvious effect when $\delta\mu/\mu$ changes from 0.1 to 0.2. As can be seen in Eq. (14.19) when $\rho = 16$, which is the critical value for which we assume to claim the detection of GW signal, then the $2/\rho$ term is about 0.1, the $0.05z$ term is also about 0.1 for $z \sim 2$ and is even larger for $z > 2$. Since there is a factor $1/4$ before the term $\delta\mu/\mu$, changing $\delta\mu/\mu$ from 0.1 to 0.2 does not affect significantly the total error on the luminosity distance $d_L(z)$. On the other hand, when $\delta\mu/\mu = 0.5$, then the last term in Eq. (14.19) dominates and this results in larger errors, by roughly $\sim 20\%$, for the GA reconstruction of $\eta(z)$, compared to when $\delta\mu/\mu$ is 0.1 or 0.2.

On the other hand, the effect of varying the number of lenses is more subtle. As can be seen in the bottom row of Fig. 14.5, for 50 lenses we have a deviation at $\sim 1\sigma$ below $z \sim 4$, while in the case of 100 lenses the errors of the GA reconstruction become smaller for $z < 4$ raising the deviation to slightly more than 1σ but at $z > 4$ surprisingly become larger again. This tightening of the errors at intermediate redshifts ($z < 4$) and enlarging at $z > 4$ as we increase the points from 50 to 100 is due to the redshift distribution of the points (for 100 points more events are located at $z < 3.5$). When we increase the number of events to 200, we see the error at high redshifts is now more uniform, even though the reconstructions start to get dominated by the systematic errors. In summary, the number of events necessary to obtain a statistically significant deviation depends both on the value of ϵ and the number of events, so for example with $N = 50$ we can have a 1σ deviation up to $z \sim 4$ while to go to higher redshifts ($z \sim 5$) we require $N = 200$.

14.4 Comparative analysis

Here we present a reconstruction of the duality parameter $\eta(z)$ using the mock data presented in Sec. 14.2 by fitting them to the parametrization of Eq. (14.2) with $\epsilon(z) = \epsilon_0$ =constant. This allows us to compare our GA and GP reconstructions to the standard parametric approach used widely in the literature.

In particular, in Fig. 14.6 we present the different fiducial mocks for $\epsilon = \{0, 0.01, 0.05, 0.1\}$ along with the best-fit parameterizations and their respective errors (blue line and blue shaded region). Comparing these against the reconstructions of Fig. 14.3 we find that they are in good agreement, albeit the parametric approach has somewhat smaller errors compared to the GA, due to its parametric nature, something which was also observed in Ref. [470]. As all three reconstructions, that of the GA, the GP and the parametric ones are in good agreement, we are confident in our methodology.

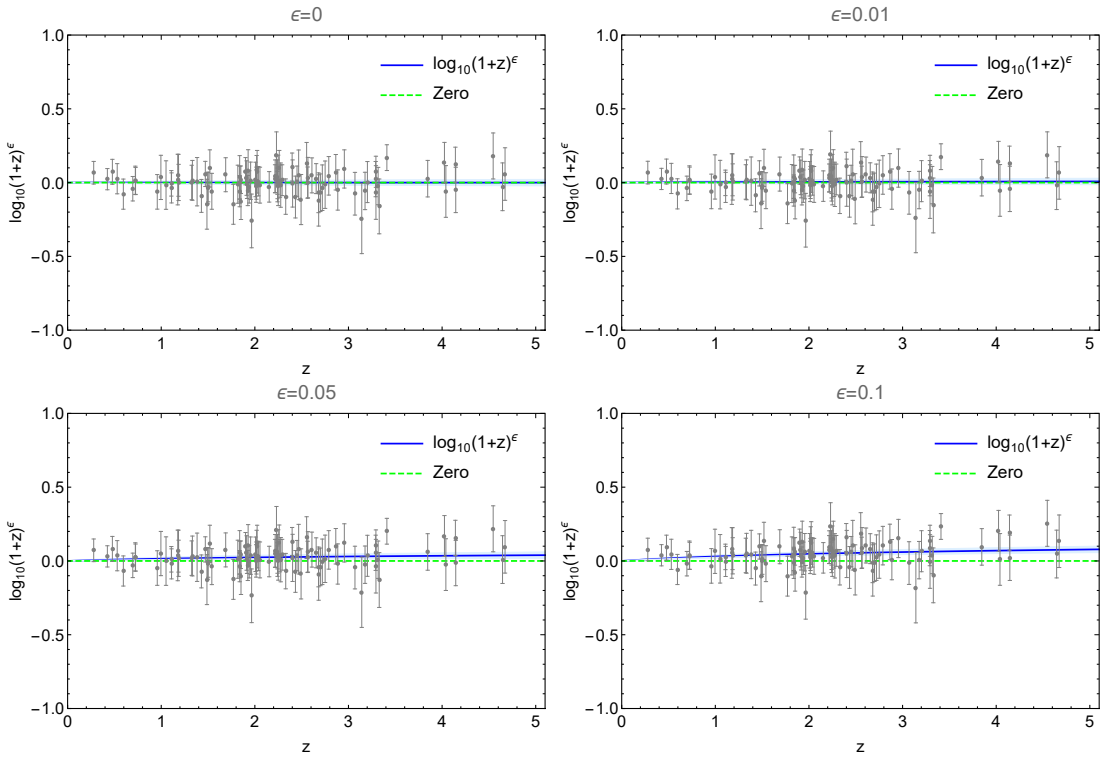

Figure 14.6: The $\eta(z)$ mocks along with the fiducial model given by Eq. (14.2) (blue line) for $\epsilon = (0, 0.01, 0.05, 0.10)$ in the top left, top right, bottom left and bottom right panels respectively and the case of $\log_{10}\eta = 0$ (dashed green line). In all cases the $\eta(z)$ data points are shown in the background as gray points with their 1σ errorbars and the shaded band corresponds to the 1σ confidence region for the best-fit fiducial model (blue band).

14.5 Conclusions

With the advent of GW observations an exciting new window has opened into the Universe. Moreover, a possible detection of strong GW lensing will allow for the testing of fundamental hypotheses of the standard cosmological model as it will provide a test of gravity in the strong field regime, but will also allow for tests of the DDR, similar to that proposed in Ref. [588] for strongly lensed SnIa systems. This exciting possibility was first proposed in Ref. [590], where parametric constraints of the DDR variable $\eta(z)$, given by Eq. (14.2) were presented.

Here, we extended the work of Ref. [590] in two crucial ways. First, we presented a methodology which allows for the direct creation of $\eta(z)$ mocks, similar to that of Ref. [588]. We showed an example of this approach using mock ET measurements of d_L and d_A from strongly lensed GW events, which were then combined to create mock $\eta(z)$ data points with an MCMC-like approach, as described in Sec. 14.2.2. It is important to stress that given the raw measurements of d_L and d_A, the measurements of $\eta(z)$ can be derived without using any dark energy model or beyond the standard model (BSM) theory.

Second, instead of using parametric models for $\eta(z)$, which may carry theoretical bias or miss important features in the data, here we used two specific ML approaches. In particular, we employed the Genetic Algorithms and the Gaussian Processes, which are two non-parametric and symbolic regression subclasses of ML methods, to reconstruct $\eta(z)$ directly without using any underlying model.

Following our methodology, we created a realization of mock $\eta(z)$ data points for $\epsilon = (0, 0.01, 0.05, 0.10)$, assuming the ET specifications, and then used the GA and the GP to directly reconstruct $\eta(z)$. The reconstructions are shown in Figs. 14.3 and 14.4 where as can be seen, both the GA and the GP capture the behavior of the data points accurately and remain close to the fiducial model, well within the 1σ region for all values of the duality parameter ϵ. In particular, on average the difference between the GA or GP best-fit and the fiducial model remains close to a percent level in all reconstructions. Furthermore, in the two most extreme cases of $\epsilon = (0.05, 0.10)$ both the GA and the GP find deviations from zero in the redshift range $0 \leq z \leq 3.5$.

We also determined the number of GW lensed events necessary to determine whether a deviation from the null hypothesis is present in the data. We find that the number of events necessary to find a deviation depends both on the value of ϵ and the number of events, so for example with $N = 50$ we can probe for deviations from the null hypothesis ($\epsilon = 0$) up to $z \sim 4$, while to go to higher redshifts we require $N = 200$.

We thus find that both machine learning approaches are capable of correctly recovering the underlying fiducial model and providing percent-level constraints when comparing the fiducial model and the reconstructions at intermediate redshifts, when applied to future Einstein Telescope data, thus opening the door to direct tests of the fundamental principles of the standard cosmological model in the coming decades.

Numerical Analysis Files: For the Gaussian process analysis we use the publicly available python package `george` found at https://github.com/dfm/george.

15

Machine Learning and cosmographic reconstructions of quintessence and the Swampland conjectures

The original content of this chapter is based on Ref. [615]. We present model independent reconstructions of quintessence and the Swampland conjectures (SC) using both Machine Learning (ML) and cosmography. In particular, we demonstrate how the synergies between theoretical analyses and ML can provide key insights on the nature of dark energy and modified gravity. Using the Hubble parameter $H(z)$ data from the cosmic chronometers we find that the ML and cosmography reconstructions of the SC are compatible with observations at low redshifts. Finally, including the growth rate data $f\sigma_8(z)$ we perform a model independent test of modified gravity cosmologies through two phase diagrams, namely $H-f\sigma_8$ and $\eta-f\sigma_8$, where the anisotropic stress parameter η is obtained via the E_g statistics, which is related to gravitational lensing data. While the first diagram is consistent within the errors with the ΛCDM model, the second one has a $\sim 2\sigma$ deviation of the anisotropic stress from unity at $z \sim 0.3$ and a $\sim 4\sigma$ deviation at $z \sim 0.9$, thus pointing toward mild deviations from General Relativity, which could be further tested with upcoming large-scale structure surveys.

15.1 Introduction

One of the more well known candidates for DE is quintessence, which is described by a slowly rolling scalar field leading to an accelerated expansion [276]. Thus, the scalar field can control the fate of the early and late Universe by dominating its energy density and posing as a source of DE respectively, see for example Ref. [616] for a review. For about a century theoretical physicists have been on the quest to develop a theory of quantum gravity which could encompass the assumptions of Einstein's theory of GR with those of quantum field theory. Although GR has demonstrated to have a very high predictive power below the Planck scale, its quantization its troublesome since it is renormalizable only at one loop [617], thus, it is believed that GR could be the low energy limit of the more fundamental higher energy theory as we have also discussed on Chapter 3.

There is an ongoing search to distinguish effective quantum field theories that can potentially arise within UV-complete quantum gravity theories (the Landscape) from those that cannot (the Swampland). In this regard, although not rigorously proven in string theory, some conjectures have been considered to discern the Swampland from the landscape. The two proposed Swampland criteria that we will consider (which we will define as SC1 and SC2) refer to the constraints on the field range of a scalar field ϕ defined by an effective field theory and to the slope of the potential of such fields respectively. In reduced Planck units these conjectures are defined as

- SC1: The scalar field net excursion has to satisfy $\frac{|\Delta\phi|}{M_{\rm pl}} < \Delta \sim O(1)$ [618].

- SC2: There is a lower bound for the gradient of the scalar field potential $M_{\rm pl}\,|\nabla_\phi V|\,/V > c \sim \mathcal{O}(1)$ in any consistent theory of gravity when $V > 0$ [619],

where Δ and c are positive constants of order one and the reduced Planck mass is $M_{\rm pl} = 1/\sqrt{8\pi G}$. The second Swampland criterion is violated in the ΛCDM model, since a positive cosmological constant or being at the minimum of a potential with positive energy density violates the bound [620], thus a rolling scalar field potential, i.e a quintessence model would be required. Hence, if the data supports the second Swampland criterion, it would imply hints for deviations of the ΛCDM model.

The Swampland criteria aim to find constructions that are compatible with a quantum theory of gravity and it has been found that specific quintessence models can satisfy the Swampland criteria at late times [620]. In Ref. [621] the authors used Gaussian Processes to reconstruct the form of the potential from the $H(z)$ data, finding hints of invalidating the Swampland criteria, while a similar analysis was performed in [622]. In Refs. [623, 624] it was found that quintessence models and current data prefer a lower value of H_0 than the ΛCDM model, thus providing robust test of the Swampland conjectures. Other analyses on the other hand, have found that string-inspired quintessence models with exponential potentials are ruled out by observations and that Swampland conjectures are in tension with viable single-field quintessence models [625, 626]. It was also proposed though that this issue might be resolved with multi-field models [627, 628]. See also Ref. [629] for the implications of the swampland conjectures on dark energy.

On the other hand, our motivation for using cosmography and Machine Learning (ML), both being model independent techniques, is because choosing a specific model can lead to model bias, which in turn would affect the conclusions drawn about fundamental physics. ML algorithms can help to remove biases due to choosing a priori a specific defined model and they are also ideal for events that are not well understood such as dark energy, dark matter or modifications of gravity. Another advantage is that we reconstruct the data without making assumptions on flatness or a dark energy model.

Here we use a particular ML method known as the genetic algorithms (GA), which can be defined as a stochastic search approach. However, in our analysis we will use both cosmography and the GA so as to compare the two methods and examine which one provides better constraints given the current data. In particular, we will focus on quintessence as an example of our approach and using the latest compilation of the Hubble parameter $H(z)$ and the growth rate data $f\sigma_8(z)$ we analyze the cosmological implications on two Swampland criteria providing constraints both via Machine Learning and cosmography. For the former approach, we reconstruct the Hubble function $H(z)$ and $f\sigma_8(z)$ using the GA, while with the later method we can express the Swampland conjectures solely via the cosmographic parameters.

Finally, in order to test and search for deviations from GR we use our ML reconstructions to analyze two phase diagrams, $H - f\sigma_8$ and $\eta - f\sigma_8$, where η is the anisotropic stress parameter. This conjoined diagrams have the asset of helping to break degeneracies between observations that are geometrical against those that come from gravitational effects and makes clearer even visually which redshift ranges should be the target of future surveys to discriminate among the plethora of DE and MG models. This approach has been used for different comparison of models, see for example Refs. [137, 141, 630–632].

This Chapter is organized as follows: In Sec. 15.2 we present the theoretical framework including the quintessence reconstruction and the cosmographic expansion. In Sec. 15.3 we describe the data used in our analysis and in Sec. 15.4 we outline our ML method, the Genetic Algorithms (GA). Then in Sec. 15.5 we set out our results and in Sec. 15.6 we provide two phase diagrams derived through our ML reconstructions. Finally in Sec. 15.7 we describe our error analysis and in Sec. 15.8 we present our conclusions.

15.2 Theory

Here we present some theoretical aspects of our analysis related to the reconstruction of quintessence and the cosmographic expansion.

15.2.1 Quintessence reconstruction

At late times, the Friedmann equations including quintessence can be written as

$$H^2 = \frac{8\pi G}{3}\left(\rho_m + \frac{1}{2}\dot{\phi}^2 + V(\phi)\right), \tag{15.1}$$

$$\dot{H} = -4\pi G\left(\rho_m + \dot{\phi}^2\right), \tag{15.2}$$

where $H \equiv \frac{\dot{a}}{a}$, for $a = \frac{1}{1+z}$ and after setting $x \equiv 1+z$ they can be solve for the potential and the kinetic terms and be rewritten as [633]

$$\frac{8\pi G}{3H_0^2}V(x) = \frac{H(x)^2}{H_0^2} - \frac{x}{6H_0^2}\frac{d(H(x)^2)}{dx} - \frac{1}{2}\Omega_{\mathrm{m},0}x^3, \tag{15.3}$$

$$\frac{8\pi G}{3H_0^2}\left(\frac{d\phi}{dx}\right)^2 = \frac{2}{3H_0^2 x}\frac{d\ln H}{dx} - \frac{\Omega_{\mathrm{m},0}x}{H^2}. \tag{15.4}$$

It is more convenient to rescale all variables and use dimensionless quantities, which can be done for example by introducing the Planck mass $M_{\rm pl} \equiv \sqrt{\frac{\hbar c}{8\pi G}} = \sqrt{\frac{1}{8\pi G}}$ in natural units ($\hbar = c = 1$) and the fact that the critical density is $\rho_c = \frac{3H_0^2}{8\pi G}$. Then we can make the redefinitions

$$\begin{aligned} E(z) &\equiv H(z)/H_0, \\ \tilde{\phi}(z) &\equiv \frac{\phi(z)}{\sqrt{3}M_{\rm pl}}, \\ \tilde{V}(z) &\equiv \frac{V(z)}{\rho_c}, \end{aligned} \tag{15.5}$$

and rewrite the reconstruction equations for the scalar field as

$$\tilde{V}(x) = E(x)^2 - \frac{x}{6}\frac{d(E(x)^2)}{dx} - \frac{1}{2}\Omega_{\mathrm{m},0}x^3, \tag{15.6}$$

$$\left(\frac{d\tilde{\phi}}{dx}\right)^2 = \frac{2}{3x}\frac{d\ln E}{dx} - \frac{\Omega_{\mathrm{m},0}x}{E(x)^2}. \tag{15.7}$$

To reconstruct the potential we then integrate Eq. (15.7) to determine $\tilde{\phi}(x)$ up to a constant, then we write x as a function of $\tilde{\phi}$ i.e $x(\tilde{\phi})$ and insert it in Eq. (15.6) to find the potential in terms in the scalar field $\tilde{V}(\tilde{\phi})$. For the ML approach the function $H(x)$ and the parameters H_0 and $\Omega_{\mathrm{m},0}$ will be given by the GA fits to the data, as described in Section 15.3, while in the case of cosmography we will determine the function $H(x)$ from the cosmographic reconstruction and we will assume a Planck 2018 prior on $\Omega_{\mathrm{m},0}$.

Note that using the aforementioned equations one may try to reconstruct any DE model, e.g. the constant equation of state w=const model or other parameterized $w(z)$ models [634].

15.2.2 Cosmography

Cosmography is a model independent series expansion in terms of the redshift z that relates the cosmological quantities, such as the Hubble parameter and luminosity distance, to a set of

cosmographic coefficients defined as the nth derivative of the scale factor [635–638]:

$$H \equiv \frac{1}{a}\frac{da}{dt}, \qquad q \equiv -\frac{1}{aH^2}\frac{d^2a}{dt^2}, \tag{15.8}$$

$$j \equiv \frac{1}{aH^3}\frac{d^3a}{dt^3}, \qquad s \equiv \frac{1}{aH^4}\frac{d^4a}{dt^4}, \tag{15.9}$$

$$l \equiv \frac{1}{aH^5}\frac{d^5a}{dt^5}, \qquad m \equiv \frac{1}{aH^6}\frac{d^6a}{dt^6}. \tag{15.10}$$

With simple algebra we can relate these quantities, evaluated today, i.e. at $z = 0$, to the series expansions of the Hubble parameter and the luminosity distance. For example, following Ref. [635] we find that the luminosity distance in a flat Universe ($\Omega_k = 0$) can be written up to fifth order in redshift as:

$$\begin{aligned} d_L(z) &= \frac{c}{H_0}\Big[z + \frac{1}{2}(1-q_0)z^2 + \frac{1}{6}(-1-j_0+q_0+3q_0^2)z^3 \\ &+ \frac{1}{24}(2+5j_0(1+2q_0) - q_0(2+15q_0(1+q_0)) + s_0)z^4 \\ &+ \frac{1}{120}\big((-6+10j_0^2 - l_0 - j_0(27+5q_0(22+21q_0)) \\ &+ 3q_0(2+q_0(27+5q_0(11+7q_0)) - 5s_0) - 11s_0)\big)z^5 + \mathcal{O}(z^6)\Big], \end{aligned} \tag{15.11}$$

while by inverting the equation of the luminosity distance that relates it to the Hubble parameter for a flat Universe, i.e. $d_L(z) = \frac{c}{H_0}(1+z)\int_0^z \frac{1}{H(u)/H_0}du$, and solving for $H(z)$ we find

$$\begin{aligned} H(z)/H_0 &= 1 + (1+q_0)z + \frac{1}{2}(j_0 - q_0^2)z^2 \\ &+ \frac{1}{6}\left(3q_0^2(1+q_0) - j_0(3+4q_0) - s_0\right)z^3 \\ &+ \frac{1}{24}\big(-4j_0^2 + l_0 - 3q_0^2(4+q_0(8+5q_0)) \\ &+ j_0(12+q_0(32+25q_0)) + (8+7q_0)s_0\big)z^4 + \mathcal{O}(z^5). \end{aligned} \tag{15.12}$$

Note that going from the luminosity distance given by Eq. (15.11) to the Hubble parameter given by Eq. (15.12), implies the use of differentiation and the presence of a term $1+z$, both of which reduce the order of the polynomial from fifth order to only fourth. This reduction of the polynomial will also be observed later on, when we derive the potential as a function of the scalar field and the cosmographic parameters.

Furthermore, it should be noted that there is an issue related to the convergence of the truncation order of the cosmographic series and the redshift range of the data. In Refs. [639–641] it has been suggested that the variable $y = \frac{z}{1+z}$ avoids the aforementioned convergence issues and is more suitable for parameterizing cosmological distances, where now y lays in the redshift interval $[0, 1]$ which encloses the range of all possible observations.

Using Eq. (15.12) we can now use the quintessence reconstruction set of equations given by Eqs. (15.6)-(15.7) to relate the cosmographic parameters to the potential $V(\phi)$, which after some simple algebra can be written in terms of the redshift z as

$$\begin{aligned} \tilde{V}(z) &= \frac{1}{6}(4 - 2q_0 - 3\Omega_{\mathrm{m},0}) + \frac{1}{6}(8 - 2j_0 + 6q_0 - 9\Omega_{\mathrm{m},0})\,z \\ &+ \frac{1}{6}(4 + 8q_0 + j_0(4+q_0) + s_0 - 9\Omega_{\mathrm{m},0})\,z^2 \\ &+ \frac{1}{18}(j_0^2 - l_0 - 9\Omega_{\mathrm{m},0} - j_0q_0(7+3q_0) - 7s_0 - 3q_0s_0)z^3 + \mathcal{O}(z^4), \end{aligned} \tag{15.13}$$

and the derivative of the scalar field $\left(\frac{d\tilde{\phi}'}{dz}\right)^2$ as

$$\begin{aligned}\tilde{\phi}'(z)^2 &= \frac{2(1+q_0)}{3} - \Omega_{\mathrm{m},0} + \frac{1}{3}\big(-4 + 2j_0 - 4q_0^2 \\ &+ 6q_0(\Omega_{\mathrm{m},0} - 1) + 3\Omega_{\mathrm{m},0}\big)z + \frac{1}{3}\big(6 - s_0 - 3\Omega_{\mathrm{m},0} \\ &+ j_0(-8 - 7q_0 + 3\Omega_{\mathrm{m},0}) + 4q_0(3 + 4q_0 + 2q_0^2 \\ &- 3(1+q_0)\Omega_{\mathrm{m},0})\big)z^2 + \mathcal{O}(z^3). \end{aligned} \tag{15.14}$$

Solving for $\tilde{\phi}$ by integrating the kinetic term over the redshift, will give two branches as

$$\tilde{\phi}(z) = \tilde{\phi}_0 + \epsilon \int_0^z \sqrt{\tilde{\phi}'(u)^2}du, \tag{15.15}$$

where $\epsilon = \pm 1$. We can then express the potential in terms of the cosmographic parameters and the scalar field $\tilde{\phi}$ as

$$\tilde{V}(\tilde{\phi}) = \tilde{V}_0 + \tilde{V}_1(\tilde{\phi} - \tilde{\phi}_0) + \tilde{V}_2(\tilde{\phi} - \tilde{\phi}_0)^2 + \tilde{V}_3(\tilde{\phi} - \tilde{\phi}_0)^3 + \mathcal{O}(\tilde{\phi}^4), \tag{15.16}$$

where we have set

$$\tilde{V}_0 = \frac{1}{6}\left(4 - 2q_0 - 3\Omega_{\mathrm{m},0}\right), \tag{15.17}$$

$$\tilde{V}_1 = \epsilon^{-1}\frac{8 - 2j_0 + 6q_0 - 9\Omega_{\mathrm{m},0}}{2\sqrt{6 + 6q_0 - 9\Omega_{\mathrm{m},0}}}, \tag{15.18}$$

$$\begin{aligned}\tilde{V}_2 &= \frac{1}{8}\left(15 + 6q_0 + \frac{4(j_0-1)^2}{\left(2 + 2q_0 - 3\Omega_{\mathrm{m},0}\right)^2} + \frac{4(2j_0 + 3q_0 + s_0)}{2 + 2q_0 - 3\Omega_{\mathrm{m},0}}\right), \\ \tilde{V}_3 &= \cdots, \end{aligned} \tag{15.19}$$

where we do not show the term $\tilde{V}_3$ as it is too long and complicated, but can be easily derived from the previous expressions.

We can now also calculate the effective mass of the scalar field as:

$$\begin{aligned} m_\phi^2 &= \frac{d^2V}{d\phi^2} \\ &= \frac{d^2\tilde{V}}{d\phi^2}H_0^2 \\ &= 2\tilde{V}_2 + 6\tilde{V}_3(\tilde{\phi} - \tilde{\phi}_0) + \cdots, \end{aligned} \tag{15.20}$$

where the coefficients V_2 and V_3 were given earlier. Then, the second Swampland conjecture (SC2) can be written as in terms of the cosmographic parameters as

$$\begin{aligned} M_{\mathrm{pl}}\frac{|V'(\phi)|}{V} &= \frac{\tilde{V}'(\tilde{\phi})}{\sqrt{3}\tilde{V}(\tilde{\phi})} \\ &= S_0 + S_1(\tilde{\phi} - \tilde{\phi}_0) + S_2(\tilde{\phi} - \tilde{\phi}_0)^2 + \cdots, \end{aligned} \tag{15.21}$$

where the coefficients S_0, S_1 and S_2 are given by

$$S_0 = \frac{\tilde{V}_1}{\sqrt{3}\tilde{V}_0}, \tag{15.22}$$

$$S_1 = -\frac{\tilde{V}_1^2 - 2\tilde{V}_0\tilde{V}_2}{\sqrt{3}\tilde{V}_0^2}, \tag{15.23}$$

$$S_2 = -\frac{\tilde{V}_1^3 - 3\tilde{V}_0\tilde{V}_1\tilde{V}_2 + 3\tilde{V}_0^2\tilde{V}_3}{\sqrt{3}\tilde{V}_0^3}. \quad (15.24)$$

Note that in the case of the cosmological constant model, we have that $\tilde{\phi}'(z) = 0$ and $\tilde{\phi}(z) = \tilde{\phi}_0$, which implies that $\tilde{V}(\tilde{\phi}) = \tilde{V}_0$ =constant, hence that $m_\phi^2 = 0$ and $S_0 = 0$ as expected. Note also that one has to take the limit to $w \to -1$ before differentiating, as the limit and the derivatives do not commute in this case.

We will present the results from the fits to the data and the cosmographic reconstructions of the conjectures in Sec.15.5.

15.3 Data

In this Chapter we will use the following cosmological data which is described in detail in Chapter 2: The Hubble rate $H(z)$ data, the growth-rate data and the $E_{\rm g}$ data.

15.4 Genetic Algorithms

A complete description on the Genetic Algorithms (GA) can be found at Chapter 10. Although it has already been covered on Sec.12.5, for completeness and for the benefit of the reader we will outline how to reconstruct the Hubble parameter $H(z)$ from the Hubble expansion history $H(z)$ data, $f\sigma_8(z)$ from the growth-rate data derived via the redshift-space distortions (RSD) and $P_2(z)$ from the Eg data. The reconstruction of $H(z)$, along with that of H_0, is needed for Eqs. (15.6) and (15.7), while our reconstruction for $f\sigma_8(z)$ is used to infer model independently the value of $\Omega_{\rm m,0}$ by means of Eq. (12.12) taken from Chapter 12. Our reconstruction of $P_2(z)$ from the Eg data is used at a latter stage in Sec. 15.6.

The outline to perform the reconstructions proceeds as follows. An initial population of functions is randomly selected so that every member of the population holds initial guesses for $H(z)$, $f\sigma_8(z)$ and $P_2(z)$. We also impose reasonable physical priors, e.g. the Hubble parameter today is given by the Hubble constant $H(z=0) = H_0$, which then allows us to estimate H_0 directly from the $H(z)$ data. For the $f\sigma_8(z)$ reconstruction we assume that the Universe at early times went through a phase of matter domination ($z \simeq 100$), then the linear growth acts as $\delta_m(a) \simeq a$ at high redshifts. However we make no assumption of a DE model or on the curvature of the Universe.

Next, the fitness of each member is computed through a χ^2 statistic, using as input the $H(z)$, growth and Eg data. Afterwards, the mutation and crossover operators are applied stochastically to the best-fitting functions in each generation, selected via the tournament selection method. This process is then repeated with different random seeds thousands of times in order to ensure convergence and not to bias the results due to a specific choice of the random seed. After the GA code has converged, the final output is a reconstruction of $H(z)$, $f\sigma_8(z)$ and $P_2(z)$.

For the estimation of the errors on the reconstructed functions we implement an analytical approach developed by Refs. [169, 417], where the errors are derived via a path integral over the whole functional space that can be scanned by the GA. See Chapter 10 for more details.

To sum up, with the GA we can reconstruct any cosmological function, for example the $H(z)$, $f\sigma_8(z)$ and $P_2(z)$ that we consider here, by applying the algorithm to any dataset of interest. There are no requirements on the specific cosmological model or assumptions on DE, hence our results are model independent. Besides executing a large number of GA runs with different random seed numbers, in order to avoid spurious reconstructions and overfitting we have imposed that all reconstructed functions, as well as their derivatives, are continuous in the range of redshifts we consider.

Model	$H(z)$	$f\sigma_8$	P_2
$\chi^2_{\Lambda\text{CDM}}$	19.476	12.238	10.516
χ^2_{GA}	17.670	12.220	5.422

Table 15.1: The χ^2 for ΛCDM and GA using the growth $f\sigma_8$, the Hubble rate $H(z)$ and the E_g statistics.

15.5 Results

15.5.1 Genetic Algorithm reconstructions

In this section we will now discuss our ML fits to the data and the corresponding reconstructions of the Swampland conjectures. First, we show in Table 15.1 the best-fit χ^2 for the GA functions for the ΛCDM model. As can be seen, in all cases the GA out-performs the ΛCDM model in terms of the best-fit χ^2.

Then, in the left panel of Fig. 15.1 we present our GA reconstruction of the scalar field potential as a function of the scalar field for the redshift range $z \in [0, 1.92]$. We can see a parabolic shape of the potential, thus pointing toward some deviations from the ΛCDM model since for the latter the potential should be flat. The black solid line corresponds with the GA best-fit and the different colours represent the errors for our reconstructions at different redshifts. In the right panel of Fig. 15.1 we see that the reconstructed kinetic term is positive from $z = 0$ to $z \sim 1.9$, hence our reconstructions of the Swampland conjectures within that redshift range should be free from ghosts and instabilities in this redshift range. The blue solid line corresponds to the GA best-fit and the grey region to the 1σ errors.

Note that the fact that at some redshift the kinetic term of the quintessence scalar field is negative, is actually a common issue of such reconstruction methods. This happens not only for quintessence models, but even for scalar tensor theories, where one naively may expect that due to the extra degree of freedom this would not happen[1]. This simply means that at some redshift the reconstruction breaks down, as obviously the kinetic term has to be both real and positive. However, due to the larger errors this is not a big problem per se, it just limits our ability to use this particular model at all redshifts.

In Fig. 15.2 we present our GA reconstructions of the first and second Swampland conjectures on the left and right panels respectively. In both cases the blue solid line and the grey region corresponds to the GA best-fit and the 1σ error respectively. As can be seen, from $z = 0.8$ onward the errors become so large that we can only draw some conclusions at low redshifts with the current available data. In specific we can see how both reconstructions are consistent with the conjectures, being both order unity, although at the same time being consistent with the ΛCDM model at the 1σ level.

15.5.2 Cosmographic reconstructions

We now present the cosmographic reconstructions of the potentials and the first and second Swampland conjectures. We find that the standard quintessence reconstruction via cosmography suffers from two issues: first, it is only valid when the square of the kinetic term given via Eq. (15.4) is positive. Second, a value of the matter density $\Omega_{\text{m},0}$ from an external source is required, as the $H(z)$ cannot provide it since Eq. (15.12) only depends on the cosmographic parameters and not at all on $\Omega_{\text{m},0}$.

We address the first issue by performing the reconstruction only in the redshift range where the kinetic term is positive, while for the value of the matter density parameter we will assume in what follows the Planck prior $\Omega_m = 0.315 \pm 0.007$ [1].

[1] See for example Fig. 5 in Ref. [642], where a similar phenomenon is also observed.

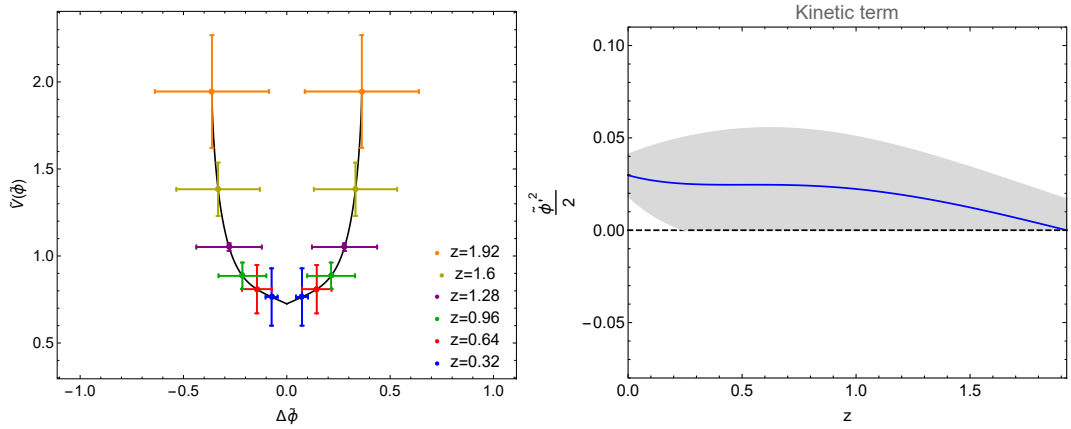

Figure 15.1: The GA reconstruction of the scalar field potential (left) and the kinetic term (right) for the redshift range $z \in [0, 1.92]$. The left panel suggests a parabolic shape of the potential, thus pointing toward some deviations from the ΛCDM model since for the latter the potential should be constant. The black solid line corresponds with the GA best-fit, the different colors represent the errors for our reconstructions at different redshifts and that $\Delta\tilde{\phi} = \tilde{\phi}(z) - \tilde{\phi}_0$. In the right panel we see that the reconstructed kinetic term is positive from $z = 0$ to $z \sim 1.9$, hence our reconstructions of the Swampland conjectures within that redshift range should be free from ghosts and instabilities. The blue solid line corresponds to the GA best-fit and the grey region to the 1σ errors. Note that in the right panel we truncate the error in the unphysical region where the kinetic term changes sign.

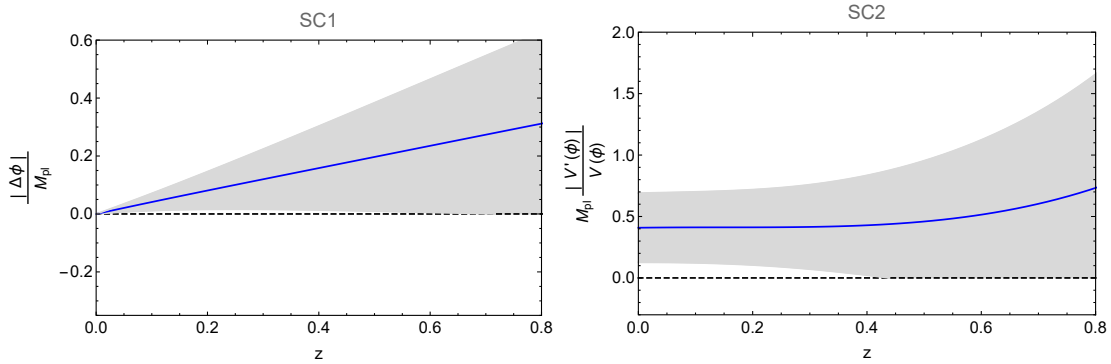

Figure 15.2: The GA reconstruction of the first and second Swampland conjectures on the left and right panels respectively. As can be seen, from $z = 0.8$ onward the errors become so large that we can only draw some conclusions at low redshifts with the current available data. Both reconstructions are consistent with the conjectures and the ΛCDM model at the 1σ level. Notice that $\Delta\phi = \phi(z) - \phi_0$ and that we truncate the error in the unphysical region where the quantities would change sign (as we take the absolute values).

Next, in Table 15.2 we show the best-fit parameters of the cosmographic parameters for the $H(z)$ data and their χ^2 values for various orders of the series expansion. We also give the values of the corrected AIC and BIC tools, which are defined as [290]:

$$\text{AIC} = \chi^2_{\text{min}} + 2k, \tag{15.25}$$

$$\text{AIC}_c = \text{AIC} + \frac{2k(k+1)}{N-k-1}, \tag{15.26}$$

$$\text{BIC} = \chi^2_{\text{min}} + k \ln N, \tag{15.27}$$

where k is the number of free parameters and N the number of data points, which for the Hubble

Order/param.	q_0	j_0	s_0	l_0	h	χ^2	$\lvert\Delta\mathrm{AIC}_c\rvert$	$\lvert\Delta\mathrm{BIC}\rvert$
2nd	0.144 ± 0.093	–	–	–	0.586 ± 0.023	24.772	5.302	5.302
3rd	-0.347 ± 0.195	0.432 ± 0.247	–	–	0.662 ± 0.040	19.172	2.088	3.286
4th	-0.851 ± 0.373	2.222 ± 1.412	2.326 ± 4.029	–	0.718 ± 0.057	17.301	2.758	4.998
5th	-0.824 ± 0.727	2.133 ± 3.951	2.091 ± 12.525	9.661 ± 34.294	0.714 ± 0.075	17.304	5.470	8.585

Table 15.2: The best fit parameters of the cosmographic expansions. For comparison the ΛCDM model has best-fit parameters $(\Omega_{\mathrm{m},0}, h) = (0.259 \pm 0.029, 0.704 \pm 0.023)$ with $\chi^2 = 19.470$, while the GA has $\chi^2 = 17.670$. The values of the differences for the AIC and BIC, are given with respect to those of the ΛCDM model.

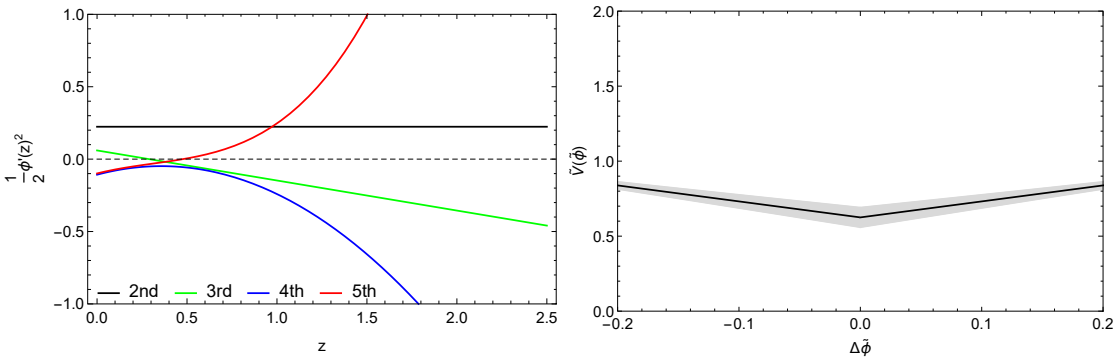

Figure 15.3: Left: Reconstruction of the kinetic term of the scalar field for various orders of the cosmographic expansion for the Planck prior $\Omega_m = 0.315 \pm 0.007$ [1]. As can be seen the third order expansion is positive in the range $z \in [0, 0.3]$, while in the other cases the reconstruction breaks down as the field is complex. Right: the third order cosmographic reconstruction on the scalar field potential, where $\Delta\tilde{\phi} = \tilde{\phi}(z) - \tilde{\phi}_0$. We only plot the quantities in the regions where the scalar field kinetic term is positive, which in this case is in the range $z \in [0, 0.3]$. As can be seen, in the aforementioned redshift range the cosmographic and the GA reconstructions are consistent.

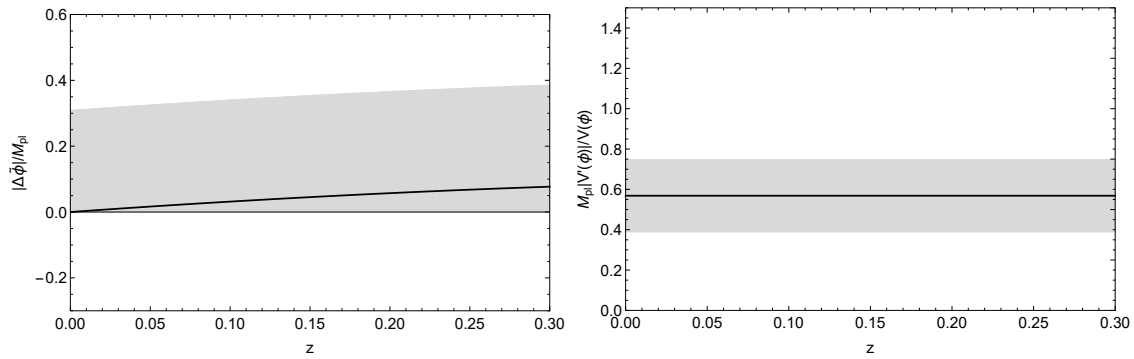

Figure 15.4: The third order cosmographic reconstruction on the scalar field potential (left) and the Swampland conjectures SC1 (center) and SC2 (right), where $\Delta\tilde{\phi} = \tilde{\phi}(z) - \tilde{\phi}_0$. We only plot the quantities in the regions where the scalar field kinetic term is positive, which in this case is in the range $z \in [0, 0.3]$. As can be seen, in the aforementioned redshift range the cosmographic and the GA reconstructions of the Swampland conjectures are consistent. Note that we truncate the error in the unphysical region where the quantities would change sign (as we take the absolute values).

data is equal to $N = 36$, while χ^2_{min} is the value of the χ^2 at the minimum.

In Table 15.2 the values of the differences of the AIC_c and BIC are given with respect to those of the ΛCDM model. In either case, the condition $\Delta\mathrm{AIC}_c \leq 2$ implies the consistency between the models, while the inequalities $2 < \Delta\mathrm{AIC}_c \leq 4$ and $4 < \Delta\mathrm{AIC}_c \leq 7$ indicate a mild and positive

evidence against the model with higher value of AIC. On the other hand, when $\Delta\text{AIC}_c \geq 10$ suggests strong evidence. The same applies to the BIC test [291]. As can be seen, in all cases the ΛCDM model seems to be favored by the data, which is also consistent with previous analyses [140]. Note that we cannot apply either of the criteria to the GA as it is a non-parametric approach.

Going back to the scalar field, the aforementioned issue with the kinetic term is also shown in Fig. 15.3 where in the left panel we show a reconstruction of the kinetic term of the scalar field for various orders of the cosmographic expansion for the Planck prior $\Omega_m = 0.315 \pm 0.007$ [1]. As can be seen the third order expansion is positive in the range $z \in [0, 0.3]$, while in the other cases the reconstruction breaks down as the field is complex. Thus, out of all cases only the second and third order expansions have a positive kinetic term at small redshifts and from these two, only the third order expansion has non-trivial phenomenology, hence we focus on this in what follows.

In the right panel of Fig. 15.3 we show the third order cosmographic reconstruction on the scalar field potential. We note that we only plot the quantities in the regions where the scalar field kinetic term is positive, which in this case is in the range $z \in [0, 0.3]$. As can be seen, in the aforementioned redshift range the cosmographic and the GA reconstructions are consistent.

Finally, we show the results for the Swampland conjecture reconstructions in Fig. 15.4. As can be seen both cases are in good agreement in the range $z \in [0, 0.3]$ within the errors with the corresponding GA reconstructions. However, given that the reconstructions are limited in range, this also significantly reduces their appeal.

15.6 Phase Diagrams

As we have seen on Chapters 4 and 5, in MG theories it is frequently assumed that the background level behaves as the ΛCDM model and its perturbations evolve differently, see for example Ref. [643]. This happens in well known DE and MG models such as the so-called designer $f(R)$ models [9, 201–204] or the designer Horndeski family of models (HDES) [10] whose background is exactly that of the ΛCDM model. However, in general, MG models can have departures from ΛCDM both at the background and at the perturbation level, as is for example the case for the Hu-Sawicki $f(R)$ gravity model [209] or the Kinetic Gravity Braiding (KGB) theory [308].

In this section we search for potential deviations from ΛCDM at the background and at the perturbation level by applying our Machine Learning reconstructions to cosmological observations. In specific we use $H(z)$ expansion rate data, the growth-rate $f\sigma_8(z)$ compilation and the Eg statistics to present two phase diagrams, $H - f\sigma_8$ and $\eta - f\sigma_8$, where η is a parameter which defines the departure of gravity from GR and can be explored by gravitational lensing.

The anisotropic stress η is conventionally modeled through the parameter $\eta = \frac{\Phi}{\Psi}$, where Φ and Ψ are the Newtonian potentials and are considered equal in GR in the absence of anisotropic stresses from other sources like neutrinos. Then, any departure of η from unity would hint to modified gravity or if neglected, it could bias the cosmological parameters inferred from the data [360].

With our GA reconstructions we demonstrate how deviations from the ΛCDM model appears in the $\eta - f\sigma_8$ diagram. In specific, in the left panel of Fig. 15.5, we plot the $H - f\sigma_8$ diagram for the redshift range of $z \in [0, 1.9]$ using the $H(z)$ and $f\sigma_8$ data. The theoretical prediction of the ΛCDM model would correspond to a point at $(1, 1)$, something which the GA best-fit reconstructions confirm within the errors. The different colors represent our reconstructions for several redshifts with their respective errors.

In the right panel of Fig. 15.5 we have the $\eta - f\sigma_8$ diagram for the redshift range of $z \in [0.27, 0.86]$ using the E_g and $f\sigma_8$ data. The theoretical prediction of the ΛCDM model would correspond to a point at $(1, 1)$. The different colors represent our reconstructions for several redshifts with their respective errors. With our GA best-fit reconstructions we find a $\sim 2\sigma$ deviation of the anisotropic stress from unity at $z \sim 0.3$ and a $\sim 4\sigma$ at $z \sim 0.9$, thus hinting toward some deviations from GR, something which was also seen in Ref. [324].

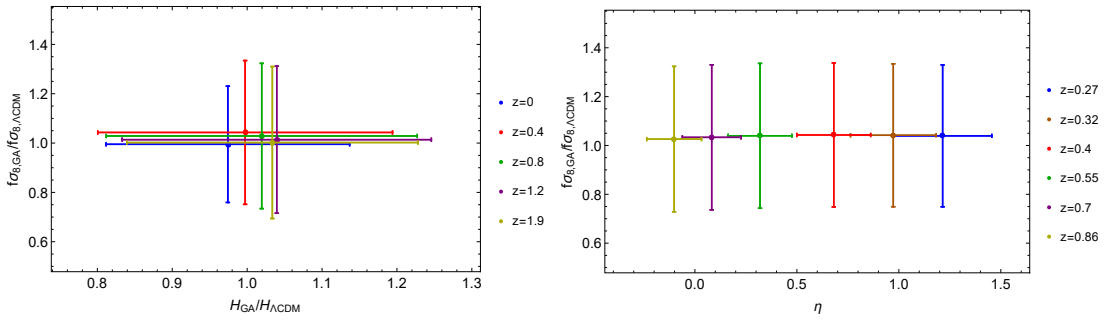

Figure 15.5: Left: $H-f\sigma_8$ diagram for the redshift range of $z \in [0, 1.9]$ using the $H(z)$ and $f\sigma_8$ data. The theoretical prediction of the ΛCDM model would correspond to a point at $(1, 1)$, something which the GA best-fit reconstructions confirm within the errors. The different colors represent our reconstructions for several redshifts with their respective errors. Right: $\eta - f\sigma_8$ diagram for the redshift range of $z \in [0.27, 0.86]$ using the E_g and $f\sigma_8$ data. The theoretical prediction of the ΛCDM model would correspond to a point at $(1, 1)$. The different colours represent our reconstructions for several redshifts with their respective errors. With our GA best-fit reconstructions we find a $\sim 2\sigma$ deviation of the anisotropic stress from unity at $z \sim 0.3$ and a $\sim 4\sigma$ at $z \sim 0.9$.

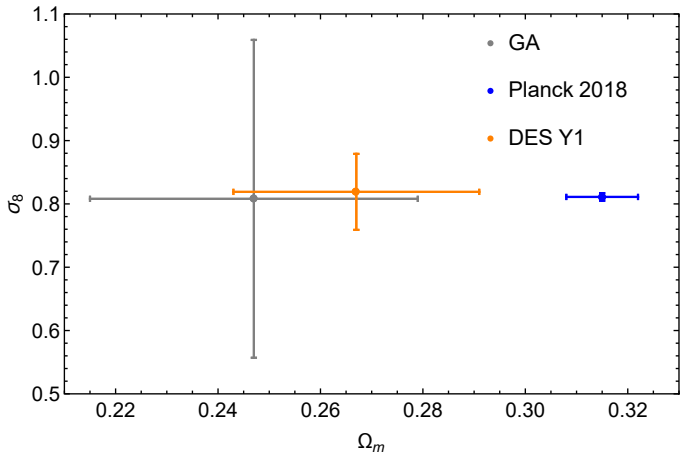

Figure 15.6: Plot for σ_8 against Ω_m from our ML reconstructions on the growth rate $f\sigma_8$ data (gray point), the Planck 2018 TT,TE,EE+lowE+lensing values (blue point) and the DES Y1 2018 results (orange point).

These deviations could be due to new physics or for the presence of unaccounted systematics and perhaps non-negligible radiative processes, as could be the case for the E_g data. The diagrams presented will be useful for future large-scale structure observations to rule out some of the modified gravity models.

Finally, we also report our results from our ML reconstruction through Eqs. (12.12) and (12.11), seen on Sec. 12.2, for the quantity S_8, quantified as $S_8 = \sigma_8\sqrt{\Omega_m/0.3}$. This parameter is in tension between Planck and cosmic shear measurements such as Kids-1000 and DES Y1 above the 2σ level, where the latter have a preference for a lower value, see for example Fig. 1 of [59] where the tension can be visualized in the $\sigma_8 - \Omega_{m,0}$ diagram. With the GA we find $S_8 = 0.733 \pm 0.275$ and in Fig. 15.6 we also provide a similar diagram, being our results more in agreement with DES Y1. Overall, these results are consistent with Ref. [59] and the analysis of [644] from the DES Y1 release, where the authors split the matter density into a "geometric" and "growth" $\Omega_{m,0}$. They are in mild tension with the Planck 2018 results though, something that has been noted repeatedly in the literature, see for example Ref. [120] and references there in. Note that the errors with the GA approach are considerably larger than those from DES Y1 and the Planck 2018 results being one

of the reasons the fact that with our reconstructions we are not making assumptions on flatness or a dark energy model, hence more agnostic.

15.7 Error analysis

In Eqs. (15.6) and (15.7) we have rewritten the reconstruction equations for the scalar field in terms of dimensionless variables. Then, by standard error propagation we find that the error for the potential and the kinetic term can be expressed as

$$\delta\tilde{V} = 2E\delta E - \frac{x}{6}\frac{d}{dx}(2E\delta E) - \frac{1}{2}\delta\Omega_{\rm m,0}x^3, \tag{15.28}$$

$$\delta\left(\frac{d\tilde{\phi}}{dx}\right)^2 = \frac{2}{3x}\frac{d}{dx}\left(\frac{\delta E}{E}\right) + \frac{2\Omega_{\rm m,0}x\delta E}{E^3} - \frac{x\delta\Omega_{\rm m,0}}{E^2}. \tag{15.29}$$

Since the Swampland conjecture 2 (SC2) is defined as

$$\mathrm{SC2} = \frac{|V_{,\phi}|}{V} \equiv \frac{|(dV/dz)/(d\phi/dz)|}{V} = \frac{|V'/\phi'|}{V}, \tag{15.30}$$

then the error will be given by

$$\delta\mathrm{SC2} = \frac{\left|\left(\frac{\delta V'\phi' - \delta\phi' V'}{\phi'^2}\right)\right| V - \delta V\,|V'/\phi'|}{V^2}, \tag{15.31}$$

where the prime is the derivative with respect to the redshift z.

15.8 Conclusions

Through a plethora of cosmological probes it has been established that the Universe is expanding in an accelerated way, being one of the biggest findings in modern cosmology and implying that 70% of the mass-energy density is made of an unknown content, usually referred to as dark energy (DE), spreading uniformly over the Universe. The cosmological constant Λ represents one of the simplest contenders of DE, however some of it caveats is that the observed energy scale of DE is much smaller than the energy scale predicted by a vacuum energy in particle physics [645]. Other viable alternatives come from the inclusion of slowly rolling scalar fields which control the accelerated expansion of the Universe at late times, being Quintessence an example of these type of models.

In the framework of string phenomenology, at present we should necessarily be in an epoch of quintessence and in the continuous search for a theory of quantum gravity there has been some Swampland conjectures proposed, which refer to some criteria that must be hold in order to have effective field theories consistent with quantum gravity [646]. Some of these conjectures have important implications in cosmology as is the case of the Swampland criteria that we have analyzed in this Chapter.

In our analysis we have presented two model independent reconstructions of the Swampland conjectures with ML and cosmography placing constraints on the first and second Swampland conjectures, finding that at low redshifts both approaches give consistent results and that, neither conjecture is ruled out by the data at a statistically significant level.

However, while the swampland bounds seem to be satisfied by the low redshift data, their reconstructed scalar potential, see Fig. 15.1, has a shape similar to a parabola. Thus, while these reconstructions may be superficially consistent with the swampland bounds, it should be noted that exponential potentials are what naturally emerges in UV complete settings.

Comparing both of our approaches, the ML algorithm seems a more robust approach for the following reasons: First, in cosmography we are assuming flatness and a Planck 2018 prior on $\Omega_{\mathrm{m},0}$, while with the GA we do not make assumptions on flatness, $\Omega_{\mathrm{m},0}$ or on a dark energy model. Second, our ML reconstructions allow us to place constraints at higher redshifts where the kinetic term reconstructed goes up to $z \sim 1.9$. while for cosmography only extends up to $z \sim 0.3$, as the scalar field kinetic term becomes negative beyond that.

Finally, using the growth rate data $f\sigma_8(z)$ we perform a model independent probe of modified gravity cosmologies through two phase diagrams, $H - f\sigma_8$ and $\eta - f\sigma_8$ where the anisotropic stress parameter η is reconstructed through the E_g statistics, related to gravitational lensing data. We see that the first diagram $H - f\sigma_8$ is consistent within the errors with the ΛCDM model, while the second diagram $\eta - f\sigma_8$ has a $\sim 2\sigma$ deviation of the anisotropic stress from unity at $z \sim 0.3$ and a $\sim 4\sigma$ at $z \sim 0.9$, thus pointing toward mild deviations from GR, which could be the future target of upcoming large-scale structure surveys.

16

Novel null tests for the spatial curvature and homogeneity of the Universe and their machine learning reconstructions

.

The original content of this chapter is based on Ref. [433]. A plethora of observational data obtained over the last couple of decades has allowed cosmology to enter into a precision era and has led to the foundation of the standard cosmological constant and cold dark matter paradigm, known as the ΛCDM model. Given the many possible extensions of this concordance model, we present here several novel consistency tests which could be used to probe for deviations from ΛCDM. First, we derive a joint consistency test for the spatial curvature $\Omega_{k,0}$ and the matter density $\Omega_{\mathrm{m},0}$ parameters, constructed using only the Hubble rate $H(z)$, which can be determined directly from observations. Second, we present a new test of possible deviations from homogeneity using the combination of two datasets, either the baryon acoustic oscillation (BAO) and $H(z)$ data or the transversal and radial BAO data, while we also introduce two consistency tests for ΛCDM which could be reconstructed via the transversal and radial BAO data. We then reconstruct the aforementioned tests using the currently available data in a model independent manner using a particular machine learning approach, namely the Genetic Algorithms. Finally, we also report on a $\sim 4\sigma$ tension on the transition redshift as determined by the $H(z)$ and radial BAO data.

16.1 Introduction

Great efforts are made to provide accurate constraints on the spatial curvature of the Universe, as measured by the parameter $\Omega_{k,0}$, since any statistically significant deviation from flatness would provide insights to the primordial inflation paradigm, aid to test physics of the early universe and also help pinpoint to high precision the age of the Universe. Moreover, accurately determining the spatial curvature of the Universe would also help in discriminating evolving dark energy density models with curvature from a flat ΛCDM model, as in general evolving dark energy and curvature are degenerate with each other [647]. In this context several consistency tests and analyses have been proposed [421, 648–655, 655, 656]. Actually, a detection of non-flatness, i.e $\Omega_{k,0} \neq 0$, would severely constrain the number of inflationary models, see e.g. Ref. [657], and future surveys, such as DESI and SKA, are targeting tighter measurements of $\Omega_{k,0}$ by breaking parameter degeneracies [658, 659].

Even though the aforementioned discrepancy might be due to unaccounted for systematic errors, there also exists the plausible possibility of new physics in the form of modified gravity (MG) or dark energy (DE) models. In fact, the ΛCDM scenario has some caveats as its main components, namely dark matter (DM) and dark energy (DE) have not yet been detected in the laboratory and are not well understood [645, 660, 661], hinting towards the idea that ΛCDM could be an approximation to a more fundamental theory that remains currently unattainable [662].

As we have already discussed in previous Chapters, one way to overcome the biases of choosing a theoretical defined model is to use non-parametric reconstruction methods and model-independent approaches [168]. In this context, machine learning (ML) algorithms have provided innovative solutions for extracting information in a theory agnostic manner [401]. These tests are ideal to check for possible tensions that could arise because of unaccounted for systematics or could provide hints of new physics. Their main advantage is that any deviations at any redshift from the expected value imply the breakdown of any assumptions made [425]. Null tests have been used extensively for the concordance ΛCDM model [168, 426, 427], interacting DE models [428], the growth-rate data [404, 425, 429], the cosmic curvature [424, 430–432] and also to probe the scale-independence of the growth of structure in the linear regime [339].

Here we provide a new method to probe the spatial curvature and homogeneity of the Universe. First, we present a new joint consistency test for the curvature $\Omega_{k,0}$ and the matter density $\Omega_{\mathrm{m},0}$ parameters, constructed using only the Hubble rate $H(z)$, which is determined directly from observational data. This null test of the ΛCDM model is an extension of the well-known $\mathcal{O}_m$ diagnostic [426], but with the added advantage that now we do not have to assume flatness. Second, we also present a null test that can be used to check for deviations from homogeneity through the combination of two datasets, either the Baryon Acoustic Oscillations (BAO) and $H(z)$ data or the transveral and radial BAO data.

Furthermore, we also introduce two new consistency tests for ΛCDM that could be tested through the transversal, also known as angular, and radial BAO respectively. The first one is derived following a similar approach to that of Ref. [419], where now we use the angular BAO scale relation $\theta(z)$ to present a new expression of ΛCDM , which we will refer to as $\mathrm{Om}_\theta(z)$. We show that this test has the advantage that it does not contain higher derivative terms, which increase the error when noisy data are used thus providing stringent constraints for the ΛCDM model. Finally, we use the radial BAO data $\Delta z(z)$ to reconstruct the Hubble parameter $H(z)$ and the deceleration parameter $q(z)$ and constrain the accelerated expansion of the Universe.

In all cases the reconstructions of the cosmological data are performed using the Genetic Algorithms (GA), which is a stochastic minimization and symbolic regression algorithm. One of its main advantages is that it is a non parametric method which allows us to make the least number of assumptions concerning the underlying cosmology and thus avoid the issue of biases.

The outline of this Chapter is as follows: in Sec. 16.2 we introduce our theoretical framework. In Sec. 16.3 we set out our spatial curvature and homogeneity test and in Sec. 16.4 we outline our ΛCDM consistency tests. Then, in Sec. 16.5 we describe the data used in our analysis and in Sec. 16.6 we discuss the Genetic Algorithms used to do the reconstructions. Later, in Sec. 16.7 we present our results, in Sec. 16.8 we present the results for the complementary joint null test for (Ω_m, Ω_k) of Ref. [663] and in Sec. 16.9 we summarize our conclusions.

16.2 Theoretical framework

In this section we review the formalism used in the analysis and the consistency tests. Assuming that at scales of order ∼100Mpc the Universe is homogeneous and isotropic, then it can be described by the Friedmann-Lemaitre-Robertson-Walker (FLRW) metric at the background level, which in reduced spherical polar coordinates can be written as:

$$ds^2 = -dt^2 + a(t)^2 \left[\frac{dr^2}{1-kr^2} + r^2 d\theta^2 + r^2 \sin^2\theta d\phi^2 \right], \tag{16.1}$$

where t is the cosmic time and the scale factor $a(t)$ is related to the redshift z as $a = \frac{1}{1+z}$. The spatial slices can be interpreted as flat Euclidean space with $k = 0$, closed hyperspherical space with $k = +1$ or open hyperbolic space with $k = -1$. The spatial curvature of the Universe can be parameterized as $\Omega_{k,0} = -\frac{c^2}{H_0} k$, thus at late times, when we can neglect radiation since $\Omega_{r,0} \sim 0$,

we find that the Friedmann equation can be written as

$$\frac{H^2(z)}{H_0^2} = \Omega_{\mathrm{m},0}(1+z)^3 + \Omega_{k,0}(1+z)^2 + (1-\Omega_{\mathrm{m},0}-\Omega_{k,0})\exp\left[3\int_0^z \frac{1+w(z')}{1+z'}dz'\right], \tag{16.2}$$

where $\Omega_{\mathrm{m},0}$ represents the matter content of the Universe, $\Omega_{k,0}$ its curvature and w the DE equation of state. Since the cosmological constant has $w=-1$, then then Eq. (16.2) gives for the ΛCDM model that

$$H(z) = H_0\sqrt{\Omega_{\mathrm{m},0}(1+z)^3 + \Omega_{k,0}(1+z)^2 + \Omega_{\Lambda,0}}, \tag{16.3}$$

where $\Omega_{\Lambda,0}$ is related to $\Omega_{\mathrm{m},0}$ and $\Omega_{k,0}$ via the consistency relation

$$\Omega_{\mathrm{m},0} + \Omega_{\Lambda,0} + \Omega_{k,0} = 1. \tag{16.4}$$

The comoving distance at some redshift z can be written as [502]

$$r(z) = \frac{c}{H_0}\frac{1}{\sqrt{-\Omega_{k,0}}}\sin\left(\sqrt{-\Omega_{k,0}}\int_0^z \frac{c}{H(z')/H_0}dz'\right), \tag{16.5}$$

while the luminosity and angular diameter distances are related via

$$d_L(z) = (1+z)\,r(z), \tag{16.6}$$

$$d_A(z) = (1+z)^{-1}r(z). \tag{16.7}$$

The deceleration parameter $q(z)$ is defined as

$$\begin{aligned} q(z) &= -\frac{\ddot{a}a}{\dot{a}^2} \\ &= -1 + (1+z)\frac{d\ln(H/H_0)}{dz}, \end{aligned} \tag{16.8}$$

and assuming Eq. (16.3), at the present time ($z=0$) it can be expressed as

$$\begin{aligned} q_0 &\equiv q(z=0) \\ &= \frac{1}{2}\left(-2 + 2\Omega_k + 3\Omega_m\right). \end{aligned} \tag{16.9}$$

Finally, assuming Eq. (16.3), the transition redshift z_t can be defined as the redshift at which the deceleration parameter changes sign, i.e. $q(z_t)=0$. This implies that

$$z_t = \left(\frac{2\Omega_{\Lambda,0}}{\Omega_{\mathrm{m},0}}\right)^{1/3} - 1 = \left(\frac{2\left(1-\Omega_{\mathrm{m},0}-\Omega_{k,0}\right)}{\Omega_{\mathrm{m},0}}\right)^{1/3} - 1, \tag{16.10}$$

which is a prediction of the ΛCDM model.

16.3 The null tests

16.3.1 Test 1: Deviations from flatness

Defining $x = 1+z$, from Eq. (16.3) we can write the matter density parameter $\Omega_{\mathrm{m},0}$ in terms of the Hubble function and the curvature $\Omega_{k,0}$ as

$$\Omega_{\mathrm{m},0} = \frac{h^2(x) - 1 + \Omega_{k,0}(1-x^2)}{x^3-1}, \tag{16.11}$$

which reminds us of the $\mathcal{O}_m$ diagnostic of Ref. [426] when $\Omega_{k,0}\to 0$ and where we have defined $h(x) = H(x)/H_0$. The problem in this case is that now the curvature parameter, which cannot be

measured in a model independent fashion, enters in the right hand side of Eq. (16.11). To avoid this problem, we can use the deceleration parameter evaluated at $z = 0$ given by Eq. (16.9), as it can indeed be determined independently from the data, see for example Ref. [419]. Thus, using Eqs. (16.3) and (16.9) we can simultaneously solve the algebraic system of equations for $\Omega_{k,0}$ and $\Omega_{\rm m,0}$ to find expressions that depend on only measurements of the Hubble rate $H(z)$. Doing so we find

$$\Omega_{\rm m,0} = \frac{2\left(-1+h^2(z)-(1+q_0)z(2+z)\right)}{z^2\left(3+2z\right)}, \tag{16.12}$$

$$\Omega_{k,0} = \frac{3-3h^2(z)+2(1+q_0)z\left(3+z(3+z)\right)}{z^2\left(3+2z\right)}, \tag{16.13}$$

where $h(z) = H(z)/H_0$.

As can be seen, the joint test of Eqs. (16.12)-(16.13), is an extension of the $\mathcal{O}_m$ diagnostic of Ref. [426] as it allows us to distinguish evolving dark energy (DE) models from the cosmological constant, without having to assume any value for the curvature parameter. Our expressions presented here resembles that of Ref. [663], but in our case we do not explicitly have derivatives of the Hubble rate $H(z)$, albeit only a derivative evaluated at a single point is implicitly contained in the deceleration parameter q_0. As we will see in later sections, this difference allows our approach to have much smaller error bars in the reconstruction compared to that of Ref. [663].

16.3.2 Test 2: Deviations from homogeneity

Here we expand on tests of homogeneity as proposed in Ref. [664]. Homogeneity implies a consistency relation that holds in FLRW between the angular diameter and comoving distances, given by $d_A(z)$ and $r(z)$ respectively, described by Eq. (16.7). Any violation of Eq. (16.7) implies we live in a non-FLRW Universe, however, one would still expect variations on the order of $\sim 10^{-5}$ due to perturbations from large-scale structure.

One way we can test this assumption is by reconstructing separately the angular diameter distance using the BAO data and the comoving distance from the $H(z)$ data. To do so, we make use of the comoving observed BAO angle, which is given by

$$\theta_{\rm BAO} = \frac{r_d}{(1+z)d_A(z)}, \tag{16.14}$$

and the same for the $H(z)$ data

$$\theta_{\rm H(z)} = \frac{r_d}{r(z)}, \tag{16.15}$$

where in both cases r_d is the comoving sound horizon at the drag epoch $r_d \equiv r_{\rm s}(z_{\rm d})$, given by

$$r_{\rm s}(z_{\rm d}) = \int_{z_{\rm d}}^{\infty} \frac{c_{\rm s}(z)}{H(z)}\,{\rm d}z\,, \tag{16.16}$$

with $z_{\rm d}$ the redshift at the drag epoch, see Eq.(4) of Ref. [98], while $c_{\rm s}(z)$ is the sound speed given by

$$c_{\rm s} = \frac{c}{\sqrt{3(1+R)}}, \tag{16.17}$$

where $R = \frac{3\rho_b}{4\rho_\gamma} = \frac{3\Omega_{\rm b,0}}{4\Omega_{\gamma,0}}a$.

Then, we can create the following expressions that can be used to search for deviations from homogeneity using BAO and $H(z)$ data:

$$\zeta = 1 - \frac{\theta_{\rm H(z)}}{\theta_{\rm BAO}}$$

$$= 1 - \frac{(1+z)d_A(z)}{r(z)}, \tag{16.18}$$

which should be zero at all z for any FLRW model.

In this case we can use BAO measurements and $H(z)$ data to directly reconstruct the angular diameter distance $d_A(z)$ and the comoving distance $r(z)$ respectively. One issue with this though is that the $H(z)$ cannot constrain the curvature parameter directly, as we reconstruct the data agnostically with the GA, thus for this test we will assume flatness, i.e. $\Omega_{k,0} = 0$ in order to calculate the comoving distance $r(z)$ from the $H(z)$ data. Furthermore, had we used any data that depend on the conservation of the number of photons to measure the luminosity distance $d_L(z)$, as is for example the case for the type Ia supernovae, then the test of Eq. (16.18) would in fact be a test of the cosmic distance duality (Etherington) relation $d_L(z) = (1+z)^2 d_A(z)$ instead.

We can also express Eq. (16.18) using alternatively the radial Δz and angular $\theta(z)$ BAO data, as $d_A(z)$ and $\theta(z)$ are related via Eq. (16.14), while the radial BAO Δz and $H(z)$ are related via the following relation

$$\Delta z = \frac{r_d \cdot H(z)}{c}, \tag{16.19}$$

where c is the speed of light. Then, by using Eqs. (16.14) and (16.19) we have also the following expression

$$\zeta = 1 - \frac{\theta_{\rm H}}{\theta_{\rm BAO}} = 1 - \left(\theta_{\rm BAO}(z)\int_0^z \frac{1}{\Delta z(z')}dz'\right)^{-1}, \tag{16.20}$$

which should be zero at all redshifts in the ΛCDM model. This test has the added advantage that the radial and angular BAO are direct observables and in fact, the sensitivity of the angular BAO scale is complementary to that of the radial BAO [665].

16.4 Complementary null tests

16.4.1 Test 1: The angular BAO

As mentioned before, the angular BAO can be expressed as

$$\theta(z, \Omega_{\rm m,0}) = \frac{r_d}{(1+z)d_A(z, \Omega_{\rm m,0})}, \tag{16.21}$$

thus, defining the following quantity

$$\tilde{\theta}(z, \Omega_{\rm m,0}) = \frac{\theta}{r_d} = \frac{1}{(1+z)d_A(z, \Omega_{\rm m,0})}, \tag{16.22}$$

we can now apply the Lagrange inversion theorem to $\tilde{\theta}(z, \Omega_{\rm m,0})$ and write $\Omega_{\rm m,0}$ as a function of $\tilde{\theta}(z)$, i.e $\Omega_{\rm m,0}(z, \tilde{\theta}(z))$ via the following steps. First, in the flat ΛCDM model and neglecting radiation, the angular diameter distance $d_A(z, \Omega_{\rm m,0})$ is given by

$$\begin{aligned} d_A(z, \Omega_{\rm m,0}) &= \frac{c}{H_0(1+z)}\int_0^z \frac{1}{H(x)}dx \\ &= \frac{c}{H_0}\frac{2(1+z)}{\sqrt{\Omega_{\rm m,0}}}\left({}_2F_1\left(\frac{1}{6}, \frac{1}{2}, \frac{7}{6}, \frac{\Omega_{\rm m,0}-1}{\Omega_{\rm m,0}}\right) - \frac{{}_2F_1\left(\frac{1}{6}, \frac{1}{2}, \frac{7}{6}, \frac{\Omega_{\rm m,0}-1}{\Omega_{\rm m,0}(1+z)^3}\right)}{\sqrt{1+z}}\right) \end{aligned} \tag{16.23}$$

Then, to derive the angular BAO test we do a series expansion on Eq. (16.22) around $\Omega_{\rm m,0} = 1$ and keep the first 10 terms in order to obtain a reliable unbiased estimation, so as to avoid theoretical systematic errors. We have chosen to keep the first 10 terms so that at high redshifts, in particular

at $z \sim 2.3$ where the last of the data points are, the theoretical systematic errors are well below $\sim 1\%$.

Then, we apply the Lagrange inversion theorem to invert the series and to write the matter density $\Omega_{\rm m,0}$ as a function of the angular BAO $\tilde{\theta}$. Then, the first two terms of the test are

$$\mathrm{Om}_\theta = 1 + \frac{28\left(-\frac{1}{2-2\sqrt{a}}\tilde{\theta}\right)}{\left(6+5\sqrt{a}+4a+3a^{3/2}+2a^2+a^{5/2}\right)} + O(\tilde{\theta}^2), \tag{16.24}$$

where the scale factor a is related to the redshift z as $a = \frac{1}{1+z}$ and when $\tilde{\theta}$ corresponds to the ΛCDM model, this should reduce to $\Omega_{\rm m,0}$. This expression has the main advantage that it does not require taking derivatives of the data as we use the angular BAO directly and the parameter r_d can also be directly obtained from the data, see Sec.16.5 for more details.

16.4.2 Test 2: The radial BAO

In a flat ΛCDM universe, the $\mathrm{Om}_H(z)$ quantity is constant and equal to the matter energy density [426]

$$\mathrm{Om}_H(z) = \frac{h^2(z)-1}{(1+z)^3-1} \equiv \Omega_{\rm m,0}, \tag{16.25}$$

where $h(z) \equiv H(z)/H_0$. From Eq. (16.19) we have that

$$h(z) = \frac{c}{100 r_{sh}}\Delta z, \tag{16.26}$$

where the combination $r_{sh} = r_d \cdot h$ can be easily determined in a model independent fashion by fitting the radial BAO with the GA, see Sec. 16.5 for more details. Then given the relation between the Hubble parameter and the radial BAO, we can also rewrite the aforementioned expression as

$$\begin{aligned} \mathrm{Om}_{\Delta z}(z) &= \frac{h(z)^2-1}{(1+z)^3-1} \\ &= \frac{\left(\frac{c}{100 r_{sh}}\right)^2 \Delta z^2(z) - 1}{(1+z)^3-1}, \end{aligned} \tag{16.27}$$

16.4.3 Test 3: The deceleration parameter

The deceleration parameter specified by Eq. (16.8) can also be estimated by using the radial BAO, see Eq. (16.19). Hence, we can measure the rate of accelerated expansion of the Universe in a model independent fashion with a different dataset other than $H(z)$ and also constrain the transition redshift z_t of the acceleration phase. In this case, we can write the deceleration parameter as

$$\begin{aligned} q(z) &= -1 + (1+z)\frac{d\ln(H/H_0)}{dz}, \\ &= -1 + (1+z)\frac{\Delta z'(z)}{\Delta z(z)}, \end{aligned} \tag{16.28}$$

and the transition redshift z_t is the value at which $q(z_t) = 0$. The main advantage in this case is that the radial BAO data have a much smaller error with respect to the $H(z)$ data, hence can provide stringent constraints on the deceleration parameter $q(z)$.

16.5 Data

The data used in this Chapter is composed of the Hubble rate data $H(z)$, baryon acoustic oscillations, the radial and angula BAO data, see Chapter 2 for a detailed discussion.

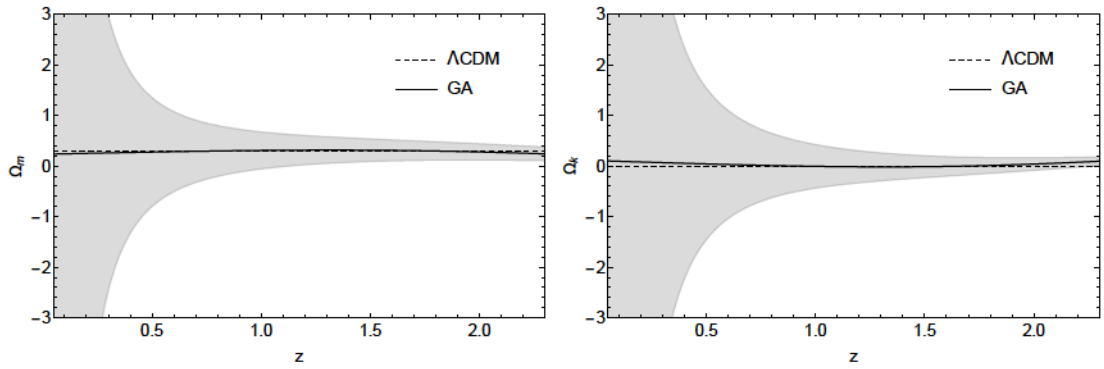

Figure 16.1: The GA reconstruction of the $\Omega_m(H, q_0)$ (left panel) and $\Omega_k(H, q_0)$ (right panel) expressions given by Eqs. (16.12) and (16.13) respectively and obtained using the $H(z)$ data. In both cases the black solid line and the grey region corresponds to the GA best-fit and the 1σ error respectively. As can be seen, both reconstructions are consistent with the flat ΛCDM model represented by the black dashed-line at the 1σ level.

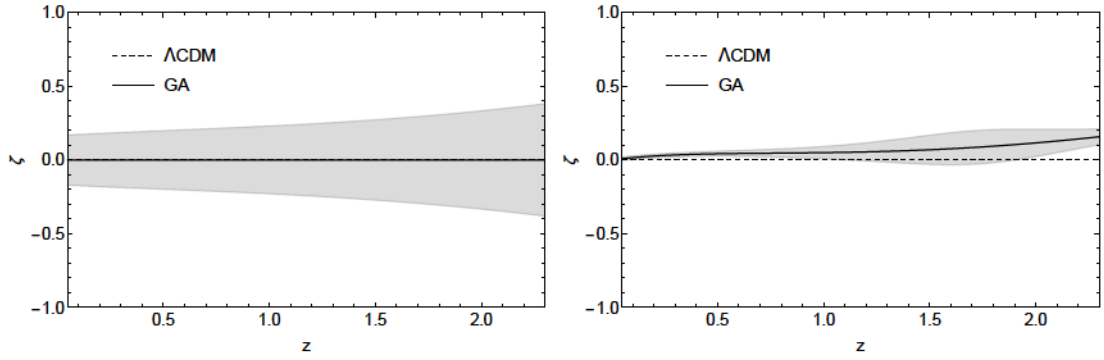

Figure 16.2: The $\zeta = 1 - \frac{\theta_H}{\theta_{\rm BAO}}$ test which aims to find deviations from homogeneity through our reconstructions from the $H(z)$ and BAO data (left panel) and our angular and radial BAO data (right panel). In both cases the black solid line and the grey region corresponds to the GA best-fit and the 1σ error respectively. As can be seen, both reconstructions are consistent with the expectation of no deviation, represented by the black dashed-line, at the 1σ level in the left and at the $\sim 2\sigma$ in the right.

16.6 Genetic Algorithms

The data set used in the analysis is described in Chapter 2, where the $H(z)$ compilation, the BAO data and the angular and radial BAO data are used to reconstruct the Hubble rate $H(z)$, the angular diameter distance $d_A(z)$, the angular BAO $\theta(z)$ and the radial BAO $\Delta z(z)$ respectively.

To perform the reconstructions in our analysis we implemented the following approach. First, our grammar included the following orthogonal basis of functions: exp, log and polynomials and a set of operations $+, -, \times, \div, \wedge$. We also specified some assumptions motivated by physical reasons. For instance at the present day $z = 0$ we have that $H(z = 0) = H_0$, $d_A(z = 0) = 0$ and similarly $\theta(z = 0) \sim \frac{rsh}{z}$ and $\Delta z(z = 0) \sim \frac{100rsh}{c}$, but we make no assumptions on the curvature of the Universe or any MG or DE model. We also imposed that all the functions the GA reconstructs are continuous and differentiable, without any singularities in the redshift scanned by the data to avoid overfitting or fake reconstructions.

The final output of the code, then is a set of smooth and analytic functions for $H(z)$, $d_A(z)$ and $\theta(z)$, $\Delta z(z)$ that describe the data.

Concerning the errors of the reconstructed functions, they are obtained through the path integral approach described in Sec. 10.0.2 of 10.

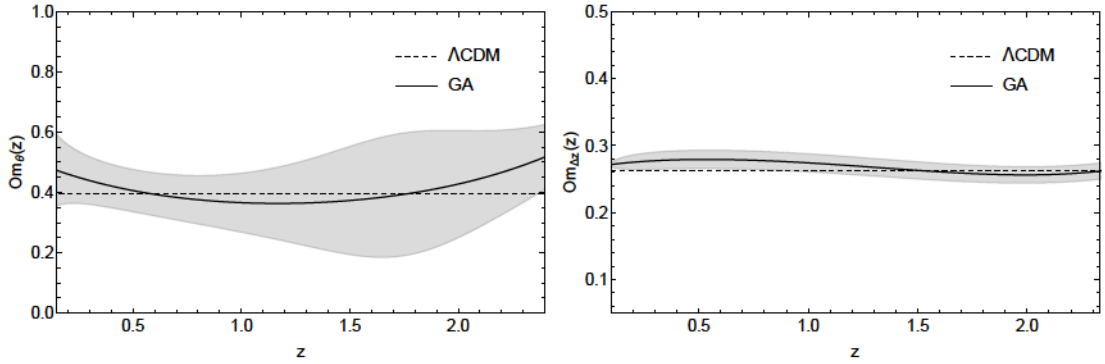

Figure 16.3: Left panel: The reconstruction of the $\mathrm{Om}_\theta(z)$ statistics obtained through our reconstruction of the angular BAO data using the GA. Right panel: The reconstruction of the $\mathrm{Om}_{\Delta z}(z)$ statistics derived through our GA reconstruction of the radial BAO data. In both cases the black solid line and the grey region corresponds to the GA best-fit and the 1σ error respectively. Both reconstructions are consistent with the best-fit flat ΛCDM model represented by the black dashed-line at the 1σ level.

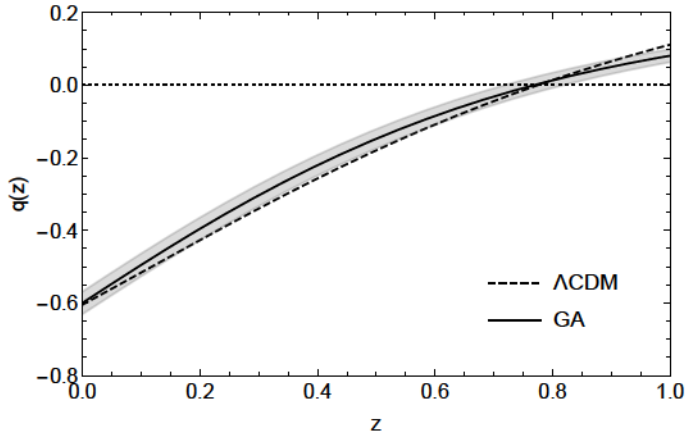

Figure 16.4: The deceleration parameter given by Eq. (16.8) as reconstructed by using Eq. (16.19). The black solid line and the grey region corresponds to the GA best-fit and the 1σ error respectively. Our model independent detection of the accelerated expansion of the Universe is consistent with the best-fit flat ΛCDM model represented by the black dashed-line at the 1σ level. The transition redshift z_{tr} corresponds to the point where $q(z)$ crosses zero.

16.7 Results

In this section we present our GA fits to the data and the corresponding consistency tests derived through our reconstructions. In Table 16.1 we show the best-fit χ^2 per degree of freedom (dof) or equivalently per number of points, for the GA functions and the best-fit ΛCDM model. As can be seen, in all cases the GA out-performs the ΛCDM model in terms of the best-fit χ^2/dof.

Concerning our probe for the curvature, in Fig. 16.1 we present the $\Omega_m(H, q_0)$ (left panel) and $\Omega_k(H, q_0)$ (right panel) expressions given by Eqs. (16.12) and (16.13) respectively, obtained through

	$H(z)$	BAO	$\theta(z)$	$\Delta z(z)$
$\chi^2_{\Lambda\rm CDM}/{\rm dof}$	0.541	0.911	0.843	0.734
$\chi^2_{\rm GA}/{\rm dof}$	0.491	0.610	0.831	0.592

Table 16.1: The $\chi^2/{\rm dof}$ for ΛCDM and GA using the Hubble rate $H(z)$, the BAO data and the angular $\theta(z)$ and radial $\Delta z(z)$ BAO data.

our GA reconstruction of the $H(z)$ data.[1] In both cases the black solid line and the grey region correspond to the GA best-fit and its 1σ error respectively. As can be seen, both reconstructions are consistent with the best-fit flat ΛCDM model, represented by the black dashed-line, at the 1σ level.

In Fig. 16.2 we show the $\zeta = 1 - \frac{\theta_H}{\theta_{BAO}}$ test which aims to find deviations from homogeneity through our reconstructions from the $H(z)$ and BAO data (left panel) and our angular and radial BAO data (right panel). In both cases the black solid line and the grey region corresponds to the GA best-fit and the 1σ error respectively. As can be seen, both reconstructions are consistent with the best-fit flat ΛCDM model, represented by the black dashed-line, at the 1σ level in the left and at $\sim 2\sigma$ in the right panel.

In Fig. 16.3 we show our consistency tests of the ΛCDM model. In particular, in the left panel we show the reconstruction of the ${\rm Om}_\theta(z)$ statistic, obtained through our reconstruction of the angular BAO data using the GA. On the right panel we have the reconstruction of the ${\rm Om}_{\Delta z}(z)$ statistics derived through our GA reconstruction of the radial BAO data. In both cases the black solid line and the grey region corresponds to the GA best-fit and the 1σ error respectively. Both reconstructions are consistent with the best-fit flat ΛCDM model, represented by the black dashed-line, at the 1σ level. It is worth noting that the best-fit value of the matter density for the flat ΛCDM model is given by $\Omega_{m,0} = 0.396 \pm 0.154$, which is somewhat higher than the one found by other observations [1]. A possible explanation for this higher value of the matter density could be due to the assumptions made on Section 16.3, where we are reducing the complex galaxy survey data to single values of $\theta(z)$.

Furthermore, in Fig. 16.4 we present the deceleration parameter given by Eq. (16.8) as reconstructed by using Eq. (16.19). The black solid line and the grey region corresponds to the GA best-fit and the 1σ error respectively. Our model independent detection of the accelerated expansion of the Universe is consistent with the best-fit flat ΛCDM model, represented by the black dashed-line, at the 1σ level. The transition redshift z_{tr} corresponds to the point where $q(z)$ crosses zero, and $q(z)$ is obtained via Eq. (16.28).

Finally, with our GA reconstructions we find the following derived parameters

$$r_s({\rm BAO}) = 101.873 \pm 2.078 \ \ {\rm Mpc/h}, \tag{16.29}$$

$$r_s({\rm transverse\ BAO}) = 103.938 \pm 2.132 \ \ {\rm Mpc/h}, \tag{16.30}$$

$$r_s({\rm radial\ BAO}) = 103.477 \pm 1.447 \ \ {\rm Mpc/h}, \tag{16.31}$$

while from the radial BAO we also find

$$q_{\rm GA,0} = -0.600 \pm 0.031, \tag{16.32}$$

$$z_{\rm GA,tr} = 0.769 \pm 0.050, \tag{16.33}$$

where $z_{\rm tr}$ is the value of the transition redshift, i.e the moment when the deceleration parameter changes sign. It should be noted that using $H(z)$ data, Ref. [419] had reported a value for the deceleration parameter today of $q_0 = -0.575 \pm 0.132$ and the transition redshift $z_{tr} = 0.662 \pm 0.027$, where the latter is $\sim 4\sigma$ away from the value reported earlier, thus hinting at a possible tension between the two datasets.

[1] In Sec. 16.8 we also present a complementary test for Ω_k containing derivatives of $H(z)$.

In this case, our constraint of the transition redshift using the $H(z)$ data and the radial BAO data comes from the same method, the GA. Actually, the main cause of the difference is due to the larger errors of the $H(z)$ data, and the associated possible systematics in the cosmic chronometers, compared to the errors of the radial BAO. This difference causes a small difference between the best-fit value from ΛCDM and the GA for the $H(z)$ data, while the radial BAO the GA and the best-fit value of ΛCDM are more in agreement. Hence, this points to possible issues with the data, even if they have a small overlap with some of the points.

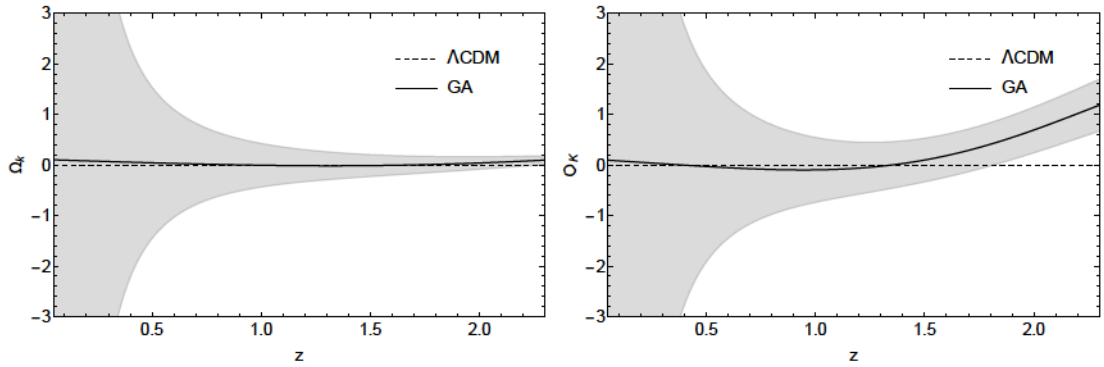

Figure 16.5: The $\Omega_k(H, q_0)$ expression presented in this Chapter (left panel) compared to the $\mathcal{O}_K(z)$ expression from Ref. [663] (right panel). In both cases we use our GA reconstruction of the $H(z)$ data, while the black solid line and the grey shaded regions correspond to the GA best-fit and the 1σ error respectively.

16.8 Complementary null tests

Here we briefly present a complementary $(\Omega_{m,0}, \Omega_{k,0})$ joint test with a similar one from Ref. [663], which is defined as

$$\mathcal{O}_m^{(2)}(z) \equiv 2\frac{(1+z)\left(1-h^2\right)+z(2+z)hh'}{z^2(1+z)(3+z)}, \tag{16.34}$$

$$\mathcal{O}_K(z) \equiv \frac{3(1+z)^2\left(h^2-1\right)-2z\left(3+3z+z^2\right)hh'}{z^2(1+z)(3+z)}, \tag{16.35}$$

where $h = H(z)/H_0$ and the prime $'$ is a derivative with respect to z. The previous tests in the ΛCDM limit reduce to

$$\mathcal{O}_m^{(2)}(z) = \Omega_{m,0}, \tag{16.36}$$

$$\mathcal{O}_K(z) = \Omega_{k,0}. \tag{16.37}$$

In Fig. 16.5 we show the two reconstructions for the curvature test, on the left panel for our test given by Eq. (16.13) and in the right panel for that of Ref. [663] given by Eq. (16.35). The main difference of the latter with our test comes at high redshifts $z > 1$, where the estimated errors of the GA are smaller with our test and also agree more at high redshifts with the expectation from Planck of a nearly flat Universe.

16.9 Conclusions

In this Chapter we have presented a set of new consistency tests for the spatial curvature and homogeneity of the Universe and the ΛCDM model, which is the target of upcoming large-scale

structure surveys. These tests will provide us alternative and complementary tests of the validity of the standard flat ΛCDM paradigm.

In our analysis we prefer to use the GA, compared to other non-parametric approaches, e.g. various kinds of orthogonal polynomials or Gaussian Processes. The reason is that the Gaussian Processes still require the choice of a mean function, arbitrarily assumed to be either some constant, e.g. zero, or the cosmological constant ΛCDM model. In previous works we have shown that the GA do not suffer from this issue, hence we believe they are quite appropriate for the problem at hand.

We have presented an extension of the consistency diagnostic of flat ΛCDM of Ref. [426], by now including both the curvature $\Omega_{k,0}$ and the matter density $\Omega_{\rm m,0}$, see Eqs. (16.12)-(16.13). We show how the latter can be derived from the Hubble rate $H(z)$ and can be determined directly from observational data. We should stress that the added advantage of our new null test of the ΛCDM model presented here is the fact that we do not have to assume a flat Universe.

Secondly, through the combination of the BAO and $H(z)$ data or the angular and radial BAO data respectively, we also presented a test to search for deviations from homogeneity, see Eqs. (16.18) and (16.20). Then, with the angular and radial BAO data we also introduce two new consistency tests for the ΛCDM model. The first one, namely $\mathrm{Om}_\theta(z)$, is derived following a similar approach as it was shown in Ref. [419] where in this case we use the angular BAO scale relation $\theta(z)$ to reconstruct null tests of the ΛCDM model, with the advantage that this null test does not contain higher derivative terms, which tend to increase the reconstruction errors when using noisy data.

Finally, we also used the radial BAO data $\Delta z(z)$ to obtain a model independent determination of the accelerated expansion of the Universe by reconstructing the deceleration parameter $q(z)$ and we applied our Δz reconstruction to the $\mathcal{O}_m$ diagnostic [426]. Overall we find that our results are consistent with the standard flat ΛCDM scenario, however we also noted a $\sim 4\sigma$ tension on the determination of the transition redshift z_t, i.e. the redshift where the Universe transitions from decelerated to accelerated expansion, between the $H(z)$ and the radial BAO data.

Overall, we find that these new tests of the spatial curvature and homogeneity of the Universe can be used, in a model-independent fashion, to test some of the fundamental assumptions of the standard cosmological model. However, our reconstructions are somewhat limited by the current data, albeit this should be resolved in the near future when high quality BAO data become available from the next stage surveys.

17

A complementary consistency test of the Copernican principle via Noether's Theorem and machine learning forecasts

The original content of this chapter is based on Ref. [666]. The Copernican principle (CP), i.e. the assumption that we are not privileged observers of the universe, is a fundamental tenet of the standard cosmological model. A violation of this postulate implies the possibility that the apparent cosmic acceleration could be explained without the need of a cosmological constant, dark energy or covariant modifications of gravity. In this letter we present a new test of the CP relating the distance and the expansion rate, derived via Noether's theorem, which is complementary to other tests found in the literature. We also simulate fiducial data based on upcoming stage IV galaxy surveys and use them to reconstruct the Hubble rate $H(z)$ and the angular diameter distance $d_A(z)$ in order to forecast how well our null test can constrain deviations from the cosmological constant model. We find that our new test can easily rule out several realistic scenarios based on the Lemaître-Tolman-Bondi void model at confidence of $\gtrsim 3\sigma$ at mid to high redshifts ($z > 0.5$).

17.1 Introduction

The standard cosmological paradigm is based on two fundamental assumptions: first, that the dynamics of space-time are governed by Einstein's field equations and second, that the universe is homogeneous and isotropic at scales larger than ∼100Mpc, a hypothesis normally referred to as the Cosmological principle, which is considered to be a generalization of the Copernican principle (CP). The latter is one of the pillars of modern cosmology, stating that we do not occupy a special place in the Universe, or in other words, that any point in space must be equivalent to any other [648]. This leads to the framework of an homogeneous and isotropic background spacetime governed by the Friedmann-Lemaître-Robertson-Walker (FLRW) metric, which describes the geometry of the universe in terms of the scale factor $a(t)$, which obeys the Friedmann equation [645].

Clearly, any violations of the CP would disprove homogeneity and would provide a plausible explanation for the observed accelerated expansion of the Universe without the need for a dark energy component. The latter could in fact have several possible explanations, such as modified gravity theories, global inhomogeneities such as a void model or novel dark fluid components currently unobserved in the laboratories [667–669].

Void models are plausible contenders to the standard cosmological model and have the particularity that they don't employ any form of dark energy components as the accelerating expansion of the Universe is interpreted from the fact that we live close to the centre of a large underdense region. These inhomogeneities can occur locally via back-reaction [670, 671] or either by having the observer in a special place in the local universe [672].

As of now, the CP has been tested with different observations such as radio-astronomy [673], time drift of cosmological redshift [674], using Type Ia supernovae [672, 675], the integrated Sachs

Wolfe effect [676], galaxy correlations and the baryon acoustic oscillations [677], the Hubble parameter [678], machine learning and cosmological distance probes [421], peculiar velocities [679], gravitational waves [680], the distortion of the Planck spectrum of the cosmic microwave background (CMB) [681], galaxy surveys [682], the first order anisotropic kinetic Sunyaev Zel'dovich (kSZ) effect [683,684] and finally with a plethora of cosmological data that can be used to constrain spatial homogeneity [685].

The simplest inhomogeneous models of the Universe are given by a spherically symmetric distribution of matter, which is mathematically described by a Lemaître-Tolman-Bondi (LTB) spacetime [686], which has been shown it can produce a Hubble diagram which until a few years ago was consistent with observations a few years ago [687], but with more recent data it has been realized that simple void models cannot be used as alternative to dark energy. Specifically, LTB models where decaying modes are not present produce a large kSZ signal [683, 688, 689], while models with large decaying modes, and correspondingly a small kSZ signal, are not viable due to y-distortions [690]. Specific cases where the void LTB models can be viable require fine-tuned initial conditions, thus leading to questions about the naturalness of these models.

Since in the near future we are going to have sufficiently good and rich cosmological data we will use the LTB models as a check for our null test to show how they can be ruled out with high confidence. Probing for deviations from the cosmological constant model (ΛCDM) is non-trivial in the absence of guiding principles or laboratory data [649]. Thus, over the years several consistency tests of the ΛCDM have appeared in the literature. In general these tests are constructed so that possible deviations from ΛCDM at any redshift are apparent and easy to quantify in the form of null tests. These are formulated such that they can be computed using reasonably directly observable quantities at any redshift, thus by computing the consistency test using data from multiple redshifts, one can examine the validity of the basic assumptions of the cosmological standard model. If these assumptions hold, the null test should be independent of redshift.

In this Chapter we present a complementary test to the well-known curvature test of Ref. [648] that can be used to falsify the CP. This null test depends solely on distance and Hubble rate observations and is derived with the aid of Noether's theorem. The advantage of our new test is that it does not suffer from divergences and provides tighter constraints at high redshifts, as we will discuss in later sections.

Our Chapter is organized as follows: In Sec. 17.2 we present the theoretical formalism, our null test named $\mathcal{O}(z)$ and a description of the LTB models used to check the consistency test. In Sec. 17.3 we describe our simulated data based on an optimistic Stage IV galaxy survey and the Machine Learning (ML) algorithm used to reconstruct the data, namely the Genetic Algorithms. Finally, in Sec. 17.4 we present our results and in Sec. 17.5 we summarize our conclusions.

17.2 Analysis

Under the assumption of a Friedmann-Lemaître-Robertson-Walker (FLRW) metric, the luminosity distance can be written as

$$d_L(z) = \frac{c(1+z)}{H_0\sqrt{-\Omega_k}} \sin\left(\sqrt{-\Omega_k}\int_0^z dz' \frac{H_0}{H(z')}\right), \tag{17.1}$$

where Ω_k is the curvature parameter today and $H(z)$ is the expansion rate. The luminosity distance $d_L(z)$ is related to the angular diameter distance $d_A(z)$ through the Etherington relation, i.e. $d_L(z) = (1+z)^2 d_A(z)$. Using the dimensionless comoving distance $D(z)$, defined as $D(z) = (1+z)d_A(z)/(c/H_0)$, we can regroup Eq. (17.1) to solve for the curvature parameter Ω_k in terms of $H(z)$ and $D(z)$ as [648]

$$\Omega_k = \frac{[H(z)D'(z)]^2 - 1}{[H_0 D(z)]^2}, \tag{17.2}$$

where the prime is a derivative with respect to the redshift $' = d/dz$ and we have set $c = 1$. The above relation allows us to estimate the spatial curvature parameter from distance and Hubble rate observations, without having to assume any particular dark energy model or other model parameters. It also allow us to test the curvature at any single redshift as it has been reconstructed in several works, see for instance Refs. [421, 648–655, 655, 656]. Since the curvature parameter Ω_k does not depend on redshift, we can differentiate this to obtain a relation that must always equal zero. This can be expressed as [648]

$$C(z) = 1 + H^2 \left(DD'' - D'^2\right) + HH'DD', \tag{17.3}$$

where $C(z)$ has to be zero at all redshifts in any model described by a FLRW metric, as was originally shown in Ref. [648]. In Sec. 17.4 we will present constraints on this test with an upcoming Stage IV survey along with a complementary CP test inspired from Noether's theorem. The advantage of following Noether's theorem to make a complementary test is that by taking into account of the symmetries of the system of equations that describe the expansion of the Universe, we can reduce the order of the differential equations that appear in the final test. This allows us to keep the errors of the reconstructions smaller, as higher order derivatives of noise data tend to make the reconstructions less robust at high redshifts, as we demonstrate in what follows.

17.2.1 Lagrangian formalism and null test

We now present a complementary test of $C(z)$ to probe the CP. Using Eq. (17.2) we can solve for D'^2, which will be given by

$$D'^2 = \frac{1 + D^2\Omega_k}{H^2}, \tag{17.4}$$

and inserting this relation into Eq. (17.3) we have

$$D'' + \frac{H'}{H}D' - \frac{\Omega_k}{H^2}D = 0. \tag{17.5}$$

To find a null test that involves the distance measure D, we will make use of the Lagrangian formalism. The first step is to find a Lagrangian for Eq. (17.5) and, with the help of the Noether's theorem, to find an associated conserved quantity. For a description of the Noether symmetry approach and applications for null tests see [420, 429].

In a nutshell, if we assume that the Lagrangian can be written as $\mathcal{L} = \mathcal{L}(z, D(z), D'(z))$. Then the Euler-Lagrange equations are:

$$\frac{\partial \mathcal{L}}{\partial D} - \frac{d}{dz}\frac{\partial \mathcal{L}}{\partial D'} = 0 \tag{17.6}$$

So, let us assume a Lagrangian of the form

$$\mathcal{L} = T - V \tag{17.7}$$

$$T = \frac{1}{2} f_1(z, H(z)) D'(z)^2 \tag{17.8}$$

$$V = \frac{1}{2} f_2(z, H(z)) D(z)^2 \tag{17.9}$$

where the f_1 and f_2 are arbitrary functions that need to be determined so that the resulting equation after implementing the Euler-Lagrange Eq. (17.6) is exactly Eq. (17.5). Therefore, substituting the former Lagrangian in the Euler-Lagrange Eq. (17.6) and comparing the result with Eq. (17.5) we are able to get the two functions f_1 and f_2 and consequently to build the Lagrangian $\mathcal{L}$ of the system:

$$\mathcal{L} = \frac{1}{2} H D'^2 + \frac{1}{2}\frac{\Omega_k}{H} D^2. \tag{17.10}$$

It is easy to see that substituting Eq. (17.10) into Eq. (17.6) results exactly to Eq. (17.5). Now that we have a Lagrangian we can use Noether's theorem to find a conserved quantity that will be later translated to the null test. So, if we have an infinitesimal transformation $\mathbf{X}$ with a generator

$$\mathbf{X} = \alpha(D)\frac{\partial}{\partial D} + \frac{d\alpha(D)}{dz}\frac{\partial}{\partial D'} \tag{17.11}$$

$$\frac{d\alpha(D)}{dz} \equiv \frac{\partial \alpha}{\partial D}D'(z) = \alpha'(z) \tag{17.12}$$

such that for the Lie derivative of the Lagrangian we have $L_X\mathcal{L} = 0$, then

$$\Sigma = \alpha(z)\frac{\partial \mathcal{L}}{\partial D'} \tag{17.13}$$

is a constant of "motion" for the Lagrangian of Eq. (17.10). From Eq. (17.13) we get that

$$\Sigma = \alpha(D)HD', \tag{17.14}$$

while from the Lie derivative we also obtain:

$$\alpha(z) = ce^{-\int_1^z \frac{\Omega_k D(x)}{H^2(x)D'(x)}dx}, \tag{17.15}$$

where c is an integration constant. Then, the constant Σ becomes

$$\Sigma = \frac{H(z)D'(z)}{H(0)D'(0)}e^{-\int_0^z \frac{\Omega_k D(x)}{H^2(x)D'(x)}dx}, \tag{17.16}$$

where we have redefined Σ to absorb c and we normalized the above equation so that the null test must be 1 for all values of z.

Finally, to write the above null test only as a function of $H(z)$ and $D(z)$ we substitute Ω_k from Eq. (17.2) into Eq. (17.16), then the null test is given by

$$\mathcal{O}(z) = \frac{H(z)D'(z)}{H_0\ D'(0)}e^{-\int_0^z \frac{H^2(x)D'^2(x)-1}{H^2(x)D(x)D'(x)}dx}. \tag{17.17}$$

17.2.2 LTB model

An alternative explanation, besides the cosmological constant Λ, for the current phase of accelerated expansion of the Universe is the idea of inhomogeneous universe models, where this expansion can be seen as an effective acceleration induced by our special position as observers residing inside a huge under-dense region of space. These models violate the CP and a simple toy model which has been studied extensively in the literature is the spherically symmetric Lemaître-Tolman-Bondi model [686, 691, 692] (LTB) which describes a local void. It actually represents a family of models coming from a spherically symmetric solution of Einstein equations exerted by pressureless matter and no cosmological constant, as one still needs to provide a matter density profile [674]. The metric for our model of interest is given by

$$ds^2 = -dt^2 + X^2(r,t)dr^2 + A^2(r,t)d\Omega^2, \tag{17.18}$$

where $d\Omega^2 = d\theta^2 + \sin^2\theta d\phi^2$ and the function $A(r,t)$ is analogous to the scale factor of the FRLW metric, albeit it also has a dependence on both time and the radial coordinate r. One can find a relation between $X(r,t)$ and $A(r,t)$ through the $0-r$ component of the Einstein equations, i.e $X(r,t) = A'(r,t)/\sqrt{1-k(r)}$, where a prime denotes a derivative with respect to the coordinate r and $k(r)$ represents an arbitrary function, being similar to the role of the spatial curvature parameter.

$\Omega_{\mathrm{m,in}}$	r[Gpc]	Δr[Gpc]	LTB models
0.298	1.0	0.30	LTB1
0.197	1.5	0.45	LTB2
0.156	1.8	0.54	LTB3
0.200	2.0	0.60	LTB4

Table 17.1: The parameters for the LTB models, where in all cases $\Omega_{\mathrm{m,out}} = 1$ and $H_0 = 77$ km/s/Mpc. Note that the actual value of the Hubble rate today as measured by a comoving observer at $z = 0$, depends on the specific profile used. Here we assume the constrained GBH LTB profile of Ref. [687], given by Eqs. (17.19)-(17.20).

This model can be totally described by the matter density $\Omega_m(r)$ and the Hubble expansion rate $H(r)$. We will check our consistency test with a particular LTB model known as the GBH parametrization [687]. In this case the matter and Hubble parameter profiles are given by

$$\Omega_{\mathrm{m}}(r) = \Omega_{\mathrm{out}} + (\Omega_{\mathrm{in}} - \Omega_{\mathrm{out}}) \frac{1 - \tanh\left[(r - r_0)/2\Delta r\right]}{1 + \tanh\left[r_0/2\Delta r\right]}, \tag{17.19}$$

$$H_0(r) = H_0 \left(\frac{1}{\Omega_{\mathrm{k}}(r)} - \frac{\Omega_{\mathrm{m}}(r)}{\sqrt{\Omega_{\mathrm{k}}(r)^3}} \sinh^{-1} \sqrt{\frac{\Omega_{\mathrm{k}}(r)}{\Omega_{\mathrm{m}}(r)}} \right), \tag{17.20}$$

where $\Omega_k(r) = 1 - \Omega_m(r)$, Ω_{out} is the value of the matter density at infinity, Ω_{in} is the value of the matter density at the center of the void, r_0 is the size of the void and Δr represents a scale that characterises the transition to uniformity. In Table 17.1 we show the four GBH parameters used in our analysis, which correspond to characteristic voids of sizes of a few Gpc, as suggested in Ref. [687].

17.3 Reconstructions

We now describe both the mock data used and the Machine Learning process used to reconstruct the null test, namely the Genetic Algorithms.

17.3.1 Mock data

Our mock Baryon Acoustic Oscillations (BAO) data for the angular diameter distance $d_A(z)$ and the Hubble rate $H(z)$ are based on a future upgrade of Dark Energy Spectroscopic Instrument (DESI) [397]. DESI is a survey with the goal of probing the expansion rate and large-scale structure (LSS) of the universe and can complement other future BAO surveys by extending the probed redshift range [470].

The DESI survey, whose operations started at the end of 2019, is expected to obtain optical spectra for tens of millions of galaxies and quasars up to redshift $z \sim 4$, which will allow for BAO and redshift-space distortion cosmological analyses. Our forecast data will cover the redshift range $z \in [0.05, 3.55]$, but their precision will also depend on the target population. The blue galaxies (BGs) will cover the redshift range $z \in [0.05, 0.45]$ in five equispaced redshift bins, the luminous red galaxies (LRGs) and emission line galaxies (ELGs) will focus on $z \in [0.65, 1.85]$ with 13 equispaced redshift bins, while the Ly-α forest quasar survey will cover $z \in [1.96, 3.55]$ with 11 equispaced redshift bins.

To create the mocks we assume the $H(z)$ and $d_A(z)$ are uniformly distributed in the range $z \in [0, 3.55]$, divided into 20 equally spaced binds of step $dz = 0.2$. The $H(z_i)$ and $d_A(z_i)$ function

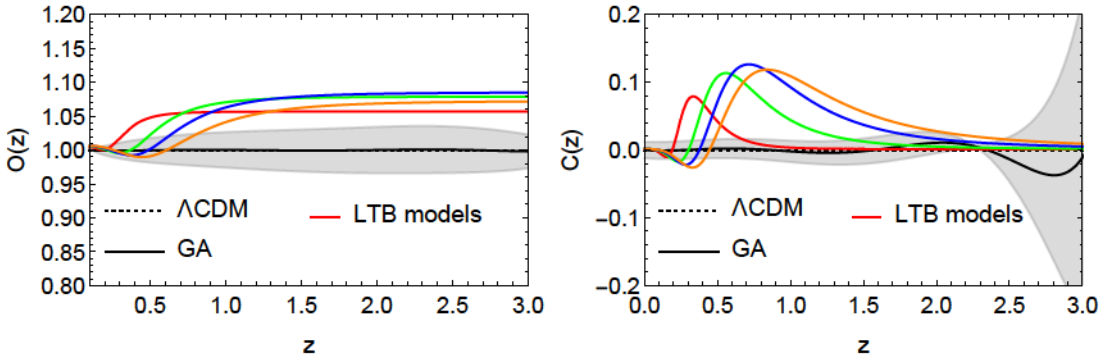

Figure 17.1: Reconstructions of the tests of the Copernican principle: the $\mathcal{O}(z)$ test of Eq. (17.17) (left panel) and the $C(z)$ test of Eq. (17.5) (right panel). The black solid line corresponds to the GA best-fit, the gray shaded region corresponds to the 68.3% confidence regions and the colored lines to the various LTB profiles described in Table 17.1.

was estimated as its theoretical value from the different cosmological models plus a gaussian error (which can be either negative or positive) and assigning an error of 0.5% of its value to $H(z)$ and for $d_A(z)$ an error of 0.28% for $z < 1.1$ and 0.39% for $z > 1.1$, which is in agreement with a similar setup to [693]. We further assume these measurements to be uncorrelated.

17.3.2 Genetic Algorithms

The implementation of the Genetic Algorithms (GA) in our analysis is explained in Chapter 10.

In our analysis we reconstruct the Hubble rate $H(z)$ and the angular diameter distance $d_A(z)$ from the mock data created, and the course of action to its reconstruction is as follows. First, our predefined grammar was formed on the following functions: exp, log, polynomials etc. and a set of operations $+, -, \times, \div$, see Table 10.1 for the complete list.

As a prior for our $H(z)$ reconstruction we imposed that at $z = 0$ it goes as $H(z = 0) = H_0$. Similarly for the $d_A(z)$ reconstruction we assumed that $d_A(z = 0) = c/H_0$ at $z = 0$ were both prior have a motivated by physical reasons. However, we make no assumptions on the curvature of the Universe or any modified gravity or dark energy model. Furthermore, in order to avoid overfitting or any spurious reconstructions we required that all functions reconstructed by the GA are continuous and differentiable, without any singularities in the redshift probed by the data.

Once the initial population has been constructed, the fitness of each member is computed by a χ^2 statistic, using the $H(z)$ and $d_A(z)$ data points directly as input. The final output of the code is a set of functions of $H(z)$ and $d_A(z)$ that describes the Hubble rate and the angular diameter distance respectively.

The error estimates of the reconstructed function are obtained via the path integral approach, see Sec. 10.0.2 for more details.

17.4 Results

In this section we present our GA fits to the simulated data and the corresponding consistency test obtained from our reconstructions on $H(z)$ and $d_A(z)$. We want to stress that the aim of this work is not simply to rule out LTB void models as contenders of dark energy models, which has already been done so, but to present a complementary consistency to test of the CP in a non-trivial but still realistic setting.

In Fig. 17.1 we show our new null test $\mathcal{O}(z)$ given by Eq. (17.17) and the $C(z)$ test given by Eq. (17.3), both of which can be used to find deviations from the CP through our reconstructions

on the Hubble rate $H(z)$ and the angular diameter distance $d_A(z)$. In both cases the black solid line and the grey region correspond to the GA best-fit and its 1σ error respectively. The black dashed-line represents the best-fit flat ΛCDM model and we see that our reconstructions recover well the fiducial cosmology. The coloured lines represent the four different LTB models, concretely defined in Table 17.1.

In the left panel of Fig. 17.1 we show our $\mathcal{O}(z)$ test and as can be seen, it is a good discriminator of all LTB models at high and intermediate redshifts, i.e. $z \sim 0.6$ and beyond, as the errors remain consistently low at all redshifts. On the other hand, in the right panel of Fig. 17.1 we present the $C(z)$ test which can discriminate the LTB model from ΛCDM at intermediate redshifts $0.5 < z < 1.5$ but at low redshifts ($z < 0.3$) and high redshifts above $z \sim 1.5$ the values of $C(z)$ of the fiducial LTB models asymptote to zero, thus being dominated by the errors.

Therefore, by comparing both panels we may infer that our test manages to detect deviations from the CP particularly well and consistently at mid to high redshifts, when the traditional $C(z)$ test does not perform equally well. Hence, our null test presented serves as a complementary consistency check of the CP and is especially useful at high redshifts.

17.5 Conclusions

In summary, we have presented a new consistency test of the Copernican principle, which is complementary to the curvature test of Ref. [648]. In particular, we used the Noether's theorem approach in order to obtain a conserved quantity that can be written in terms of the Hubble rate $H(z)$ and the comoving distance $D(z)$.

In order to forecast how well our new test, given by Eq. (17.17), can constrain deviations from the Copernican principle at large scales, we created mock datasets based on specifications of the DESI survey and using the ΛCDM model for the fiducial cosmology, for a variety of different profiles. This approach allows us to quantify any deviations using realistic scenarios.

Then, to reconstruct the $\mathcal{O}(z)$ statistic given by Eq. (17.17) from the mock data, we preferred to use the machine learning approach, namely the GA, as this will allow us to obtain non-parametric and theory agnostic reconstructions of the data, in the form of $H(z)$ and $D(z)$, that we can in turn use to reconstruct $\mathcal{O}(z)$. With the same functions we also reconstructed the $C(z)$ function of Ref. [648] given by Eq. (17.5).

Following this approach, we find that the GA with the $\mathcal{O}(z)$ statistic can correctly predict the underlying fiducial cosmology at all redshifts covered by the data, as seen in the left panel Fig. 17.1 and can easily rule out several realistic LTB scenarios at confidence of $\gtrsim 3\sigma$ at mid to high redshifts ($z > 0.5$). On the other hand, the $C(z)$ statistic, while it successfully rules out the same LTB profiles at small redshifts at a confidence of $\sim 8\sigma$ at intermediate redshifts ($0.5 < z < 1.0$), it does not fare equally well at higher redshifts ($z > 1.5$) as the errors become larger and the value of $C(z)$ asymptotes to zero, thus diminishing its predictive power.

To conclude, we find that the $\mathcal{O}(z)$ test provides complementary to other tests, information on possible deviations of homogeneity at different redshift regimes and can help test one of the fundamental assumptions of the standard cosmological model at high redshifts, something which is the goal of several current and upcoming surveys in the coming years.

18

Machine Learning improved fits of the sound horizon at the baryon drag epoch

The original content of this chapter is based on Ref. [694]. The baryon acoustic oscillations (BAO) have proven to be an invaluable tool in constraining the expansion history of the Universe at late times and are characterized by the comoving sound horizon at the baryon drag epoch $r_{\rm s}(z_{\rm d})$. The latter quantity can be calculated either numerically using recombination codes or via fitting functions, such as the one by Eisenstein and Hu (EH), made via grids of parameters of the recombination history. Here we quantify the accuracy of these expressions and show that they can strongly bias the derived constraints on the cosmological parameters using BAO data. Then, using a machine learning approach, called the genetic algorithms, we proceed to derive new analytic expressions for $r_{\rm s}(z_{\rm d})$ which are accurate at the $\sim 0.003\%$ level in a range of 10σ around the Planck 2018 best-fit or $\sim 0.018\%$ in a much broader range, compared to $\sim 2-4\%$ for the EH expression, thus obtaining an improvement of two to three orders of magnitude. Moreover, we also provide fits that include the effects of massive neutrinos and an extension to the concordance cosmological model assuming variations of the fine structure constant. Finally, we note that our expressions can be used to ease the computational cost required to compute $r_{\rm s}(z_{\rm d})$ with a Boltzmann code when deriving cosmological constraints from current and upcoming surveys.

18.1 Introduction

Some of the strongest constraints on the expansion of the Universe at late times come from baryon acoustic oscillations (BAO) data. The BAO were formed in the early Universe, while it was very homogeneous (as probed today by the CMB) except for tiny fluctuations, and the photons and baryons were tightly coupled [37]. As the Universe expanded, it became cooler and less dense, while the fluctuations grew due to gravity. Acoustic waves were generated as the photon-baryon fluid was attracted and fell onto the overdensities producing compressions and rarefactions due to the gravitational collapse and radiation pressure.

These acoustic waves propagated until the Universe became cool enough for the electrons and protons to recombine and then the baryons and photons decoupled. The time when the baryons were "released" from the drag of the photons is known as the drag epoch, $z_{\rm d}$ [26]. From then on, photons expanded freely while the acoustic waves "freezed in" the baryons in a scale given by the size of the sound horizon at the drag epoch, dubbed $r_{\rm s}(z_{\rm d})$. Progressively, baryons fell into dark matter potential wells but also dark matter was attracted to baryon overdensities. Neutrinos did not interact, so they streamed away while dark matter responded to gravity and fell onto the overdensity.

The perturbations were dominated by photons and baryons as they were coupled, resulting in overdensities and overpressure which tried to equalize with the surrounding resulting in an expanding sound wave moving at the speed of sound, approximately $\sim 2/3$ the speed of light. The perturbation in photons and baryons was carried outward and the photons and baryons continued

to expand whereas neutrinos spread out. Dark matter continued to fall into perturbations, which kept growing.

As the expanding Universe continued to cool down, it reached a point when the electrons and protons began to combine. Since photons did not scatter as efficiently they started to decouple. The sound speed dropped and the pressure wave slowed down. The process continued until the photons where completely decoupled and then the perturbations smoothed out[1]. In fact, the sound speed of the baryon perturbation dropped so much that the pressure wave stalled. Thus, the original dark matter perturbation was left surrounded by a baryon perturbation in a shell. The two components attracted each other and the perturbations started to mix[2].

The BAO provides a characteristic scale that is "frozen" in the galaxy distribution providing a standard ruler that can be measured as a function of redshift in either the galaxy correlation function or the galaxy power spectrum. The BAO determination of the geometry of the Universe is quite robust against systematics and has been measured by several surveys, such as the SDSS [695] and 2dFGRS [696]. The BAO signature provides a standard ruler that can be used to measure the geometry of the Universe and it can measure both the angular diameter distance $d_A(z)$ and the expansion rate $H(z)$. Measurements of the BAO only provide the combination of H_0 and $r_{\rm s}(z_{\rm d})$, which means the two parameters are fully degenerate. As a result, the constraints obtained from the analysis of the BAO can be influenced significantly on the assumption of $r_{\rm s}(z_{\rm d})$ [697].

In order to accurately estimate $r_{\rm s}(z_{\rm d})$, one may use either recombination codes, such as `RECFAST` [698], `CosmoRec` [699] or `HyRec` [700, 701], or analytic approximations based on fits of grids of parameters of the recombination history. A prominent example of the latter approach is the formula by Eisenstein and Hu [98], hereafter known as EH, which provides a fit of $r_{\rm s}(z_{\rm d})$ in terms of the matter and baryon density parameters. This formula has been extensively used in the literature in analyses of the BAO data, see for example Refs. [90, 317, 470, 702, 703]. However, as already observed in Ref. [98], this expression is only accurate to the $\sim 2\%$ level and as a result is not appropriate for deriving cosmological constraints from BAO data in a percent cosmology era with current and upcoming surveys.

Over the years attempts to improve the EH formula have appeared. For example, the dependence of $r_{\rm s}(z_{\rm d})$ on various parameters, including massive and massless neutrinos, was examined in Ref. [704]. On the other hand, fits of $r_{\rm s}(z_{\rm d})$ including neutrinos and relativistic species were found in Ref. [705] and in Ref. [81]. Finally, how the fraction of the baryonic mass in Helium Y_P and the relativistic degrees of freedom $N_{\rm eff}$ affects the sound horizon and how both are degenerate, was studied in Ref. [706].

The main limitation of the aforementioned analyses is that some ad-hoc parametrizations were fitted to grids of parameters and $r_{\rm s}(z_{\rm d})$, thus being limited from the start on how accurate they can be. Hence, in our work we use machine learning to provide, in a data driven approach, extremely accurate fits to the comoving sound horizon at the baryon drag epoch $r_{\rm s}(z_{\rm d})$. We then compare these expressions against both the original formula of EH and the exact numerical estimation of the sound horizon, in order to quantify the amount of bias this expression introduces in the constraints.

In our analysis we also consider separately the effect of massive neutrinos and a varying fine structure constant and we find that our fits provide an improvement of a factor of three compared to other simple parametrizations and can be used in current and upcoming surveys to derive cosmological constraints so as to ease the computational cost that would be required when computing $r_{\rm s}(z_{\rm d})$ via a Boltzmann code.

The structure of this Chapter is as follows: in Sec. 18.2 we present the theoretical background and main assumptions in our work, while in Sec. 18.3 we present some details on our machine learning approach used to improve the sound horizon fits. In Sec. 18.4 we present our main results, while in Sec. 18.5 we present some complementary fits for the redshift at the drag and recombination epochs. Finally in Sec. 18.6 we summarize our conclusions.

[1] http://mwhite.berkeley.edu/BAO
[2] https://lweb.cfa.harvard.edu/~deisenst/acousticpeak/

18.2 Theory

The comoving sound horizon at the drag epoch is given by

$$r_{\rm s}\left(z_{\rm d}\right) = \frac{1}{H_0}\int_{z_{\rm d}}^{\infty}\frac{c_{\rm s}(z)}{H(z)/H_0}\,{\rm d}z, \tag{18.1}$$

where $z_{\rm d}$ is the redshift at the drag epoch, see Eq. (4) of Ref. [98], while $c_{\rm s}(z)$ is the sound speed in the baryon-photon fluid given by

$$c_{\rm s} = \frac{c}{\sqrt{3(1+R)}}, \tag{18.2}$$

where $R = \frac{3\rho_b}{4\rho_\gamma} = \frac{3\Omega_{b,0}}{4\Omega_{\gamma,0}}a$ and c is the speed of light in vacuum. By definition, the sound horizon at the baryon drag epoch is the comoving distance a wave can travel prior to $z_{\rm d}$ and it depends on the epoch of recombination, the expansion of the Universe and the baryon-to-photon ratio. The sound horizon is well determined by the Cosmic Microwave Background (CMB) measurements of the acoustic peaks.

Regarding the neutrinos, neutrino flavour oscillation experiments have shown that they are massive [707], providing a direct evidence for physics beyond the Standard Model. Cosmology is a very propitious stage to probe neutrino properties since they leave an imprint in the CMB and in the distribution of Large-Scale Structure (LSS) in the Universe. The energy density of massive neutrinos, $\rho_\nu = \sum m_{\nu,i}n_{\nu,i}$, corresponds to

$$\Omega_\nu h^2 \sim \frac{\sum m_{\nu,i}}{94{\rm eV}}, \tag{18.3}$$

where n_ν represents number density of neutrinos.

We also consider variations of fundamental constants, which are usually assumed to be constant over space-time. These constants are defined operationally, meaning that nature by itself does not force it to be constant. They have to be obtained experimentally since they are not given by the theory, see for instance Ref. [539] for a review on the variation of fundamental constants. Here we will probe the interesting case where the fine structure constant, defined as $\alpha_0 = \frac{e^2}{\hbar c}$, is not constant and we will express its relative variation over its standard model value as α/α_0.

If there are eventually signatures of a variation it would have imprints in different physical mechanisms such as the CMB anisotropies [522]. Constraints on this variation, both temporal and spatial, have been performed already [514,540–545], and this variation can be produced for example through an evolving scalar field which is coupled to the electromagnetic Lagrangian [514, 708–710]. This will give rise to variations of the fine structure constant, a violation of the Weak Equivalence principle and violations of the standard $T_{\rm CMB}(z)$ law, as the number of photons is no longer conserved. These kinds of models can in principle be constrained by future large scale structure surveys using high-resolution spectroscopic data in combination with local astrophysical data, see Ref. [711] for updated constraints with current data and Ref. [712] for recent forecasts with upcoming surveys.

Another class of models where this occurs is the Bekenstein-Sanvik-Barrow-Magueijo (BSBM) model [546], where the electric charge is allowed to vary. Although such theories preserve the local gauge and Lorentz invariance, the fine structure constant will vary during the matter dominated era.

18.3 The Genetic Algorithms

A full description concerning the Genetic Algorithms (GA) that will be used in our analysis to improve the sound horizon fits can be found in Chapter 10. In our analysis we reconstruct the $r_{\rm s}(z_{\rm d})$ function considering that it depends on the following variables: $\{\Omega_m h^2, \Omega_b h^2\}$, $\{\Omega_m h^2, \Omega_b h^2, \Omega_\nu h^2\}$

and $\{\Omega_m h^2, \Omega_b h^2, \alpha/\alpha_0\}$ respectively. Our reconstruction procedure is as follows. First, our predefined grammar was constructed on the following functions: exp, log, polynomials etc. and a set of operations $+, -, \times, \div$, see Table 10.1 for the complete list.

Once the initial population has been constructed, the fitness of each member is computed by a χ^2 statistic, using the $r_{\rm s}(z_{\rm d})$ data points directly as input. Then, through a tournament selection process, the best-fitting functions in each generation are chosen and the two stochastic operations of crossover and mutation are used. The final output of the code is a mathematical function of $r_{\rm s}(z_{\rm d})$ that describes the sound horizon at the drag epoch in terms of the various cosmological parameters of interest.

18.4 Results

In this section we now present our machine learning fits to the sound horizon at the baryon drag epoch $r_{\rm s}(z_{\rm d})$. First, we will only include the dependence on the matter and baryon density parameters $\{\Omega_m h^2, \Omega_b h^2\}$, while later we will also consider the effect of massive neutrinos and a varying fine structure constant, i.e. the parameter vectors will be $\{\Omega_m h^2, \Omega_b h^2, \Omega_\nu h^2\}$ and $\{\Omega_m h^2, \Omega_b h^2, \alpha/\alpha_0\}$ respectively.

To calculate the sound horizon we use the code `CLASS` by Ref. [232] and the `HYREC-2` recombination module `Hyrec2020` [700, 701]. We then make grids of parameters and $r_{\rm s}(z_{\rm d})$ and fit the values with both traditional minimization approaches and with the genetic algorithms, as described in Sec. 18.3. To simplify our notation we make the following definitions that will be used throughout the text: $\omega_b = \Omega_b h^2$, $\omega_m = \Omega_m h^2$ and $\omega_\nu = \Omega_\nu h^2$. In what follows, we will now describe our approach in more detail and present the results for the various cases.

18.4.1 Matter and baryons only

First, we consider the standard case of matter and baryons, as was also studied in Ref. [98] (hereafter denoted as EH). This case was obtained by simulating values for $\Omega_m h^2 \in [0.025, 0.5]$ and $\Omega_b h^2 \geq 0.0125$ and is given by [98]

$$r_{\rm s}\left(z_{\rm d}\right) \simeq \frac{44.5 \ln\left(\frac{9.83}{\omega_m}\right)}{\sqrt{1 + 10\ \omega_b^{3/4}}} \text{Mpc}, \tag{18.4}$$

which is accurate up to $\sim 2\%$. Since now the recombination codes have more improved physics (for example an improved post-Saha expansion at early phases of hydrogen recombination, see Refs. [700, 713] for a discussion), we have considered the same parametrization as in EH but with the coefficients as free parameters. By fitting the parametrization to a grid of values for $r_{\rm s}(z_{\rm d})$ for the range $\Omega_m h^2 \in [0.13, 0.15]$ and $\Omega_b h^2 \in [0.0214, 0.0234]$, which is around 10σ from the Planck best-fit, we find the following improved expression

$$r_{\rm s}\left(z_{\rm d}\right) = \frac{45.5337 \ln\left(\frac{7.20376}{\omega_m}\right)}{\sqrt{1 + 9.98592\ \omega_b^{0.801347}}}\ \text{Mpc}, \tag{18.5}$$

which is accurate up to $\sim 0.009\%$. Using the same grid of values with the GA we find the following fit which is even better

$$r_{\rm s}(z_{\rm d}) = \frac{1}{a_1 \omega_b^{a_2} + a_3 \omega_m^{a_4} + a_5 \omega_b^{a_6} \omega_m^{a_7}} \text{Mpc}, \tag{18.6}$$

where

$$\begin{aligned} a_1 &= 0.00785436, a_2 = 0.177084, a_3 = 0.00912388, a_4 = 0.618711, a_5 = 11.9611, \\ a_6 &= 2.81343, a_7 = 0.784719. \end{aligned}$$

Method	Param	best-fit	mean$\pm\sigma$	95% lower	95% upper
Num.	$\omega_{\rm m,0}$	0.1968	$0.1641^{+0.04}_{-0.051}$	0.0788	0.251
	$r_{s,d}h$	102.1	$101.7^{+1.9}_{-1.8}$	97.91	105.4
EH	$\omega_{\rm m,0}$	0.1816	$0.1488^{+0.036}_{-0.044}$	0.07544	0.2222
	$r_{s,d}h$	100.3	$99.9^{+2.2}_{-1.9}$	95.74	103.9
GA	$\omega_{\rm m,0}$	0.1959	$0.1645^{+0.04}_{-0.054}$	0.07738	0.2535
	$r_{s,d}h$	102.3	$101.7^{+1.9}_{-1.8}$	97.94	105.5

Table 18.1: The best-fit, mean and 95% limits for $(\omega_{\rm m,0}, r_{s,d}h)$ as discussed in the text. As seen, the older EH approach biases the estimated mean values for the parameters by almost half a σ, even though they share the same value of the χ^2 at the minimum $\chi^2_{\rm min} = 10.95$. The contours are shown in Fig. 18.1.

In this case, our GA improved expression given by Eq. (18.6) is accurate up to $\sim 0.003\%$.

Next, we also consider a broader range of values for the parameter grid in order to allow for the fitting function to be used in BAO analyses without compromising its accuracy. In particular, we consider the range $\Omega_m h^2 \in [0.05, 0.25]$ and $\Omega_b h^2 \in [0.016, 0.03]$ and we find with the GA the following fit

$$r_{\rm s}(z_{\rm d}) = \left[\frac{1}{a_1\omega_b^{a_2} + a_3\omega_b^{a_4}\omega_m^{a_5} + a_6\omega_m^{a_7}} - \frac{a_8}{\omega_m^{a_9}}\right]{\rm Mpc}, \tag{18.7}$$

where

$$\begin{aligned} a_1 &= 0.00257366, a_2 = 0.05032, a_3 = 0.013, a_4 = 0.7720642, a_5 = 0.24346362, \\ a_6 &= 0.00641072, a_7 = 0.5350899, a_8 = 32.7525, a_9 = 0.315473. \end{aligned}$$

which is accurate up to $\sim 0.018\%$, i.e. a two orders of magnitude improvement from the EH expression of Eq. (18.4).

In order to quantify the bias introduced in deriving constraints on the cosmological parameters by using the less accurate expression of Eq. (18.4), we will now present the confidence contours and parameter constraints obtained via a Markov chain Monte Carlo (MCMC) with the code `MontePython 3` of Ref. [334], using the currently available BAO data as described in Ref. [324] and the aforementioned $r_{\rm s}(z_{\rm d})$ expressions. As mentioned earlier, $r_{\rm s}(z_{\rm d})$ and $h \equiv H_0/100$ are degenerate, we in what follows we will consider the combination $r_{s,d}h = r_{\rm s}(z_{\rm d})h$.

In particular, in Fig. 18.1 we show a comparison of the confidence contours for the EH expression for the sound horizon given by Eq. (18.4) (blue contour) against the machine learning improved expression (GA) given by Eq. (18.7) (red contours) and the exact numerical approach (Num.) calculated via `Hyrec2020` (green contour). Furthermore, in Table 18.1 we show the best-fit, mean and 95% limits for $(\omega_{\rm m,0}, r_{s,d}h)$ obtained from the MCMC runs. As can be seen, using the older and less accurate expression biases strongly the constraints for both $\omega_{\rm m,0}$ and $r_{\rm s}(z_{\rm d})h$ by almost half a σ and shifts the best-fit $\omega_{\rm m,0}$ by $\sim 9.3\%$ from its true value, which is obtained using the full numerical approach.

18.4.2 Matter, baryons and massive neutrinos

Next, we also include massive neutrinos and this time we compare with the expression of Ref. [705], where the following fit was presented

$$r_{\rm s}(z_{\rm d}) \approx \frac{55.154\exp\left[-72.3\left(\omega_\nu + 0.0006\right)^2\right]}{\omega_m^{0.25351}\omega_b^{0.12807}}{\rm Mpc}, \tag{18.8}$$

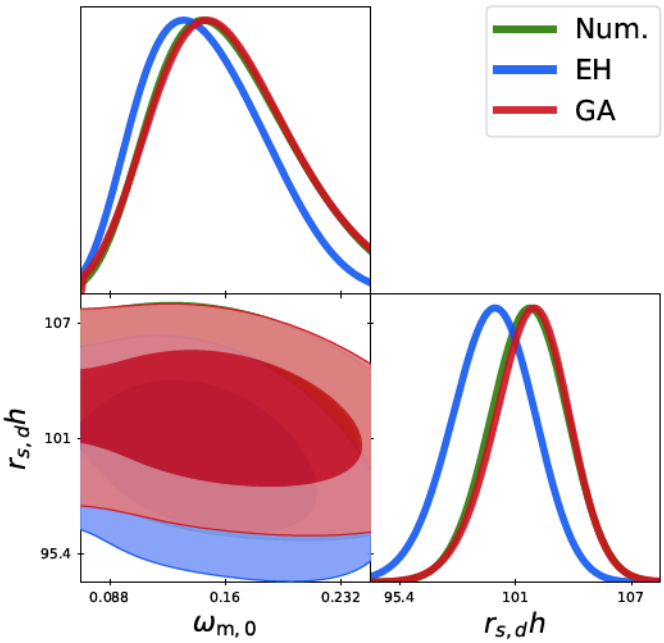

Figure 18.1: A comparison of the confidence contours for the expression by Eisenstein-Hu (EH) for the sound horizon given by Eq. (18.4) (blue contour) against the improved expression found by the machine learning approach (GA) given by Eq. (18.7) (red contours) and the exact numerical approach (Num.) calculated via `Hyrec2020` (green contour), using the current BAO data as described in Ref. [324].

which is accurate up to 0.29% within our range of values considered. Notice that this expression is accurate up to 0.021% if we limit to the range within 3σ of values derived by Planck and that $\omega_\nu = 0.0107\,(\sum m_\nu/1.0\text{eV})$.

In our case we consider the parameters in the range $\Omega_m h^2 \in [0.13, 0.15]$, $\Omega_b h^2 \in [0.0214, 0.0234]$, which is around 10σ from Planck, and for the massive neutrinos in the range $0 < \sum m_\nu < 0.6\text{eV}$. Then, with the GA we find the improved fit which reads as follows

$$r_s(z_d) = \frac{a_1\ e^{a_2(a_3+\omega_\nu)^2}}{a_4\ \omega_b^{a_5} + a_6\ \omega_m^{a_7} + a_8\,(\omega_b\ \omega_m)^{a_9}}\ \text{Mpc}, \tag{18.9}$$

where the coefficients take the following values

$$\begin{aligned} a_1 &= 0.0034917, a_2 = -19.972694, a_3 = 0.000336186, a_4 = 0.0000305, a_5 = 0.22752, \\ a_6 &= 0.00003142567, a_7 = 0.5453798, a_8 = 374.14994, a_9 = 4.022356899, \end{aligned} \tag{18.10}$$

which is accurate up to 0.0076%, i.e. roughly a factor of three improvement over Eq. (18.8).

18.4.3 Matter, baryons and the fine structure constant

Finally, we also consider the effects of a varying fine structure constant on the sound horizon at the drag redshift. The fine structure constant is only included in the recombination code `Hyrec2020` [700, 701], thus the only modification in the code in this case that was needed, was passing an extra parameter to `CLASS`.

Then, we simulate values of the $r_s(z_d)$ for the range $\Omega_m h^2 \in [0.13, 0.15]$, $\Omega_b h^2 \in [0.0214, 0.0234]$ and $\alpha/\alpha_0 \in [0.98, 1.02]$. The range for α/α_0 might seem restrictive, but in Ref. [714] it was shown that with current data any variations are constrained to $\Delta\alpha/\alpha_0 \sim 10^{-3}$, while with future large

scale structure data and local astrophysical measurements the constraints can be further reduced to $\Delta\alpha/\alpha_0 \sim 10^{-6}$. Following the same procedure as before we find the following fitting formula using an EH-like parametrization

$$r_{\rm s}\left(z_{\rm d}\right) = \frac{a_1 \ln\left(\frac{a_2}{\omega_m}\right)}{\sqrt{1+a_3\ \omega_b^{a4}}}\left(\alpha/\alpha_0\right)^{a_5}\ {\rm Mpc}, \tag{18.11}$$

which is accurate up to $\sim 0.026\%$ and the parameters are given by

$$a_1 \;=\; 45.504, a_2 = 7.15391, a_3 = 9.98792, a_4 = 0.805083, a_5 = -1.34678.$$

On the other hand, with the GA we have found an improved fit which reads as follows

$$r_{\rm s}(z_{\rm d}) = \frac{1}{a_1\omega_b^{a_2}\omega_m^{a_3}\left[\left(\alpha/\alpha_0\right)^{a_4}+\omega_b^{a_5}\omega_m^{a_6}\right]+a_7\omega_m^{a_8}}\ {\rm Mpc}, \tag{18.12}$$

where the coefficients take the following values

$$\begin{aligned} a_1 \;&=\; 0.00759287, a_2 = 0.0865956, a_3 = 0.104933, a_4 = 2.05112, a_5 = 0.327626, \\ a_6 \;&=\; 0.045884, a_7 = 0.00723555, a_8 = 0.933333, \end{aligned} \tag{18.13}$$

which is accurate up to 0.0062%, which is roughly a factor of four improvement over the EH-like parametrization of Eq. (18.11).

18.5 Fits for the redshift of the drag epoch and the photon-decoupling surface

Here we provide some fits for the redshift at the drag epoch $z_{\rm d}$, which can be used in Eq. (18.1) as a complementary fit instead of the analytic fit of $r_{\rm s}(z_{\rm d})$ and also a fit to the redshift at the photon-decoupling surface z_*.

18.5.1 The drag redshift $z_{\rm d}$

The fit for the drag redshift from Ref. [98] is given by

$$z_d = \frac{1291\left(\omega_m\right)^{0.251}}{1+0.659\left(\omega_m\right)^{0.828}}\left[1+b_1\left(\omega_b\right)^{b2}\right], \tag{18.14}$$

where

$$\begin{aligned} b_1 \;&=\; 0.313\left(\omega_m\right)^{-0.419}\left[1+0.607\left(\omega_m\right)^{0.674}\right], \\ b_2 \;&=\; 0.238\left(\omega_m\right)^{0.223}, \end{aligned}$$

and which is accurate up to $\sim 3.7\%$.

To improve this fit, we simulate values for $z_{\rm d}$ in the range $\Omega_m h^2 \in [0.13, 0.15]$ and $\Omega_b h^2 \in [0.0214, 0.0234]$ which is around 10σ from Planck. Then, with the GA we find

$$z_{\rm d} = \frac{1+428.169\omega_b^{0.256459}\omega_m^{0.616388}+925.56\omega_m^{0.751615}}{\omega_m^{0.714129}}. \tag{18.15}$$

which is accurate up to $\sim 0.001\%$.

18.5.2 The redshift at recombination z_*

The fit for the redshift to the photon-decoupling surface z_* from Ref. [715] is given by

$$z_* = 1048\left[1+0.00124\left(\Omega_b h^2\right)^{-0.738}\right]\left[1+g_1\left(\Omega_m h^2\right)^{g_2}\right], \tag{18.16}$$

where

$$\begin{aligned} g_1 &= \frac{0.0783\left(\Omega_b h^2\right)^{-0.238}}{1+39.5\left(\Omega_b h^2\right)^{0.763}}, \\ g_2 &= \frac{0.560}{1+21.1\left(\Omega_b h^2\right)^{1.81}}, \end{aligned}$$

and which is accurate up to $\sim 0.3\%$.

To improve this fit, we simulate values for z_* for the range $\Omega_m h^2 \in [0.13, 0.15]$ and $\Omega_b h^2 \in [0.0214, 0.0234]$ which is around 10σ from Planck. Then, as before, with the GA we find

$$z_* = \frac{391.672\omega_m^{-0.372296} + 937.422\omega_b^{-0.97966}}{\omega_m^{-0.0192951}\omega_b^{-0.93681}} + \omega_m^{-0.731631}, \tag{18.17}$$

which is accurate up to $\sim 0.0005\%$.

18.6 Conclusions

In summary, we have presented extremely accurate machine learning fits to the comoving sound horizon at the baryon drag epoch $r_{\rm s}(z_{\rm d})$ as a function of cosmological parameters and we compared our results with other expressions found in the literature. In particular, we considered the widely used Eisenstein-Hu fitting formula given by Eq. (18.4), which is accurate to the $\sim 2\%$ level, and showed how it may strongly bias any constraints on the matter density parameter obtained by using the current BAO data as described in Ref. [324].

In particular, we found that the confidence contours are biased by roughly half a sigma, while the matter density parameter $\omega_{\rm m,0}$ is shifted at a $\sim 9.3\%$ level from its correct value, which is obtained using the full numerical analysis. On the other hand, our machine learning fits given by Eq. (18.6) do not suffer from this issue, as they are accurate to within $\sim 0.003\%$. Furthermore, in our analysis we also considered the effect of massive neutrinos, see Eq. (18.9) and a varying fine structure constant, see Eq. (18.12), finding that our fits have an improvement of a factor of three to four compared to other simple EH-like parametrizations.

To conclude, we presented machine learning improved expressions for the sound horizon at the drag redshift, which are more accurate in some cases even by two orders of magnitude compared to other similar expressions already found in the literature. The advantage of our approach is that the new expressions do not bias the parameter constraints obtained from BAO data, thus they can be used in BAO analyses coming from current and upcoming surveys to derive cosmological constraints and ease the computational cost that would be required when computing $r_{\rm s}(z_{\rm d})$ with a full Boltzmann code.

The expressions of the fits can be found at https://github.com/RubenArjona.

19
Conclusions

So much Universe, and so little time.
Terry Pratchett

One of the major challenges in Cosmology is to explain the origin of the accelerated expansion of the Universe at late times. This phase of accelerated expansion on very large scales has been confirmed through measurements of distant type Ia supernovae at the turn of the previous century, baryon acoustic oscillations (BAO) and in analyses of the galaxy clustering. The nature of this repulsive force that dominates over gravity at cosmological scales remains a mystery, and implies that a fraction of the Universe must consist of some unknown component, commonly called Dark Energy (DE), or that General Relativity (GR) breaks down on cosmological scales.

This dissertation is focused in exploring the nature of this phenomena from the theoretical point of view through modifications of the theory of gravity and in the analysis of cosmological data in a model independent way through Machine Learning (ML) algorithms, with the goal of testing dark energy models accurately and probing fundamental properties of gravity. The Standard Cosmological model is widely used as the de facto theoretical model by current and upcoming surveys like Euclid and the Dark Energy Survey, hence it should be extensively tested without using the model itself as a benchmark to avoid the problem of model bias.

Current and upcoming surveys will require sub-percent agreement in theoretical accuracy to test the different cosmological and gravity scenarios, something which can be performed with Boltzmann solvers, i.e. codes that solve the linear evolution of cosmological perturbations. Given the plethora of gravity models, it is crucial to have a standardized unified way to describe all of them and take them into account in a Boltzmann code like `CAMB` [1] or `CLASS` [2]. DE and Modified Gravity (MG) models, although at a first glance quite dissimilar, it is possible to unify them within the same framework. One way to do this is to map the MG models, to linear order, to some DE fluid via the effective fluid approach. Then, MG models can be interpreted as DE fluids described by an equation of state $w(a)$, a pressure perturbation $\delta P(k, a)$, and an anisotropic stress $\sigma(k, a)$. In Chapters 4 and 5 it is shown how to implement this approach in `CLASS` for $f(R)$ and Horndeski theories respectively obtaining competitive results at the level of $\sim 0.1\%$ in a much simpler and less error-prone approach compared to other MG codes like `hi_class`, see Fig. 5.5 [3]. In Chapter 4 we also showed that the viscosity parameter c^2_{vis} in realistic models is not constant as commonly assumed, but rather evolves significantly over several orders of magnitude, something which could affect forecasts of upcoming surveys. In Chapter 5 we have also presented a family of designer Horndeski models, i.e. models that have a background exactly equal to that of the ΛCDM model but perturbations given by the Horndeski theory. By linking the effective fluid approach to MontePython, a Monte Carlo code for cosmological parameter extraction, in Chapter 6 we derived rigorous cosmological constraints on three Modified Gravity (MG) models using the recent available

[1] Code for Anisotropies in the Microwave Background
[2] Cosmic Linear Anisotropy Solving System
[3] Horndeski in the Cosmic Linear Anisotropy Solving System

data (i.e., Planck 2018, CMB lensing, BAO, SNIa Pantheon compilation, H0 from SHOES, and RSD Gold-18 compilation) and by not fixing the neutrino mass which could obscure its relation to MG parameters. Two models, the Designer f(R) and Designer Horndeski have a background matching ΛCDM, while the third model, the Hu & Sawicki $f(R)$ model the background differs from the standard model. In summary, our results do not conclusively indicate the presence of modifications to GR. Since our MG constraints are prior dominated we conclude ΛCDM is still the preferred model.

The exact nature of dark energy is currently unknown and its cosmological perturbations, when dark energy is assumed not to be the cosmological constant, are usually modeled as adiabatic. In Chapter 7 we explore the possibility that DE might have a nonadiabatic component and we examine how it would affect several key cosmological observables. We present analytical solutions for the growth rate and growth index of matter density perturbations and compare them to both numerical solutions of the fluid equations and an implementation in the Boltzmann code `CLASS`, finding that they all agree to well below one percent. We also perform a Monte Carlo analysis to derive constraints on the parameters of the nonadiabatic component using the latest cosmological data and find that the amplitude of the nonadiabatic pressure perturbation is consistent with zero within 1σ.

Chapter 8 was motivated for the following reason. In order to calculate the unperturbed density and pressure for neutrinos current implementations in Boltzmann solvers, such as `CLASS`, employ numerical methods. Shortcomings of the numerical approach include nontrivial weighting scheme to carry out the numerical integration, possible limited precision, increase of computing time, but more importantly hindering the understanding of the underlying physics. We provide explicit analytical solutions for the neutrino's unperturbed density, pressure, number density, and pseudo-pressure. Our expressions agree with the fully numerical implementation of the code `CLASS`. We have implemented our solutions in `CLASS` and verified that the fully numerical approach (the current implementation) and the fully analytical approach are in very good agreement. These changes in the code leave precision and computing time unchanged.

Another important part of this dissertation was to lead the process of transforming the emerging field of model independent reconstruction methods and machine learning (ML) in cosmology into a mature scientific discipline and solidify the way to model bias free and sub-percent measurements in cosmology. In this regard we have developed and coded a particular ML algorithm known as the Genetic Algorithms (GA) which specialize in unsupervised symbolic regression of data. This means that the GA can reconstruct in an agnostic manner an analytic function that describes the data, using one or more variables. In fact, one can reconstruct any cosmological function by applying the GA to any dataset of choice and it has been tested with mock data, finding that the GA can properly recover the fiducial cosmology. No assumptions on the specific cosmological model or the behaviour of DE need to be made, hence the results are model independent. With the GA we have presented a unified ML analysis of all the currently available cosmological data in order to reconstruct several key background and perturbations variables in a model independent manner in order to explore the nature of DE.

In Chapter 11 we reconstructed with the GA the Hubble expansion $H(z)$ dataset (see Chapter 2 for more details) and then we made a $\sim 4.5\sigma$ model independent detection of the accelerated expansion by estimating the deceleration parameter $q(z)$. We also place constraints on the transition redshift of the acceleration phase ($z_{\rm tr} = 0.662 \pm 0.027$) and find a deviation from ΛCDM at high redshifts, albeit within the errors, hinting toward the recently alleged tension between the SnIa/quasar data and the cosmological constant ΛCDM model at high redshifts ($z \gtrsim 1.5$). Finally, we showed the GA can be used in complementary null tests of the ΛCDM via reconstructions of the luminosity distance.

Recently, several high profile analyses, e.g. by Risaliti et al [56] or Di Valentino et al [58], have claimed the existence of deviations from flat the standard cosmological model. Such deviations could be due to modifications of gravity on large scales or exotic dark energy models, both of which in general also exhibit an anisotropic stress, i.e. a difference in the 00 and ij parts of the metric of space-time, which are known as the Newtonian potentials Φ and Ψ (assumed equal in GR).

Chapter 12 is a marked improvement over the aforementioned analyses by Risaliti et al and Di Valentino et al, as instead of using simple cosmographic expansions (which have convergence issues) or the ΛCDM itself, we use a totally agnostic approach based on Machine Learning to explore the nature of dark energy and reconstruct its properties in a model independent fashion, which is much broader than traditional statistical inference and model selection. Using a plethora of observational data, we find mild evidence for the existence of anisotropic stress, a $\sim 2\sigma$ deviation from unity at low redshifts and $\sim 4\sigma$ at high redshifts, based on direct reconstructions of the anisotropic stress itself, but also reconstructions of the dark energy equation of state $w(z)$ and its speed of propagation of perturbations, i.e. the "sound speed", since the latter provides indirect information on the behavior of dark energy perturbations and we find that it is negative at the $\sim 2.5\sigma$ level at $z = 0.1$. These results hint towards either the presence of an non-adiabatic component in the DE sound speed or the presence of DE anisotropic stress, thus hinting at possible deviations from the ΛCDM model.

Continuing with the reconstruction approach, on Chapter 13 we present a model independent and non-parametric reconstruction of data coming from the redshift evolution of the CMB temperature which allowed us to estimate the cosmic duality relation and place constraints on a temporal varying fine structure constant. Overall we find that our results are consistent with ΛCDM within the confidence region. We also constrain in a model independent manner deviations from the cosmic distance duality relation by simulating strongly lensed gravitational wave events from the Einstein Telescope on Chapter 14. In particular, we use two machine learning approaches, the Genetic Algorithms and Gaussian Processes, to reconstruct the mock data and we show that both approaches are capable of correctly recovering the underlying fiducial model and can provide percent-level constraints at intermediate redshifts when applied to future Einstein Telescope data, thus opening the door to direct tests of the fundamental principles of the standard cosmological model in the coming decades.

There is an ongoing search to distinguish effective quantum field theories that can potentially arise within UV-complete quantum gravity theories (the Landscape) from those that cannot (the Swampland). In this regard, although not rigorously proven in string theory, some conjectures have been considered to discern the Swampland from the landscape. The Swampland criteria aim to find constructions that are compatible with a quantum theory of gravity and it has been found that specific quintessence models can satisfy the Swampland criteria at late times. In Chapter 15 we present model independent reconstructions of quintessence and the Swampland conjectures (SC) using both Machine Learning (ML) and cosmography. In particular, using the Hubble parameter $H(z)$ data from the cosmic chronometers we find that the ML and cosmography reconstructions of the SC are compatible with observations at low redshifts.

Chapters 16 and 17 are concerned in presenting null tests of ΛCDM. These tests are ideal to check for possible tensions that could arise because of unaccounted for systematics or could provide hints of new physics. Given the many possible extensions of this concordance model, we present here several novel consistency tests which could be used to probe for deviations from ΛCDM. In Chapter 16 we presented an extension of the consistency diagnostic of flat ΛCDM of Ref. [426], by now including both the curvature $\Omega_{k,0}$ and the matter density $\Omega_{\mathrm{m},0}$. We show how the latter can be derived from the Hubble rate $H(z)$ and can be determined directly from observational data. We should stress that the added advantage of our new null test presented here is the fact that we do not have to assume a flat Universe. Secondly, through the combination of the BAO and $H(z)$ data or the angular and radial BAO data respectively, we also presented a test to search for deviations from homogeneity. Then, with the angular and radial BAO data we also introduce two new consistency tests for the ΛCDM model. The first one, namely $\mathrm{Om}_\theta(z)$, is derived following a similar approach as it was shown in Ref. [419] where in this case we use the angular BAO scale relation $\theta(z)$ to reconstruct null tests of the ΛCDM model, with the advantage that this null test does not contain higher derivative terms, which tend to increase the reconstruction errors when using noisy data. Finally, we also used the radial BAO data $\Delta z(z)$ to obtain a model independent determination of the accelerated expansion of the Universe by reconstructing the deceleration parameter $q(z)$ and we applied our Δz reconstruction to the $\mathcal{O}_m$ diagnostic [426]. We find that our results are

consistent with the standard flat ΛCDM scenario, however we also noted a $\sim 4\sigma$ tension on the determination of the transition redshift z_t, i.e. the redshift where the Universe transitions from decelerated to accelerated expansion, between the $H(z)$ and the radial BAO data.

Overall, we find that these new tests of the spatial curvature and homogeneity of the Universe can be used, in a model-independent fashion, to test some of the fundamental assumptions of the standard cosmological model. However, our reconstructions are somewhat limited by the current data, albeit this should be resolved in the near future when high quality BAO data become available from the next stage surveys.

In Chapter 17 we have presented a new consistency test of the Copernican principle, which is complementary to the curvature test of Ref. [648]. In particular, we used the Noether's theorem approach in order to obtain a conserved quantity that can be written in terms of the Hubble rate $H(z)$ and the comoving distance $D(z)$. In order to forecast how well our new test can constrain deviations from the Copernican principle at large scales we created mock datasets based on specifications of the DESI survey and using the ΛCDM model for the fiducial cosmology, for a variety of different profiles. This approach allows us to quantify any deviations using realistic scenarios. We find that the GA can correctly predict the underlying fiducial cosmology at all redshifts covered by the data and can easily rule out several realistic LTB scenarios at confidence of $\gtrsim 3\sigma$ at mid to high redshifts ($z > 0.5$).

Finally, in order to ease the computational cost that would be required when computing the sound horizon at the drag redshift $r_{\rm s}(z_{\rm d})$ with a full Boltzmann code, in Chapter 18 we have presented extremely accurate machine learning fits to $r_{\rm s}(z_{\rm d})$ as a function of cosmological parameters. In particular, we considered the widely used Eisenstein-Hu (EH) fitting formula, which is accurate to the $\sim 2\%$ level, and showed how it may strongly bias any constraints on the matter density parameter obtained by using the current BAO data as described in Ref. [324].

In particular, we found that the confidence contours are biased by roughly half a sigma, while the matter density parameter $\omega_{\rm m,0}$ is shifted at a $\sim 9.3\%$ level from its correct value, which is obtained using the full numerical analysis. In the other hand, our machine learning fits given by Eq. (18.6) do not suffer from this issue, as they are accurate to within $\sim 0.003\%$. Furthermore, in our analysis we also considered the effect of massive neutrinos, see Eq. (18.9) and a varying fine structure constant, see Eq. (18.12), finding that our fits have an improvement of a factor of three to four compared to other simple EH-like parametrizations.

To conclude, we presented machine learning improved expressions for the sound horizon at the drag redshift, which are more accurate in some cases even by two orders of magnitude compared to other similar expressions already found in the literature. The advantage of our approach is that the new expressions do not bias the parameter constraints obtained from BAO data, thus they can be used in BAO analyses coming from current and upcoming surveys to derive cosmological constraints.

Outlook

The natural goal would be now to explore the nature of Dark Matter with Modified Gravity and Machine Learning. For example, such possible avenues would be to explore formation mechanisms of Primordial Black Holes (PBH) in the Early Universe through Modified Gravity theories and in the Gravitational Wave signatures that they would imprint which opens the possibility to probe the primordial power spectrum at small-scales. The Machine learning tools developed thus far can also be used for Gravitational Wave waveform reconstruction for Virgo and Burst template generation for LISA.

Concerning some extensions of this thesis we present some of the following plans related to Modified Gravity (MG) theories:

- Extend the effective fluid approach to include more MG models such as non-local gravity theories, models with higher derivatives or with extra degrees of freedom which are not at this time included in Boltzmann codes.

- Derive the effective fluid approach for MG models to second order in perturbation theory. Then we could calculate useful cosmological quantities such as the bispectrum or non-linear corrections to the matter power spectrum.
- Determine if it is possible to remove instabilities of the theories containing higher order invariants with "a la Horndeski" type corrections to keep the equations of motion to second order.

Related to Machine Learning some possible avenues are:

- Use the upcoming release of surveys like EUCLID, LSST or DESI, where we will reach a high enough sensitivity to apply ML methods and have a covariance matrix for all data covered by the surveys like SnIa, BAO, RSD or Weak Lensing, to treat the data properly accounting for correlations, complement and extend the redshift probed and perform a joint and simultaneous analysis to quantify how the ability of present and future surveys can improve the current cosmological constraints, both at the background and at the perturbation level.
- Reconstruct the Newtonian potentials through synergies between the Genetic Algorithms (GA) and the effective fluid approach.
- Train Neural Networks (NN) using a plethora of cosmological data such as RSD, BAO or SnIa to help classify different cosmological scenarios and distinguish between standard and modified gravity models.

20
Conclusiones

Uno de los mayores desafíos de la cosmología es explicar el origen de la expansión acelerada del Universo en épocas tardías. Esta fase de expansión acelerada a escalas muy grandes se ha confirmado mediante mediciones de supernovas distantes de tipo Ia a principios del siglo anterior, oscilaciones acústicas bariónicas (BAO) y en análisis de la agrupación de galaxias. La naturaleza de esta fuerza repulsiva que domina la gravedad a escalas cosmológicas sigue siendo un misterio, e implica que una fracción del Universo debe consistir en algún componente desconocido, comúnmente llamado Energía Oscura (DE), o que la Relatividad General (GR) se descompone en escalas cosmológicas.

Esta disertación está enfocada en explorar la naturaleza de este fenómeno desde el punto de vista teórico a través de modificaciones de la teoría de la gravedad y en el análisis de datos cosmológicos de forma independiente del modelo a través de algoritmos de Machine Learning (ML), con el objetivo de testear dark modelos de energía con precisión y sondeando las propiedades fundamentales de la gravedad. El modelo cosmológico estándar es ampliamente utilizado como modelo teórico de facto por encuestas actuales y futuras como Euclid y Dark Energy Survey, por lo que debe probarse ampliamente sin usar el modelo en sí como punto de referencia para evitar el problema del sesgo del modelo.

Los estudios actuales y futuros requerirán un acuerdo del sub-porcentaje en la precisión teórica para probar los diferentes escenarios cosmológicos y gravitacionales, algo que se puede realizar con los solucionadores de Boltzmann, es decir, códigos que resuelven la evolución lineal de las perturbaciones cosmológicas. Dada la plétora de modelos de gravedad, es crucial tener una forma unificada estandarizada de describirlos todos y tenerlos en cuenta en un código de Boltzmann como `CAMB` [1] o `CLASS` [2]. Los modelos DE y Modified Gravity (MG), aunque a primera vista son bastante diferentes, es posible unificarlos dentro de un mismo marco. Una forma de hacer esto es mapear los modelos MG, en orden lineal, a algún fluido DE a través del enfoque de fluido efectivo. Entonces, los modelos MG pueden interpretarse como fluidos DE descritos por una ecuación de estado $w(a)$, una perturbación de presión $\delta P(k,a)$ y una tensión anisotrópica $\sigma(k,a)$. En los Capítulos 4 y 5 se muestra cómo implementar este enfoque en `CLASS` para las teorías $f(R)$ y Horndeski respectivamente obteniendo resultados competitivos al nivel de $\sim 0.1\%$ en un enfoque mucho más simple y menos propenso a errores en comparación con otros códigos MG como `hi_class`, ver Fig. 5.5. [3] En el Capítulo 4 también mostramos que el parámetro de viscosidad c^2_{vis} en modelos realistas no es constante como comúnmente asumido, pero más bien evoluciona significativamente en varios órdenes de magnitud, algo lo que podría afectar las previsiones de las próximas encuestas. En el capítulo 5 también hemos presentado una familia de modelos Designer Horndeski, es decir, modelos que tienen un trasfondo exactamente igual al del modelo ΛCDM pero perturbaciones dadas por la teoría de Horndeski. Al vincular el enfoque de fluido efectivo a MontePython, un código de Monte Carlo para la extracción de parámetros cosmológicos, en el Capítulo 6 derivamos restricciones cosmológicas rigurosas en tres modelos de Gravedad Modificada (MG) utilizando los datos disponibles recientes (es decir, Planck 2018 , CMB

[1] Code for Anisotropies in the Microwave Background
[2] Cosmic Linear Anisotropy Solving System
[3] Horndeski in the Cosmic Linear Anisotropy Solving System

lensing, BAO, SNIa Pantheon compilation, H0 de SHOES y compilación RSD Gold-18) y no fijando la masa de neutrinos que podría oscurecer su relación con los parámetros de MG. Dos modelos, Designer f(R) y Designer Horndeski tienen un fondo que coincide con ΛCDM, mientras que el tercer modelo, el modelo Hu & Sawicki $f(R)$, el fondo difiere del modelo estándar. En resumen, nuestros resultados no indican de manera concluyente la presencia de modificaciones en GR. Dado que nuestras restricciones de MG están dominadas a priori, concluimos que ΛCDM sigue siendo el preferido modelo.

La naturaleza exacta de la energía oscura se desconoce actualmente y sus perturbaciones cosmológicas, cuando se supone que la energía oscura no es la constante cosmológica, por lo general se modela como adiabática. En el capítulo 7 exploramos la posibilidad de que DE pueda tener un componente no adiabático y examinamos cómo afectaría a varios observables cosmológicos clave. Presentamos soluciones analíticas para la tasa de crecimiento e índice de crecimiento de las perturbaciones de la densidad de la materia y compararlos con ambos soluciones de las ecuaciones de fluidos y una implementación en el código de Boltzmann `CLASS`, encontrando que todos están de acuerdo en muy por debajo del uno por ciento. También realizamos un análisis de Monte Carlo para derivar restricciones. en los parámetros del componente no adiabático utilizando los últimos datos cosmológicos y encuentre que la amplitud de la perturbación de la presión no adiabática es consistente con cero dentro de 1σ.

El capítulo 8 fue motivado por la siguiente razón. Para calcular la densidad y la presión no perturbada de los neutrinos, las implementaciones actuales en los solucionadores de Boltzmann, como `CLASS`, emplean métodos numéricos. Las deficiencias del enfoque numérico incluyen un esquema de ponderación no trivial para llevar a cabo la integración numérica, posible precisión limitada, aumento del tiempo de computación, pero lo que es más importante, dificulta la comprensión de la física subyacente. Ofrecemos soluciones analíticas explícitas para la densidad, la presión, la densidad numérica y la pseudopresión imperturbables del neutrino. Nuestras expresiones concuerdan con la implementación completamente numérica del código `CLASS`. Hemos implementado nuestro soluciones en `CLASS` y se verificó que el enfoque completamente numérico (la implementación actual) y el enfoque completamente analítico concuerdan muy bien. Estos cambios en el código no modifica la precisión ni el tiempo de cálculo.

Otra parte importante de esta disertación fue liderar el proceso de transformación del campo emergente de los métodos de reconstrucción independientes de modelos y el aprendizaje automático (ML) en cosmología en una disciplina científica madura y solidificar la forma de modelar mediciones libres de sesgo y sub-porcentaje en cosmología. En este sentido, hemos desarrollado y codificado un algoritmo ML particular conocido como Algoritmos Genéticos (GA) que se especializan en regresión simbólica de datos no supervisada. Esto significa que el GA puede reconstruir de manera agnóstica una función analítica que describe los datos, utilizando una o más variables. De hecho, se puede reconstruir cualquier función cosmológica aplicando el GA a cualquier conjunto de datos de elección y se ha probado con datos simulados, encontrando que el GA puede recuperar correctamente la cosmología fiducial. No es necesario hacer suposiciones sobre el modelo cosmológico específico o el comportamiento de DE, por lo que los resultados son independientes del modelo. Con el GA hemos presentado un análisis ML unificado de todos los datos cosmológicos actualmente disponibles para reconstruir varias variables clave de antecedentes y perturbaciones de una manera independiente del modelo para explorar la naturaleza de DE.

En el Capítulo 11 reconstruimos con el GA el conjunto de datos de la expansión $H(z)$ de Hubble (consultar el Capítulo 2 para obtener más detalles) y luego hicimos una detección de $\sim 4.5\sigma$ independiente del modelo de la expansión acelerada estimando el parámetro de desaceleración $q(z)$. También colocamos restricciones sobre el corrimiento al rojo de transición de la fase de aceleración ($z_{\rm tr} = 0.662 \pm 0.027$) y encontramos una desviación de ΛCDM en corrimientos al rojo altos, aunque dentro de los errores, apuntando hacia la reciente supuesta tensión entre los datos de SnIa / cuásar y el modelo cosmológico constante ΛCDM a altos desplazamientos al rojo ($z \gtrsim 1.5$). Finalmente, mostramos que los GA se puede usar en pruebas nulas complementarias de ΛCDM mediante reconstrucciones de la distancia de luminosidad.

Recientemente, varios análisis de alto perfil, p. ej. por Risaliti et al [56] o Di Valentino

et al [58], han reclamado la existencia de desviaciones del modelo cosmológico estándar plano. Semejantes desviaciones podrían deberse a modificaciones de la gravedad a gran escala o modelos exóticos de energía oscura, algunos de los cuales en general también exhiben un estrés anisotrópico, es decir, una diferencia en las partes de 00 e ij de la métrica del espacio-tiempo, que se conocen como los potenciales newtonianos Φ y Ψ (asumidos iguales en GR). El capítulo 12 es una mejora notable con respecto a los análisis antes mencionados de Risaliti et al y Di Valentino et al, donde en lugar de utilizar expansiones cosmográficas simples (que tienen problemas de convergencia) o el modelo ΛCDM en sí, utilizamos un enfoque totalmente agnóstico basado en el aprendizaje automático para explorar la naturaleza de energía oscura y reconstruir sus propiedades de una manera independiente del modelo, que es mucho más amplia que inferencia estadística tradicional y selección de modelos. Usando una plétora de datos de observación, encontramos evidencia leve de la existencia de estrés anisotrópico, una desviación $\sim 2\sigma$ de la unidad en corrimientos al rojo bajos y $\sim 4\sigma$ en corrimientos al rojo altos, basada en reconstrucciones directas de la estrés anisotrópico en sí, pero también reconstrucciones de la ecuación de energía oscura del estado $w(z)$ y su velocidad de propagación de perturbaciones, es decir, la "velocidad del sonido", ya que esta última proporciona información indirecta sobre el comportamiento de las perturbaciones de energía oscura y encontramos que es negativo en el nivel $\sim 2.5\sigma$ en $z = 0.1$. Estos resultados apuntan hacia la presencia de un componente no adiabático en la velocidad del sonido DE o la presencia de estrés anisotrópico DE, lo que sugiere posibles desviaciones del modelo ΛCDM.

Continuando con el enfoque de reconstrucción, en el Capítulo 13 presentamos un modelo de reconstrucción independiente y no paramétrica de datos que vienen de la evolución del corrimiento al rojo de la temperatura del CMB que nos permitió estimar la relación de dualidad cósmica y poner restricciones en una constante de estructura fina variable temporal. En general, encontramos que nuestros resultados son consistentes con ΛCDM dentro de la región de confianza. También restringimos de manera independiente del modelo las desviaciones de la relación de dualidad de distancia cósmica simulando eventos de ondas gravitacionales con lentes fuertes para el Telescopio de Einstein (ET) en el Capítulo 14. En particular, utilizamos dos enfoques de aprendizaje automático, los algoritmos genéticos y los procesos gaussianos, para reconstruir los datos simulados y mostramos que ambos enfoques son capaces de recuperar correctamente el modelo fiducial subyacente y pueden proporcionar restricciones de nivel porcentual en desplazamientos al rojo intermedios cuando se aplican a datos futuros del telescopio Einstein, lo que abre la puerta a pruebas directas de los principios fundamentales del modelo cosmológico estándar en las próximas décadas.

Hay una búsqueda continua para distinguir las teorías efectivas de campo cuántico que pueden surgir potencialmente dentro de las teorías de gravedad cuántica completa UV (the Landscape) de aquellas que no pueden (the Swampland). En este sentido, aunque no está rigurosamente probado en la teoría de cuerdas, se han considerado algunas conjeturas para discernir el Swampland del Landscape. Los criterios de Swampland apuntan a encontrar construcciones que son compatibles con una teoría cuántica de la gravedad y se ha descubierto que modelos específicos de quintaesencia pueden satisfacer los criterios de Swampland en épocas tardías. En el capítulo 15 presentamos reconstrucciones independientes de modelos de la quintaesencia y las conjeturas de Swampland (SC) utilizando tanto aprendizaje automático (ML) como cosmografía. En particular, usando el parámetro de Hubble $H(z)$ datos de los cronómetros cósmicos, encontramos que las reconstrucciones ML y cosmografía del SC son compatibles con observaciones a bajos corrimientos al rojo.

Los capítulos 16 y 17 tratan de presentar pruebas nulas de ΛCDM. Estas pruebas son ideales para verificar posibles tensiones que podrían surgir debido a errores sistemáticos no contabilizados o podrían proporcionar indicios de nueva física. Dadas las muchas posibles extensiones de este modelo de concordancia, presentamos aquí varias pruebas de consistencia novedosas que podrían usarse para probar desviaciones de ΛCDM. En el capítulo 16 presentamos una extensión del diagnóstico de consistencia del modelo plano ΛCDM de Ref. [426], que ahora incluye tanto la curvatura $\Omega_{k,0}$ como la densidad de materia $\Omega_{\mathrm{m},\,0}$. Mostramos cómo este último puede derivarse de la tasa de Hubble $H(z)$ y puede determinarse directamente a partir de datos de observación. Debemos enfatizar que la ventaja adicional de nuestra nueva prueba nula presentada aquí es el hecho de que no tenemos

que asumir un Universo plano. En segundo lugar, a través de la combinación de los datos BAO y $H(z)$ o los datos BAO angulares y radiales respectivamente, también presentamos una prueba para buscar desviaciones de la homogeneidad. Luego, con los datos BAO angulares y radiales, también presentamos dos nuevas pruebas de consistencia para el modelo ΛCDM . El primero, a saber, $\mathrm{Om}_\theta(z)$, se deriva siguiendo un enfoque similar al que se muestra en Ref. [419] donde en este caso usamos la relación de escala BAO $\theta(z)$ para reconstruir pruebas nulas del modelo ΛCDM , con la ventaja de que esta prueba nula no contiene términos derivados superiores, que tienden a incrementar los errores de reconstrucción cuando se utilizan datos ruidosos. Finalmente, también usamos los datos radiales BAO $\Delta z(z)$ para obtener una determinación independiente del modelo de la expansión acelerada del Universo mediante la reconstrucción del parámetro de desaceleración $q(z)$ y aplicamos nuestra reconstrucción Δz al diagnóstico $\mathcal{O}_m$ [426]. Encontramos que nuestros resultados son consistentes con el escenario estándar CDM plano Λ, sin embargo, también notamos una tensión $\sim 4\sigma$ en la determinación del corrimiento al rojo de transición z_t, es decir, el corrimiento al rojo desde donde el Universo hace la transición desacelerado a una expansión acelerada, entre $H(z)$ y los datos radiales BAO. En general, encontramos que estas nuevas pruebas de la curvatura espacial y la homogeneidad del Universo pueden usarse, de manera independiente del modelo, para probar algunas de las suposiciones fundamentales del modelo cosmológico estándar. Sin embargo, nuestras reconstrucciones están algo limitadas por los datos actuales, aunque esto debería resolverse en un futuro cercano cuando los datos BAO de alta calidad estén disponibles en los experimentos de la siguiente etapa.

En el capítulo 17 hemos presentado una nueva prueba de consistencia del principio copernicano, que es complementaria a la prueba de curvatura de Ref. [648]. En particular, utilizamos el enfoque del teorema de Noether para obtener una cantidad conservada que se puede escribir en términos de la tasa de Hubble $H(z)$ y la distancia comovil $D(z)$. Para pronosticar qué tan bien nuestra nuevo test puede limitar las desviaciones del principio copernicano a gran escala, creamos conjuntos de datos simulados basados en las especificaciones del experimento DESI y utilizando el modelo ΛCDM para la cosmología fiducial, para una variedad de perfiles diferentes. Este enfoque nos permite cuantificar cualquier desviación utilizando escenarios realistas. Descubrimos que el GA puede predecir correctamente la cosmología fiducial subyacente en todos los desplazamientos al rojo cubiertos por los datos y puede descartar fácilmente varios escenarios LTB realistas con una confianza de $\gtrsim 3\sigma$ en desplazamientos al rojo medios a altos ($z > 0,5$).

Finalmente, para aliviar el coste computacional que se requeriría al calcular el horizonte de sonido en el desplazamiento al rojo de arrastre $r_\mathrm{s}(z_\mathrm{d})$ con un código de Boltzmann completo, en el Capítulo 18 hemos presentado ajustes de aprendizaje automático extremadamente precisos para $r_\mathrm{s}(z_\mathrm{d})$ como una función de parámetros cosmológicos. En particular, consideramos la fórmula de ajuste de Eisenstein-Hu (EH) ampliamente utilizada, que es precisa al nivel $\sim 2\%$, y mostramos cómo puede sesgar fuertemente cualquier restricción en el parámetro de densidad de materia obtenido al usar los datos actuales de BAO como se describe en Ref. [324]. En particular, encontramos que los contornos de confianza están sesgados por aproximadamente la mitad de un sigma, mientras que el parámetro de densidad de materia $\omega_{\mathrm{m},0}$ se desplaza a un nivel de $\sim 9.3\%$ de su valor correcto, que se obtiene mediante el análisis numérico completo. Por otro lado, nuestros ajustes de aprendizaje automático dados por la Ec. (18.6) no sufren este problema, ya que tienen una precisión de $\sim 0.003\%$. Además, en nuestro análisis también consideramos el efecto de neutrinos masivos, ver Ec. (18.9) y una constante de estructura fina variable, ver Ec. (18.12), encontrando que nuestros ajustes tienen una mejora de un factor de tres a cuatro en comparación con otras parametrizaciones simples similares a EH. Para concluir, presentamos expresiones mejoradas de aprendizaje automático para el horizonte de sonido en el desplazamiento al rojo de arrastre, que son más precisas en algunos casos incluso en dos órdenes de magnitud en comparación con otras expresiones similares que ya se encuentran en la literatura. La ventaja de nuestro enfoque es que las nuevas expresiones no sesgan las restricciones de parámetros obtenidas de los datos BAO, por lo que pueden usarse en análisis BAO provenientes de encuestas actuales y futuras para derivar restricciones cosmológicas.

Part IV

Appendices

A

The Effective Fluid Approach for f(R)

A.1 Useful formulae and the integrated sachs wolfe effect effect

In this section we present some useful formulas related to the effective fluid approach and the integrated sachs wolfe (ISW) effect. Using the definitions of the effective pressure perturbation, the anisotropic stress and the effective sound speed one can easily obtain the following expressions:

$$\delta P_{DE} = \frac{1}{3}T, \tag{A.1}$$

$$\Sigma^i_j = T^i_j - \frac{1}{3}\delta^i_j T, \tag{A.2}$$

$$(\bar{\rho}+\bar{P})\sigma = -(\hat{k}_i\hat{k}_j - \frac{1}{3}\delta_{ij})\Sigma^{ij}, \tag{A.3}$$

$$\pi_{DE} = \frac{3}{2}(1+w)\sigma, \tag{A.4}$$

$$c^2_{s,eff}\delta\rho_{DE} = \delta P_{DE} - \frac{2}{3}\bar{\rho}_{DE}\pi_{DE}, \tag{A.5}$$

which lead to

$$\bar{\rho}_{DE}\pi_{DE} = -\frac{3}{2}\left(\hat{k}_i\hat{k}_j T^{ij} - \frac{T}{3}\right) \tag{A.6}$$

and

$$c^2_{s,eff}\delta\rho_{DE} = \hat{k}_i\hat{k}_j T^{ij} \tag{A.7}$$

where $T = T^i_i$, $\hat{k}_i$ is a unit vector in Fourier space and in the above expressions we have only kept the 1st order parts.

In what follows we present the theoretical expressions used to calculate the low multipoles for Fig. 4.8. In this regard, we mostly follow Ref. [315]. The contribution of the ISW effect on the angular CMB power spectrum is given by [315]:

$$C^{\rm ISW}_\ell = 4\pi\int\frac{dk}{k}I^{\rm ISW}_\ell(k)^2\frac{9}{25}\frac{k^3P_\zeta}{2\pi^2}, \tag{A.8}$$

where we have used the fact the power spectrum P_ζ is given in terms of the primordial power spectrum times a transfer function

$$\frac{k^3P_\zeta}{2\pi^2} = A_s\left(\frac{k}{k_0}\right)^{n_s-1}T(k)^2, \tag{A.9}$$

where A_s is the primordial amplitude, k_0 is the pivot scale and $T(k)$ is the usual matter-radiation transfer function (see Eq. (7.71) in Ref. [316]). Furthermore, the kernel $I^{\rm ISW}_\ell(k)$ is given by

$$I_\ell^{\rm ISW}(k) = 2\int dz \frac{dG}{dz} j_\ell(k\, r(z)), \tag{A.10}$$

where $j_n(x)$ is the spherical bessel function, $r(z) = \int_0^z dz/H(z)$ is the comoving distance and the function $G(z,k)$ is the scale dependent potential growth rate

$$G(a,k) = \frac{\Phi(a,k)+\Psi(a,k)}{\Phi(a_{ini},k)+\Psi(a_{ini},k)}. \tag{A.11}$$

Also, the contribution to the spectrum due to the usual Sachs-Wolfe (SW) effect is given by:

$$C_\ell^{\rm SW} = \frac{2\pi}{25} A_s \frac{\Gamma\left(\frac{3}{2}\right)\Gamma\left(1-\frac{n_s-1}{2}\right)\Gamma\left(\ell+\frac{n_s-1}{2}\right)}{\Gamma\left(\frac{3}{2}-\frac{n_s-1}{2}\right)\Gamma\left(\ell+2-\frac{n_s-1}{2}\right)}, \tag{A.12}$$

where $\Gamma(x)$ is the usual Gamma function. The previous expression for $n_s = 1$ simplifies to the well-known result for the SW plateau

$$\frac{\ell(\ell+1)}{2\pi} C_\ell^{\rm SW} = \frac{A_s}{25}. \tag{A.13}$$

Finally, the total contribution from the SW and ISW effects will be given by the sum of Eqs. (A.8) and (A.12), that is,

$$C_\ell^{\rm total} = C_\ell^{\rm SW} + C_\ell^{\rm ISW}. \tag{A.14}$$

In our analysis we used $A_s = 2.3\times10^{-9}$, $n_s = 1$, $k_0 = 0.05h/\text{Mpc}$, $\Omega_{m0} = 0.3$ and $T_{\rm CMB} = 2.726K$. Note that to convert the result of Eq. (A.14) to μK^2, as is the standard in the CMB community, one needs to multiply the C_ℓ with $T_{\rm CMB}^2 \cdot 10^{12}$.

A.2 CLASS implementation

In this section we present our implementation of the effective fluid approach in the `CLASS` code [232], which we call `EFCLASS`. As shown in the previous sections, even with these minimal changes our approach gives results in agreement with other codes, such as `EFTCAMB`, `MGCAMB`, `FRCAMB` and `CLASS_EOS_FR`.

The only changes we made in the code are in the following two places:

1. In the *background.c* file we included the correct expansion history for the $f(R)$ models. For the HS model this is given by Eq. (4.58).
2. In the *perturbations.c* file we included the proper perturbations for the effective DE fluid given by Eqs. (4.7) and (4.9).

We found that the most straight-forward and least error-prone way to make these changes is to modify the ΛCDM model equations in the aforementioned parts of the code, as we can just increment the background equations of ΛCDM with the one of the HS model (for the DES model, no change is needed) and in the case of the perturbations, ΛCDM has none so we can just add the appropriate new terms given by Eqs. (4.7) and (4.9).

In more detail, first we consider the background evolution, where we consider two cases: that of the DES model, where the background is fixed to that of the ΛCDM model, and that of the HS model where the Friedman equation is modified. For the DES model we obviously do not make any change as the Hubble parameter for the ΛCDM is already included in the `CLASS` code. For the HS model we introduce the extremely accurate approximations for the Hubble parameter given by Eq. (4.58). In Ref. [286] is shown that this expression works to a level of accuracy better than $\sim 10^{-5}\%$ for $b \in [0, 0.1]$. Finally, we also had to include an expression for the equation of state parameter w_{DE} and effective density ρ_{DE}. Both were calculated to second order in b from Eqs. (4.25) and (4.24) by using Eq. (4.58).

Regarding the perturbations, we treat both models equally. In this case we found that the best place to implement the modifications were in the *perturb_einstein* routine of `CLASS`, which solves the Einstein equations in the conformal Newtonian gauge given by Eqs. (4.7) and (4.9). Then, it is simple to just add in the right-hand-side of the aforementioned equations our expressions for the effective fluid DE velocity and anisotropic stress given by Eqs. (4.44) and (4.45).

Our analytic approach has several advantages: First, given that most viable $f(R)$ models can be written as small perturbations around ΛCDM model, such as the HS model, it is always possible to derive extremely accurate expressions for the background, as was shown in Ref. [286]. Second, regarding the perturbations our improved subhorizon approximation gives much more accurate results compared to codes that are based on the default subhorizon approximation. Also, the accuracy is comparable to codes that treat the perturbations exactly by numerically solving the relevant equations. However, our approach has a much smaller overhead in terms of new lines of code and as a result is more straight-forward and less error-prone.

B

Horndeski's gravity

B.1 Scalar and Gravitational field equations

For completeness, in this Appendix we show how to compute both the gravitational and the scalar-field equations derived from the Horndeski action (5.21).

B.1.1 Scalar field equation

For a function of a single variable with higher derivatives, the stationary values of the functional [716]

$$I[f] = \int_{x_0}^{x_1} \mathcal{L}\left(x, f, f', f'', \cdots, f^{(k)}\right) dx; \quad f' \equiv \frac{df}{dx},$$
$$f'' \equiv \frac{d^2 f}{dx^2},\ f^{(k)} \equiv \frac{d^k f}{dx^k}, \tag{B.1}$$

can be obtained from the Euler-Lagrange equation

$$\frac{\partial \mathcal{L}}{\partial f} - \frac{d}{dx}\left(\frac{\partial \mathcal{L}}{\partial f'}\right) + \frac{d^2}{dx^2}\left(\frac{\partial \mathcal{L}}{\partial f''}\right) - \ldots (-1)^k \frac{d^k}{dx^k}\left(\frac{\partial \mathcal{L}}{\partial f^k}\right) = 0. \tag{B.2}$$

Since our Lagrangian $\mathcal{L}_i$ functions defined in the Horndeski action (5.21) depend on the scalar field ϕ and its first and second derivatives, we can use the Euler-Lagrange equation (B.2) to compute the scalar field equation for $\mathcal{L}_2$, $\mathcal{L}_3$ and $\mathcal{L}_4$. For $\mathcal{L}_2$ we have

$$\mathcal{L}_2\left(\phi, \partial_\mu \phi\right) = \frac{\partial \mathcal{L}_2}{\partial \phi}\delta\phi + \frac{\partial \mathcal{L}_2}{\partial_\mu \phi}\delta\left(\partial_\mu \phi\right) = \frac{\partial \mathcal{L}_2}{\partial \phi}\delta\phi - \partial_\mu \frac{\partial \mathcal{L}_2}{\partial_\mu \phi}\delta\phi,$$

$$\begin{aligned} \frac{\partial \mathcal{L}_2}{\partial \phi} - \partial_\mu \frac{\partial \mathcal{L}_2}{\partial_\mu \phi} &= P_\phi^2 - \nabla^\mu J_\mu^2 \\ &= 0. \end{aligned} \tag{B.3}$$

Since $\mathcal{L}_2 = K\left(\phi, X\right)$, applying Eq. (B.3) leads to

$$P_\phi^2 = \frac{\partial \mathcal{L}_2}{\partial \phi} = K_\phi, \tag{B.4}$$

$$\nabla^\mu J_\mu^2 = \partial_\mu \frac{\partial \mathcal{L}_2}{\partial_\mu \phi} = \nabla^\mu\left(\frac{\partial K}{\partial^\mu \phi}\right) = \nabla^\mu\left(\frac{\partial K}{\partial X}\frac{\partial X}{\partial^\mu \phi}\right) = -\nabla^\mu\left(K_X \nabla_\mu \phi\right), \tag{B.5}$$

where we have replaced the partial derivatives by covariant derivatives and we are using the fact that $X = -\frac{1}{2}\partial_\mu\phi\partial^\mu\phi$. Hence, for $\mathcal{L}_2$ the scalar field equation reads

$$K_\phi + \nabla^\mu\left(K_X\nabla_\mu\phi\right) = 0. \tag{B.6}$$

For the term $\mathcal{L}_3$ we follow the same approach

$$\begin{aligned}\mathcal{L}_3\left(\phi,\partial_\mu\phi,\partial_\mu\partial_\nu\phi\right) &= \frac{\partial\mathcal{L}_3}{\partial\phi}\delta\phi + \frac{\partial\mathcal{L}_3}{\partial_\mu\phi}\delta\left(\partial_\mu\phi\right) + \frac{\partial\mathcal{L}_3}{\partial_\mu\partial_\nu\phi}\delta\left(\partial_\mu\partial_\nu\phi\right)\\ &= \frac{\partial\mathcal{L}_3}{\partial\phi}\delta\phi - \partial_\mu\frac{\partial\mathcal{L}_3}{\partial_\mu\phi}\delta\phi + \partial_\mu\partial_\nu\frac{\partial\mathcal{L}_3}{\partial_\mu\partial_\nu\phi}\delta\phi,\end{aligned} \tag{B.7}$$

$$\frac{\partial\mathcal{L}_3}{\partial\phi} - \partial_\mu\frac{\partial\mathcal{L}_3}{\partial_\mu\phi} + \partial_\mu\partial_\nu\frac{\partial\mathcal{L}_3}{\partial_\mu\partial_\nu\phi} = 0. \tag{B.8}$$

Knowing that $\mathcal{L}_3 = -G_3\left(\phi,X\right)$ $[\Box\phi = g^{\mu\nu}\nabla_\mu\nabla_\nu\phi]$, applying Eq. (B.8) gives

$$\frac{\partial\mathcal{L}_3}{\partial\phi} = -G_{3\phi}\Box\phi, \tag{B.9}$$

$$\partial_\mu\frac{\partial\mathcal{L}_3}{\partial_\mu\phi} = \nabla^\mu\left(\frac{\partial G_3}{\partial^\mu\phi}\Box\phi\right) = \nabla^\mu\left(\frac{\partial G_3}{\partial X}\frac{\partial X}{\partial^\mu\phi}\Box\phi\right) = -\nabla^\mu\left(G_{3X}\nabla_\mu\phi\Box\phi\right), \tag{B.10}$$

$$\begin{aligned}\partial_\mu\partial_\nu\frac{\partial\mathcal{L}_3}{\partial_\mu\partial_\nu\phi} &= -\nabla_\mu\left(\nabla_\nu g^{\mu\nu}G_3\right)\\ &= -\nabla^\mu\left(G_{3\phi}\nabla_\mu\phi + G_{3X}\nabla_\mu X\right),\end{aligned} \tag{B.11}$$

where we have replaced again the partial derivatives by covariant derivatives. We can then conclude that, for $\mathcal{L}_3$ the scalar field equation reads

$$-G_{3\phi}\Box\phi - \nabla^\mu\left(G_{3X}\nabla_\mu\phi\Box\phi\right) - \nabla^\mu\left(G_{3\phi}\nabla_\mu\phi\right) - \nabla^\mu\left(G_{3X}\nabla_\mu X\right) = 0. \tag{B.12}$$

and we make the following assignment

$$P^3_\phi = \nabla_\mu G_{3\phi}\nabla^\mu\phi, \tag{B.13}$$

$$\nabla^\mu J^3_\mu = \nabla^\mu\left(-G_{3X}\nabla_\mu\phi + G_{3X}\nabla_\mu X + 2G_{3\phi}\nabla_\mu\phi\right). \tag{B.14}$$

For $\mathcal{L}_4$ we have

$$\mathcal{L}_4\left(\phi\right) = \frac{\partial\mathcal{L}_4}{\partial\phi}\delta\phi, \tag{B.15}$$

$$\frac{\partial\mathcal{L}_4}{\partial\phi} = P^4_\phi = 0. \tag{B.16}$$

Since $\mathcal{L}_4 = G_4\left(\phi\right)R$, applying Eq. (B.16) leads to

$$P^4_\phi = G_{4\phi}R. \tag{B.17}$$

Our result for the scalar field equation considering $G_{4X} = 0$ and $G_5 = 0$ is in full agreement with Ref. [302]. Hence, the scalar-field equation can be written as

$$\nabla^\mu\left(\sum_{i=2}^{4}J^i_\mu\right) = \sum_{i=2}^{4}P^i_\phi. \tag{B.18}$$

B.1.2 Gravitational field equations

Defining the arbitrary functions $\mathcal{L}_i$ from the action (5.21) as

$$\mathcal{L}_2 = K(\phi, X), \tag{B.19}$$
$$\mathcal{L}_3 = -G_3(\phi, X)\,\Box\phi, \tag{B.20}$$
$$\mathcal{L}_4 = G_4(\phi)R, \tag{B.21}$$

we can then vary the action with respect to the metric tensor; using the principle of least action, this leads to

$$\delta S = \delta S_2 + \delta S_3 + \delta S_4 + \delta\left(\sqrt{-g}\mathcal{L}_m\right) = 0. \tag{B.22}$$

For δS_2 we have

$$\delta S_2 = \int d^4x \left[\delta\sqrt{-g}K + \sqrt{-g}\delta K\right], \tag{B.23}$$

and using the fact that

$$\delta\sqrt{-g} = -\frac{1}{2}\sqrt{-g}g_{\mu\nu}\delta g^{\mu\nu}, \tag{B.24}$$

and that the variation of K with respect to the metric can be written as

$$\delta K(\phi, X) = K_X \delta g^{\mu\nu}\left(-\frac{1}{2}\nabla_\mu\phi\nabla_\nu\phi\right), \tag{B.25}$$

we get

$$\delta S_2 = \int d^4x\sqrt{-g}\delta g^{\mu\nu}\left[-\frac{1}{2}Kg_{\mu\nu} - \frac{1}{2}K_X\nabla_\mu\phi\nabla_\nu\phi\right]. \tag{B.26}$$

For δS_3 we have

$$\delta S_3 = \int d^4x\left[-\delta\sqrt{-g}G_3\Box\phi - \sqrt{-g}\delta\left(G_3\Box\phi\right)\right]. \tag{B.27}$$

The variations of G_3 with respect to the metric can be written as

$$\begin{aligned}\delta\left(G_3(\phi, X)\,\Box\phi\right) &= \delta G_3\Box\phi + G_3\delta\left(\Box\phi\right)\\ &= G_{3X}\delta g^{\mu\nu}\left(-\frac{1}{2}\nabla_\mu\phi\nabla_\nu\phi\right)\Box\phi + G_3\delta\left(\Box\phi\right),\end{aligned} \tag{B.28}$$

hence

$$\delta S_3 = \int d^4x\sqrt{-g}\left[\frac{1}{2}g_{\mu\nu}\delta g^{\mu\nu}G_3\Box\phi + \frac{1}{2}\delta g^{\mu\nu}G_{3X}\Box\phi\nabla_\mu\phi\nabla_\nu\phi + G_3\delta\left(\Box\phi\right)\right]. \tag{B.29}$$

The last term of the above equation can be expanded in the following way

$$\delta\Box\phi = \delta g^{ab}\nabla_a\nabla_b\phi + g^{ab}\delta\left(\nabla_a\nabla_b\phi\right) = \delta g^{ab}\nabla_a\nabla_b\phi + \Box\left(\delta\phi\right) - g^{ab}\delta\Gamma^\gamma_{ab}\partial_\gamma\phi, \tag{B.30}$$

since

$$\nabla_a\nabla_b\phi = \partial_a\partial_b\phi - \Gamma^\gamma_{ab}\partial_\gamma\phi, \tag{B.31}$$

and

$$\delta\left(\nabla_a\nabla_b\phi\right) = \nabla_a\nabla_b\left(\delta\phi\right) - \delta\Gamma^\gamma_{ab}\partial_\gamma\phi. \tag{B.32}$$

Also we have that $g^{ab}\Gamma^{\gamma}_{ab} = \ldots = -\nabla_a \delta g^{\gamma a} + \frac{1}{2} g_{ab} g^{\gamma\lambda} \nabla_\lambda \delta g^{ab}$, so we get for the last term in Eq. (B.29):

$$\begin{aligned}
\delta S_{\text{last-term}} &= \int d^4x\sqrt{-g}\,(-G_3)\left(\delta g^{ab}\nabla_a\nabla_b\phi + \Box\delta\phi + \left(\nabla_a\delta g^{\gamma a} - \frac{1}{2}g_{ab}g^{\gamma\lambda}\nabla_\lambda\delta g^{ab}\right)\partial_\gamma\phi\right) \\
&= \int d^4x\sqrt{-g}\left[-\delta g^{\mu\nu}\left(\nabla_\mu\nabla_\nu\right)G_3 + \delta g^{\gamma a}\nabla_a\left(G_3\nabla_\gamma\phi\right) - \frac{1}{2}\delta g^{ab}g_{ab}g^{\gamma\lambda}\nabla_\lambda\left(G_3\nabla_\gamma\phi\right)\right] \\
&= \int d^4x\sqrt{-g}\left[-\delta g^{\mu\nu}\left(\nabla_\mu\nabla_\nu\right)G_3 + \delta g^{\mu\nu}\nabla_\nu\left(G_3\nabla_\mu\phi\right) - \frac{1}{2}\delta g^{\mu\nu}g_{\mu\nu}\nabla^\gamma\left(G_3\nabla_\gamma\phi\right)\right] \\
&= \int d^4x\sqrt{-g}\delta g^{\mu\nu}\left[\left(\nabla_{(\mu}\phi\right)\left(\nabla_{\nu)}G_3\right) - \frac{1}{2}g_{\mu\nu}\nabla^\gamma\left(G_3\nabla_\gamma\phi\right)\right]. \qquad \text{(B.33)}
\end{aligned}$$

Combining all terms we have

$$\delta S_3 = \int d^4x\sqrt{-g}\delta g^{\mu\nu}\left[\frac{1}{2}G_{3X}\Box\phi\nabla_\mu\phi\nabla_\nu\phi + \nabla_{(\mu}G_3\nabla_{\nu)}\phi - \frac{1}{2}g_{\mu\nu}\nabla_\lambda G_3\nabla^\lambda\phi\right]. \qquad \text{(B.34)}$$

For δS_4 we have

$$\delta S_4 = \int d^4x\left[\delta\sqrt{-g}G_4R + \sqrt{-g}G_4\delta R\right], \qquad \text{(B.35)}$$

where

$$\begin{aligned}
\delta R &= \delta\left(g^{\mu\nu}R_{\mu\nu}\right) \\
&= R_{\mu\nu}\delta g^{\mu\nu} + g^{\mu\nu}\delta R_{\mu\nu} \\
&= R_{\mu\nu}\delta g^{\mu\nu} + g^{\mu\nu}\left(\nabla_\rho\delta\Gamma^\rho_{\nu\mu} - \nabla_\nu\delta\Gamma^\rho_{\rho\mu}\right). \qquad \text{(B.36)}
\end{aligned}$$

Since $\delta\Gamma^\lambda_{\mu\nu}$ is the difference of two connections, it should transform as a tensor. Therefore, it can be written as

$$\delta\Gamma^\lambda_{\mu\nu} = \frac{1}{2}g^{\lambda\alpha}\left(\nabla_\mu\delta g_{\alpha\nu} + \nabla_\nu\delta g_{\alpha\mu} - \nabla_\alpha\delta g_{\mu\nu}\right). \qquad \text{(B.37)}$$

Then, substituting Eq. (B.37) into (B.36), we get

$$\delta R = R_{\mu\nu}\delta g^{\mu\nu} + g_{\mu\nu}\Box\left(\delta g^{\mu\nu}\right) - \nabla_\mu\nabla_\nu\left(\delta g^{\mu\nu}\right), \qquad \text{(B.38)}$$

hence

$$\begin{aligned}
\delta S_4 &= \int d^4x\sqrt{-g}\left[-\frac{1}{2}g_{\mu\nu}\delta g^{\mu\nu}G_4R + G_4R_{\mu\nu}\delta g^{\mu\nu} + G_4\left(g_{\mu\nu}\Box\left(\delta g^{\mu\nu}\right) - \nabla_\mu\nabla_\nu\left(\delta g^{\mu\nu}\right)\right)\right] \\
&= \int d^4x\sqrt{-g}\delta g^{\mu\nu}\left[G_{\mu\nu}G_4 + g_{\mu\nu}\Box G_4 - \nabla_\mu\nabla_\nu G_4 + \text{total derivatives}\right] \\
&= \int d^4x\sqrt{-g}\delta g^{\mu\nu}\Big[G_{\mu\nu}G_4 + g_{\mu\nu}\left(G_{4\phi}\Box\phi - 2XG_{4\phi\phi}\right) - G_{4\phi}\nabla_\mu\nabla_\nu\phi - G_{4\phi\phi}\nabla_\mu\phi\nabla_\nu\phi \\
&\quad + \text{total derivatives}\Big] \qquad \text{(B.39)}
\end{aligned}$$

where

$$\begin{aligned}
-\nabla_\mu\left(\nabla_\nu G_4\right) &= -\nabla_\mu\left(\nabla_\nu\phi G_{4\phi}\right) \\
&= -\nabla_\mu\nabla_\nu\phi G_{4\phi} - \nabla_\mu\phi\nabla_\nu\phi G_{4\phi\phi}, \qquad \text{(B.40)}
\end{aligned}$$

$$g_{\mu\nu}\Box G_4 = g_{\mu\nu}\left(g^{ab}\nabla_a\nabla_b G_4\right)$$

$$
\begin{aligned}
&= g_{\mu\nu}\left(g^{ab}\nabla_a\left(\nabla_b\phi G_{4\phi}\right)\right)\\
&= g_{\mu\nu}\left(g^{ab}\nabla_a\nabla_b\phi G_{4\phi}+g^{ab}\nabla_b\phi\nabla_a G_{4\phi}\right)\\
&= g_{\mu\nu}\left(\Box\phi G_{4\phi}-2XG_{4\phi\phi}\right). \qquad \text{(B.41)}
\end{aligned}
$$

Since the energy-momentum tensor is defined as

$$
T^{(m)}_{\mu\nu}=-\frac{2}{\sqrt{-g}}\frac{\delta\left(\sqrt{-g}\mathcal{L}_m\right)}{\delta g^{\mu\nu}}, \qquad \text{(B.42)}
$$

the gravitational field equation can be written

$$
\begin{aligned}
&T^{(m)}_{\mu\nu}=-K_X\nabla_\mu\phi\nabla_\nu\phi-Kg_{\mu\nu}+G_{3X}\Box\phi\nabla_\mu\phi\nabla_\nu\phi+2\nabla_{(\mu}G_3\nabla_{\nu)}\phi-g_{\mu\nu}\nabla_\lambda G_3\nabla^\lambda\phi+2G_4G_{\mu\nu}\\
&+2g_{\mu\nu}\left(G_{4\phi}\Box\phi-2XG_{4\phi\phi}\right)-2G_{4\phi}\nabla_\mu\nabla_\nu\phi\\
&-2G_{4\phi\phi}\nabla_\mu\phi\nabla_\nu\phi. \qquad \text{(B.43)}
\end{aligned}
$$

B.2 Coefficients

Here we show the coefficients for the perturbations in the Horndeski theory in Eq. (5.21). They are given by:

$$
A_1 = -3\dot\phi^3G_{3X}+12HG_4+6\dot\phi G_{4\phi}, \qquad \text{(B.44)}
$$

$$
\begin{aligned}
A_2 &= -\dot\phi\left(K_X+\dot\phi^2K_{XX}\right)+2\dot\phi G_{3\phi}-3H\dot\phi^2\left(3G_{3X}+\dot\phi^2G_{3XX}\right)\\
&+ \dot\phi^3G_{3\phi X}+6HG_{4\phi}, \qquad \text{(B.45)}
\end{aligned}
$$

$$
A_3 = 4G_4, \qquad \text{(B.46)}
$$

$$
\begin{aligned}
A_4 &= \dot\phi^2\left(K_X+\dot\phi^2K_{XX}\right)-2\dot\phi^2G_{3\phi}-\dot\phi^4G_{3\phi X}+3H\dot\phi^3\left(4G_{3X}+\dot\phi^2G_{3XX}\right)\\
&-12H\left(HG_4+\dot\phi G_{4\phi}\right), \qquad \text{(B.47)}
\end{aligned}
$$

$$
A_6 = -\dot\phi^2G_{3X}+2G_{4\phi}, \qquad \text{(B.48)}
$$

$$
\mu=-K_\phi+\dot\phi^2K_{\phi X}-\dot\phi^2G_{3\phi\phi}+3H\dot\phi^3G_{3\phi X}-6H^2G_{4\phi}-6H\dot\phi G_{4\phi\phi}, \qquad \text{(B.49)}
$$

$$
B_1 = 12G_4, \qquad \text{(B.50)}
$$

$$
B_2 = -3\dot\phi^2G_{3X}+6G_{4\phi}, \qquad \text{(B.51)}
$$

$$
B_3 = 12\left(\dot\phi G_{4\phi}+3HG_4\right), \qquad \text{(B.52)}
$$

$$
B_4=3\left[\dot\phi K_X-2\dot\phi G_{3\phi}-2\dot\phi\ddot\phi G_{3X}-\dot\phi^3\left(G_{3\phi X}+\ddot\phi G_{3XX}\right)+4HG_{4\phi}+4\dot\phi G_{4\phi\phi}\right], \qquad \text{(B.53)}
$$

$$
B_5 = 3\left(\dot\phi^3G_{3X}-4HG_4-2\dot\phi G_{4\phi}\right), \qquad \text{(B.54)}
$$

$$B_6 = 4G_4, \quad B_7 = 4G_{4\phi}, \quad B_8 = 4G_4, \tag{B.55}$$

$$\begin{aligned} B_9 &= -3K_X\dot{\phi}^2 + 6G_{3\phi}\dot{\phi}^2 + 3G_{3\phi X}\dot{\phi}^4 + 12G_{3X}\dot{\phi}^2\ddot{\phi} + 3G_{3XX}\dot{\phi}^4\ddot{\phi} - 36G_4H^2 - 24G_4\dot{H} \\ &- 24G_{4\phi}H\dot{\phi} - 12G_{4\phi\phi}\dot{\phi}^2 - 12G_{4\phi}\ddot{\phi}, \end{aligned} \tag{B.56}$$

and using Eq.(5.50) to eliminate G_4 in favor of K we can express B_9 as

$$B_9 = 3\left(2K - \dot{\phi}^2K_X + 2\dot{\phi}^2\ddot{\phi}G_{3X} + \dot{\phi}^4G_{3\phi X} + \dot{\phi}^4\ddot{\phi}G_{3XX}\right), \tag{B.57}$$

$$\begin{aligned} \nu &= K_\phi - \dot{\phi}^2\left(G_{3\phi\phi} + \ddot{\phi}G_{3\phi X}\right) + 2\left(3H^2 + 2\dot{H}\right)G_{4\phi} + 2\left(\ddot{\phi} + 2H\dot{\phi}\right)G_{4\phi\phi} \\ &+ 2\dot{\phi}^2G_{4\phi\phi\phi}, \end{aligned} \tag{B.58}$$

$$C_1 = 4G_4, \tag{B.59}$$

$$C_2 = -\dot{\phi}^2G_{3X} + 2G_{4\phi}, \tag{B.60}$$

$$C_3 = \dot{\phi}^3G_{3X} - 4HG_4 - 2\dot{\phi}G_{4\phi}, \tag{B.61}$$

$$C_4 = \dot{\phi}\left(K_X - 2G_{3\phi} + 2G_{4\phi\phi}\right) + H\left(3\dot{\phi}^2G_{3X} - 2G_{4\phi}\right), \tag{B.62}$$

$$D_1 = -3\left(\dot{\phi}^2G_{3X} - 2G_{4\phi}\right), \tag{B.63}$$

$$D_2 = -K_X - \dot{\phi}^2K_{XX} + 2G_{3\phi} - 6H\dot{\phi}G_{3X} + \dot{\phi}^2G_{3\phi X} - 3H\dot{\phi}^3G_{3XX}, \tag{B.64}$$

$$D_3 = -3\left(\dot{\phi}K_X - 2\dot{\phi}G_{3\phi} + 6H\dot{\phi}^2G_{3X} + 2\dot{\phi}\ddot{\phi}G_{3X} + \dot{\phi}^3G_{3\phi X} + \dot{\phi}^3\ddot{\phi}G_{3XX} - 8HG_{4\phi}\right), \tag{B.65}$$

$$\begin{aligned} D_4 &= \frac{d}{dt}D_2 + 3HD_2 \\ &= -3HK_X - K_{\phi X}\dot{\phi} - K_{\phi XX}\dot{\phi}^3 - K_{XXX}\dot{\phi}^3\ddot{\phi} - 3K_{XX}\left(H\dot{\phi}^2 + \dot{\phi}\ddot{\phi}\right) + 6HG_{3\phi} \\ &+ 2G_{3\phi\phi}\dot{\phi} - 6G_{3X}\left(3H^2\dot{\phi} + \dot{H}\dot{\phi} + H\ddot{\phi}\right) + G_{3\phi X}\left(-3H\dot{\phi}^2 + 4\dot{\phi}\ddot{\phi}\right) + G_{3\phi\phi X}\dot{\phi}^3 \\ &- 3G_{3XX}\dot{\phi}^2\left(3H^2\dot{\phi} + \dot{H}\dot{\phi} + 5H\ddot{\phi}\right) + G_{\phi XX}\left(H\dot{\phi}^3\ddot{\phi} - 3H\dot{\phi}^4\right) - 3G_{3XXX}H\dot{\phi}^4\ddot{\phi}, \end{aligned} \tag{B.66}$$

$$D_5 = \dot{\phi}\left(K_X + \dot{\phi}^2_{XX} - 2G_{3\phi} - \dot{\phi}^2G_{3\phi X}\right) + 3H\left(3\dot{\phi}^2G_{3X} + \dot{\phi}^4G_{3XX} - 2G_{4\phi}\right), \tag{B.67}$$

$$D_7 = 4G_{4\phi}, \tag{B.68}$$

$$D_8 = 9H\dot{\phi}^{-1}K + 3K_\phi - 3\left(\ddot{\phi} + 3H\dot{\phi}\right)K_X - 3\dot{\phi}^2\left(K_{\phi X} + \ddot{\phi}K_{XX}\right) + 3\left(2\ddot{\phi} + 3H\dot{\phi}\right)G_{3\phi}$$

$$
\begin{aligned}
&- \quad 9\dot{\phi}\left(3H\ddot{\phi}+3H^2\dot{\phi}+\dot{H}\dot{\phi}\right)G_{3X}+3\dot{\phi}^2G_{3\phi\phi}+3\dot{\phi}^2\left(\ddot{\phi}-3H\dot{\phi}\right)G_{3\phi X}-9H\dot{\phi}^3\ddot{\phi}G_{3XX}\\
&+ \quad 18H\dot{\phi}^{-1}\left(3H^2+2\dot{H}\right)G_4+18\dot{\phi}^{-1}\left(H\ddot{\phi}+4H^2\dot{\phi}+\dot{H}\dot{\phi}\right)G_{4\phi}+18H\dot{\phi}G_{4\phi\phi}, \qquad \text{(B.69)}
\end{aligned}
$$

and using Eqs. (5.50) and (5.56) we find that

$$
D_8 \quad = \quad 0, \qquad \text{(B.70)}
$$

$$
\begin{aligned}
D_9 &= -K_X+2G_{3\phi}-4H\dot{\phi}G_{3X}-\ddot{\phi}\left(2G_{3X}+\dot{\phi}^2G_{3XX}\right)-\dot{\phi}^2G_{3\phi X}, && \text{(B.71)}\\
D_{10} &= -\dot{\phi}^2G_{3X}+2G_{4\phi}, && \text{(B.72)}\\
D_{11} &= K_\phi+\left(\ddot{\phi}+3H\dot{\phi}\right)K_X+\dot{\phi}^2\left(4\ddot{\phi}+3H\dot{\phi}\right)K_{XX}+\dot{\phi}^4\left(K_{\phi XX}+\ddot{\phi}K_{XXX}\right)\\
&- 2\left(\ddot{\phi}+3H\dot{\phi}\right)G_{3\phi}+9\dot{\phi}\left(2H\ddot{\phi}+3H^2\dot{\phi}+\dot{H}\dot{\phi}\right)G_{3X}-\dot{\phi}^2G_{3\phi\phi}\\
&- \dot{\phi}^2\left(5\ddot{\phi}-3H\dot{\phi}\right)G_{3\phi X}-\dot{\phi}^4G_{3\phi\phi X}+3\dot{\phi}^3\left(7H\ddot{\phi}+3H^2\dot{\phi}+\dot{H}\dot{\phi}\right)G_{3XX}\\
&- \dot{\phi}^4\left(\ddot{\phi}-3H\dot{\phi}\right)G_{3\phi XX}+3H\dot{\phi}^5\ddot{\phi}G_{3XXX}-6\left(2H^2+\dot{H}\right)G_{4\phi}, && \text{(B.73)}\\
M^2 &= -K_{\phi\phi}+\left(\ddot{\phi}+3H\dot{\phi}\right)K_{\phi X}+\dot{\phi}^2K_{\phi\phi X}+\dot{\phi}^2\ddot{\phi}K_{\phi XX}\\
&- \ddot{\phi}\left[2G_{3\phi\phi}+\dot{\phi}^2G_{3\phi\phi X}-3H\dot{\phi}\left(2G_{3\phi X}+\dot{\phi}^2G_{3\phi XX}\right)\right]\\
&- 6H\dot{\phi}G_{3\phi\phi}+3\dot{\phi}^2\left(3H^2+\dot{H}\right)G_{3\phi X}-\dot{\phi}^2G_{3\phi\phi\phi}\\
&+ 3H\dot{\phi}^3G_{3\phi\phi X}-6\left(2H^2+\dot{H}\right)G_{4\phi\phi}. && \text{(B.74)}
\end{aligned}
$$

For the DE effective perturbation equations we found the following coefficients

$$
\mathcal{F}_1=\left(A_6-B_7\right)B_7G_4G_{4\phi}^2\Big(B_7G_4-\left(B_6-2\right)G_{4\phi}\Big), \qquad \text{(B.75)}
$$

$$
\begin{aligned}
\mathcal{F}_2 &= \left(A_6-B_7\right)B_7G_4\Big(3\nu G_{4\phi}^2+2B_2G_{4\phi\phi}^2\dot{\phi}^2\\
&- G_{4\phi}\Big(B_4G_{4\phi\phi}\dot{\phi}+B_2G_{4\phi\phi\phi}\dot{\phi}^2+B_2G_{4\phi\phi}\ddot{\phi}\Big)\Big)\\
&+ G_{4\phi}^2\Big(B_2B_7\left(B_7-A_6\right)G_{4\phi\phi}\dot{\phi}^2+G_{4\phi}\Big(B_9\left(B_7^2-2D_9\right)\\
&+ \left(A_6-B_7\right)B_7\left(B_4\dot{\phi}+B_2\ddot{\phi}\right)\Big)\Big), && \text{(B.76)}
\end{aligned}
$$

$$
\mathcal{F}_3 \quad = \quad B_6B_9M^2G_{4\phi}^3, \qquad \text{(B.77)}
$$

$$
\mathcal{F}_4 \quad = \quad G_{4\phi}, \qquad \text{(B.78)}
$$

$$
\mathcal{F}_5 \quad = \quad B_6\left(A_6^2-2A_6B_7+B_6D_9\right)G_{4\phi}^2, \qquad \text{(B.79)}
$$

$$
\mathcal{F}_6 \quad = \quad -B_6^2M^2G_{4\phi}^2, \qquad \text{(B.80)}
$$

$$
\mathcal{F}_7=G_{4\phi}\Big(A_6\left(A_6-B_7\right)B_7G_4+\left(B_6-2\right)\left(B_6D_9-A_6B_7\right)G_{4\phi}\Big), \qquad \text{(B.81)}
$$

$$\begin{aligned}\mathcal{F}_8 &= \Big(G_{4\phi}^2\Big(A_4\left(B_7^2-B_6D_9\right)-\left(B_6-2\right)B_6M^2\\ &+ 6\left(B_7^2-B_6D_9\right)H^2+A_2\left(A_6-B_7\right)B_7\dot{\phi}\Big)\\ &- \left(A_6-B_7\right)B_7G_4\left(\mu G_{4\phi}+A_2G_{4\phi\phi}\dot{\phi}\right)\Big),\end{aligned} \tag{B.82}$$

$$\mathcal{F}_9 = B_6M^2G_{4\phi}^2\left(A_4+6H^2\right) \tag{B.83}$$

$$\begin{aligned}\mathcal{F}_{10} &= G_{4\phi}\Big(\left(A_6-B_7\right)B_7C_4G_4\\ &+ \left(B_7^2-B_6D_9\right)G_{4\phi}\left(C_3+2H\right)\Big)\\ &+ \left(A_6-B_7\right)B_7C_2\left(G_{4\phi}^2-G_4G_{4\phi\phi}\right)\dot{\phi},\end{aligned} \tag{B.84}$$

$$\mathcal{F}_{11} = B_6M^2G_{4\phi}^2\left(C_3+2H\right). \tag{B.85}$$

The coefficients for the KGB DE effective perturbation equations are

$$\hat{\mathcal{F}}_2 = -B_9D_9+3A_6\nu-6D_9\left(3H^2+2\dot{H}\right), \tag{B.86}$$

$$\hat{\mathcal{F}}_3 = M^2\left(B_9+18H^2+12\dot{H}\right) \tag{B.87}$$

$$\hat{\mathcal{F}}_5 = A_6^2+B_6D_9, \tag{B.88}$$

$$\hat{\mathcal{F}}_6 = -B_6M^2, \tag{B.89}$$

$$\hat{\mathcal{F}}_7 = -A_6^2-\left(B_6-2\right)D_9, \tag{B.90}$$

$$\hat{\mathcal{F}}_8 = A_4D_9+M^2\left(B_6-2\right)+A_6\mu+6D_9H^2, \tag{B.91}$$

$$\hat{\mathcal{F}}_9 = -M^2\left(A_4+6H^2\right), \tag{B.92}$$

$$\hat{\mathcal{F}}_{10} = M^2\left(C_3+2H\right), \tag{B.93}$$

$$\hat{\mathcal{F}}_{11} = A_6C_4-C_3D-9-2D_9H. \tag{B.94}$$

C

The RSD likelihood

The publicly available RSD Montepython likelihood for the growth rate $f\sigma_8$ data set, introduced in this paper for the first time, is based on the compilation shown in Table 2.4 and can be found at https://github.com/snesseris/RSD-growth.

Here we describe the RSD likelihood we used for the MCMC analysis done in Chapters 6 and 7. In particular, we implement in python a likelihood for the "Gold 2018" growth rate $f\sigma_8$ compilation with $N = 22$ data points given in Ref. [116] and shown in Table 2.4 with the corresponding references of each point. See Chapter 2 for more details.

The redshift correction for the Alcock-Paczynski effect as described in Ref. [120], is given in terms of a correction factor of

$$\mathrm{fac}(z^i) = \frac{H(z^i)\, d_A(z^i)}{H^{\mathrm{ref},i}(z^i)\, d_A^{\mathrm{ref},i}(z^i)} \,, \tag{C.1}$$

where the label "ref, i" stands for the fiducial cosmology used on each data point at the redshift z^i. As a result, the now corrected growth rate is [717]

$$f\sigma_8^{\mathrm{th,i}} \to \frac{f\sigma_8^{\mathrm{th,i}}}{\mathrm{fac}(z^i)} \,. \tag{C.2}$$

We can then define the data vector $\boldsymbol{V}$ as:

$$\mathbf{V} = \mathbf{f}\boldsymbol{\sigma}_{\mathbf{8}}^{\mathrm{obs,i}} - \frac{f\sigma_8^{\mathrm{th,i}}}{\mathrm{fac}(z^i)}, \tag{C.3}$$

and the chi-squared of our likelihood via

$$\chi^2 = \mathbf{x}^T \mathbf{C}^{-1} \mathbf{x} \,. \tag{C.4}$$

Finally, in `CLASS` we can obtain the scale-dependent growth $\delta(k, z)$ at each redshift via the matter power spectrum as $\delta(k, z) = \sqrt{\frac{P(k,z)}{P(k,0)}}$, where the matter power spectrum $P(k, z)$ is obtained from the code itself via the function `cosmo.pk(k,z)`. Then, $f\sigma_8(k, z)$ can be obtained with simple cubic interpolations and direct differentiation from Eq. (7.56).

Bibliography

[1] Planck, N. Aghanim *et al.*, (2018), arXiv:1807.06209.

[2] A. Heavens *et al.*, Phys. Rev. Lett. **119**, 101301 (2017), arXiv:1704.03467.

[3] T. Clifton, P. G. Ferreira, A. Padilla, and C. Skordis, Phys. Rept. **513**, 1 (2012), arXiv:1106.2476.

[4] E. Bertschinger, Phil. Trans. Roy. Soc. Lond. **A369**, 4947 (2011), arXiv:1111.4659.

[5] E. J. Copeland, M. Sami, and S. Tsujikawa, Int. J. Mod. Phys. **D15**, 1753 (2006), arXiv:hep-th/0603057.

[6] M. Kunz and D. Sapone, Phys. Rev. **D74**, 123503 (2006), arXiv:astro-ph/0609040.

[7] G. Gubitosi, F. Piazza, and F. Vernizzi, JCAP **1302**, 032 (2013), arXiv:1210.0201, [JCAP1302,032(2013)].

[8] B. Hu, M. Raveri, N. Frusciante, and A. Silvestri, Phys. Rev. **D89**, 103530 (2014), arXiv:1312.5742.

[9] R. Arjona, W. Cardona, and S. Nesseris, Phys. Rev. **D99**, 043516 (2019), arXiv:1811.02469.

[10] R. Arjona, W. Cardona, and S. Nesseris, Phys. Rev. **D100**, 063526 (2019), arXiv:1904.06294.

[11] R. Arjona, The effective fluid approach for modified gravity, in *2nd Hermann Minkowski Meeting on the Foundations of Spacetime Physics*, 2020, arXiv:2010.04764.

[12] I. Sawicki and E. Bellini, Phys. Rev. **D92**, 084061 (2015), arXiv:1503.06831.

[13] J. J. Stachel, (2005).

[14] e. a. Abbott, Benjamin P, Physical review letters **116**, 061102 (2016).

[15] T. Clifton, P. G. Ferreira, A. Padilla, and C. Skordis, Physics reports **513**, 1 (2012).

[16] R. Penrose, *Fashion, faith, and fantasy in the new physics of the universe* (Princeton University Press, 2016).

[17] F. Bezrukov and M. Shaposhnikov, Physics Letters B **659**, 703 (2008).

[18] e. a. Akrami, Y., arXiv preprint arXiv:1807.06205 (2018).

[19] e. a. Astier, Pierre, Astronomy & Astrophysics **447**, 31 (2006).

[20] e. a. Eisenstein, Daniel J., The Astrophysical Journal **633**, 560 (2005).

[21] e. a. Aghanim, N., arXiv preprint arXiv:1807.06209 (2018).

[22] S. M. Carroll, Living reviews in relativity **4**, 1 (2001).

[23] S. Weinberg, Reviews of modern physics **61**, 1 (1989).

[24] A. L. Maroto and J. Ramirez, arXiv preprint astro-ph/0409280 (2004).

[25] D. Lovelock, Journal of Mathematical Physics **13**, 874 (1972).

[26] S. Weinberg, *Cosmology* (Oxford university press, 2008).

[27] E. Hubble, Proceedings of the national academy of sciences **15**, 168 (1929).

[28] e. a. Aghanim, N, Astronomy & Astrophysics **594**, A11 (2016).

[29] E. Kolb, *The early universe* (CRC Press, 2018).

[30] S. Capozziello and M. De Laurentis, Physics Reports **509**, 167 (2011).

[31] T. Ortín, *Gravity and strings* (Cambridge University Press, 2004).

[32] C. W. Misner, K. S. Thorne, and J. A. Wheeler, *Gravitation* (Princeton University Press, 2017).

[33] S. Dodelson, *Modern cosmology* (Academic press, 2003).

[34] C.-P. Ma and E. Betschinger, Astrophys. J. **455**, 7 (1995), arXiv:astro-ph/9506072.

[35] L. Amendola, S. Fogli, A. Guarnizo, M. Kunz, and A. Vollmer, Physical Review D **89**, 063538 (2014).

[36] D. Baumann, Available onlin e: www. damtp. cam. ac. uk/user/db275/Cosmology. pdf (accessed on 15 December 2016) (2015).

[37] S. Dodelson, *Modern cosmology* (Elsevier, 2003).

[38] A. Riotto, ICTP Lect. Notes Ser. **14**, 317 (2003), arXiv:hep-ph/0210162.

[39] Supernova Search Team, A. G. Riess *et al.*, Astron. J. **116**, 1009 (1998), arXiv:astro-ph/9805201.

[40] Supernova Cosmology Project, S. Perlmutter *et al.*, Astrophys. J. **517**, 565 (1999), arXiv:astro-ph/9812133.

[41] E. V. Linder, Reports on Progress in Physics **71**, 056901 (2008).

[42] A. Silvestri and M. Trodden, Reports on Progress in Physics **72**, 096901 (2009).

[43] P. Steinhardt, V. Fitch, and D. R. Marlow, edited by VL Fitch et al. DR Marlow & MAE Dementi (Princeton Univ. 1997) (1997).

[44] H. Velten, R. vom Marttens, and W. Zimdahl, The European Physical Journal C **74**, 3160 (2014).

[45] S. Zaabat and K. Nouicer, arXiv preprint arXiv:1807.00700 (2018).

[46] A. G. Riess, S. Casertano, W. Yuan, L. M. Macri, and D. Scolnic, Astrophys. J. **876**, 85 (2019), arXiv:1903.07603.

[47] M. Benetti and S. Capozziello, (2019), arXiv:1910.09975.

[48] DES, T. M. C. Abbott *et al.*, Mon. Not. Roy. Astron. Soc. **480**, 3879 (2018), arXiv:1711.00403.

[49] SPT, J. W. Henning *et al.*, Astrophys. J. **852**, 97 (2018), arXiv:1707.09353.

[50] V. Bonvin *et al.*, Mon.Not.Roy.Astron.Soc. **465**, 4914 (2017), arXiv:1607.01790.

[51] A. G. Riess, Nature Rev. Phys. **2**, 10 (2019), arXiv:2001.03624.

[52] P. Lemos, E. Lee, G. Efstathiou, and S. Gratton, Mon. Not. Roy. Astron. Soc. **483**, 4803 (2019), arXiv:1806.06781.

[53] E. Di Valentino *et al.*, (2021), arXiv:2103.01183.

[54] G. Efstathiou, (2020), arXiv:2007.10716.

[55] L. Perivolaropoulos and F. Skara, (2021), arXiv:2105.05208.

[56] G. Risaliti and E. Lusso, Nat. Astron. **3**, 272 (2019), arXiv:1811.02590.

[57] W. Handley, (2019), arXiv:1908.09139.

[58] E. Di Valentino, A. Melchiorri, and J. Silk, Nat. Astron. (2019), arXiv:1911.02087.

[59] E. Di Valentino *et al.*, (2020), arXiv:2008.11285.

[60] D. J. Schwarz, C. J. Copi, D. Huterer, and G. D. Starkman, Class. Quant. Grav. **33**, 184001 (2016), arXiv:1510.07929.

[61] Planck, Y. Akrami *et al.*, Astron. Astrophys. **641**, A7 (2020), arXiv:1906.02552.

[62] A. Del Popolo and M. Le Delliou, Galaxies **5**, 17 (2017), arXiv:1606.07790.

[63] J. S. Bullock and M. Boylan-Kolchin, Ann. Rev. Astron. Astrophys. **55**, 343 (2017), arXiv:1707.04256.

[64] H. Velten and S. Gomes, (2019), arXiv:1911.11848.

[65] E. Di Valentino, A. Melchiorri, O. Mena, and S. Vagnozzi, (2019), arXiv:1910.09853.

[66] W. Lin, K. J. Mack, and L. Hou, (2019), arXiv:1910.02978.

[67] D. Camarena and V. Marra, (2019), arXiv:1906.11814, [Phys. Rev. Research.2,013028(2020)].

[68] W. Handley and P. Lemos, Phys. Rev. **D100**, 043504 (2019), arXiv:1902.04029.

[69] S. Gariazzo, Neutrino Properties and the Cosmological Tensions in the ΛCDM Model, in *15th Marcel Grossmann Meeting on Recent Developments in Theoretical and Experimental General Relativity, Astrophysics, and Relativistic Field Theories (MG15) Rome, Italy, July 1-7, 2018*, 2018, arXiv:1812.00638.

[70] R.-Y. Guo, J.-F. Zhang, and X. Zhang, JCAP **1902**, 054 (2019), arXiv:1809.02340.

[71] E. Gaztanaga, A. Cabre, and L. Hui, Mon. Not. Roy. Astron. Soc. **399**, 1663 (2009), arXiv:0807.3551.

[72] R. Jimenez and A. Loeb, Astrophys. J. **573**, 37 (2002), arXiv:astro-ph/0106145.

[73] M. Moresco *et al.*, JCAP **1605**, 014 (2016), arXiv:1601.01701.

[74] H. Yu, B. Ratra, and F.-Y. Wang, Astrophys. J. **856**, 3 (2018), arXiv:1711.03437.

[75] R.-Y. Guo and X. Zhang, Eur. Phys. J. **C76**, 163 (2016), arXiv:1512.07703.

[76] C. Zhang, H. Zhang, S. Yuan, T.-J. Zhang, and Y.-C. Sun, Res. Astron. Astrophys. **14**, 1221 (2014), arXiv:1207.4541.

[77] D. Stern, R. Jimenez, L. Verde, M. Kamionkowski, and S. A. Stanford, JCAP **1002**, 008 (2010), arXiv:0907.3149.

[78] M. Moresco *et al.*, JCAP **1208**, 006 (2012), arXiv:1201.3609.

[79] C.-H. Chuang and Y. Wang, Mon. Not. Roy. Astron. Soc. **435**, 255 (2013), arXiv:1209.0210.

[80] C. Blake *et al.*, Mon. Not. Roy. Astron. Soc. **425**, 405 (2012), arXiv:1204.3674.

[81] BOSS, L. Anderson *et al.*, Mon. Not. Roy. Astron. Soc. **441**, 24 (2014), arXiv:1312.4877.

[82] M. Moresco, Mon. Not. Roy. Astron. Soc. **450**, L16 (2015), arXiv:1503.01116.

[83] BOSS, T. Delubac *et al.*, Astron. Astrophys. **574**, A59 (2015), arXiv:1404.1801.

[84] J. C. Wheeler and R. P. Harkness, Reports on Progress in Physics **53**, 1467 (1990).

[85] B. E. Stahl, T. de Jaeger, W. Zheng, and A. V. Filippenko, (2021), arXiv:2105.04446.

[86] G. T. 1 *et al.*, (2021), arXiv:2104.00172.

[87] A. G. Riess *et al.*, The Astronomical Journal **116**, 1009 (1998).

[88] D. M. Scolnic *et al.*, Astrophys. J. **859**, 101 (2018), arXiv:1710.00845.

[89] SNLS, A. Conley *et al.*, Astrophys. J. Suppl. **192**, 1 (2011), arXiv:1104.1443.

[90] F. Beutler *et al.*, Mon. Not. Roy. Astron. Soc. **416**, 3017 (2011), arXiv:1106.3366.

[91] X. Xu, N. Padmanabhan, D. J. Eisenstein, K. T. Mehta, and A. J. Cuesta, Mon. Not. Roy. Astron. Soc. **427**, 2146 (2012), arXiv:1202.0091.

[92] A. J. Ross *et al.*, Mon. Not. Roy. Astron. Soc. **449**, 835 (2015), arXiv:1409.3242.

[93] H. Gil-Marin *et al.*, Mon. Not. Roy. Astron. Soc. **460**, 4210 (2016), arXiv:1509.06373.

[94] DES, T. M. C. Abbott *et al.*, Mon. Not. Roy. Astron. Soc. **483**, 4866 (2019), arXiv:1712.06209.

[95] M. Blomqvist *et al.*, Astron. Astrophys. **629**, A86 (2019), arXiv:1904.03430.

[96] J. E. Bautista *et al.*, Astrophys. J. **863**, 110 (2018), arXiv:1712.08064.

[97] M. Ata *et al.*, Mon. Not. Roy. Astron. Soc. **473**, 4773 (2018), arXiv:1705.06373.

[98] D. J. Eisenstein and W. Hu, Astrophys. J. **496**, 605 (1998), arXiv:astro-ph/9709112.

[99] S. Alam, S. Ho, and A. Silvestri, Mon. Not. Roy. Astron. Soc. **456**, 3743 (2016), arXiv:1509.05034.

[100] eBOSS, S. Alam *et al.*, (2020), arXiv:2007.08991.

[101] R. C. Nunes, S. K. Yadav, J. F. Jesus, and A. Bernui, Mon. Not. Roy. Astron. Soc. **497**, 2133 (2020), arXiv:2002.09293.

[102] E. Sanchez *et al.*, Mon. Not. Roy. Astron. Soc. **411**, 277 (2011), arXiv:1006.3226.

[103] E. de Carvalho, A. Bernui, G. Carvalho, C. Novaes, and H. Xavier, JCAP **04**, 064 (2018), arXiv:1709.00113.

[104] G. Carvalho *et al.*, Astropart. Phys. **119**, 102432 (2020), arXiv:1709.00271.

[105] G. Carvalho, A. Bernui, M. Benetti, J. Carvalho, and J. Alcaniz, Phys. Rev. D **93**, 023530 (2016), arXiv:1507.08972.

[106] J. S. Alcaniz, G. C. Carvalho, A. Bernui, J. C. Carvalho, and M. Benetti, Fundam. Theor. Phys. **187**, 11 (2017), arXiv:1611.08458.

[107] J. M. LoSecco, G. J. Mathews, and Y. Wang, Phys. Rev. **D64**, 123002 (2001), arXiv:astro-ph/0108260.

[108] D. J. Fixsen, Astrophys. J. **707**, 916 (2009), arXiv:0911.1955.

[109] G. Luzzi *et al.*, The Astrophysical Journal **705**, 1122 (2009).

[110] R. Srianand, P. Noterdaeme, C. Ledoux, and P. Petitjean, Astronomy & Astrophysics **482**, L39 (2008).

[111] J. Cui, J. Bechtold, J. Ge, and D. M. Meyer, The Astrophysical Journal **633**, 649 (2005).

[112] J.-a. Ge, J. Bechtold, and J. H. Black, Astrophys. J. **474**, 67 (1997), arXiv:astro-ph/9607145.

[113] R. Srianand, P. Petitjean, and C. Ledoux, Nature **408**, 931 (2000), arXiv:astro-ph/0012222.

[114] G. Hurier, N. Aghanim, M. Douspis, and E. Pointecouteau, Astron. Astrophys. **561**, A143 (2014), arXiv:1311.4694.

[115] P. Molaro, S. A. Levshakov, M. Dessauges-Zavadsky, and S. D'Odorico, Astron. Astrophys. **381**, L64 (2002), arXiv:astro-ph/0111589.

[116] B. Sagredo, S. Nesseris, and D. Sapone, Phys. Rev. **D98**, 083543 (2018), arXiv:1806.10822.

[117] W. J. Percival and M. White, Mon. Not. Roy. Astron. Soc. **393**, 297 (2009), arXiv:0808.0003.

[118] Y.-S. Song and W. J. Percival, JCAP **0910**, 004 (2009), arXiv:0807.0810.

[119] S. Nesseris and L. Perivolaropoulos, JCAP **0701**, 018 (2007), arXiv:astro-ph/0610092.

[120] S. Nesseris, G. Pantazis, and L. Perivolaropoulos, Phys. Rev. **D96**, 023542 (2017), arXiv:1703.10538.

[121] L. Kazantzidis and L. Perivolaropoulos, Phys. Rev. **D97**, 103503 (2018), arXiv:1803.01337.

[122] S. Nesseris and S. Tsujikawa, Phys. Rev. **D90**, 024070 (2014), arXiv:1402.4613.

[123] G.-B. Zhao *et al.*, (2018), arXiv:1801.03043.

[124] D. Huterer, D. Shafer, D. Scolnic, and F. Schmidt, JCAP **05**, 015 (2017), arXiv:1611.09862.

[125] S. J. Turnbull *et al.*, Mon. Not. Roy. Astron. Soc. **420**, 447 (2012), arXiv:1111.0631.

[126] M. J. Hudson and S. J. Turnbull, Astrophys. J. Lett. **751**, L30 (2013), arXiv:1203.4814.

[127] M. Davis *et al.*, Mon. Not. Roy. Astron. Soc. **413**, 2906 (2011), arXiv:1011.3114.

[128] M. Feix, A. Nusser, and E. Branchini, Phys. Rev. Lett. **115**, 011301 (2015), arXiv:1503.05945.

[129] C. Howlett, A. Ross, L. Samushia, W. Percival, and M. Manera, Mon. Not. Roy. Astron. Soc. **449**, 848 (2015), arXiv:1409.3238.

[130] C. Blake *et al.*, Mon. Not. Roy. Astron. Soc. **436**, 3089 (2013), arXiv:1309.5556.

[131] L. Samushia, W. J. Percival, and A. Raccanelli, Mon. Not. Roy. Astron. Soc. **420**, 2102 (2012), arXiv:1102.1014.

[132] A. G. Sanchez *et al.*, Mon. Not. Roy. Astron. Soc. **440**, 2692 (2014), arXiv:1312.4854.

[133] C.-H. Chuang *et al.*, Mon. Not. Roy. Astron. Soc. **461**, 3781 (2016), arXiv:1312.4889.

[134] A. Pezzotta *et al.*, Astron. Astrophys. **604**, A33 (2017), arXiv:1612.05645.

[135] T. Okumura *et al.*, Publ. Astron. Soc. Jap. **68**, 38 (2016), arXiv:1511.08083.

[136] G.-B. Zhao *et al.*, Mon. Not. Roy. Astron. Soc. **482**, 3497 (2019), arXiv:1801.03043.

[137] B. Sagredo, J. S. Lafaurie, and D. Sapone, (2018), arXiv:1808.05660.

[138] L. Kazantzidis, L. Perivolaropoulos, and F. Skara, Phys. Rev. D **99**, 063537 (2019), arXiv:1812.05356.

[139] F. Skara and L. Perivolaropoulos, (2019), arXiv:1911.10609.

[140] S. Basilakos, S. Nesseris, F. K. Anagnostopoulos, and E. N. Saridakis, JCAP **1808**, 008 (2018), arXiv:1803.09278.

[141] S. Basilakos and S. Nesseris, Phys. Rev. **D96**, 063517 (2017), arXiv:1705.08797.

[142] S. Basilakos and S. Nesseris, Phys. Rev. **D94**, 123525 (2016), arXiv:1610.00160.

[143] P. Zhang, M. Liguori, R. Bean, and S. Dodelson, Phys. Rev. Lett. **99**, 141302 (2007), arXiv:0704.1932.

[144] R. Reyes *et al.*, Nature **464**, 256 (2010), arXiv:1003.2185.

[145] A. M. Pinho, S. Casas, and L. Amendola, JCAP **1811**, 027 (2018), arXiv:1805.00027.

[146] M. C. Guzzetti, N. Bartolo, M. Liguori, and S. Matarrese, Riv. Nuovo Cim. **39**, 399 (2016), arXiv:1605.01615.

[147] R. Utiyama and B. S. DeWitt, Journal of Mathematical Physics **3**, 608 (1962).

[148] G. t Hooft and M. J. Veltman, Ann. Henri Poincaré **20**, 69 (1974).

[149] N. D. Birrell, N. D. Birrell, and P. Davies, *Quantum fields in curved space* (Cambridge university press, 1984).

[150] I. Buchbinder, S. Odintsov, and I. Shapiro, Riv. Nuovo Cim. 12N10 **1** (1989).

[151] G. Vilkovisky, Classical and Quantum Gravity **9**, 895 (1992).

[152] L. Kofman and A. A. Starobinsky, Sov. Astron. Lett. **11**, 271 (1985), [Pisma Astron. Zh.11,643(1985)].

[153] WMAP, G. Hinshaw *et al.*, Astrophys. J. Suppl. **208**, 19 (2013), arXiv:1212.5226.

[154] DES, T. M. C. Abbott *et al.*, Phys. Rev. **D98**, 043526 (2018), arXiv:1708.01530.

[155] J. Pérez-Romero and S. Nesseris, Physical Review D **97**, 023525 (2018).

[156] E. J. Copeland, Int. J. Mod. Phys. D **15**, 1753 (2006).

[157] S. Tsujikawa, Modified gravity models of dark energy, in *Lectures on Cosmology*, pp. 99–145, Springer, 2010.

[158] M. Kunz, S. Nesseris, and I. Sawicki, Physical Review D **94**, 023510 (2016).

[159] M. Kunz, S. Nesseris, and I. Sawicki, Physical Review D **92**, 063006 (2015).

[160] S. Nojiri and S. D. Odintsov, International Journal of Geometric Methods in Modern Physics **4**, 115 (2007).

[161] A. D. Dolgov and M. Kawasaki, Physics Letters B **573**, 1 (2003).

[162] S. Nojiri and S. D. Odintsov, Physical Review D **74**, 086005 (2006).

[163] E. J. Copeland, M. Sami, and S. Tsujikawa, International Journal of Modern Physics D **15**, 1753 (2006).

[164] T. E. Collett *et al.*, Science **360**, 1342 (2018), arXiv:1806.08300.

[165] LIGO Scientific and Virgo Collaborations, B. P. Abbott *et al.*, Phys. Rev. Lett. **116**, 221101 (2016).

[166] B. Ratra and P. J. E. Peebles, Phys. Rev. **D37**, 3406 (1988).

[167] C. Armendariz-Picon, V. F. Mukhanov, and P. J. Steinhardt, Phys. Rev. Lett. **85**, 4438 (2000), arXiv:astro-ph/0004134.

[168] S. Nesseris and A. Shafieloo, Mon. Not. Roy. Astron. Soc. **408**, 1879 (2010), arXiv:1004.0960.

[169] S. Nesseris and J. Garcia-Bellido, JCAP **1211**, 033 (2012), arXiv:1205.0364.

[170] Virgo, LIGO Scientific, B. P. Abbott *et al.*, Phys. Rev. Lett. **119**, 141101 (2017), arXiv:1709.09660.

[171] P. Creminelli and F. Vernizzi, Phys. Rev. Lett. **119**, 251302 (2017), arXiv:1710.05877.

[172] J. Sakstein and B. Jain, Phys. Rev. Lett. **119**, 251303 (2017), arXiv:1710.05893.

[173] J. M. Ezquiaga and M. Zumalacárregui, Phys. Rev. Lett. **119**, 251304 (2017), arXiv:1710.05901.

[174] T. Baker *et al.*, Phys. Rev. Lett. **119**, 251301 (2017), arXiv:1710.06394.

[175] L. Amendola, M. Kunz, I. D. Saltas, and I. Sawicki, Phys. Rev. Lett. **120**, 131101 (2018), arXiv:1711.04825.

[176] M. Crisostomi and K. Koyama, Phys. Rev. **D97**, 084004 (2018), arXiv:1712.06556.

[177] N. Frusciante, S. Peirone, S. Casas, and N. A. Lima, Phys. Rev. D **99**, 063538 (2019), arXiv:1810.10521.

[178] R. Kase and S. Tsujikawa, (2018), arXiv:1809.08735.

[179] R. McManus, L. Lombriser, and J. Penarrubia, JCAP **1611**, 006 (2016), arXiv:1606.03282.

[180] L. Lombriser and A. Taylor, JCAP **1603**, 031 (2016), arXiv:1509.08458.

[181] E. J. Copeland, M. Kopp, A. Padilla, P. M. Saffin, and C. Skordis, (2018), arXiv:1810.08239.

[182] G. W. Horndeski, Int. J. Theor. Phys. **10**, 363 (1974).

[183] S. Nadkarni-Ghosh and A. Refregier, Mon. Not. Roy. Astron. Soc. **471**, 2391 (2017), arXiv:1612.06697.

[184] N. Sugiyama, Progress of Theoretical Physics **81**, 1021 (1989).

[185] C.-P. Ma and E. Bertschinger, Astrophys. J. **455**, 7 (1995), arXiv:astro-ph/9506072.

[186] A. Lewis, A. Challinor, and A. Lasenby, Astrophys. J. **538**, 473 (2000), arXiv:astro-ph/9911177.

[187] J. Lesgourgues, (2011), arXiv:1104.2932.

[188] D. Alonso, E. Bellini, P. G. Ferreira, and M. Zumalacárregui, Phys. Rev. **D95**, 063502 (2017), arXiv:1610.09290.

[189] M. Kunz, Comptes Rendus Physique **13**, 539 (2012), arXiv:1204.5482.

[190] D. Huterer, Gen. Rel. Grav. **42**, 2177 (2010), arXiv:1001.1758.

[191] W. Cardona, R. Arjona, and S. Nesseris, (2019), arXiv:1907.10130.

[192] M. Kunz and D. Sapone, Phys. Rev. Lett. **98**, 121301 (2007), arXiv:astro-ph/0612452.

[193] L. Pogosian, A. Silvestri, K. Koyama, and G.-B. Zhao, Phys. Rev. **D81**, 104023 (2010), arXiv:1002.2382.

[194] S. Capozziello, S. Nojiri, and S. D. Odintsov, Phys. Lett. **B634**, 93 (2006), arXiv:hep-th/0512118.

[195] S. Capozziello, S. Nojiri, S. D. Odintsov, and A. Troisi, Phys. Lett. **B639**, 135 (2006), arXiv:astro-ph/0604431.

[196] S. Capozziello, C. A. Mantica, and L. G. Molinari, Int. J. Geom. Meth. Mod. Phys. **16**, 1950008 (2019), arXiv:1810.03204.

[197] T. P. Sotiriou and V. Faraoni, Rev. Mod. Phys. **82**, 451 (2010), arXiv:0805.1726.

[198] A. De Felice and S. Tsujikawa, Living Rev. Rel. **13**, 3 (2010), arXiv:1002.4928.

[199] S. Nojiri, S. D. Odintsov, and V. K. Oikonomou, Phys. Rept. **692**, 1 (2017), arXiv:1705.11098.

[200] S. Nojiri and S. D. Odintsov, Phys. Rept. **505**, 59 (2011), arXiv:1011.0544.

[201] T. Multamaki and I. Vilja, Phys. Rev. **D73**, 024018 (2006), arXiv:astro-ph/0506692.

[202] A. de la Cruz-Dombriz and A. Dobado, Phys. Rev. **D74**, 087501 (2006), arXiv:gr-qc/0607118.

[203] L. Pogosian and A. Silvestri, Phys. Rev. **D77**, 023503 (2008), arXiv:0709.0296, [Erratum: Phys. Rev.D81,049901(2010)].

[204] S. Nesseris, Phys. Rev. **D88**, 123003 (2013), arXiv:1309.1055.

[205] S. Tsujikawa, Phys. Rev. **D76**, 023514 (2007), arXiv:0705.1032.

[206] S. Nesseris and D. Sapone, Phys. Rev. **D92**, 023013 (2015), arXiv:1505.06601.

[207] C. A. Luna, S. Basilakos, and S. Nesseris, Phys. Rev. **D98**, 023516 (2018), arXiv:1805.02926.

[208] J. Perez-Romero and S. Nesseris, Phys. Rev. **D97**, 023525 (2018), arXiv:1710.05634.

[209] W. Hu and I. Sawicki, Phys. Rev. **D76**, 064004 (2007), arXiv:0705.1158.

[210] W. Hu and I. Sawicki, Phys. Rev. **D76**, 104043 (2007), arXiv:0708.1190.

[211] T. Koivisto and D. F. Mota, Phys. Lett. **B644**, 104 (2007), arXiv:astro-ph/0606078.

[212] T. Koivisto and D. F. Mota, Phys. Rev. **D75**, 023518 (2007), arXiv:hep-th/0609155.

[213] A. de la Cruz-Dombriz, A. Dobado, and A. L. Maroto, Phys. Rev. **D77**, 123515 (2008), arXiv:0802.2999.

[214] W. Hu and I. Sawicki, Phys. Rev. D **76**, 104043 (2007).

[215] A. A. Starobinsky, JETP Lett. **86**, 157 (2007), arXiv:0706.2041.

[216] R. Bean, D. Bernat, L. Pogosian, A. Silvestri, and M. Trodden, Phys. Rev. **D75**, 064020 (2007), arXiv:astro-ph/0611321.

[217] Y.-S. Song, L. Hollenstein, G. Caldera-Cabral, and K. Koyama, JCAP **1004**, 018 (2010), arXiv:1001.0969.

[218] R. Bean and M. Tangmatitham, Phys. Rev. **D81**, 083534 (2010), arXiv:1002.4197.

[219] R. Caldwell, A. Cooray, and A. Melchiorri, Phys. Rev. **D76**, 023507 (2007), arXiv:astro-ph/0703375.

[220] E. Bertschinger and P. Zukin, Phys. Rev. **D78**, 024015 (2008), arXiv:0801.2431.

[221] T. Baker, P. G. Ferreira, C. Skordis, and J. Zuntz, Phys. Rev. D **84**, 124018 (2011).

[222] A. Silvestri, L. Pogosian, and R. V. Buniy, Phys. Rev. **D87**, 104015 (2013), arXiv:1302.1193.

[223] T. Clifton and V. A. A. Sanghai, (2018), arXiv:1803.01157.

[224] M. Ishak, Living Rev. Rel. **22**, 1 (2019), arXiv:1806.10122.

[225] G.-B. Zhao, L. Pogosian, A. Silvestri, and J. Zylberberg, Phys. Rev. **D79**, 083513 (2009), arXiv:0809.3791.

[226] A. Hojjati, L. Pogosian, and G.-B. Zhao, JCAP **1108**, 005 (2011), arXiv:1106.4543.

[227] J.-h. He, Phys. Rev. **D86**, 103505 (2012), arXiv:1207.4898.

[228] L. Xu, (2015), arXiv:1506.03232.

[229] Planck, P. A. R. Ade *et al.*, Astron. Astrophys. **594**, A14 (2016), arXiv:1502.01590.

[230] J. Li and G.-B. Zhao, (2018), arXiv:1806.05022.

[231] R. A. Battye, B. Bolliet, and J. A. Pearson, Phys. Rev. **D93**, 044026 (2016), arXiv:1508.04569.

[232] D. Blas, J. Lesgourgues, and T. Tram, JCAP **1107**, 034 (2011), arXiv:1104.2933.

[233] R. A. Battye, B. Bolliet, and F. Pace, Phys. Rev. **D97**, 104070 (2018), arXiv:1712.05976.

[234] I. D. Saltas and M. Kunz, Phys. Rev. D **83**, 064042 (2011).

[235] W. Cardona, L. Hollenstein, and M. Kunz, JCAP **1407**, 032 (2014), arXiv:1402.5993.

[236] T. Koivisto and D. F. Mota, Phys. Rev. **D73**, 083502 (2006), arXiv:astro-ph/0512135.

[237] D. F. Mota, J. R. Kristiansen, T. Koivisto, and N. E. Groeneboom, Mon. Not. Roy. Astron. Soc. **382**, 793 (2007), arXiv:0708.0830.

[238] D. Sapone and E. Majerotto, Phys. Rev. D **85**, 123529 (2012).

[239] W. Hu, Astrophys. J. **506**, 485 (1998), arXiv:astro-ph/9801234.

[240] R. de Putter, D. Huterer, and E. V. Linder, Phys. Rev. **D81**, 103513 (2010), arXiv:1002.1311.

[241] R. C. Batista and V. Marra, JCAP **1711**, 048 (2017), arXiv:1709.03420.

[242] A. Lewis and S. Bridle, Phys. Rev. D **66**, 103511 (2002), arXiv:astro-ph/0205436.

[243] SDSS, M. Tegmark *et al.*, Phys. Rev. **D69**, 103501 (2004), arXiv:astro-ph/0310723.

[244] L. Amendola, M. Kunz, and D. Sapone, JCAP **04**, 013 (2008), arXiv:0704.2421.

[245] L. Amendola, I. Sawicki, M. Kunz, and I. D. Saltas, JCAP **1808**, 030 (2018), arXiv:1712.08623.

[246] E. V. Linder, JCAP **1803**, 005 (2018), arXiv:1801.01503.

[247] A. Peel, V. Pettorino, C. Giocoli, J.-L. Starck, and M. Baldi, (2018), arXiv:1805.05146.

[248] D. Sapone, E. Majerotto, M. Kunz, and B. Garilli, Phys. Rev. **D88**, 043503 (2013), arXiv:1305.1942.

[249] S. F. Daniel and E. V. Linder, Phys. Rev. **D82**, 103523 (2010), arXiv:1008.0397.

[250] Y.-S. Song *et al.*, Phys. Rev. **D84**, 083523 (2011), arXiv:1011.2106.

[251] L. Amendola, M. Kunz, M. Motta, I. D. Saltas, and I. Sawicki, Phys. Rev. D **87**, 023501 (2013).

[252] I. D. Saltas, I. Sawicki, L. Amendola, and M. Kunz, Phys. Rev. Lett. **113**, 191101 (2014), arXiv:1406.7139.

[253] L. Amendola, G. Ballesteros, and V. Pettorino, Phys. Rev. **D90**, 043009 (2014), arXiv:1405.7004.

[254] L. Amendola, S. Fogli, A. Guarnizo, M. Kunz, and A. Vollmer, Phys. Rev. **D89**, 063538 (2014), arXiv:1311.4765.

[255] M. Raveri, C. Baccigalupi, A. Silvestri, and S.-Y. Zhou, Phys. Rev. D **91**, 061501 (2015).

[256] C. Bonvin and P. Fleury, JCAP **1805**, 061 (2018), arXiv:1803.02771.

[257] S. Hagstotz, M. Costanzi, M. Baldi, and J. Weller, (2018), arXiv:1806.07400.

[258] C. M. S. Barbosa, H. Velten, J. C. Fabris, and R. O. Ramos, (2018), arXiv:1807.03357.

[259] E. V. Linder and D. Polarski, (2018), arXiv:1810.10547.

[260] A. Peel *et al.*, Phys. Rev. **D100**, 023508 (2019), arXiv:1810.11030.

[261] M. Zaldarriaga, D. N. Spergel, and U. Seljak, Astrophys. J. **488**, 1 (1997), arXiv:astro-ph/9702157.

[262] J. R. Bond, G. Efstathiou, and M. Tegmark, Mon. Not. Roy. Astron. Soc. **291**, L33 (1997), arXiv:astro-ph/9702100.

[263] E. V. Linder, Phys. Rev. Lett. **90**, 091301 (2003), arXiv:astro-ph/0208512.

[264] P. Marshall, N. Rajguru, and A. Slosar, Phys. Rev. **D73**, 067302 (2006), arXiv:astro-ph/0412535.

[265] R. Trotta, Contemp. Phys. **49**, 71 (2008), arXiv:0803.4089.

[266] E. Di Valentino, A. Melchiorri, Y. Fantaye, and A. Heavens, Phys. Rev. D **98**, 063508 (2018).

[267] Planck, P. A. R. Ade *et al.*, Astron. Astrophys. **594**, A13 (2016), arXiv:1502.01589.

[268] G.-B. Zhao *et al.*, Nat. Astron. **1**, 627 (2017), arXiv:1701.08165.

[269] W. L. Freedman, Nat. Astron. **1**, 0121 (2017), arXiv:1706.02739.

[270] J. Renk, M. Zumalacarregui, F. Montanari, and A. Barreira, JCAP **1710**, 020 (2017), arXiv:1707.02263.

[271] R. C. Nunes, JCAP **1805**, 052 (2018), arXiv:1802.02281.

[272] M.-X. Lin, M. Raveri, and W. Hu, (2018), arXiv:1810.02333.

[273] M. Benetti, S. Santos da Costa, S. Capozziello, J. S. Alcaniz, and M. De Laurentis, Int. J. Mod. Phys. **D27**, 1850084 (2018), arXiv:1803.00895.

[274] V. Poulin, K. K. Boddy, S. Bird, and M. Kamionkowski, Phys. Rev. D **97**, 123504 (2018).

[275] Z. Sakr, S. Ilic, and A. Blanchard, (2018), arXiv:1803.11170.

[276] L. Amendola and S. Tsujikawa, *Dark Energy* (Cambridge University Press, 2015).

[277] V. F. Mukhanov, H. A. Feldman, and R. H. Brandenberger, Phys. Rept. **215**, 203 (1992).

[278] D. Sapone and M. Kunz, Phys. Rev. **D80**, 083519 (2009), arXiv:0909.0007.

[279] R. M. Wald, Pr. 491p (1984).

[280] J. Santos, J. Alcaniz, N. Pires, and M. J. Reboucas, Physical Review D **75**, 083523 (2007).

[281] M. Visser and C. Barcelo, Energy conditions and their cosmological implications, in *Cosmo-99*, pp. 98–112, World Scientific, 2000.

[282] G. Cognola *et al.*, Phys. Rev. **D77**, 046009 (2008), arXiv:0712.4017.

[283] P. K. S. Dunsby, E. Elizalde, R. Goswami, S. Odintsov, and D. S. Gomez, Phys. Rev. **D82**, 023519 (2010), arXiv:1005.2205.

[284] S. Nojiri and S. D. Odintsov, Phys. Rev. **D74**, 086005 (2006), arXiv:hep-th/0608008.

[285] E. Elizalde, S. Nojiri, S. D. Odintsov, L. Sebastiani, and S. Zerbini, Phys. Rev. **D83**, 086006 (2011), arXiv:1012.2280.

[286] S. Basilakos, S. Nesseris, and L. Perivolaropoulos, Phys. Rev. **D87**, 123529 (2013), arXiv:1302.6051.

[287] M. Kunz, S. Nesseris, and I. Sawicki, Phys. Rev. **D94**, 023510 (2016), arXiv:1604.05701.

[288] Y. Wang and M. Dai, Phys. Rev. **D94**, 083521 (2016), arXiv:1509.02198.

[289] H. Akaike, IEEE transactions on automatic control **19**, 716 (1974).

[290] A. R. Liddle, Mon. Not. Roy. Astron. Soc. **377**, L74 (2007), arXiv:astro-ph/0701113.

[291] S. Nesseris and J. Garcia-Bellido, JCAP **1308**, 036 (2013), arXiv:1210.7652.

[292] S. Nesseris, C. Blake, T. Davis, and D. Parkinson, JCAP **1107**, 037 (2011), arXiv:1107.3659.

[293] R. Gannouji, L. Kazantzidis, L. Perivolaropoulos, and D. Polarski, (2018), arXiv:1809.07034.

[294] E. Bellini *et al.*, Phys. Rev. **D97**, 023520 (2018), arXiv:1709.09135.

[295] T. Baker, P. G. Ferreira, and C. Skordis, Phys. Rev. **D87**, 024015 (2013), arXiv:1209.2117.

[296] J. Noller and A. Nicola, (2018), arXiv:1811.03082.

[297] C. de Rham and S. Melville, Phys. Rev. Lett. **121**, 221101 (2018), arXiv:1806.09417.

[298] C. Deffayet, O. Pujolas, I. Sawicki, and A. Vikman, JCAP **1010**, 026 (2010), arXiv:1008.0048.

[299] M. Zumalacarregui, E. Bellini, I. Sawicki, J. Lesgourgues, and P. G. Ferreira, JCAP **1708**, 019 (2017), arXiv:1605.06102.

[300] D. W. Hogg *et al.*, Astrophys. J. **624**, 54 (2005), arXiv:astro-ph/0411197.

[301] Planck, P. A. R. Ade *et al.*, Astron. Astrophys. **594**, A16 (2016), arXiv:1506.07135.

[302] T. Kobayashi, M. Yamaguchi, and J. Yokoyama, Prog. Theor. Phys. **126**, 511 (2011), arXiv:1105.5723.

[303] T. Chiba, Phys. Lett. **B575**, 1 (2003), arXiv:astro-ph/0307338.

[304] C. Brans and R. H. Dicke, Phys. Rev. **124**, 925 (1961), [,142(1961)].

[305] I. Quiros, (2019), arXiv:1901.08690.

[306] Q. Fang, S. Chen, and J. Jing, (2018), arXiv:1811.07479.

[307] M. Kopp, C. Skordis, D. B. Thomas, and S. Ilić, Phys. Rev. Lett. **120**, 221102 (2018).

[308] R. Kimura and K. Yamamoto, JCAP **1104**, 025 (2011), arXiv:1011.2006.

[309] A. De Felice, T. Kobayashi, and S. Tsujikawa, Phys. Lett. **B706**, 123 (2011), arXiv:1108.4242.

[310] J. Matsumoto, (2018), arXiv:1806.10454.

[311] R. J. Scherrer, Phys. Rev. Lett. **93**, 011301 (2004), arXiv:astro-ph/0402316.

[312] R. de Putter and E. V. Linder, Astropart. Phys. **28**, 263 (2007), arXiv:0705.0400.

[313] O. Pujolas, I. Sawicki, and A. Vikman, JHEP **11**, 156 (2011), arXiv:1103.5360.

[314] J. M. Ezquiaga and M. Zumalacarregui, Front. Astron. Space Sci. **5**, 44 (2018), arXiv:1807.09241.

[315] Y.-S. Song, W. Hu, and I. Sawicki, Phys. Rev. **D75**, 044004 (2007), arXiv:astro-ph/0610532.

[316] S. Dodelson, *Modern Cosmology* (Academic Press, Amsterdam, 2003).

[317] Z. Zhai and Y. Wang, (2018), arXiv:1811.07425.

[318] L. Perenon, J. Bel, R. Maartens, and A. de la Cruz-Dombriz, (2019), arXiv:1901.11063.

[319] J. Noller and A. Nicola, (2018), arXiv:1811.12928.

[320] A. Spurio Mancini *et al.*, (2019), arXiv:1901.03686.

[321] W. Cardona, R. Arjona, A. Estrada, and S. Nesseris, (2020), arXiv:2012.05282.

[322] LIGO Scientific, Virgo, Fermi-GBM, INTEGRAL, B. P. Abbott *et al.*, Astrophys. J. Lett. **848**, L13 (2017), arXiv:1710.05834.

[323] A. Zucca, L. Pogosian, A. Silvestri, and G.-B. Zhao, JCAP **05**, 001 (2019), arXiv:1901.05956.

[324] R. Arjona and S. Nesseris, (2020), arXiv:2001.11420.

[325] F. Pace *et al.*, (2020), arXiv:2011.05713.

[326] BOSS, S. Alam *et al.*, Mon. Not. Roy. Astron. Soc. **470**, 2617 (2017), arXiv:1607.03155.

[327] R. Arjona, J. García-Bellido, and S. Nesseris, (2020), arXiv:2006.01762.

[328] H. Motohashi, A. A. Starobinsky, and J. Yokoyama, Prog. Theor. Phys. **124**, 541 (2010), arXiv:1005.1171.

[329] H. Motohashi, A. A. Starobinsky, and J. Yokoyama, Phys. Rev. Lett. **110**, 121302 (2013), arXiv:1203.6828.

[330] A. S. Chudaykin, D. S. Gorbunov, A. A. Starobinsky, and R. A. Burenin, JCAP **05**, 004 (2015), arXiv:1412.5239.

[331] Planck, P. A. R. Ade *et al.*, Astron. Astrophys. **571**, A16 (2014), arXiv:1303.5076.

[332] S. Sharma, Annual Review of Astronomy and Astrophysics **55**, 213 (2017), arXiv:1706.01629.

[333] B. Audren, J. Lesgourgues, K. Benabed, and S. Prunet, JCAP **1302**, 001 (2013), arXiv:1210.7183.

[334] T. Brinckmann and J. Lesgourgues, (2018), arXiv:1804.07261.

[335] H. Desmond and P. G. Ferreira, Phys. Rev. D **102**, 104060 (2020), arXiv:2009.08743.

[336] J. Garcia-Bellido, J. Phys. Conf. Ser. **840**, 012032 (2017), arXiv:1702.08275.

[337] Y. Tada and S. Yokoyama, Phys. Rev. **D91**, 123534 (2015), arXiv:1502.01124.

[338] L.-M. Wang and P. J. Steinhardt, Astrophys. J. **508**, 483 (1998), arXiv:astro-ph/9804015.

[339] F. O. Franco, C. Bonvin, and C. Clarkson, (2019), arXiv:1906.02217.

[340] Planck, Y. Akrami *et al.*, (2018), arXiv:1807.06205.

[341] S. Hannestad, Phys. Rev. D **71**, 103519 (2005), arXiv:astro-ph/0504017.

[342] W. Zimdahl, H. Borges, S. Carneiro, J. Fabris, and W. Hipolito-Ricaldi, JCAP **04**, 028 (2011), arXiv:1009.0672.

[343] H. Velten and R. Fazolo, Phys. Rev. D **96**, 083502 (2017), arXiv:1707.03224.

[344] W. Zimdahl, J. Fabris, H. Velten, and R. Herrera, (2019), arXiv:1911.12084.

[345] A. E. Romano and S. A. Vallejo Pena, Phys. Lett. B **784**, 367 (2018), arXiv:1806.01941.

[346] M. A. J. Rodrguez, A. E. Romano, and S. A. Vallejo-Pena, (2020), arXiv:2006.03395.

[347] A. J. Christopherson and K. A. Malik, Phys. Lett. B **675**, 159 (2009), arXiv:0809.3518.

[348] G. Ballesteros and J. Lesgourgues, JCAP **10**, 014 (2010), arXiv:1004.5509.

[349] S. Tsujikawa, Lect. Notes Phys. **800**, 99 (2010), arXiv:1101.0191.

[350] S. Nesseris, Phys. Rev. D **79**, 044015 (2009), arXiv:0811.4292.

[351] S. Nesseris and A. Mazumdar, Phys. Rev. D **79**, 104006 (2009), arXiv:0902.1185.

[352] A. Bueno Belloso, J. Garcia-Bellido, and D. Sapone, JCAP **10**, 010 (2011), arXiv:1105.4825.

[353] G. Jelic-Cizmek, F. Lepori, C. Bonvin, and R. Durrer, (2020), arXiv:2004.12981.

[354] B. Bose, K. Koyama, W. A. Hellwing, G.-B. Zhao, and H. A. Winther, Phys. Rev. D **96**, 023519 (2017), arXiv:1702.02348.

[355] M. Kunz, S. Nesseris, and I. Sawicki, Phys. Rev. D **92**, 063006 (2015), arXiv:1507.01486.

[356] I. A. Brown, A. J. Christopherson, and K. A. Malik, Mon. Not. Roy. Astron. Soc. **423**, 1411 (2012), arXiv:1108.0639.

[357] S. Zaroubi, M. Viel, A. Nusser, M. Haehnelt, and T.-S. Kim, Mon. Not. Roy. Astron. Soc. **369**, 734 (2006), arXiv:astro-ph/0509563.

[358] R. Takahashi, M. Sato, T. Nishimichi, A. Taruya, and M. Oguri, Astrophys. J. **761**, 152 (2012), arXiv:1208.2701.

[359] M. Viel, K. Markovic, M. Baldi, and J. Weller, Mon. Not. Roy. Astron. Soc. **421**, 50 (2012), arXiv:1107.4094.

[360] R. Arjona, W. Cardona, and S. Nesseris, JCAP **10**, 060 (2019), arXiv:1906.03160.

[361] G. Bertone and D. Hooper, Rev. Mod. Phys. **90**, 045002 (2018).

[362] DES, T. M. C. Abbott *et al.*, Phys. Rev. Lett. **122**, 171301 (2019), arXiv:1811.02375.

[363] M. Maltoni, T. Schwetz, M. A. Tortola, and J. W. F. Valle, New J. Phys. **6**, 122 (2004), arXiv:hep-ph/0405172.

[364] G. L. Fogli, E. Lisi, A. Marrone, and A. Palazzo, Prog. Part. Nucl. Phys. **57**, 742 (2006), arXiv:hep-ph/0506083.

[365] I. Esteban, M. C. Gonzalez-Garcia, A. Hernandez-Cabezudo, M. Maltoni, and T. Schwetz, JHEP **01**, 106 (2019), arXiv:1811.05487.

[366] P. F. de Salas, D. V. Forero, C. A. Ternes, M. Tortola, and J. W. F. Valle, Phys. Lett. **B782**, 633 (2018), arXiv:1708.01186.

[367] F. Capozzi, E. Lisi, A. Marrone, and A. Palazzo, Prog. Part. Nucl. Phys. **102**, 48 (2018), arXiv:1804.09678.

[368] J. Lesgourgues and S. Pastor, Phys. Rept. **429**, 307 (2006), arXiv:astro-ph/0603494.

[369] J. Lesgourgues and S. Pastor, New J. Phys. **16**, 065002 (2014), arXiv:1404.1740.

[370] M. Lattanzi and M. Gerbino, Front.in Phys. **5**, 70 (2018), arXiv:1712.07109.

[371] K. N. Abazajian and M. Kaplinghat, Ann. Rev. Nucl. Part. Sci. **66**, 401 (2016).

[372] S. Mishra-Sharma, D. Alonso, and J. Dunkley, Phys. Rev. D **97**, 123544 (2018).

[373] W. Hu, D. J. Eisenstein, and M. Tegmark, Phys. Rev. Lett. **80**, 5255 (1998).

[374] D. J. Eisenstein, W. Hu, and M. Tegmark, Astrophys. J. **518**, 2 (1999), arXiv:astro-ph/9807130.

[375] J. Lesgourgues, S. Pastor, and L. Perotto, Phys. Rev. D **70**, 045016 (2004).

[376] D. Blas, J. Lesgourgues, and T. Tram, Journal of Cosmology and Astro-Particle Physics **2011**, 034 (2011), arXiv:1104.2933.

[377] J. Lesgourgues and T. Tram, Journal of Cosmology and Astro-Particle Physics **2011**, 032 (2011), arXiv:1104.2935.

[378] G. Mangano, G. Miele, S. Pastor, O. Pisanti, and S. Sarikas, Phys. Lett. **B708**, 1 (2012), arXiv:1110.4335.

[379] E. Castorina *et al.*, Phys. Rev. **D86**, 023517 (2012), arXiv:1204.2510.

[380] Y. Y. Y. Wong, Phys. Rev. D **66**, 025015 (2002).

[381] A. D. Dolgov *et al.*, Nucl. Phys. **B632**, 363 (2002), arXiv:hep-ph/0201287.

[382] K. N. Abazajian, J. F. Beacom, and N. F. Bell, Phys. Rev. **D66**, 013008 (2002), arXiv:astro-ph/0203442.

[383] P. D. Serpico and G. G. Raffelt, Phys. Rev. **D71**, 127301 (2005), arXiv:astro-ph/0506162.

[384] V. Barger, J. P. Kneller, P. Langacker, D. Marfatia, and G. Steigman, Phys. Lett. **B569**, 123 (2003), arXiv:hep-ph/0306061.

[385] A. Cuoco *et al.*, Int. J. Mod. Phys. **A19**, 4431 (2004), arXiv:astro-ph/0307213.

[386] T. Padmanabhan, *Theoretical Astrophysics: Volume 3, Galaxies and Cosmology* (Cambridge University Press, 2002).

[387] I. S. Gradshteyn and I. M. Ryzhik, *Table of integrals, series, and products*, Seventh ed. (Elsevier/Academic Press, Amsterdam, 2007), Translated from the Russian, Translation edited and with a preface by Alan Jeffrey and Daniel Zwillinger.

[388] M. Abramowitz and I. Stegun, *Handbook of Mathematical Functions with Formulas, Graphs, and Mathematical Tables* (Dover Publications, New York, 1972).

[389] J. Lesgourgues, G. Mangano, G. Miele, and S. Pastor, *Neutrino Cosmology* (Cambridge University Press, 2013).

[390] J. Lesgourgues and S. Pastor, Adv. High Energy Phys. **2012**, 608515 (2012), arXiv:1212.6154.

[391] V. Moll, *Special Integrals of Gradshteyn and Ryzhik: the Proofs-Volume II* (Chapman and Hall/CRC, 2015).

[392] T. Bringmann and S. Hofmann, Journal of Cosmology and Astroparticle Physics **2007**, 016 (2007).

[393] A. Sarkar, S. Das, and S. K. Sethi, Journal of Cosmology and Astroparticle Physics **2015**, 004 (2015).

[394] LSST Science, LSST Project, P. A. Abell *et al.*, (2009), arXiv:0912.0201.

[395] SDSS, M. R. Blanton *et al.*, Astron. J. **154**, 28 (2017), arXiv:1703.00052.

[396] J-PAS, N. Benitez *et al.*, (2014), arXiv:1403.5237.

[397] DESI, A. Aghamousa *et al.*, (2016), arXiv:1611.00036.

[398] C. L. Carilli and S. Rawlings, New Astron. Rev. **48**, 979 (2004), arXiv:astro-ph/0409274.

[399] C. M. Trott and J. C. Pober, (2019), arXiv:1909.12491.

[400] R. Bellman and K. M. R. Collection, *Adaptive Control Processes: A Guided Tour*Princeton Legacy Library (Princeton University Press, 1961).

[401] M. Ntampaka *et al.*, (2019), arXiv:1902.10159.

[402] E. A. Huerta *et al.*, Nature Rev. Phys. **1**, 600 (2019), arXiv:1911.11779.

[403] R. Arjona, (2020), arXiv:2002.12700.

[404] D. Benisty, (2020), arXiv:2005.03751.

[405] L. Amendola *et al.*, Living Rev. Rel. **21**, 2 (2018), arXiv:1606.00180.

[406] C. Wetterich, Nucl. Phys. **B302**, 668 (1988), arXiv:1711.03844.

[407] R. R. Caldwell, R. Dave, and P. J. Steinhardt, Phys. Rev. Lett. **80**, 1582 (1998), arXiv:astro-ph/9708069.

[408] C. Armendariz-Picon, V. F. Mukhanov, and P. J. Steinhardt, Phys. Rev. **D63**, 103510 (2001), arXiv:astro-ph/0006373.

[409] J.-P. Uzan, Phys. Rev. **D59**, 123510 (1999), arXiv:gr-qc/9903004.

[410] F. Perrotta, C. Baccigalupi, and S. Matarrese, Phys. Rev. **D61**, 023507 (1999), arXiv:astro-ph/9906066.

[411] A. Riazuelo and J.-P. Uzan, Phys. Rev. **D66**, 023525 (2002), arXiv:astro-ph/0107386.

[412] T. Dent, S. Stern, and C. Wetterich, JCAP **0901**, 038 (2009), arXiv:0809.4628.

[413] A. A. Starobinsky, Phys. Lett. **91B**, 99 (1980), [,771(1980)].

[414] M. C. Bento, O. Bertolami, and A. A. Sen, Phys. Rev. **D66**, 043507 (2002), arXiv:gr-qc/0202064.

[415] C. Deffayet, G. R. Dvali, and G. Gabadadze, Phys. Rev. **D65**, 044023 (2002), arXiv:astro-ph/0105068.

[416] S. Nojiri and S. D. Odintsov, eConf **C0602061**, 06 (2006), arXiv:hep-th/0601213, [Int. J. Geom. Meth. Mod. Phys.4,115(2007)].

[417] S. Nesseris and J. Garcia-Bellido, Phys. Rev. **D88**, 063521 (2013), arXiv:1306.4885.

[418] P. Mehta and D. J. Schwab, arXiv preprint arXiv:1410.3831 (2014).

[419] R. Arjona and S. Nesseris, (2019), arXiv:1910.01529.

[420] S. Nesseris, D. Sapone, and J. Garcia-Bellido, Phys. Rev. **D91**, 023004 (2015), arXiv:1410.0338.

[421] D. Sapone, E. Majerotto, and S. Nesseris, Phys. Rev. **D90**, 023012 (2014), arXiv:1402.2236.

[422] V. Rajpaul, Genetic algorithms in astronomy and astrophysics, in *Proceedings, 56th Annuall Conference of the South African Institute of Physics (SAIP 2011): Gauteng, South Africa, July 12-15, 2011*, pp. 519–524, 2012, arXiv:1202.1643.

[423] A. Montiel, R. Lazkoz, I. Sendra, C. Escamilla-Rivera, and V. Salzano, Phys. Rev. **D89**, 043007 (2014), arXiv:1401.4188.

[424] S. Yahya, M. Seikel, C. Clarkson, R. Maartens, and M. Smith, Phys. Rev. **D89**, 023503 (2014), arXiv:1308.4099.

[425] V. Marra and D. Sapone, Phys. Rev. D **97**, 083510 (2018), arXiv:1712.09676.

[426] V. Sahni, A. Shafieloo, and A. A. Starobinsky, Phys. Rev. D **78**, 103502 (2008), arXiv:0807.3548.

[427] C. Zunckel and C. Clarkson, Phys. Rev. Lett. **101**, 181301 (2008), arXiv:0807.4304.

[428] R. von Marttens, V. Marra, L. Casarini, J. E. Gonzalez, and J. Alcaniz, Phys. Rev. **D99**, 043521 (2019), arXiv:1812.02333.

[429] S. Nesseris and D. Sapone, Int. J. Mod. Phys. **D24**, 1550045 (2015), arXiv:1409.3697.

[430] R.-G. Cai, Z.-K. Guo, and T. Yang, Phys. Rev. **D93**, 043517 (2016), arXiv:1509.06283.

[431] D. Benisty and D. Staicova, Astron. Astrophys. **647**, A38 (2021), arXiv:2009.10701.

[432] Y.-L. Li, S.-Y. Li, T.-J. Zhang, and T.-P. Li, Astrophys. J. Lett. **789**, L15 (2014), arXiv:1404.0773.

[433] R. Arjona and S. Nesseris, Phys. Rev. D **103**, 103539 (2021), arXiv:2103.06789.

[434] M. Ho *et al.*, (2019), arXiv:1902.05950.

[435] J. Caldeira *et al.*, (2018), arXiv:1810.01483.

[436] S. He *et al.*, Proc. Nat. Acad. Sci. **116**, 13825 (2019), arXiv:1811.06533.

[437] S. Ravanbakhsh, F. Lanusse, R. Mandelbaum, J. Schneider, and B. Poczos, (2016), arXiv:1609.05796.

[438] C. Escamilla-Rivera, M. A. C. Quintero, and S. Capozziello, (2019), arXiv:1910.02788.

[439] ANTARES, G. Narayan *et al.*, Astrophys. J. Suppl. **236**, 9 (2018), arXiv:1801.07323.

[440] F. Lanusse *et al.*, Mon. Not. Roy. Astron. Soc. **473**, 3895 (2018), arXiv:1703.02642.

[441] N. Aggarwal *et al.*, (2020), arXiv:2011.12414.

[442] M. Hannam, Gen. Rel. Grav. **46**, 1767 (2014), arXiv:1312.3641.

[443] B. Sathyaprakash and S. Dhurandhar, Phys. Rev. D **44**, 3819 (1991).

[444] S. Klimenko *et al.*, Phys. Rev. D **93**, 042004 (2016), arXiv:1511.05999.

[445] B. Allen and J. D. Romano, Phys. Rev. D **59**, 102001 (1999), arXiv:gr-qc/9710117.

[446] D. George and E. Huerta, Phys. Lett. B **778**, 64 (2018), arXiv:1711.03121.

[447] H. Gabbard, M. Williams, F. Hayes, and C. Messenger, Phys. Rev. Lett. **120**, 141103 (2018), arXiv:1712.06041.

[448] E. Cuoco *et al.*, (2020), arXiv:2005.03745.

[449] D. George and E. Huerta, Phys. Rev. D **97**, 044039 (2018), arXiv:1701.00008.

[450] M. Zevin *et al.*, Class. Quant. Grav. **34**, 064003 (2017), arXiv:1611.04596.

[451] M. Coughlin *et al.*, Class. Quant. Grav. **34**, 044004 (2017), arXiv:1611.09812.

[452] P. Graff, F. Feroz, M. P. Hobson, and A. Lasenby, Mon. Not. Roy. Astron. Soc. **421**, 169 (2012), arXiv:1110.2997.

[453] A. J. Chua and M. Vallisneri, Phys. Rev. Lett. **124**, 041102 (2020), arXiv:1909.05966.

[454] H. Gabbard, C. Messenger, I. S. Heng, F. Tonolini, and R. Murray-Smith, (2019), arXiv:1909.06296.

[455] A. L. Miller *et al.*, Phys. Rev. D **100**, 062005 (2019), arXiv:1909.02262.

[456] C. Dreissigacker, R. Sharma, C. Messenger, R. Zhao, and R. Prix, Phys. Rev. D **100**, 044009 (2019), arXiv:1904.13291.

[457] LIGO Scientific, Virgo, R. Abbott *et al.*, (2020), arXiv:2010.14550.

[458] Y.-C. Lin and J.-H. P. Wu, (2020), arXiv:2007.04176.

[459] E. Huerta *et al.*, (2020), arXiv:2012.08545.

[460] M. W. Coughlin, Nature Astron. **4**, 550 (2020).

[461] G. Allen *et al.*, arXiv preprint arXiv:1902.00522 (2019).

[462] R. J. Foley *et al.*, (2019), arXiv:1903.04553.

[463] M. Lightman *et al.*, J. Phys. Conf. Ser. **32**, 58 (2006).

[464] C. Bogdanos and S. Nesseris, JCAP **0905**, 006 (2009), arXiv:0903.2805.

[465] SDSS, M. Betoule *et al.*, Astron. Astrophys. **568**, A22 (2014), arXiv:1401.4064.

[466] R. Mohayaee, M. Rameez, and S. Sarkar, (2020), arXiv:2003.10420.

[467] A. Shafieloo, A. G. Kim, and E. V. Linder, Phys. Rev. **D85**, 123530 (2012), arXiv:1204.2272.

[468] V. C. Busti, C. Clarkson, and M. Seikel, IAU Symp. **10**, 25 (2014), arXiv:1407.5227.

[469] C. A. P. Bengaly, C. Clarkson, and R. Maartens, (2019), arXiv:1908.04619.

[470] EUCLID, M. Martinelli *et al.*, (2020), arXiv:2007.16153.

[471] N. B. Hogg, M. Martinelli, and S. Nesseris, (2020), arXiv:2007.14335.

[472] S.-M. Udrescu and M. Tegmark, (2019), arXiv:1905.11481.

[473] Y. Setyawati, M. Pürrer, and F. Ohme, Class. Quant. Grav. **37**, 075012 (2020), arXiv:1909.10986.

[474] H. Vaddireddy, A. Rasheed, A. E. Staples, and O. San, arXiv preprint arXiv:1911.05254 (2019).

[475] K. Liao, A. Shafieloo, R. E. Keeley, and E. V. Linder, Astrophys. J. Lett. **886**, L23 (2019), arXiv:1908.04967.

[476] E. Belgacem, S. Foffa, M. Maggiore, and T. Yang, Phys. Rev. D **101**, 063505 (2020), arXiv:1911.11497.

[477] Y. Li, Y. Hao, W. Cheng, and R. Rainer, (2019), arXiv:1904.05683.

[478] M. Bernardini, L. Mayer, D. Reed, and R. Feldmann, (2019), arXiv:1912.04299.

[479] A. Gómez-Valent and L. Amendola, H_0 from cosmic chronometers and Type Ia supernovae, with Gaussian processes and the weighted polynomial regression method, in *15th Marcel Grossmann Meeting on Recent Developments in Theoretical and Experimental General Relativity, Astrophysics, and Relativistic Field Theories*, 2019, arXiv:1905.04052.

[480] R. Hogan, M. Fairbairn, and N. Seeburn, Mon. Not. Roy. Astron. Soc. **449**, 2040 (2015), arXiv:1412.5997.

[481] X.-L. Luo, J. Feng, and H.-H. Zhang, (2019), arXiv:1907.01090.

[482] G. De Geyter, M. Baes, J. Fritz, and P. Camps, Astron. Astrophys. **550**, A74 (2013), arXiv:1212.0538.

[483] J. De La Calleja and O. Fuentes, Monthly Notices of the Royal Astronomical Society **349**, 87 (2004), https://onlinelibrary.wiley.com/doi/pdf/10.1111/j.1365-2966.2004.07442.x.

[484] Y. Akrami, P. Scott, J. Edsjo, J. Conrad, and L. Bergstrom, JHEP **04**, 057 (2010), arXiv:0910.3950.

[485] B. C. Allanach, D. Grellscheid, and F. Quevedo, JHEP **07**, 069 (2004), arXiv:hep-ph/0406277.

[486] D. G. Ireland, S. Janssen, and J. Ryckebusch, Nucl. Phys. **A740**, 147 (2004), arXiv:nucl-th/0312103.

[487] S.-H. Chen, editor, *Genetic Algorithms and Genetic Programming in Computational Finance* (Springer, 2002).

[488] P. Kroha and M. Friedrich, Comparison of genetic algorithms for trading strategies, in *SOFSEM 2014: Theory and Practice of Computer Science*, edited by V. Geffert, B. Preneel, B. Rovan, J. Štuller, and A. M. Tjoa, pp. 383–394, Cham, 2014, Springer International Publishing.

[489] H. J. Dikhil, M. Shkoukani, and S. S. Owais, International Journal of Advanced Research in Artificial Intelligence **5** (2016).

[490] C. Bogdanos and S. Nesseris, AIP Conf. Proc. **1241**, 200 (2010).

[491] S. Nesseris, J. Phys. Conf. Ser. **283**, 012025 (2011), arXiv:1011.1859.

[492] E. Lusso *et al.*, Astron. Astrophys. **628**, L4 (2019), arXiv:1907.07692.

[493] S. Capozziello and O. Luongo, Cosmographic transition redshift in $f(R)$ gravity, in *International Conference on Quantum Field Theory and Gravity (QFTG 2014) Tomsk, Russia, July 28-August 3, 2014*, 2014, arXiv:1411.2350.

[494] O. Farooq, F. R. Madiyar, S. Crandall, and B. Ratra, Astrophys. J. **835**, 26 (2017), arXiv:1607.03537.

[495] N. Rani, D. Jain, S. Mahajan, A. Mukherjee, and N. Pires, JCAP **1512**, 045 (2015), arXiv:1503.08543.

[496] J. F. Jesus, R. F. L. Holanda, and S. H. Pereira, JCAP **1805**, 073 (2018), arXiv:1712.01075.

[497] J. F. Jesus, R. Valentim, A. A. Escobal, and S. H. Pereira, (2019), arXiv:1909.00090.

[498] J. T. Nielsen, A. Guffanti, and S. Sarkar, Sci. Rep. **6**, 35596 (2016), arXiv:1506.01354.

[499] J. Colin, R. Mohayaee, M. Rameez, and S. Sarkar, Astron. Astrophys. **631**, L13 (2019), arXiv:1808.04597.

[500] D. Rubin and B. Hayden, Astrophys. J. **833**, L30 (2016), arXiv:1610.08972.

[501] V. C. Busti and C. Clarkson, JCAP **1605**, 008 (2016), arXiv:1505.01821.

[502] S. Weinberg, *Cosmology* (Oxford university press, 2008).

[503] A. Moradinezhad Dizgah and R. Durrer, JCAP **1609**, 035 (2016), arXiv:1604.08914.

[504] B. Ghosh and R. Durrer, JCAP **1906**, 010 (2019), arXiv:1812.09546.

[505] J. Garcia-Bellido, Cosmology and astrophysics, in *2004 European School of High-Energy Physics, Sant Feliu de Guixols, Spain, 30 May - 12 June 2004*, pp. 267–342, 2005, arXiv:astro-ph/0502139.

[506] E. Hubble, Proc. Nat. Acad. Sci. **15**, 168 (1929).

[507] G. Gamow, Phys. Rev. **70**, 572 (1946).

[508] A. A. Penzias and R. W. Wilson, Astrophys. J. **142**, 419 (1965).

[509] M. H. Abitbol, J. C. Hill, and J. Chluba, (2019), arXiv:1910.09881.

[510] J. Chluba, Mon. Not. Roy. Astron. Soc. **443**, 1881 (2014), arXiv:1405.1277.

[511] J. A. S. Lima, A. I. Silva, and S. M. Viegas, Mon. Not. Roy. Astron. Soc. **312**, 747 (2000).

[512] J. Jaeckel and A. Ringwald, Ann. Rev. Nucl. Part. Sci. **60**, 405 (2010), arXiv:1002.0329.

[513] T. Damour and A. M. Polyakov, Nucl. Phys. **B423**, 532 (1994), arXiv:hep-th/9401069.

[514] I. De Martino, C. J. A. P. Martins, H. Ebeling, and D. Kocevski, Universe **2**, 34 (2016), arXiv:1612.06739.

[515] B. D. Sherwin *et al.*, Phys. Rev. Lett. **107**, 021302 (2011), arXiv:1105.0419.

[516] R. F. L. Holanda, S. H. Pereira, and D. Jain, Phys. Rev. **D97**, 023538 (2018), arXiv:1801.04344.

[517] L. Zhou, X. Fu, Z. Peng, and J. Chen, Phys. Rev. **D100**, 123539 (2019), arXiv:1912.02327.

[518] R. F. L. Holanda, S. H. Pereira, and S. Santos da Costa, Phys. Rev. **D95**, 084006 (2017), arXiv:1612.09365.

[519] J. Lima, A. Silva, and S. Viegas, Monthly Notices of the Royal Astronomical Society **312**, 747 (2000).

[520] J. Lima, A. Germano, and L. Abramo, Physical Review D **53**, 4287 (1996).

[521] E. Menegoni, S. Galli, J. G. Bartlett, C. Martins, and A. Melchiorri, Phys. Rev. D **80**, 087302 (2009), arXiv:0909.3584.

[522] J.-P. Uzan, Living Rev. Rel. **14**, 2 (2011), arXiv:1009.5514.

[523] P. Jetzer and C. Tortora, Phys. Rev. **D84**, 043517 (2011), arXiv:1107.4610.

[524] S. Muller *et al.*, Astron. Astrophys. **551**, A109 (2013), arXiv:1212.5456.

[525] G. F. Ellis, General Relativity and Gravitation **39**, 1047 (2007).

[526] B. A. Bassett and M. Kunz, Phys. Rev. **D69**, 101305 (2004), arXiv:astro-ph/0312443.

[527] S. Rasanen, J. Valiviita, and V. Kosonen, JCAP **1604**, 050 (2016), arXiv:1512.05346.

[528] R. Lazkoz, S. Nesseris, and L. Perivolaropoulos, JCAP **0807**, 012 (2008), arXiv:0712.1232.

[529] G. F. R. Ellis, R. Poltis, J.-P. Uzan, and A. Weltman, Phys. Rev. **D87**, 103530 (2013), arXiv:1301.1312.

[530] C. Ma and P.-S. Corasaniti, Astrophys. J. **861**, 124 (2018), arXiv:1604.04631.

[531] V. F. Cardone, S. Spiro, I. Hook, and R. Scaramella, Physical Review D **85**, 123510 (2012).

[532] S. Khedekar and S. Chakraborti, Phys. Rev. Lett. **106**, 221301 (2011), arXiv:1105.1138.

[533] R. F. L. Holanda and V. C. Busti, Phys. Rev. **D89**, 103517 (2014), arXiv:1402.2161.

[534] X. Zheng *et al.*, (2020), arXiv:2002.09909.

[535] A. Rana, D. Jain, S. Mahajan, and A. Mukherjee, JCAP **1607**, 026 (2016), arXiv:1511.09223.

[536] S. More, J. Bovy, and D. W. Hogg, The Astrophysical Journal **696**, 1727 (2009).

[537] A. Avgoustidis, L. Verde, and R. Jimenez, Journal of Cosmology and Astroparticle Physics **2009**, 012 (2009).

[538] R. Nair, S. Jhingan, and D. Jain, Journal of Cosmology and Astroparticle Physics **2012**, 028 (2012).

[539] S. J. Landau, Variation of fundamental constants and white dwarfs, in *IAU Symposium 357: White Dwarfs as probes of fundamental physics and tracers of planetary, stellar & galactic evolution Hilo, Big Island, Hawaii, United States, October 21-25, 2019*, 2020, arXiv:2002.00095.

[540] M. T. Clara and C. J. A. P. Martins, Astron. Astrophys. **633**, L11 (2020), arXiv:2001.01787.

[541] I. de Martino, C. J. A. P. Martins, H. Ebeling, and D. Kocevski, Phys. Rev. **D94**, 083008 (2016), arXiv:1605.03053.

[542] A. Hees, O. Minazzoli, and J. Larena, Phys. Rev. D **90**, 124064 (2014), arXiv:1406.6187.

[543] L. Colacco, R. Holanda, and R. Silva, (2020), arXiv:2004.08484.

[544] L. Lopez-Honorez, O. Mena, S. Palomares-Ruiz, P. Villanueva-Domingo, and S. J. Witte, (2020), arXiv:2004.00013.

[545] M. R. Wilczynska *et al.*, (2020), arXiv:2003.07627.

[546] H. B. Sandvik, J. D. Barrow, and J. Magueijo, Phys. Rev. Lett. **88**, 031302 (2002), arXiv:astro-ph/0107512.

[547] A. Avgoustidis, C. Martins, A. Monteiro, P. Vielzeuf, and G. Luzzi, JCAP **06**, 062 (2014), arXiv:1305.7031.

[548] W. H. Press, S. A. Teukolsky, W. T. Vetterling, and B. P. Flannery, *Numerical recipes 3rd edition: The art of scientific computing* (Cambridge university press, 2007).

[549] R. Arjona, H.-N. Lin, S. Nesseris, and L. Tang, Phys. Rev. D **103**, 103513 (2021), arXiv:2011.02718.

[550] LIGO Scientific, Virgo, B. Abbott *et al.*, Astrophys. J. Lett. **882**, L24 (2019), arXiv:1811.12940.

[551] LIGO Scientific, Virgo, B. Abbott *et al.*, Phys. Rev. Lett. **123**, 011102 (2019), arXiv:1811.00364.

[552] LIGO Scientific, Virgo, B. Abbott *et al.*, Phys. Rev. D **100**, 104036 (2019), arXiv:1903.04467.

[553] LIGO Scientific, Virgo, 1M2H, Dark Energy Camera GW-E, DES, DLT40, Las Cumbres Observatory, VINROUGE, MASTER, B. Abbott *et al.*, Nature **551**, 85 (2017), arXiv:1710.05835.

[554] e. a. Abbott, BP, The Astrophysical Journal Letters **848**, L13 (2017).

[555] L. Lombriser and N. A. Lima, Phys. Lett. B **765**, 382 (2017), arXiv:1602.07670.

[556] M. Maggiore *et al.*, JCAP **03**, 050 (2020), arXiv:1912.02622.

[557] LISA, P. Amaro-Seoane *et al.*, (2017), arXiv:1702.00786.

[558] G. Cusin, R. Durrer, and I. Dvorkin, (2019), arXiv:1912.11916.

[559] J. M. Ezquiaga, D. E. Holz, W. Hu, M. Lagos, and R. M. Wald, (2020), arXiv:2008.12814.

[560] M. Oguri, Mon. Not. Roy. Astron. Soc. **480**, 3842 (2018), arXiv:1807.02584.

[561] X.-L. Fan, K. Liao, M. Biesiada, A. Piórkowska-Kurpas, and Z.-H. Zhu, Physical Review Letters **118**, 091102 (2017).

[562] K. Liao, X.-L. Fan, X. Ding, M. Biesiada, and Z.-H. Zhu, Nature Communications **8**, 1 (2017).

[563] J. M. Ezquiaga and M. Zumalacárregui, (2020), arXiv:2009.12187.

[564] H. Ohanian, Int. J. Theor. Phys. **9**, 425 (1974).

[565] K. S. Thorne, (1997), arXiv:gr-qc/9704042.

[566] R. Takahashi and T. Nakamura, Astrophys. J. **595**, 1039 (2003), arXiv:astro-ph/0305055.

[567] Y. Wang, A. Stebbins, and E. L. Turner, Phys. Rev. Lett. **77**, 2875 (1996), arXiv:astro-ph/9605140.

[568] K. K. Ng, K. W. Wong, T. Broadhurst, and T. G. Li, Phys. Rev. D **97**, 023012 (2018), arXiv:1703.06319.

[569] O. Hannuksela *et al.*, Astrophys. J. Lett. **874**, L2 (2019), arXiv:1901.02674.

[570] M. Biesiada, X. Ding, A. Piorkowska, and Z.-H. Zhu, JCAP **10**, 080 (2014), arXiv:1409.8360.

[571] M. Sereno *et al.*, Phys. Rev. Lett. **105**, 251101 (2010), arXiv:1011.5238.

[572] S.-S. Li, S. Mao, Y. Zhao, and Y. Lu, Mon. Not. Roy. Astron. Soc. **476**, 2220 (2018), arXiv:1802.05089.

[573] S. Jung and C. S. Shin, Phys. Rev. Lett. **122**, 041103 (2019), arXiv:1712.01396.

[574] K.-H. Lai *et al.*, Phys. Rev. D **98**, 083005 (2018), arXiv:1801.07840.

[575] L. Dai, S.-S. Li, B. Zackay, S. Mao, and Y. Lu, Phys. Rev. D **98**, 104029 (2018), arXiv:1810.00003.

[576] M. Sereno, P. Jetzer, A. Sesana, and M. Volonteri, Mon. Not. Roy. Astron. Soc. **415**, 2773 (2011), arXiv:1104.1977.

[577] S. Mukherjee, B. D. Wandelt, and J. Silk, Phys. Rev. D **101**, 103509 (2020), arXiv:1908.08950.

[578] S. Mukherjee, B. D. Wandelt, and J. Silk, Mon. Not. Roy. Astron. Soc. **494**, 1956 (2020), arXiv:1908.08951.

[579] S. Mukherjee, T. Broadhurst, J. M. Diego, J. Silk, and G. F. Smoot, (2020), arXiv:2006.03064.

[580] I. Etherington, General Relativity and Gravitation **39**, 1055 (2007).

[581] P. S. Corasaniti, Mon. Not. Roy. Astron. Soc. **372**, 191 (2006), arXiv:astro-ph/0603833.

[582] P. Tiwari, Phys. Rev. D **95**, 023005 (2017), arXiv:1610.06583.

[583] K. Liao *et al.*, Astrophys. J. **822**, 74 (2016), arXiv:1511.01318.

[584] X. Li and H. N. Lin, Mon. Not. Roy. Astron. Soc. **474**, 313 (2018), arXiv:1710.11361.

[585] H.-N. Lin, M.-H. Li, and X. Li, Mon. Not. Roy. Astron. Soc. **480**, 3117 (2018), arXiv:1808.01784.

[586] R. Holanda, V. Busti, and J. Alcaniz, JCAP **02**, 054 (2016), arXiv:1512.02486.

[587] R. Holanda, V. Busti, F. Lima, and J. Alcaniz, JCAP **09**, 039 (2017), arXiv:1611.09426.

[588] F. Renzi, N. B. Hogg, M. Martinelli, and S. Nesseris, (2020), arXiv:2010.04155.

[589] H.-N. Lin and X. Li, Chin. Phys. C **44**, 075101 (2020), arXiv:1911.00263.

[590] H.-N. Lin, X. Li, and L. Tang, Chinese Physics C **45**, 015109 (2021).

[591] S. Mollerach and E. Roulet, (2002).

[592] A. S. Bolton *et al.*, Astrophys. J. **682**, 964 (2008), arXiv:0805.1931.

[593] T. E. Collett, Astrophys. J. **811**, 20 (2015), arXiv:1507.02657.

[594] S. H. Suyu *et al.*, Mon. Not. Roy. Astron. Soc. **468**, 2590 (2017), arXiv:1607.00017.

[595] A. Aghamousa and A. Shafieloo, Astrophys. J. **834**, 31 (2017), arXiv:1603.06331.

[596] H.-W. Rix and S. D. M. White, MNRAS **254**, 389 (1992).

[597] S. Cao *et al.*, Sci. Rep. **9**, 11608 (2019), arXiv:1910.10365.

[598] W. Zhao, C. Van Den Broeck, D. Baskaran, and T. G. F. Li, Phys. Rev. D **83**, 023005 (2011).

[599] B. Sathyaprakash and B. Schutz, Living Rev. Rel. **12**, 2 (2009), arXiv:0903.0338.

[600] T. G. F. Li, (2015).

[601] C. K. Mishra, K. G. Arun, B. R. Iyer, and B. S. Sathyaprakash, Phys. Rev. D **82**, 064010 (2010).

[602] Y. Wang, A. Stebbins, and E. L. Turner, Phys. Rev. Lett. **77**, 2875 (1996).

[603] H.-Y. Chen, M. Fishbach, and D. E. Holz, Nature **562**, 545 (2018), arXiv:1712.06531.

[604] C. E. Rasmussen and C. K. I. Williams, *Gaussian Processes for Machine Learning* (MIT Press, 2006).

[605] T. Holsclaw *et al.*, Physical Review D **82**, 103502 (2010), arXiv:1009.5443.

[606] T. Holsclaw *et al.*, Physical Review Letters **105**, 241302 (2010), arXiv:1011.3079.

[607] T. Holsclaw *et al.*, Physical Review Letters **84**, 083501 (2011), arXiv:1104.2041.

[608] M. Seikel, C. Clarkson, and M. Smith, Journal of Cosmology and Astroparticle Physics **6**, 036 (2012), arXiv:1204.2832.

[609] M.-J. Zhang and H. Li, European Physical Journal C **78**, 460 (2018), arXiv:1806.02981.

[610] M. Martinelli, N. B. Hogg, S. Peirone, M. Bruni, and D. Wands, Monthly Notices of the Royal Astronomical Society **488**, 3423 (2019), arXiv:1902.10694.

[611] F. Gerardi, M. Martinelli, and A. Silvestri, JCAP **1907**, 042 (2019), arXiv:1902.09423.

[612] N. B. Hogg, M. Bruni, R. Crittenden, M. Martinelli, and S. Peirone, Phys. Dark Univ. **29**, 100583 (2020), arXiv:2002.10449.

[613] M. Seikel and C. Clarkson, (2013), arXiv:1311.6678.

[614] S. Ambikasaran, D. Foreman-Mackey, L. Greengard, D. W. Hogg, and M. O'Neil, IEEE Transactions on Pattern Analysis and Machine Intelligence **38**, 252 (2016), arXiv:1403.6015.

[615] R. Arjona and S. Nesseris, (2020), arXiv:2012.12202.

[616] S. Tsujikawa, Class. Quant. Grav. **30**, 214003 (2013), arXiv:1304.1961.

[617] N. Birrell and P. Davies, *Quantum Fields in Curved Space*Cambridge Monographs on Mathematical Physics (Cambridge Univ. Press, Cambridge, UK, 1984).

[618] H. Ooguri and C. Vafa, Nucl. Phys. B **766**, 21 (2007), arXiv:hep-th/0605264.

[619] G. Obied, H. Ooguri, L. Spodyneiko, and C. Vafa, (2018), arXiv:1806.08362.

[620] P. Agrawal, G. Obied, P. J. Steinhardt, and C. Vafa, Phys. Lett. B **784**, 271 (2018), arXiv:1806.09718.

[621] E. Elizalde and M. Khurshudyan, Phys. Rev. D **99**, 103533 (2019), arXiv:1811.03861.

[622] T. Yang, Phys. Rev. D **102**, 083511 (2020), arXiv:2006.14511.

[623] E. O. Colgáin and H. Yavartanoo, Phys. Lett. B **797**, 134907 (2019), arXiv:1905.02555.

[624] A. Banerjee *et al.*, (2020), arXiv:2006.00244.

[625] Y. Akrami, R. Kallosh, A. Linde, and V. Vardanyan, Fortsch. Phys. **67**, 1800075 (2019), arXiv:1808.09440.

[626] M. Raveri, W. Hu, and S. Sethi, Phys. Rev. D **99**, 083518 (2019), arXiv:1812.10448.

[627] S. K. Garg and C. Krishnan, JHEP **11**, 075 (2019), arXiv:1807.05193.

[628] Y. Akrami, M. Sasaki, A. R. Solomon, and V. Vardanyan, (2020), arXiv:2008.13660.

[629] L. Heisenberg, M. Bartelmann, R. Brandenberger, and A. Refregier, Phys. Rev. D **98**, 123502 (2018), arXiv:1808.02877.

[630] M. Moresco and F. Marulli, Mon. Not. Roy. Astron. Soc. **471**, L82 (2017), arXiv:1705.07903.

[631] E. V. Linder, Astropart. Phys. **86**, 41 (2017), arXiv:1610.05321.

[632] J. Matsumoto, T. Okumura, and M. Sasaki, JCAP **07**, 059 (2020), arXiv:2005.09227.

[633] V. Sahni and A. Starobinsky, Int. J. Mod. Phys. D **15**, 2105 (2006), arXiv:astro-ph/0610026.

[634] R. J. Scherrer, Phys. Rev. D **92**, 043001 (2015), arXiv:1505.05781.

[635] M. Visser, Gen. Rel. Grav. **37**, 1541 (2005), arXiv:gr-qc/0411131.

[636] S. Capozziello, V. Cardone, and V. Salzano, Phys. Rev. D **78**, 063504 (2008), arXiv:0802.1583.

[637] S. Capozziello, R. D'Agostino, and O. Luongo, Int. J. Mod. Phys. D **28**, 1930016 (2019), arXiv:1904.01427.

[638] A. Aviles, C. Gruber, O. Luongo, and H. Quevedo, Phys. Rev. D **86**, 123516 (2012), arXiv:1204.2007.

[639] C. Cattoen and M. Visser, (2007), arXiv:gr-qc/0703122.

[640] R. Lazkoz, J. Alcaniz, C. Escamilla-Rivera, V. Salzano, and I. Sendra, JCAP **12**, 005 (2013), arXiv:1311.6817.

[641] A. C. Guimaraes and J. A. S. Lima, Class. Quant. Grav. **28**, 125026 (2011), arXiv:1005.2986.

[642] S. Nesseris and L. Perivolaropoulos, Phys. Rev. D **73**, 103511 (2006), arXiv:astro-ph/0602053.

[643] T. Tröster *et al.*, (2020), arXiv:2010.16416.

[644] DES, J. Muir *et al.*, (2020), arXiv:2010.05924.

[645] S. Weinberg, Rev. Mod. Phys. **61**, 1 (1989), [,569(1988)].

[646] M. Cicoli, F. G. Pedro, and G. Tasinato, JCAP **07**, 044 (2012), arXiv:1203.6655.

[647] J. M. Virey, D. Talon-Esmieu, A. Ealet, P. Taxil, and A. Tilquin, JCAP **12**, 008 (2008), arXiv:0802.4407.

[648] C. Clarkson, B. Bassett, and T. H.-C. Lu, Phys. Rev. Lett. **101**, 011301 (2008), arXiv:0712.3457.

[649] A. Shafieloo and C. Clarkson, Phys. Rev. D **81**, 083537 (2010), arXiv:0911.4858.

[650] E. Mortsell and J. Jonsson, (2011), arXiv:1102.4485.

[651] S. Räsänen, K. Bolejko, and A. Finoguenov, Phys. Rev. Lett. **115**, 101301 (2015), arXiv:1412.4976.

[652] B. L'Huillier and A. Shafieloo, JCAP **01**, 015 (2017), arXiv:1606.06832.

[653] M. Denissenya, E. V. Linder, and A. Shafieloo, JCAP **03**, 041 (2018), arXiv:1802.04816.

[654] C.-G. Park and B. Ratra, Astrophys. J. **882**, 158 (2019), arXiv:1801.00213.

[655] S. Cao, J. Ryan, and B. Ratra, (2021), arXiv:2101.08817.

[656] N. Khadka and B. Ratra, (2020), arXiv:2012.09291.

[657] A. H. Guth, D. I. Kaiser, and Y. Nomura, Phys. Lett. B **733**, 112 (2014), arXiv:1312.7619.

[658] E. Di Dio *et al.*, JCAP **06**, 013 (2016), arXiv:1603.09073.

[659] M. Vardanyan, R. Trotta, and J. Silk, Mon. Not. Roy. Astron. Soc. **397**, 431 (2009), arXiv:0901.3354.

[660] G. Bertone and D. Hooper, Rev. Mod. Phys. **90**, 045002 (2018), arXiv:1605.04909.

[661] S. M. Carroll, Living Rev. Rel. **4**, 1 (2001), arXiv:astro-ph/0004075.

[662] E. Di Valentino *et al.*, (2020), arXiv:2008.11283.

[663] M. Seikel, S. Yahya, R. Maartens, and C. Clarkson, Phys. Rev. D **86**, 083001 (2012), arXiv:1205.3431.

[664] R. Maartens, Phil. Trans. Roy. Soc. Lond. A **369**, 5115 (2011), arXiv:1104.1300.

[665] E. Sanchez, D. Alonso, F. Sanchez, J. Garcia-Bellido, and I. Sevilla, Mon. Not. Roy. Astron. Soc. **434**, 2008 (2013), arXiv:1210.6446.

[666] R. Arjona and S. Nesseris, (2021), arXiv:2105.09049.

[667] K. Tomita, Mon. Not. Roy. Astron. Soc. **326**, 287 (2001), arXiv:astro-ph/0011484.

[668] R. K. Barrett and C. A. Clarkson, Class. Quant. Grav. **17**, 5047 (2000), arXiv:astro-ph/9911235.

[669] M.-N. Celerier, Astron. Astrophys. **353**, 63 (2000), arXiv:astro-ph/9907206.

[670] T. Buchert, Gen. Rel. Grav. **32**, 105 (2000), arXiv:gr-qc/9906015.

[671] D. L. Wiltshire, Phys. Rev. Lett. **99**, 251101 (2007), arXiv:0709.0732.

[672] T. Clifton, P. G. Ferreira, and K. Land, Phys. Rev. Lett. **101**, 131302 (2008), arXiv:0807.1443.

[673] H. L. Bester, J. Larena, and N. T. Bishop, "" (2017), arXiv:1705.00994.

[674] J.-P. Uzan, C. Clarkson, and G. F. R. Ellis, Phys. Rev. Lett. **100**, 191303 (2008), arXiv:0801.0068.

[675] K. Bolejko and J. S. B. Wyithe, JCAP **02**, 020 (2009), arXiv:0807.2891.

[676] K. Tomita and K. T. Inoue, Phys. Rev. D **79**, 103505 (2009), arXiv:0903.1541.

[677] S. February, C. Clarkson, and R. Maartens, JCAP **03**, 023 (2013), arXiv:1206.1602.

[678] Z.-S. Zhang, T.-J. Zhang, H. Wang, and C. Ma, Phys. Rev. D **91**, 063506 (2015), arXiv:1210.1775.

[679] W. A. Hellwing, A. Nusser, M. Feix, and M. Bilicki, Mon. Not. Roy. Astron. Soc. **467**, 2787 (2017), arXiv:1609.07120.

[680] S. Alexander, L. Jenks, P. Jirousek, J. Magueijo, and T. Zlosnik, Physical Review D **102**, 044039 (2020).

[681] R. R. Caldwell and A. Stebbins, Phys. Rev. Lett. **100**, 191302 (2008), arXiv:0711.3459.

[682] F. S. Labini and Y. V. Baryshev, JCAP **06**, 021 (2010), arXiv:1006.0801.

[683] P. Zhang and A. Stebbins, Phys. Rev. Lett. **107**, 041301 (2011), arXiv:1009.3967.

[684] C.-M. Yoo, T. Kai, K.-i. Nakao, and M. Sasaki, Testing the Copernican Principle with the kSZ Effect, in *19th Workshop on General Relativity and Gravitation in Japan*, 2009.

[685] W. Valkenburg, V. Marra, and C. Clarkson, Mon. Not. Roy. Astron. Soc. **438**, L6 (2014), arXiv:1209.4078.

[686] H. Bondi, Mon. Not. Roy. Astron. Soc. **107**, 410 (1947).

[687] J. Garcia-Bellido and T. Haugboelle, JCAP **04**, 003 (2008), arXiv:0802.1523.

[688] J. Garcia-Bellido and T. Haugboelle, JCAP **09**, 016 (2008), arXiv:0807.1326.

[689] J. P. Zibin and A. Moss, Class. Quant. Grav. **28**, 164005 (2011), arXiv:1105.0909.

[690] J. P. Zibin, Phys. Rev. D **84**, 123508 (2011), arXiv:1108.3068.

[691] A. G. Lemaître, General Relativity and Gravitation **29**, 641 (1997).

[692] R. C. Tolman, Proc. Nat. Acad. Sci. **20**, 169 (1934).

[693] DESI, M. Vargas-Magaña, D. D. Brooks, M. M. Levi, and G. G. Tarle, Unraveling the Universe with DESI, in *53rd Rencontres de Moriond on Cosmology*, 2018, arXiv:1901.01581.

[694] A. Aizpuru, R. Arjona, and S. Nesseris, (2021), arXiv:2106.00428.

[695] A. de Mattia *et al.*, Mon. Not. Roy. Astron. Soc. **501**, 5616 (2021), arXiv:2007.09008.

[696] W. J. Percival *et al.*, Mon. Not. Roy. Astron. Soc. **381**, 1053 (2007), arXiv:0705.3323.

[697] A. Cuceu, J. Farr, P. Lemos, and A. Font-Ribera, JCAP **10**, 044 (2019), arXiv:1906.11628.

[698] S. Seager, D. D. Sasselov, and D. Scott, Astrophys. J. Lett. **523**, L1 (1999), arXiv:astro-ph/9909275.

[699] J. Chluba and R. M. Thomas, Mon. Not. Roy. Astron. Soc. **412**, 748 (2011), arXiv:1010.3631.

[700] N. Lee and Y. Ali-Haïmoud, Phys. Rev. D **102**, 083517 (2020), arXiv:2007.14114.

[701] Y. Ali-Haimoud and C. M. Hirata, Phys. Rev. D **83**, 043513 (2011), arXiv:1011.3758.

[702] WMAP, E. Komatsu *et al.*, Astrophys. J. Suppl. **192**, 18 (2011), arXiv:1001.4538.

[703] K. Bamba, S. Capozziello, S. Nojiri, and S. D. Odintsov, Astrophys. Space Sci. **342**, 155 (2012), arXiv:1205.3421.

[704] K. Thepsuriya and A. Lewis, JCAP **01**, 034 (2015), arXiv:1409.5066.

[705] E. Aubourg *et al.*, Phys. Rev. D **92**, 123516 (2015), arXiv:1411.1074.

[706] Z. Hou, R. Keisler, L. Knox, M. Millea, and C. Reichardt, Phys. Rev. D **87**, 083008 (2013), arXiv:1104.2333.

[707] S. Bilenky, Nucl. Phys. B **908**, 2 (2016), arXiv:1602.00170.

[708] T. R. Taylor and G. Veneziano, Phys. Lett. B **213**, 450 (1988).

[709] J. A. Casas, J. Garcia-Bellido, and M. Quiros, Nucl. Phys. B **361**, 713 (1991).

[710] J. A. Casas, J. Garcia-Bellido, and M. Quiros, Class. Quant. Grav. **9**, 1371 (1992), arXiv:hep-ph/9204213.

[711] L. Hart and J. Chluba, Mon. Not. Roy. Astron. Soc. **493**, 3255 (2020), arXiv:1912.03986.

[712] M. Martinelli *et al.*, "" (2021), arXiv:2105.09746.

[713] J. A. Rubino-Martin, J. Chluba, W. A. Fendt, and B. D. Wandelt, Mon. Not. Roy. Astron. Soc. **403**, 439 (2010), arXiv:0910.4383.

[714] Planck, P. A. R. Ade *et al.*, Astron. Astrophys. **580**, A22 (2015), arXiv:1406.7482.

[715] W. Hu and N. Sugiyama, Astrophys. J. **471**, 542 (1996), arXiv:astro-ph/9510117.

[716] R. Courant and D. Hilbert, Inc., New York , 106 (1953).

[717] E. Macaulay, I. K. Wehus, and H. K. Eriksen, Phys. Rev. Lett. **111**, 161301 (2013), arXiv:1303.6583.